

---

**HIGH ENERGY RESEARCH AND APPLICATIONS (HERA)**

**PULSED POWER AND PULSED POWER SYSTEMS R&D FOR  
MAGNETIZED TARGET FUSION USING FIELD REVERSED  
CONFIGURATIONS (MTF-FRC)**

**Wayne Sommars, et al.**

**Science Applications International Corporation  
2109 Air Park Road SE  
Albuquerque, NM 87106**

**Final Report**

Approved for public release; distribution is unlimited.



**AIR FORCE RESEARCH LABORATORY  
Directed Energy Directorate  
3550 Aberdeen Ave SE  
AIR FORCE MATERIEL COMMAND  
KIRTLAND AIR FORCE BASE, NM 87117-5776**

---

## NOTICE AND SIGNATURE PAGE

Using Government drawings, specifications, or other data included in this document for any purpose other than Government procurement does not in any way obligate the U.S. Government. The fact that the Government formulated or supplied the drawings, specifications, or other data does not license the holder or any other person or corporation; or convey any rights or permission to manufacture, use, or sell any patented invention that may relate to them.

This report was cleared for public release by the Air Force Research Laboratory [insert TD site] Public Affairs Office and is available to the general public, including foreign nationals. Copies may be obtained from the Defense Technical Information Center (DTIC) (<http://www.dtic.mil>).

AFRL-RD-PS-TR-2013-0020 HAS BEEN REVIEWED AND IS APPROVED  
FOR PUBLICATION IN ACCORDANCE WITH ASSIGNED  
DISTRIBUTION STATEMENT.

//Signed//  
JAMES DEGNAN, DR-IV  
Project Officer

//Signed//  
STEPHEN T. MARTINICK, DR-IV  
Chief, High Power Electromagnetics Division

This report is published in the interest of scientific and technical information exchange, and its publication does not constitute the Government's approval or disapproval of its ideas or findings.

REPORT DOCUMENTATION PAGE			Form Approved OMB No. 0704-0188	
Public reporting burden for this collection of information is estimated to average 1 hour per response, including the time for reviewing instructions, searching existing data sources, gathering and maintaining the data needed, and completing and reviewing this collection of information. Send comments regarding this burden estimate or any other aspect of this collection of information, including suggestions for reducing this burden to Department of Defense, Washington Headquarters Services, Directorate for Information Operations and Reports (0704-0188), 1215 Jefferson Davis Highway, Suite 1204, Arlington, VA 22202-4302. Respondents should be aware that notwithstanding any other provision of law, no person shall be subject to any penalty for failing to comply with a collection of information if it does not display a currently valid OMB control number. <b>PLEASE DO NOT RETURN YOUR FORM TO THE ABOVE ADDRESS.</b>				
1. REPORT DATE (DD-MM-YYYY) 12 Mar 2013		2. REPORT TYPE Final Report		3. Feb COVERED (From - To) 11 Aug 2011-12 Mar 2013
4. TITLE AND SUBTITLE  High Energy Research and Applications (HERA) Pulsed Power and Pulsed Power Systems R&D for Magnetized Target Fusion Using Field Reversed Configurations (MTF-FRC)			5a. CONTRACT NUMBER FA9451-08-D-0170/ 0002	
			5b. GRANT NUMBER	
			5c. PROGRAM ELEMENT NUMBER 69120H	
			5d. PROJECT NUMBER	
6. AUTHOR(S) Gerald F Kiuttu, Sean Coffey, Frank Camacho, Al Lerma, Mark Kostora, Wayne Sommars			5e. TASK NUMBER D01U	
			5f. WORK UNIT NUMBER PPM00001079	
			8. PERFORMING ORGANIZATION REPORT NUMBER	
7. PERFORMING ORGANIZATION NAME(S) AND ADDRESS(ES) AND ADDRESS(ES) Science Applications International Corporation 2109 Air Park Road SE Albuquerque, NM 87106			10. SPONSOR/MONITOR'S ACRONYM(S) AFRL/RDHP	
9. SPONSORING / MONITORING AGENCY NAME(S) AND ADDRESS(ES) Air Force Research Laboratory 3550 Aberdeen Ave SE Kirtland AFB, NM 87117-5776			11. SPONSOR/MONITOR'S REPORT NUMBER(S) AFRL-RD-PS-TR-2013-0020	
12. DISTRIBUTION / AVAILABILITY STATEMENT Approved for public release; distribution is unlimited.				
13. SUPPLEMENTARY NOTES Public Affairs Release #377ABW-2013-0731				
14. ABSTRACT We described efforts to advance the state of the art for Magnetized Target Fusion (MTF) using Field Reversed Configuration (FRC) plasmas. The work is primarily experimental. We document production, translation, and trapping of FRCs in a coaxial system, and initial efforts to drive cylindrical aluminum liners with the Shiva Star fast capacitor bank to compress magnetic flux and magnetized plasma. We describe the pulsed power systems used to create and manipulate the plasma and the diagnostics employed to determine magnetic field and plasma characteristics. We also describe modifications to the plasma system for puffed gas injection, radio frequency (RF) systems for pre-preionization of the gas, and use of biased rings to attempt to control the rotation and subsequent instability of the plasma				
15. SUBJECT TERMS Magnetized Target Fusion (MTF), Field Reversed Configurations (FRC),				
16. SECURITY CLASSIFICATION OF:			17. LIMITATION OF ABSTRACT	18. NUMBER OF PAGES
a. REPORT Unclassified	b. ABSTRACT Unclassified	c. THIS PAGE Unclassified	SAR	368
			19a. NAME OF RESPONSIBLE PERSON James Degnan	
			19b. TELEPHONE NUMBER (include area code)	

Standard Form 298 (Rev. 8-98)  
Prescribed by ANSI Std. Z39.18

**This page intentionally left blank.**



# TABLE OF CONTENTS

<b>1.0</b>	<b>SUMMARY.....</b>	<b>1</b>
<b>2.0</b>	<b>INTRODUCTION.....</b>	<b>4</b>
2.1	BACKGROUND .....	4
2.1.1	<i>Laboratory Nuclear Fusion Approaches.....</i>	<i>4</i>
2.1.2	<i>Field Reversed Configuration Plasmas.....</i>	<i>7</i>
2.1.3	<i>Technical Challenges .....</i>	<i>8</i>
2.1.4	<i>Report Organization.....</i>	<i>9</i>
<b>3.0</b>	<b>METHODS, ASSUMPTIONS, AND PROCEDURES.....</b>	<b>10</b>
3.1	SHIVA STAR COMPRESSION TESTS.....	10
3.1.1	<i>Initial Hardware Preparation .....</i>	<i>11</i>
3.1.2	<i>Vacuum Magnetic Field Compression .....</i>	<i>34</i>
3.1.3	<i>Plasma Compression.....</i>	<i>108</i>
3.2	PLASMA SYSTEM DEVELOPMENT .....	205
3.2.1	<i>Diagnostic Development .....</i>	<i>206</i>
3.2.2	<i>Gas Puff System.....</i>	<i>243</i>
3.2.3	<i>Preionization and Pre-Preionization .....</i>	<i>261</i>
3.2.4	<i>Bias Ring System.....</i>	<i>314</i>
<b>4.0</b>	<b>RESULTS AND DISCUSSION.....</b>	<b>325</b>
4.1	SHIVA STAR COMPRESSION TESTS .....	325
4.1.1	<i>FRCHX-2.....</i>	<i>325</i>
4.1.2	<i>FRCHX-3.....</i>	<i>327</i>
4.2	PLASMA SYSTEM DEVELOPMENT .....	329
<b>5.0</b>	<b>CONCLUSIONS.....</b>	<b>340</b>
<b>6.0</b>	<b>RECOMMENDATIONS .....</b>	<b>342</b>
<b>7.0</b>	<b>REFERENCES .....</b>	<b>344</b>
<b>8.0</b>	<b>ABBREVIATIONS .....</b>	<b>346</b>

# LIST OF FIGURES

FIGURE 1. CUTAWAY OF FRCHX CONFIGURATION .....	1
FIGURE 2. VARIOUS CAPACITOR BANKS AND COILS FOR FRCHX .....	3
FIGURE 3. FRC FORMATION PROCESS.....	7
FIGURE 4. SHIVA BANK PORTION OF EXPERIMENT HIGH BAY .....	11
FIGURE 5. FLOOR, SIDES, AND CEILING OF THE B-ARM TUNNEL LINED WITH SHEETS OF INSULATING MATERIAL .....	12
FIGURE 6. PNEUMATIC LIFTERS (AEROGo “AERO-PLANKS”).....	13
FIGURE 7. PROCESS OF MOVING THE MAIN BANK.....	14
FIGURE 8. PI BANK MOVED BEHIND MAIN BANK UNDER B-ARM.....	15
FIGURE 9. CROSS-SECTION DIAGRAMS OF INITIAL (A) AND FINAL (B) CONICAL THETA COILS .....	16
FIGURE 10. 2.66° CONICAL THETA COIL (A) PARTIALLY ASSEMBLED; (B) AFTER ASSEMBLY WAS COMPLETE .....	18
FIGURE 11. ARRANGEMENT OF THE VARIOUS FIELD COILS AROUND THE QUARTZ TUBE AND LINER FOR FRCHX .....	19
FIGURE 12. FIRST GUIDE AND MIRROR COIL ASSEMBLY, WHILE CHARACTERIZATION MEASUREMENTS WERE BEING PERFORMED .....	20
FIGURE 13. (A) INDUCTANCE; (B) RESISTANCE FOR FIRST GUIDE AND MIRROR COIL SET .....	21
FIGURE 14. (A) MOVING GUIDE AND MIRROR COIL ASSEMBLY TO THE VACUUM AND FIELD COIL STAND; (B) ASSEMBLY IN PLACE ABOVE THETA COIL.....	22
FIGURE 15. CROSS-SECTION OF TRANSLATION AND LINER AND CAPTURE REGIONS OF VACUUM AND FIELD COIL STAND .....	23
FIGURE 16. (A) FLUX-CONSERVING TUBE BEING LOWERED INTO PLACE; (B) TUBE IN PLACE ON VACUUM AND FIELD COIL STAND .....	24
FIGURE 17. (A) VACUUM AND FIELD COIL STAND AFTER CABLES FOR ALL BANKS WERE CONNECTED; (B) SUPPORTS FOR BIAS AND GUIDE/MIRROR BANK CABLES ATTACHED TO B-ARM CATWALK .....	25
FIGURE 18. TRIGGER AND CHARGING CABLES ON NEW CABLE TRAY .....	26
FIGURE 19. PI 40168 TRIGGER AMPLIFIER IN HOFFMAN ENCLOSURE.....	27
FIGURE 20. (A) GAS LINES RUN TO INSERTED TEST POSITION; (B) FITTINGS FOR SHUTOFF VALVES .....	28
FIGURE 21. DRY NITROGEN AND DEUTERIUM BOTTLES MOVED UNDER C-ARM NEXT TO SF6 BOTTLE .....	29
FIGURE 22. QUICK-CONNECT FITTINGS.....	30
FIGURE 23. (A) FORMATION, TRANSLATION, AND CAPTURE TEST SETUP; (B) FIELD-COMPRESSION TEST SETUP.....	32
FIGURE 24. FIELD-MAPPING PROBE ASSEMBLY CONFIGURED FOR MAKING MEASUREMENTS IN FORMATION, TRANSLATION, AND CAPTURE TEST SETUP.....	33
FIGURE 25. FIELD MAP FOR THE PRESENT FRC FORMATION, TRANSLATION, CAPTURE TEST SETUP USING LARGE-AREA B-DOT PROBE DATA.....	33
FIGURE 26. CROSS-SECTION DIAGRAM OF LINER ASSEMBLY.....	36
FIGURE 27. CENTERING RING, ACRYLIC.....	37

FIGURE 28. UPPER CLAMP DETAIL .....	38
FIGURE 29. LOWER CLAMP AND DIAGNOSTIC SPOOL .....	38
FIGURE 30. CLOSE-UP OF DIAGNOSTIC SPOOL, MOCK BELLOWS, AND THEIR VACUUM SEALS .....	39
FIGURE 31. 3D VIEW OF DIAGNOSTIC SPOOL.....	39
FIGURE 32. GUIDE AND MIRROR COIL ASSEMBLY ON SUPPORT TABLE, SHORTLY BEFORE FIELD-COMPRESSION TEST ..	41
FIGURE 33. PROBE ASSEMBLY CONFIGURED FOR MAKING MEASUREMENTS IN FIELD-COMPRESSION TEST SETUP .....	41
FIGURE 34. (A) PROBE ASSEMBLY BELOW GUIDE AND MIRROR COILS; CLOSE-UP VIEW UNDER COIL TABLE SHOWING PROBE ASSEMBLY IN PLACE.....	42
FIGURE 35. AXIAL MAGNETIC FIELD VS. AXIAL POSITION IN THE FIELD-COMPRESSION TEST SETUP.....	43
FIGURE 36. AXIAL MAGNETIC FIELD VS. TIME AT SEVERAL POSITIONS NEAR TOP OF THE LINER .....	44
FIGURE 37. AXIAL MAGNETIC FIELD VS. TIME FOR THREE DIFFERENT GUIDE/MIRROR BANK-CHARGE VOLTAGES .....	45
FIGURE 38. CURRENT (BLUE TRACE) MEASURED BY SHIVA FARADAY ROTATION DIAGNOSTIC DURING FIELD- COMPRESSION TEST .....	48
FIGURE 39. CROSS-SECTION DIAGRAM OF LINER, LOWER VACUUM SECTION, AND B-DOT PROBE PACKAGE .....	49
FIGURE 40. MICRO B-DOT BENCH CALIBRATION SETUP.....	49
FIGURE 41. TYPICAL MICRO B-DOT PROBE CONSTRUCTION.....	50
FIGURE 42. MICRO B-DOT PROBE WINDING FIXTURE.....	51
FIGURE 43. B-DOT PROBE SIGNAL (V PEAK-TO-PEAK) VS. NUMBER OF TURNS IN PROBE.....	51
FIGURE 44. B-DOT PROBE FABRICATION AND ASSEMBLY PROCESS.....	53
FIGURE 45. LINER B-DOT PROBE ARRAY POSITIONAL AND PHYSICAL PARAMETERS .....	54
FIGURE 46. MICRO B-DOT SIGNALS OVERLAID WITH SIGNALS RECORDED WITH TWO “NULL TEST” SIDE-ON OPTICAL FIBER ARRAY FIBER SIGNALS.....	54
FIGURE 47. IMAGES FROM X-RAY #1 IMAGING SYSTEM (TOP AND MIDDLE); SETUP IMAGE TAKEN BEFORE THE SHOT (BOTTOM).....	56
FIGURE 48. ONE IMAGE FROM X-RAY #2 IMAGING SYSTEM (TOP); SETUP IMAGE TAKEN BEFORE SHOT (BOTTOM) .....	57
FIGURE 49. SOLIDWORKS BASIC HARDWARE ARRANGEMENT .....	58
FIGURE 50. RADIANT EMISSION SPECTRUM OF A BLACKBODY AT 5,000 K .....	60
FIGURE 51. OPTICAL PYROMETER SCHEMATIC .....	61
FIGURE 52. PYROMETRY DATA RECORDED DURING FIELD-COMPRESSION TEST .....	63
FIGURE 53. PHOTODIODE DATA AND CALIBRATED INTENSITY RATIO.....	64
FIGURE 54. ALIGNMENT AND FOCUSING TARGET LOCATED INSIDE LINER .....	67
FIGURE 55. IMPLoding LINER DURING SHOT .....	68
FIGURE 56. SCHEMATIC OF STREAK CAMERA SETUP FOR FIELD-COMPRESSION TEST .....	69
FIGURE 57. STREAK CAMERA “FOCUS MODE” IMAGE OF TUNGSTEN-LAMP FILAMENT .....	70
FIGURE 58. STREAK IMAGE OF TUNGSTEN FILAMENT, RECORDED WITH A 2 $\mu$ S/MM STREAK RATE .....	71
FIGURE 59. STREAK IMAGE OF A REPETITIVELY PULSED LED .....	72

FIGURE 60. LOCATION ON STREAK IMAGE (IN PIXEL NUMBER) OF THE CENTERS OF CONSECUTIVE LED PULSES VS. TIME DELAY FROM STREAK CAMERA TRIGGER .....	73
FIGURE 61. LABVIEW PANEL .....	75
FIGURE 62. NEW SOFTWARE PANELS .....	76
FIGURE 63. CROSS-SECTION OF CURRENT FEED AND INSULATOR DESIGN FOR FRCHX-1 .....	78
FIGURE 64. CROSS-SECTION OF CURRENT FEED AND INSULATOR DESIGN IMPLEMENTED FOR FRCHX-2 .....	79
FIGURE 65. AXIAL-MAGNETIC FIELD VS. AXIAL POSITION OBTAINED FROM MEASUREMENTS IN FRCHX-1 TEST SETUP .....	80
FIGURE 66. UPPER LINER-CLAMPING ASSEMBLY .....	81
FIGURE 67. COMSOL MULTIPHYSICS CALCULATIONS OF AXIAL-MAGNETIC FIELD WITH MIRROR 2 COILS MODIFIED.82	
FIGURE 68. NEW UPPER MIRROR COIL ARRANGEMENT .....	83
FIGURE 69. GUIDE AND MIRROR COIL GEOMETRY ENTERED INTO QUICK FIELD .....	84
FIGURE 70. CALCULATION OF MAGNETIC FIELD ALONG AXIS (BOTTOM) OF GEOMETRY SHOWN IN FIGURE 67.....	85
FIGURE 71. CALCULATION OF LORENTZ FORCES ON COILS AND HARDWARE SHOWN IN FIGURE 70.....	86
FIGURE 72. QUICK FIELD CALCULATES A NET FORCE OF (A) 93.4 kN ( $2.11 \times 10^4$ LB) ON MIRROR 2 COILS; (B) 84.5 kN ( $1.90 \times 10^4$ LB) ON MIRROR 3 COILS .....	87
FIGURE 73. GUIDE AND MIRROR COIL STRUCTURE WITH NEW CLAMPING ASSEMBLY ON EACH SIDE OF UPPER COIL SET .....	88
FIGURE 74. ATTACHMENT OF LINER-RETURN CONDUCTOR TO LOWER SHIVA CURRENT FEED .....	89
FIGURE 75. BONDING LINER-RETURN-CONDUCTOR INSULATOR TO SHIVA CURRENT-FEED INSULATOR.....	90
FIGURE 76. (A) APPLICATION OF ANOTHER LAYER OF ViSIL ABOVE INSULATOR OVERLAP; (B) WEEP HOLES CONFIRMED REGION HAD BEEN THOROUGHLY FILLED WITH ViSIL .....	90
FIGURE 77. LOWER-HARDWARE CONFIGURATION FOR FRCHX-2.....	91
FIGURE 78. (A) INSIDE HOFFMAN BOX; (B) COPPER TUBE USED TO RUN B-DOT PROBE TWISTED PAIR LEADS TO HOFFMAN BOX .....	92
FIGURE 79. GUIDE AND MIRROR ASSEMBLY (A) INDUCTANCE AND (B) RESISTANCE MEASURED WITH QUADTECH LCR BRIDGE .....	93
FIGURE 80. FIELD-MAPPING-PROBE ASSEMBLY .....	94
FIGURE 81. AXIAL-MAGNETIC FIELD VS. AXIAL POSITION IN FIELD-COMPRESSION TEST SETUP .....	95
FIGURE 82. AXIAL-MAGNETIC FIELD VS. TIME FOR THREE GUIDE AND MIRROR BANK-CHARGE VOLTAGES .....	97
FIGURE 83. OVERLAY OF CURRENT WAVEFORMS RECORDED FOR EACH OF SHIVA STAR ARMS .....	100
FIGURE 84. SUMMATION OF EACH OF ARM-CURRENT WAVEFORMS FROM FIGURE 84.....	101
FIGURE 85. SHIVA CW AND CCW LOAD ROGOWSKI CURRENT WAVEFORMS, SHOWN OVERLAID.....	102
FIGURE 86. CURRENT MEASURED WITH CW AND CCW ROGOWSKI COIL PAIRS, AFTER CORRECTING FOR COMMON-MODE NOISE .....	102
FIGURE 87. WAVEFORMS FROM THREE UPPER-RETURN CONDUCTOR B-DOT PROBES, SHOWN OVERLAID .....	103
FIGURE 88. THREE SHIVA VOLTAGE-PROBE WAVEFORMS, SHOWN OVERLAID .....	104
FIGURE 89. SHIVA-MTF MICRO B-DOT PROBE CONFIGURATION .....	105

FIGURE 90. MTF LINER B-DOT PROBE ARRAY POSITIONAL AND PHYSICAL PARAMETERS.....	105
FIGURE 91. PROBE AND SHIELDING LOCATIONS.....	106
FIGURE 92. (A) SETUP IMAGES RECORDED WITH RAD #1 IMAGING SYSTEM BEFORE FRCHX-2 TEST; (B) SHOT IMAGE TAKEN DURING THE TEST (AT 21.81 $\mu$ S).....	107
FIGURE 93. (A) SETUP IMAGES RECORDED WITH RAD #2 IMAGING SYSTEM BEFORE FRCHX-2 TEST; (B) SHOT IMAGE TAKEN DURING TEST (AT 22.78 $\mu$ S).....	108
FIGURE 94. (A) FRONT AND (B) BACK SIDES OF DAMAGED MYLAR ON SHIVA MODULE F-1.....	109
FIGURE 95. A SHIVA BANK MODULE AFTER REPLACEMENT OF BROWN PAPER BELOW HOT BUS PLATE ON THIS HALF OF THE MODULE .....	111
FIGURE 96. (A) SMALLER SUPPORTS BETWEEN MODULES; (B) “TALL” SUPPORTS ON MODULES CLOSEST TO SHIVA CENTER SECTION .....	111
FIGURE 97. CROSS-SECTION VIEW OF SHIVA DUMMY LOAD .....	114
FIGURE 98. A 0.060- $\Omega$ FRANKLIN RESISTOR, SHOWN WITH A TAPE MEASURE FOR SCALE .....	114
FIGURE 99. RINGS TO BE USED TO JOIN TWO GROUPS OF FRANKLIN RESISTORS TOGETHER AT MID-PLANE OF LOAD ..	115
FIGURE 100. UPPER CONDUCTOR PLATE OF LOAD SHOWN WITH EXHAUST LINES AND MANIFOLD CONNECTED TO ITS FITTINGS .....	116
FIGURE 101. LOWER CONDUCTOR PLATE WITH GAS LINES IN THE PROCESS OF BEING CONNECTED .....	117
FIGURE 102. RESISTIVE TEST LOAD MOUNTED TO CURRENT-FEED PLATES AT CENTER OF SHIVA BANK .....	118
FIGURE 103. SHIVA STAR FINAL COMPOSITE CHARGE VOLTAGE VS. SET-POINT CONTROL SETTING.....	119
FIGURE 104. SHIVA STAR SET-POINT CONTROL SETTING VS. FINAL COMPOSITE CHARGE VOLTAGE.....	120
FIGURE 105. MEASURED AXIAL MAGNETIC FIELD VS. AXIAL POSITION FOR FRCHX-2 COIL SET.....	122
FIGURE 106. AXIAL MAGNETIC FIELD VS. AXIAL POSITION AT T = 6 MS FOLLOWING START OF GUIDE/MIRROR BANK CURRENT.....	124
FIGURE 107. (A) NEW GUIDE AND MIRROR COIL SET; (B) CLOSE-UP OF UPPER MIRROR COILS AND CLAMPING STRUCTURE .....	125
FIGURE 108. LARGE-AREA B-DOT PROBE AND HALL PROBE ASSEMBLY .....	127
FIGURE 109. (A) AXIAL MAGNETIC FIELD MEASURED WHEN ONLY GUIDE AND MIRROR COILS WERE PULSED; (B) MEASURED FIELD WITH GUIDE, MIRROR, BIAS, AND CUSP COILS PULSED .....	128
FIGURE 110. TWO DISTINCT BIAS CURRENT WAVEFORMS, FROM CONSECUTIVE FIELD-MAPPING TESTS .....	130
FIGURE 111. THETA COIL-CURRENT WAVEFORMS SHOW VARIATIONS IN BIAS BANK CURRENT FOR THREE TESTS.....	131
FIGURE 112. NORTH BIAS BANK IGNITRON WITH COPPER STRAP TYING ITS CATHODE TO ISOLATION-INDUCTOR TERMINAL.....	132
FIGURE 113. (A) IGNITRON-TRIGGER-GENERATOR OUTPUT PULSES; (B) TRIGGER PULSES AT OUTPUT OF EACH SECONDARY OF ISOLATION TRANSFORMER.....	133
FIGURE 114. IGNITRON-TRIGGER-ISOLATION TRANSFORMER IN PLACE NEXT TO BIAS BANK IGNITRONS.....	134
FIGURE 115. (A) AND (B) TRIGGER PULSES MEASURED AT SECONDARIES OF NEW TRIGGER-ISOLATION TRANSFORMER .....	135
FIGURE 116. ARC OCCURRED AT LOW END OF IGNITRON-ISOLATION TRANSFORMER .....	136
FIGURE 117. PLACEMENT OF FRCHX MAIN AND PI BANKS RELATIVE TO SHIVA B-ARM MODULES .....	141

FIGURE 118. PROPER GAPPING OF (A) CB #1 AND (B) CB #2; IN (C) CB #3 AND (D) CB #4 THE GAPPING TOOL TILTS SLIGHTLY LEFT .....	143
FIGURE 119. MOST RECENT CROWBAR-TRIGGER-BOARD CIRCUIT .....	144
FIGURE 120. CROWBAR-TRIGGER BOARD BEFORE MOVING THE MAIN BANK UNDER B-ARM.....	145
FIGURE 121. (A) CROWBAR-TRIGGER-BOARD SETUP (PRE-14 MARCH 2007); (B) LATER SETUP WITH ADDITIONAL BLOCKING CAPACITORS .....	146
FIGURE 122. TRIGGER-BOARD SETUP 18 MAY 2007, CONFIGURED FOR END-RAIL-GAP-ONLY (CB #1 AND CB #4) TESTS.....	147
FIGURE 123. THE “UNDER SHIVA” CROWBAR-TRIGGER BOARD .....	150
FIGURE 124. (A) MIDDLE PORTION OF CROWBAR-TRIGGER BOARD IN PLACE ABOVE CROWBAR SWITCH; (B) END SECTION OF BOARD ON WORKBENCH .....	150
FIGURE 125. CROWBAR RAIL-GAP-TRIGGER CIRCUIT USED BEFORE JUNE 2009 TESTS.....	151
FIGURE 126. MODIFIED CROWBAR RAIL-GAP-TRIGGER CIRCUIT, END OF JUNE 2009.....	152
FIGURE 127. CROWBAR RAIL-GAP-TRIGGER CIRCUIT, SEP 2009 .....	154
FIGURE 128. CURRENT-JOINT SURFACES OF THETA COIL SEGMENTS LEFT ASSEMBLED ON VACUUM STAND .....	156
FIGURE 129. (A) AND (B) CLOSE-UP VIEWS OF THREE SEGMENTS FROM FIGURE 128 .....	156
FIGURE 130. NEW WINDOW ASSEMBLY, TOP OF QUARTZ TUBE.....	157
FIGURE 131. TWO PE FIXTURES TO KEEP STAINLESS FLUX CONSERVER CENTERED WITHIN GUIDE AND MIRROR COILS.....	158
FIGURE 132. (1) GROUND CABLES; (2) MOVEMENT OF CONNECTION POINT FOR TRIGGER-SYSTEM-GROUNDING INDUCTOR.....	159
FIGURE 133. WITHOUT GROUNDING CABLES, ARCS WOULD OCCUR AROUND BALUNS ON PRE-FIRE DETECTION SENSOR CABLE.....	160
FIGURE 134. (A) PREVIOUS MAIN BANK-TRIGGER SYSTEM; (B) NEW CONFIGURATION AFTER CHANGES .....	161
FIGURE 135. CLOSER VIEW OF PTA OUTPUT CABLE AND MTG POWER-SUPPLY-CONTROL CABLE FERRITE-CORE STACKS.....	161
FIGURE 136. DAMAGED CHARGING INDUCTOR BETWEEN MODULES 2 AND 3.....	163
FIGURE 137. NEW INDUCTOR BETWEEN GUIDE/MIRROR MODULES 2 AND 3.....	163
FIGURE 138. (A) DAMAGED INDUCTOR JOINING MODULES 3 AND 6; (B) MODULE 3-6 AND 5-6 INDUCTORS WERE ALSO REMADE.....	164
FIGURE 139. (A) TRIGGER TRANSFORMER AFTER DAMAGE BY MAIN BANK PRE-FIRE; (B) ARC MARKS OBSERVED ON CABLE FROM TRIGGER UNIT TO TRANSFORMER.....	167
FIGURE 140. ARC MARKS BETWEEN (A) WEST MODULE PEARSON COIL AND BANK FRAME; (B) PEARSON COIL AND DIAGNOSTIC CABLE.....	167
FIGURE 141. REPAINTED BIAS PEARSON COILS IN PLACE .....	168
FIGURE 142. (A) SIGNS OF ARC ON MYLAR; (B) ARC INITIATION POINT; (C) DAMAGE TO MYLAR ON RAIL-GAP SWITCH .....	169
FIGURE 143. PI BANK AFTER MYLAR PACK WAS REFURBISHED.....	170
FIGURE 144. PI RAIL-GAP SWITCH AFTER NEW MYLAR PACKS WERE REATTACHED AND RTV APPLIED .....	171

FIGURE 145. PI BANK AFTER REPAIRS AND REASSEMBLY WAS COMPLETED .....	171
FIGURE 146. CABLES BETWEEN PI 40168 AND MTG WERE WRAPPED AROUND FERRITE CORES.....	175
FIGURE 147. (A) BRAID PLACED AROUND 40168-MTG CONTROL CABLE; (B) VARIAC MOVED INSIDE 40168 ENCLOSURE .....	176
FIGURE 148. ELECTRODES OF FOUR CLOSING SWITCH RAIL GAPS AFTER 150+ SHOTS .....	177
FIGURE 149. ELECTRODES OF FOUR CROWBAR SWITCH RAIL GAPS AFTER 150+ SHOTS .....	178
FIGURE 150. (A) INITIATION POINT OF ARC ON BANK SIDE HOT BUS PLATE; (B) DAMAGE TO MYLAR ON RAIL-GAP SWITCH AT LOCATION FACING ARC INITIATION POINT.....	179
FIGURE 151. PAINTED END OF PI HOT BUS PLATE, WHERE RAIL-GAP SWITCH IS MOUNTED .....	179
FIGURE 152. TYGON TUBING PLACED UNDERNEATH RAIL-GAP SWITCH TO FORM ARC BARRIER BETWEEN BANK AND LOAD SIDES OF SWITCH .....	180
FIGURE 153. ARC DAMAGE OBSERVED ON HIGH-VOLTAGE END OF BOARD FOR PI BANK POWER SUPPLY .....	181
FIGURE 154. PI POWER SUPPLY DIODE BOARD AFTER CHANGES IMPLEMENTED.....	181
FIGURE 155. PI BANK CABLE HEADER AFTER (A) ARC EVENT 12 MARCH; (B) ARC EVENT 15 MARCH 2010 .....	182
FIGURE 156. TWO ENDS OF CHARGING INDUCTOR, AFTER THE FAULT .....	183
FIGURE 157. CHARGING INDUCTORS (A) THE UPPER MODULES OF GUIDE/MIRROR BANK; (B) LOWER MODULES OF GUIDE/MIRROR BANK .....	184
FIGURE 158. ARC DAMAGE PRODUCED WHEN LEADS OF GUIDE COIL #2 DEVELOPED A SHORT.....	184
FIGURE 159. SHIVA FRANKLIN RESISTOR LOAD, FRCHX VACUUM STAND IN BACKGROUND .....	185
FIGURE 160. MAGNETIC DIAGNOSTIC DATA AND CALCULATED EXCLUDED FLUX RADII, TESTS 8 AND 9 .....	191
FIGURE 161. MAGNETIC DIAGNOSTIC DATA AND CALCULATED EXCLUDED FLUX RADII, TESTS 10 AND 11 .....	192
FIGURE 162. LINE-INTEGRATED ELECTRON DENSITY VS. TIME (A) TEST 4 AND (B) TEST 8 .....	193
FIGURE 163. SHIVA STAR ARM ROGOWSKI COIL SIGNALS FOR FRCHX-3 .....	195
FIGURE 164. SHIVA STAR ARM ROGOWSKI COIL SIGNAL SUM FOR FRCHX-3 .....	196
FIGURE 165. SHIVA STAR UNCORRECTED CENTER SECTION ROGOWSKI COIL SIGNALS FOR FRCHX-3 .....	197
FIGURE 166. SHIVA STAR CORRECTED CENTER SECTION ROGOWSKI COIL SIGNALS FOR FRCHX-3 .....	198
FIGURE 167. RAW FARADAY ROTATION PROBE SIGNALS.....	199
FIGURE 168. INTERPRETED CURRENT FROM THE FARADAY ROTATION SIGNALS.....	200
FIGURE 169. CURRENT INFERRED FROM B-DOT PROBES .....	201
FIGURE 170. SHIVA STAR VOLTAGE PROBE SIGNALS .....	202
FIGURE 171. RADIOGRAPHY PIN PHOTODIODE SIGNALS.....	203
FIGURE 172. MTF FOUR-CHORD INTERFEROMETER SYSTEM OPTICAL TABLE .....	207
FIGURE 173. INTERFERENCE SIGNALS AT 80 MHZ OBTAINED FROM RECOMBINED PROBE AND REFERENCE BEAMS....	208
FIGURE 174. INTERFERENCE SIGNALS SHOWING AMPLITUDE MODULATED OF FIBER PROBE AND AIR-REFERENCE- INTERFERENCE SIGNAL .....	209
FIGURE 175. DEMODULATOR-OUTPUT SIGNALS FOR CHANNEL NO. 1, SHIVA STAR IMPLODING LINER TEST .....	210

FIGURE 176. DEMODULATOR-OUTPUT SIGNALS MEASURED FOR CHANNEL NO. 2, SHIVA STAR IMPLoding LINER TEST.....	211
FIGURE 177. DEMODULATOR-OUTPUT SIGNALS MEASURED FOR CHANNEL NO. 3, SHIVA STAR IMPLoding LINER TEST.....	212
FIGURE 178. DEMODULATOR-OUTPUT SIGNALS FOR CHANNEL NO. 4, SHIVA STAR IMPLoding LINER TEST .....	212
FIGURE 179. INTERFERENCE SIGNALS FROM RECOMBINED PROBE AND REFERENCE BEAMS HIGHLIGHTING AMPLITUDE MODULATION .....	213
FIGURE 180. INTERFERENCE SIGNAL OBTAINED FROM RECOMBINED PROBE AND REFERENCE BEAMS .....	216
FIGURE 181. EXPANDED VIEW OF FIGURE 180 INTERFERENCE SIGNAL.....	216
FIGURE 182. INTERFEROMETER SYSTEM OPTICAL TABLE IN NEW LOCATION BETWEEN TWO ARMS OF SHIVA STAR ...	218
FIGURE 183. INTERFEROMETER SYSTEM OPTICAL TABLE BETWEEN A AND B ARMS.....	219
FIGURE 184. FIBERGLASS PLATFORM SUPPORTING THE RECEIVE FIBER COUPLER AND ITS TURNING MIRROR .....	219
FIGURE 185. SINGLE-CHORD FIBER-PROBE INTERFEROMETER G10 OPTICAL PLATFORM AND ASSOCIATED COMPONENTS .....	222
FIGURE 186. PLOT OF I AND Q DEMODULATOR SIGNALS .....	223
FIGURE 187. EXPANDED VIEW OF I AND Q DEMODULATOR SIGNALS AROUND THE TIME OF FRC FORMATION .....	223
FIGURE 188. PLOT OF PLASMA-ELECTRON DENSITY .....	224
FIGURE 189. EXPANDED VIEW OF PLASMA-ELECTRON DENSITY AROUND THE TIME OF FRC FORMATION .....	224
FIGURE 190. (A) NEW INTERFEROMETER DATA ACQUISITION ENCLOSURE; (B) COMPONENT LAYOUT IN ENCLOSURE ..	226
FIGURE 191. TWO 1-IN. THICK INTERFEROMETER OPTICAL PLATFORMS MOUNTED ON FRCHX VACUUM STAND.....	226
FIGURE 192. OPTICAL TABLE OF THE FIBER-PROBE INTERFEROMETER SYSTEM.....	228
FIGURE 193. LAUNCH AND RECEIVE OPTICS FOR “E/F” CHORD AND “T2” CHORD AT TESTSTAND.....	229
FIGURE 194. DIAGRAM OF OPTICAL PLATFORM TO BE USED FOR FOUR-CHORD FIBER-PROBE INTERFEROMETRY SYSTEM .....	230
FIGURE 195. OPTICAL TABLE OF THE FIBER-PROBE INTERFEROMETER SYSTEM.....	231
FIGURE 196. OPTICAL PLATFORM FOR THE FOUR-CHORD INTERFEROMETRY SYSTEM TO BE PLACED AT T4 AXIAL LOCATION.....	232
FIGURE 197. DIAGRAM OF THE OPTICAL PLATFORM TO BE USED FOR THE FOUR-CHORD FIBER-PROBE INTERFEROMETRY SYSTEM THAT WILL CONDUCT DENSITY MEASUREMENTS OF THE PLASMA INSIDE MOCK LINER AT DIFFERENT IMPACT PARAMETERS.....	233
FIGURE 198. ACCESS HOLES ON SLOTTED RETURN CONDUCTOR THROUGH WHICH FOUR INTERFEROMETRY BEAMS CAN ENTER MOCK LINER. MOCK LINER IS SITUATED INSIDE RETURN CONDUCTOR WITH VACUUM SEALED QUARTZ WINDOWS COVERING ITS ACCESS HOLES .....	234
FIGURE 199. OPTICAL PLATFORM FOR E/F DIAMETER CHORD ON MTF TESTSTAND—CHORD IS NOW OPERATIONAL ..	235
FIGURE 200. PLOT OVERLAY OF THE PMT SIGNAL BEFORE AND AFTER DECONVOLUTION .....	238
FIGURE 201. PLOT OVERLAY OF THE $H_{\alpha}$ AND $H_{\beta}$ SIGNALS FROM FRCHX TEST .....	239
FIGURE 202. PLOT OVERLAY OF THE EMISSION LIGHT COLLECTED BY CHORDS 1 THROUGH 4 .....	240
FIGURE 203. PLOT OVERLAY OF THE EMISSION LIGHT COLLECTED BY CHORDS 5 THROUGH 8 .....	240



FIGURE 204. MTF FRCHX PUFF FILL SCHEME.....	243
FIGURE 205. MTF PUFF-FILL TWO-CHANNEL DRIVER BOX .....	244
FIGURE 206. COMPARISON OF GAS PUFF HARDWARE AND ACTUAL EXPERIMENT .....	245
FIGURE 207. LOCATIONS OF FAST ION GAUGES FOR TESTSTAND MOCK-UP .....	246
FIGURE 208. 6AH6 FAST ION GAUGE CONTROL CIRCUIT.....	247
FIGURE 209. COMPARISON OF THE DESIGNED AND ACTUAL GAS PUFF HARDWARE GAS PUFF EXPERIMENT .....	248
FIGURE 210. 12.2 PSIA, 5 MS GAS PUFF PRESSURE DATA .....	249
FIGURE 211. 5 PSIA, 5 MS GAS PUFF PRESSURE DATA .....	250
FIGURE 212. 50 PSIA 2.5 MS GAS PUFF DATA .....	250
FIGURE 213. THREE CONSECUTIVE 40 PSIA, 2.0 MS GAS PUFFS .....	252
FIGURE 214. THREE CONSECUTIVE 45 PSIA, 750 $\mu$ S, 100 V GAS PUFFS .....	253
FIGURE 215. THREE CONSECUTIVE 40 PSIA, 1 MS, 100 V GAS PUFFS .....	254
FIGURE 216. THREE CONSECUTIVE 35 PSIA, 1 MS, 100 V GAS PUFFS .....	255
FIGURE 217. THREE CONSECUTIVE 30 PSIA, 1 MS, 100 V GAS PUFFS .....	255
FIGURE 218. GAS-PUFF DRIVER ELECTRONICS .....	256
FIGURE 219. GAS-PUFF DRIVER ENCLOSURE.....	257
FIGURE 220. PUFF-VALVE ASSEMBLY .....	258
FIGURE 221. PUFF-VALVE ASSEMBLY MOUNTED ON THE EXPERIMENT .....	258
FIGURE 222. GAS PUFF VALVE DRIVER ENCLOSURE.....	259
FIGURE 223. GAS PUFF VALVE DRIVER CIRCUIT.....	260
FIGURE 224. POWER SUPPLY PATCH PANEL .....	260
FIGURE 225. 46 MHZ OR 146 MHZ LPRF PRE-PREIONIZATION SYSTEM FOR MTF FRCHX.....	263
FIGURE 226. MTF FRCHX LPRF PPI MODES OF OPERATION .....	265
FIGURE 227. MTF FRCHX LPRF PPI 1 kW SOURCE.....	266
FIGURE 228. MTF FRCHX LPRF INTERFACED TO THE EXPERIMENT.....	268
FIGURE 229. MTF FRCHX OF RF GLOW GAS BREAKDOWN OVER A RANGE OF FILL PRESSURES .....	269
FIGURE 230. NEW RF RING ASSEMBLY .....	270
FIGURE 231. MTF RF PPI PIN DIODE FAST TRIGGER SWITCH MODULE AND CONTROLLER .....	271
FIGURE 232. MTF FRCHX RF PPI FAST SWITCH PLASMA BREAKDOWN TRIGGER CONTROLLER .....	273
FIGURE 233. RF PPI PIN DIODE FAST SWITCH INITIAL DATA SHOWING SWITCHING PARAMETERS.....	274
FIGURE 234. COPPER STRIP ELECTRODE IN HOLDER .....	275
FIGURE 235. CIRCUMFERENTIAL GAP IN THE ELECTRODES TO PREVENT FLUX EXCLUSION .....	276
FIGURE 236. ELECTRODE ASSEMBLY SURROUNDING QUARTZ TUBE .....	276
FIGURE 237. MICRO-CAP MODEL OF CABLE DISCHARGE CIRCUIT .....	278
FIGURE 238. CABLE PULSER TEST SETUP .....	278

FIGURE 239. 40168 HPRF TEST SETUP .....	279
FIGURE 240. RF ENCLOSURE FOR MODEL 40168 .....	280
FIGURE 241. HYDROGEN FRACTIONAL DISSOCIATION AND IONIZATION FROM SAHA EQUILIBRIUM FOR A TOTAL NUMBER DENSITY OF $1.77 \times 10^{21} \text{ m}^{-3}$ .....	282
FIGURE 242. DENSITIES OF MOLECULAR, ATOMIC, AND IONIZED HYDROGEN AS A FUNCTION OF TEMPERATURE FOR A PRESSURE OF 50 MTORR FROM THE SAHA EQUATION .....	283
FIGURE 243. ELECTRIC FIELD STRENGTH IN FORMATION REGION—PRE-BREAKDOWN, 10 kV APPLIED .....	284
FIGURE 244. ELECTRIC FIELD VECTORS IN VICINITY OF UPPER ELECTRODE—PRE-BREAKDOWN CASE .....	285
FIGURE 245. EQUIPOTENTIAL CONTOURS NEAR BOTTOM OF UPPER ELECTRODE—PRE-BREAKDOWN .....	286
FIGURE 246. ELECTRIC FIELD CONTOURS NEAR BOTTOM OF UPPER ELECTRODE—PRE-BREAKDOWN .....	287
FIGURE 247. ELECTRIC FIELD AMPLITUDE IN VICINITY OF ELECTRODES—POST-BREAKDOWN .....	288
FIGURE 248. EQUIPOTENTIAL CONTOURS NEAR UPPER ELECTRODE—POST-BREAKDOWN .....	289
FIGURE 249. ELECTRIC FIELD STRENGTH NEAR BOTTOM OF UPPER ELECTRODE—POST-BREAKDOWN .....	290
FIGURE 250. ELECTRIC FIELD VECTORS NEAR BOTTOM OF UPPER ELECTRODE—POST-BREAKDOWN .....	291
FIGURE 251. DRIFT VELOCITIES AS A FUNCTION OF ELECTRIC FIELD WITH AND WITHOUT MAGNETIC FIELD .....	301
FIGURE 252. FIRST TOWNSEND COEFFICIENT (INVERSE IONIZATION MEAN FREE PATH) AS A FUNCTION OF ELECTRIC FIELD WITH AND WITHOUT MAGNETIC FIELD .....	302
FIGURE 253. IONIZATION RATE AS A FUNCTION OF ELECTRIC FIELD WITH AND WITHOUT MAGNETIC FIELD .....	303
FIGURE 254. IONIZATION TIME AS A FUNCTION OF ELECTRIC FIELD WITH AND WITHOUT MAGNETIC FIELD .....	303
FIGURE 255. AVERAGE ELECTRON ENERGY AS A FUNCTION OF ELECTRIC FIELD .....	304
FIGURE 256. ELECTRON DIFFUSION COEFFICIENT AS A FUNCTION OF ELECTRIC FIELD WITH AND WITHOUT MAGNETIC FIELD .....	304
FIGURE 257. IONIZATION AND DIFFUSION LOSS RATES AS A FUNCTION OF ELECTRIC FIELD WITH AND WITHOUT MAGNETIC FIELD .....	305
FIGURE 258. NET IONIZATION-LOSS RATES AS A FUNCTION OF ELECTRIC FIELD WITH AND WITHOUT MAGNETIC FIELD .....	306
FIGURE 259. NET IONIZATION RATE AS A FUNCTION OF MAGNETIC FLUX DENSITY FOR VARIOUS VALUES OF ELECTRIC FIELD .....	307
FIGURE 260. NET ELECTRON EXPONENTIATION TIME AS A FUNCTION OF MAGNETIC FLUX DENSITY FOR VARIOUS VALUES OF ELECTRIC FIELD .....	307
FIGURE 261. ELECTRON POPULATION HISTORY FOR THE CASE CORRESPONDING TO THE PRESENT FRCHX CONFIGURATION .....	311
FIGURE 262. ELECTRON POPULATION HISTORY FOR THE CASE OF 0.5 T BIAS FIELD AND 400 V/CM INITIAL PEAK ELECTRIC FIELD .....	312
FIGURE 263. ELECTRON POPULATION HISTORY FOR THE CASE OF 0.5 T BIAS FIELD AND 665 V/CM PEAK INITIAL ELECTRIC FIELD .....	313
FIGURE 264. ELECTRON POPULATION HISTORY FOR THE CASE OF 0.5 T BIAS FIELD AND -665 V/CM ELECTRIC FIELD .....	314
FIGURE 265. MAGNETIC FIELD CONFIGURATION WITH EQUIPOTENTIAL RINGS .....	315
FIGURE 266. DESIGN DRAWINGS FOR EQUIPOTENTIAL RINGS .....	315

FIGURE 267. EQUIPOTENTIAL RING ASSEMBLY .....	316
FIGURE 268. LOCATION OF EP RINGS IN VACUUM CHAMBER.....	316
FIGURE 269. BIAS CIRCUIT DESIGN FOR EP RINGS .....	317
FIGURE 270. TOP OF BIAS BANK .....	318
FIGURE 271. EQUIPOTENTIAL RING VOLTAGE DATA .....	319
FIGURE 272. ACTIVELY BIASED RING CURRENT DATA .....	320
FIGURE 273. COMPARISON OF FAST CAMERA IMAGES FOR SHOTS WITH AND WITHOUT RING BIAS.....	321
FIGURE 274. NEW CABLES INSTALLED TO LOWER INDUCTANCE OF RING BANK SYSTEM .....	322
FIGURE 275. COPPER STRIP SHUNTS SHOWN CONNECTED TO RING ASSEMBLY FOR RESONANCE-INDUCTANCE MEASUREMENTS .....	322
FIGURE 276. ANOTHER VIEW OF COPPER STRIP SHUNTS .....	323
FIGURE 277. BENCH MOCK SIMULATION OF RING BANK CAPACITANCE AND INDUCTANCE WITH 50-W AMPLIFIER ....	323
FIGURE 278. CLOSE-UP OF MOCK-UP BANK TO CHARACTERIZE RESONANCE FOR DERIVING INDUCTANCE .....	324
FIGURE 279. OVERLAY OF ARM ROGOWSKI CURRENTS, LOAD ROGOWSKI CURRENTS, AND UPPER RETURN CONDUCTOR B-DOT PROBES SIGNALS .....	325
FIGURE 280. RADIOGRAPHIC RESULTS FROM THE FRCHX-2 TEST .....	326
FIGURE 281. RESULTS OF A MACH2 MHD SIMULATION FOR FRCHX-2, WITH RADIOGRAPHIC DATA SUPERIMPOSED.....	327
FIGURE 282. FRCHX-3 CURRENT DIAGNOSTICS OVERLAY .....	328
FIGURE 283. RADIOGRAPHY #2 STATIC IMAGE .....	329
FIGURE 284. RADIOGRAPHY #2 DYNAMIC IMAGE AT 22.985 $\mu$ S .....	329
FIGURE 285. FIELD-MAPPING RESULTS FOR VARIOUS COMBINATIONS OF COIL BANK DISCHARGES .....	330
FIGURE 286. ELECTRON DENSITY MEASUREMENTS WITH AND WITHOUT RF PPI.....	331
FIGURE 287. FRCHX CONFIGURATION .....	332
FIGURE 288. COMPARISON OF T4 B-DOT SIGNALS FOR VARIOUS PI-MAIN DELAYS FOR LOW-VOLTAGE OPERATION..	333
FIGURE 289. COMPARISON OF T4 B-DOT SIGNALS FOR VARIOUS PI-MAIN DELAYS FOR FULL-VOLTAGE OPERATION.	334
FIGURE 290. COMPARISON OF FIRST-CYCLE AND SECOND-CYCLE PI BANK DELAYS .....	335
FIGURE 291. COMPARISON OF SECOND-CYCLE PI BANK DELAYS WITH GAS PUFF AND 50-mTORR STATIC FILL .....	335
FIGURE 292. COMPARISON OF DATA OVER CONDITIONING OF VACUUM VESSEL .....	336
FIGURE 293. COMPARISON OF DIFFERENT GAS-PUFF-TO-PI DELAYS.....	337
FIGURE 294. COMPARISON OF PI-MAIN DELAYS FOR 3.75-MS PUFF-PI DELAY .....	337
FIGURE 295. T4 B-DOT DATA FOR MULTIPLE-CYCLE DELAYS OF PI TO MAIN DISCHARGE.....	338
FIGURE 296. EXCLUDED FLUX RADIUS FOR THE DATA OF FIGURE 295 .....	339

## LIST OF TABLES

TABLE 1. OPTIMUM STREAK CAMERA SETTINGS .....	72
TABLE 2. SHIVA STAR FINAL COMPOSITE VOLTAGES RECORDED FOR SET-POINTS INDICATED ...	119
TABLE 3. CALCULATED SET-POINTS FOR INDICATED FINAL COMPOSITE CHARGE VOLTAGES— SHIVA STAR BANK .....	120
TABLE 4. VARIATIONS IN MIRROR 2 AND MIRROR 3 COILS CONSIDERED IN RECENT COMSOL CALCULATIONS.....	123
TABLE 5. BLOCKING CAPACITANCE BETWEEN TRIGGER CABLES AND TRIGGER TERMINAL AT EACH CROWBAR RAIL GAP .....	145
TABLE 6. MAIN BANK CURRENT QUARTER-CYCLE TIMES VS. PI-TO-MAIN BANK TRIGGER DELAY AND LOAD CONDITIONS .....	173
TABLE 7. POSITIONS OF B-DOT PROBES, FLUX LOOPS, OPTICAL FIBER PROBES, AND INTERFEROMETER PROBES.....	187
TABLE 8. CAMAC CRATE PHOTO DETECTOR SENSITIVITIES .....	237
TABLE 9. HAMAMATSU PMT 1 THROUGH PMT 5 SENSITIVITIES .....	237
TABLE 10. CHORDAL LENGTH FOR EACH OF THE PMT DATA CHANNELS.....	241
TABLE 11. GAS PUFF TEST MATRIX.....	261

**This page intentionally left blank**

## 1.0 SUMMARY

The Air Force Research Laboratory (AFRL), in collaboration with Los Alamos National Laboratory (LANL) was funded and tasked by the Department of Energy Office of Fusion Energy Sciences (DOE-OFES) to investigate an alternative approach to achieving controlled thermonuclear fusion, or achieve high-energy-density plasma (HEDP) conditions relevant to fusion. SAIC and its subcontractor team supported this work at AFRL's Shiva Star facility under the Pulsed Power and Pulsed Power Systems R&D for Magnetized Target Fusion (MTF) portion (Task Order 2) of the High Energy Research and Applications (HERA) contract. This effort was more than four years. During this time, we set up an experiment to test field-reversed configuration (FRC) magnetized plasmas, called FRCHX, for FRC Heating Experiment. The testing involved forming plasma in deuterium gas using multiple theta-coil discharges, translating the plasma from the formation region to a capture region using magnetic guide fields, injecting the plasma into a compression region inside a 1-mm-thick, 30-cm long cylindrical aluminum liner, and trapping it there using mirror magnetic fields above and below the liner. Figure 1 shows a cutaway rendering of the FRCHX configuration.

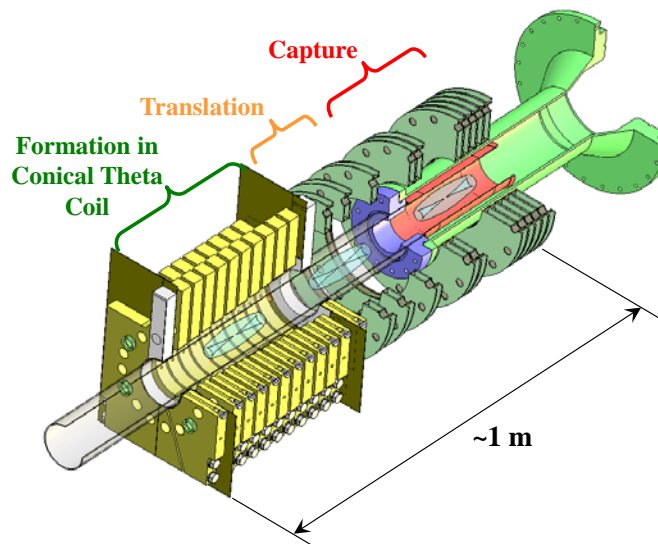


Figure 1. Cutaway of FRCHX configuration

The purpose of these experiments was to develop a magnetized plasma suitable for subsequent compression by the liner, driven by the Shiva Star 10-MJ fast capacitor bank. Two-dimensional

magnetohydrodynamic (MHD) simulations, performed by NumerEx, LLC (NumerEx), had shown that it might be possible, by such a technique, to compress the plasma to nuclear-fusion-relevant conditions.

To achieve these conditions, it would be necessary to produce a pre-compression FRC plasma with a lifetime in excess of the inherent 20- $\mu$ s timescale of the Shiva Star drive. While such lifetimes have been measured in other FRC experiments, they were achieved at significantly lower plasma densities than what is required for compression to fusion conditions by liner compression with Shiva Star (of order  $10^{17}$  cm<sup>-3</sup>). In addition to the density requirement, compression to the approximately 10-keV temperature required for fusion implies that the initial plasma should have a temperature of approximately 200 eV. Much of the work described in this report involved applying multiple strategies for achieving the requisite pre-compression plasma conditions. The strategies included optimizing magnetic field amplitudes, profiles, and timings, studying gas puff injection for plasma formation, using RF electric fields to pre-ionize the gas to increase the amount of magnetic flux trapped in the FRC, and develop the ability to apply radial electric fields in the vicinity of the plasma using electrically biased rings above the plasma to counter the  $n = 2$  rotational instability known to shorten FRC plasma lifetimes.

To successfully carry out the experimental campaign, we developed command and control systems for the complex pulsed power operation (at least five separate capacitor bank discharges for the plasma system, alone, shown in Figure 2) and data acquisition systems for collecting and recording diagnostic measurement signals and processing them. In addition, we developed and fielded advanced diagnostics, including a multi-chord fiber-optic HeNe laser interferometer.

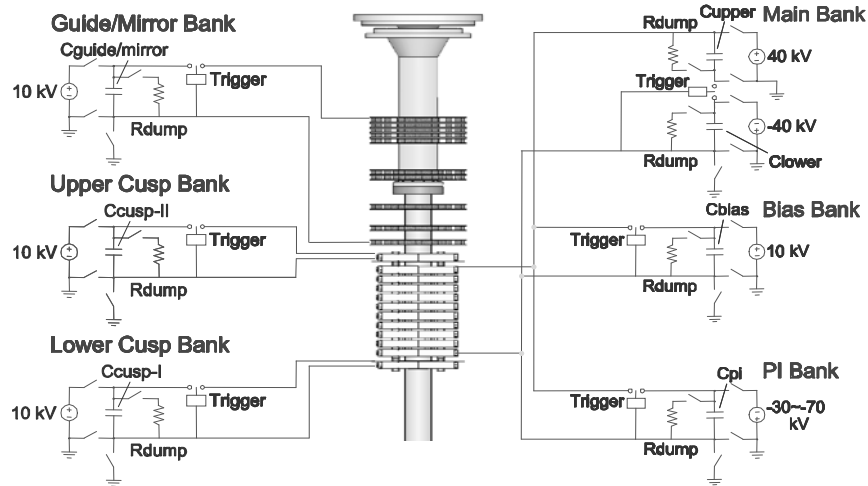


Figure 2. Various capacitor banks and coils for FRCHX

By the end of the contract period of performance (POP), we had successfully produced FRCs with electron plus ion temperature 200–300 eV, and density within a factor of two of that required. Furthermore, we increased FRC plasma lifetimes (formation to capture decay) from less than 10  $\mu$ s to approximately 20  $\mu$ s.

Another important goal of the work was to demonstrate that the FRC plasma system could be integrated with Shiva Star, and both systems successfully operated to actually compress a magnetized plasma at the multi-mega joule energy level. To prepare for such a complex experiment, two inherently destructive Shiva Star experiments with liners compressing vacuum magnetic flux were performed. The second of these successfully demonstrated essentially instability-free liner radial convergence of 10 times and an interpreted peak compressed magnetic field of 500 T. A successful integrated plasma compression experiment was demonstrated in April 2010, although the plasma had substantially decayed by the time of compression.

Based on these successes, as well as advanced analysis and advancement of the state of the art, both at AFRL and in other laboratories, we believe production of fusion-relevant plasmas is within technical reach with existing facilities such as Shiva Star.



## **2.0 INTRODUCTION**

This technical report documents the work performed by SAIC and its subcontractors, VariTech Services (VTS), NumerEx, Fiore Industries, Inc. (Fiore), and Voss Scientific (Voss), in support of the Pulsed Power and Pulsed Power Systems R&D for Magnetized Target Fusion (MTF) portion (Task Order 2) of the HERA contract over the period 11 August 2008 through 11 February 2013. Work was performed at the AFRL Shiva Star facility and involved carrying out experiments to form, translate, capture, and compress—using the Shiva Star fast capacitor bank FRC plasmas. Implicit in this work were designing, fabricating, assembling, maintaining, and testing hardware; fielding diagnostics; acquiring, post-processing, and analyzing data; providing logistical support; and carrying out supporting calculations and analysis. For this effort, we worked closely not only with AFRL personnel, but also with scientists, engineers, and technicians from Los Alamos National Laboratory (LANL), the University of New Mexico (UNM), and the University of Nevada Reno (UNR). We also interacted with consultants (Dr. Loren Steinhuaer) and other AFRL and DOE contractors (e.g., Woodruff Scientific), and participated actively in professional conferences to keep abreast of relevant efforts and developments around the world.

SAIC and its team members were already familiar with AFRL's desire to develop this technology, and we supported their work in this area since the spring of 2000 under both the DEHPM and the DETAR contracts. Forming and compressing magnetized plasmas such as the FRC is recognized by SAIC to be important for meeting the goals and objectives outlined by AFRL's customer—the DOE-OFES, both as an alternative path to achieving laboratory nuclear fusion and as a potential testbed for High Energy Density Physics.

### ***2.1 Background***

#### **2.1.1 Laboratory Nuclear Fusion Approaches**

Historically, there have been two major approaches to achieving controlled thermonuclear fusion, i.e., Magnetic Fusion energy (MFE) and Inertial Confinement Fusion (ICF). The MFE approach is one in which a relatively low-density plasma is confined for relatively long times using magnetic fields produced by external field coils. Scientists have investigated conventional

MFE—with plasma density  $n$  at approximately  $10^{14} \text{ cm}^{-3}$  and a magnetic field provided by superconducting magnets—continuously since at least the mid-1950s when Igor Tamm and Andrei Sakharov and others developed the toroidal tokamak concept, based on an idea of Oleg Lavrentyev in the Soviet Union [1].

In contrast with MFE, ICF involves ultra-high fuel pressures, created by an implosion driven by a radiation field, to confine a high-density plasma for relatively short (inertial) periods. Intense lasers or particle beams create this radiation field, directly or indirectly. ICF researchers have investigated laser-driven ICF—with peak density  $n$  at approximately  $10^{25} \text{ cm}^{-3}$  and a measured confinement time of several nanoseconds—continuously since soon after the invention of the laser in 1960 [2].

The Magnetized Target Fusion (MTF, or MIF – for Magneto-Inertial Fusion) approach to controlled thermonuclear fusion involves compression of a magnetized plasma “target,” but the plasma is intermediate in density between Magnetic Fusion Energy (MFE) and Inertial Confinement Fusion (ICF) plasmas. The main advantage of MTF over either MFE or ICF is its relative cost and compactness owing to the fact that the MTF fusion volume is much smaller than that of MFE and the driver power requirements for MTF are much lower than those of ICF [3].

High thermonuclear fusion reaction rates take place in high-temperature fuels such as deuterium ( $\text{D}_2$ ) or a deuterium-tritium (D-T) mixture. Like MFE, MTF requires a magnetic field, but the main purpose of the MTF field is to suppress thermal conduction from the heating fuel to its surroundings. Like ICF, MTF requires a pulsed high pressure to create a high-density fuel, but because the applied magnetic field suppresses thermal conduction, the high pressure can be created over a longer timescale than that required for ICF, and the compression process can proceed nearly adiabatically.

The means of compressing the MTF plasma chosen by AFRL is by electromagnetic implosion of a solid cylindrical metal shell, or liner, using the Shiva Star fast capacitor bank. Several authors discussed using imploding liners to drive MTF in the 1980s, including Sherwood [4], Kirkpatrick, and Lindemuth [5]. Excitement grew in the mid-1980s as the Russian MAGO (see Glossary) concept [6] came to the attention of U.S. researchers.

The relatively slower implosion timescale of MTF (of order 10  $\mu$ s) relative to ICF (of order 1 ns) enables the use of less expensive pulsed power drivers. Experiments at AFRL's Shiva Star facility during the past two decades have shown that high-current-driven implosions of initially solid shells up to 10 centimeters in diameter can produce sufficiently high pressures to drive targets to a radial compression of 10 times or more without substantial degradation in implosion quality from a class of Rayleigh-Taylor-like fluid instabilities [7, 8]. These results provided confidence that MTF is possible in the Shiva Star facility.

The MTF system comprises a plasma formation subsystem, translation/injection region, and trapping/compression region. The compression region is the interior of a cylindrical aluminum shell, or liner. During compression, the liner is imploded radially by a high-current Z-pinch discharge of the Shiva Star capacitor bank.

The experimental work described in this report consists of three Shiva Star liner implosion shots—two compressing magnetic flux in vacuum, and one integrated plasma compression test—and multiple series of non-destructive FRC formation and translation experiments. By nature, the Shiva Star tests are destructive to the liner hardware as well as many of the guide and mirror field coils positioned around it. Most of the core experimental systems are located in the northeast corner of the Experiment high bay for both types of tests. However, the compression-heating experiments involved moving the vacuum and field coil assembly, and two of the pulsed power banks to a position under the Shiva Star high-energy capacitor bank, to enable injecting the FRC into the 30-cm tall, 10-cm diameter aluminum solid liner that the Shiva Star bank implodes. The compression-heating experiment was a milestone in our program because it represents the culmination of a design and analysis effort spanning several months, and it was a proof-of-principle demonstration for the MTF concept described here. After the first compression-heating experiment occurred, subsequent test series focused on incremental improvements in the overall system to increase such parameters as initial FRC lifetime or density. Subsequent test series also focused on suppressing instabilities such as the “n=2” instability that was observed in the FRC.

### 2.1.2 Field Reversed Configuration Plasmas

The version of magnetized plasma preferred by the AFRL for compression is the FRC, which is a type of compact toroid [9]. An ideal FRC has only a poloidal magnetic field and no toroidal field. The FRC is formed from a theta-pinch discharge through the external field coils in an initially neutral gas. If the gas becomes ionized with an embedded ambient axial magnetic field, and a subsequent main theta coil discharge occurs that produces magnetic field in the opposite direction, the two opposing fields tend to spontaneously reconnect to form closed poloidal (i.e., in the  $r$ - $z$  plane only) field lines, as shown in Figure 3 [10]. Once the injected magnetic flux exceeds the ambient flux, additional flux injection produces a vacuum boundary flux of open magnetic field lines, as indicated in the figure.

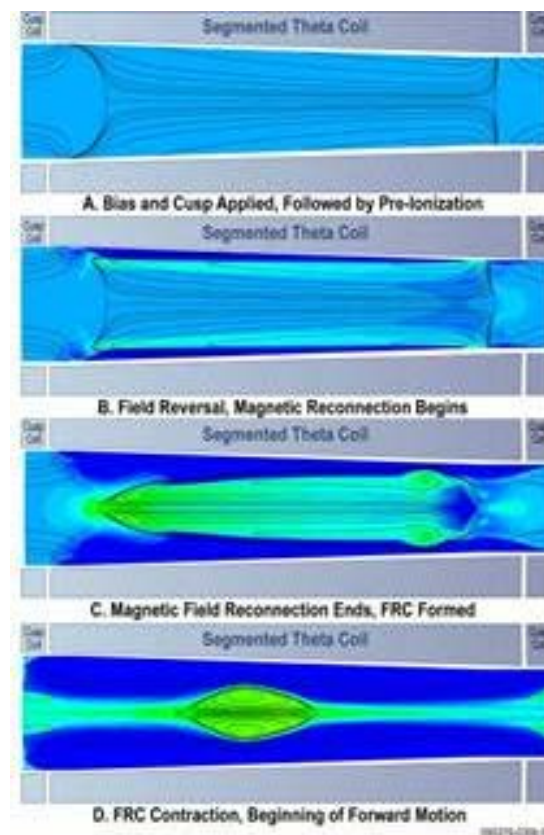


Figure 3. FRC formation process<sup>1</sup>

<sup>1</sup> Contour and field line plots in this figure taken from recent NumerEx simulations conducted under an independent contract.

The FRC has advantages of high power density and a  $\beta \approx 1$  (i.e., ratio of plasma energy density to magnetic energy density) magnetic equilibrium [11]. Glen Wurden's group at LANL analyzed the compression of such a magnetized target plasma inside a flux-conserving shell and presented this work at the 20th IAEA Fusion Energy Conference held in Vilamoura, Portugal, in November 2004. Wurden et al. designed an FRC with a relatively high initial density ( $n$  approximately  $10^{17} \text{ cm}^{-3}$ ) and temperature (100–300 eV) that is expected to increase to more than  $10^{19} \text{ cm}^{-3}$  and to the multi-keV range after compression, driven by a solid liner implosion with the Shiva Star High Energy Capacitor Bank. A combined AFRL–Los Alamos effort at LANL Tech Area 35 developed the ability to form suitable FRCs with these initial densities and temperatures. The FRC parameters attained are very close to the desired parameters—radius approximately 2 cm, length approximately 10–20 cm, density approximately  $0.5 \times 10^{17} \text{ cm}^{-3}$ , ion temperature approximately 200 eV, axial magnetic field approximately 1–2 Tesla, and lifetime approximately 15–20 microseconds [12].

### **2.1.3 Technical Challenges**

The basic approach to MTF adopted by AFRL, LANL, and SAIC, appears to be technically sound, based on previous experimental work and two-dimensional magnetohydrodynamic (MHD) simulations. An integrated plasma compression experiment involves four phases:

1. Creation of a magnetized plasma (Formation)
2. Moving the plasma from its formation region to its compression region (Translation)
3. Capturing the plasma in the compression region (Trapping)
4. Compressing the plasma by surrounding liner implosion (Compression)

Each of these phases has its technical challenges. Although FRCs have been produced in the laboratory for many years, the requirement for compression to fusion conditions means that the initial FRC plasma must have higher density and temperature, and longer lifetime, by comparison, and also be essentially rotation-free. While the minimum density and temperature were achieved in the FRX-L experiment at LANL, the lifetime (of order 10  $\mu\text{s}$ ) was marginal. Additionally, it is known that FRC plasmas rotate. If the FRC is rotating at the time of liner compression, conservation of angular momentum implies that the rotation rate will increase with diminishing radius. There are two problems with this rotation. First, rotation leads to a well-

known  $n=2$  distortion instability that causes the FRC to collapse prematurely. Second, rotational energy increases the compression driver requirement because the rotating plasma is harder to compress.

Because the plasma is compressed by an effective flux conserver, it is impossible to create it in the compression region directly. Therefore, it must be formed in a separate region and transported with guide magnetic fields to the liner region. This axial transport is effected back in the formation region by using a set of segmented theta coils with a conical bore for the reversed theta pinch formation process. Calculations, discussed later, showed that the conical bore would not only form the plasma, but also impart an axial momentum sufficient for the plasma to penetrate the mirror magnetic field at the entrance to the trapping/compression region; but this concept had to be demonstrated. In addition, if the plasma has too much axial momentum, it will pass through the capture region and out the other end. So, there had to be a second mirror field peak at the upper end of the capture region to prevent the plasma from escaping. If the entrance mirror field is insufficient, the plasma can bounce back from the upper mirror and escape back into the translation region. The mirror fields, therefore, had to be tuned for optimal capture. Finally, the integrated plasma-compression system had to be integrated, and a highly complex set of pulsed power discharges performed to accomplish a proof-of-principle demonstration. These challenges were quite daunting. Nevertheless, almost all of them were accomplished.

#### **2.1.4 Report Organization**

The remainder of this report is organized as follows. In the next section, we discuss in detail performance of Shiva Star vacuum-magnetic-field (FRCHX-1 and FRCHX-2) and plasma compression (FRCHX-3) experiments. Following that discussion, we describe the development of the magnetized target plasma over the course of the contract. Plasma development entailed development, fielding, and interpreting diagnostic measurements, and those diagnostics are discussed as appropriate for the various experiments. In Section 4, we summarize and discuss results. We state our conclusions in Section 5, and we make recommendations for future work in Section 6. References are listed in Section 7 and Section 8 contains a glossary of acronyms and abbreviations.

## **3.0 METHODS, ASSUMPTIONS, AND PROCEDURES**

The bulk of the MTF work performed under the HERA contract is described here. There are two main parts. In Section 3.1, we describe the two vacuum magnetic flux compression experiments (FRCHX-1 and FRCHX-2) and the integrated plasma compression experiment (FRCHX-3) performed with the Shiva Star capacitor bank. Section 3.2 contains a description of the plasma formation, translation and trapping experiments that were performed to produce an optimized FRC plasma for compression. Several subsystems were developed and incorporated in an attempt to both improve plasma lifetime and control rotation, including implementation of gas puff injection, construction and testing of two different types of RF “pre-preionization,” and development of a set of electrically biased rings to help control plasma rotation.

### ***3.1 SHIVA STAR Compression Tests***

The main goal of this effort was to prepare for and conduct a solid liner-plasma-implosion demonstration. Prior to conducting the fully integrated test, it was decided to perform at least one test with only the Guide and Mirror fields injected into the liner. The primary impetus for performing a magnetic-field-only compression test was to determine the magnetic field’s effects on the liner, specifically how uniform the implosion of the deformable contact liner would be with a strong magnetic field inside it, as well as at what time instabilities might develop in the liner and what factor of field compression could be obtained.

Much hardware design, fabrication, assembly, and testing was required before any compression experiments could be performed, and this initial hardware preparation is discussed in Section 3.1.1. The first field-compression test (FRCHX-1) was performed, but two serious problems arose during the test that prevented it from yielding the desired information, as described in Section 3.1.2.1. The problems were identified and corrected, and a second field-compression test (FRCHX-2) was performed, with substantially better results. It is described in Section 3.1.2.2. At that point, the various plasma formation, translation, and capture hardware was integrated under the Shiva Star capacitor bank, and a fully integrated plasma compression test was conducted, described in Section 3.1.2.3. That test, while fully successful in terms of demonstrating the proof

of principle, showed that the target plasma had insufficient lifetime, and the rest of the contract effort was spent addressing that shortfall.

### 3.1.1 Initial Hardware Preparation

Despite the decision to conduct a field-compression test with the Shiva bank ahead of the first FRC compression-heating test, SAIC and subcontractor personnel moved the FRCHX Main and Preionization (PI) banks underneath the B-Arm of Shiva and to move the vacuum and field coil stand under the load section of the Shiva bank (Figure 4). Instead of placing the vacuum and field coil stand directly under the center of the Shiva load section, however, it was necessary to place the stand to the south side, toward the A-arm, to leave adequate room for field-compression-test setup. Because both the FRCHX vacuum and field coil stand and the field-compression Guide/Mirror coils would require use of the Guide/Mirror bank, this arrangement provided the simplest means of enabling near-simultaneous tests to be performed with both. Furthermore, the preparation time for the follow-on FRC compression-heating test would be greatly reduced with the FRCHX banks and cabling already in place under the Shiva bank.

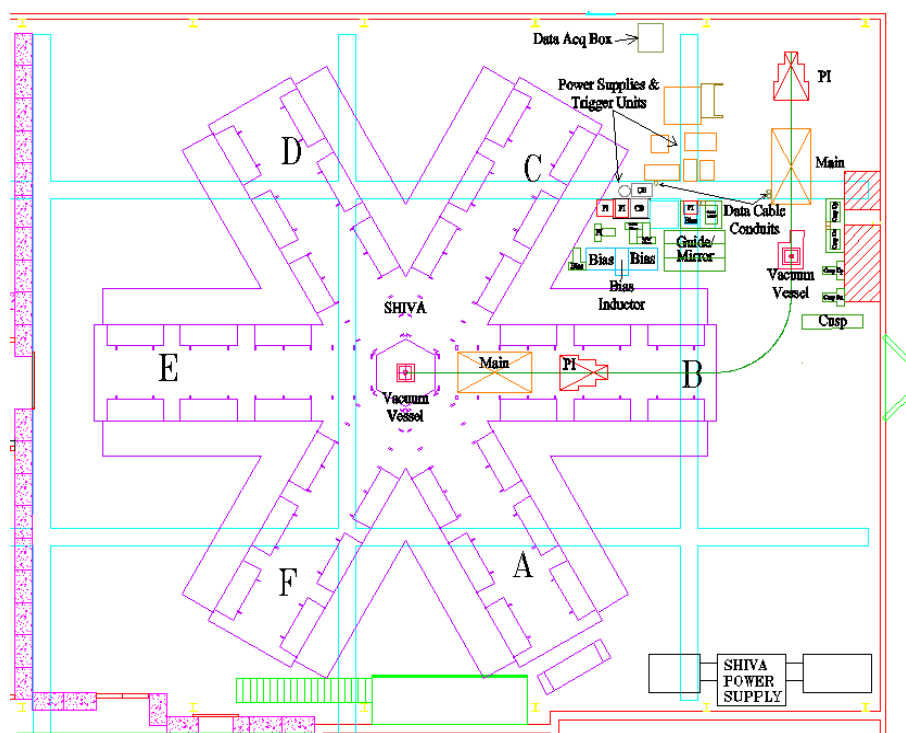


Figure 4. Shiva Bank portion of Experiment high bay



Figure 4 shows both the “retracted” position of the FRCHX Main and PI banks and vacuum stand (where tests had been performed) and the “inserted” position (where tests would be performed next).

The FRCHX Main and PI banks operate on relatively fast time scales ( $\mu\text{s}$ ) compared to all the other FRCHX banks, which operate on much slower times scales (tens of  $\mu\text{s}$  to  $\text{ms}$ ). As such, bank and cable inductance must be kept at a minimum, and therefore the Main and PI banks must follow the vacuum and field coil stand as it moves between the two test locations shown in Figure 4. Because of the limited clearance between the FRCHX Main bank and the support structure under Shiva B-Arm, it was necessary to line the section of the B-Arm support structure where the Main bank would reside with an insulating material to prevent the Main bank from arcing to the structure. High-density polyethylene (HDPE) sheets, 0.5-in. thick, were used to line the sides and ceiling of the first 16 ft of the B-Arm support structure closest to the Shiva center section. We placed 0.0625-in. and 0.125-in. sheets of HDPE and Lexan on the floor to insulate the bank from the Shiva ground plane (Figure 5). Brown craft paper, proven to be effective at grading the voltage and inhibiting static buildup on the Shiva module Mylar packs, was placed over the HDPE sheets on the walls in areas where the Main bank trigger-electrodes and bus plates would be closest.



Figure 5. Floor, sides, and ceiling of the B-Arm tunnel lined with sheets of insulating material

Moving the PI bank into its new position under B-Arm was straightforward, because it is small and was fabricated on a cart with wheels. To move the larger and heavier Main bank, we used a pair of pneumatic lifters manufactured by AeroGo (Figure 6).

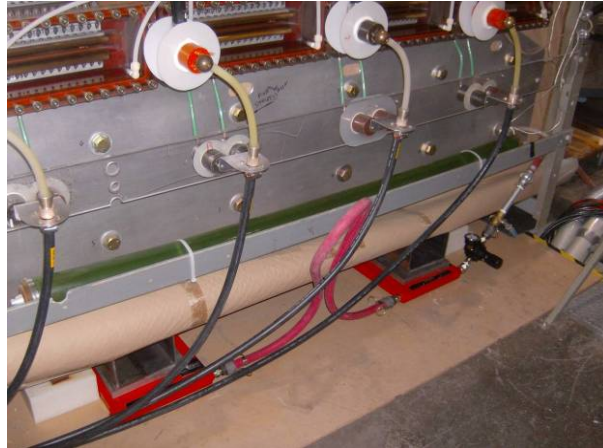


Figure 6. Pneumatic lifters (AeroGo "Aero-Planks")

Lifters were positioned under the bank to elevate it on a cushion of air and enable it to be pushed under the Shiva bank. These lifters require a pressure of 25 approximately 40 psi and an air flow of approximately 125 scfm for operation, and to provide this pressure and flow it was necessary to rent an air compressor. Each lifter is capable of lifting 12,000 lb, though, and capable of moving the weight very smoothly on level surfaces. They proved to be a very effective means for moving the Main bank.

The RG 17/14 transmission line cables and the RG 218 trigger cables for the closing and crowbar switches were all left attached to the bank, because there would not be adequate room to reattach them once the bank was under the B-Arm of Shiva. To assist with moving these cables while the bank was moved, the cables were coiled up and placed in carts going in front of and behind the bank. Figure 7 shows the process of moving the Main bank: (a) Initial "retracted" position; (b) and (c) bank starts to go under B-Arm; (d) final "inserted" position from Shiva load region; (e) view from east end of B-Arm.



(a)



(b)



(c)



(d)



(e)

Figure 7. Process of moving the Main bank

In Figure 7 a, the RG 17/14 cables were placed in a cart in front of the bank and RG-218 trigger cables for the closing and crowbar switches were placed on a cart in back. In Figure 7 e, the RG 218 trigger cables are being run to the north side of the arm where they will be placed into a tray running to the trigger units.

Figure 8 shows the PI bank placement behind the Main bank after the Main bank move was completed.

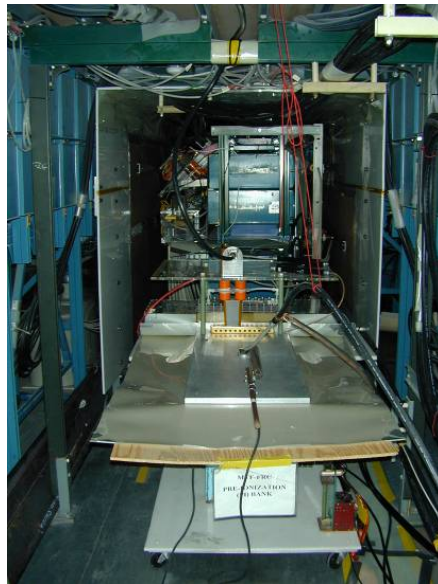
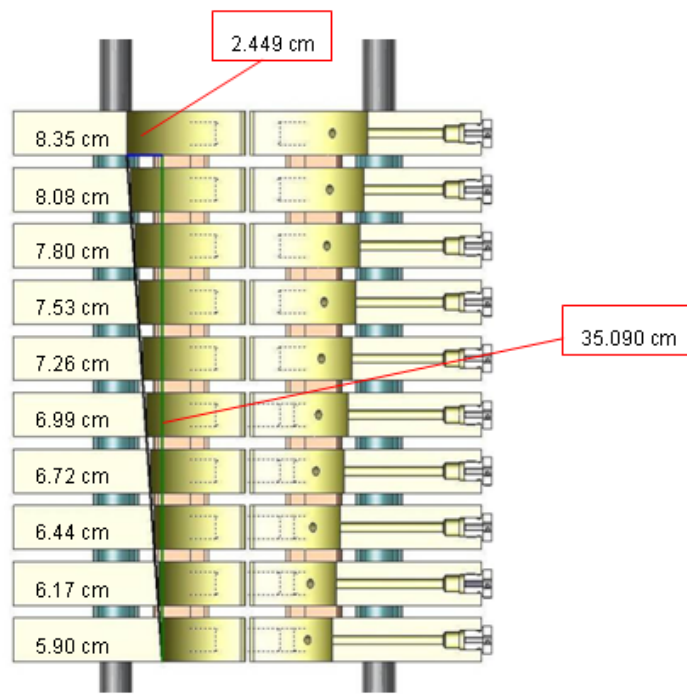
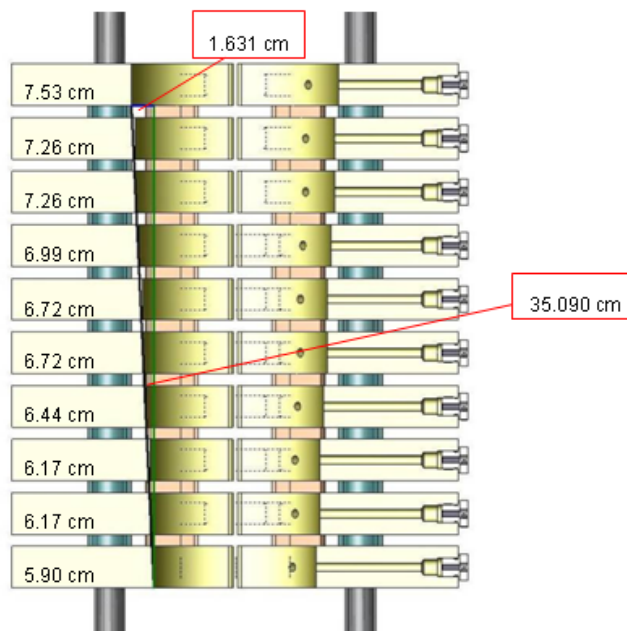


Figure 8. PI bank moved behind Main bank under B-Arm

Following the conclusion of previous static FRC formation tests the cylindrical Theta coil and much of the vacuum stand had been completely disassembled to prepare for build-up of the conical Theta coil and the addition of the Guide and Mirror coils. Figure 9a shows 4° cone angle cross-section; Figure 9b shows 2.66° cone angle cross-section.



(a)



(b)

Figure 9. Cross-section diagrams of initial (a) and final (b) conical Theta coils

This reassembly work commenced at the end of the summer of 2008, beginning with the Theta coil, and the Theta coil was re-assembled at that time with its bore having a 4° cone angle (Figure 9a). This cone angle was chosen based upon analyses performed by FRX-L personnel at LANL showing that an angle of this value would impart a sufficiently fast translation speed (10 cm/μs to approximately 20 cm/μs) to the FRC so that it could be injected into the liner and compressed well before its lifetime ended. This translation speed was later verified by experiments on FRX-L, in which personnel measured a velocity of approximately 14 cm/μs with a side-on optical fiber array that detected the light from the FRC as it passed by.

More recent modeling results obtained by NumerEx showed, however, that if the FRC were formed in a Theta coil with this cone angle during a compression-heating test it would not have sufficient momentum to pass through the lower mirror and enter the liner. This situation results because the lower mirror would have been compressed slightly and raised in amplitude due to the liner compression by the time the FRC reached it. To ensure that the FRC entered the liner it was necessary to have an average magnetic field in the Theta coil that was at least as large as the partially compressed lower mirror field, and so the bore angle needed to be reduced. Further simulations conducted by NumerEx personnel showed that unless the Main-bank-discharge current were increased, a reduced cone angle closer to 2.5° would be needed.

A review of the numbers of coil segments in our inventory and their inner radii showed that it was possible to fashion a Theta coil with a 2.66° cone angle (Figure 9b). NumerEx simulations confirmed that forming the FRC with such a cone angle would now allow sufficient momentum to be imparted to it. Furthermore, the velocity at which it would be launched up into the liner would not be significantly different from that which would have been provided by the 4° cone-angle coil. AFRL and SAIC personnel, therefore, disassembled the top eight segments of the Theta coil (because the lower two were the same for both cone angles) and reassembled the coil with the segments necessary to form the 2.66° cone angle. Figure 10 shows the coil.



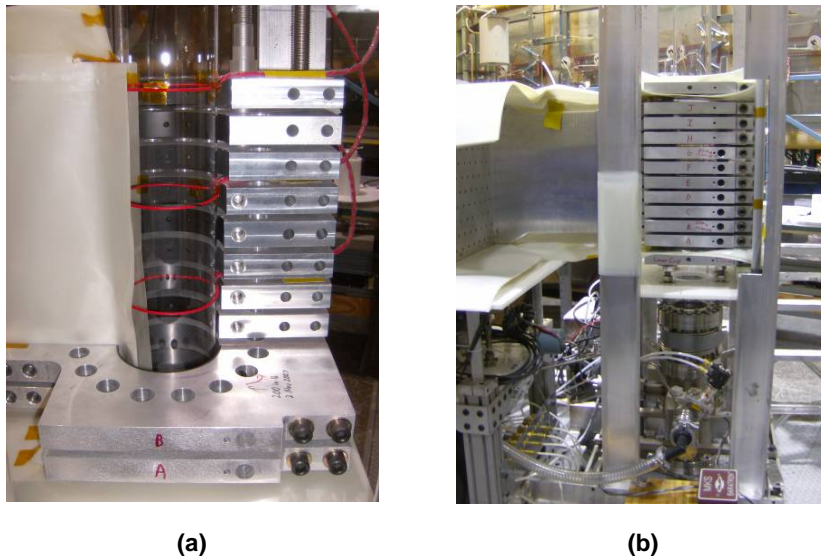


Figure 10. 2.66° conical Theta coil (a) partially assembled; (b) after assembly was complete

Figure 10a shows the coil when only the back half of the top eight segments had been reassembled, illustrating the profile of the coil bore. Flux loops were placed at segments D, G, and J. Figure 10b shows the coil when the coil assembly had been completed.

As the Theta coil was being reassembled with a bore cone angle of 2.66°, SAIC personnel were also completing the assembly of the first Guide and Mirror coil set. The original design prescribed by FRX-L personnel (Figure 11) called for three Guide coils distributed over the FRC translation region, two “Mirror 1” coils at the base of the liner to provide the lower mirror field, and two “Mirror 2” and three “Mirror 3” coils stacked together around the upper half of the liner to form the upper mirror. (The Mirror 2 coils are pulsed with opposite polarity to all the other coils and help to form the “pocket” in the liner region in which to capture the FRC.)

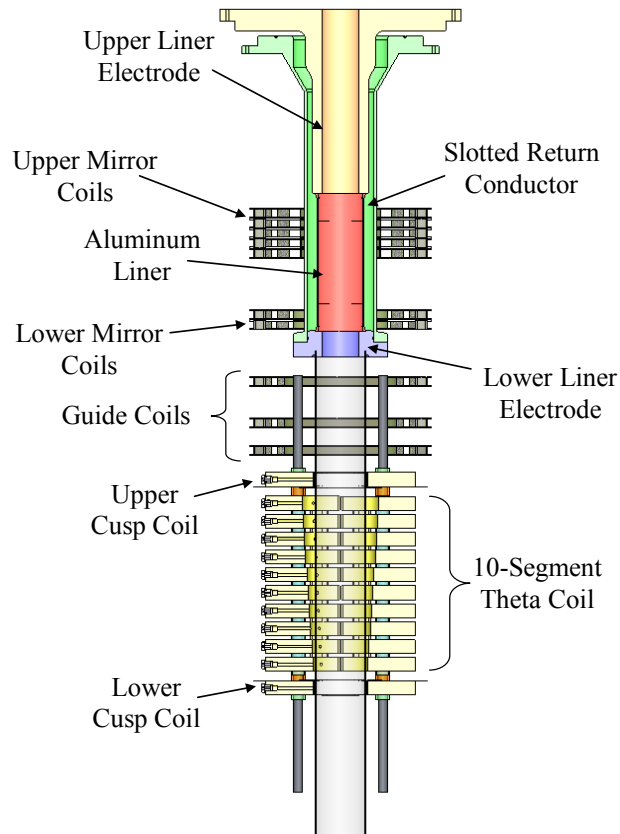


Figure 11. Arrangement of the various field coils around the quartz tube and liner for FRCHX

The modeling results from NumerEx, as well as independent Comsol calculations that were being conducted by AFRL personnel, indicated that the upper mirror field was actually needlessly large. As a result, it was suggested that one of the Mirror 3 coil segments be removed and the two Mirror 2 segments be moved up to fill the empty space. This change thus had the secondary benefit of reducing the number of coils by one that would have to be fabricated for each FRC compression-heating test. Figure 12 shows the first Guide and Mirror coil set after this change had been implemented.



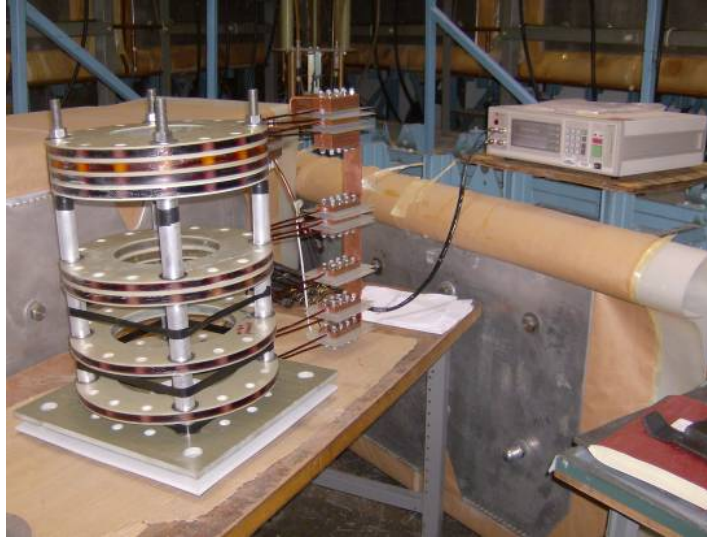
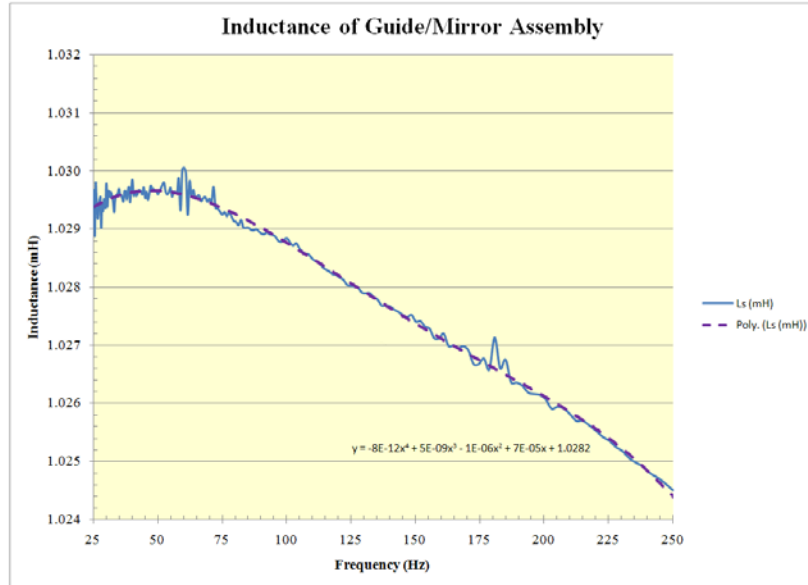
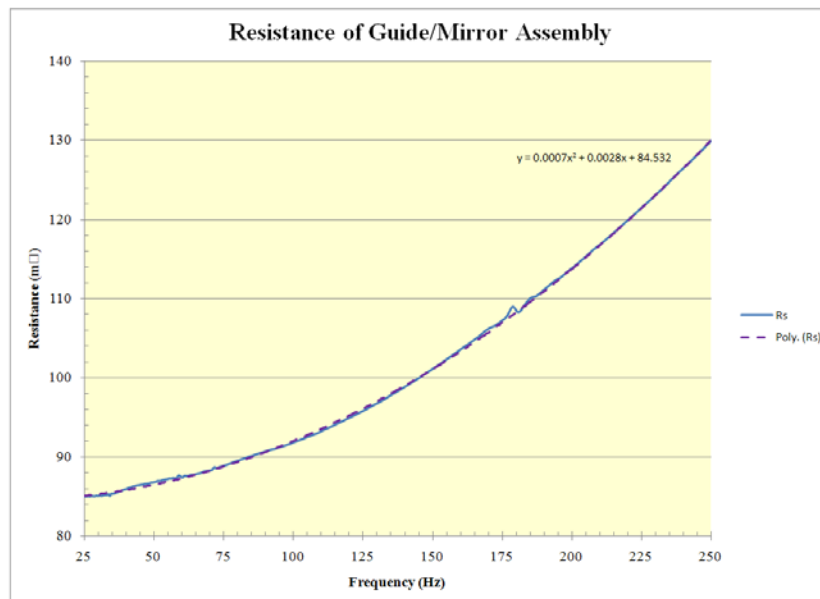


Figure 12. First Guide and Mirror coil assembly, while characterization measurements were being performed. Before placing the coil assembly on the vacuum and field coil stand, the inductance and resistance of the coils were measured with a QuadTech LCR meter to characterize the coils and enable an accurate circuit model to be developed for the Guide/Mirror bank. Figure 13 shows plots of the inductance and resistance as a function of frequency from 25 to 250 Hz. A curve fit for each trace was calculated by Excel, shown as a dashed line in the respective plots, along with the analytical equation for the curve fit. As can be seen, the inductance varies by only 0.5% over this frequency range; using the upper value for the inductance, approximately 1.03 mH, and the Guide/Mirror bank capacitance of 12 mF, an oscillation frequency of approximately 45 Hz is roughly estimated for the Guide/Mirror bank circuit, which corresponds to a quarter-cycle rise time of 5.5 ms.



(a)



(b)

Figure 13. (a) Inductance; (b) resistance for first Guide and Mirror coil set

Once the QuadTech measurements were completed, the coils lifted by crane as one unit and guided into place around the quartz tube on the vacuum and field coil stand. Figure 14a shows Voss Scientific technicians during the moving process. Figure 14b shows a view after the Guide and Mirror coils were set in place.



(a)



(b)

Figure 14. (a) Moving Guide and Mirror coil assembly to the vacuum and field coil stand; (b) assembly in place above Theta coil

The motivation for performing the FRC formation, translation, and capture tests before the field-compression test was twofold: (1) it was desired to verify as soon as possible that we were forming, translating, and capturing FRCs with the appropriate parameters, such as density, temperature, and lifetime, needed for the FRC compression-heating test; and (2) the FRC parameters measured in these tests would be extremely useful in benchmarking the NumerEx simulation results and would allow NumerEx personnel to refine their calculations further and improve their predictive capabilities for the FRC compression-heating test. Given the desire to start testing quickly, it was not possible to produce a realistic mockup of the liner, electrodes, and return conductor to allow these tests to be truly representative of the FRC compression-heating test. To benchmark and refine the simulation models, however, this mockup was not necessary. All that was needed was to provide an accurate description of the geometry that we did have to NumerEx personnel, and we would then be able to compare results. Furthermore, while FRC parameters might vary once the liner and other hardware was introduced, it did not seem likely that there should be gross variations.

Therefore, a much longer quartz tube was installed in the vacuum and field coil stand for these tests, i.e., one that extended above the upper mirror coils. A 20-in. length of stainless steel pipe

having a 6-in. (15.24 cm) O.D. and a 0.205-in. (5.21 mm) wall thickness was placed around the tube in what would be the FRC translation and liner and compression regions (Figure 15). This pipe would act as a flux conserver for the FRC to keep it from expanding once it entered the region. With regard to its effect on the diffusion of the Guide and Mirror fields through it, its thickness was approximately equivalent to 0.038 in. (0.98 mm) of aluminum, and therefore appropriate for loosely mimicking structural conditions around the middle of the liner region. (Note that at the ends of the liner, where there are much thicker flanges and/or electrodes, the stainless tube was not an appropriate approximation.) In Figure 15, the radial separation between flux-conserving tube and the quartz tube is 0.635 in. allowing for easy placement of flux loops.

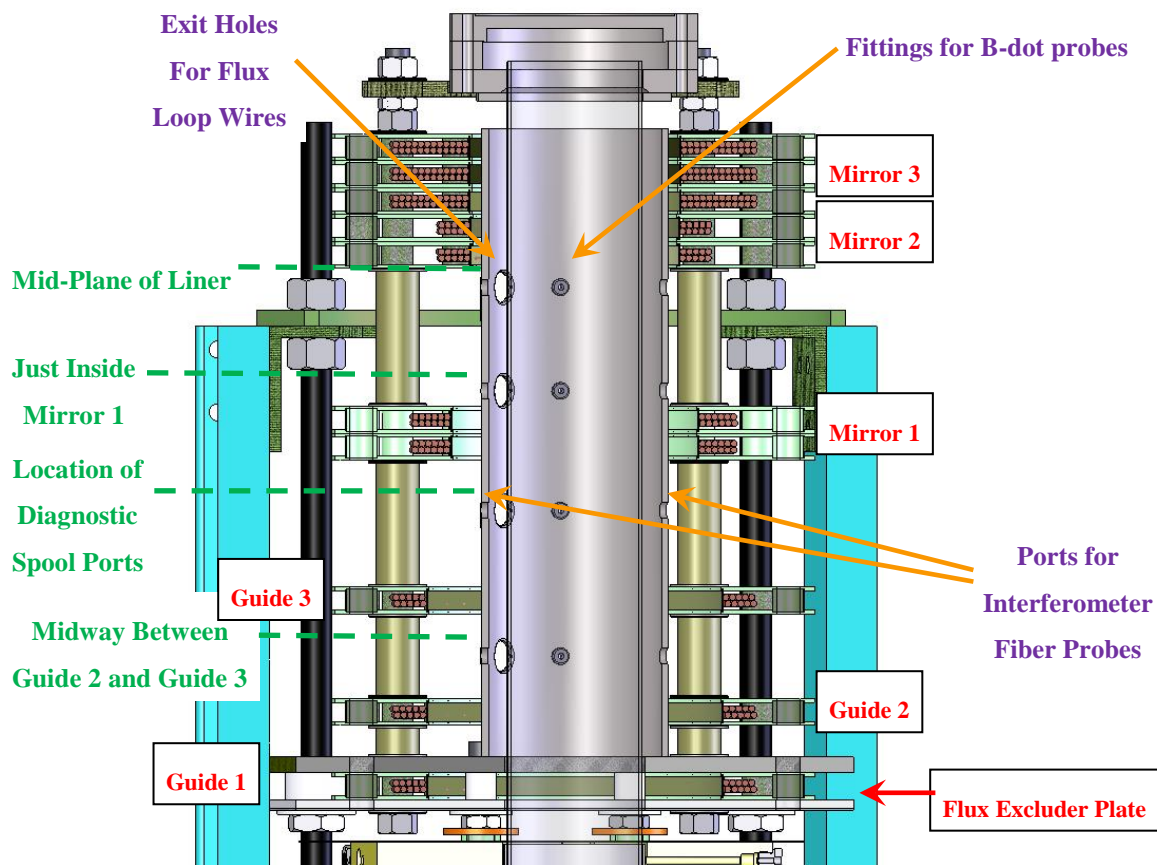


Figure 15. Cross-section of translation and liner and capture regions of vacuum and field coil stand

The use of a quartz tube throughout the entire length of the translation and compression regions facilitated optical diagnostic access throughout this entire length. To take advantage of this capability, holes 90° apart at four axial locations were placed in the walls of the stainless steel

pipe to allow for insertion of interferometer beams and the mounting of B-dot probes and side-on optical fiber array fibers. In addition, flux-loop wires were wrapped around the quartz tube and brought out a larger fifth hole that was placed in the pipe wall.

Figure 16 shows the vacuum and field coil stand taken during and after the stainless steel pipe was put in place.

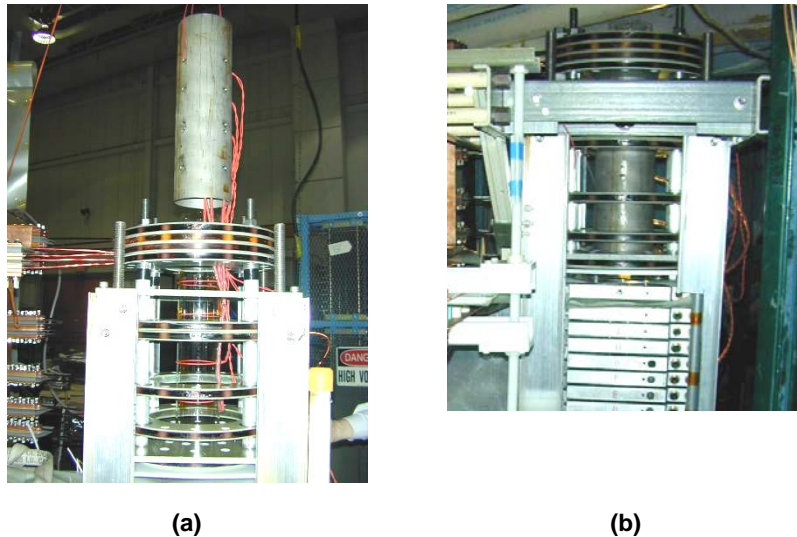


Figure 16. (a) Flux-conserving tube being lowered into place; (b) tube in place on vacuum and field coil stand

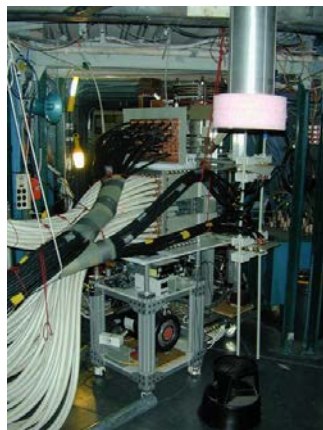
In Figure 16a, the flux-conserving tube was lowered into place by crane; before lowering it to the level of the quartz tube the flux-loop wires were fed through the ports for these wires in the tube. In Figure 16b, the flux-conserving tube is shown in place on the vacuum and field coil stand.

After the flux-conserving pipe was placed around the upper quartz tube, the assembly of the field coil and vacuum stand was essentially complete, and it was moved down the A-Arm of the Shiva bank and into position at the south side of the load section. Once there, our efforts centered on completing all the cable and gas-line connections to the Main and PI banks and the vacuum and field coil stand. The rest of Section 3.1.1 highlights this work. Because it was the first move of the banks and the vacuum and field coil stand, there were a number of new gas lines, control lines, and diagnostic lines that had to be run and that will not have to be run again in the future. Thus, it should be possible to implement future transitions between the “retracted” and “inserted” test positions somewhat more expediently.



The RG 17/14 transmission-line cables coming from the Main and PI banks were moved into place with their respective banks and were therefore immediately ready to be connected to the Theta coil-cable header. However, the bias cables, as well as the YK 198 cables for the upper and lower cusp banks, had to be rerouted from their overhead cable trays over to the B-Arm catwalk and then run under the catwalk to the Shiva load section. Because the Guide/Mirror bank had not been operated before, the YK 198 cables for it had to be connected to the bank-cable headers first, and then run to the Shiva load section under the B-Arm catwalk.

As soon as the cables were in place at the vacuum and field coil stand, personnel began connecting them to their respective cable headers. Figure 17a shows the stand once all the transmission-line cables had been connected. Figure 17b shows a photo of the transmission-line-cable supports that were fabricated to guide the bias and Guide/Mirror cables from the bank-cable headers to the floor by the catwalk. The upper and lower cusp cables, being fewer in number, were easier to run; they were run from their respective headers to the floor, being secured to a wooden support already attached to both bank frames, and then run west along the floor over to the B-Arm catwalk. A wooden tray with a cover was fabricated to protect them from foot traffic. Figure 17 shows the rerouting and extensive numbers of connections that had to be made for the many transmission-line cables.



(a)



(b)

Figure 17. (a) Vacuum and field coil stand after cables for all banks were connected; (b) supports for Bias and Guide/Mirror bank cables attached to B-Arm catwalk

Duplicate sets of RG 218 cables were fabricated for the PI bank and the Main bank closing and crowbar switches, which allowed the original cables to be left in place in the overhead cable trays running to the retracted position. Their ends were simply disconnected from the trigger units and secured to something out of the way. Duplicate charging cables were also fabricated with the originals being left in place in the cable trays, as was done with the trigger cables. A new cable tray running from the triggering and charging systems over to Shiva B-Arm was then fabricated to take the new cables to their respective banks. Figure 18 shows the Main and PI bank charging and trigger cables coming together in a bundle on the new cable tray (center, background), which takes the cables over to Shiva B-Arm to where the banks have been moved.



Figure 18. Trigger and charging cables on new cable tray

Efforts were also made at this time to move the PI bank 40168 trigger amplifier into a shielded enclosure, much like the one in which the crowbar switch 40168 was placed. These efforts were made because the bank-trigger-timing scenarios for an FRC compression-heating test may possibly require the Shiva bank to be triggered before the PI bank. Experience with the crowbar 40168 trigger amplifier earlier showed that the unit was prone to pre-trigger with either the Main or PI bank triggers due to the noise generated by these triggers, until it was placed in its present enclosure. Because the noise generated by the Shiva triggers was expected to be at least as intense if not more so, it was felt that it would be wise to prepare such an enclosure for the PI 40168. The enclosure was fabricated using the same size Hoffman box (Figure 19). Power filters

and a cooling fan were added inside, and a number of cut-off waveguide and optical fiber feedthroughs were placed on the back to allow compressed air, pneumatic control, and the high-voltage-output lines to enter and exit the box. In Figure 19, the crowbar switch 40168 enclosure, which was the model for the PI enclosure, can be seen in the background.



Figure 19. PI 40168 trigger amplifier in Hoffman enclosure

Care was taken to maintain the same grounding scheme that had been established when the Main and PI banks and the vacuum and field coil stand were in the “retracted” test position. Namely, all banks and trigger systems are tied to building ground, but these grounds are lifted during a shot, and the only ground that is maintained continuously, even during a shot, is the one on the return side of the Theta coil. Thus, copper ground straps were run to the new locations for the PI and Main banks from the same building grounding point, and these straps were tied to the Ross relays on the banks to allow these grounds to be lifted just before a shot. Similarly, the return side of the Theta coil was tied to the fourth data-cable conduit that had recently been run to the Shiva load section from the data acquisition box (discussed later in this section), as the data cable conduits have a single-point connection to the building ground.

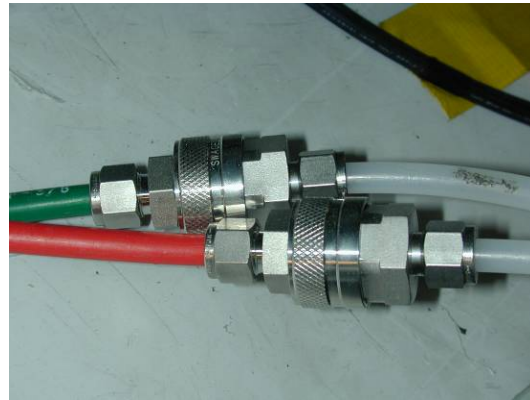
As mentioned earlier, it was decided to run new gas lines for the PI and Main banks rather than attempt to reroute the existing lines over to the new bank locations. This action was done to simplify transitions between the two test locations in the future. The new SF<sub>6</sub>/Ar supply and return lines for the rail-gap switches on these banks were simply teed into the old lines attached



to the back of the FRCHX gas-control panel under Shiva C-Arm. These new lines were then run through a PVC conduit, which had been put in place a few years ago for data cables, to the Shiva load section (Figure 20a). Similarly, a compressed air line for the crowbar-switch-peaking gaps and an SF6 line for the Main, PI, and Theta coil cable headers were teed into their existing lines and run with these other gas lines to the Shiva load section. After emerging from the PVC conduit at the Shiva load section, the gas lines were then run to their appropriate locations. Quick-connect fittings with shut-off valves were placed on the ends of both the new and the old gas lines, and the appropriate mating fittings were placed on short lines running to the switches (Figure 20b). Aside from making the gas line connections very quick before or after a move, the quick-connect fittings on the unused lines served to seal them off.



(a)



(b)

Figure 20. (a) Gas lines run to inserted test position; (b) fittings for shutoff valves

The deuterium and dry nitrogen gas bottles were moved from the retracted test location to the end of Shiva C-Arm to shorten the amount of line needed to run to the vacuum and field coil stand (Figure 21). A plastic gas line for the dry nitrogen was then run along with the bundle of other lines in the PVC conduit, and a new length of 0.25-in. stainless steel tubing was run along the center of the ceiling of Shiva C-Arm to carry the deuterium to the vacuum and field coil stand. Lastly, to actuate the plenum and vacuum valves on the vacuum and field coil stand, a new house airline was run through the Shiva support structure and the cable trays over to a valve in a cable tray along the north wall of the high bay.



Figure 21. Dry nitrogen and deuterium bottles moved under C-Arm next to SF<sub>6</sub> bottle

With the exception of two pneumatic control lines that are connected to switches on the Main bank, we followed the same concept of running a second set of pneumatic and fiber optic control lines for systems in the inserted test position as was done for the switch and cable-header gas lines. The new pneumatic lines were teed into the existing lines at a convenient point in the cable trays near the Compact Field Point (cFP) controller. Because there is not a convenient way to tee into an optical fiber, the new fiber optic lines were run directly to the cFP controller, and the old lines were disconnected and tied up out of the way. As with the switch and cable header gas lines, quick connect fittings with shutoff valves were placed on the ends of both the old and new pneumatic control lines, and the appropriate mating fittings were placed on short lines running to the pneumatic switches on the vacuum and field coil stand or other component (Figure 22). The quick-connect fittings would simplify the transition between the inserted and retracted test positions.



Figure 22. Quick-connect fittings

When the remote data acquisition box was first set up, provisions were made for a fourth data-cable conduit that would be run to the Shiva load section for use during testing in the inserted test position. A portion of that fourth conduit was even run at that time (as far as Shiva C-Arm) but was not completed. During this past quarter, personnel completed that run of conduit, prepared and pulled 25 RG 223 data cables for the conduit, and fabricated a patch panel for the cables at the end of the conduit. Because of the numbers of diagnostics such as B-dot probes and flux loops planned for the vacuum and field coil stand, the Main and PI bank diagnostic data cables were not run to this new patch panel but to one of the other patch panels located near the FRCHX power supplies and trigger units. The length of the run to this other patch panel required that personnel fabricate several additional RG 223 patch cables for these diagnostics, but the connectors and cable were already in house.

Once all the pneumatic and fiber optic control lines were reconnected to their proper system components, SAIC personnel began checking the control-system operation to make sure everything still performed as it should. First, all the control and status channels for the cFP controller were checked individually to verify proper operation of the lines, as well as proper operation of the particular component that was being controlled. Then, the LabVIEW<sup>®</sup> control program was stepped through its charging and firing and sequences for the Main, PI, and Guide/Mirror banks to verify proper operation of the bank components at their proper times. This

checking was actually the first such test for the Guide/Mirror bank, as this bank had not been brought on line up until this point.

After completing the control-system checks, “live” tests with the Guide/Mirror bank discharging into the Guide and Mirror coil load started right away, because this bank would be needed for the field-compression test, and it had not been operated before. A problem with getting all six of the bank modules to fire was uncovered on the first day of testing, but it later turned out to be a problem with a charging connection between two of the modules. The bank performed as expected after the connection was fixed.

Before any experiments were performed with either the formation, translation, and capture test setup or the field-compression test setup, having a knowledge of the axial field profile in these test setups was desired. As a result, a modular field-mapping probe package having two 10-turn, large-area B-dot probes backed up by two Hall probes was designed and fabricated. The B-dot probes were wound on nylon spools using 20 AWG magnet wire, with a loop diameter of 1.0 in (2.54 cm). The Hall probes are BH-700 series probes (specifically, model # BH-704) manufactured by F. W. Bell and are mounted on one side of the large-area B-dot probe spools. An external battery box was assembled, as well, for the two Hall probes to provide the 100 mA of control current they need. The box has two independent regulated current supplies, one for each probe, that are each powered by two 9-V batteries.

Figure 23 shows SolidWorks<sup>®</sup> drawings of the field-mapping B-dot probes.

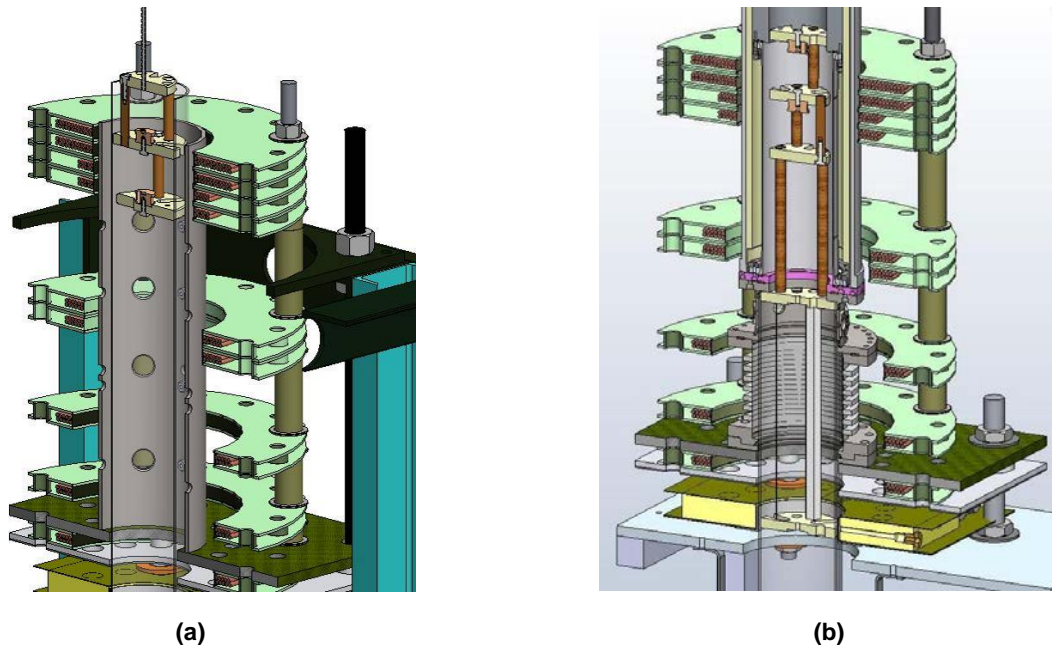


Figure 23. (a) Formation, translation, and capture test setup; (b) field-compression test setup

The support structure for the probes was such that it could be assembled for use within the 10.5-cm-diameter quartz tube of the formation, translation, and capture setup (Figure 23a) or within the 10-cm-diameter solid liner, which has 8-cm-diameter apertures on each end (Figure 23b).

When beginning the field-mapping measurements, the probes were placed first at the top of the liner and capture region (Figure 23a) and moved downward in 1.5-in. (3.81 cm) increments until the lower probe reached the first Guide coil.

Figure 24 shows the probe package assembled for making measurements within the formation, translation, and capture setup.

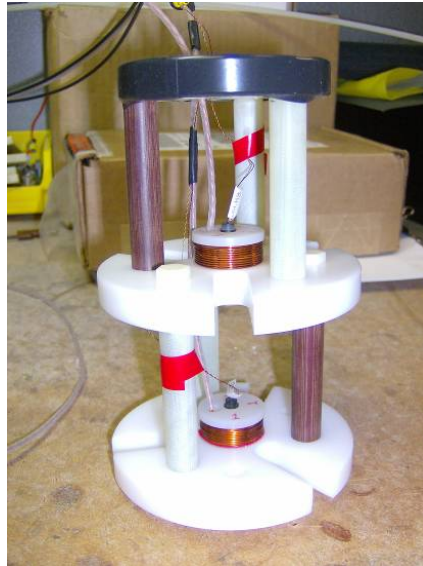


Figure 24. Field-mapping probe assembly configured for making measurements in formation, translation, and capture test setup

Figure 25 shows a plot of selected data that was recorded during this mapping exercise vs. the axial position of the probes.

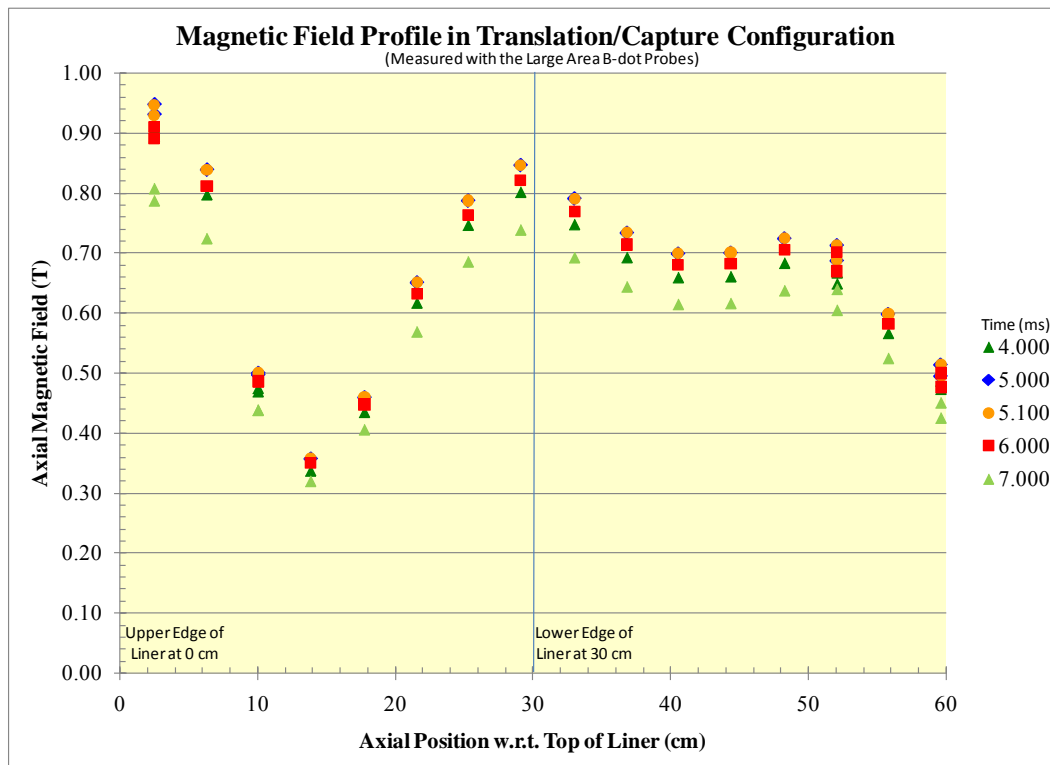


Figure 25. Field map for the present FRC formation, translation, capture test setup using large-area B-dot probe data

The data is from the large-area B-dot probes, and each data set shown corresponds to a different time after the start of the Guide/Mirror current pulse. We see that the largest field appears at approximately 5.1 ms; this time compares with a time of approximately 4.83 ms observed for the peak of the Guide/Mirror bank current pulse. As indicated in the graph, “0 cm” corresponds to where the top of the liner would be, and “30 cm” corresponds to where the bottom of the liner would be. The Guide/Mirror bank was charged to 2 kV for these tests, so to achieve the desired 2T peak for the upper mirror field the bank will have to be charged to slightly greater than 4 kV.

A few tests were performed at 3 kV and one at 4 kV during the field-mapping exercise, and it was noted that the upper set of four coils (the Mirror 2 and Mirror 3 coils) began to exhibit signs of cracking and bulging. (We recall that the Mirror 2 coils are being driven oppositely to the Mirror 3 coils to shape the FRC capture region, and therefore the coils are repelling each other.) Additional all-thread stubs were placed in the unused holes around the perimeter of the coils, and nuts and washers were placed on the top and bottom to clamp the coils together better. Unfortunately, the repulsive forces acting on the coils are closer to the inner radii of the coils, because that is where the windings are physically located (Figure 23a).

### **3.1.2 Vacuum Magnetic Field Compression**

The primary impetus for performing magnetic-field-only compression tests was to determine the magnetic field’s effects on the liner, specifically how uniform the implosion of the deformable contact liner would be with a strong magnetic field inside it, as well as at what time instabilities might develop in the liner and what factor of field compression could be obtained. The first test, designated FRCHX-1, was conducted on 19 December 2008. There were multiple failures on that test. They were corrected and a second field-compression test, FRCHX-2, was conducted on 1 April 2009. This test was generally successful. Preparations for the two tests, diagnostics, and results are presented in the following sections.

#### **3.1.2.1 FRCHX-1**

Two serious problems arose during the test that prevented it from yielding the desired information. The first problem was that the Guide/Mirror bank did not fire during the test, and therefore the liner did not have a magnetic field in it when it started imploding. It is felt that the

LabVIEW control program prematurely entered a dumping and safing sequence for the bank, one of the first steps of which is to turn off the trigger units for the bank. This action would explain why the bank-charge voltage was observed to begin a slow decay just a few seconds before the trigger was to occur and why even with approximately 3.3 kV remaining voltage on the bank it did not trigger at all when the command trigger was sent. The second problem, which ultimately made the first problem of no consequence, was that solid dielectric insulation in the current feed to the liner failed, apparently at an overlapped joint between two insulator pieces. The failure is attributed to either not enough Vi-Sil™ encapsulant being present at the dielectric joint to displace all the air in the joint, not enough weight on the dielectric joint after the Vi-Sil was put down to keep the dielectric seal intact, and or not enough of an overlap between the two solid dielectric pieces.

#### *3.1.2.1.1 Shot Preparation*

Here, we discuss preparation for the field-compression test, specifically the hardware design, the setting up of the Guide and Mirror coils around the liner hardware, and magnetic field mapping that was conducted in this test setup, respectively. Then we describe the various diagnostics fielded for this test and the procedures followed for setting them up and calibrating them.

Though this test did not perform in the desired manner, the results that were obtained with the diagnostics are also briefly discussed, as they provided some valuable information with regard to baseline noise levels, signal levels, and light intensities that can be expected for subsequent tests.

1. The liner assembly was designed and fabricated to support the liner while maintaining adequate vacuum and enable passage of electrical current with the lowest possible resistance (Figure 26).



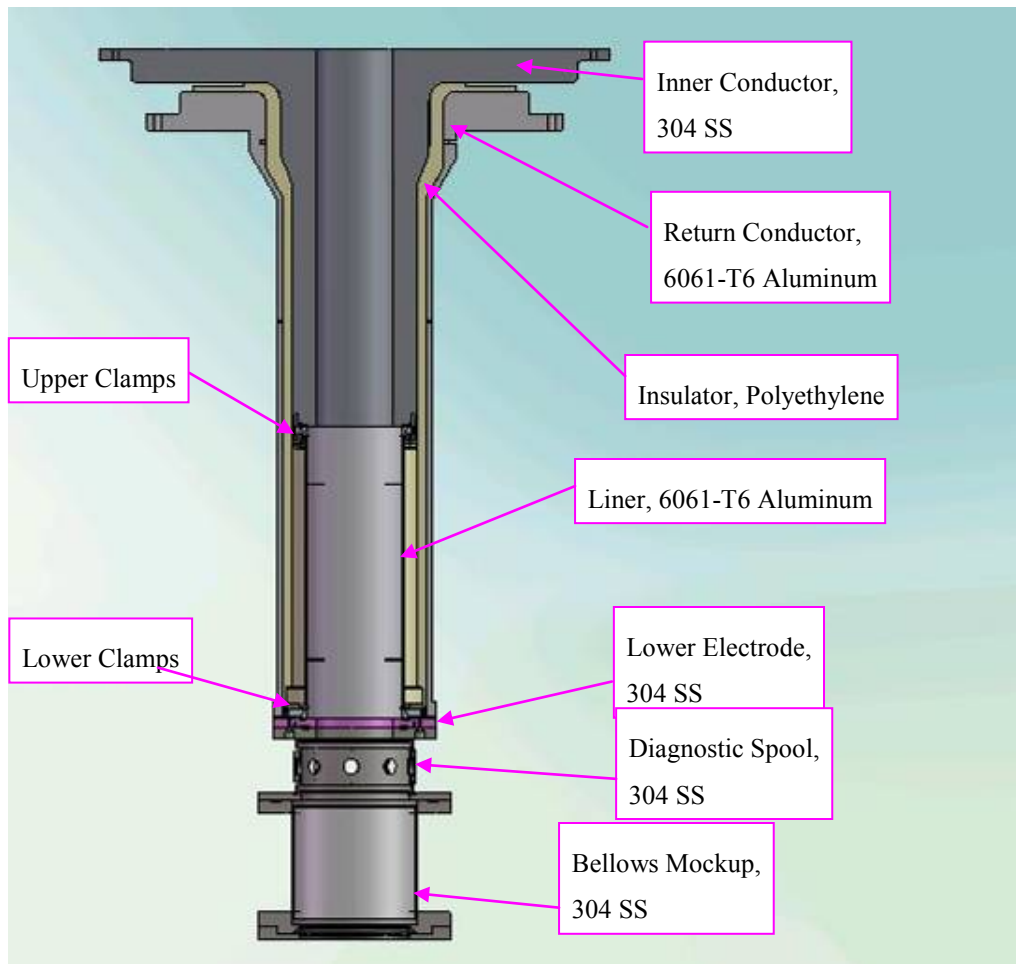


Figure 26. Cross-section diagram of liner assembly

Not shown are the quartz tube and lower B-dot probe package. Sixteen axial slots were placed in the return conductor to allow the Mirror fields to penetrate more quickly into the interior of the liner. The basic sequence of assembly was as follows:

2. Insert insulator into return conductor
3. Raise return conductor, with insulator, and attach to lower Shiva current-feed plate
4. Insert inner conductor using overhead crane, and attach to upper Shiva current-feed plate
5. Insert liner and upper clamps. Use centering ring to center bottom of liner in return conductor while tightening screws at upper clamps (See Figure 27)
6. Attach lower electrode
7. Attach diagnostic spool

8. Install magnet assembly underneath, and raise up as much as possible
9. Move table into position underneath liner assembly
10. Lower magnetic assembly to table and attach
11. Install diagnostic spool
12. Install bellows mockup

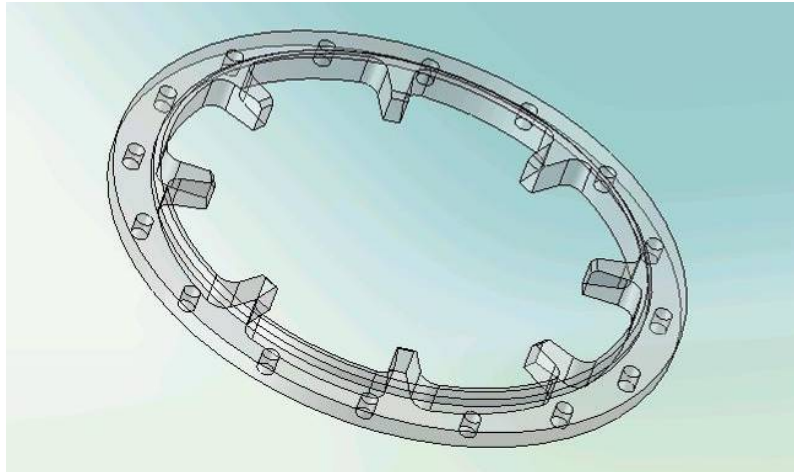


Figure 27. Centering ring, acrylic

The liner was secured to the inner conductor by clamping two G-10 half-rings with a titanium clamp ring, which was then covered with an aluminum cap ring to round the sharp edges of the clamp ring (Figure 28). A conical surface on a circular nib at the upper end of the liner was pressed into a mating conical groove in the inner conductor to provide tight contact for low electrical resistance. The configuration takes advantage of current induced electromagnetic force to improve the contact as the current ramps up.

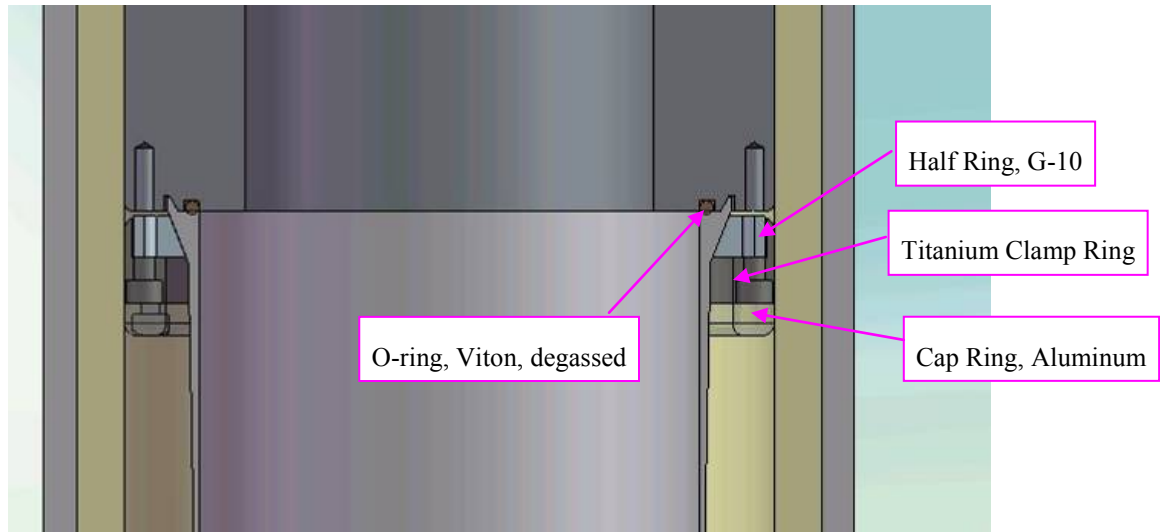


Figure 28. Upper clamp detail

The configuration of the lower clamp, shown in Figure 29, was similar to the upper clamp. A separate cap was not required because there was room to radius the corners of the lower clamp ring.

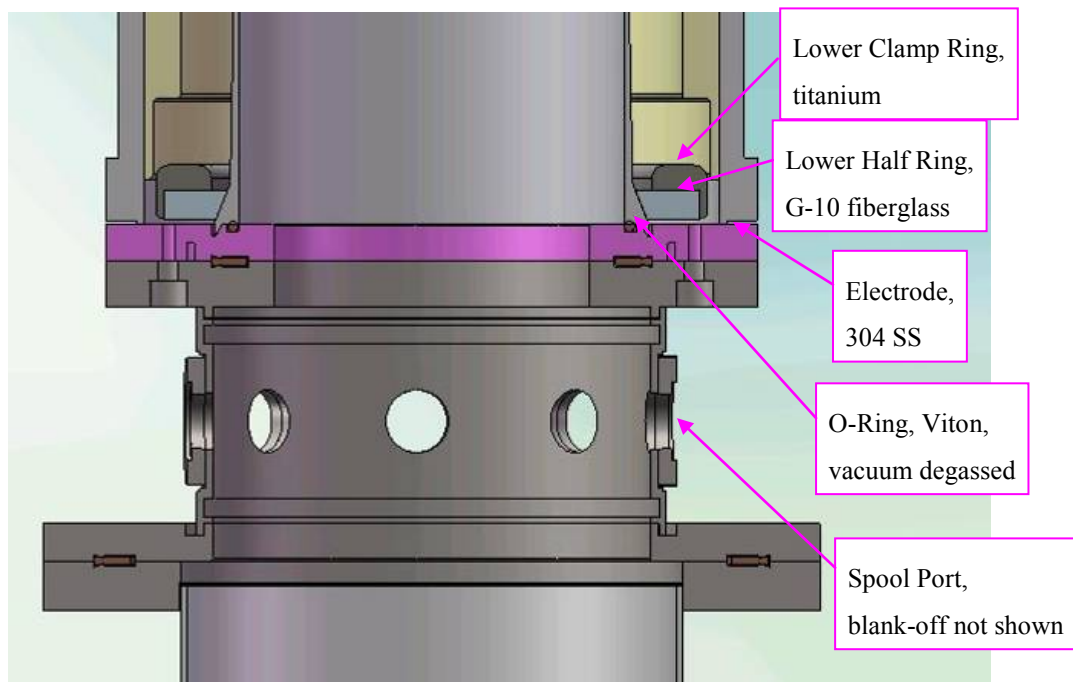


Figure 29. Lower clamp and diagnostic spool

A mock bellows, shown in Figure 30, was attached below the diagnostic spool (Figure 31) and the final vacuum seal to the quartz tube and B-dot probe package was made at the bottom of the

mock bellows. This so-called mock bellows consisted essentially of a rigid stainless steel tube with flanges attached at each end, and it served its purpose well.

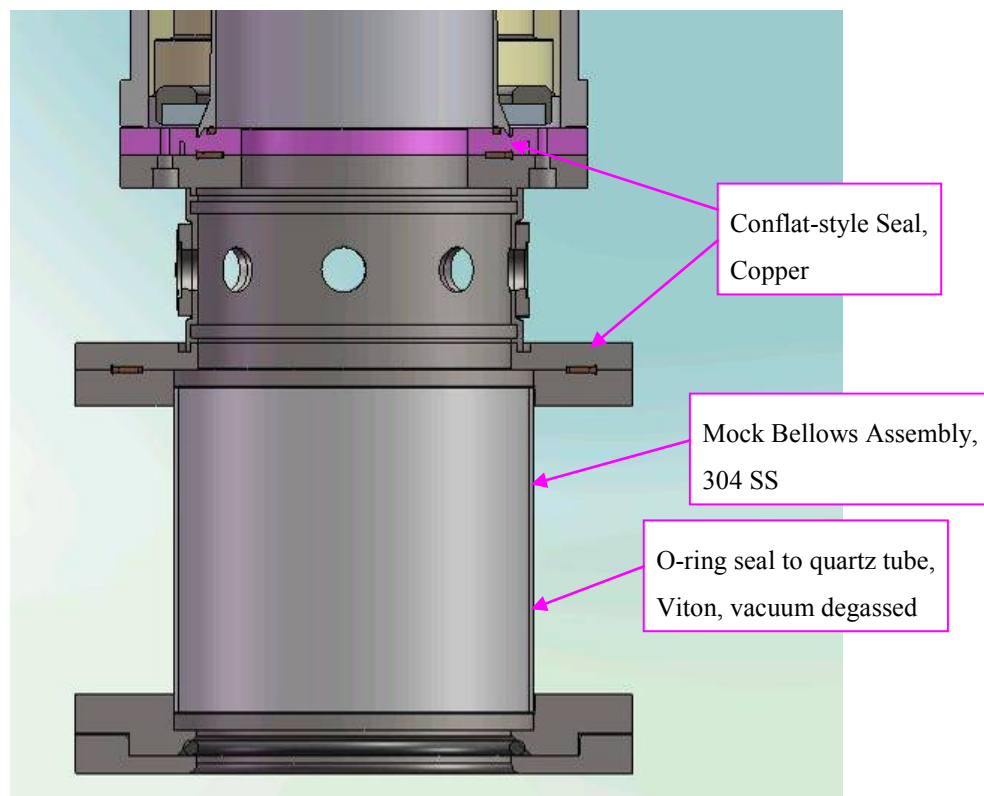


Figure 30. Close-up of diagnostic spool, mock bellows, and their vacuum seals

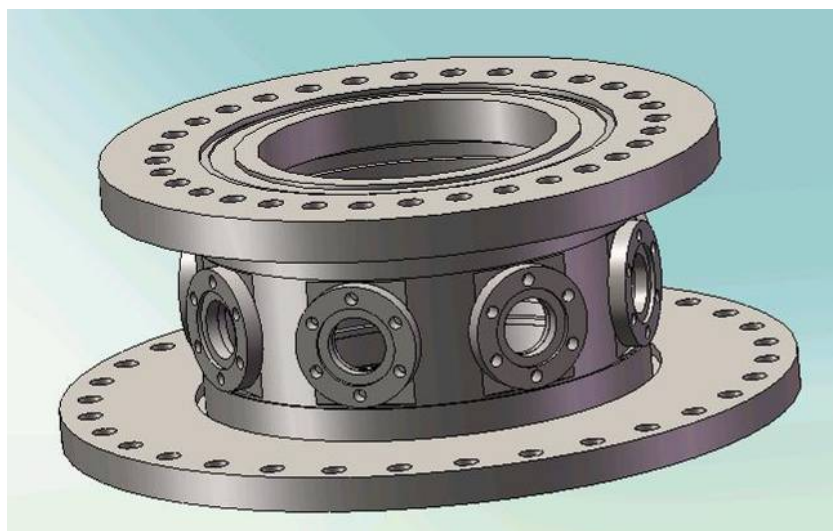


Figure 31. 3D view of diagnostic spool

Because of the desire to move forward with FRC formation, translation, and capture tests while preparations were simultaneously being made for the field-compression test, SAIC personnel began fabricating a second set of Guide and Mirror coils to be used in the field-compression test as soon as the first set was completed. The final coil assembly was nearly identical to the first, the only differences being that a flux-excluder plate was not placed below the bottom Guide coil (because there were no fast formation fields to be excluded), and a more robust clamping structure was placed above and below the set of upper four coils to keep them from deforming. However, a mock upper cusp coil was placed below the lower Guide coil to incorporate any effects that the large aluminum coil might have on the lower Guide field profile. It also served as a damage target during the field-compression test and supplied an indication of the amount of damage that the Theta and cusp coils might take during an FRC compression-heating test.

A new stand was now needed on which to place the coil assembly when it was time to put it into position around the liner and its return conductor because the original support stand was being used for the formation, translation, and capture test setup. A relatively simple 2 ft x 4 ft table was designed using “80–20” hardware. Wheels were placed on the table so that it would be easy to move into position, and once in the Shiva load section the table could be raised up using adjustable feet to set the Guide and Mirror coils at the appropriate height with respect to the liner hardware. Figure 32 shows the completed Guide and Mirror coil assembly and its support table after both had been moved into place around the liner and return conductor. Between the coils, 0.5-in. HDPE blocks were added at this time for additional strength against the magnetic forces.



(a)



(b)

Figure 32. Guide and Mirror coil assembly on support table, shortly before field-compression test

After the Guide and Mirror coils were moved into place around the liner and return conductor, the fields throughout the translation and liner and compression regions were mapped using the same large-area B-dot and Hall probe assembly that was described in previously, with the exception that it was configured this time as shown in Figure 23b. Figure 33 shows the probe assembly in this configuration.

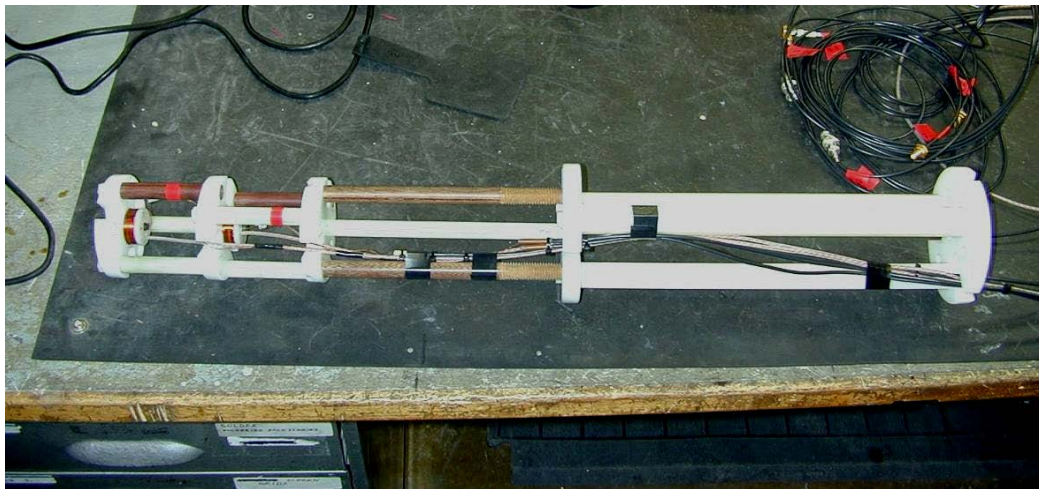


Figure 33. Probe assembly configured for making measurements in field-compression test setup



Figure 34 includes two more views of the probe assembly in the field-compression test setup while the fields were being mapped. A 34-in. long quartz tube was inserted up into the mock bellows and diagnostic spool as far as the bottom of the lower electrode (Figure 30) to serve as a guide for the field-mapping-probe assembly.

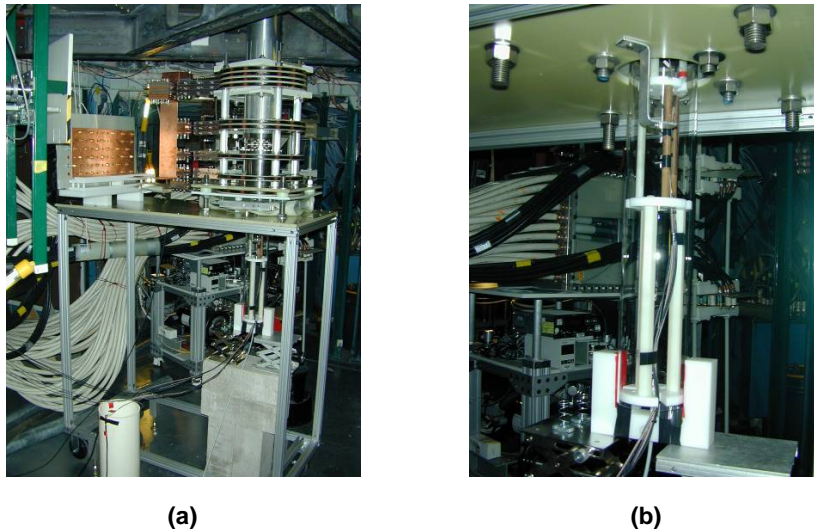


Figure 34. (a) Probe assembly below Guide and Mirror coils; close-up view under coil table showing probe assembly in place

When performing the field-mapping measurements this time, the probes were moved in smaller increments of 0.75 in (1.91 cm) to generate a map with a more refined resolution. The mapping of the upper B-dot probe spanned from the bottom of the lowest Guide coil to the top edge of the liner. Figure 35 shows a plot of selected large-area B-dot probe data that was recorded during these measurements.

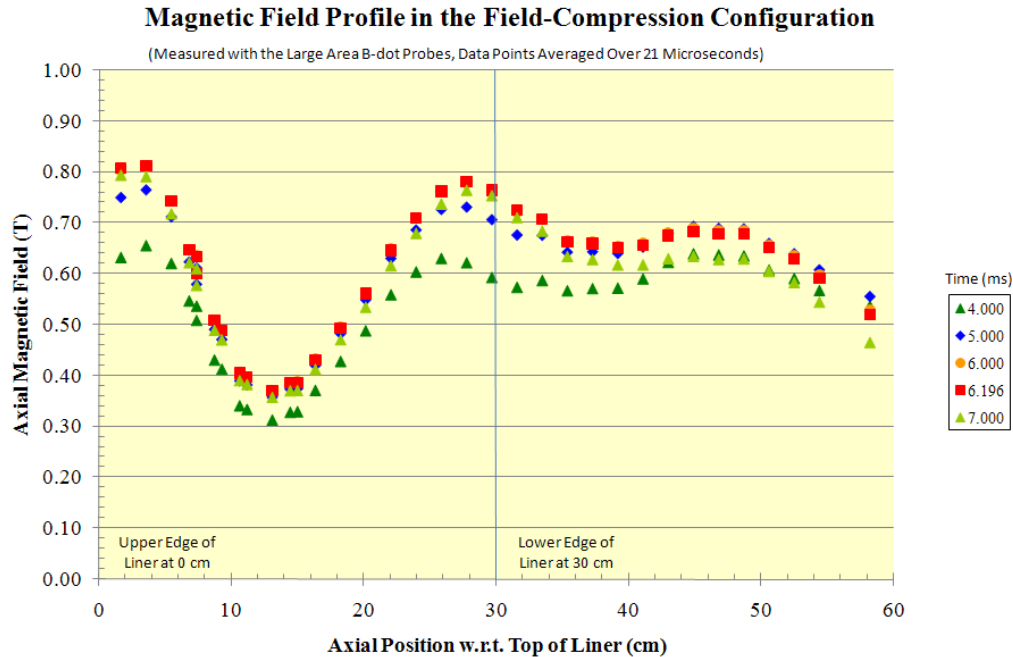


Figure 35. Axial magnetic field vs. axial position in the field-compression test setup

As with Figure 25, each data set in Figure 35 corresponds to a different time after the start of the Guide/Mirror current pulse. As is indicated in the graph, “0 cm” corresponds to where the top of the liner would be, and “30 cm” corresponds to where the bottom of the liner would be, and the Guide/Mirror bank was charged to 2 kV for each of these measurements.

We see that the largest field now appears at approximately 6.2 ms, compared to 5.1 ms for the FRC formation, translation, compression setup, and approximately 4.83 ms observed for the peak of the Guide/Mirror bank current pulse. Thus, on average the stainless steel flux conserver in the other test setup needed to be about twice as thick to provide the same magnetic field-diffusion time that the liner, return conductor, electrodes, and related vacuum hardware introduce. A secondary effect of the longer diffusion time is that the amplitude of the field on axis is reduced everywhere, by approximately 8%, compared to the formation, translation, and capture test setup. Figure 36 shows that by plotting several of the large-area B-dot probe waveforms together it can be seen that the diffusion time is not the same everywhere, which is, of course, due to the fact that the thickness of the surrounding structures varies along the length of the translation and liner and capture regions. The vertical line indicates the time of the field maximum for  $z = 3.513$  cm, the position having the highest measured field.



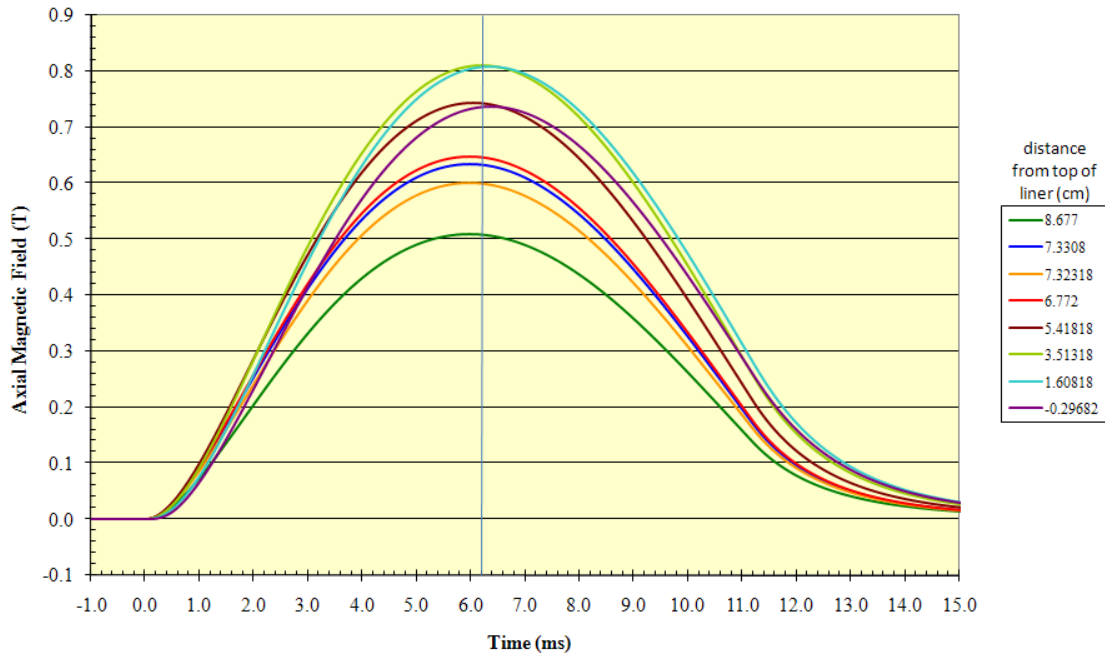


Figure 36. Axial magnetic field vs. time at several positions near top of the liner

While the data in Figure 25 and Figure 33 show that the axial magnetic field is generally reduced by approximately 8% in the field-compression-test setup, we note that the upper mirror is reduced considerably more, by approximately 14%. It is felt that the liner upper electrode is responsible for this decrease. NumerEx personnel are currently modeling this reduced upper mirror in their FRC compression-heating simulations to determine how much this hinders the FRC capture. However, we anticipate having to make some changes to the upper Mirror coil arrangement before performing the FRC compression-heating test to bring the amplitude of this mirror field back up.

Each of the field-mapping measurements in Figure 35 was performed with a Guide/Mirror bank-charge voltage of 2 kV. In preparation for the more immediate field-compression test, the charge voltage was increased and the field was measured at the peak field location (3.51 cm) to determine what charge voltage would be needed to achieve a field of 2 T.

Figure 37 shows a plot of the magnetic field vs. time for charge voltages of 2 kV, 3 kV, and 4 kV. At 4 kV, the peak field was only 1.7 T; using these data it was estimated that a charge

voltage of approximately 4.7 kV would be needed to inject a 2 T field into the liner at this location during the field-compression test.

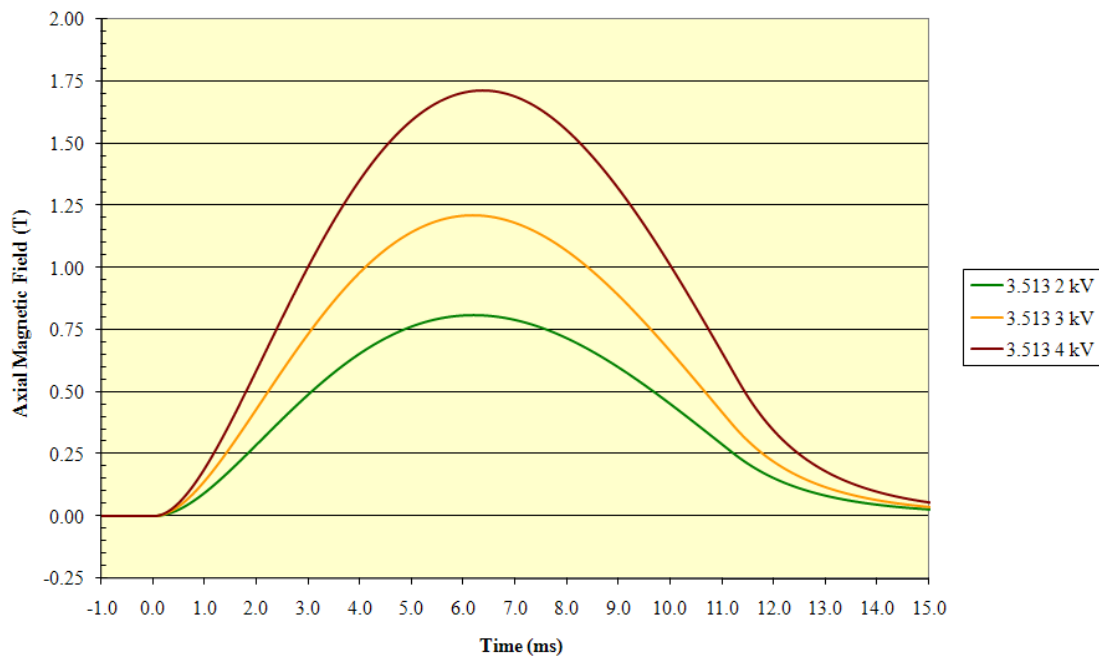


Figure 37. Axial magnetic field vs. time for three different Guide/Mirror bank-charge voltages

An attempt was not made to charge the bank to this voltage and measure the field one last time, as the upper four mirror coils had begun to exhibit signs of cracking again when the voltage was raised to 3 kV. Some of the pieces of the clamping supports also began to come apart. It should be recalled that this setup was a new set of coils that had not been tested until the field mapping began, and frequent inspections during the field mapping, with a 2 kV charge voltage, showed no signs of any problems. Thus, it was decided to save this last 4.7 kV test for the field-compression test for fear that irreparable damage might be done to the coils.

#### 3.1.2.1.2 Diagnostics and Test Results

We show a list of shot diagnostics categorized according to importance for this test and with the typical Shiva experiment diagnostics folded into it.

## Primary Performance Diagnostics

- Typical performance (pulsed power) diagnostics: Shiva arm and load Rogowski coils, load B-dot probes and V-dot probes, and Faraday rotation. Also included with these is the Guide/Mirror cable header Rogowski coil for measuring the total Guide/Mirror current.
- Axial B-dot probe array inserted into the liner to measure injected and compressed magnetic fields. These probes will need to be as small as possible, possibly sub-millimeter in diameter, so as to not perturb the liner as it approaches maximum compression.
- Radiography to provide side-on images of the liner. Two heads will be used, with two image times, and armored digital film packs. The images will show how axially uniform the implosion is, at least within the field of view, and give evidence of fluting if abnormal wall thicknesses are observed. Concerns about fluting in the liner during the implosion arise from the slots in the return conductor.
- Secondary Performance Diagnostics
  - Streak camera to look at luminosity of the liner surface. The optical path will be through one of the six-sided ports installed on top of Shiva, providing a quasi-axial view through the liner. Current thinking is that the liner will become self-luminous above 1-2 Megagauss.
  - Photodiode pair to look also at luminosity on the liner surface, but with much greater dynamic range and sensitivity. The optical path will also be through one of the six-sided ports installed on top of Shiva, again for a quasi-axial view through the liner.
  - Fast-framing camera for capturing a 2D record of the light intensity emitted from the liner surface, as well as an end-on image of the liner profile. The optical path will again be through one of the six-sided ports installed on top of Shiva. Concerns are that the slotted return conductor might cause fluting of the liner's surface, and the end-on 2D camera image would more clearly confirm or dispute that.

- Null measurements: a B-dot probe-flux loop pair typically used for FRC flux-exclusion measurements, and one of the fibers from the side-on optical fiber array.

The designation of “primary” or “secondary” was decided as follows: The primary diagnostics were those critical to confirming that the liner successfully imploded and that the field compression was of sufficient magnitude to adequately compress an FRC. The secondary diagnostics were those that would possibly provide additional scientific information of interest during this test, but would certainly become “primary” diagnostics on the subsequent FRC compression-heating experiment. Thus, the performance of this field-compression test was an opportunity to bring many of the FRC compression-heating experiment diagnostics on line early and obtain information regarding baseline noise, signal amplitudes, and light intensities that could be expected; all of which would be useful in preparing for the FRC compression-heating test.

We discuss each of these diagnostics, with the exception of the null measurement diagnostics, as their set-up and operation has been described in past reports on this work, is discussed in more detail in the sub-sections that follow.

The usual complement of Shiva Star current and voltage diagnostics was fielded on this test, which includes the six Shiva arm Rogowski coils used to measure the current delivered by each arm of the Shiva bank: four load section Rogowski coils, wrapped in clockwise and counter-clockwise pairs, used to measure the total current delivered to the load; a Faraday rotation diagnostic used as a second total load current diagnostic; three load B-dot probes used to measure the azimuthal uniformity of the current delivered to the load; and three V-dot probes placed at the perimeter of the load section to measure the azimuthal uniformity of the load voltage.

Because of the failure in the Shiva current-feed insulator, these diagnostics measured somewhat abnormal values. The current obtained from the Faraday rotation diagnostic is an example (Figure 38). The expected current was approximately 12-13 MA, but the measured current was approximately 18 MA.

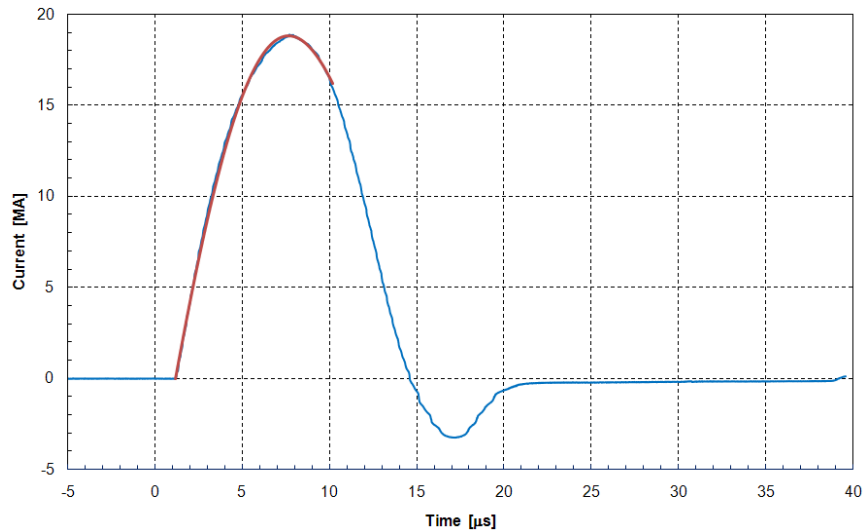


Figure 38. Current (blue trace) measured by Shiva Faraday rotation diagnostic during field-compression test. NumerEx personnel did an analytical fit to this curve (red trace) using a bank capacitance of 1300  $\mu\text{F}$ , a net circuit resistance of 1.23  $\text{m}\Omega$ , a net circuit inductance of 16 nH, and a bank-charge voltage of 84.4 kV. The Shiva circuit inductance should have been approximately 44 nH, so there is a difference of 28 nH in the real vs. the expected inductances. By incrementally adding the inductances upstream from the liner lower electrode until an inductance of 28 nH is obtained, the probable position of the fault can be found, which corresponds approximately to the joint between the disk insulator in the Shiva current feed and the coaxial insulator placed between the liner and its return conductor.

A set of seven probes was constructed and characterized for use in the field-compression test to monitor fields injected from the Guide-Mirror-magnet array and trapped within the collapsing liner (Figure 39). The micro B-dot probes were calibrated with both a benchtop setup (Figure 40) and a Helmholtz coil calibration teststand. The micro B-dot probes were then installed on the field-compression experimental setup.

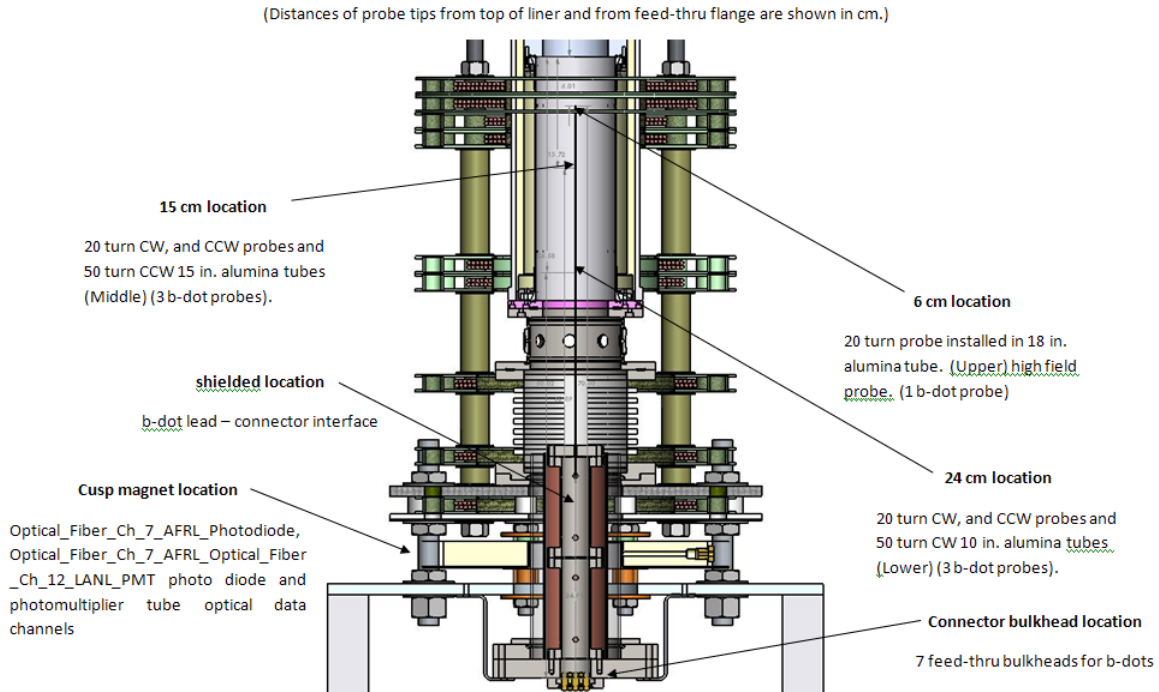


Figure 39. Cross-section diagram of liner, lower vacuum section, and B-dot probe package

#### MTF liner b-dot electrical bench calibration

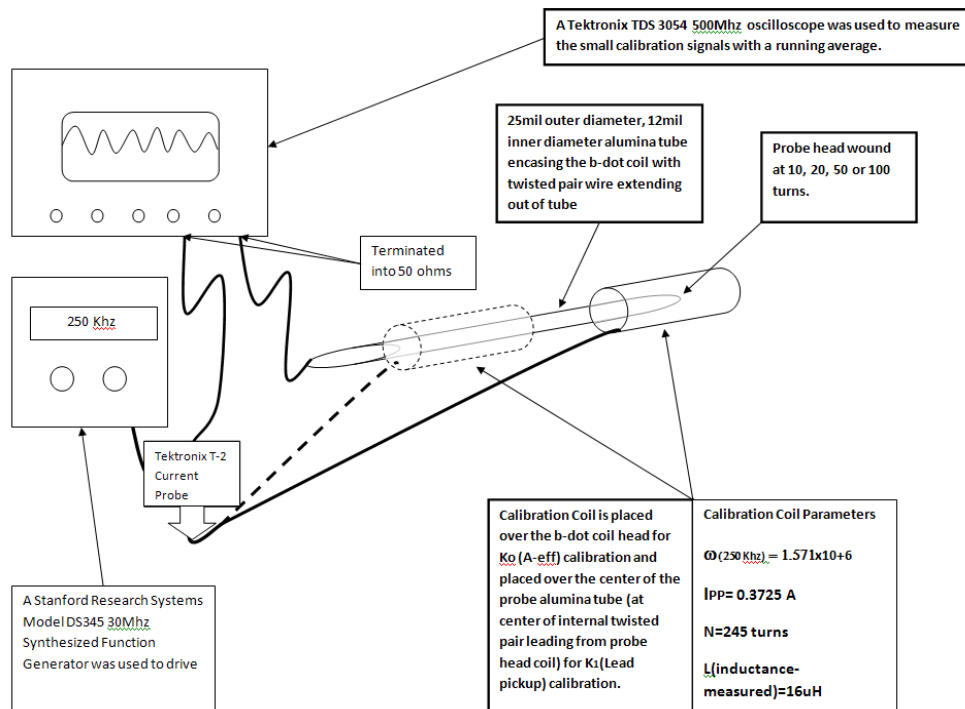


Figure 40. Micro B-dot bench calibration setup

The micro B-dots were fabricated using a 43 AWG copper wire insulated with a polyamide (Kapton) coating with a thickness of 0.2 mil (Figure 41). For perspective, a 10-turn B-dot coil measures approximately 0.8 mm long and approximately 0.2 mm wide. The B-dot probes were wound with 10-, 20-, 50-, and 100-turn coils for electrical and physical characterization, from which five 20- and two 50-turn B-dots were then chosen for use in the final probe assembly.

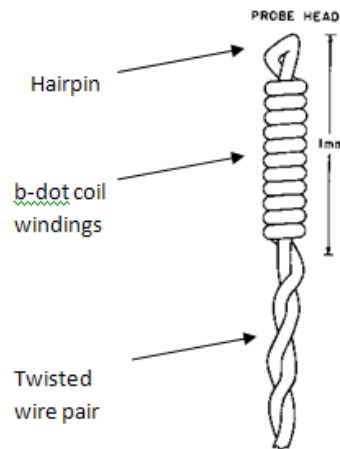


Figure 41. Typical micro B-dot probe construction

The micro B-dot probes were wound on a custom winding fixture, shown in Figure 42. The wide field magnet allows for control of the feed angle during the coil-head-winding process. After winding the probe heads, the leads are then twisted at a pitch of about two turns per millimeter. The maximum length of the probes using this winding fixture is approximately 19 in. (48.26 cm).

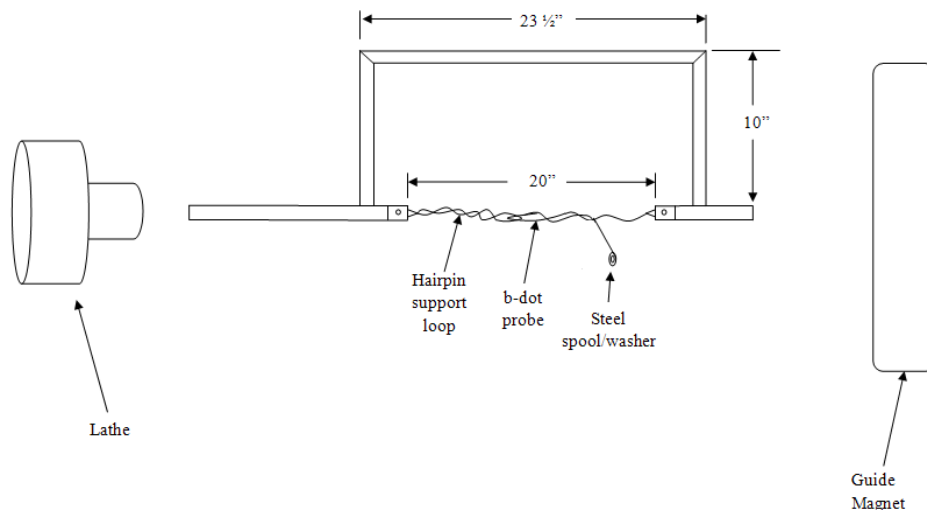


Figure 42. Micro B-dot probe winding fixture

After fabrication, the probes were pulled into 10-, 15-, and 18-in. long (25.4-, 38.1-, and 45.7-cm long) alumina tubes. These tubes had inner and outer diameters of 12 mil (0.30 mm) and 25 mil (0.64 mm), respectively, and served to protect the probes, as well as position them at their appropriate elevations in the liner, ultimately at 24, 15, and 6 cm from the top of the liner, as shown in Figure 39. Probe calibrations were performed once the probes had been placed in these protective tubes.

The plot in Figure 43 shows a sampling of the calibration data obtained using the set shown in Figure 40. Here, the voltage induced in the probe coil is plotted vs. the number of turns in the probe coil.

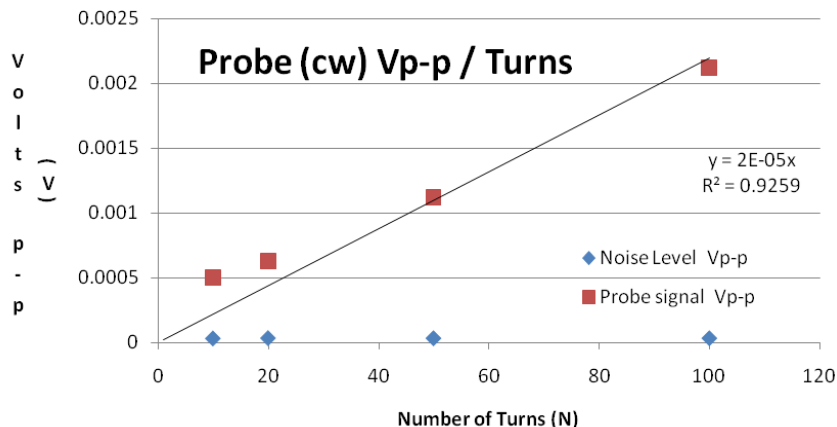


Figure 43. B-dot probe signal (V peak-to-peak) vs. number of turns in probe



The linear trend line that is shown is related to Faraday's law of induction and the geometrical characteristics of the probe and probe leads. We noted that probes with only 10 turns tended to unravel slightly causing the induced voltage to rise above the trend line (due to the increased probe head area), resulting in our decision to use 20 turn probes for the "low sensitivity" probes.

After the calibrations were performed and after it was determined which probes would be used in the final probe assembly, those that were chosen were secured in their alumina tubes using a drop of Torr-Seal epoxy placed at the bottom of the alumina tube where the twisted pair leads exited. The bundle of seven alumina tubes was then placed into a 2.75-in. conflat flange that had a small hole drilled into it, and then the twisted pair leads of the probes were soldered onto short semi-rigid coaxial cables. The cables were attached to SMA vacuum feedthroughs on an acrylic disk at the bottom of the probe assembly, and after the soldering was completed the 2.75-in. conflate flange was bolted to two short pipes that were placed around the semi-rigid coaxial cables to shield the solder connections. Lastly, a copper tube to provide magnetic shielding followed by a short 10-in. quartz tube that served as the vacuum envelope were placed around the short pipes now supporting the 2.75-in. conflat flange and alumina tubes.

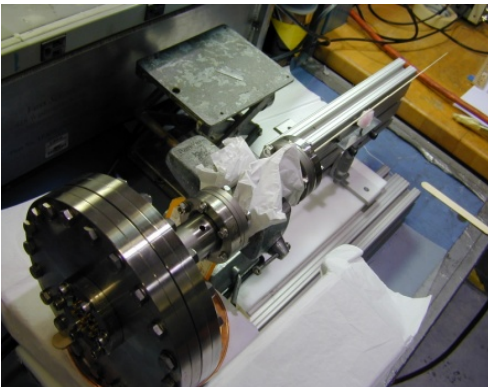
Figure 44 shows the B-dot probe fabrication and assembly process: (a) B-dot probe winding fixture, magnet assembly on left; (b) 7 probes shown before hookup to connector assembly; (c) gluing and alignment of probe assembly; (d) complete micro B-dot assembly; (e) installation below Guide/Mirror coil table; (f) micro B-dot assembly installed, diagnostic cables connected.



(a)



(b)



(c)



(d)



(e)



(f)

Figure 44. B-dot probe fabrication and assembly process

Figure 45 shows a listing of the final channel assignments, physical properties, and positions of the seven micro B-dot probes used in the field-compression experiment. The  $K_o$  parameters

(calibration constants) were determined using the benchtop calibration setup (Figure 40). Prior to the field-compression experiment all seven of the probes showed good continuity, indicating that none of the leads had been broken during the final assembly process. At the PXI data acquisition chassis all the probes were terminated with 50  $\Omega$ . In addition, the 20 turn probes had 100x attenuation and the 50 turn probes had 200x attenuation.

Probe #	Connector Channel #	K <sub>0</sub> (250Khz)	N direction	Description	Length of tube	Length of twisted pair Approx.	Continuity Resistance in Ohms	Liner position (from top of liner)
A	7	5.38X10+6 T/V-S	20 CW	Upper	18 in.	20.5 in.	7.2	6 cm
B	2	5.95X10+6 T/V-S	20 CW	Middle	15 in.	18 in.	8.4	15 cm
C	6	7.85X10+6 T/V-S	20 CCW (18)	Middle	15 in.	18.5 in.	7.8	15 cm
D	4	2.28X10+6 T/V-S	50 CCW	Middle	15 in.	19 in.	7.8	15 cm
E	3	6.74X10+6 T/V-S	20 CCW (18)	Lower	10 in.	14 in.	6.6	24 cm
F	5	6.78X10+6 T/V-S	20 CW	Lower	10 in.	14.5 in.	5.9	24 cm
G	1	3.13X10+6 T/V-S	50 CW	Lower	10 in.	16 in.	7.4	24 cm

Figure 45. Liner B-dot probe array positional and physical parameters

Because the Guide/Mirror bank did not fire, there was unfortunately no magnetic field data recorded during the field-compression test. As a result, the B-dot probe package became more of a time-of-impact probe (Figure 46)

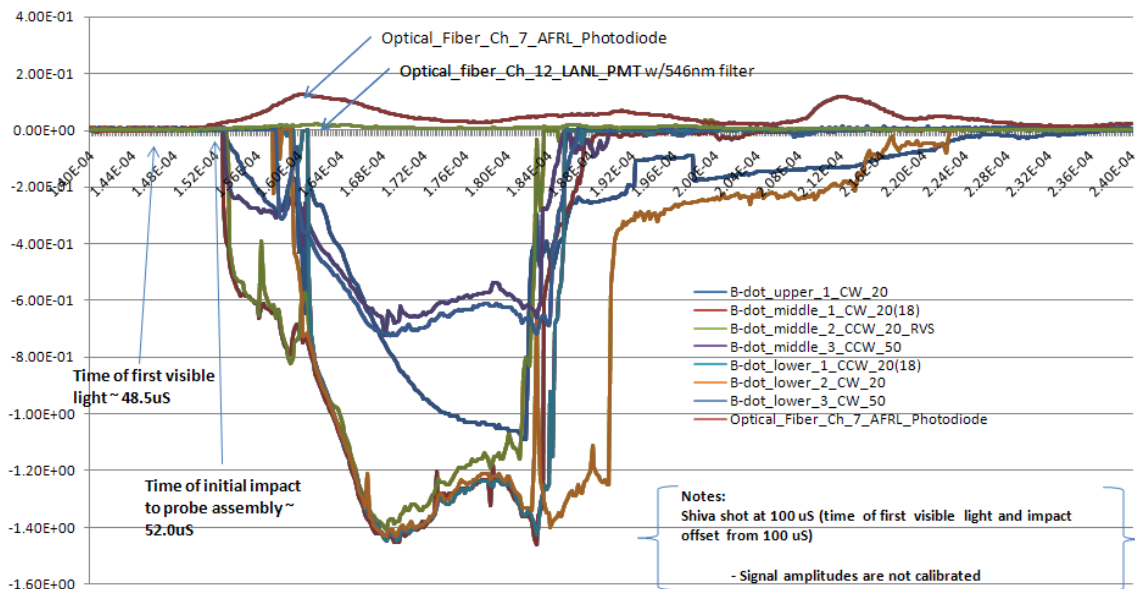


Figure 46. Micro B-dot signals overlaid with signals recorded with two "null test" side-on optical fiber array fiber signals. The time-of-impact probe was evidenced by the fact that all the probe signals were negative, despite two being wound counter to the others. The recorded data does show, however, that the

electrical noise environment for the B-dot probes during the implosion and even at the time of the liner stagnation when it has impacted the probes is not as severe of a problem as originally thought. It may not be necessary to install the oppositely wound probes for the purpose of eliminating common mode noise on the next field-compression test.

For FRCHX-1, we used two 300 kV radiography (X-ray) imaging systems, operating at approximately 250 kV. To maximize imaging resolution we used our in-house-built X-ray-tube heads with source spot sizes less than 1 mm. Digital film was used for recording all images. In each imaging-film-pack assembly we loaded two pieces of film with each film in its own separate "package." The extra film was a backup in case of some unforeseen issue or problem. Due to the Guide and Mirror coils enclosing much of the liner, the only X-ray imaging region available was centered approximately 18.5 cm below the liner top plane. As such, both imaging systems were vertically positioned to view this region but were azimuthally separated to be perpendicular to each other. Also, because of Guide and Mirror coil constraints, X-ray # 1 film pack needed to be mounted between two of the current feeds to the coils, dictating a smaller film pack size for this imaging system. Both imaging systems needed to image through approximately 6 cm of high-density polyethylene (used for protection of the X-ray heads and film packs and to support the Guide and Mirror coils structurally). Such a large amount of HDPE contributes to scatter, and image quality is reduced.

X-ray system #1 was located at a radius of 130 cm from centerline, and its film pack was at a radius of 36 cm, producing an image magnification = 1.28X. With an axial field of view of 5.7 cm we were able to image the liner from 15.7 cm through 21.4 cm (centered at 18.5 cm) with regard to the top of the liner plane.

The desired X-ray #1 system imaging time of 21.8  $\mu$ s actually came in at 21.714  $\mu$ s, or 86 ns earlier.

The X-ray #1 film pack suffered some damage due to shot-generated fragments. However, we were still able to retrieve the image from the damaged film.

X-ray system #2 was located at a radius of 128 cm from centerline, and its film pack was at a radius of 44 cm, producing an image magnification = 1.35X. With an axial field of view of 8.3

cm we were able to image the liner from 14.4 cm through 22.65 cm (centered at 18.5 cm) with regard to the top of the liner plane.

The desired X-ray #2 system imaging time of 22.5  $\mu$ s actually came in at 22.357  $\mu$ s, or 143 ns earlier.

X-ray #2 film pack did not suffer any damage due to shot-generated fragments.

Figure 47 shows the two-shot images and the setup images for X-ray #1 imaging system. (Both shot images are shown to illustrate the usable information still obtained despite the damage to the film.)



Figure 47. Images from X-ray #1 imaging system (top and middle); setup image taken before the shot (bottom)  
Figure 48 shows the setup and shot images for X-ray #2 imaging system.

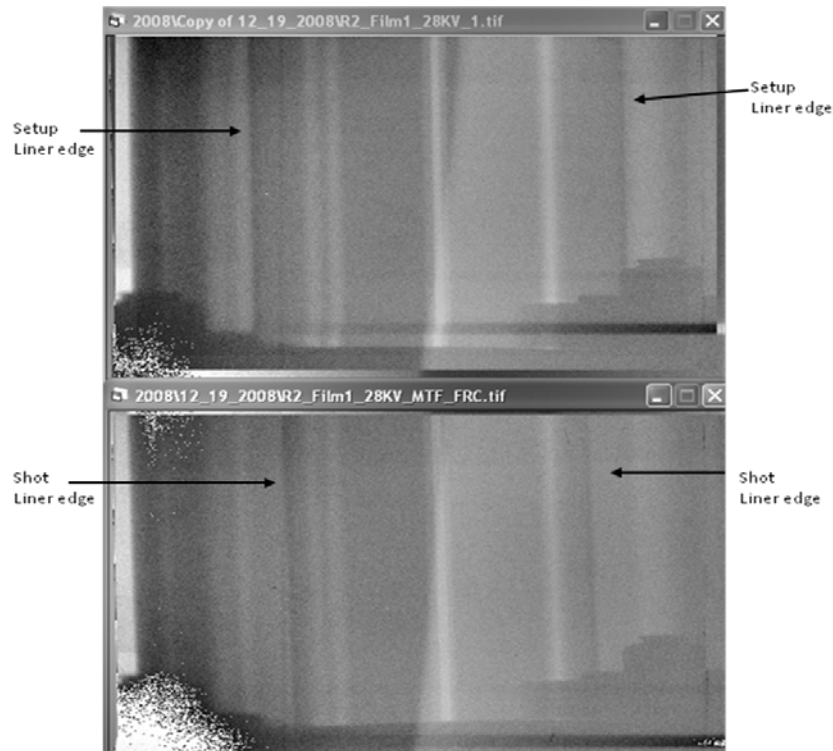


Figure 48. One image from X-ray #2 imaging system (top); setup image taken before shot (bottom)

On the damaged section of the two-shot film packs of Figure 47, the first film was so damaged we had to cut out the section so that we would not damage the film scanner when reading the film.

The slots in the return conductor are easily visible throughout the image. Two such slots are aligned in the center of this image. The shot imploding liner diameter measures 8.25 cm on film #1 and 8.35 cm on film #2.

In Figure 48, the slots in the return conductor are easily visible throughout the image. Two slots are also aligned in the center of this image. The shot imploding liner diameter measures 8.2 cm for film #1.

An average velocity of 1.6 km per second is calculated from the two X-ray images.

Before discussing each of the secondary performance diagnostics, we present a brief description of how the optical paths were set up for them on top of Shiva. Figure 49 shows a pair of SolidWorks drawings illustrating the basic hardware arrangement: (a) Vacuum and optical

hardware on top of Shiva load section; (b) cross-section of (a) showing pyramidal mirror assembly supported above aperture in upper electrode

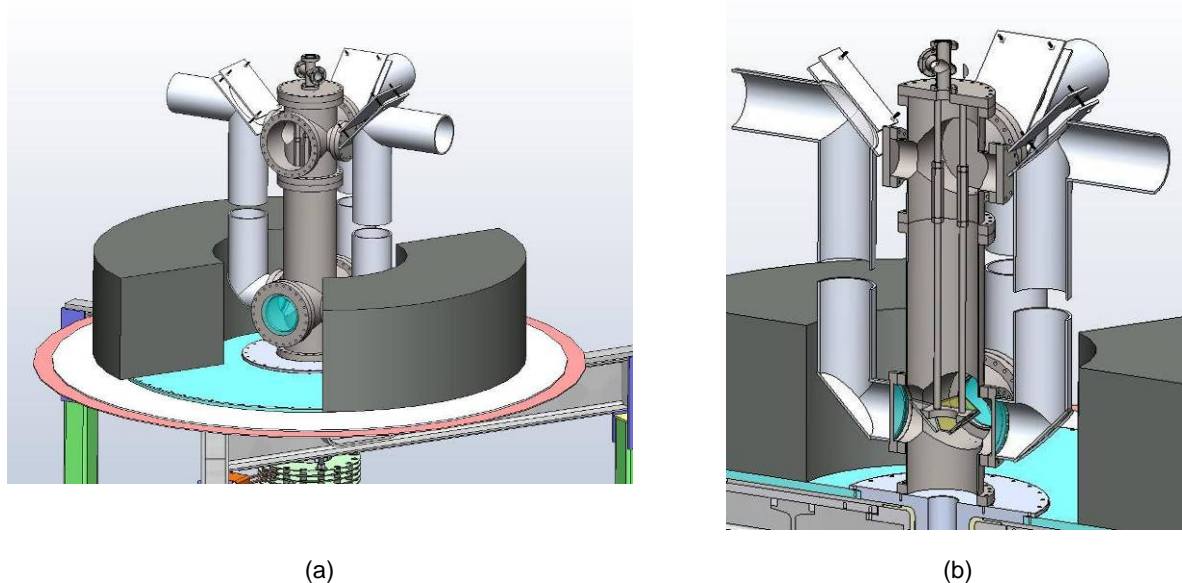


Figure 49. SolidWorks basic hardware arrangement

To provide the quasi-axial view through the liner, a four-sided pyramidal mirror assembly was designed by AFRL personnel. The pyramidal mirror, or “Mirramid,” was hung above the aperture in the liner upper electrode, being supported by four two-piece all-thread rods, the upper piece of which had left-handed threads and was screwed into the top plate of an upper vacuum vessel. The height of the Mirramid was then adjusted by turning four coupling nuts that joined the all-thread pairs together, and it was set in such a way as to align the mirrors with the four side ports on the vacuum vessel. (This vessel was also the means for connecting the vacuum system to the experimental setup to allow the liner interior to be evacuated.) Though up to four optical diagnostics could be placed around the upper vacuum vessel, only the three already described were used on this test. Additional mirrors in S-shaped periscope assemblies then aligned the respective optical paths with the lenses in front of or inside each of the diagnostic enclosures.

An optical pyrometer was fielded on FRCHX-1. The pyrometer was designed to measure the temperature of the inside surface of the aluminum cylinder (liner) that was imploded to compress an axial magnetic field. Simulations showed that as the liner compresses the field, field strength

increases dramatically from around 2.0 T to over 600 T inside the liner. Much of the magnetic field is expected to diffuse into the liner, heating it according to the following equation:

$$C\Delta T = \beta(B^2/2\mu_0)$$

where, C is the volumetric heat capacity of Al, ( $\text{J/m}^3\text{-}^\circ\text{K}$ ),  $\beta$  is the surface enhancement factor (approximately 1, or slightly greater than 1),  $\Delta T$  is the change in temperature of the Al liner ( $^\circ\text{K}$ ), and  $B^2/2\mu_0$  is the magnetic energy density in vacuum (or non-ferromagnetic medium, such as Al) ( $\text{J/m}^3$ ).

The pyrometer is designed to measure the intensities of two different wavelengths of light emanating from the magnetically heated inner surface of the imploding liner. By assuming that the liner emits radiation as a quasi-blackbody radiator, and is a diffuse emitter, or Lambertian (i.e., the intensity of the observed radiation is independent of the angle of view), the two intensities can be used to define a blackbody-radiation-emission spectrum for a unique temperature.

The radiant emission spectrum of a surface of emissivity  $e$  is:

$$I(\lambda) = e(2hc^2/\lambda^5)/(\exp(hc/\lambda kT)-1)$$

where  $e$  is the emissivity ( $0 < e < 1$ ;  $e = 1$  for BB),  $h$  is Planck's constant =  $6.6261\text{e-}34$  J-s,  $c$  is the speed of light in vacuum =  $2.9979\text{e}+8$  m/sec,  $\lambda$  is the wavelength of light (m),  $k$  is Boltzmann's constant =  $1.3807\text{e-}23$  J/K, and  $T$  is the blackbody temperature (K) (see Figure 50). The units of  $I(\lambda)$  are Watts per steradian per unit wavelength per unit area of emitter.



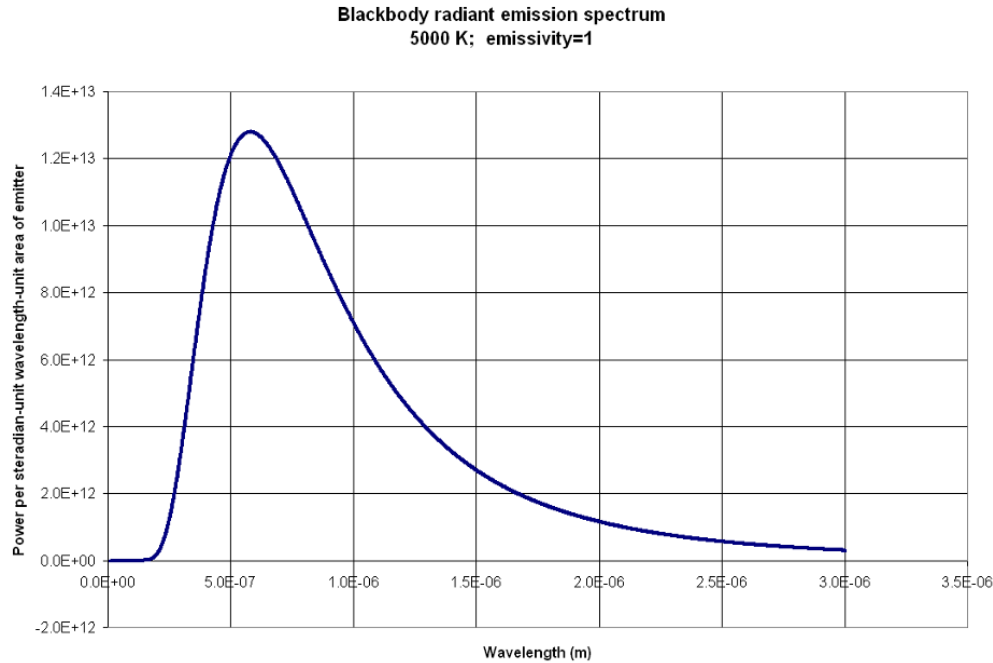


Figure 50. Radiant emission spectrum of a blackbody at 5,000 K

If we measure the intensity of the radiant emission of a blackbody at two different wavelengths,  $\lambda_0$  and  $2\lambda_0$ , then we can solve for the temperature  $T$  in terms of  $\lambda_0$  and the ratio,

$$R = I(\lambda_0)/I(2\lambda_0).$$

Then,

$$T(\lambda_0, R) = (hc/2\lambda_0 k) / \ln((32-R)/R),$$

where  $0 < R < 16$ .

Figure 51 shows a schematic representation of the pyrometer as it was fielded on the field-compression experiment. The liner was 10 cm in diameter. As described previously, the optics were positioned so the pyrometer could “look” down into the bore of the liner, focusing on an image plane about 6 cm from the top of the 30-cm-long liner and capturing an image of the center approximately 2.5 cm in diameter. The liner was expected to be crushed down to a diameter of less than 2 mm at its maximum compression, and significant heating from the magnetic diffusion was not expected to occur until after the liner had been compressed down to at least 2 cm in diameter.

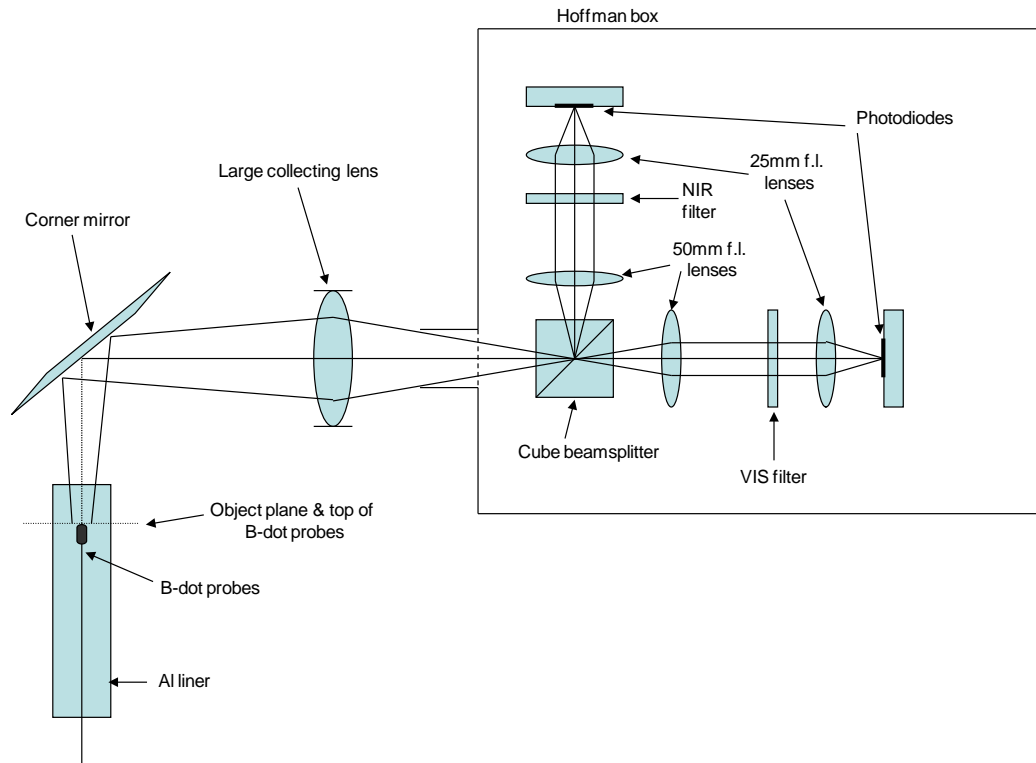


Figure 51. Optical pyrometer schematic

The object plane was at 2 m from the large collecting lens, and the image came to a focus at about 25 cm behind the lens. The cubic beam splitter was positioned near the image focal plane, and the light was split into a visible leg (transmitted) and a near infrared (NIR) leg (reflected). The light in each leg was collimated by the 50 mm focal length lenses and condensed, or focused, onto the photodiodes by the 25 mm focal length lenses. The desired wavelength band in each leg was selected by the use of an appropriate line filter – one for 532 nm (visible) and the other for 1064 nm (NIR).

The photodiodes were powered by internal 12 V batteries. The electrical signals from each photodiode were routed via a short, 6-in. long coaxial cable to fiber optic converter and transmitter boxes. These converter and transmitter boxes converted the photodiode electrical signals to digital optical signals and transmitted them via multimode fiber optic cables from the top of the Shiva bank to matching receiver and converter boxes in the Shiva screen room. There, the optical signal was then converted back to an electrical signal and recorded on a fast digitizing oscilloscope.

The converter and transmitter boxes were powered by 12 V batteries with 9 V regulators, and the receiver and converters in the Shiva screen room were powered by wall-powered voltage regulators. The batteries, voltage regulators, converter and transmitters, photodiodes, and all the optics, except for the large collecting lens, were contained within a shielded Hoffman box on top of the Shiva bank.

The pyrometer was calibrated with a Tungsten filament incandescent lamp. The lamp was powered with 12 V DC. At that voltage the filament has a temperature of approximately 3,300 K, and the emissivity of the filament is 0.44 at 532 nm and 0.35 at 1064 nm. From that information it was calculated that the ratio of the radiant intensities of the Tungsten filament –  $I(532)/I(1064)$  – at that temperature is

$$R(\text{Tungsten @ } 3,300 \text{ }^{\circ}\text{K}) = 0.654.$$

The incandescent filament was placed at the position where the object plane would be in the actual experiment, at 2 m from the large collecting lens, and the relative intensities in the two legs were recorded and a ratio computed. The ratio was,

$$R_{\text{sig}} = 0.333.$$

To get the actual ratio of radiant intensities one must multiply the signal ratio,  $R_{\text{sig}}$ , by approximately 2. So,

$$R_{\text{sig}} * 2 = R(\text{Tungsten @ } 3,300 \text{ }^{\circ}\text{K}).$$

We can generalize this result to say,

$$R_{\text{sig}} * 2 = R(\text{actual, of any radiant source})$$

It is the calibration required for the experiment.

The Guide and Mirror field coils around the liner did not get energized during this field-compression test. As a result, there was no axial magnetic field set up inside the liner prior to the Shiva bank firing. There was a short between the upper and lower Shiva current feed plates, and some of the current was shunted around the load. The result was a weaker compression of the liner, which took about 40  $\mu\text{s}$  to reach maximum compression, instead of the expected 24  $\mu\text{s}$ , or so. However, there was still a strong optical signal detected by both legs of the pyrometer, starting at 40  $\mu\text{s}$ , which rapidly increased off scale (greater than 3 V) in both detectors.

The data, reproduced in Figure 52, show clearly the trigger noise from the Shiva Star bank firing (commencement of current) at approximately  $2\ \mu\text{s}$ , and then both signals begin taking off  $40\ \mu\text{s}$  later.

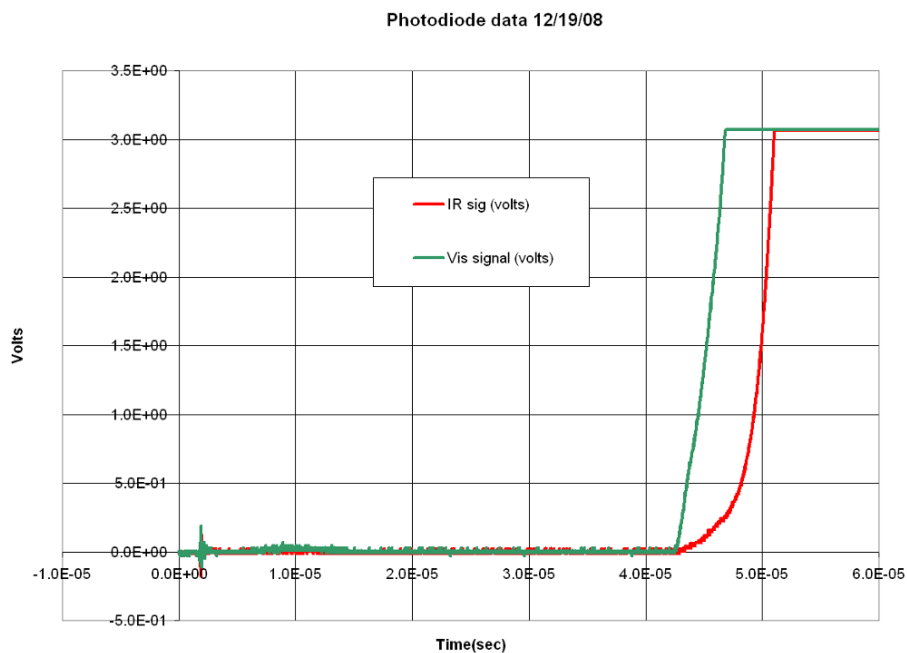


Figure 52. Pyrometry data recorded during field-compression test

The visible signal is much stronger and grows more rapidly than the NIR signal, but the timing correlates well with the measurement from other diagnostics for the maximum compression of the liner. This light is also known as a “stagnation flash,” the result of the liner imploding upon itself and creating an aluminum plasma jet.

Figure 53 shows an expanded view of the photodiode data and the calibrated ratio of the measured intensities.

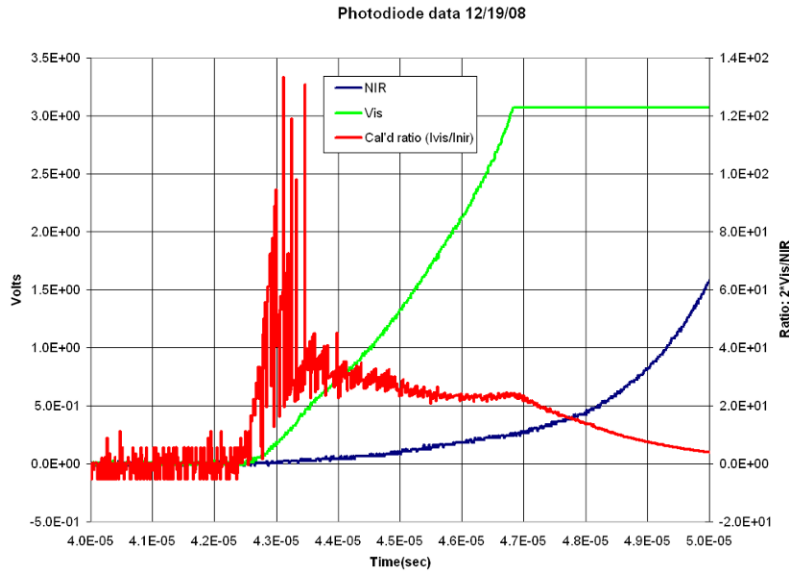


Figure 53. Photodiode data and calibrated intensity ratio

The photodiodes are linear only up to 1 V. Furthermore, the intensity ratio is greater than 16—actually between 25 and 40 in the region of interest—indicating the source does not have a blackbody characteristic. The formula for temperature assumes the emissivity of the liner/radiator is the same for both wavelengths. If this assumption is not true, the formula is not valid. For a true blackbody of uniform emissivity across the spectrum,  $R$  is bounded:  $R$  approaches 0 for  $T$  near 0 K, and  $R$  approaches 16 for  $T$  approaching infinity.

A Princeton Instruments PI-MAX image intensified CCD framing camera was used as part of the photometry-diagnostics suite fielded for the magnetic field-compression experiment of 19 December 2008 on the Shiva Star bank. The purpose of this diagnostic was to obtain an axial image of the imploding aluminum liner at  $t = 22.22 \mu\text{s}$  after the start of Shiva current. This point in time is when the liner's outer diameter was predicted to be about 1 cm, and the compressed axial field was predicted to be about 400 T, based on 1D MACH code simulations. The goal of this diagnostic was to measure the intensity of light emitted from the compressed, heated liner in a narrow band of wavelengths (in this case, visible light in the range  $512 \text{ nm} \leq \lambda \leq 552 \text{ nm}$  with the use of a line filter centered at  $\lambda_0 = 532 \text{ nm}$ ). Assuming that the light is the result of blackbody radiation, the purpose was to obtain an estimate of the liner-surface temperature by comparing this measurement with a calibration measurement obtained using a tungsten-filament halogen

lamp whose blackbody radiant emission spectrum is known. Knowledge of the liner surface temperature can then, in principle, be used to estimate the local magnetic field. Therefore, this diagnostic could serve as an independent means of measuring the axial field in the compressed liner to determine if the field strength required for a successful FRC compression-heating experiment could be attained. In addition, an axial view of the liner at an advanced stage of compression would also serve as a useful visual diagnostic for detecting the development of a “fluting” instability around the perimeter of the liner structure.

The PI-MAX camera was equipped with a 400-mm-focal-length  $f/2.8$  Nikon telephoto lens. Placed directly in front of the Nikon lens was a 1.83-m-focal-length  $f/13$  achromat used as a close-up lens. This additional lens was required to obtain an adequate focus and field of view at the imaging distance used on this experiment. The 532-nm line filter was placed immediately in front of the camera’s photocathode window. With this arrangement, calibration measurements were made using a 100-W tungsten-filament halogen lamp (OSRAM HLX 64625) that has a true temperature of 0.284 eV and an emissivity of 0.44. These values yield a radiant emission of  $3.40 \times 10^{11} \text{ W sr}^{-1} \text{ m}^{-3}$  at  $\lambda_0 = 532 \text{ nm}$  (as obtained from Planck’s law for blackbody radiation), which translates to a certain number of counts on the PI-MAX CCD camera for a given gain setting, exposure time, imaging distance, and  $f$ -stop setting.

The lamp was set at an imaging distance of approximately 2 m, the same imaging distance used on the actual experiment, which focuses on the liner at an axial location about 6 cm below its upper current joint. Calibration images were taken with the gain of the image intensifier set to its maximum value, an exposure time of 50 ns controlled by a gate pulse applied to the image intensifier, and the Nikon lens set to  $f/2.8$  with a distance setting of about 20 m. A peak value of approximately 7900 counts on the CCD detector was measured under these conditions, which is about 1/8 of the full-scale reading for the 16-bit dynamic range of the PI-MAX camera’s CCD detector.

The expected temperature of the imploding liner at the time of interest is 0.24 eV, corresponding to a radiant emission of  $1.66 \times 10^{11} \text{ W sr}^{-1} \text{ m}^{-3}$  at  $\lambda_0 = 532 \text{ nm}$ , which is about a factor of two less than the radiant emission from the calibration lamp at the same wavelength. To provide an

adequate safety margin for avoiding the possibility of saturating the CCD detector, in the event that the actual liner temperature were higher by as much as a factor of two from the expected value of 0.24 eV, the Nikon lens was set to  $f/5.3$  for the experimental image instead of  $f/2.8$ . This change would reduce the amount of light collected by a factor of about 3.6 from the lowest  $f$ -stop setting and allow the camera and other lens settings to be kept the same. With these settings, it should be possible to measure a radiant emission approximately 64.5 times larger than expected—the emission associated with twice the expected temperature at  $\lambda_0 = 532$  nm—and still obtain a good full-scale reading on the camera.

A periscope assembly with visible light mirrors was fabricated and attached to a viewing port on the upper vacuum vessel to transport light from the liner region to the PI-MAX camera (Figure 49). An RF-shielding enclosure was placed on a platform set up on the upper Shiva load section; the camera, lens assembly, and associated electronics were situated within this “screen box.” To maintain the RF-shielding integrity of the screen box, a copper mesh was placed over the opening through which the camera viewed its target. This mesh, while attenuating the level of light recorded by the camera by a factor of about 1.8, did not significantly compromise image quality. (The mesh’s attenuation factor was taken into account when determining the optical and electronic settings for the camera.) In addition, a 0.25-in. thick piece of glass was placed in front of the mesh to protect the camera assembly from the hot gases and blasted debris arising from the shot, both of which could damage the camera.

To obtain good in situ alignment and focusing, a reflective viewing target was lowered into the liner through the upper electrode aperture to the desired imaging location. Figure 54 shows the image that was recorded of that viewing target. Uniform illumination of the surface could not be obtained, but a good portion of the reflective disk and the slot cut through it can be seen.

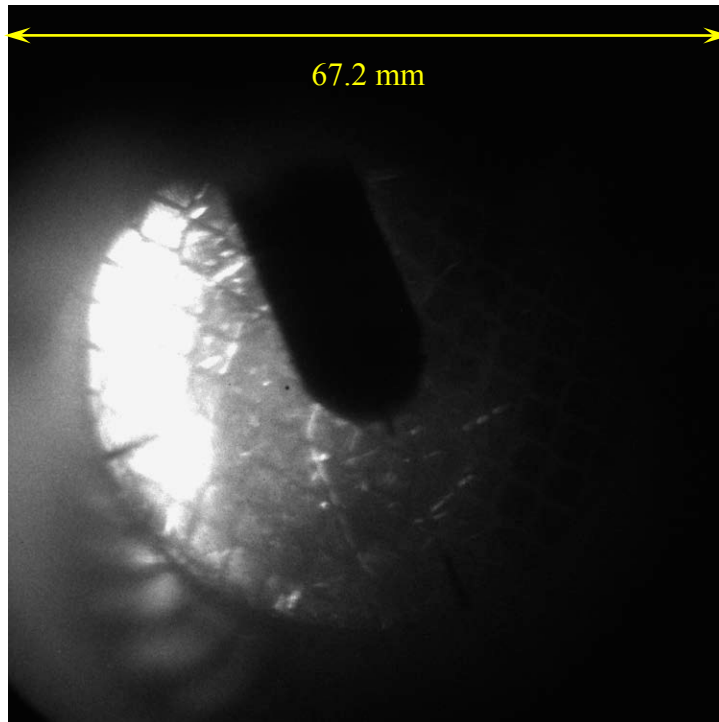


Figure 54. Alignment and focusing target located inside liner

As a result of the fact that the insulator between the Shiva bank's current feed plates failed prior to delivering its full current to the load, the liner did not compress as quickly and uniformly as expected. In addition, no initial axial magnetic field was established within the liner because the Guide and Mirror coils did not get energized. Therefore, the PI-MAX camera image could not be used to obtain any quantitative temperature information, as the liner was not at the expected level of heating to produce blackbody radiation. However, Figure 55 does appear to give a view of the tip of the long, thin alumina tube that housed the upper magnetic field probe that was inserted along the axis of the liner. In addition, what appears to be at least part of the imploding liner, can be seen in this image. The image was taken at approximately  $20.49 \mu\text{s}$  with respect to the start of the Shiva current pulse, about  $1.73 \mu\text{s}$  earlier than desired due to a timing miscalculation.



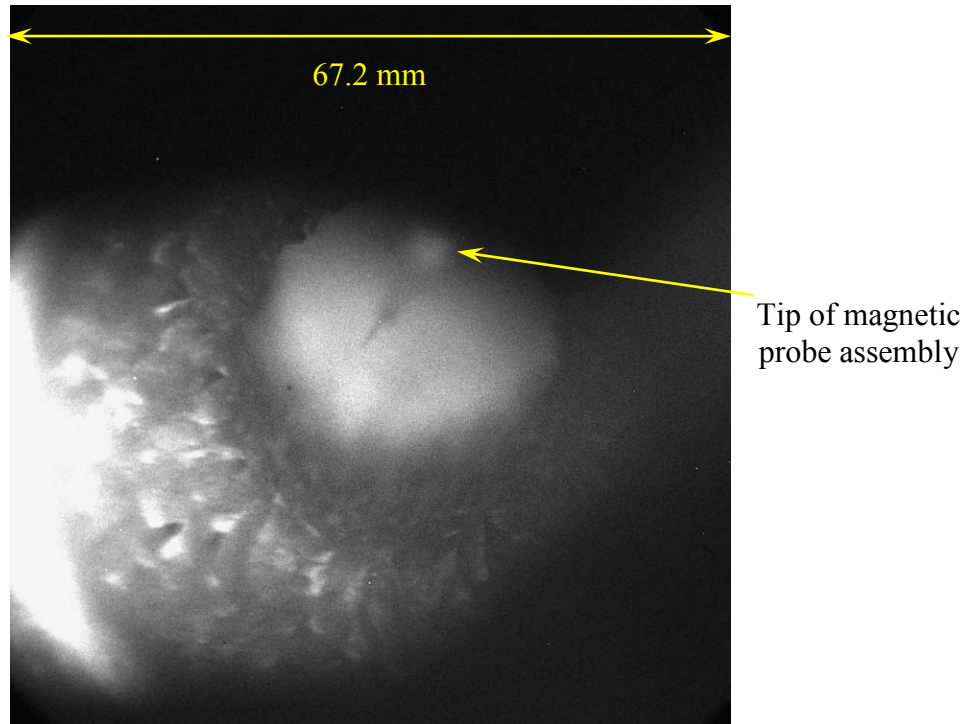


Figure 55. Imploding liner during shot

Following the field-compression test, the camera and lens assembly emerged undamaged, as the glass-blast shield and periscope assembly provided adequate protection from the hot gases and flying debris associated with the shot.

A Cordin Model 173-3 digital streak camera was fielded to measure light intensity vs. time at two different wavelengths simultaneously. The two wavelengths were  $\lambda_0 = 532$  nm and  $\lambda_1 = 2 * \lambda_0 = 1064$  nm, chosen for the ready availability of narrow line filters at these wavelengths. The goal was to estimate an imploding liner's surface temperature by using the intensities at these two wavelengths and fitting them to a blackbody spectrum. The setup of the system is illustrated in Figure 56.

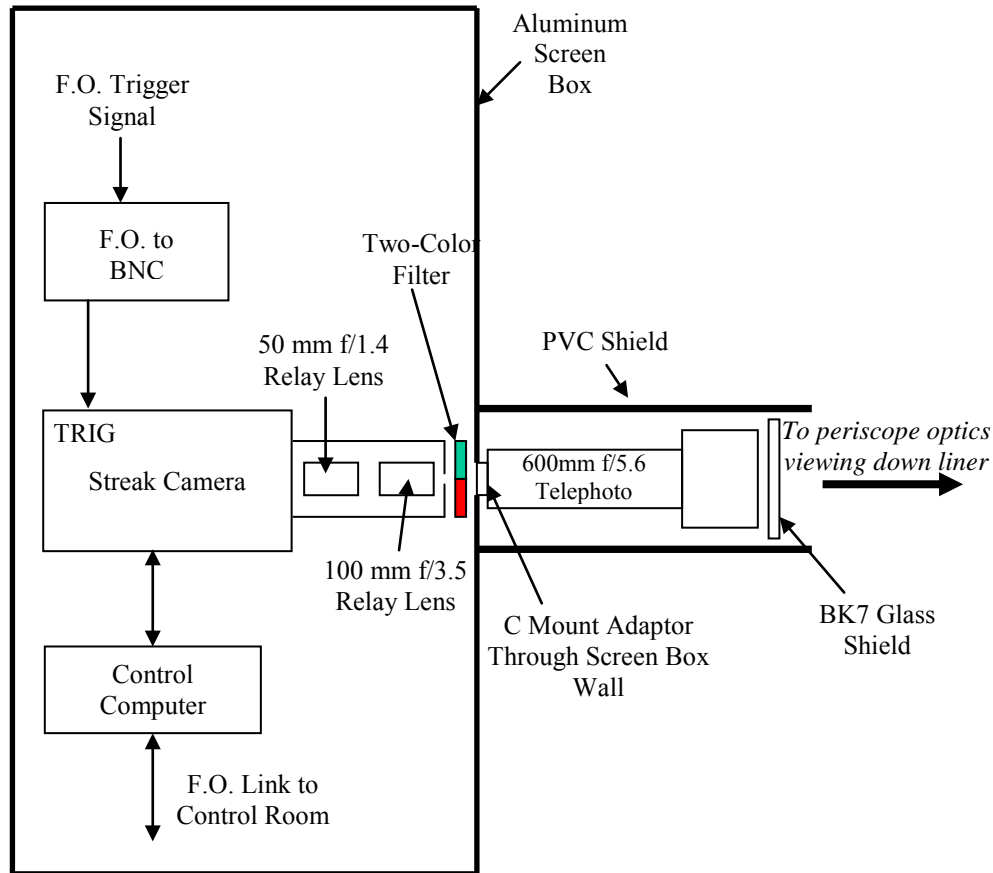


Figure 56. Schematic of streak camera setup for field-compression test

A custom two-color filter was fabricated in-house by first grinding down and then bonding together side by side the two line filters. The two-color filter was then mounted directly in front of the streak camera entrance slit. The camera face was pushed up against a machined alignment plate that fixed the (x,y,z) location of the camera slit relative to a 600-mm f/4 Nikon telephoto lens. Because of optical path considerations, the telephoto lens was mounted outside the screen box housing the camera, but it was secured to the screen box using a threaded C-mount adaptor that was bolted to a fiberglass shelf, in turn mounted to the screen-box exterior. The exterior lens assembly was housed in a 1/4-in. thick PVC cylinder to protect it from debris during the liner shot. Furthermore, the front of the lens was protected by a 1/4-in. thick optical quality slab of BK7 glass that was secured in an aluminum ring attached to the telephoto lens face.

Triggering was done using an in-house fiber-optic-to-electrical-trigger converter, with an optical trigger pulse provided from the Shiva screen room. Control and data retrieval from the streak

camera were handled by a computer located inside the camera screen box, and a fiber optic Ethernet connection allowed this computer (and the camera) to be controlled remotely from the Shiva screen room.

Calibration of the system was performed using a 100-W tungsten-halogen lamp of known temperature and spectral emission properties. The lamp was placed at the same distance from the telephoto lens as the liner would be during the shot. The streak camera optical setup was identical to that shown in Figure 56 (used during the actual liner shot) with the exception of these differences: In the calibration setup the telephoto lens used  $f/4$  instead of  $f/5.6$  and the periscope optics were not used. The  $f/\#$  difference was taken into account when determining the calibration, though, and the periscope optics were expected to have negligible effect on the light transmission.

The camera alignment and focus were adjusted by putting the camera in “focus mode,” which allows it to take a full-frame image instead of a streak; Figure 57 shows an example image. During this step it was noticed that the 532 nm and 1064 nm wavelengths needed significantly different focal lengths to produce a sharp, bright image due to the difference in refractive index of the telephoto lens at the longer wavelength. It was decided to optimize the focus for 1064 nm to maximize the light collected at this wavelength, because the streak camera is less sensitive in the NIR. The upper spot is 532 nm; lower spot is 1064 nm.



Figure 57. Streak camera “focus mode” image of tungsten-lamp filament

A large number of streak images were taken at several different streak speeds, camera slit widths, and camera gain settings. Figure 58 shows an example of 532 nm upper, 1064 nm lower filament.

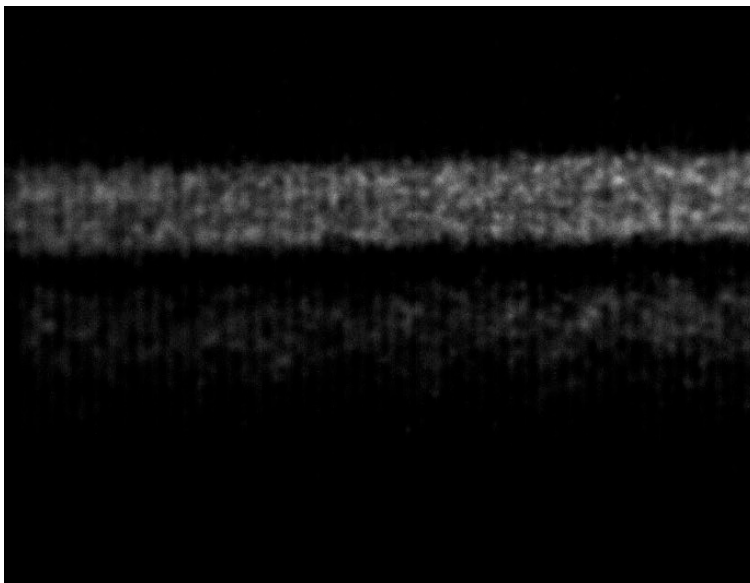


Figure 58. Streak image of tungsten filament, recorded with a 2  $\mu\text{s}/\text{mm}$  streak rate

The camera has independent gain settings for the CCD and MCP (micro-channel plate) amplification stages, and both were adjusted during calibration. Varying levels of neutral density (ND) filtering were also used on the green (532 nm) side of the two-color filter to compensate for the camera's greater sensitivity at this wavelength. It should be noted that the streak rate also changes the effective camera sensitivity, because a faster streak gives less time for a given pixel to collect light. Thus, a calibration must be done at the streak speed that is intended to be used during the actual experiment.

The final settings were largely constrained by the low sensitivity of the camera response to the NIR (gain settings) and the desire for good time resolution (streak speed and slit-width settings). Based on the predicted light intensity and liner-compression speeds estimated from simulations, the optimum streak camera settings are listed in Table 11.

Table 1. Optimum streak camera settings

Parameter	Setting
CCD gain	MAX
MCP gain	MAX
streak rate	500 ns/mm
slit width	0.04 mm
ND filtering	532 nm: 0.9 ND 1064 nm: None

These settings were expected to give a full-scale signal on the 8-bit streak camera CCD for 532 nm at a temperature  $T = T_{\text{max}} = 0.37$  eV and 1064 nm at  $T = 2 \cdot T_{\text{max}} = 0.74$  eV.

The streak camera has a small time delay between receiving its trigger and beginning a streak image. This delay varies with the chosen streak speed. So the timing between the camera trigger and the absolute time window of the streak image must be experimentally determined for each streak rate. This determination was done using a delay generator to trigger an LED light pulse with a variable delay after the camera was triggered. Figure 59 shows a representative series of such light pulses during a streak image.



Figure 59. Streak image of a repetitively pulsed LED

In Figure 59, time increases to the right. The camera had a 1  $\mu\text{s}/\text{mm}$  streak rate, and each pulse is 1  $\mu\text{s}$  in duration.

For each time delay, a 2D Gaussian profile was fit to a single light pulse and the location of the peak of the Gaussian was then determined. Figure 60 shows a plot of pulse center vs. time delay for one streak rate. The streak rate was 2  $\mu\text{s}/\text{mm}$ .

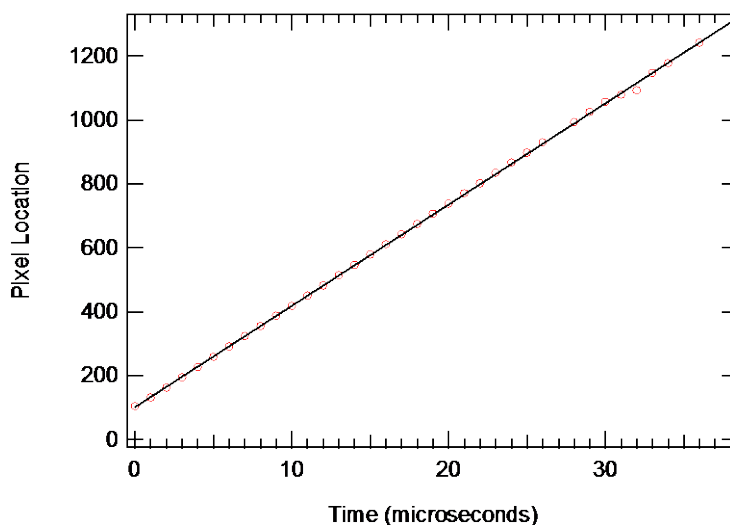


Figure 60. Location on streak image (in pixel number) of the centers of consecutive LED pulses vs. time delay from streak camera trigger

Fortunately, the streak rate was found to be constant throughout the streak and well fit by a linear function, allowing the timing of the features in the streak image to be determined relative to other diagnostics and events in the experiment. Equipment and analysis software has been developed to allow characterization of the streak timing shown in Figure 60 to be done rapidly for any desired streak rate.

#### 3.1.2.2 FRCHX-2

As discussed in the previous section, the first field-compression had two serious problems. The first was that the Guide and Mirror bank did not fire, so there was no flux injected for compression. The second problem was that the solid-dielectric insulation in the current feed to the liner failed at a joint between two insulator sections. We, therefore, corrected the problems so that we could repeat the experiment.

One of the findings that arose from the mapping of the axial-magnetic field in the liner prior to the first field-compression test was that the upper-mirror field was much lower in amplitude than anticipated with respect to the lower mirror and other regions of the axial field. Modeling performed by NumerEx personnel showed this mirror would not be adequate for stopping the FRC in the liner; that is, after entering the liner the FRC would be able to pass through the upper mirror and exit from the top of the liner. As a result, AFRL, NumerEx, and SAIC personnel spent several days determining why the upper-mirror field was lower than anticipated and developed a plan for increasing the amplitude of this field to something more appropriate. An improved clamping structure for the upper four coils was also designed and is briefly described in this section.

The field-compression test, FRCHX-2, was performed on 1 Apr 2009.

#### *3.1.2.2.1 Changes Made to FRCHX*

As mentioned above, the first serious problem encountered during the first field-compression test was that the Guide and Mirror fields did not set up inside the liner as intended during the shot. Just 1 or 2 s after the Guide and Mirror bank had reached its targeted charge voltage the voltage on the bank began falling rapidly. We believe the LabVIEW control program prematurely entered the dumping sequence for the bank, which has as one of its first steps turning off all trigger units. This program's action would explain not only why the bank voltage began a steady decay just a few seconds before the trigger was to have occurred, but also why the bank failed to trigger when the command trigger was sent – despite the fact the bank still had a voltage of approximately 3.3 kV.

Personnel examined the routines in the LabVIEW control program and identified the most likely reasons for the software to have entered the dump sequence: (1) The operator accidentally pressed the software button intended to initiate the dump sequence after the shot or the computer erroneously detected that the software button had been pressed; or (2) an interlock opened somewhere, which would have caused the computer to immediately halt all charging operations and start the dump sequence. Possible open-interlock scenarios include the wind jarring an external door enough to cause a door interlock to open briefly; a battery failing in a door interlock box; the batteries failing in the remote Emergency Abort control—as this control works

by shutting off a fiber-optic link with the Compact Field Point (cFP) controller in the event of an emergency, which then discharges all banks; or electrical noise causing one of the rail-gap trigger-units, which were turned on for timing purposes, to drop out of “ready” status. Each of these potential problems was addressed.

Once all banks reach their targeted voltage, the panel shown in Figure 61 is displayed on the computer monitor. It asks the operator for input regarding whether (and when) to proceed with the dump sequence once the trigger has occurred or to have the cFP controller send an immediate trigger pulse, after which the dump sequence automatically begins.

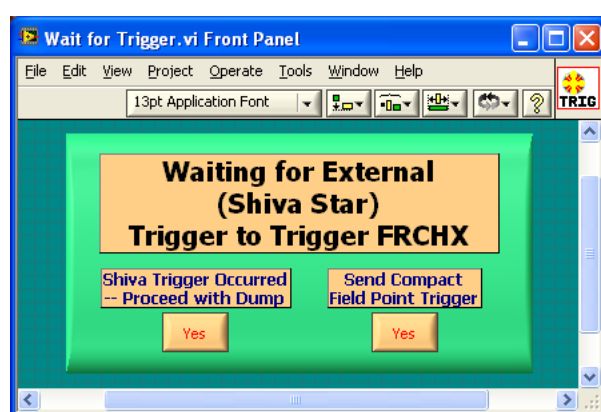


Figure 61. LabVIEW panel

In an effort to prevent any accidental operator input from directing the controller to start the dump sequence too soon through either of these two avenues, or the erroneous detection by the computer of such inputs (e.g., through some means such as a static discharge), additional steps were incorporated into the LabVIEW control program that requires a confirmation for either of these inputs.

Figure 62 shows the software panels asking FRCHX operator for confirmation: (a) starting dumping and safing sequence and (b) sending cFP command trigger pulse.

Figure 62a shows a new panel asking for confirmation before starting the dump sequence, the left panel input in Figure 61. A panel asking for the confirmation of the cFP trigger, the right panel input in Figure 61, was also added at this time and is shown in Figure 62b.



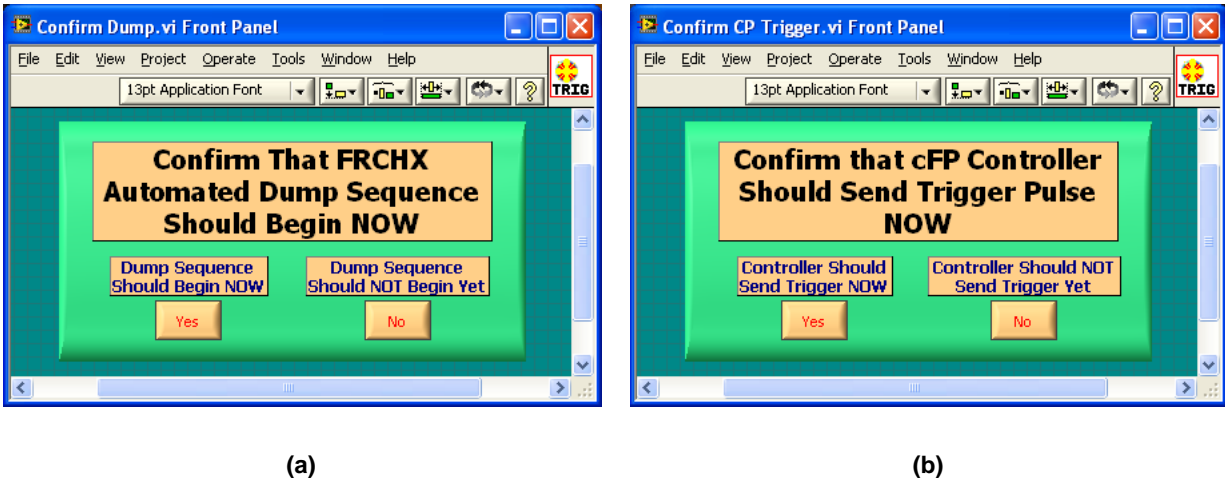


Figure 62. New software panels

Presently, the only interlocks the cFP controller polls regularly to determine their status are those that have been mounted on the doors and those on the rail-gap 40168 trigger amplifiers. Because it is known that no one was attempting to open one of the test cell doors during the FRCHX-1 test, it is hypothesized one of the doors may have been jarred by the wind. To deal with an intermittent opening such as this one in a door interlock, a software filter was added to the interlock-polling routine. If an open door is detected, no action is taken right away by the program; instead a timer, with an operator-defined time limit (currently chosen to be 1.0 s) is set, and only if the door is still open after that time limit expires does the program begin immediately to shut down the experimental systems. If the door has closed, the assumption is the door was bumped, because no one would be able to open and close the test-cell doors that quickly. The program then takes no action, but allows all operations to continue uninterrupted.

A low charge on the batteries in either the door-interlock boxes or in the Emergency-Abort control, which is not polled, but nonetheless could have caused the bank to dump, did not seem to be a likely cause of the control-system problem. However, it was felt the possibility should not be overlooked. The batteries in the door-interlock boxes were actually checked during the month prior to the test (November) and were found to be good. They were checked again following the test by operating the interlock system for an extended period of time, and no problems were encountered. The batteries in the Emergency-Abort control had not been checked prior to the December test. They were found to be a little low in voltage when they were inspected later in

January, although the control still appeared to be operational. Nevertheless, the batteries were replaced.

The most likely interlock failure to have occurred is that one of the rail-gap 40168 trigger amplifiers dropped out of ready status during the test. These units had been turned on so that their sync-out signals could be recorded to confirm proper timing of their triggers had the PI bank, Main bank, and/or crowbar switch been used. The Pre-Ionization (PI) 40168, in particular, had been observed to have such intermittent problems in earlier tests, although they were not frequent and occurred only following the operation of the PI or Main bank high-voltage triggers. Because such an event is a valid reason to abort a shot (because the 40168 requires approximately 5–10 minutes to return to ready status once it drops out), a software filter was not added to the LabVIEW routine reading in the status of these interlocks. It was decided to observe the trigger unit closely when FRC formation, translation, and capture tests begin. If the problem with it dropping out of ready status continues to occur, efforts will be made to troubleshoot and if necessary modify this interlock within the 40168. The interlock is in place to prohibit operation of the high-voltage systems in the 40168 before the thyatron inside it has had sufficient time to warm up; a hardware timer or a software timer that is not sensitive to any power fluctuations could replace the present interlock components.

As a final precaution, aimed more at catching future FRCHX bank problems sooner during tests rather than necessarily trying to eliminate them, the FRCHX control computer was moved to the Shiva control console where more personnel will be able to observe the Guide and Mirror and other FRCHX bank charge voltages, once the Shiva Star bank has started charging. At least one person will be present who should be able to alert everyone else of a potential problem that is occurring, and the shot can be aborted.

After examining the hardware following FRCHX-1 and the original design drawings for the hardware, failure in the current-feed insulator can most likely be attributed to (1) not enough encapsulant being present at the dielectric joint between the current-feed-disk insulator and the liner-return conductor insulator brim to displace all of the air in the joint; (2) not enough compressive force (weight) on the dielectric joint after the ViSil was put down to keep the

dielectric seal intact; (3) not enough of an overlap between the two solid-dielectric pieces; (4) bulk dielectric failure, possibly due to field enhancements near the stepped flange in the lower current feed; or (5) a combination of two or more of these factors. In the Jan-Mar quarter SAIC personnel redesigned the current-feed insulator and several features of the hardware around the insulator joint, concentrating on how best to mitigate each of these issues.

Figure 63 shows a detailed cross-sectional diagram of the hardware as it existed for the FRCHX-1 test.

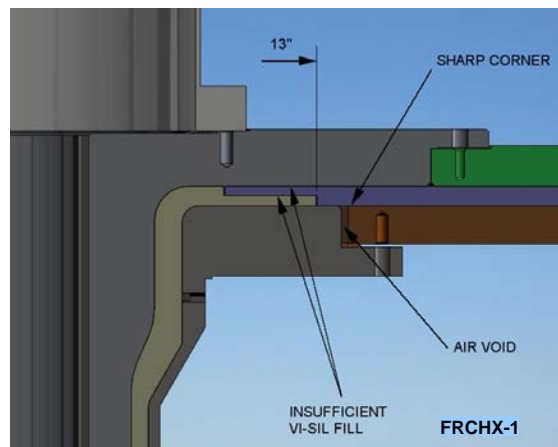


Figure 63. Cross-section of current feed and insulator design for FRCHX-1

Shown in the drawing are the upper and lower Shiva current-feed plates, the upper liner electrode, and the liner-return conductor in the region surrounding the insulator overlap. Also indicated in the drawing are an air void and a sharp corner that may have contributed to the bulk dielectric breakdown mentioned above. The two insulators had a 2-in. overlap, and the 13-in. brim of the cylindrical insulator between the upper electrode and return conductor was observed to end rather close to a seam in the lower current-feed plate.

Figure 64 shows a drawing of the hardware similar to that presented in Figure 63, with the new design changes incorporated.

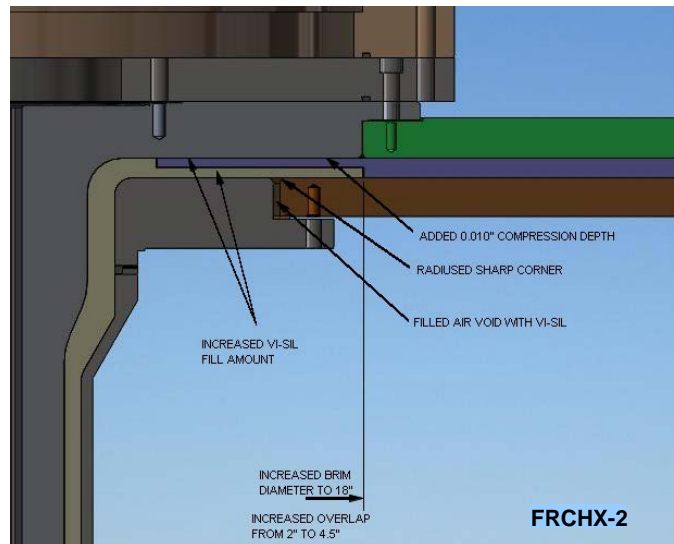


Figure 64. Cross-section of current feed and insulator design implemented for FRCHX-2

The most notable change is the increase in the brim diameter for the cylindrical insulator. This change increases the insulator overlap from 2 in to 4.5 in and moves the edge of the brim away from the seam in the lower current-feed plate. Also noted are the rounding of the sharp edge on the lower current-feed plate and an increase in the amount of ViSil to be used in the region around the insulator joint. Increased compression on the insulator joint was to be obtained by cutting an additional 0.010 in from the current joint on the upper liner electrode. Doing so effectively lowers the entire upper electrode, bringing it down more tightly against the insulator joint as the bolts that fasten it to the upper current-feed plate are tightened and as the lead weights are placed on the feed plate. This design was implemented for the second field-compression test, FRCHX-2, and the changes were found to be successful in preventing a breakdown from occurring again between the Shiva current-feed plates.

When the data that was recorded during the field mapping of the FRCHX-1 experimental setup was plotted, it was noted that the upper mirror field was considerably lower than was expected, based upon both numerical calculations and the field mapping that was performed earlier on the FRC formation, translation, and capture test setup. We show the data again here in Figure 65. Each data set shown corresponds to a different time after the start of the Guide and Mirror current pulse, and, as is indicated by the text in the graph, 0 cm corresponds to the location of the

top of the liner, and 30 cm corresponds to the bottom of the liner. The Guide and Mirror bank was charged to 2 kV for each of these measurements.

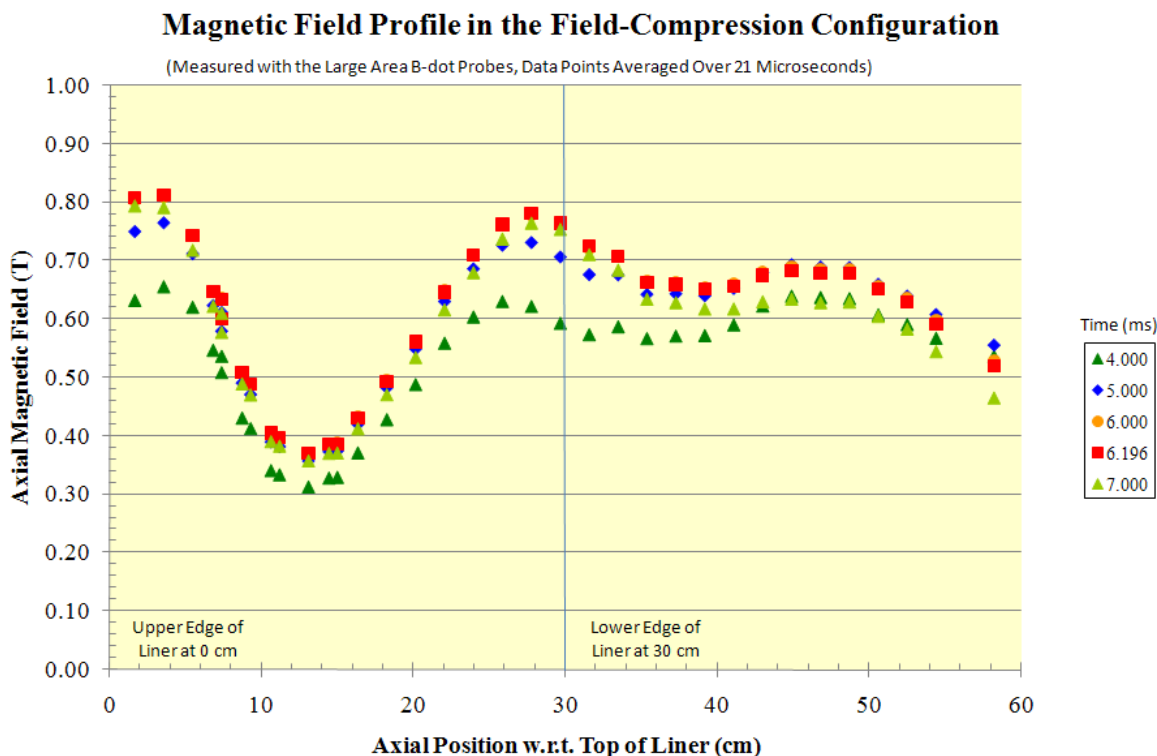


Figure 65. Axial-magnetic field vs. axial position obtained from measurements in FRCHX-1 test setup

The data shows that the ratio of the upper mirror field to the lower mirror field is 1.04, and the ratio of the trough field between the mirrors to the lower mirror field is 0.46. From their numerical modeling NumerEx personnel have found that there is a “sweet spot” for capturing the FRC after the start of liner compression when the ratios are 1.18 and 0.50, respectively. That is, the time at which the FRC is injected into the liner can be varied fairly broadly with these ratios compared to other field ratios. As mentioned, for the 1.04 ratio that was measured here, the FRC was not captured at all but passed through the liner or, if it was launched late enough in time, it bounced off the first mirror and went back into the formation region.

Initially, it was felt that the lower amplitude for the upper mirror field was caused primarily by the nearby presence of the thick upper electrode. After reviewing the design drawings, however, personnel were reminded that some additional rings had also been placed around the liner to hold

it in place against the upper electrode. Figure 66 shows a diagram of the upper end of the liner illustrating this clamping arrangement.

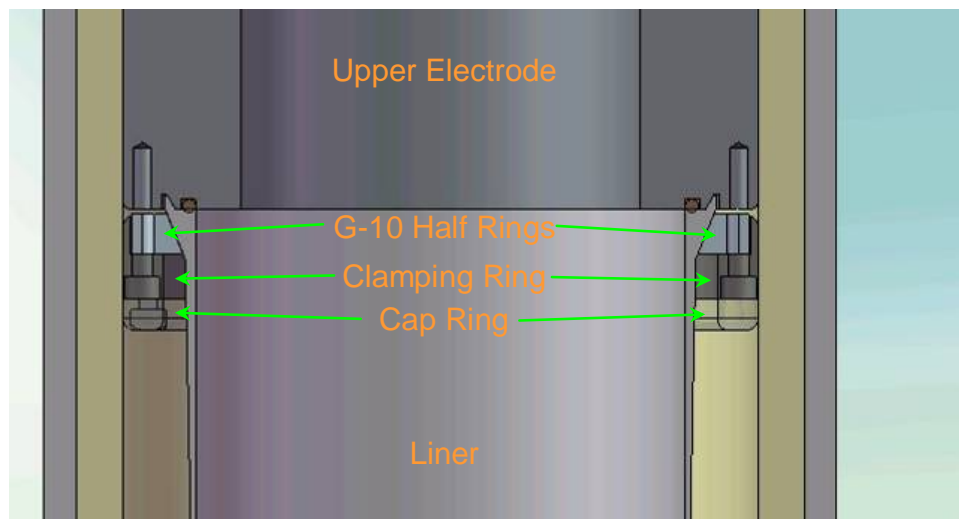


Figure 66. Upper liner-clamping assembly

The liner was gripped by two G-10 half-rings, and these were held against the liner by a titanium clamping ring. Titanium screws drew the clamping ring against the upper electrode, compressing the liner-upper electrode current joint. The titanium clamping ring was then covered with an aluminum cap ring to round the sharp edges of the clamp ring. The lower liner-electrode configuration was similar, except that the titanium clamping ring was slightly larger, which allowed its corners to be rounded, and therefore the aluminum cap ring was not used.

Titanium has a resistivity that is somewhat comparable to stainless steel ( $55 \mu\Omega\text{-cm}$  vs.  $72 \mu\Omega\text{-cm}$ ), but the presence of the titanium ring was an additional component through which the magnetic field needed to diffuse. Aluminum has a much lower resistivity of  $2.7 \mu\Omega\text{-cm}$ ; therefore, the cap ring appears to have been the predominant cause for the upper mirror being lower in amplitude. When preparing for the second field-compression test, the cap ring was fabricated of stainless steel.

Though the change from aluminum to stainless steel for the cap ring was an improvement, simulations performed by AFRL personnel with COMSOL Multiphysics, a finite element physics and engineering analysis package, indicated that further changes were still needed to bring up the amplitude of the upper mirror field. Keeping the positions of the mirror coils fixed

(so that changes to the Guide and Mirror coil support hardware and their bus work would not be required), variations in the winding arrangement of the coils, in particular that of the Mirror 2 coils, were explored.

Figure 67 shows axial field profiles calculated by COMSOL Multiphysics for four of these variations.

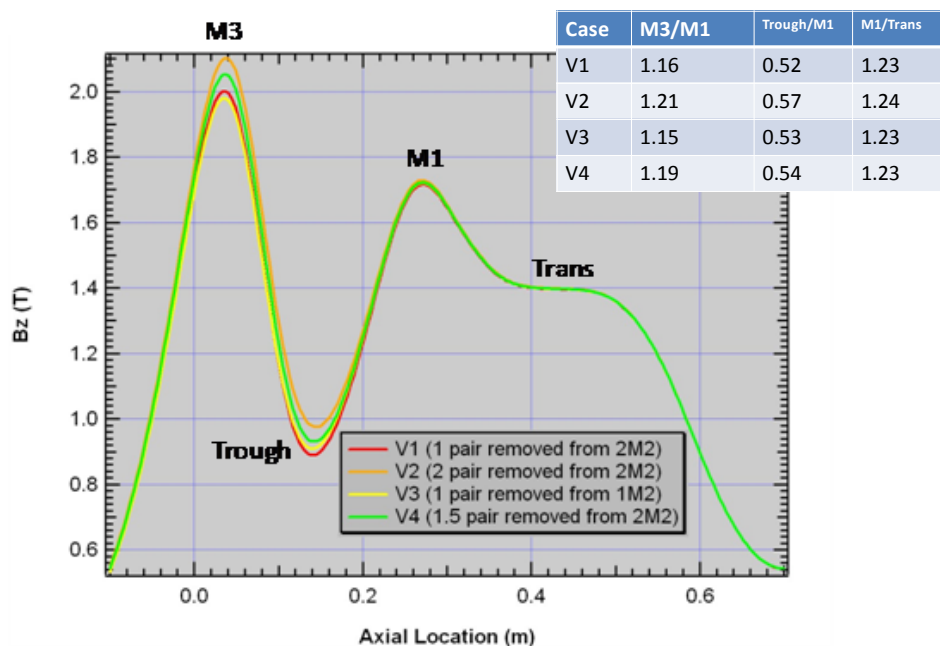


Figure 67. COMSOL Multiphysics calculations of axial-magnetic field with Mirror 2 coils modified

Variation 1 involved removing a pair of windings from the top Mirror 2 coil (the one adjacent to the Mirror 3 coils, “2M2” in the graph); variation 2 involved removing two pairs of windings from this coils; variation 3 replaced the windings on the top Mirror 2 coil and removed a pair of windings from the lower Mirror 2 coil (“1M2”); and variation 4 focused again on the upper Mirror 2 coil, removing three windings from it (1.5 pairs). As can be seen from the graph, this last variation provided the closest match to what was desired, because the ratio of the upper mirror to the lower mirror exceeded the target of 1.18, while the ratio of the trough field to the lower mirror was kept the closest to its target of 0.5. Figure 68 illustrates the new winding scheme for the set of Mirror 2 and Mirror 3 coils. With three windings removed from the top Mirror 2 coil, there are three windings remaining in the top winding layer of this coil that are

closest to the Mirror 3 coils and four windings in the layer just below it. The lower Mirror 2 coil was left unchanged.

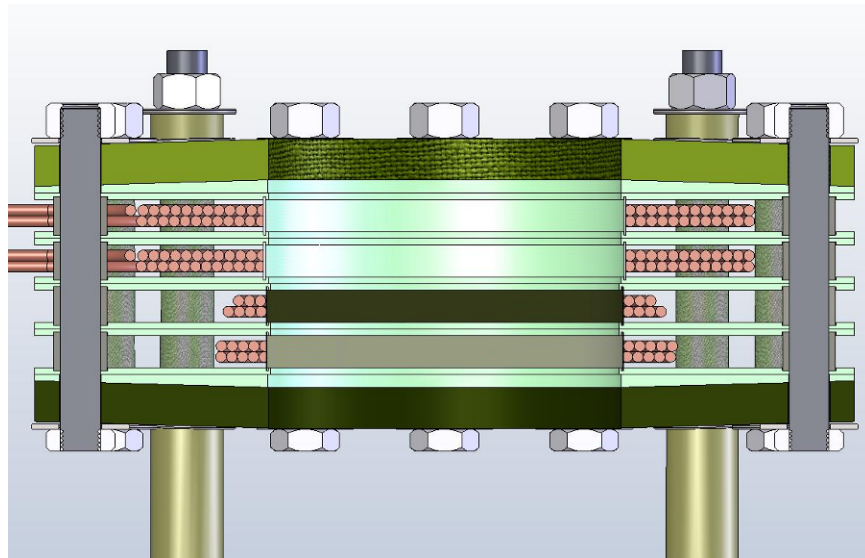


Figure 68. New upper mirror coil arrangement

Having modified the configuration of the upper mirror coils slightly by removing these three windings, the Quick Field™ Lorentz force analyses that were presented earlier were repeated to determine if the net forces on these coils would be changed. Recalling that the Mirror 2 coils are pulsed with a polarity opposite that of the Mirror 3 coils and that they therefore want to push away from each other, it was still anticipated that a robust clamping scheme would be needed to keep these upper four coils from cracking and deforming during full-current tests.

Figure 69 shows a diagram of the coil geometry as it was entered into Quick Field.



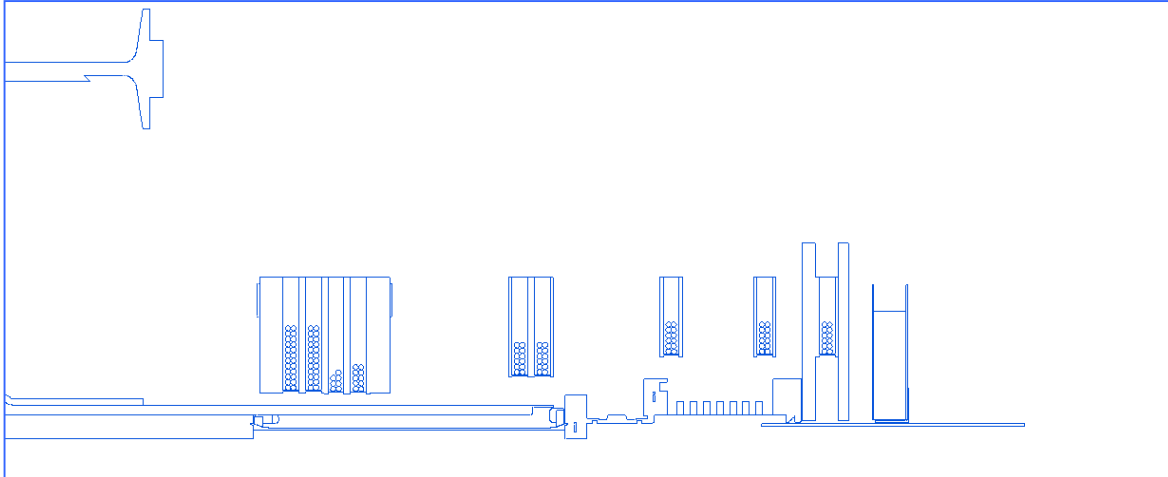


Figure 69. Guide and Mirror coil geometry entered into Quick Field

“Up” is to the left in the illustration, and “down” is to the right. Note that along with the coil windings and their dielectric support structures the model now also includes the liner, its electrodes, the return conductor, and other metallic structures within the bore of the coils. The peak winding current was set at the same amplitude as in the previous analysis, 11.3 kA, and the windings in the Mirror 2 coils again had a negative current to represent their opposite polarity. Using this geometry and these parameters, a time harmonic magnetic analysis was performed again at a frequency that is appropriate for the Guide and Mirror bank current waveform, which is approximately 50 Hz.

To check quickly for blatant errors in the Quick Field model before proceeding, the peak magnetic field on axis was plotted (Figure 70) and then compared to the COMSOL Multiphysics results shown in Figure 67 for variation 4.

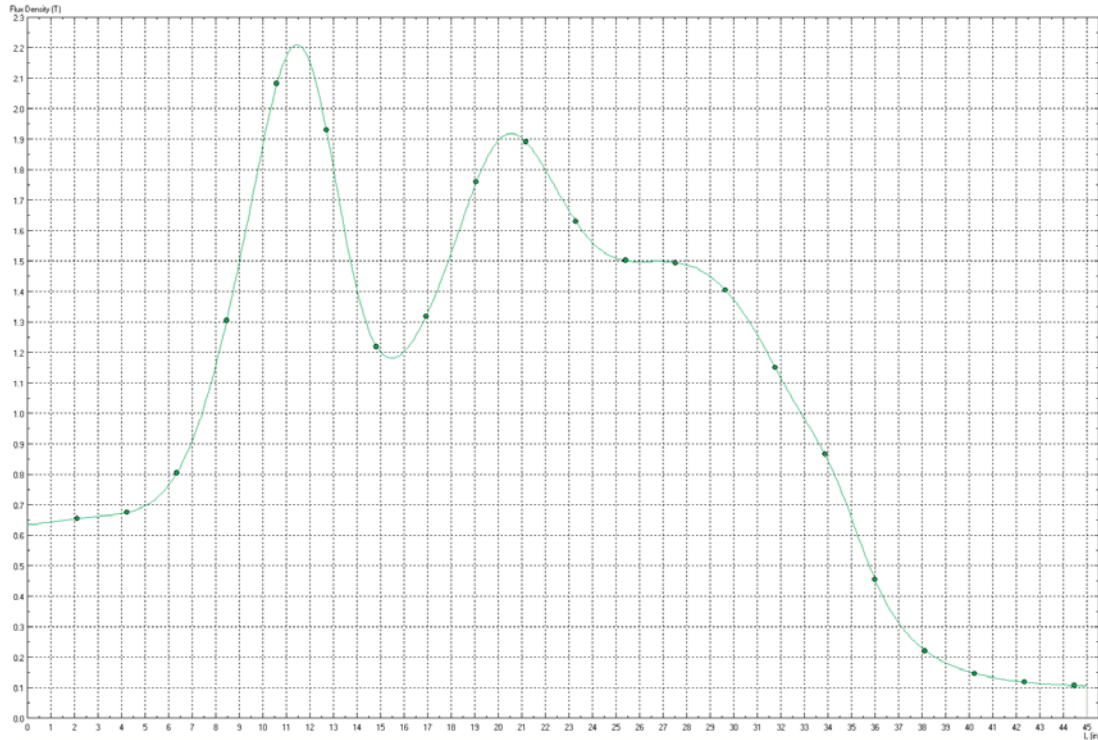


Figure 70. Calculation of magnetic field along axis (bottom) of geometry shown in Figure 67

The top of the liner in the Quick Field graph is located at  $L = 10$  in, and the bottom of the liner is at  $L = 21.81$  in. Though the ratios of the upper mirror to the lower mirror and the trough field to the lower mirror are observed to differ slightly from that calculated by COMSOL Multiphysics, being 1.15 and 0.61, respectively, the profile of the field is generally consistent with that shown in Figure 68. The differences that are present are likely a result of the fact that the Quick Field analysis is, again, a time harmonic analysis and not a true transient analysis. The time harmonic Lorentz force calculations on the coils should be much closer to the transient results because the fields of interest do not have to diffuse through any metallic structures. These results are therefore expected to be able to guide reliably the final design of the clamping structure for the coils.

Figure 71 shows a Quick Field color contour plot of the instantaneous Lorentz forces on the structures in this model calculated at the peak of the current.

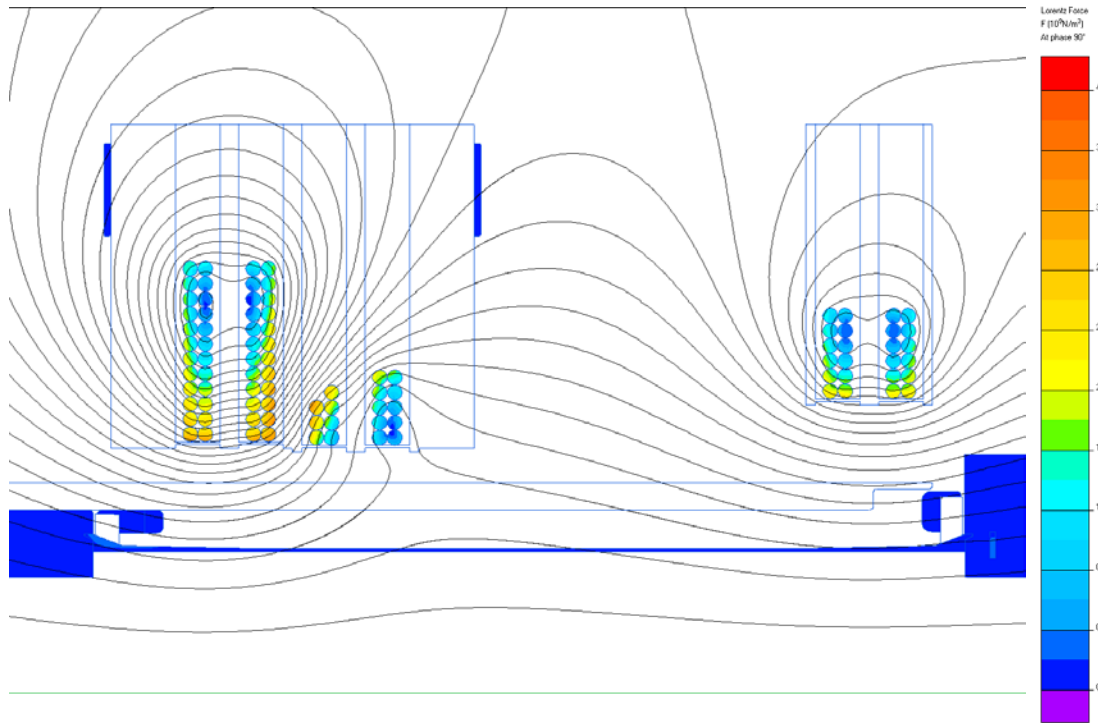


Figure 71. Calculation of Lorentz forces on coils and hardware shown in Figure 70

Overlaid on this plot are magnetic field line contours. Both the color shading on the Mirror 2 and Mirror 3 coils and the distribution and orientation of the magnetic field lines highlight the rather large forces that are present on these coils when they are pulsed.

Figure 72 illustrates the placement of contours around the Mirror 2 and Mirror 3 coil pairs for the purpose of calculating the net forces on these coils, and values of 93.4 kN and 84.5 kN, respectively, were calculated. Again, these are the instantaneous peak forces that occur at the current maximum, and it is interesting to note that they are down by 25% compared to the values calculated before the three windings were removed. Thus, removing the windings from the upper Mirror 2 coil has also served to decrease the forces between the Mirror 2 and Mirror 3 coil pairs.

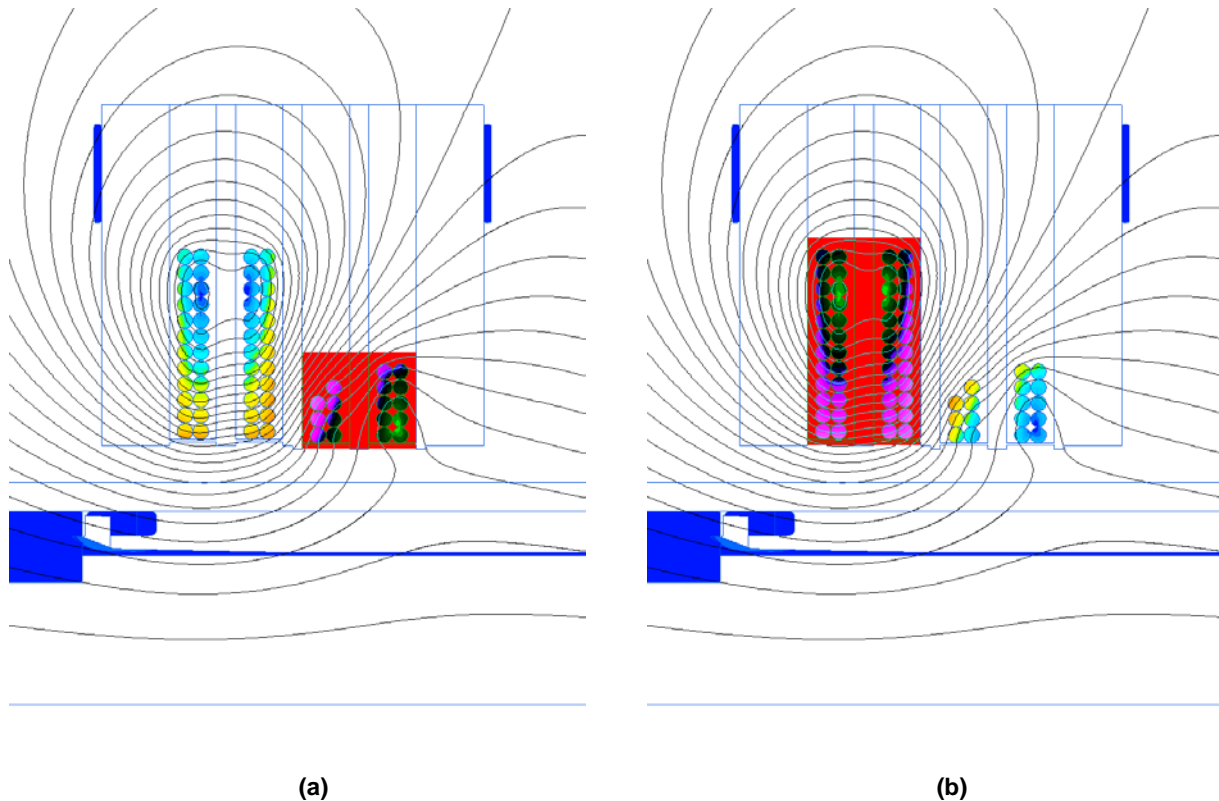


Figure 72. Quick Field calculates a net force of (a) 93.4 kN ( $2.11 \times 10^4$  lb) on Mirror 2 coils; (b) 84.5 kN ( $1.90 \times 10^4$  lb) on Mirror 3 coils. SAIC mechanical engineers took the data from these calculations and inserted it into a Rasna analysis of the upper set of four coils to develop a more robust method for clamping the coils. The initial starting point for the new clamping structure involved simply using very thick G-10 plates above and below these coils. With the Quick Field forces and the Rasna calculations, personnel were able to devise a way of using thin beveled plates between the thick G-10 plates and the coils to place a pre-load on the coils that the magnetic forces would have to overcome before they could begin to deform the coils and the G-10 plate. The SolidWorks diagram in Figure 68 shows how these beveled plates are sandwiched between the coils and the thick G-10 plates, to the point of distorting the G-10 plates when the coil assembly is bolted together. Figure 73 shows the actual Guide and Mirror coil assembly fabricated for the FRCHX-2 test.

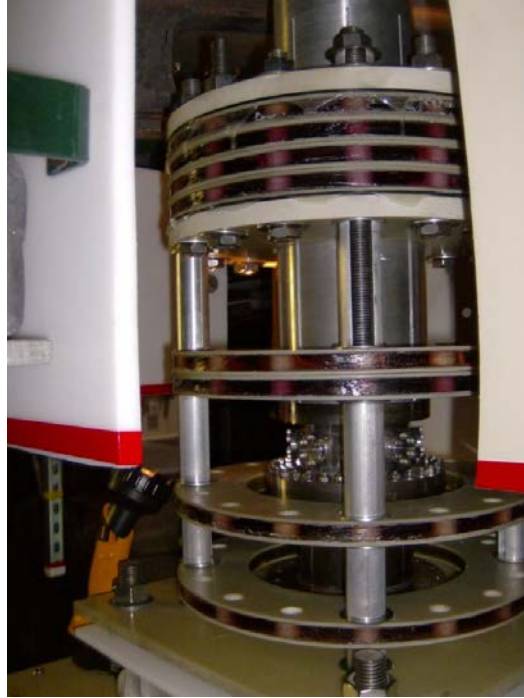


Figure 73. Guide and Mirror coil structure with new clamping assembly on each side of upper coil set

#### 3.1.2.2.2 Shot Preparations

This section focuses on the final hardware assembly and other preparations that were made for FRCHX-2 once the changes to software and hardware designs that were discussed in the previous section were implemented. We present a brief overview of the liner-hardware assembly, followed by a similar overview of the assembly of the Guide and Mirror coils and other “lower” hardware. The mapping of the axial Guide and Mirror inside and just below the liner is outlined next, followed by a discussion of a fault that occurred on the Guide and Mirror bank when trying to charge the bank to the voltage needed for operation for FRCHX-2. This section concludes with a presentation of the various diagnostics that were fielded for FRCHX-2 and the data that was obtained with them during the test. It should be noted here that the upper half of Module F-1 of the Shiva bank had a momentary arc fault to its frame just before the command trigger was initiated for the shot. Though the pulsed power systems performed successfully in all other respects, the net voltage on the upper half of the Shiva bank was reduced to 36.7 kV (vs. -42.3 kV on the lower half of the Shiva bank).

We briefly outline the various assembly steps associated with putting together the Shiva current feed and the liner-load components that attach to it. Highlighted in particular is the installation of the dielectric insulator that goes between the liner and its return conductor, where the fault occurred during FRCHX-1. First, the return conductor is attached to the lower Shiva current-feed plate (Figure 74).

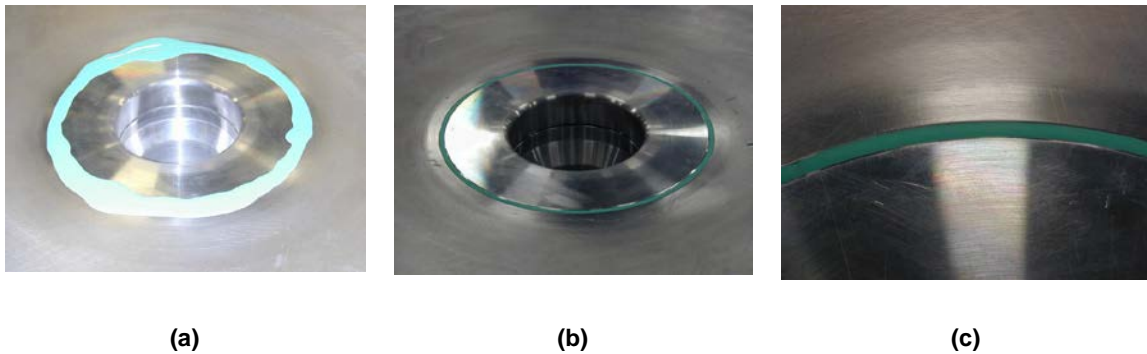


Figure 74. Attachment of liner-return conductor to lower Shiva current feed

Particular care was taken to ensure that the air void between the return-conductor flange and the Shiva lower conductor disk was filled with ViSil (Figure 74a). Once cured, the ViSil was trimmed flush with the conductor surface (Figure 74b). The close-up view in Figure 74c shows how the sharp corner on the lower conductor plate was radiused prior to assembly to reduce any field enhancements at this location.

Once the return conductor was installed, the Shiva current-feed (disk) insulator was placed down onto the lower current feed, and the liner-return-conductor insulator was inserted into the return conductor. Again, ample ViSil was applied to the insulator-overlap region (Figure 75). That the ViSil thoroughly fills the overlap region can be seen by the pale green coloring within the stepped region (inside the fictitious violet circle).

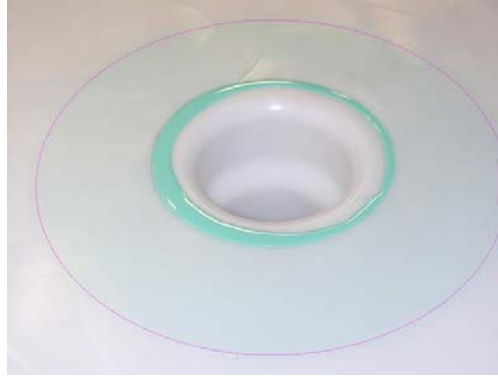
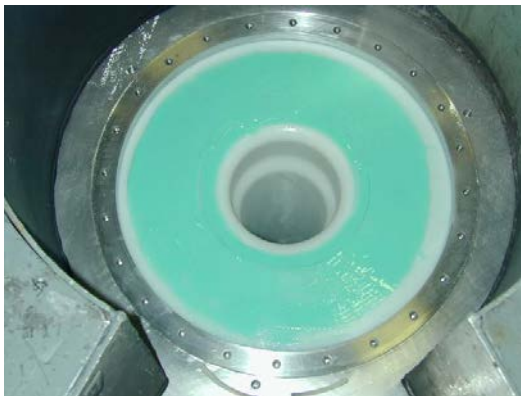


Figure 75. Bonding liner-return-conductor insulator to Shiva current-feed insulator

The next step was to place the Shiva upper current feed onto the disk insulator and bolt the feed plate down to the hex plate surrounding it. Afterwards, the liner upper electrode was then lowered into place and bolted down to the feed plate. Just prior to the installation of the upper electrode, however, more ViSil was applied above the insulator overlap (this was not done previously for FRCHX-1) to displace any air between the insulator and the upper electrode (Figure 76a).



(a)



(b)

Figure 76. (a) Application of another layer of ViSil above insulator overlap; (b) weep holes confirmed region had been thoroughly filled with ViSil

Six weep holes were placed in the upper electrode; these provided an exit path for the excess ViSil and in doing so also gave confirmation that the air voids were filled. For the FRCHX-2 assembly shown here, all six weep holes were observed to have excess seepage (Figure 76b). We noted that after disassembling the FRCHX-1 hardware, only one weep hole and a portion of a second showed any evidence of excess ViSil within this region.



With both the upper electrode and the return conductor now in place, the liner was ready to be installed next. The clamping scheme outlined in Figure 66 was used again to attach the liner to the upper electrode. Section 2.3 mentioned a similar clamping assembly used to fasten the lower electrode to the liner. The remaining vacuum components positioned below the liner-lower electrode were installed after the Guide and Mirror coils were moved into place.

Following the FRCHX-2 test, the current-feed hardware was disassembled with no evidence of any tracking or arcing on any of the insulator surfaces. Thus, the changes to the insulator and the assembly procedures outlined here appear to have successfully corrected the current-feed problem encountered during FRCHX-1.

With the exception of the improved clamping scheme for the upper mirror coils and an RF enclosure added for the B-dot probe package, the setup for the Guide and Mirror coil assembly and its support table was generally the same as for FRCHX-1. Figure 77 shows an illustration of this hardware configuration.

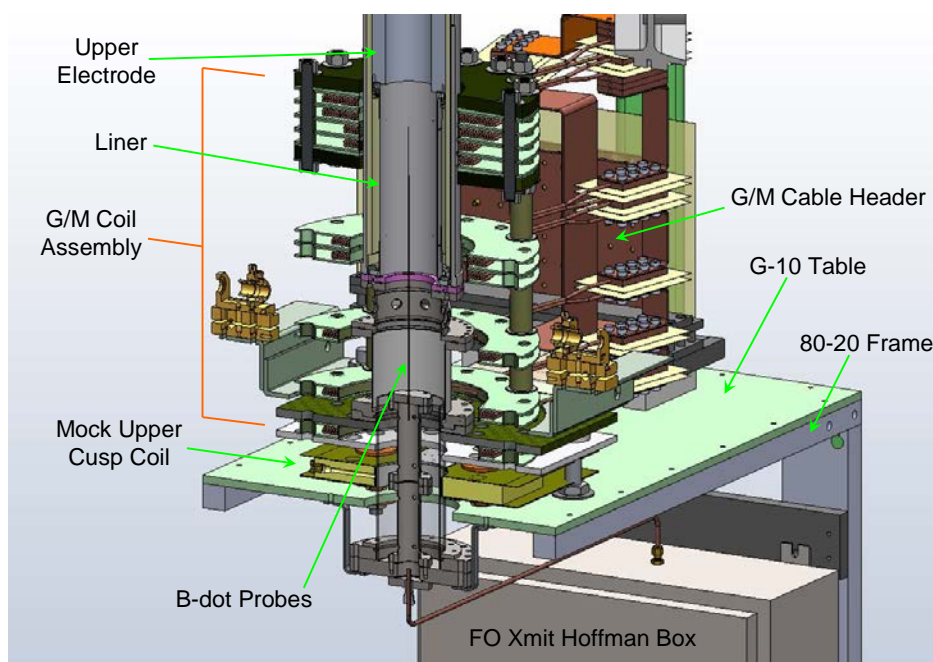


Figure 77. Lower-hardware configuration for FRCHX-2

A mock Upper Cusp coil was again placed below the lower Guide coil to take into account any effects that the large aluminum coil might have on the lower Guide field profile, as well as to



provide an indication of the amount of damage that the Theta and Cusp coils might take during an FRC compression-heating test. The mock Upper Cusp coil, the Guide and Mirror coil assembly, and the Guide and Mirror cable header were placed on the same 2 ft by 4 ft G-10 table that was used for FRCHX-1, though the “80-20” frame for the table had been rebuilt following that last shot. Once the coils and table were in place, the diagnostic spool and mock bellows, both of which were also used in the last shot, were inserted within the bore of the Guide and Mirror coils and then attached to the lower liner electrode. The B-dot probe package was the last item to be raised up into position, which was done following the mapping of the Guide and Mirror fields, to be discussed next.

The RF enclosure (Hoffman box) that was added was mounted to the frame below the G-10 table and was used to house three fiber-optic transmitters that were set up to transmit the B-dot probe signals to the FRCHX remote data acquisition box (Figure 78a). The twisted pair leads from the B-dot probes were run directly from the vacuum vessel to the Hoffman box through a copper tube conduit (Figure 78b), the opening of which was filled with Torr Seal to seal off the conduit.



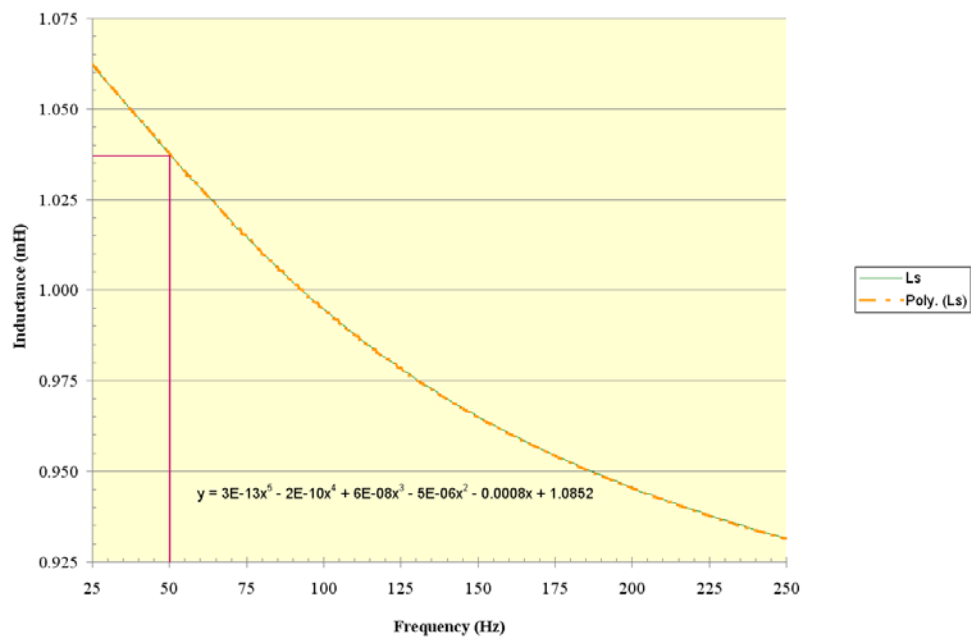
(a)



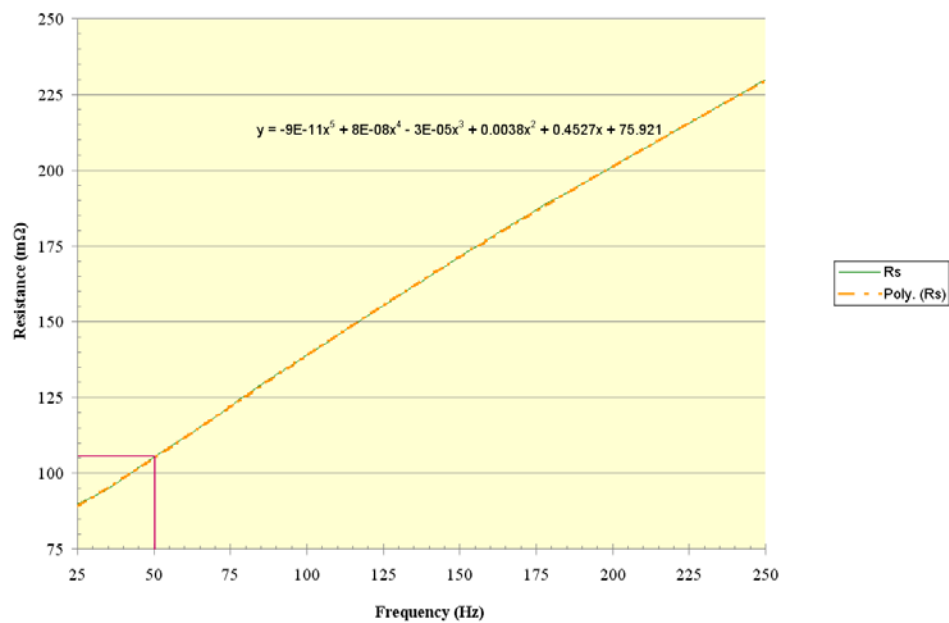
(b)

Figure 78. (a) Inside Hoffman box; (b) copper tube used to run B-dot probe twisted pair leads to Hoffman box

Once the Guide and Mirror coil assembly had been set up on the G-10 table, the inductance and resistance of the coils were measured with a QuadTech LCR meter to characterize the coils and enable comparisons to be made with the earlier sets of coils that were fabricated. Figure 79 shows plots of the inductance and resistance as a function of frequency from 25 to 250 Hz.



(a)



(b)

Figure 79. Guide and Mirror assembly (a) inductance and (b) resistance measured with QuadTech LCR bridge

A curve fit for each trace was calculated by Microsoft Excel, shown as a dashed line in the respective plots along with the analytical equation for the curve fit. As can be seen by the red markers in each plot, the inductance and resistance at approximately 50 Hz, which again is the approximate ringing frequency of the Guide and Mirror circuit measured in earlier bank tests, are approximately 1.037 mH and 106 m $\Omega$ , respectively. These values compare well with the inductance and resistance measured for the coils on the FRC formation and translation test setup, 1.030 mH and 86 m $\Omega$ , respectively.

At this time the fields throughout the translation and liner and compression regions were mapped using the same large-area B-dot assembly that was described in Section 3.1.2.1.2. Figure 80 shows the probe assembly again for reference. The probe assembly also has two Hall probes in it, but because of problems encountered with their current supply, they were not able to be used in the field-mapping measurements described here. As was the case for the FRCHX-1 field-mapping exercise, a 34-in. long quartz tube was inserted up into the mock bellows and diagnostic spool as far as the bottom of the lower electrode (Figure 77); this tube served as a guide for the field-mapping-probe assembly.

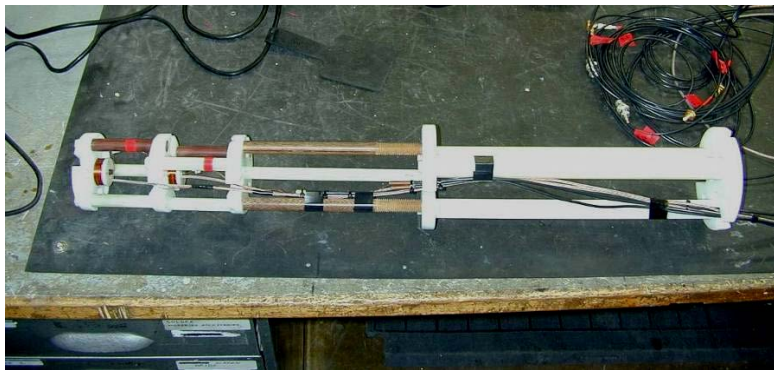


Figure 80. Field-mapping-probe assembly

When performing the field-mapping measurements, the probes were moved in increments of 0.75 in (1.91 cm). The mapping of the upper B-dot probe (“B-dot probe #1”) spanned from the bottom of the lowest Guide coil to the top edge of the liner. Figure 81 shows a plot of selected large-area B-dot probe data that was recorded during these measurements.

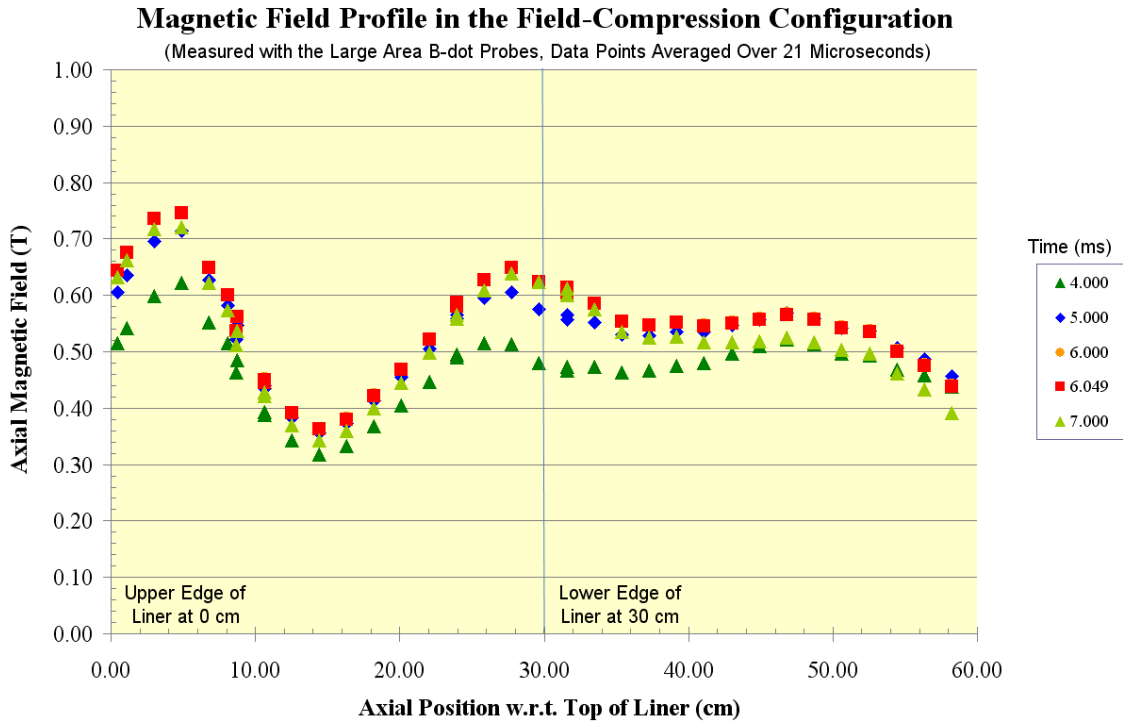


Figure 81. Axial-magnetic field vs. axial position in field-compression test setup

Each data set shown here corresponds to a different time after the start of the Guide and Mirror current pulse. As is also indicated in the graph, “0 cm” corresponds to where the top of the liner is located, and “30 cm” corresponds to where the bottom of the liner should be. For each of these measurements the Guide and Mirror bank was charged to 2 kV. Several interesting observations can be made when comparing this data with the FRCHX-1 data in Figure 65.

First, we see that the field reaches its peak within the liner slightly sooner than before, at approximately 6.049 ms instead of 6.2 ms. Also, the upper mirror to lower mirror and the trough field to lower mirror ratios are now 1.15 and 0.58, respectively. When compared to the ratios obtained from the data in Figure 65, which are 1.04 and 0.46, one can see that removing the three windings in the top Mirror 2 coil and replacing the aluminum cap ring with the stainless ring have yielded close to the desired results. While these values do differ slightly from the desired values of 1.18 and 0.50, as well as from the values that were predicted by COMSOL Multiphysics (1.19 and 0.54 as seen in Figure 67), they should still be acceptable and are definitely an improvement. Interestingly, the measured values actually agree slightly better with

the ratios calculated from the Quick Field time harmonic data shown in Figure 70, which are 1.15 and 0.61.

One final observation to be made is that despite the increased ratios just discussed the actual magnetic field values shown in Figure 81 are generally lower everywhere than those shown in Figure 65. The upper mirror is reduced by approximately 9% and the lower mirror and guide fields are reduced considerably more, by approximately 16 %. The trough field, interestingly, is relatively unchanged. Given that the Guide and Mirror coil-assembly inductances were very similar between the FRCHX-1 and FRCHX-2 coil sets and that the current rise times for both coil sets were very similar, it does not seem likely that there were any changes with the Guide and Mirror circuit that could account for this difference. It is possible that the liner-return conductor, which had only eight slots in it for the FRCHX-2 setup, is responsible for this decrease in field within the liner. With fewer slots present the magnetic diffusion time may be expected to be longer everywhere throughout the liner region. With a longer diffusion time the field, of course, will not reach the same amplitude before the current pulse passes through its maximum. The difference in return-conductor slots should not have affected the guide field amplitude, however, as the hardware in this region is unchanged. Although the cause of the lower field was not clear, the fact that it was lower meant that the Guide and Mirror bank had to be charged to a higher voltage to set up the same target field (2T) inside the liner during the field-compression test.

During the final field-mapping tests, the charge voltage was therefore increased to determine how the field was scaling with charge voltage and at what charge voltage to which the bank needed to be charged to achieve a field of 2 T at the upper mirror. Figure 82 shows a plot of the magnetic field vs. time for charge voltages of 2 kV, 3 kV, and 4 kV.

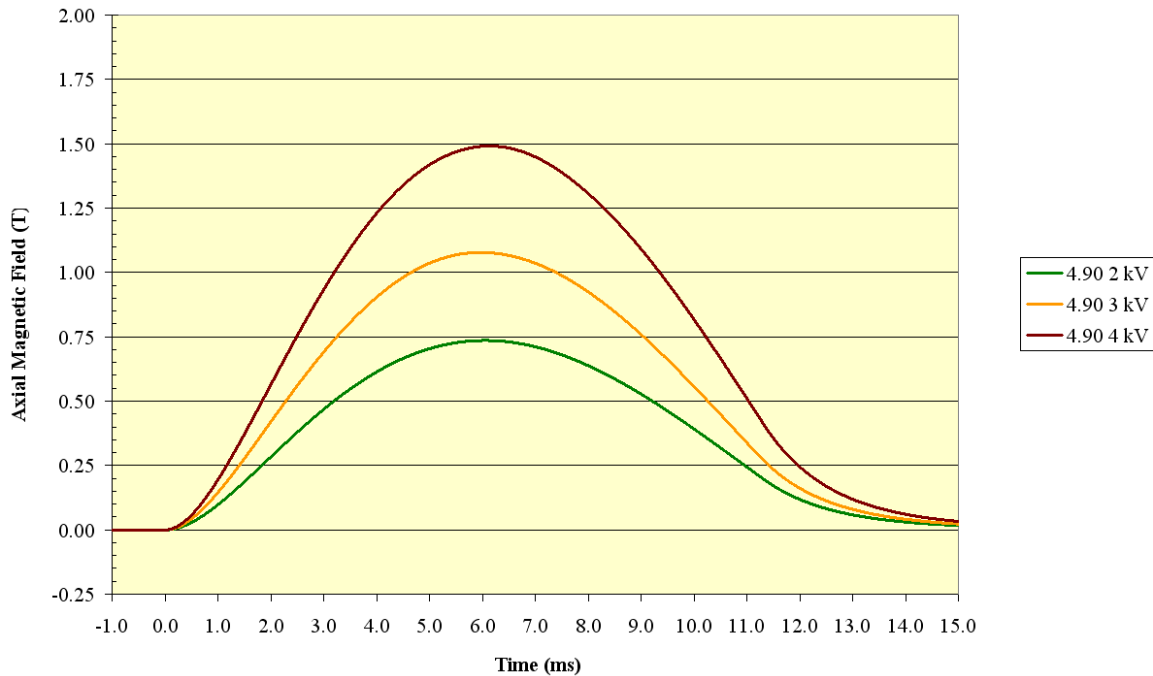


Figure 82. Axial-magnetic field vs. time for three Guide and Mirror bank-charge voltages

These measurements were made at 4.90 cm from the top of the liner, the location where the maximum field was observed in the upper mirror in Figure 81. Using this data, it was estimated that a charge voltage of 5.3–5.4 kV would be needed to inject a 2 T field into the liner at this location during the field-compression test.

These final field-mapping tests also served as an opportunity to test the new clamping scheme for the upper four mirror coils. While the G-10 clamping disks seemed to be holding up well to the higher coil currents and exhibited no signs of unusual stress, it was noted that the epoxy in the upper four mirror coils, which was the same as that used in the previous coil sets, had immediately begun to exhibit signs of cracking once the bank charge voltage was raised to 3 kV and above. As was the case at this point during the FRCHX-1 field mapping, it was therefore decided not to test the coils at any higher currents but to wait until the actual field-compression test to pulse them at their target current for fear that irreparable damage might be done to them. However, with confirmation that the new clamping setup for the coils at least seemed to be working, personnel began looking at alternative epoxies that are less brittle as a possible potting compound for these upper four mirror coils. If sufficient space is available in the coil spools, a

strip of fiberglass cloth may also be wrapped around the coil windings before potting them in their respective spools.

With the failure of the Guide and Mirror bank to hold charge during the FRCHX-1 test, a number of charge-and-dump tests with the Guide and Mirror bank were performed to determine if the problem could be repeated. These tests involved charging the bank to its FRCHX-1 target voltage of 4.7 kV, sometimes with the Shiva bank also being charged (to only  $\pm 5$  kV) in an attempt to duplicate all the conditions during the FRCHX-1 test. In all cases the Guide and Mirror bank was allowed to hold its charge for approximately 15–20 s before dumping it, but the problem could not be replicated. Therefore, the findings of these tests left only the software-related problems that were listed earlier as being the possible causes for the problem encountered during the FRCHX-1 test. The software edits discussed in this section were then implemented in an effort to address this issue.

When it was determined that the target charge voltage for FRCHX-2 needed to be higher (5.4 kV), we wanted to perform at least one charge-and-dump test at this new voltage both to obtain a measurement of the time required for the bank to reach this voltage and to make sure that the bank experienced no problems when being charged to a higher voltage. Prior to this time, the highest voltage that the bank had been charged to was 4.7 kV, and it was charged to this voltage for these recent tests. Unfortunately, when attempting to perform the charge-and-dump test at 5.4 kV, there was an arc near one of the insulators between the bus plates on one of the Guide and Mirror bank modules. The arc occurred at just 4.8 kV.

Because of the desire not to have such an arc repeat itself while performing the actual field-compression test, the circumstances surrounding the arc (specifically the placement of cables, the conditions of the bus plates, and other details) were examined thoroughly. In addition, Quick Field simulations were performed to examine electric field distributions in the vicinity of the arc. From these simulations, we concluded that it was likely that field enhancements at edges and corners, in combination with close proximity between the capacitor charge cables and hot conductors, was likely responsible for the arc. We made several changes to the Guide and Mirror bank modules, and believe that the problem was fixed.

It is encouraging to note that once the repairs and changes to the Guide and Mirror bank were completed, the charge-and-dump tests were attempted a second time, and no problems were encountered. During these tests the bank was charged several times to 5.5 kV, slightly beyond the 5.4 kV required for FRCHX-2.

#### *3.1.2.2.3 Diagnostics and Test Results*

A relatively large number of diagnostics was fielded on the first field-compression test, primarily in an effort to ready them for use on the first FRC compression-heating test, though some were also expected to yield pertinent data on FRCHX-1. To simplify the second field-compression test, however, the number of diagnostics was reduced to include only those most essential or those that were not able to be readied in time for the first test. The following list, categorized according to importance for this test, identifies the diagnostics that were fielded for FRCHX-2.

##### Primary Performance Diagnostics:

- *Typical performance (pulsed power) diagnostics.* These include Shiva arm and load Rogowski coils, load B-dot probes and V-dot probes, and Faraday rotation. Also included among these was the Guide and Mirror cable header Rogowski coil for measuring the total Guide and Mirror current.
- *Axial B-dot probe array.* This was an array of probes inserted into the liner to measure injected and compressed magnetic fields. The number of probes was reduced for FRCHX-2 to include only one probe at each of the three measurement locations. In addition, their signals were transmitted to digitizers this time through fiber-optic links to improve signal bandwidth.
- *Radiography to provide side-on images of the liner.* As with FRCHX-1, two heads were used, with two image times, and armored digital film packs. The images were to show how axially uniform the implosion was (at least within the field of view) and give evidence of fluting if abnormal wall thicknesses were observed. Concerns about fluting in the liner during the implosion arose from the slots in the return conductor.



## Secondary Diagnostics:

- *Interferometer with optical fiber probe (null test).* This was the first test of an interferometer probe beam transmitted to and from the interferometer optics board through fiber-optic cables. For this test, however, the fibers were not run to the center of Shiva but rather left coiled up near the optics board.

A detailed listing of the pulsed power diagnostics for this shot includes 10 Rogowski coils to monitor discharge current (one per Shiva arm and four in the center section); a single-turn Faraday fiber-optic probe to monitor the discharge current; three B-dot probes located near the load and 120° apart at a radius of 9.36 cm; three voltage monitor probes to monitor the voltage on Shiva; and Shiva Arm Rogowski Coils.

As is normal for Shiva Star capacitor-bank shots, there were Rogowski coils at the end of each of the six transmission arms comprising the capacitor bank. After removing cable-signal delays, the average start time for these current signals is 1.125  $\mu\text{s}$ , which will be referenced when giving times with respect to the start of Shiva current. Figure 83 shows the individual arm Rogowski coil signals.

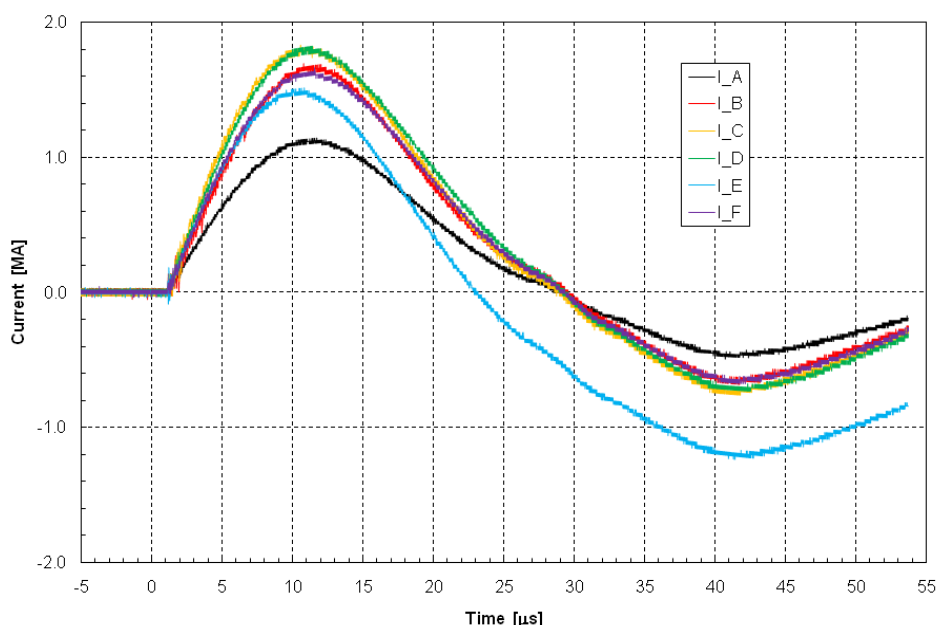


Figure 83. Overlay of current waveforms recorded for each of Shiva Star arms

The data from the six arm Rogowski coils is then summed. This result is shown in Figure 84.

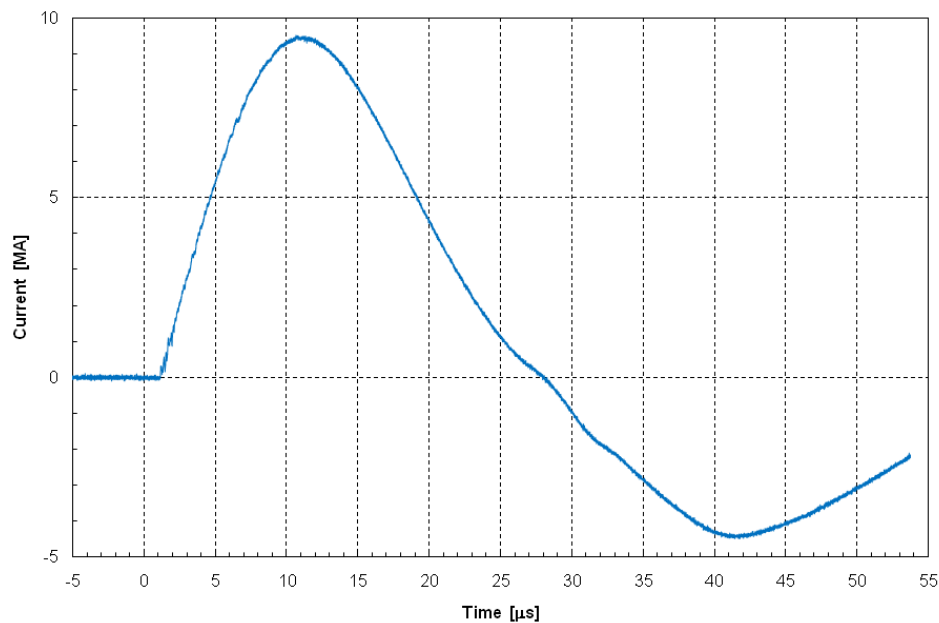


Figure 84. Summation of each of arm-current waveforms from Figure 84

In Figure 84, the peak value of the signal is  $I_{\text{sum}} = 9.54 \text{ MA}$ , and it occurs at  $10.640 \mu\text{s}$  ( $9.515 \mu\text{s}$  with respect to the start of Shiva current).

The four Rogowski coils located near the center section of the Shiva bank were divided into two groups with a pair of coils per group. Each pair of coils measures opposite halves of the discharge current, with each pair looped around the center in the same direction. Hence, the prefix designation for the coil names is CW and CCW for clockwise and counter-clockwise, respectively. By summing the respective CW and CCW signals we get the total current delivered. By adding the summed CW and CCW signals together we should get zero current—i.e., the CW (CCW) signal is  $+ (-) \times A$ . The value of current remaining after adding the summed CW and CCW data is the common-mode noise (CMN) current. This CMN current is divided in half and subtracted from the summed CW (CCW) data, and these results are referred to as the corrected CW (CCW) currents. Figure 85 shows the discharge current data.

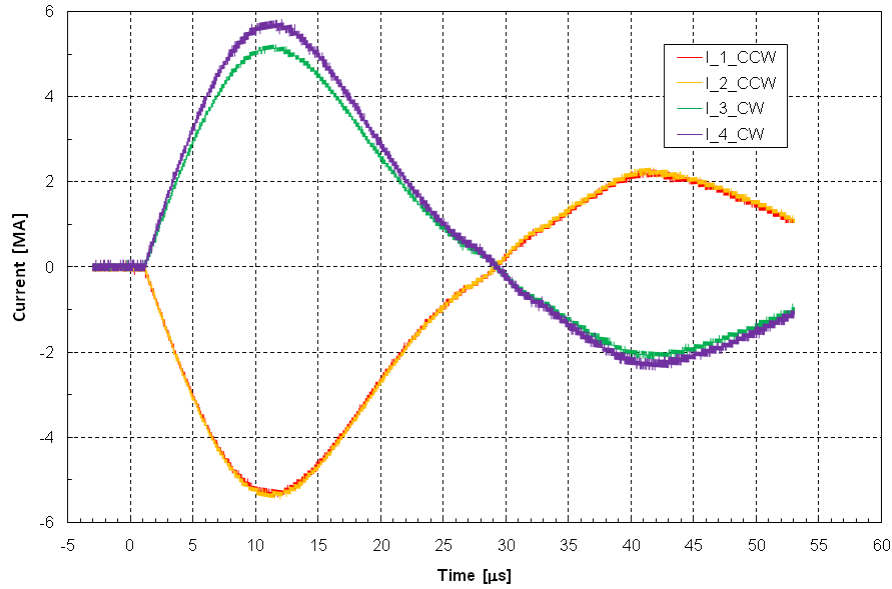


Figure 85. Shiva CW and CCW load Rogowski current waveforms, shown overlaid

The peak values of the above signals are  $|I_{1\_CCW}| = 5.40$  MA,  $|I_{2\_CCW}| = 5.43$  MA,  $I_{3\_CW} = 5.23$  MA,  $I_{4\_CW} = 5.84$  MA.

Using the Shiva center section Rogowski coils, the common-mode noise current and the two corrected CW/CCW discharge currents are calculated. Figure 86 shows the total Shiva load current.

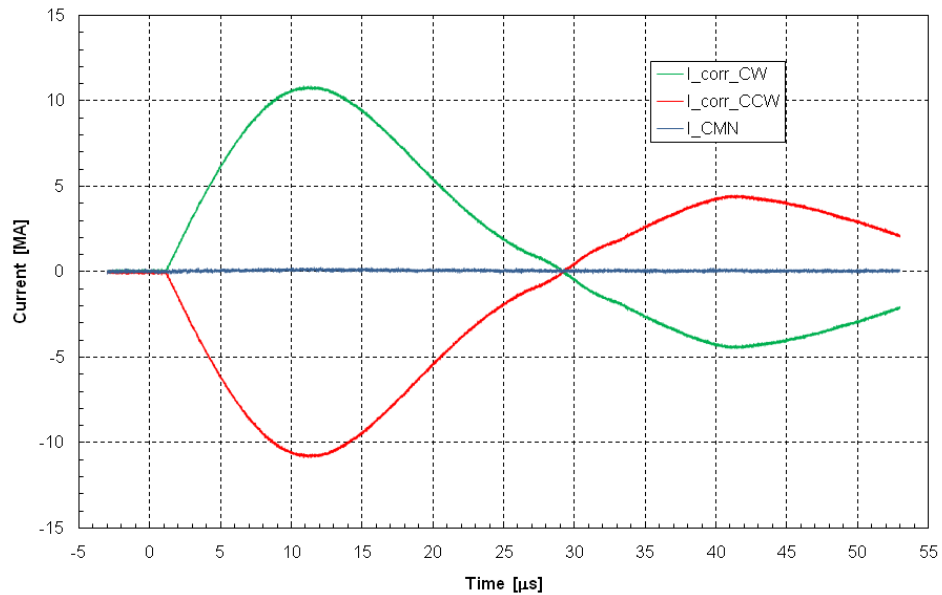


Figure 86. Current measured with CW and CCW Rogowski coil pairs, after correcting for common-mode noise

The peak values of the signals are  $I_{\text{corr\_CW}} = -I_{\text{corr\_CCW}} = 10.86 \text{ MA}$  and  $I_{\text{CMN}} = 234.7 \text{ kA}$ , with the peaks of the corrected CW/CCW Rogowski coil currents occurring at  $11.371 \mu\text{s}$  ( $10.246 \mu\text{s}$  with respect to the start of Shiva current).

We also had a Faraday rotation fiber-optic probe installed for monitoring the Shiva discharge current. Physically, this probe was located very near the locations of the four CW/CCW Rogowski coils. Unfortunately, on this particular shot, the battery on the UPS used to power the probe laser failed, so no Faraday rotation current data was recorded.

The three B-dot probes were located at a radius of  $9.36 \text{ cm}$ , placed  $120^\circ$  apart, and located near the liner load. The three probes were azimuthally aligned such that first probe (B-dot 5) was centered with the middle of Shiva B arm, while B-dot probes 6 and 7 were aligned with Shiva D and F arms, respectively. Figure 87 shows the discharge current as measured by these probes.

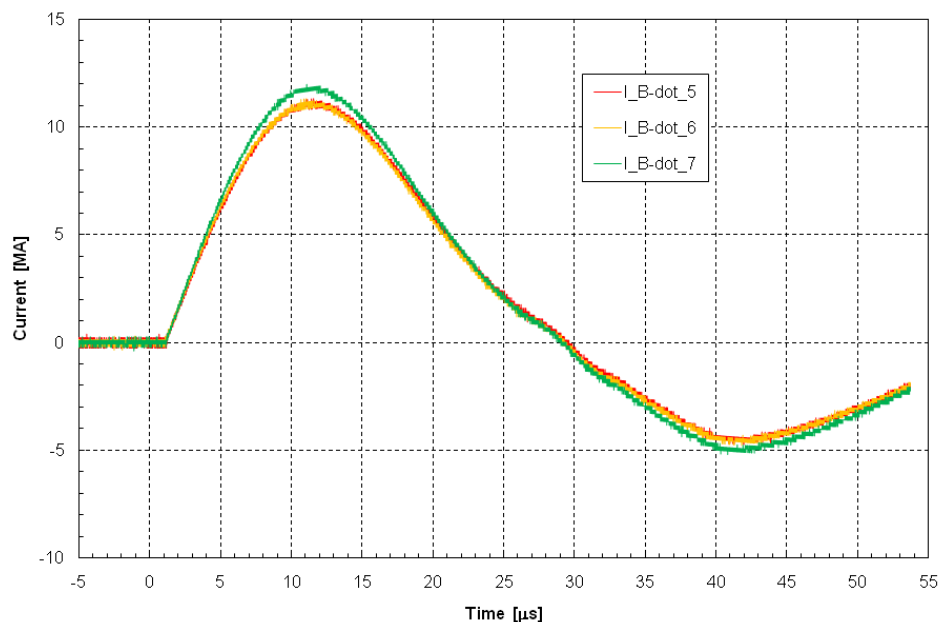


Figure 87. Waveforms from three upper-return conductor B-dot probes, shown overlaid

The peak currents measured with the B-dot probes are as follows:  $I_{\text{B-dot5}} = 11.36 \text{ MA}$ ,  $I_{\text{B-dot6}} = 11.5 \text{ MA}$ , and  $I_{\text{B-dot7}} = 12.0 \text{ MA}$ .

Located on the lower portion of the Shiva transmission line hex plate were three capacitive voltage probes. Physically, the probes were located at a radial position of  $46 \text{ in}$  and are labeled

V1, V2, and V3. They are azimuthally positioned between Shiva arms A-B, C-D, and E-F, respectively. If  $0^\circ$  is defined to be along A arm, then V1, V2, and V3 are located at  $30^\circ$ ,  $150^\circ$ , and  $270^\circ$ , respectively. Figure 88 shows the overlay plot of the probe outputs  $V_1$ ,  $V_2$ , and  $V_3$ .

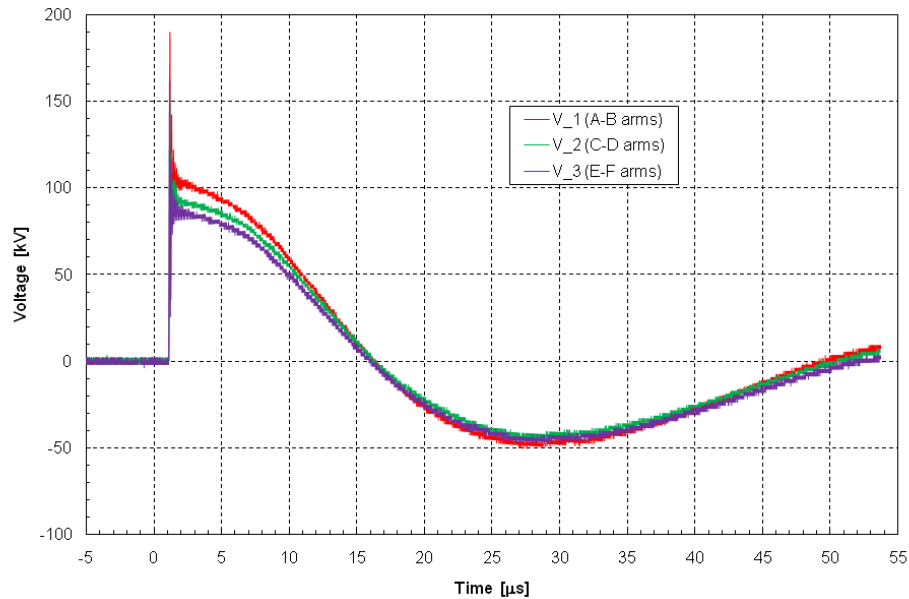


Figure 88. Three Shiva voltage-probe waveforms, shown overlaid

Several probes were constructed and characterized for use on MTF liner shots to monitor the B field extending from the guide-mirror-magnet array to the collapsing liner. The micro B-dot probes were characterized and bench-calibrated with changes and improvements established after the previous Shiva-MTF shot. The presently used micro B-dot probes are similar to the 7 micro B-dots placed on the FRCHX-1 MTF experiment. This discussion lists the details of the MTF B-dot probe diagnostic (Figure 89–Figure 91) that are more specific to the FRCHX-2 implementation.

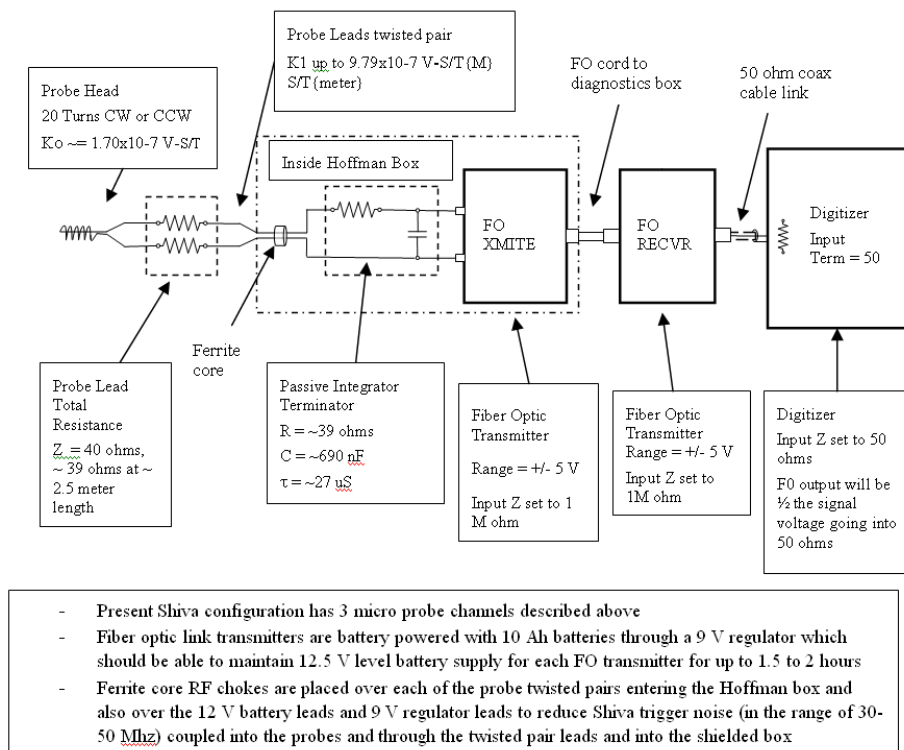


Figure 89. Shiva-MTF micro B-dot probe configuration

Probe #	Connector Channel #	K0(300 KHz) 5 cm x 4 mm Cal coil	K1(300 KHz) 10 cm x 3.3 mm Cal coil	N direction
A	#1(Top)	$+1.73 \times 10^{-7} \text{ V-s/T}$	$-9.88 \times 10^{-8} \text{ V-s/T (M)}$	20 CW
B	#2(Middle)	$+1.70 \times 10^{-7} \text{ V-s/T}$	$-9.56 \times 10^{-8} \text{ V-s/T (M)}$	20 CW
C	#3(Bottom)	$-2.01 \times 10^{-7} \text{ V-s/T}$	$+9.62 \times 10^{-8} \text{ V-s/T (M)}$	20 CW
Connector Channel #	Length of tube	Length of twisted pair Approx.	Continuity Resistance in Ohms	Liner position
#1(Top)	45.72 cm	2.4 m	33.3	6 cm
#2(Middle)	38.1 cm	2.5 m	34.4	15 cm
#3(Bottom)	25.4 cm	2.0 m	28.9	24 cm
Integrator parameters				
Probe	R	C	Integrator Time Constant	
#1 (Top)	39.26 ohms	$472+218=690\text{nF}$	27.09 $\mu\text{s}$	
#2 (Middle)	39.07 ohms	$473+219=692\text{nF}$	27.04 $\mu\text{s}$	
#3 (Bottom)	38.96 ohms	$476+218=694\text{nF}$	27.04 $\mu\text{s}$	

Figure 90. MTF liner B-dot probe array positional and physical parameters



Figure 91. Probe and shielding locations

Prior to the MTF Liner shot all three B-dot probes showed good continuity with their characteristic resistance allowing the probes to be individually identifiable by length and the total lead and probe head resistance. The data links for the middle and bottom probes lost communications during the course of the Shiva shot, so data was lost from two of the three probes. The top probe did produce data.

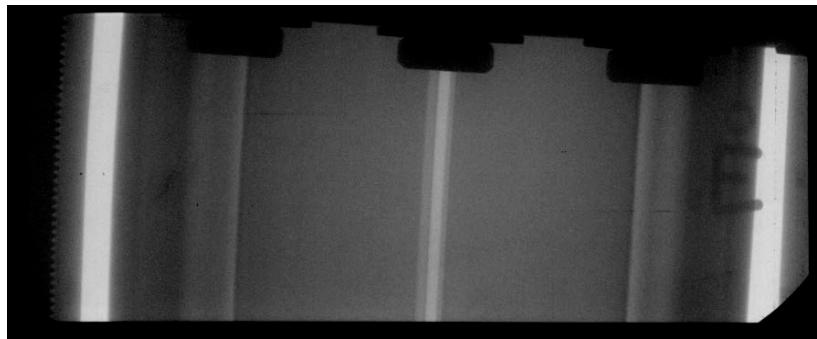
As was the case with FRCHX-1, for this experimental test we again used two radiography systems to record dynamic X-ray images of the liner. The imaging scheme employed had the heads positioned at two different azimuthal locations that were 90° apart. The first head (Rad #1) was located at E arm, and the other (Rad #2) was located between C and D arms. Both heads imaged a field of view that was centered on the liner region and was bounded above and below by the Mirror 2 and Mirror 1 coil pairs. To improve the image quality over that which was obtained for FRCHX-1 both heads were moved closer to the experiment, to a radius of about 24 in. from the liner axis.

Digital film was used for recording all the images. The film pack for Rad #1 was at a radius of 16 in from the liner axis, whereas the one for Rad #2 was at a 20-in. radius. In each imaging film pack assembly we loaded two pieces of film with each film in its own separate “package.” The extra film was a backup in case of some unforeseen issue or problem. Because of the constraints introduced by the Guide and Mirror coils, the Rad # 1 film pack was mounted (again) between two of the current feeds to the coils, dictating a smaller film pack size for this imaging system.

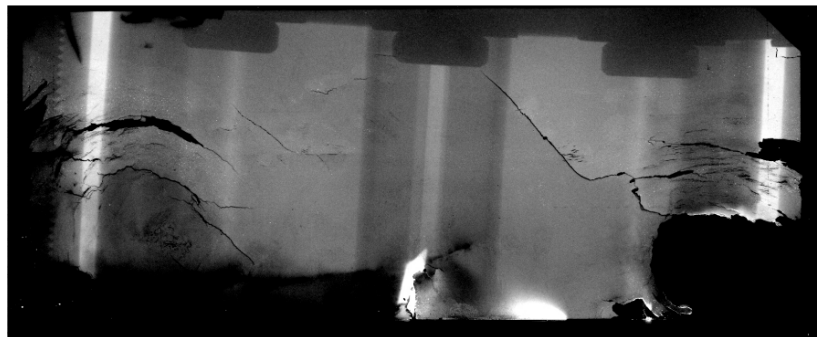
Unlike the case for FRCHX-1, the 1-in. thick pieces of high-density polyethylene were not placed between the Mirror 1 and Mirror 2 coils for this test. This setup meant that the imaging systems needed to image through less polyethylene than for the previous test, and as a result there was not as much scatter, and the image quality was much better.

Figure 92 shows setup and shot images for the Rad #1 imaging system. The initial outer diameter of the liner is 10 cm; using this value to find the scale for the images in Figure 92, the outer diameter of the liner in Figure 92b (which is at  $t = 21.81 \mu\text{s}$ ) is then determined to be 3.73 cm.

Figure 93 presents the setup and shot images for the Rad #2 imaging system in a similar fashion. Again using the known initial outer diameter of the liner to determine the scale from Figure 92a, the diameter at  $t = 22.78 \mu\text{s}$  in Figure 92b is found to be 3.15 cm. From these two diameters and their respective times, the implosion velocity is calculated to be  $0.6 \text{ cm}/\mu\text{s}$ .



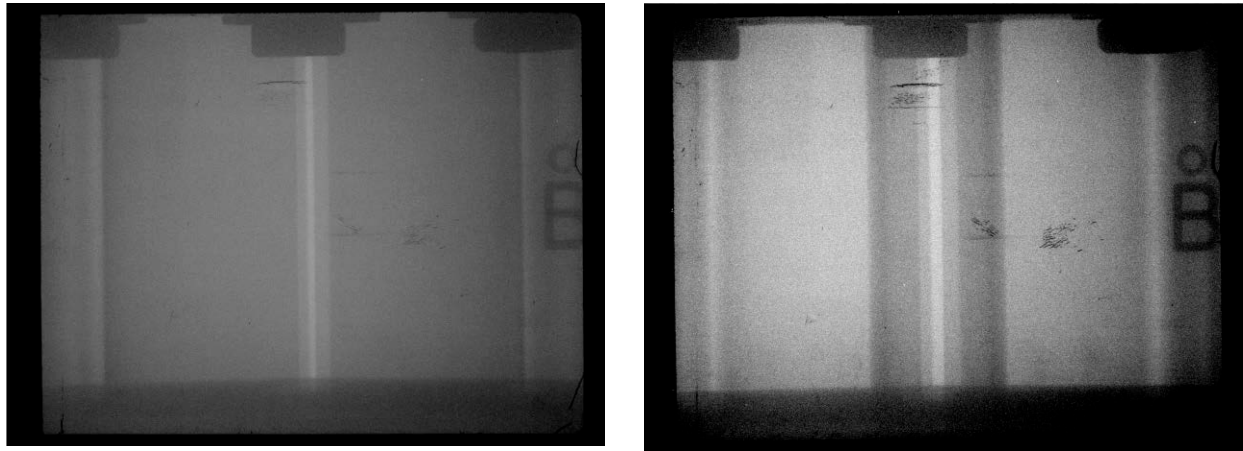
(a)



(b)

Figure 92. (a) Setup images recorded with Rad #1 imaging system before FRCHX-2 test; (b) shot image taken during the test (at  $21.81 \mu\text{s}$ )





(a)

(b)

Figure 93. (a) Setup images recorded with Rad #2 imaging system before FRCHX-2 test; (b) shot image taken during test (at 22.78 $\mu$ s). Because of the arc fault on Shiva Star module F-1 and the resulting drop in charge voltage on the upper half of the Shiva bank, the liner drive current was slightly lower than what was anticipated. The lower drive current then caused the implosion to occur somewhat more slowly, and as a result the shot images show a somewhat larger liner radius than was expected for these times. Within the field of view, the profile of the liner is very uniform, however. It does not appear, at least at these “early” times, that the fluting instability, or any other instabilities, had become a problem for the liner. The concern over the fluting instability, in particular, had arisen from simulation results that included the effects of the slotted return conductor.

### 3.1.3 Plasma Compression

Prior to performing an integrated plasma compression experiment, several tasks had to be completed. First, the Shiva Star capacitor bank had to undergo repairs and refurbishment. This task is described in the following section. Second, FRCHX systems had to be readied, and this task is described in Section 3.1.3.2. Third, FRCHX had to be characterized and maintained. The characterization led to further modifications. These tasks took nearly a full year and are described in Section 3.1.3.3. The actual integrated experiment, FRCHX-3, occurred on 16 April 2010 and discussed in Section 3.1.3.4.

### 3.1.3.1 Shiva Star Maintenance

#### 3.1.3.1.1 *Shiva Star Mylar Repair*

Figure 94 shows the damage done to the Mylar insulation on the top half of Shiva module F-1 following the arc fault during the FRCHX-2 test.

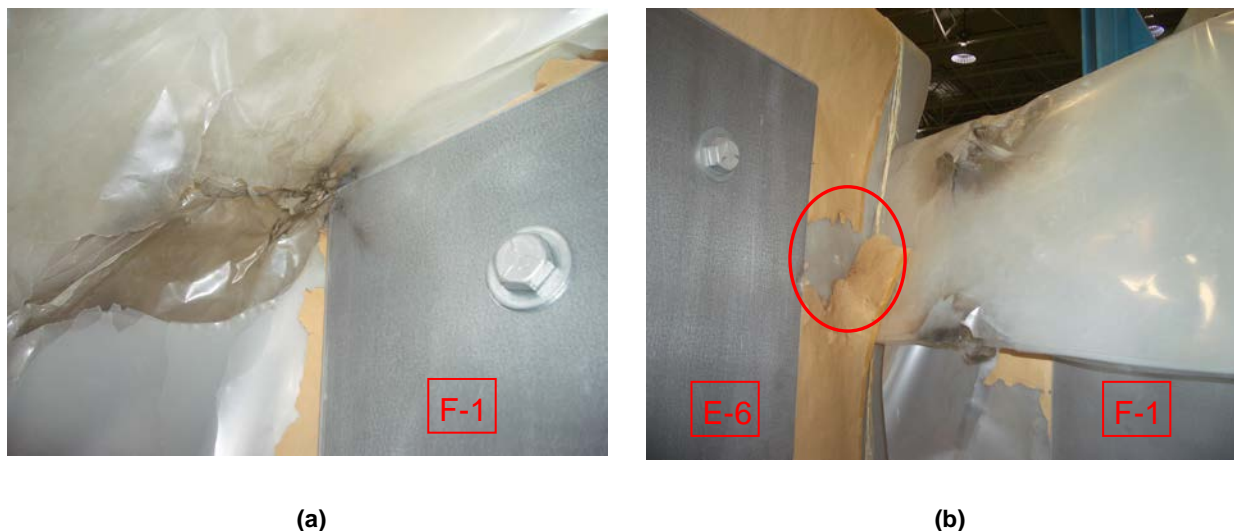


Figure 94. (a) Front and (b) back sides of damaged Mylar on Shiva module F-1

Figure 94a is a view of the front of the Mylar showing that the arc punched through at the corners of the bus plates. Because this module is closest to the center section of Shiva, and the side where the fault occurred is directly facing the center section, it is hypothesized that there may have been a small piece of debris from the previous test (FRCHX-1, conducted in December 2008) that lodged itself within the Mylar at this location and precipitated the fault. Such a possibility has led to greater standards being implemented for inspecting and cleaning the Shiva bank prior to a test.

Figure 94b shows the Mylar folded down so that the extent of the damage on the back side can be seen. The wider field of view also brings into sight a damage spot found on the E-6 module Mylar, highlighted with a red circle. Because of its close proximity to the E-6 module bus plates, it was felt that this spot warranted completely replacing the Mylar pack on the top half of this module, as well, along with that on the top half of F-1.

Replacement of the module Mylar packs was relatively straightforward; once the trigger boards were removed from in front of the modules and the transmission-line-clamping bars were unbolted in back, the crane was then be used to pick up the top module halves and move them to a spot between the bank arms where the front (hot) bus plate could be unbolted. The new Mylar packs were prepared in advance on the Mylar Mezzanine in the high bay; there they were cut to size; taped together, including the brown paper on the front; and had holes punched in them at the appropriate locations for the capacitor terminals. As the bus plate was removed from each module, the old Mylar pack was taken away, the new one was held up in its place, and the bus plate was bolted back down onto the module, sandwiching the Mylar pack between the plate and the rest of the module. At this point, the module half was hoisted with the crane back into its original position on the bank, and the disassembly process was reversed to integrate the module back into the bank.

As mentioned, not only was there damage to the upper halves of modules E-6 and F-1 due to the arc fault, but the brown paper covering the Mylar of many of the modules was torn up quite badly following the concussion from the “normal” Shiva discharge that followed shortly thereafter. Because the brown paper is important for grading the voltage across the surfaces of the Mylar and thereby prevents the buildup of a static charge that might lead to a surface breakdown, it was imperative that the paper be repaired. In most cases this was best accomplished by trimming the paper back to the edge of the bus plate and sliding a new sheet of brown paper up under the bus plate. The new paper was cut such that it covered approximately the same amount of Mylar surface area that the old brown paper covered. Figure 95 shows one of the Shiva modules after the brown paper had been repaired and replaced on it. In this particular instance, only the brown paper below the hot bus place was replaced, as the original paper to either side of the plate was still in good condition.



Figure 95. A Shiva bank module after replacement of brown paper below hot bus plate on this half of the module. In addition, a large number of the  $\frac{1}{4}$ -in. thick acrylic supports holding up the Mylar sheets on either side of the modules were snapped off, also due to the concussion from the Shiva discharge. Figure 96 shows new supports in place.



(a)



(b)

Figure 96. (a) Smaller supports between modules; (b) "tall" supports on modules closest to Shiva center section. Figure 96a shows the predominant (and smaller) supports that hold up the Mylar between modules. The second type of support in Figure 96b is very similar, but is mounted on the sides of

the modules closest to the center section, and their longer vertical face serves as somewhat of a debris shield for the exposed sides of the capacitors in these modules. Because of the large numbers of these acrylic supports that needed to be replaced, it was decided to have an outside machine shop fabricate them. This decision was also done in part so that in-house personnel could then concentrate on completing the other bank cleaning and refurbishment tasks and only needed to turn attention to the new supports once they had arrived in-house from the outside machine shop.

While replacing the brown paper and removing the broken acrylic supports on each of the modules, SAIC and AFRL personnel also thoroughly wiped down all the exposed surfaces of the Mylar to remove all dust and any other debris that may have been stuck to the Mylar surfaces. The Tygon® tubing that is wedged in between the Mylar sheets near the bus plate edges to block the line of sight between the bus plate and the Mylar edge was also replaced at this time; much of it was either missing or had become stiff with age and was not staying in place.

In addition to this extensive work on the modules, some repairs were also necessary on the Shiva high-flow purge system for the rail-gap switches, because the control wires for several of the filling and purging solenoid valves for the C-arm modules had been severed by flying debris. These wires were repaired, and afterwards the operation of the system was observed from beginning to end a couple of times to verify that it was indeed working correctly again. Several of the pre-fire detection-signal cables, which were located close to the purge system wires that were damaged, were also found to have been severed. Repairs to these cables are being carried out at this time and should be completed within another day or two.

#### *3.1.3.1.2 Repairs to the Shiva Star Pre-Fire Detection System*

The last of the repair tasks to be performed on the Shiva bank were carried out during the summer of 2009 and involved the bank's pre-fire detection system. Following the 1 April 2009 Field-Compression test ("FRCHX 2") it was discovered that several of the pre-fire detection-signal cables had been severed by flying debris. The cables were severed close enough to the signal mixer to which they are connected that in all but one or two cases it was possible simply to install new BNC connectors where they were severed and then pull out the slack along their

run to connect them again to the mixer. In the few cases where this change was not possible, new RG-58 cables were prepared and run between the mixer and the bank-module-current sensor.

Once the cable repairs were completed, tests were performed on the entire system (except for pre-fire sensors themselves) to ensure that no damaged cables had been overlooked and that the repaired cables had no remaining problems. These tests also allowed each of the mixer inputs to be checked for proper operation. The tests were conducted as follows. Each of the sensor cables was disconnected one at a time from its respective module pre-fire sensors and was connected instead to a small battery-operated pulser. Personnel pressed a manual fire button on the pulser to activate it several times while other personnel in the Shiva Star screen room monitored an oscilloscope, observing that the signals were indeed received on the pre-fire detection-signal line located in the screen room. As soon as one cable had been tested several times, it was reconnected to its sensor, and the next cable was then disconnected from its sensor and attached to the pulser. In this manner, all the cables and their mixer inputs were checked except those going to the sensors on modules B-1 and B-6; these were inaccessible, and all were found to be operating reliably.

#### *3.1.3.1.3 Resistive Test Load for Shiva Star*

The arc fault that occurred during the FRCHX-2 test did so immediately after the target Shiva charge voltage was achieved and just before the command trigger was sent. In addition to highlighting the need for a more vigilant effort in inspecting and cleaning the Shiva bank prior to a test, the occurrence of the fault also suggested that a means of charging the bank up to its target voltage before an experiment had been set up on it to determine if there were any voltage hold-off problems would be extremely useful. If a fault occurred during such a charge-and-dump test, particularly a fault that would lead to the pre-firing of the rail-gap switches, then even though repairs might be required on the bank the experiment itself would not be lost. Such a charge test could not be performed on the bank without any load in place; however, as any module(s) discharging into their transmission line would drive the transmission line to arc over at the Mylar insulation at the center section of the bank. This arc would create a significant amount of additional damage beyond that caused directly by any fault. As a result, SAIC personnel spent a couple of weeks designing a test load to be used on the Shiva bank during such charge tests.

Figure 97 shows a SolidWorks illustration of the test, or “dummy,” load hardware.

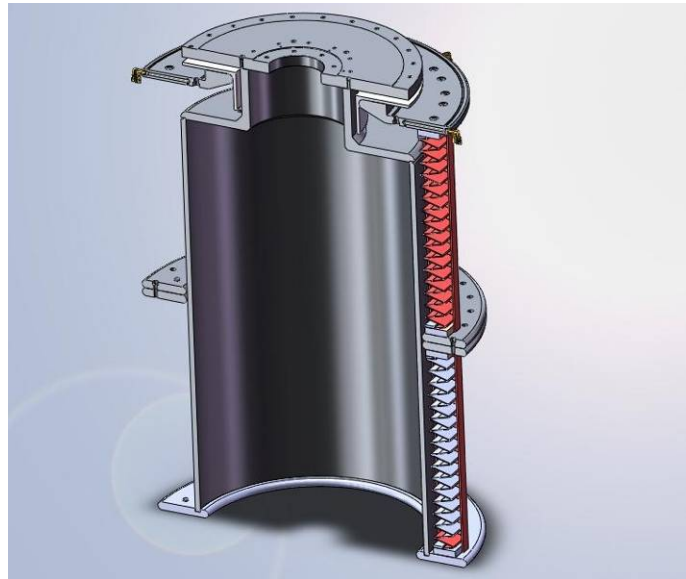


Figure 97. Cross-section view of Shiva dummy load

The load consists of two stacked arrays of Franklin resistors, and the assembly mates to the existing Shiva solid dielectric (non-vacuum) center conductor plates. The load inner conductor is approximately 18.5 in in diameter and has a length of 30 in. As it is being assembled, the cylinder is first wrapped with 10 layers of 0.010-in. Mylar along its full length to insulate it from the sets of Franklin resistors placed around it.

There are a total of 32 Franklin resistors used in the load, 16 in each level. Figure 98 shows one of the resistors that is used.



Figure 98. A 0.060- $\Omega$  Franklin resistor, shown with a tape measure for scale



As can be seen from the tape measure, the Franklin resistors are approximately 16 in. long. Each resistor has a resistance of  $0.060\ \Omega$  and an inductance of 250 nH, and they are rated for 100,000 J each. As is indicated by Figure 97, the Franklin resistors attach to intermediate rings at the midpoint of the load. Figure 99 shows the two rings.

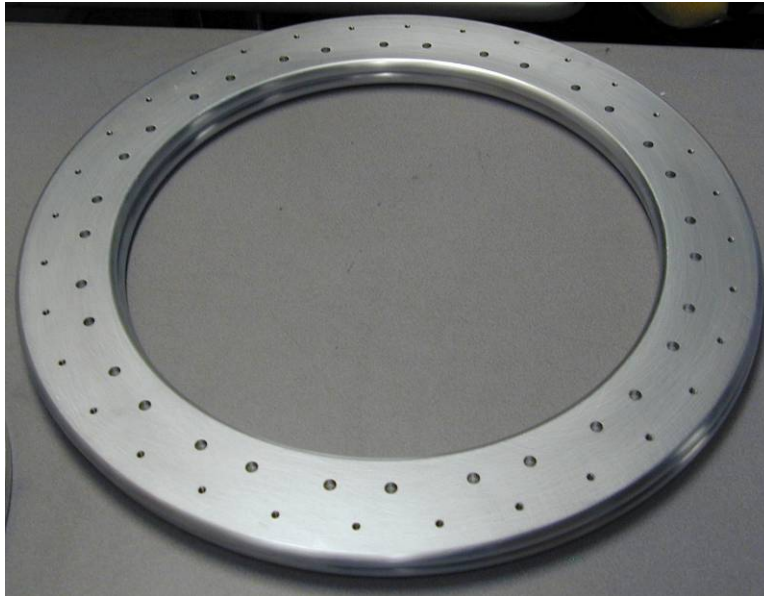


Figure 99. Rings to be used to join two groups of Franklin resistors together at mid-plane of load  
The rings are being used to facilitate assembly of the resistors in a series/parallel combination, which was necessary to achieve the desired total resistance and Joule rating for the load. This arrangement also provides a convenient means for physically mating the two sets of resistors end to end during assembly, and it also serves to grade the field along the length of the load.

As mentioned, the connections to the load have been designed such that they will readily mate to the Shiva current feed plates that have the solid dielectric insulator. The top plate of the load, which is attached to the load's inner conductor, mates directly onto the Shiva upper current-feed plate. Figure 100 shows the load top plate.





Figure 100. Upper conductor plate of load shown with exhaust lines and manifold connected to its fittings. Fittings are provided in the plate to allow for an  $\text{SF}_6$  purge of the load. These fittings are connected to a common manifold as shown, which in turn directs the gas into a single discharge tube that is routed to the outside of the building. A polyethylene “top hat” insulator (shown in white in Figure 97) is placed below the upper load-conductor plate to isolate it from the lower load plate. As is the standard practice for dielectric joints in the Shiva load region, the joint between this insulator and the Shiva current-feed-disk insulator will be filled with ViSil™ to displace any air pockets that might otherwise remain in this region.

Like the upper load-conductor plate, the lower load-conductor plate mates directly onto its corresponding Shiva current feed plate. As can be seen in Figure 97, the top end of the upper set of Franklin resistors also attach to this plate. Figure 101 shows the lower load plate.

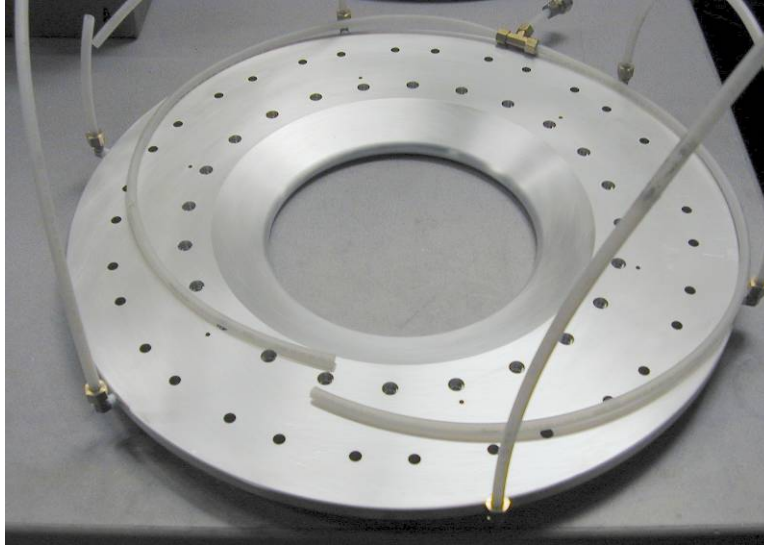


Figure 101. Lower conductor plate with gas lines in the process of being connected

Six gas fittings at the outer brim of the lower load plate are routed to a common manifold, in a manner similar to that which is being done for the upper load plate's  $\text{SF}_6$  fittings. This manifold will likewise be discharged to the outside of the building. The fill points for the  $\text{SF}_6$  in the load, not visible in Figure 97, are located at the upper end of the load inner cylinder, on its inside surface.

As soon as the above assembly was completed, charge-and-dump, or hi-pot, tests with the load on the Shiva bank then commenced. Figure 102 shows the 7.5-m $\Omega$ , 31.25-nH resistive load, once it was in place at the center of the Shiva Star bank.



Figure 102. Resistive test load mounted to current-feed plates at center of Shiva bank

The gas lines seen in Figure 102 are used carry  $\text{SF}_6$  to and from the load.  $\text{SF}_6$  is used here to prevent arcing from occurring. The lines prevent arcing between the center conductor, which connects the hot (top) current-feed plate of the Shiva bank to the bottom of the resistive load, and the array of Franklin resistors, of which the resistive load is comprised and that tie the center conductor back to the lower (ground) current-feed plate on the Shiva bank.

Three charge-and-dump tests were performed on 16 July 2009, and these had target composite charge voltages of 20 kV, 40 kV, and 65 kV. Three additional tests, with target composite voltages of 75 kV, 85 kV, and 90 kV, were performed on 1 Sep 2009. In all these tests the bank was successfully charged to (or slightly above) the intended voltage without any arc-fault or self-triggering incidents. Thus, the integrity of the bank was deemed worthy again for liner-implosion tests, included the upcoming FRC compression-heating test.

In addition to checking the integrity of the bank, these charge-and-dump tests also provided an opportunity to correlate the set-point controls on the Shiva Star control console with the actual voltage to which the bank was charged. Such a “calibration” of the set-point control is useful in

the upcoming FRC compression-heating test, because the set-point control can be used to stop the charging of the Shiva bank more precisely than was possible in the past with just the operator pressing the manual stop-charge button. Table 12 summarizes the set-point and final composite charge-voltage data recorded during several of the Shiva Star charge-and-dump tests.

Table 2. Shiva Star final composite voltages recorded for set-points indicated

Set Point (± kV)	Final Composite (kV)
10.0	18.04
21.4	40.01
33.5	66.00
34.1	68.20
37.5	77.50

Though six charge-and-dump tests were performed, we show data from only the first four. During the last two of these tests the set-point dial on the Shiva Star control console appeared to be allowing the bank to charge well beyond the intended voltage and, as a result, the manual stop-charge was used. Table 12 includes data from a Shiva test performed on 17 August 2009 (the middle data set), though, as the set-point control was able to stop the bank charge at the indicated voltage. All this data is plotted in Figure 103.

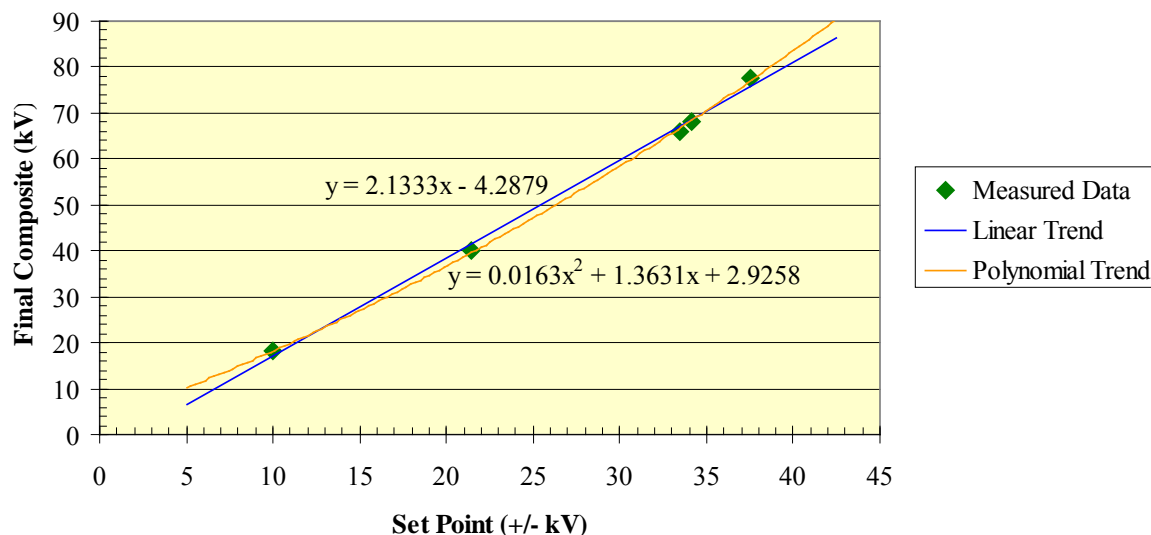


Figure 103. Shiva Star final composite charge voltage vs. set-point control setting

As can be seen, the best curve fit to the data is not a straight line but a second order polynomial. This finding explains why it was not possible in the past to use set-point and charge-voltage data at lower charge voltages to predict what a set-point would be for a higher Shiva charge voltage. If the ordinate and abscissa in the plot in Figure 103 are interchanged, the plot in Figure 104 is obtained.

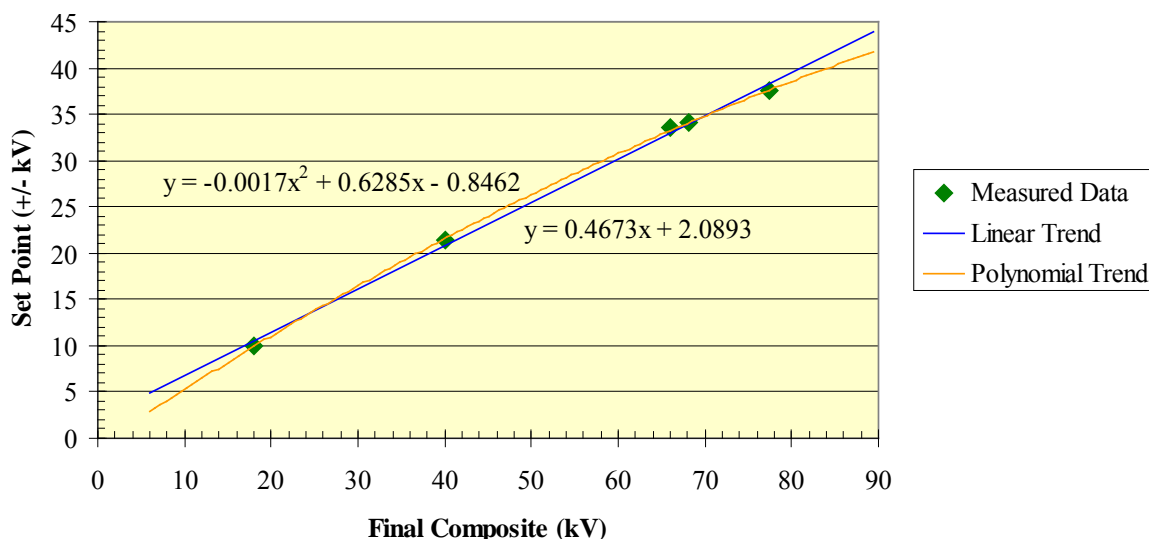


Figure 104. Shiva Star set-point control setting vs. final composite charge voltage

Using the equation for the second-order polynomial curve fit shown, it will now be possible to calculate appropriate set-points for any desired Shiva composite charge voltage. Table 13 shows the calculated set-points for a range of final composite charge voltages, which includes the target final composite voltage needed for the FRC compression-heating test (85 kV).

Table 3. Calculated set-points for indicated final composite charge voltages—Shiva Star Bank

Target Final Composite (kV)	Calculated Set Point (± kV)
60	30.7
65	32.8
75	36.7
85	40.3
90	41.9

Though the integrity of the Shiva Star bank has been verified at voltages relevant for the FRC compression-heating test, we planned to conduct several more charge-and-dump tests in tandem

with the FRC formation, translation, and capture tests. Performing one or two Shiva Star charge-and-dump tests (at 85 kV) would be extremely helpful both to determine the appropriate time to start the Shiva bank charge relative to the start time of the charging sequence for all the FRCHX banks and to confirm that the set-point calculation (Table 13) for an 85 kV charge voltage is correct. In addition, a test in which the Shiva bank is actually fired into the resistive load would be useful for revealing any adverse effects that the bank may have on any of the FRCHX pulsed power systems—particularly trigger systems—and diagnostics. Such a charge-and-fire test would be limited to 60 kV composite charge voltage on the Shiva Star bank; load currents produced with charge voltages above this limit are likely to cause some deformation of the Franklin resistors in the resistive load.

#### 3.1.3.2 FRCHX Preparation

As has been discussed at various times, before attempting to perform the FRC compression heating test with the Shiva bank, it must be verified that FRCs that are in fact suitable for compression are being formed, translated into the liner region, and successfully captured between the upper and lower mirrors. As a result, one of the tasks focused upon was that of attempting to increase the physical strength of the upper Mirror coils and improving upon the magnetic field profile in the capture region. Each of the FRCHX banks was also tested up to the charge voltage at which it was operated previously. Once the new upper mirror coils had been fabricated and mounted on the vacuum stand, mapping began of the magnetic field from the capture region down to the translation region and then to the formation region. Unfortunately, problems with the Crowbar switch on the Main bank were encountered again during the Main bank tests. Specifically, only one rail-gap switch in the Crowbar—generally rail gap #1 (“CB #1”)—was consistently conducting. Because excessive wear and even some damage would likely occur to a single crowbar rail gap when operating the Main bank at higher charge voltages, a considerable effort was spent this past quarter attempting to diagnose and correct the reasons for this problem. The rest of this section describes in further detail the redesign of the upper mirror coils, the bank tests, and the issues uncovered with the Crowbar switch.

### 3.1.3.2.1 Further Redesign of the FRCHX Upper Mirror Coils to Boost the Upper Mirror Amplitude

Numerical calculations performed by NumerEx showed that the magnetic field profile in the liner region appears to be optimized for capturing an FRC when the ratio of the upper mirror field to the lower mirror field is 1.18 or slightly greater, and the ratio of the trough field between the mirrors to the lower mirror field is approximately 0.5. With such a magnetic field profile, the time at which the FRC is injected into the liner after the liner compression begins can be varied fairly broadly. This situation is not necessarily the case if the field profile is allowed to vary much from these values.

Previously, we described a redesign effort for the upper mirror coils that was conducted during the weeks following the FRCHX-1 test in an effort to adjust the field profile in the liner region so that it followed more closely the profile indicated by NumerEx as being the optimum. The result of this effort was, of course, the coil set that was fabricated for the FRCHX-2 test setup; Figure 105 shows a plot of the field profile that was measured for this coil set.

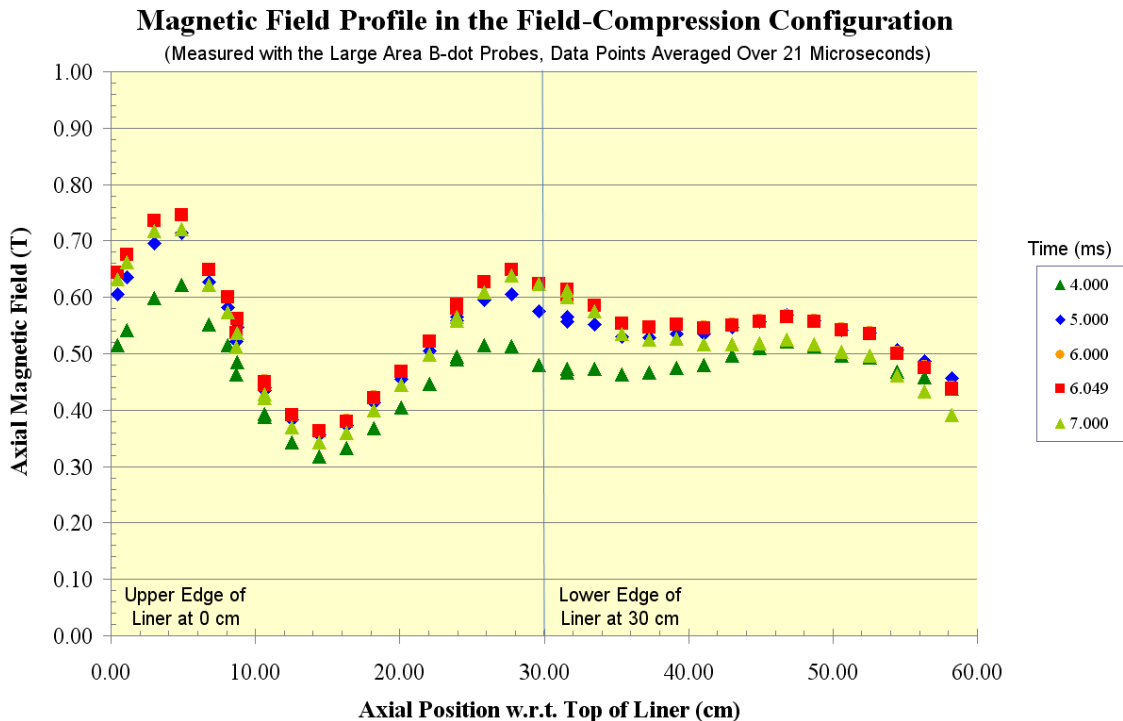


Figure 105. Measured axial magnetic field vs. axial position for FRCHX-2 coil set

Each data set in the graph corresponds to a different time after the start of the Guide/Mirror current pulse, and as is also indicated in the graph, “0 cm” corresponds to where the top of the liner is located, and “30 cm” corresponds to where the bottom of the liner should be. Upon inspection of this profile it can be seen that it is close to that which was targeted; that is, the upper-mirror-to-lower-mirror and the trough-field-to-lower-mirror ratios are 1.15 and 0.58, respectively. NumerEx personnel expressed some concern that the first ratio was still somewhat too low, however; AFRL and SAIC personnel began examining additional changes to the coil configuration at the beginning of this quarter.

Using COMSOL to calculate the field profile on axis within the liner hardware, possible variations in only the Mirror 3 coils were explored first as a means of boosting the upper mirror field. Such changes involved placing additional windings on these coils, but this placement also led to a greater trough-to-lower-mirror ratio. The focus was then turned to variations in the Mirror 2 coils and, in particular, to eliminating the upper Mirror 2 coil but leaving the lower Mirror 2 coil in its original location. Additional windings were then placed on the lower Mirror 2 coil to compensate. Table 14 shows a listing of the Mirror 2 and Mirror 3 winding variations, with the upper Mirror 2 coil removed, which were considered next with COMSOL.

Table 4. Variations in Mirror 2 and Mirror 3 coils considered in recent COMSOL calculations

	Case 5 –	Case 6 –	Case 7 –
Upper Mirror 3	2 x 12 windings	2 x 12 windings	2 x 12 windings
Lower Mirror 3	2 x 12 windings	2 x 12 windings	2 x 11 windings
Upper Mirror 2	no windings (replaced with spacer)	no windings (replaced with spacer)	no windings (replaced with spacer)
Lower Mirror 2	1 x 9 windings top layer, 1 x 10 windings bottom layer	1 x 10 windings top layer, 1 x 9 windings bottom layer	1 x 9 windings top layer, 1 x 10 windings bottom layer

	Case 8 –	Case 9 –	Case 10 –
Upper Mirror 3	2 x 12 windings	2 x 12 windings	2 x 11 windings
Lower Mirror 3	2 x 11 windings	2 x 11 windings	2 x 12 windings
Upper Mirror 2	no windings (replaced with spacer)	no windings (replaced with spacer)	no windings (replaced with spacer)
Lower Mirror 2	1 x 10 windings top layer, 1 x 9 windings bottom layer	2 x 9 windings	2 x 9 windings



Figure 106 shows a plot of the field profiles (at  $t = 6$  ms) that were calculated by COMSOL for each of these cases shown in Table 14. The graph is shown courtesy of M. Domonkos.

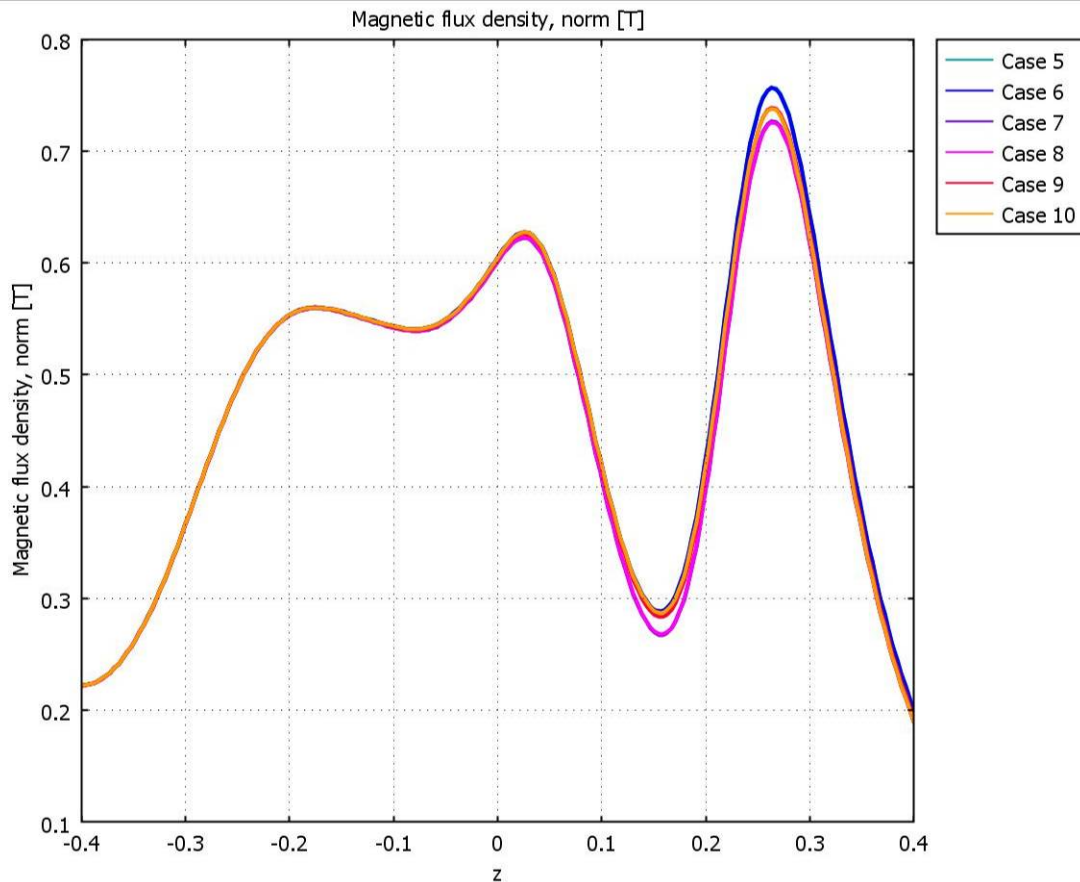


Figure 106. Axial magnetic field vs. axial position at  $t = 6$  ms following start of Guide/Mirror bank current

As can be seen from this graph, changing only one or two windings in the Mirror 2 or Mirror 3 coils produced only small variations in the upper mirror or trough fields as had been hoped. Thus, it appears that fine tailoring of the liner field profile can be accomplished through such means when it is needed. Case 5 and Case 6 yielded nearly identical results, and their profiles provided the best match with targeted profile; the ratio of the upper mirror field to the lower mirror field is approximately 1.21, and the ratio of the trough field between the mirrors to the lower mirror field is 0.46. As noted, having a mirror ratio that is slightly greater than 1.18 is acceptable, and it is better if it is slightly greater than slightly less than this value. Also, although care was taken to include all materials and their material properties in the COMSOL model, the

real material properties can vary a little, and the mirror ratio in the final experimental setup could be slightly lower; thus, there is somewhat of a buffer built into this coil-set design.

Once this design for the upper mirror coils was settled upon, fabrication of the new Mirror 2 and Mirror 3 coils was begun immediately so that these coils would be ready for installation on the FRCHX vacuum stand well before axial field-mapping measurements were ready to begin. Though the design of the Mirror 3 coils ended up not changing, these coils were still replaced because of the damage they had incurred during the field mapping and other coil tests performed last fall. Furthermore, a different and expected to be better epoxy (Crystal Clear<sup>®</sup> 220) was identified for use as an encapsulant for the mirror coils this time. This epoxy is less brittle than the epoxy used up to this point (Stycast W 19), and it was desired to have all the upper mirror coils potted with this new material. Though the breakdown voltage for this new material is not as high as that for the Stycast W 19, voltages across each coil are low enough that breakdown should not be an issue. A less brittle potting material should improve the strength of these coils and enable them to be pulsed many times at the appropriate field and current levels needed for FRC capture tests without being damaged.

Figure 107 shows two views of the new Mirror 2 and Mirror 3 coils after they were installed on the FRCHX vacuum and field-coil stand.



Figure 107. (a) New Guide and Mirror coil set; (b) close-up of upper mirror coils and clamping structure

Note that the Guide and Mirror 1 coils in the assembly are the original ones that were used during the tests last fall. As can be seen, the upper Mirror 2 coil has been eliminated and replaced instead with two G-10 spacer disks to fill in the 0.875-in. gap. The same clamping structure design used for the upper mirror coils on the FRCHX-2 coil set was used again here: Lexan disks (black) that are approximately 0.25 in. thick at their inner radius and 0.125 in. thick at their outer radius are placed on the top and bottom of the coil set, and 0.75-in. G-10 disks are placed above and below these to compress the entire assembly. The thicker inner portion of the Lexan disks places an additional compressive force on the coils that the magnetic forces must first overcome before they can begin to deform the coils outwardly. During the few high-field tests that were performed with the FRCHX-2 coil set, this clamping assembly performed well and did not experience any cracking or visible deformation that earlier clamping approaches had after pulsing the coils.

There are several advantages to eliminating the upper Mirror 2 coil in this new coil set. The first is that it eliminates one coil that must be fabricated for each FRC compression-heating test. Generally, the time required to fabricate a coil, from starting the winding in the casting mold to potting the pre-cast windings in their spool, is two or three days. A second advantage is that it provides a greater separation between the pulsed (Mirror 3) and counter-pulsed (Mirror 2) coils, and thus the repulsive forces on these coils should be lessened.

Figure 108 shows the large-area B-dot and Hall probe assembly configured for mapping the FRC formation, translation, and capture test setup.

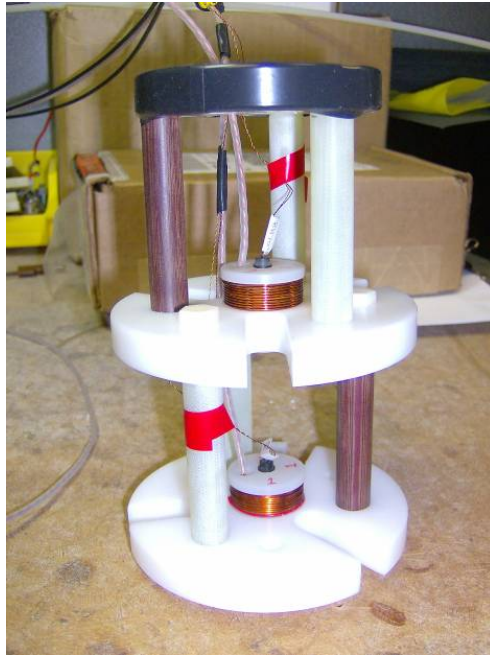


Figure 108. Large-area B-dot probe and Hall probe assembly

Though the assembly is smaller than that used when mapping the axis of the field-compression-test setup, the B-dot and Hall probe pairs are still spaced 3 in (7.62 cm) apart, and the assembly was moved in increments of 0.75 in (1.91 cm) along the axis, as has been done in the past. However, unlike the previous field-mapping effort performed in this test setup earlier, the formation region was also mapped this time. Field measurements were therefore made with the Bias and Upper and Lower Cusp banks being discharged at their appropriate times in conjunction with the Guide/Mirror bank.

With a new upper Mirror coil assembly in place on the FRCHX vacuum and field-coil stand, it was important to perform another series of field-mapping tests to determine if the changes made to the coil configuration had indeed improved the Upper Mirror-to-Lower Mirror ratio. Furthermore, mapping of the entire FRCHX axial magnetic field profile, i.e., mapping throughout the formation region, as well as throughout the translation and capture regions, was also of interest to obtain a picture of what the combined Bias, Upper and Lower Cusp, Guide, and Mirror field structures look like just before FRC formation begins. This information would then be useful not only in guiding the FRC experiments but also for comparison with past Mach2 simulations and for providing input to future simulations.

In an attempt to isolate the slow, millisecond-time-scale fields from the faster, microsecond-time-scale fields, two measurements were made at each mapping position in the translation and capture regions. The first measurement was made with only the slow Guide and Mirror coils being pulsed, and the second was made with the faster Upper and Lower Cusp and Bias coils being pulsed at their appropriate times in conjunction with the Guide and Mirror coils. In the formation region only the second measurement with all of the field components was made. A plot of the data from the first measurement set is shown in Figure 109a, and a similar plot of data from the second measurement set is shown in Figure 109b.

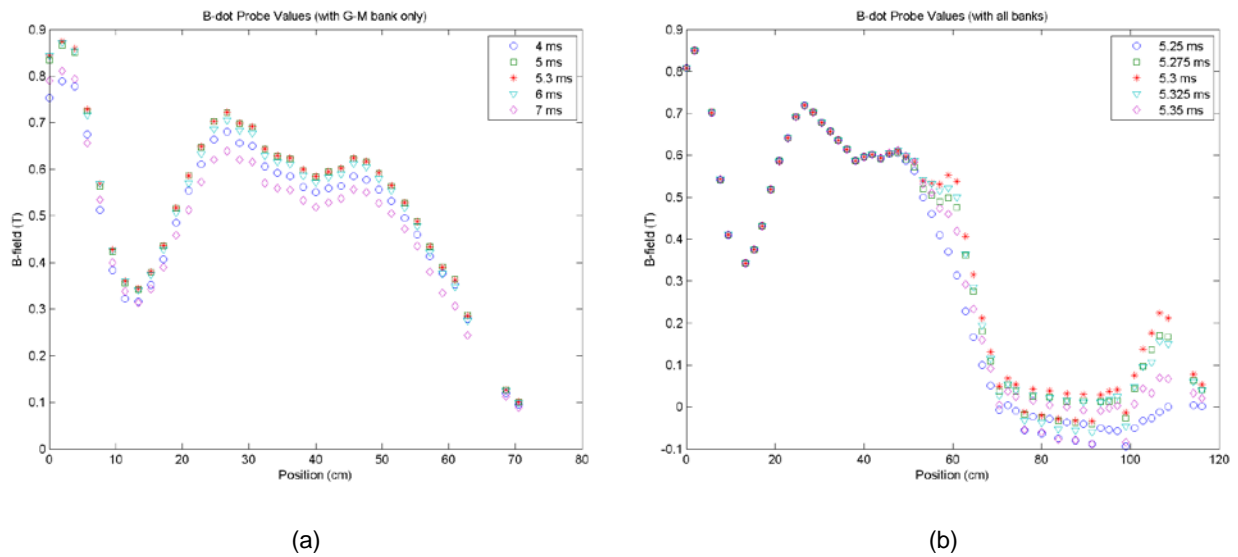


Figure 109. (a) Axial magnetic field measured when only Guide and Mirror coils were pulsed; (b) measured field with Guide, Mirror, Bias, and Cusp coils pulsed

In all these tests the Guide/Mirror bank was charged to 2 kV, the Bias bank was charged to 2.5 kV, and the Upper and Lower Cusp banks were charged to 2 kV. The time at which the Upper Mirror field peaked was observed to be at  $\sim 5.3$  ms, so the triggering of the Bias and Cusp banks was timed such that these fields also peaked at this time.

Several interesting features can be identified in the graph in Figure 109b. First, the ratio of the Upper Mirror to the Lower Mirror is 1.182, and the ratio of the trough field to the Lower Mirror is 0.477. Thus, the new coil configuration (at least in the translation-only test setup) now

provides a Mirror field profile around the capture region that matches the profile identified earlier by Mach 2 as being optimal for FRC capture.

Second, the local peak seen at 59 cm and the peak at 114 cm are identified as being the Upper and Lower Cusp field maxima. One notes that the Upper Cusp field is almost twice as large as the Lower Cusp field despite the identical charge voltages on their respective banks. It is a result, however, of the Upper Cusp field being superimposed upon the Guide field that is trailing off into the formation region. In fact, the Upper Cusp field should be raised slightly so as to smooth out the transition from the Upper Cusp region into the Guide region.

Also, there is a peculiar alternating appearance to the Bias field in the formation region (approximately between 70 cm and 100 cm). This appearance was later identified—after reviewing several of the Theta coil current waveforms from these tests—as being caused by two different “modes of operation” for the Bias bank. In one mode both ignitrons on the bank triggered as intended, yielding a bank current of  $\sim 80$  kA with a quarter-cycle rise time of  $\sim 135$   $\mu$ s; in the other mode only one ignitron was successfully triggered, resulting in a bank current of just  $\sim 52$  kA and a slightly shorter quarter-cycle rise time (approximately 115  $\mu$ s). The plot of Theta coil-current waveforms in Figure 110 illustrates this changing bank output current behavior. Again, for each of these tests the Bias bank charge voltage was kept at a constant 2.5 kV.

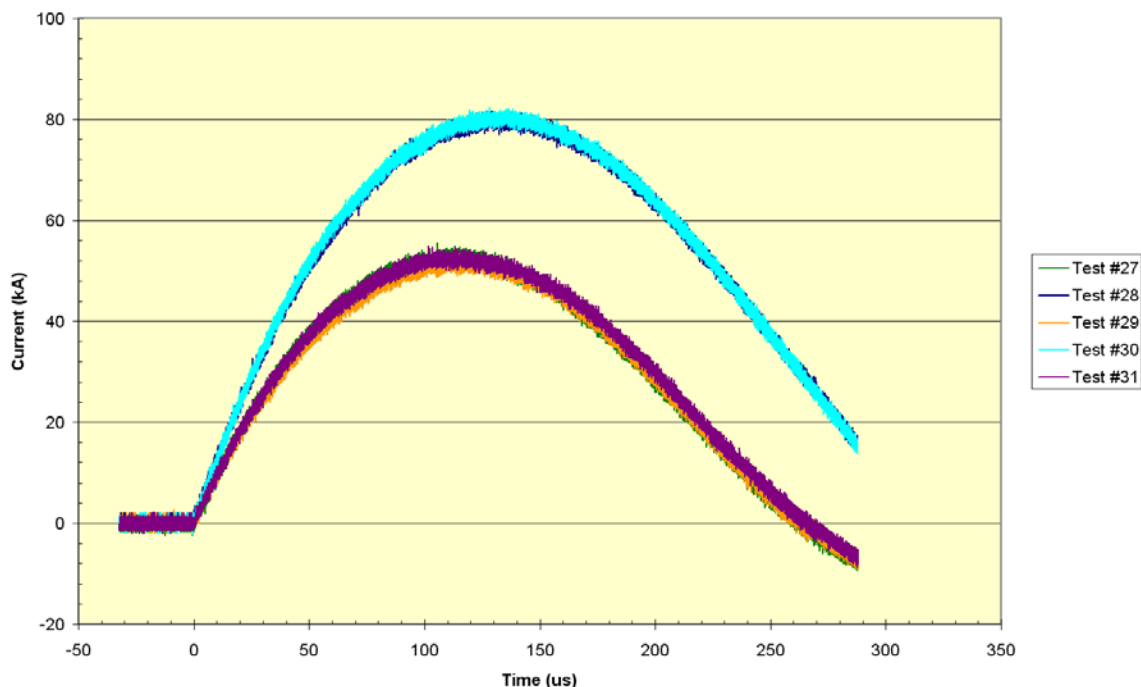


Figure 110. Two distinct Bias current waveforms, from consecutive field-mapping tests

Such a random variation in behavior is unacceptable for the FRC formation tests, so several days were spent diagnosing and correcting this problem. That the problem was an ignitron-triggering issue was largely confirmed by performing a couple of Bias bank tests with only the west module of the Bias bank being charged and fired. Such tests were accomplished simply by disconnecting both the charging cable from the east module and the trigger transformer lead from the east module ignitron's igniter pin. (East-module-only tests were not performed at this time because of the added complication of having to move the charge voltage monitor, which has been set up semi-permanently on the west module, over to the east module.) Figure 111 shows a plot of Theta coil-current waveform from one of these west-module-only tests ("Test 17") overlaid with two full-Bias-bank Theta coil-current waveforms in which only one ("Test 4") and then both ("Test 14") ignitrons triggered successfully.

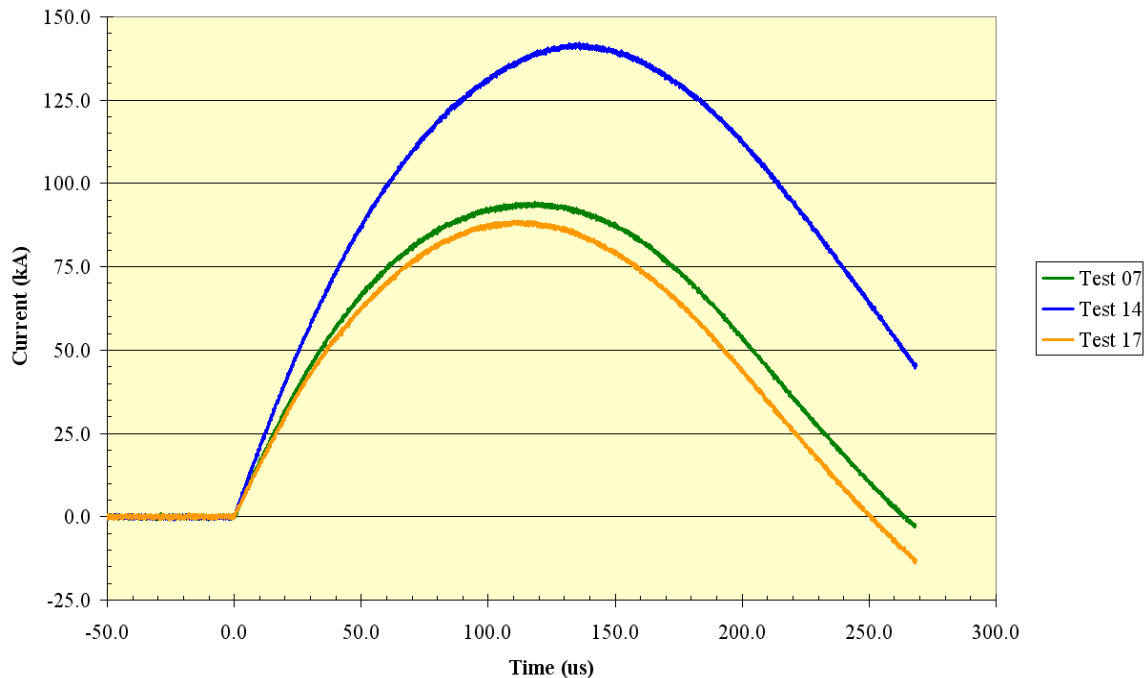


Figure 111. Theta coil-current waveforms show variations in Bias bank current for three tests

The charge voltage on the Bias bank was 4 kV for all these tests. As can be seen, the current amplitude and waveform for the west-module-only test is very similar to that of the lower-current, full-bank test, which suggests that only one module triggered and conducted during the latter. Appropriately located current monitors were not in place at the time to indicate which ignitron was having difficulty conducting during the full-bank tests.

The reason that one ignitron was suddenly now having difficulty conducting was not clear. However, the basic phenomenon appeared to be that the “good” ignitron was closing too quickly at times, and when it did the voltage on the neighboring ignitron’s cathode rose to match its anode voltage. With no net voltage drop across it, the “slow” ignitron” had no incentive to close and begin conduction. Two independent solutions were derived to attempt to address this problem, regardless of which ignitron was having the difficulty with conducting.

The first solution involved fabricating new bus work for the ignitrons. The original bus work consisted of common bus bars joining the bottoms of the ignitrons and the bottoms of the Bias bank isolation inductors, and these two bars were joined by an aluminum rod that was positioned between the two ignitrons. The new bus-work scheme replaced this structure with two 2-in. wide



by 0.125-in. thick copper straps that joined each ignitron to the isolation inductor directly above it. Thus, direct contact between the two ignitrons was broken, and the closure of one ignitron now would not immediately affect the net voltage drop across the other. Figure 112 shows one of the ignitrons and the new copper strap (painted with a red voltage-insulating paint) joining its cathode to the bank-isolation inductor immediately above it.

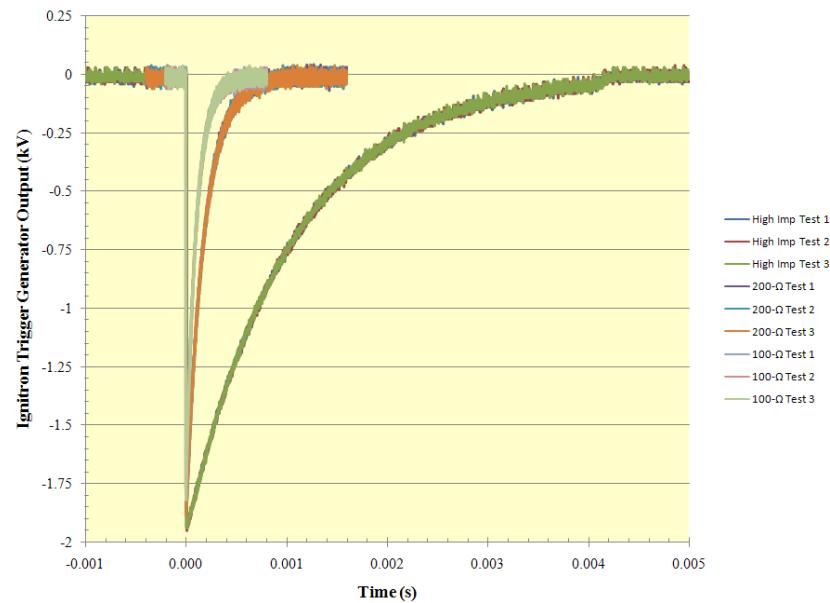


Figure 112. North Bias bank ignitron with copper strap tying its cathode to isolation-inductor terminal

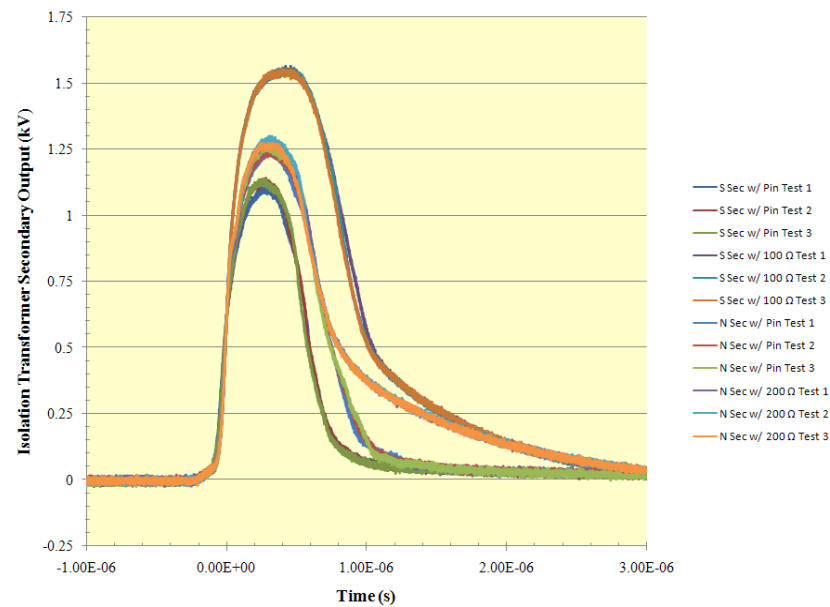
Because the bank-isolation inductors have nominally the same inductance, and the transmission-line cables joining the other end of the isolation inductors to the Theta coil-cable header have close to the same inductance—one inductor has 10 cables connected to it and the other has 9. Therefore, each module and ignitron would be driving essentially the same load impedance, so their current rise times and amplitudes should be nearly the same.

The second solution implemented to deal with the ignitron-triggering problem was directed at increasing the energy in the trigger pulse delivered to each ignitron. Figure 113a shows the direct output of the Bias bank ignitron-trigger generator with both a high-impedance and a 100- $\Omega$  load; Figure 113b shows the profiles of the trigger pulses that were actually being delivered to each

ignitron through the two secondary windings of the trigger-isolation transformer. Note that the transformer inverts the polarity of the trigger pulse.



(a)



(b)

Figure 113. (a) Ignitron-trigger-generator output pulses; (b) trigger pulses at output of each secondary of isolation transformer

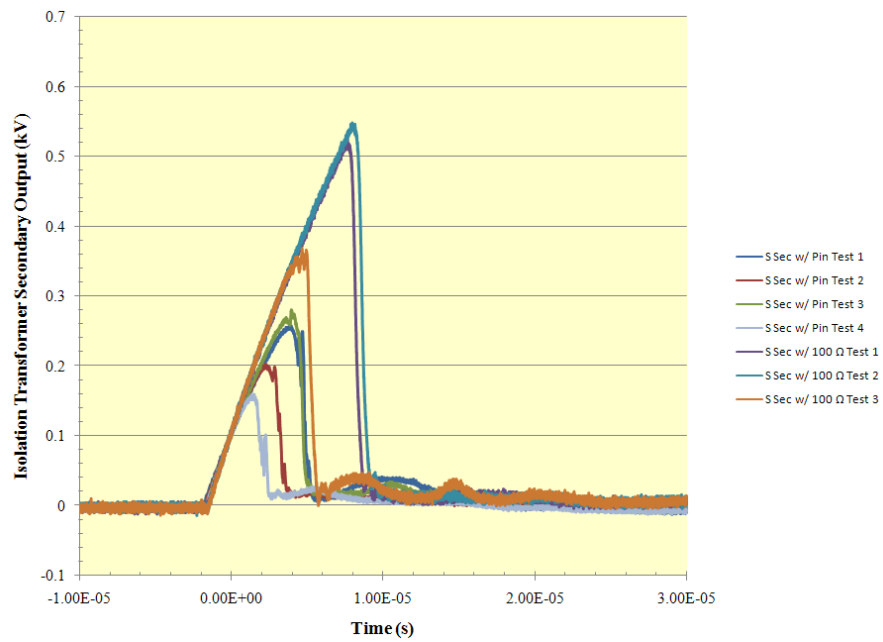
Though the rise time of the pulses at the two secondaries is quite good and the amplitudes of the pulses are appropriate for the trigger generator driving two parallel loads, the widths of these pulses at the transformer secondaries is substantially reduced compared to that being supplied to the transformer primary. Thus, it seems likely that for the numbers of turns that were in the windings (12 turns each for the primary and the two secondaries) and for the cross-sectional area of the core of the transformer, the transformer was saturating rather quickly. A new transformer was then designed with a substantially larger number of turns: 85 turns for the primary and 105 turns for each secondary, and with a core cross-section that was 33% larger.

A slight increase was made in number of turns in each secondary compared with the primary to give the voltage a boost and thereby help to initiate the breakdown in each ignitron more quickly. It was possible to obtain these increases in the number of turns in both the primary and the two secondaries by using a smaller-diameter magnet wire (20 AWG) instead of the core and center conductor of RG-58 cable, with which the previous transformer had been wound. Because of the reduced insulation of the magnet wire, though, the primary had to be physically separated from the secondaries on the core, and the windings toward the “hot” side of the secondaries could not overlap the windings closer to their low sides without some additional insulation. The pair of resistor and parallel diode strings that had been placed across each secondary on the first transformer was also used with this new transformer to prevent voltage reversals from taking place that might damage the ignitron-trigger generator. Figure 114 shows the new transformer after it was put into place and connected to the trigger generator and the two ignitrons.

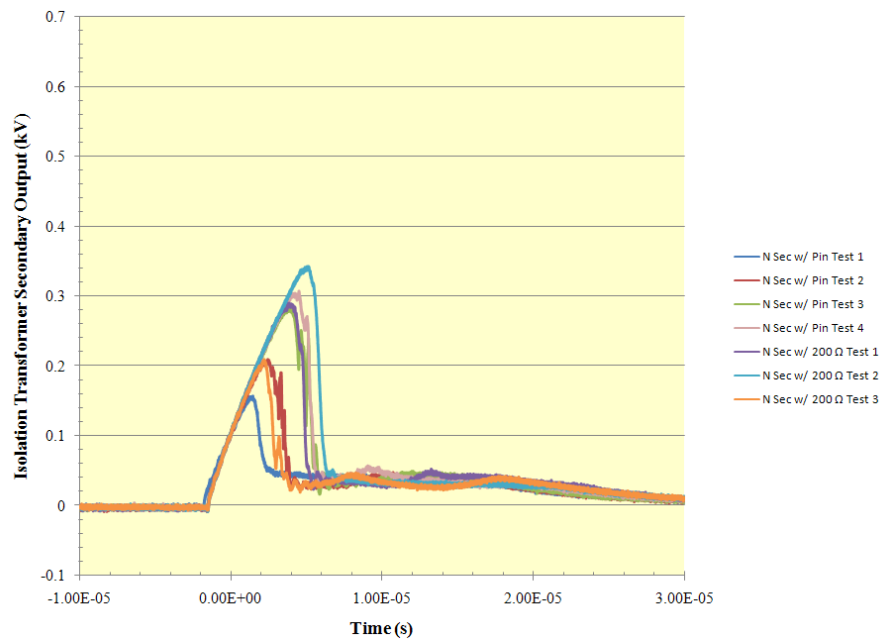


Figure 114. Ignitron-trigger-isolation transformer in place next to Bias bank ignitrons

Figure 115 shows the trigger pulses that were being delivered to each of the ignitrons.



(a)



(b)

Figure 115. (a) and (b) Trigger pulses measured at secondaries of new trigger-isolation transformer

Comparing the data with the data shown in Figure 113b, though the amplitude and rise time are not as good, the pulse duration is now 5 to 15 times greater. The variation in the pulse duration, however, implies that now there is a greater spread in the times at which the igniter pin breaks down to the mercury and starts the current conduction through the ignitron; i.e., the jitter has increased for the ignitrons. For the south ignitron this jitter appears to be  $\pm 1.5 \mu\text{s}$ , and for the north ignitron it is slightly greater at  $\pm 2.0 \mu\text{s}$ . However, with a quarter-cycle rise time of approximately  $135 \mu\text{s}$  for the Bias bank, this jitter should not be noticeable.

When tests began again with the Bias bank, both ignitrons were conducting successfully for every shot, so the transformer and bus-work changes were successful in fixing this problem. For the first iteration of this new transformer design, however, the two secondaries were wound on top of each other with their windings interleaved. This placement was possible because the amplitudes of their respective output pulses were nearly the same, and so there was then no net voltage drop between the corresponding windings of the two secondaries. Unfortunately, it appears that after a day and a half of testing in one shot one of the ignitrons failed to close as quickly as the other one. This closure delay resulted in the secondary of one transformer floating up to the ignitron-anode voltage while the secondary of the ignitron that was still non-conducting remained at ground potential. The result was an arc between several of the windings at the “low” ends of the secondaries (Figure 116).

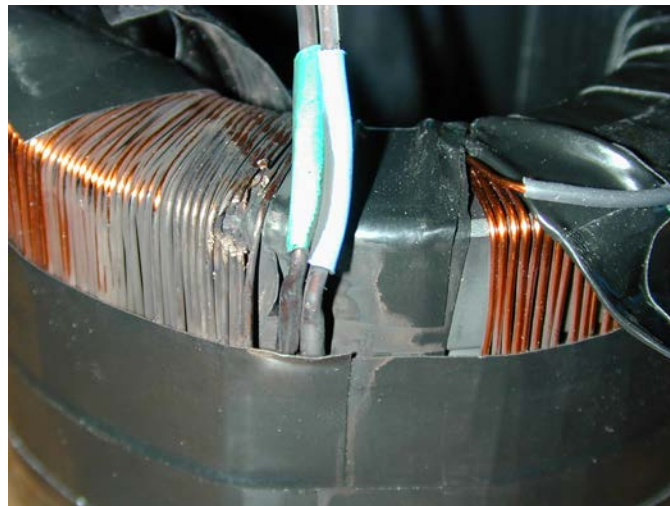


Figure 116. Arc occurred at low end of ignitron-isolation transformer

The diodes in one of the resistor and diode strings all failed as a result of this arc, as well. The field-mapping tests were able to resume quickly, however, with the use of the original ignitron-trigger-isolation transformer and replacement of the failed resistor and diode string. The isolation provided by the change in the bus work alone appears to have been sufficient in enabling both ignitrons to conduct now.

Despite the fact that both ignitrons were triggering now, a second trigger-isolation transformer was fabricated shortly thereafter, to be installed at a later date. Having a more energetic trigger pulse was still desired to increase the likelihood that there would be no problems with getting both ignitrons to conduct during future tests. To avoid the arcing problem encountered with the first transformer, the new transformer was not wound with the two secondaries interwoven but with them physically separated around the perimeter of the core, just as they were from the primary. The new transformer was not tested or set up on the Bias bank until October 2009.

The mapping of the formation region was repeated on 9–10 September 2009 once the Bias bank behavior had been stabilized. It was also necessary to remap the Upper Mirror fields after the stainless steel upper window-flange assembly was replaced with a non-metallic structure; the previous structure, though consisting of poorly-conducting stainless steel, still had an effect of the field profile. Remapping of this region was carried out on 23 September 2009.

#### *3.1.3.2.2 Initial Preparations for and Performance of Pulsed Power Tests with the FRCHX Banks*

Just prior to beginning the field-mapping measurements in the FRC formation, translation, and capture test setup, each of the FRCHX banks was carefully cleaned, inspected, and then charged and fired into its respective coils. The charge-and-fire tests were started at a nominally low charge voltage, after which the voltage was slowly increased up to the typical operating voltage used in tests last spring. This section briefly outlines the tests that were performed on each bank.

Because these banks were not moved from their original location for FRCHX-1, the only potential problems that were expected were associated with their transmission-line cables or the connections of these cables to the Upper and Lower Cusp coil-cable headers. Problems with the cables, specifically some sort of physical damage, may have been introduced when they were all

rerouted from the “retracted” test location to below the Shiva bank B-Arm catwalk and then to the Shiva bank center section. Thus far, there appear to be no such problems.

The charge-and-fire tests were successfully performed with the banks starting at a 1 kV charge voltage and thereafter in increments of 1 kV up to a final charge voltage of 4 kV. The peak Lower Cusp current is observed to be approximately 102 kA with a 4 kV charge voltage, and the peak Upper Cusp current is approximately 113 kA at this voltage. Both bank circuits have a quarter-cycle rise time of 49  $\mu$ s.

Like the Upper and Lower Cusp banks, the Bias bank has not been moved from its original location, so the only potential problems that were expected to be encountered were associated with its transmission-line cables, because they also had to be rerouted, or the connections of these cables to the Theta-coil-cable header. Fortunately, no such problems were encountered with this bank, either.

The charge-and-fire tests were successfully performed with the Bias bank starting at a 1 kV charge voltage and thereafter in increments of 1 kV up to a final charge voltage of 5 kV. The peak Bias current is approximately 200 kA with a 5 kV charge voltage on the bank, and the quarter-cycle rise time of its circuit is approximately 135 ~ 140  $\mu$ s.

The PI bank actually underwent the greatest number of changes, because not only was it moved under Shiva B-arm, but the new negative polarity, 100-kV Spellman power supply was set up to charge the bank. Though a number of exercises with the control program were carried out in earlier months to check the operation of the power supply by the Compact Field Point controller and its LabVIEW control program, this was the first opportunity to charge the PI bank with the new supply.

Charge-and-dump tests were performed first at voltages of 5, 10, and 20 kV, after which charge-and-fire tests were carried out. These tests were performed in 10 kV increments until a charge voltage of 50 kV was reached, and all of them were essentially successful. The peak pre-ionization current is approximately 144 kA with a 50 kV charge voltage on the bank, and the quarter-cycle rise time of its circuit is approximately 1.08  $\mu$ s.

There were a number of pre-fires with the rail-gap switch on the bank during these tests, and the required pressure to hold off the voltage was unusually high. It was later found to be caused by an incorrect gapping of the rail-gap switch, which has since been corrected. It was not deemed to be necessary to repeat the charge-and-fire tests after the switch was regapped, as the charging supply and circuit worked extremely well during the first tests, and the bank was, in fact, successfully charged and fired at 50 kV, though the switch pressure was not the standard pressure.

The Main bank was the bank that personnel were most concerned about possibly encountering problems with due to its size and resultant close proximity to the sides, floor, and ceiling of Shiva B-arm. The fear was that there would be a high probability of the bank arcing to its surroundings despite the 0.5-in. thick polyethylene sheets with which the interior of B-arm was lined. Furthermore, some of the Bias bank transmission-line cables had to be run fairly close to the hot bus plate on the lower half of the Main bank, creating further arcing concerns despite additional rigorous efforts at shielding the cables from the bank.

Fortunately, the charge-and-fire tests were successful with respect to the bank charging to its intended voltage and then discharging into the Theta-coil load without any evidence of arcing problems. Tests were performed at composite charge voltages of 35, 40, and 50 kV, and bank tests were also performed at voltages of 60 and 70 kV. These are the highest anticipated charge voltages at which the bank will be operated during FRC formation, translation, and capture tests. The peak Main bank current is approximately 1.26 MA with a 70 kV composite charge voltage on the bank, and it was most interesting to discover that the quarter-cycle rise time of the Main bank circuit is now 3.12  $\mu$ s, approximately. This time is 240 ns less than the quarter-cycle rise time that had been observed for the bank during tests conducted the previous two years in the bank's retracted position.

Though the bank, in principle, performed well, the Crowbar switch, which is integral with the bank and important for extending the duration of the reverse field that forms the FRC, experienced the familiar problem that it had earlier, in which not all four Crowbar rail gaps were conducting when the Crowbar was triggered. Indeed, during the 35, 40, and 50 kV tests



conducted at the end of this quarter, generally only Crowbar rail gap #1 (“CB #1”) conducted, though once CB #2 conducted and during one other test both CB #1 and #2 conducted together. The Crowbar-switch problem has essentially been the only significant problem encountered with any of the FRCHX systems during these tests. Because of the considerable difficulties that the Crowbar-triggering problem has caused in the past, not only with FRCHX previously, but also throughout the history of FRX-L, we present a discussion of this problem and an outline of the possible solutions for it.

Formal charge-and-fire tests with the Guide/Mirror bank were not necessary, because this bank had been operated regularly throughout the previous field-mapping exercises with the FRC formation, translation, and capture test setup and the FRCHX-1 and -2 test setups. The more recent field-mapping effort further confirmed that the bank was still operating as it should be, at least at charge voltages up to 2 kV. At this voltage and with this new coil set, the peak Guide and Mirror coil current is approximately 4.16 kA, and the quarter-cycle rise time of its circuit is approximately 4.21 ms.

#### *3.1.3.2.3 Main Bank Crowbar Switch Issues and Mitigation*

While problems were almost anticipated with the Main bank, given its move and the tight space into which it had now been placed, it was quite unexpected to observe that the Crowbar switch was experiencing problems again. The Crowbar switch had operated successfully in the “retracted” test position and without fail, except in one instance when the DG-535 delay generator was set incorrectly. In that case, the delay between the Main bank and Crowbar-switch triggers had inadvertently been set to 4.3  $\mu$ s instead of 3.3  $\mu$ s, and as a result not all the Crowbar rail gaps had conducted. Thus, once the 240-ns change in the Main bank rise time was discovered, the Crowbar-switch-trigger time was immediately adjusted to be 240 ns earlier (i.e., at 3.06  $\mu$ s following the Main bank trigger), but this change, unfortunately, did not solve the problem. Nothing obvious had been changed in the Crowbar-trigger system or on the Crowbar-trigger board when moving the Main bank under Shiva B-arm, except that new trigger cables were run to the switch from its master trigger generator and these cables now followed a different path.

The change in the quarter-cycle rise time of the Main bank circuit combined with the fact that CB #1 was conducting almost exclusively suggested that there was something associated with the new location of the Main bank that was connected to this problem. Figure 117 shows a portion of the floor layout in the high bay indicating the position of the Main bank under Shiva B-arm relative to the Shiva bank modules on either side of it. We note that CB #1 is the only Crowbar rail gap not immediately adjacent to the south Shiva module structure.

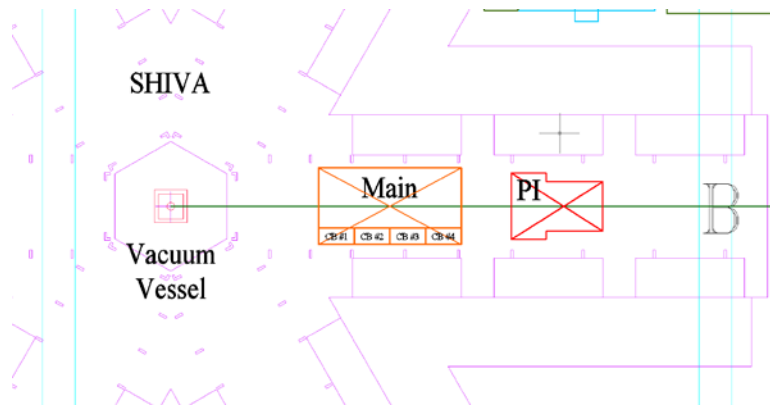


Figure 117. Placement of FRCHX Main and PI banks relative to Shiva B-arm modules

To explain the observed behavior, it is suspected that the metal ground plane below the Main bank, the Shiva B-arm transmission line above it, and the modules to either side are acting as a Faraday cage, keeping the magnetic fields around the bank from radiating outward. Confining these fields close to the bank has the effect of lowering its inductance, but this effect is not uniform on the north and south sides because the Shiva modules do not extend the full length of the Main bank. The west end of the Main bank, for example, where CB #1 is located, may thus be expected to have a slightly higher local inductance than the rest of the bank, particularly in the cable-header region on the south side of the bank. On the other hand, the header inductance should be reduced much more next to CB #2, CB #3, and CB #4 as it is closest to the Shiva Star module structure in this area. How this situation may explain CB #1 closing (i.e., starting to conduct) and not the others is perhaps because the higher local inductance around CB #1 is effectively downstream of this Crowbar rail gap. In other words, because the Crowbar rail gaps have a very low inductance internally, the higher the inductance (or impedance) that is downstream of the Crowbar rail gap, the more favorable a path the rail gap appears to be for the

current coming from the Main bank to start flowing in the rail gap once the Crowbar is triggered. The inductance downstream of CB #2, CB #3, and CB #4 (and in CB #1 once it is triggered) is low enough that the current is not diverted through these other rail gaps when they are triggered.

To obtain an estimate of how much the overall Main bank inductance has been lowered by all the metal structure around it, the total circuit inductance in both test locations is first determined based upon its oscillation frequency before and after it was moved. This calculation is done using the relation

$$t_{1/4} \cong \frac{\pi}{2} \sqrt{LC}$$

where  $t_{1/4}$  is the quarter-cycle rise time of the Main bank circuit, and L and C are the circuit inductance and capacitance ( $= 36 \mu\text{F}$ ), respectively. The rise time was  $3.36 \mu\text{s}$  in the “retracted” position, and it dropped to  $3.12 \mu\text{s}$  when the bank was moved under Shiva B-arm, thus the change in circuit inductance is approximately  $-17.51 \text{ nH}$ . It should be noted, however, that in the “retracted” position the cylindrical 10-segment Theta coil was used, which has a calculated inductance of  $42.84 \text{ nH}$ . In the “inserted” position under Shiva, the  $2.66^\circ$  conical Theta coil is being used, which has a calculated inductance of  $46.93 \text{ nH}$ . Changing the Theta coil configuration should, therefore, have increased the circuit inductance by  $4.09 \text{ nH}$ . Thus, the total decrease in bank inductance due to its new location is actually  $17.51 + 4.09 = 21.6 \text{ nH}$ .

While these arguments appeared to provide a satisfactory explanation for the Crowbar-triggering problem, it was felt that the rail-gap switches and the trigger-board components should be inspected more closely to rule out any more obvious causes. Rather than move the Main bank out from under Shiva B-arm to perform this inspection, personnel attempted to carry out this work with the bank in place in an effort to save some time. Therefore, a slow component-by-component disassembly of the trigger board above the Crowbar switch was begun, followed by a slow disassembly of the Crowbar switch itself.

When the covers on the Crowbar rail gaps were removed, there were no real surprises regarding the condition of the different sets of rail electrodes: CB #1 had the greatest signs of use, while CB #2 had some signs consistent with the one shot in which it was observed to conduct. Crowbar

rail gaps #3 and #4 were dusty, but had no signs of use, as expected. When placing the gapping tools between the rail electrodes (the  $\pm 40$  kV tool for CB #1 and CB #4, and the  $\pm 35$  kV tool for CB #2 and CB #3) to check the gap spacing, it was noted that the spacing was fine for all four rail-gap switches, but the gapping for CB #3 and CB #4 was slightly off center. Figure 118 shows that the rail electrodes appear to be shifted such that the trigger electrode was closer to the hot electrodes in these rail-gap switches than they should have been.

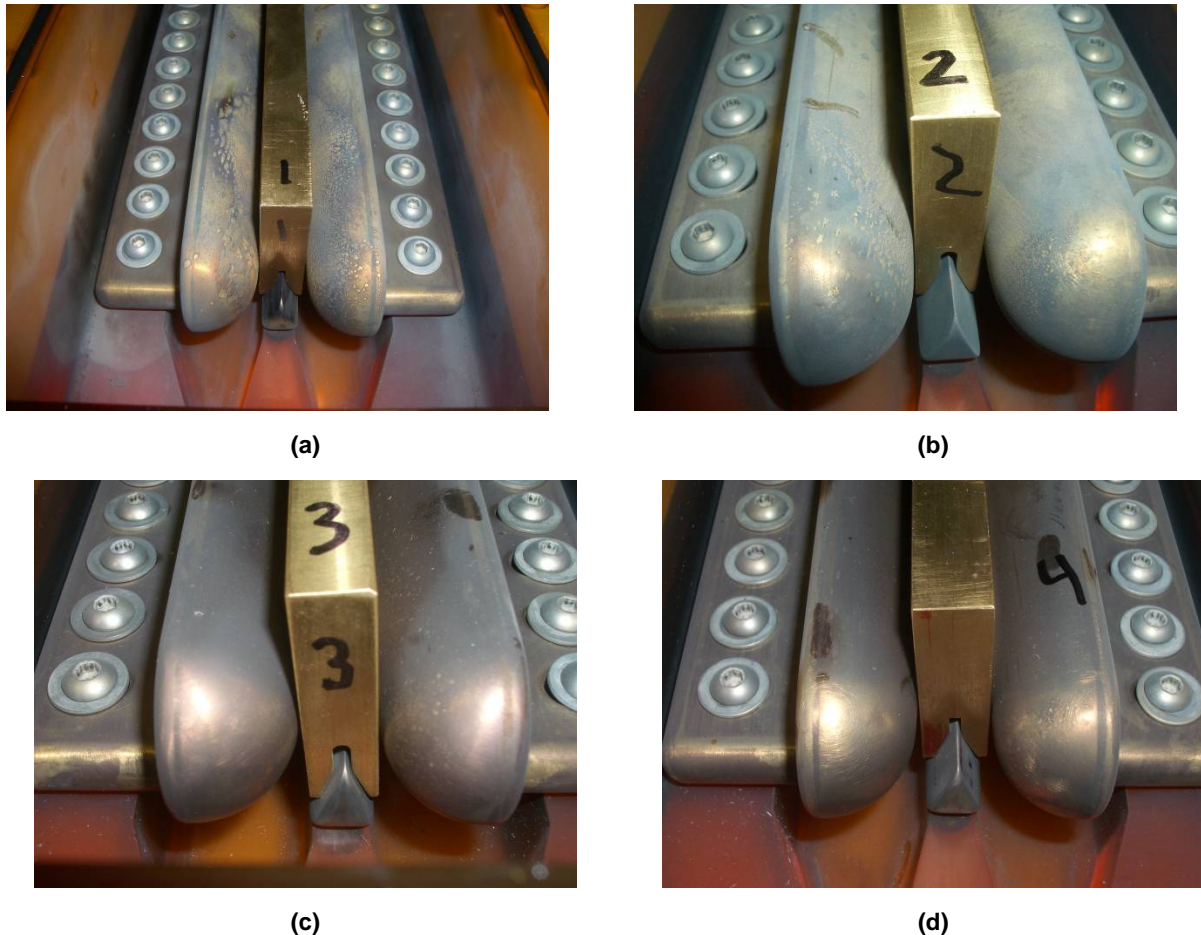


Figure 118. Proper gapping of (a) CB #1 and (b) CB #2; in (c) CB #3 and (d) CB #4 the gapping tool tilts slightly left. The shift was slight, however, and it is not felt that this small aberration in the gapping could have been responsible for these two switches not conducting during tests. Because everything was already disassembled, all four Crowbar rail-gap switches were cleaned and regapped before their covers were replaced.

With all the components removed from the Crowbar-trigger board, a systematic check of each of these components was then performed using a QuadTech 7600 LCR meter. Figure 119 is a schematic diagram showing the various components on the trigger board for each Crowbar rail gap and all their interconnections.

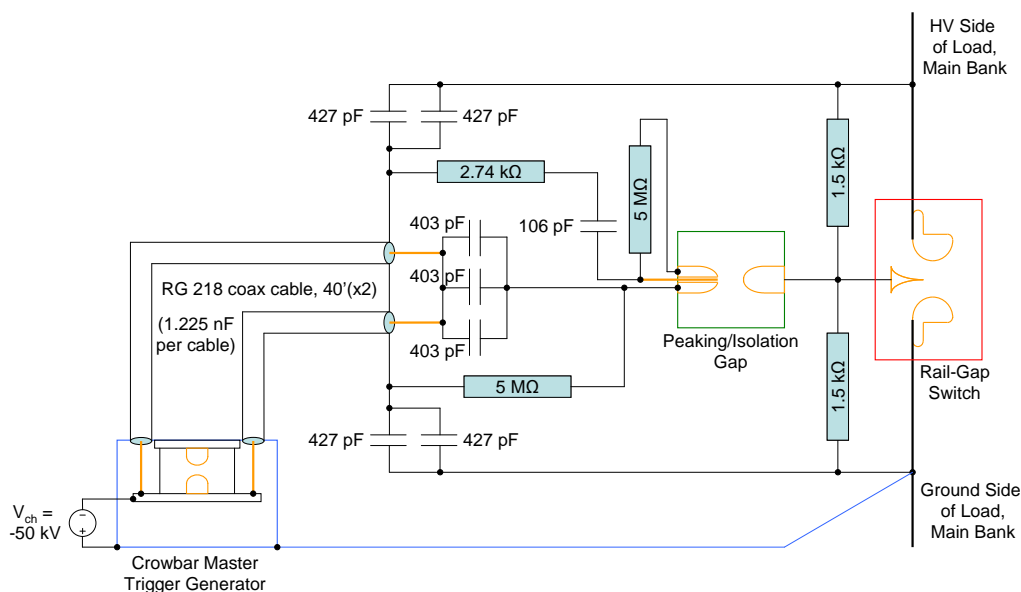


Figure 119. Most recent Crowbar-trigger-board circuit

Measurements of the various capacitors and resistors were made at 80 kHz, which is the approximate frequency of the Main bank discharge, and at 2 MHz, which is the upper limit of the QuadTech. (The approximate frequency of the trigger pulse is 4 MHz, so the 2-MHz measurements should be fairly representative of what the component values are for the trigger circuit.) The average values measured for these components at 2 MHz are indicated in the schematic diagram, except in the case of the 5-MΩ resistors, which due to their high resistance were difficult to measure reliably with the meter.

In general, the component values were all very consistent between the four Crowbar rail-gap circuits, except in the case of the 427-pF capacitors tied to the trigger-cable ground braid and the 403-pF capacitors tied to the trigger-cable center conductors. (All these are actually pairs of nominally 1-nF capacitors in series.) It was found for these components that the brown capacitors in use quite often had much lower values at 2 MHz than the orange capacitors did (Figure 120).



Figure 120. Crowbar-trigger board before moving the Main bank under B-arm

Furthermore, among the CB #2 center conductor capacitors one or two of the orange capacitors here even had somewhat lower-than-normal values. Table 15 lists the measured values for the three pairs of capacitors (combined) that were tied to each pair of trigger-cable center conductors at each rail-gap switch; note that Figure 121 shows two pairs of brown capacitors at this location for CB #3, which explains its abnormally low measurement.

Table 5. Blocking Capacitance between Trigger Cables and Trigger Terminal at Each Crowbar Rail Gap

	CB #1	CB #2	CB #3	CB #4
Capacitance (Measured at 2 MHz)	1.278 nF	1.032 nF	0.843 nF	1.321 nF

Though not all are visible in Figure 121, each Crowbar rail gap also had at least one pair of brown capacitors tied to the trigger-cable ground braid, and CB #1 had only brown capacitors connecting the trigger-cable braid to the hot and ground sides of the Crowbar switch.

While these measurements revealed that all the brown needed to be replaced, it is worth noting again that these were the same components used on the Crowbar-switch-trigger board during the previous year, and the Crowbar switch experienced no triggering problems at that time. With a fair number of blocking capacitors in use that appear to be below average, especially in the CB #1 triggering circuit, the questions remain about why the triggering worked so well last year and why was CB #1 the only Crowbar rail gap to conduct consistently in recent tests. These findings do appear to leave only the moving of the Main bank and the subsequent change in the rise time and inductance of the bank current as being responsible for the return of the Crowbar-triggering problem, however.



To develop a viable mitigation plan for the Crowbar-triggering problem, SAIC spent some time searching the literature for previous Crowbar-switch-development efforts, as well as attempting to understand better how the FRCHX Crowbar-triggering circuit is operating and why it was so successful last spring. Before 14 March 2007, the triggering circuit for each Crowbar rail gap included only one trigger cable per rail-gap switch, one pair of blocking capacitors between the trigger-cable center conductor and the peaking gap, and one pair of blocking capacitors between the trigger-cable braid and the ground side of the Crowbar switch (Figure 121a).

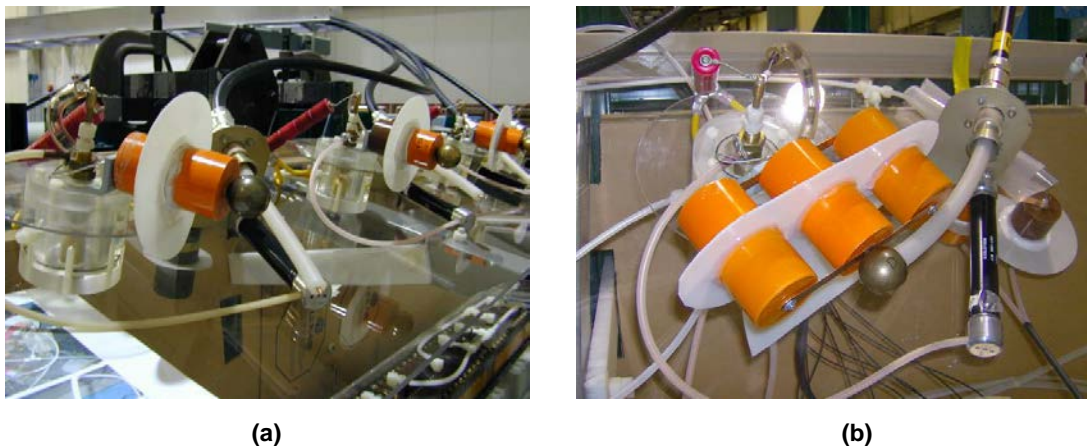


Figure 121. (a) Crowbar-trigger-board setup (pre-14 March 2007); (b) later setup with additional blocking capacitors. There were no blocking capacitors between the trigger-cable braid and the hot side of the Crowbar switch. Whether or not the Crowbar rail gaps would conduct appeared to be rather random, and when they would conduct there were sometimes long delays ( $>1 \mu\text{s}$ ) between the Crowbar trigger and the start of conduction in the rail gap. After increasing the numbers of blocking capacitors on the trigger-cable center conductor to three pairs, and after putting two pairs between the cable braid and the Crowbar ground side and another two pairs between the cable braid and the hot side of the Crowbar switch (Figure 121b), the long delays between triggering and start of conduction completely went away, though still not all Crowbar rail gaps conducted. The fact that CB #3 was the least likely of the Crowbar rail gaps to conduct seems to make sense now in light of the blocking capacitance data shown in Table 15.

By moving the trigger cables attached to CB #2 and CB #3 over the CB #1 and CB #4 (Figure 122) later in May 2007, reliable conduction was obtained in these two end rail gaps. Finally,

when the trigger cables were doubled up going to each Crowbar rail gap, reliable conduction was obtained in all four rail gaps (Figure 122).

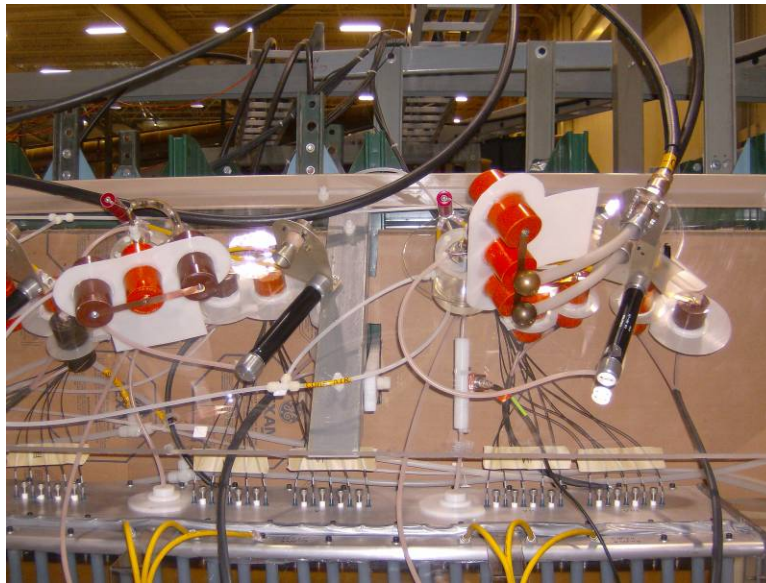


Figure 122. Trigger-board setup 18 May 2007, configured for end-rail-gap-only (CB #1 and CB #4) tests

P. M. Barnes, et al. [13] describe in some detail how the inductance of the bank circuit sets the threshold for the reliability of parallel switches being able to close. This reliability is tied to the voltage across the switches—if the voltage falls quickly because circuit inductance is low, it may be difficult to get parallel switches to conduct if there is a fair amount of jitter in the switch-closure time. In cases where the inductance between neighboring switches is low (i.e., there is no transit-time isolation), the voltage may be pulled down quickly by neighboring switches, as well, and again the jitter in the switch closure plays a role in how reliably the parallel switches will conduct. Such effects may partially explain why during recent tests only CB #1 has conducted.

However, the triggering of the Crowbar switch in our case is generally done when the voltage is very low across the switch, and as was proven last spring, good parallel operation of the rail gaps was obtained only with such triggering; the parallel operation was poorer (i.e., not all the Crowbar rail gaps conducted) when triggering was done when there should have been more voltage across the switch. There are likely a variety of physical effects occurring here that deserve a detailed analysis to understand them fully, but for the moment it is sufficient to note that the successful closure of the parallel Crowbar rail gaps during tests last spring must have



been dominated through other mechanisms. The clues to these mechanisms are linked to the information that we obtained during the Crowbar-switch tests performed in 2007.

The Crowbar-trigger system is based upon storing the trigger energy in the trigger cables, and the amount of energy, or perhaps more appropriately, the amount of charge that can be passed from the cables into the rail-gap switches is determined by the size of the blocking capacitance. When increasing the blocking capacitance in March 2007, more charge was then injected into the rail gaps during each trigger pulse. To a certain extent the initial trigger-pulse current, or charge per unit time, was also increased by increasing the blocking capacitance. Because the brown capacitors appear to be somewhat poor at high frequencies, however, not all the rail-gap switches received the same amount of charge. This situation again explains why CB #3 had the poorest operation. Upon examination of the circuit diagram in Figure 119, the brown capacitors attached to the trigger-cable braid would appear to have been less detrimental to the trigger circuit than those attached to the trigger-cable center conductor, because of the presence of the ground connection between the ground side of the Crowbar switch and the master trigger generator. This would explain why CB #1 has operated well with only the brown capacitors connected between the Crowbar switch and the braid of its trigger cables.

When doubling up the trigger cables on each rail-gap switch, the total charge delivered to each rail gap was not changed, but the trigger-pulse current was doubled meaning that the initial amount of charge delivered to the rail-gap switches was doubled. It is this change – putting in more charge sooner into the rail gaps – that appears to be what enabled them to all start conducting reliably.

Based upon the previous discussion, a plan was devised and implemented to mitigate the Crowbar switch-triggering problem. First, to make the change in inductance more uniform along the entire length of the cable header on the Main bank, so that one Crowbar rail gap would not be influenced differently than the others, sheets of 0.063-in. aluminum were placed between the Shiva module just south of the Main bank and the polyethylene sheets lining the tunnel containing the Main bank. At the Main bank frequency (approximately 80.1 kHz), the magnetic diffusion time of 0.063 in. of aluminum is approximately 231  $\mu$ s, so aluminum sheets will appear

as a uniform boundary, like the ground plane below the Main bank and the Shiva transmission-line plate above, for well beyond the start of current flow in the Crowbar switch and even beyond the FRC formation and translation events occurring in and around the Theta-coil load of the Main bank.

Next, because injecting charge appears to be the key in initiating conduction in a switch with little voltage across it, all the brown capacitors were replaced with orange capacitors that were confirmed good at frequencies up to 2 MHz, which again is the frequency up to which the QuadTech 7600 was able to measure. The questionable orange capacitors tied to the CB #2 trigger terminal were also replaced. In addition, the amount of blocking capacitance at the trigger-cable center conductors was increased for each Crowbar rail gap from approximately 1.2 nF to 2.6 nF. Doing so will now allow all the charge that is stored in the pair of trigger cables for each rail gap to be dumped into the rail gap, with the current path being completed either by the blocking capacitors attached to the trigger-cable braid or by the ground connection between the Crowbar assembly and the master trigger generator.

A. E. Bishop, et al. [14] state that in the case where a switch is required to start conducting when the voltage across it passes through zero, it is important to break down the gap between the trigger electrode and the hot side of the switch first. If the gap between the trigger electrode and the ground side of the switch is broken down first, “the trigger pulse is short-circuited to earth, and the trigger energy is dissipated, before complete breakdown of the switch can be achieved.” With this information in mind, the last change to be implemented as part of the mitigation plan was to connect all four pairs of blocking caps that are tied to the trigger-cable ground braid to the hot side of the Crowbar rail gaps. Doing so creates a fairly low-inductance path through which a significant portion of the charge stored in the trigger cables can be injected quickly into the top half of the Crowbar rail gaps. The remaining stored charge will still be injected but into the lower half of the Crowbar rail gaps and presumably at a slightly slower rate, because the path back to the master trigger generator is likely to be more inductive.

Figure 123 shows the Crowbar-trigger board after it was rebuilt to accommodate the changes just discussed.



Figure 123. The "under Shiva" Crowbar-trigger board

The board doubles the blocking capacitance at the trigger-cable center conductor and ties all trigger-cable braid capacitors to the hot side of the Crowbar. In addition, the board itself was split into three parts, a middle section and two sections on each end, to facilitate easier installation and removal of the trigger board in the future, thereby making it possible to clean the Crowbar rail gaps readily while the Main bank remains in place under Shiva B-arm (Figure 124).



(a)



(b)

Figure 124. (a) Middle portion of Crowbar-trigger board in place above Crowbar switch; (b) end section of board on workbench

The Crowbar switch and its trigger board were reassembled, and Crowbar switch tests with the new trigger-board arrangement were performed with nearly complete success. At Main bank composite charge voltages of 50 and 60 kV, three tests were performed, and in each case all four Crowbar rail gaps conducted. Tests were then conducted with a Main bank composite voltage of

70 kV, and unfortunately there was some noise of sufficient amplitude at this voltage to cause the Crowbar 40168 trigger amplifier to pre-trigger as much as  $1.8 \mu\text{s}$  early. When this pre-triggering happens, only two or three Crowbar rail gaps conduct. The pre-triggering does not always occur, though; two tests were performed in which the triggering occurred at the correct time, and in these cases all four Crowbar rail gaps conducted.

We continued to follow up previous efforts to return the Crowbar switch to reliable four-gap operation. Several series of tests were performed in the summer of 2009 with the Main bank and Crowbar switch to evaluate the effectiveness of previous changes and to refine them further. As background for the discussion of these tests, we show the original Crowbar triggering circuit (before June 2009), followed by the new circuit that implemented the June modifications, in Figure 125 and Figure 126, respectively.

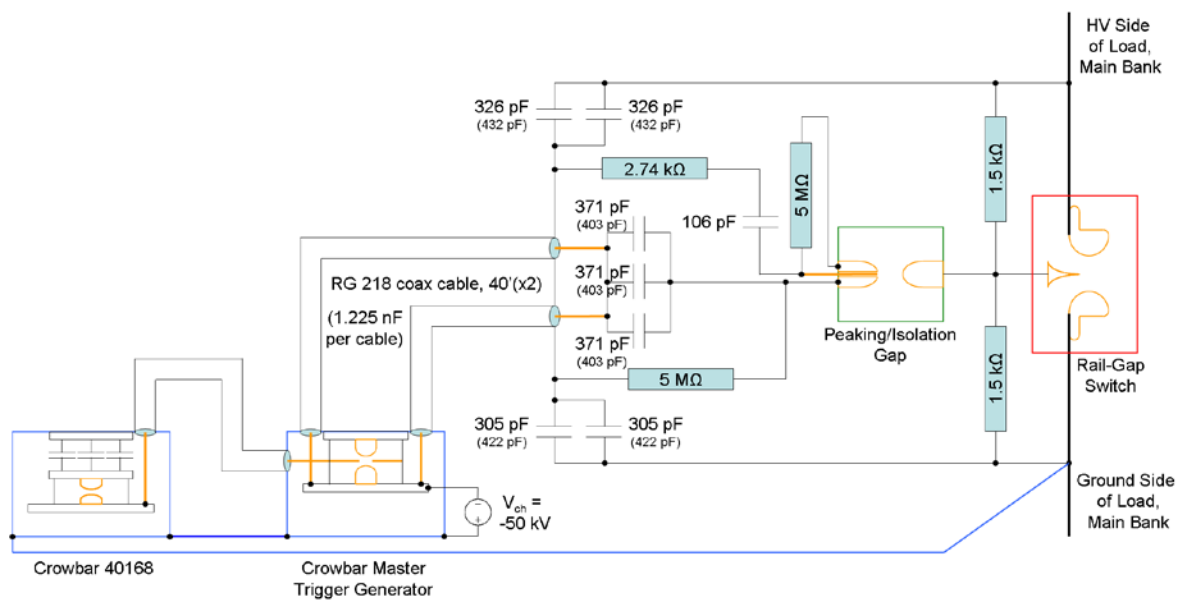


Figure 125. Crowbar rail-gap-trigger circuit used before June 2009 tests

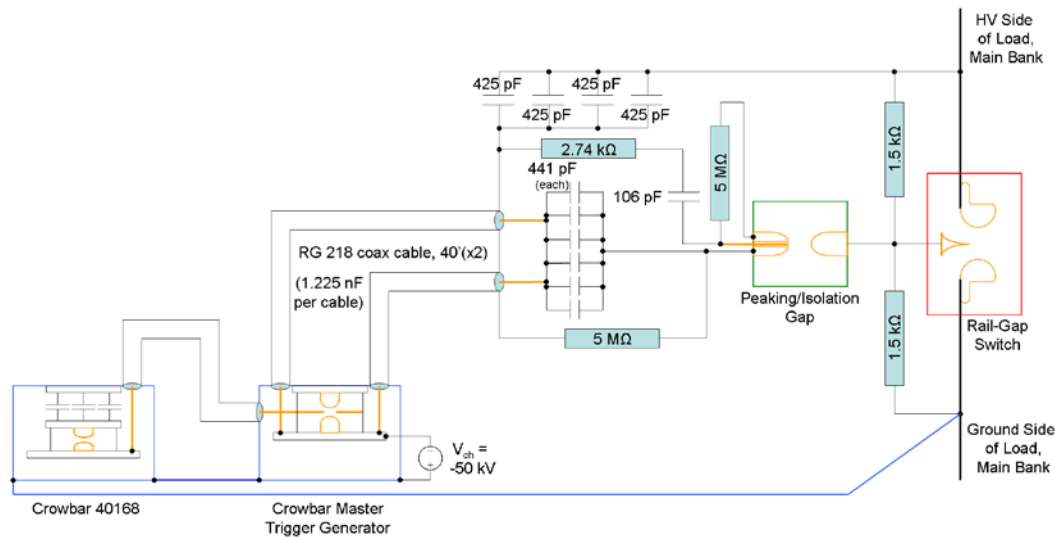


Figure 126. Modified Crowbar rail-gap-trigger circuit, end of June 2009

All values shown in Figure 125 and Figure 126 are averages for the particular components among the four rail-gap-trigger circuits. Where symbols for single capacitors are shown in the diagram there are generally two or more physical capacitors connected in series at these locations. In Figure 125, two types of capacitors, one brown and the other orange, were used in assembling the capacitor pairs, and these pairs of orange or brown capacitors were intermixed on the trigger board. The capacitance values shown in parentheses in Figure 125 were obtained using only the values measured for the orange capacitor pairs on the trigger board. The increase in blocking capacitance made by merely replacing all the brown capacitor pairs in the various rail-gap-trigger circuits with orange capacitor pairs is therefore readily evident.

The first tests performed with the Crowbar triggering circuit shown in Figure 126 were carried out on 7 July 2009. As the test series began, three tests were performed first at Main bank composite charge voltages of 50 and 60 kV. The results were very encouraging, as in each case all four Crowbar rail gaps conducted. Several tests were then conducted with a Main bank composite voltage of 70 kV, but unfortunately at this voltage problems were encountered in which the Crowbar switch would often pre-trigger. There apparently was some noise of sufficient amplitude at this voltage—which was not present at the lower voltages—that caused the Crowbar 40168 trigger amplifier to pre-trigger as much as 1.8  $\mu$ s early. When this event happened, only two or three of the four Crowbar rail gaps conducted. The pre-triggering did not

always occur, though; two tests were performed in which the triggering occurred at the correct time, and in these cases all four Crowbar rail gaps conducted. It is likely that by connecting all four pairs of blocking capacitors between the hot side of the Crowbar switch and the trigger-cable ground braid (Figure 125 and Figure 126) the Crowbar trigger system was then made more susceptible to voltage transients from the Main bank that in turn caused the trigger system to pre-trigger.

To address this problem, efforts were made to isolate more completely the Crowbar 40168 from transients in the rest of the circuit. These efforts included disconnecting the ground strap tying the 40168 enclosure to the Master Trigger Generator (MTG, which was redundant anyway because of the connections to the braid on the trigger cable between the 40168 and the MTG). The set of three ground cables that ties the trigger system to the ground side of the Main bank was then moved from the 40168 enclosure over to the MTG; and the trigger cable between the 40168 and the MTG was wrapped around a set of ferrite cores several times to suppress high-frequency transients on this cable. As an added precaution and to complete the isolation of the Crowbar 40168, the cable running between the MTG's -50 kV power supply and its controller was also wrapped around a set of ferrite cores several times. The motivation for wrapping the control cable around ferrite cores was that the power-supply controller and the 40168 are powered from the same 120 AC source.

Another series of Main bank and Crowbar switch tests was then performed on 7 August 2009. The pre-triggering problem had been completely eliminated by the changes; however, it was now observed that the changes to the trigger circuit made in June, while resulting in substantial improvements, did not provide 100% reliability in ensuring that all four Crowbar rail gaps would conduct. Out of six tests, four had all four Crowbar rail gaps conducting but two had only three rail gaps conducting. Thus, the reliability of having all four rail gaps conduct was apparently only 67%, indicating that performance had still not been returned to the level attained during the spring 2008 tests carried out in the "retracted" test location.

Following these tests, several smaller iterative changes were made to see if the percentage at which all four rail gaps would conduct would increase any. These changes included moving the

connection from one of the four ground-braid-capacitor pairs from the hot side of the Crowbar switch to the ground side and later returning the connection to this capacitor pair back to the hot side of the Crowbar while installing two new sets of capacitors between the trigger-cable ground braid and the ground side of the Crowbar switch. The additional capacitors themselves were mounted to the side of Crowbar switch for the latter because of space consideration on the trigger board, but this arrangement proved to be prone to induce arcing on the trigger board. As a result, a third trigger-circuit iteration involved combining the four “hot” blocking capacitor pairs into a single assembly, much like what was done for the trigger-cable center-conductor-blocking capacitors, to make more room on the trigger board; then it was possible to place the new “ground” blocking capacitor pairs on the trigger board, as well. Only one pair of ground blocking capacitor pairs was installed at this time, however. Figure 127 shows the Crowbar triggering circuit following this latest change.

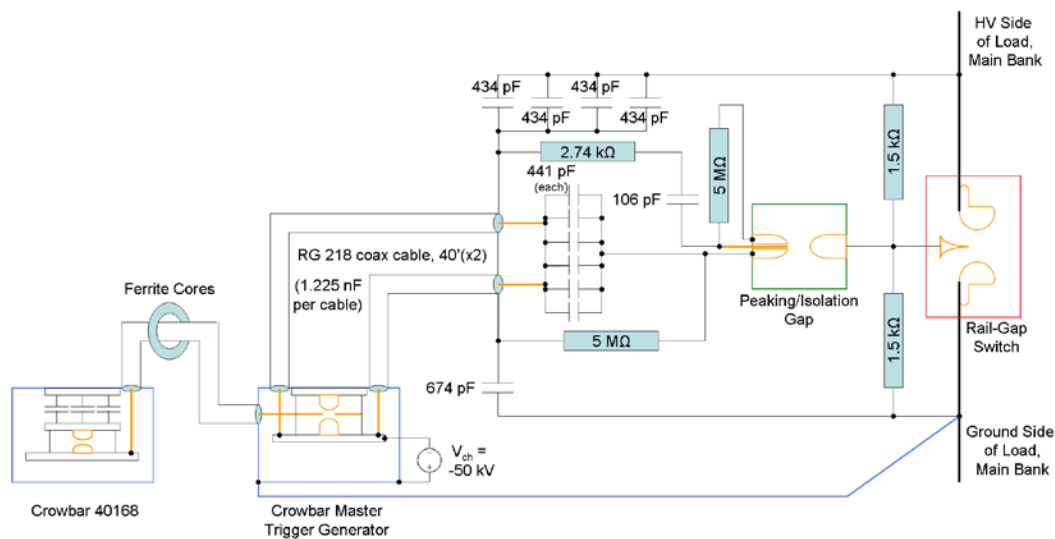


Figure 127. Crowbar rail-gap-trigger circuit, Sep 2009

Note that reassembling the four hot blocking capacitor pairs into a single, compact package actually increased their average capacitance by a small amount.

The rationale for implementing these last three changes was to determine if injecting charge into the gap between the trigger and ground electrodes of the Crowbar rail gaps—at a faster rate than that provided by the ground connection between the bank and the trigger system—would be more likely to encourage switch closure. Unfortunately, the first test with the first modification

(25 Aug 2009) still resulted in only three Crowbar rail gaps conducting, and as was already mentioned the second modification (tested 11 Sep 2009) did not work because the changes led to arcs between components on the trigger board. Tests with the third iterative change went somewhat better.

#### *3.1.3.2.4 Quartz Tube Replacement*

The movement of the stainless steel window flange above the Upper Mirror coils when the coils were being pulsed ultimately broke the quartz tube. Fortunately, only the end of the tube was broken (Figure 128), and it was possible, therefore, to complete several other test series before finally replacing the quartz tube so that the system could be put under vacuum.

The task of replacing the tube was completed in just 7½ working days, beginning on 14 September 2009 and finishing up by mid-day on 23 September. In fact, the re-mapping of the upper mirror field was carried out that afternoon. Replacement of the tube provided the opportunity to inspect the current joints on each of the Theta coil segments now that a number of Main bank tests had been performed with the coil. We recall that these current joints had been redesigned following the observation of considerable arcing at the joints on some of the segments when the cylindrical Theta coil was disassembled after tests occurring during the spring of 2008 under the previous contract (DETAR TO 16).

Figure 128 shows an overall view of the current joint surfaces on all 10 of the grounded-side Theta coil segments. Figure 129 shows a close-up view of three of the segment-current-joint surfaces close to their inner radii.





Figure 128. Current-joint surfaces of Theta coil segments left assembled on vacuum stand

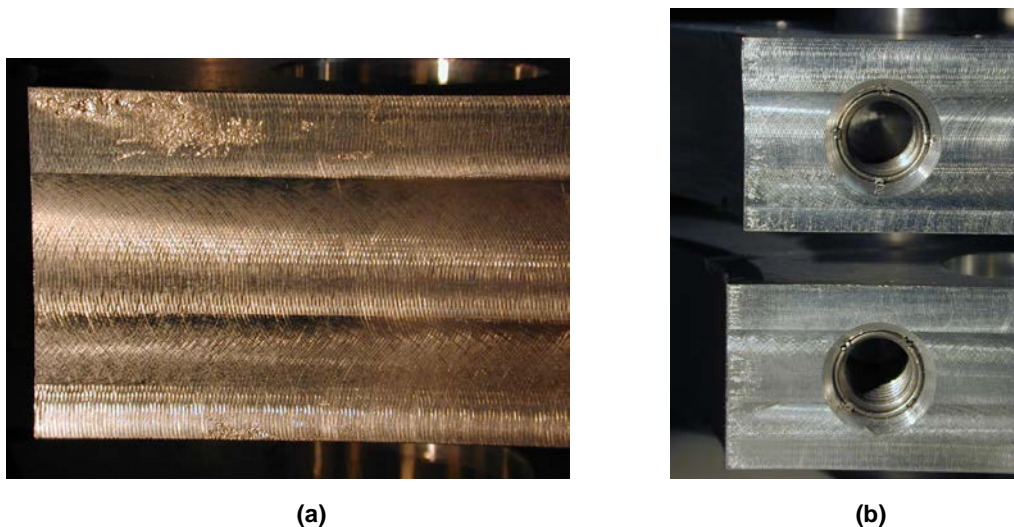


Figure 129. (a) and (b) Close-up views of three segments from Figure 128

By this time, approximately 25 Main bank tests had been performed with discharge currents as high as 1.1 MA, and, as can be seen, there is very little pitting on these surfaces. Thus, the design changes to the segments and their copper gaskets were successful.

After the new quartz tube was installed in the vacuum and field-coil stand and reassembly of the field coils and diagnostics had begun around it, personnel began giving careful thought to how

the window could be better secured at the top of the quartz tube. Because present window assembly had a non-magnetic and relatively poor conductor such as stainless steel in it and because it still moved in the pulsed magnetic fields, it was decided to try fabricating the next assembly using only non-metallic materials to eliminate any possibility of motion due to the fields. Figure 130 shows the window assembly developed by SAIC machinists.



Figure 130. New window assembly, top of quartz tube

A 0.75-in. thick piece of glass is used for the window, and its flange structure is made out of G-10. Nylon bolts are used to hold it together, and a single O-ring makes the vacuum seal between the quartz tube and the window glass. To keep the tube and glass from touching each other directly, a thin polyethylene ring cap—the only plastic component to be in the vacuum—has been placed around the top edge of the quartz tube. A thin lip around the inside diameter of the ring cap keeps it centered on the tube. Thus far, vacuum pressures as low as approximately  $2 \times 10^{-8}$  Torr, which are very comparable to the base pressures obtained during the spring 2008 tests, have been achieved with this new window structure.

SAIC machinists also fabricated two centering plates for the stainless flux-conserving tube that is placed around the quartz tube in the FRC translation region (Figure 131).

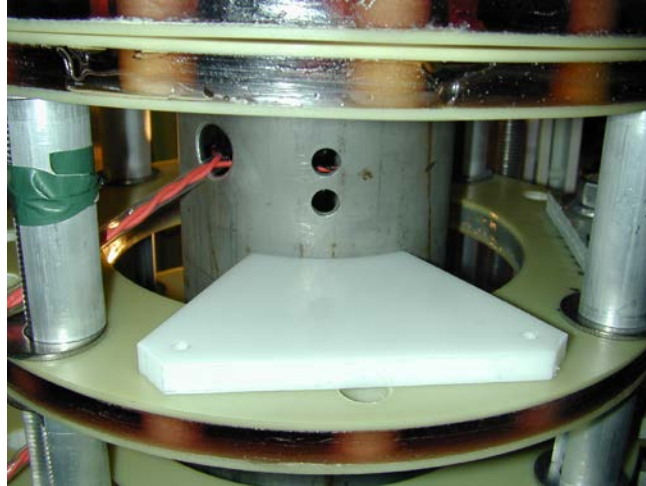


Figure 131. Two PE fixtures to keep stainless flux conserver centered within Guide and Mirror coils  
Just as with the upper window flange, there was evidence that the stainless tube was moving under the influence of the pulsed high magnetic fields, as well. The new centering plates will keep the tube centered within the coils and will therefore keep the B-dot probes and fiber optic light monitors from moving from their designated locations.

Much time was spent tying the flux loops around the quartz tube at their designated locations and then trying to keep them from moving. A plastic holder in which they could be secured and that could be just slid down around the quartz tube would save a considerable amount of time. Furthermore, if a tube were to break again and if the flux loops were wrapped in special holders instead of on the surface of the tube, it might be possible to remove the broken tube and install the new tube without disassembling the Theta coil or removing the Guide and Mirror coil assembly from the vacuum stand. Such a tube exchange could then be performed in a much shorter amount of time than the 7½ days required for this exchange.

#### *3.1.3.2.5 Main Bank Triggering*

The pre-triggering problem with the Main bank triggering system became prominent after three parallel grounding cables were run between the Main bank frame and the Main bank triggering system, at which point they were tied to the MTG. Figure 132 shows the ground cables for the Main bank trigger system at the connection point to the MTG (#1)

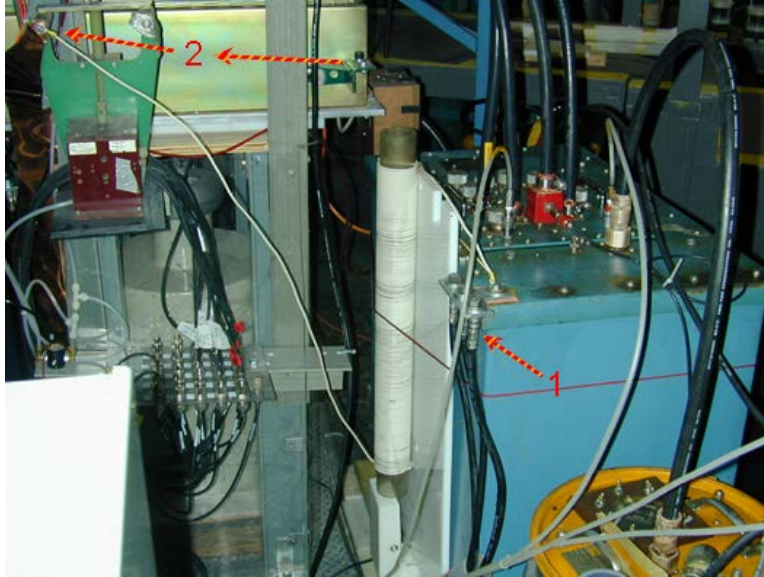


Figure 132. (1) Ground cables; (2) movement of connection point for trigger-system-grounding inductor

These cables, the manner in which they were connected between the bank and the trigger system, and their purpose—that of ensuring that the trigger system floats at the same potential as the bank during a shot—were all essentially identical to those put into place nearly three years previously for the PI and Crowbar triggering systems. These triggering systems, however, had not been prone to self-triggering, and thus it was somewhat of a mystery as to why the Main bank trigger system was experiencing this problem with the ground cables connected. It was also preferable not to remove the grounding cables again and return to the original configuration for the trigger system. With the previous configuration arcing had been commonly observed around the ferrite core choke on the Main bank pre-fire detection sensor (B-dot) cable each time the Main bank trigger system was fired (Figure 133).

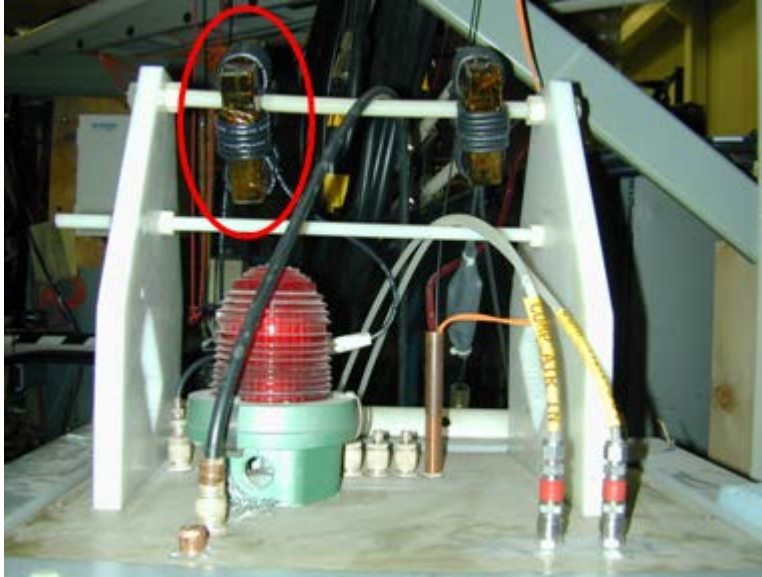


Figure 133. Without grounding cables, arcs would occur around Baluns on pre-fire detection sensor cable. No such arcing was observed with the grounding cables in place, but instead the trigger system operated very quietly.

To address this problem, personnel began by looking at the MTG spark gap switch. It was removed from its oil tank, cleaned, and then inspected. The biasing and gapping were determined to be correct for the switch; however, the electrode surfaces were quite dirty and in need of cleaning. Though it was uncertain whether it was the MTG initiating the pre-fires or the PTA, cleaning the MTG switch should at least improve the performance of the MTG.

During the process of removing the switch, the MTG grounding inductor was also noted to be incorrectly grounded to the Crowbar 40168 Hoffman box. This connection was therefore moved over to the nearby earth-ground strap on the Crowbar trigger-system ground-lift relay (#2 in Figure 132), which was a more appropriate location for it. In addition to this change, a few other external changes were made to the Main bank-trigger system to make its configuration more like that of the Crowbar trigger system. These changes included removing a redundant copper braid that tied the PTA rack and the MTG to each other and assembling two stacks of five ferrite cores, around which the PTA output cable and the input AC power line to the MTG's external power supply were wrapped. The placement of the ferrite cores in the system effectively isolates the MTG and its power supply from the PTA rack and the power-supply controller. Figure 134



highlights the external changes made to the trigger-system configuration, and Figure 135 shows a closer view to the two ferrite-core stacks.

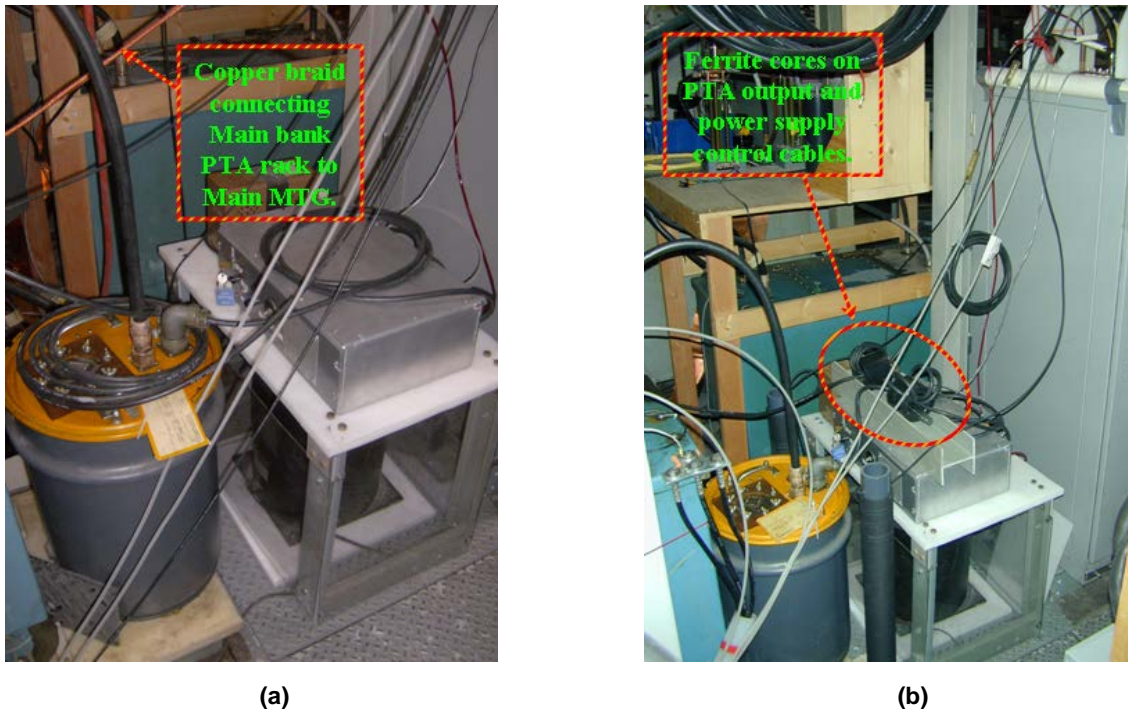


Figure 134. (a) Previous Main bank-trigger system; (b) new configuration after changes

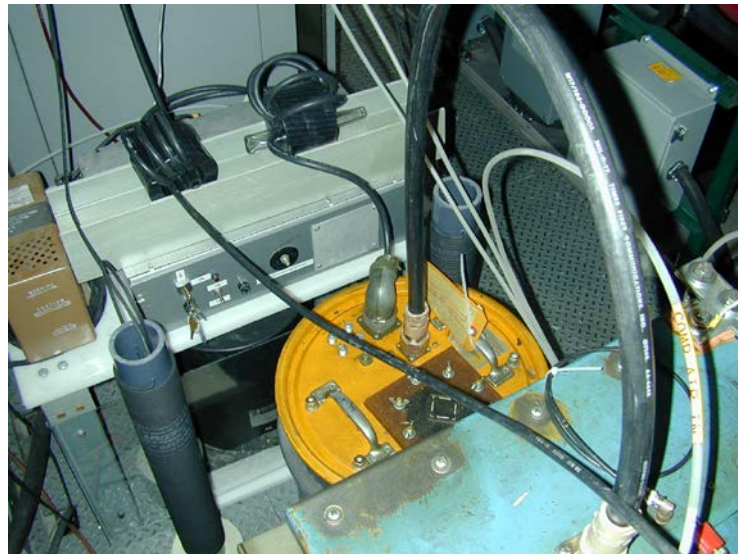


Figure 135. Closer view of PTA output cable and MTG power-supply-control cable ferrite-core stacks

Lastly, the PTA spark-gap switch was removed, disassembled, cleaned, and inspected as was done with the MTG switch. The PTA switch was found to be very clean but was noted to have several cracks that radiated out from each of the electrode bolt holes. Many of these cracks passed under the O-ring channels on each side and at least one was found to leak substantially. Should the leak have been sufficient to lower the pressure in the switch, the lower-than-desired pressure could have led to the pre-fires. An attempt was made to seal this and other possible leaks by brushing in Rhodosil™ silicone encapsulant around the O-ring grooves and bolt holes on each side, but it was unsuccessful. Another switch, which unfortunately leaked as well, but did so at a much slower rate than the original switch, was found to replace it. Before installing the replacement switch in the PTA, the electrodes were inspected and the irradiation-pin-gap spacing was set per the manufacturer's instructions. Specifically, a DC voltage was applied between the pin and the mid-plane electrode, and the distance of the pin from the mid-plane was adjusted such that the voltage at which the gap broke down was  $\sim 900 \text{ V} \pm 50 \text{ V}$ .

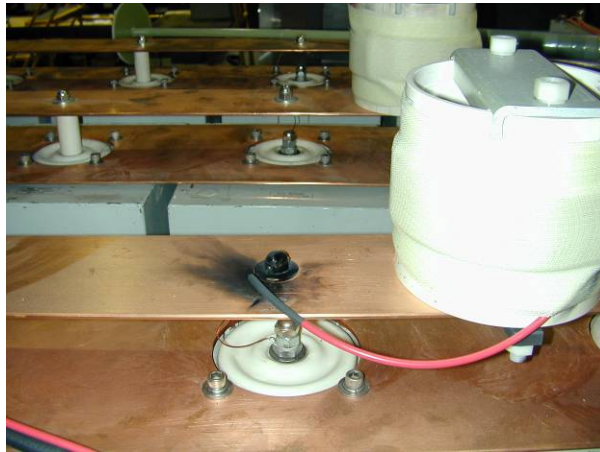
Trigger tests performed on 30 September 2009 then showed that the Main bank trigger system was now exceptionally quiet (i.e., all undesired air arcs continued to be suppressed, in particular those observed around the pre-fire detection probe ferrite cores). Furthermore, the system now exhibited no instances of self-triggering on its own.

#### *3.1.3.2.6 Final FRCHX Pulsed Power Changes*

Several problems were encountered with the FRCHX pulsed power systems during further testing, so we present here the various means employed to correct them. For simplicity the specific problems are grouped according to the bank or other systems that they affected.

##### **Guide/Mirror Bank**

A somewhat unexpected problem was encountered with the Guide/Mirror bank involving the charging inductors linking the different modules. During two tests on different days in early October 2009 the inductor connecting modules 2 and 3 of the bank was damaged, apparently by excessive current flow (Figure 136).



(a)



(b)

Figure 136. Damaged charging inductor between modules 2 and 3

The recorded time window for the module current waveforms captured just one-half of a cycle during both these tests, but nothing abnormal was observed during that time in any of the waveforms.

A heavier gauge wire (approximately 0.125 in in diameter with a 0.375-in. diameter polyethylene insulation around it) was used to construct the inductor the second time. Connectors were not used this time at the ends of the wires, as these locations in particular seemed to be a weak point. Instead, the wire was bent into a hook and flattened to allow each end of the inductor to be fastened with a bolt onto the neighboring module bus plates. Figure 137 shows this new and more robust inductor in place.



Figure 137. New inductor between Guide/Mirror modules 2 and 3



The time window for recording the current waveforms was also increased to enable observation of anything occurring later in time that could cause the inductors to fail. Subsequent tests showed that the bank modules actually tended to conduct for only one-half cycle; the ignitrons on each module appeared to shut off when the current reached zero and would not restrike. However, it was eventually observed during one of the tests that a few of the module ignitrons did restrike and allow for a reversed current flow. Following this particular test, the new inductor between modules 2 and 3 incurred no damage, but the inductor connecting modules 3 and 6 was damaged during a third fault (Figure 138a).

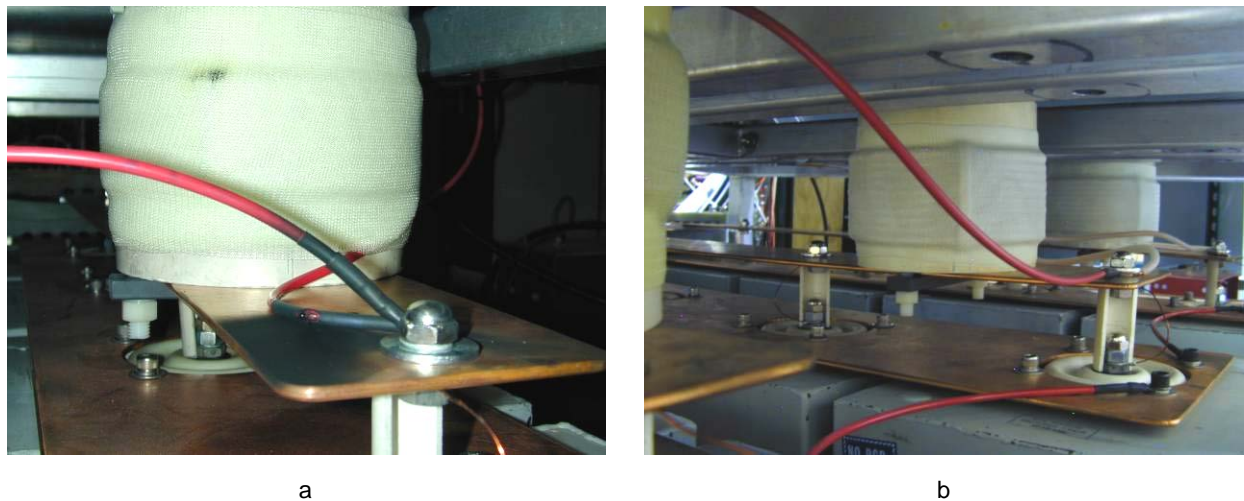


Figure 138. (a) Damaged inductor joining modules 3 and 6; (b) module 3-6 and 5-6 inductors were also remade. With some modules reversing and not others, the reason for the charging inductors incurring damage was now readily apparent: the non-reversing modules would have a residual voltage with an opposite polarity to that of the modules that did have reversed current flow, and the charging inductors that tied those adjacent modules together would then have that net voltage difference applied across them. With a voltage drop of 100s of V to a few kV suddenly across them, significantly greater currents than those occurring during normal charging would then flow through the inductors as the charges on the neighboring modules attempted to equalize. The excessive current flow then resulted in the rapid failure of these inductors. Following this third fault, it would appear that the wire used to remake the module 2-3 inductor was better suited for such conditions. Therefore, both the module 3-6 inductor, which was damaged on the last fault, and the neighboring module 5-6 inductor were remade using this thicker wire (Figure 138b).

While no obvious damage was seen on the inductor between modules 5-6, it was decided to remake it anyway because of some suspicious markings on it.

### Bias Bank

The Bias bank was the most problematic bank during the FRC formation, translation, and capture tests in the during the fall of 2009. At the very start of the plasma tests at the beginning of October it began experiencing a number of pre-fires while it was being charged. This problem was soon determined to be due to a failing ignitron. The bank has two ignitrons, one for each of its modules. To identify the particular ignitron experiencing the voltage hold-off problem, a high-voltage power supply was connected using a series-charging resistor across the ignitrons one at a time, and then the current meter on the supply was monitored as the voltage was increased. The voltage was also measured directly on the ignitron anode using a North Star PVM-5 high voltage probe, and this measurement was compared with that indicated by the voltage meter on the power supply.

It was found that the north ignitron began to conduct when the supply voltage reached 3.2 kV. The south ignitron showed no current conduction as the supply was raised all the way to its maximum voltage of 10 kV. Fortunately, three spare ignitrons of the same size and construct were located in-house, and so it was possible to replace the ignitron rather rapidly. Because the test setup was already assembled, the voltage hold-off of the Jennings dump switch for the bank was also checked in this manner. The switch electrodes are contained inside a vacuum-insulated enclosure, and should a leak ever develop in the switch's enclosure it could also begin causing premature discharges of the bank. Fortunately, the switch checked out well, because the power supply did not show any indication of current flow between the electrodes for voltages up to 10 kV.

When tests resumed after the replacement of the north ignitron, it was noted the "new" north ignitron appeared to be triggering late compared to the south ignitron. This behavior gave rise to a somewhat oddly shaped double-hump profile for the Bias bank current. The delay in triggering was readily corrected by replacing the trigger-isolation transformer again with one that provided a more energetic trigger pulse to each ignitron. This new transformer was similar to the one

described previously, except that the two secondaries were not wound on top of each other this time but instead separated spatially around the perimeter of the ferrite cores. Following the installation of the new transformer, the Bias bank-current waveform again appeared normal; a Rogowski coil installed around the bus bar tied to the output of the ignitron confirmed that the north ignitron was starting conduction at the appropriate time.

Unfortunately, during the first half of November 2009, after just a few weeks of testing, the replacement north ignitron began to have difficulty holding off the bank voltage and started to pre-fire during charging as the old ignitron had done. That it was the north ignitron that was failing again was apparent from the excessive condensation of mercury vapor on the glass envelope at the top of the ignitron. This situation was confirmed by performing the voltage hold-off tests again with the high-voltage power supply. Heating the top of the ignitron drove away the mercury-vapor droplets and would allow the ignitron to hold off voltage, but the recovery was only temporary. The ignitron would operate well again for fewer than 10 shots, and then the mercury-vapor droplets would have condensed sufficiently again on the glass to reduce the voltage hold-off. After replacing the ignitron with another one of the spares, the bank operated well again, and no longer exhibited any signs of pre-firing.

FRX-L personnel commented about experiencing problems in the past with their bank ignitrons pre-firing. While the bank ignitrons are, of course, being operated only in a single-shot manner, personnel found that running cooling water through the jackets around the ignitrons encourages the mercury vapor to re-condense at the bottom of the ignitron rather than on the glass envelope. The voltage hold-off capability of the ignitrons is therefore preserved.

Because of the connection to a common field coil (the theta coil), problems with Main bank pre-firing also led to problems on the Bias bank. A Main bank pre-fire on 6 November 2009 was suspected to have caused a number of component failures inside the Bias bank's ignitron-trigger unit. The trigger unit was repaired the following week using spare components that were on hand. Several days later on 17 November a similar Main bank pre-fire event damaged the ignitron-trigger-isolation transformer again (Figure 139).



(a)



(b)

Figure 139. (a) Trigger transformer after damage by Main bank pre-fire; (b) Arc marks observed on cable from trigger unit to transformer

Ordinarily the isolation inductors on the load side of each of the Bias bank ignitrons would help protect the bank from the higher Main bank voltages. However, if the Bias bank has not started to conduct yet when the voltage is impressed upon the inductors, the same voltage on the load side of the inductors appears on the bank side of the inductors, and the lower-voltage-rated trigger components are then damaged. Therefore, these events initiated an effort to develop an overvoltage-protection module for the Bias bank.

When examining the damaged Bias bank-trigger-isolation transformer following the 17 November test, personnel discovered some arcing between one of the bank's two Pearson coils and the bank bus work and frame (Figure 140).



(a)



(b)

Figure 140. Arc marks between (a) west module Pearson coil and bank frame; (b) Pearson coil and diagnostic cable

This arcing, if it was recent, may explain some anomalous late-time behavior in a number of the diagnostic signals that started appearing during tests performed on 16–17 November 2009. Following this discovery, the Pearson coils were removed from the bank, cleaned, and then painted with a red high-voltage-insulating paint before reinstalling them (Figure 141).



Figure 141. Repainted Bias Pearson coils in place

### Upper Cusp Bank

On 19 October 2009, the Upper Cusp bank began exhibiting problems during charging. Specifically, its charging waveform was changing slope (charging more slowly) at about halfway to the target-charge voltage, and the final charge voltage was then barely reached. Furthermore, the voltage began falling off rapidly as charging stopped just before firing.

The capacitors in the bank were checked to determine if one of them might have failed, but they were found to be good. The voltage-to-frequency converter box used to transmit the bank-charge voltage to the control system was also checked to determine if its battery was getting weak, but it was also found to be good. After a few additional tests were performed with the bank, it began to pre-fire. Thus, it became apparent that, like the Bias bank, its ignitron was beginning to fail.

Hi-potting the ignitron with the high-voltage power supply in the same manner as done with the Bias bank ignitrons showed current draw starting between 8 and 10 kV. This amount was somewhat higher than the voltages at which the change in the charging waveform was observed during the tests just performed; however, it was decided to replace the ignitron anyway. Several spare ignitrons for the Upper and Lower Cusp and the Guide/Mirror banks had been brought

down from the FRX-L facility during the previous week in light of the recent failure of the Bias bank ignitron. After the ignitron was replaced, the charging behavior of the bank returned to normal.

### PI Bank

When FRC formation, translation, and capture tests began in October it was noticed that the PI bank would occasionally fail to fire. Checks of the various trigger and rail-gap-switch pressures revealed that the problem was caused by the pressure in the MTG spark-gap switch drifting and becoming too high for the unit to operate properly. The problem was therefore resolved initially by simply monitoring the pressure more closely between tests. Later, when time finally permitted it, the pressure regulator for the MTG was replaced with a new one that would keep the pressure more constant.

On 3 November 2009 an arc fault occurred on the PI bank during one of several tests with an intended charge voltage of 49 kV. Originating from the hot bus plate, the arc punched through the Kapton tape on the bus plate and the layers of Mylar sheets attached to the bank side of the rail-gap switch. It then propagated underneath the switch to the hot bus plate on the load side of the switch. Figure 142 shows the damage.

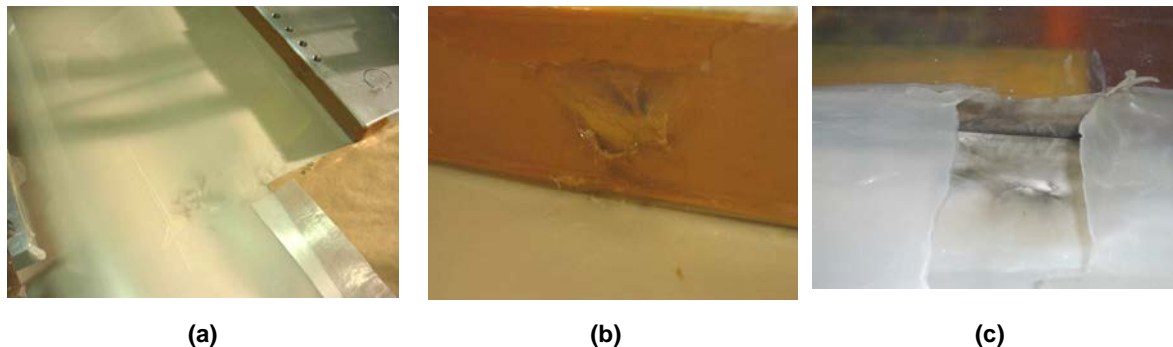


Figure 142. (a) Signs of arc on Mylar; (b) arc initiation point; (c) damage to Mylar on rail-gap switch

Figure 142a shows damage with the rail-gap switch removed; Figure 142b shows the arc's initiation point on the bank-side hot bus plate. Though somewhat involved, the repair procedures were able to be completed within a 24-hour period. These procedures entailed cleaning the Mylar pack that runs the full length of the bank and then turning it over to place the side with the arc



damage (Figure 142a) toward the ground bus plate. A sheet of brown kraft paper was then placed over the new top surface of the Mylar. While this procedure was being done, personnel were also machining a larger radius on all the corners of the hot bus plate, and then placing new Kapton tape on the face and corners of the plate where the rail-gap switch is attached. These modifications were made to mitigate the likelihood of future arc faults on the bank.

Before placing the hot bus plate back onto the Mylar pack and torquing it down to the capacitor, a thin coating of Rhodosil<sup>TM</sup> encapsulant was spread onto the existing encapsulant filling the PI capacitor header. The reapplication of the Rhodosil was done to fill some air pockets that were found within the encapsulant material in the header, as well as to help form a seal again between the header encapsulant and the Mylar. Figure 143 shows the bank after the hot bus plate was finally torqued back down to the capacitor terminal.

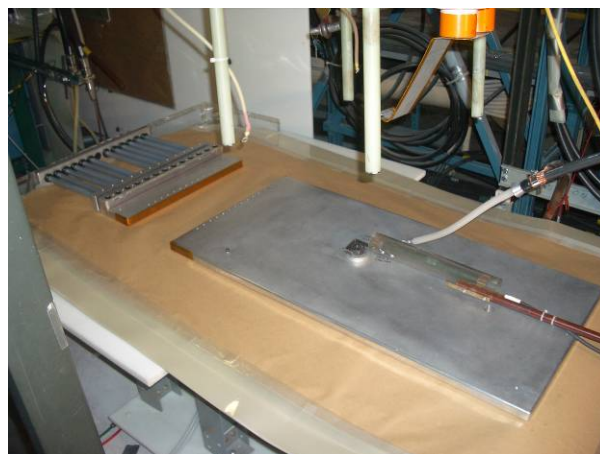


Figure 143. PI bank after Mylar pack was refurbished

Meanwhile, new Mylar sheets were being cut to replace both the small Mylar packs that are clamped down to the sides of the rail-gap switch. Brown kraft paper was also placed on what would be the top surface of the longer pack. When the packs were completed, they were attached to the sides of the rail-gap switch with the switch's brass clamping bars, and a bead of Room Temperature Vulcanizing (RTV) silicone was run along the corners of the switch next to the Mylar packs to form a seal between the two. The switch was then raised up on a workbench such that the Mylar packs could hang down vertically, and the RTV was allowed to cure overnight (Figure 144).

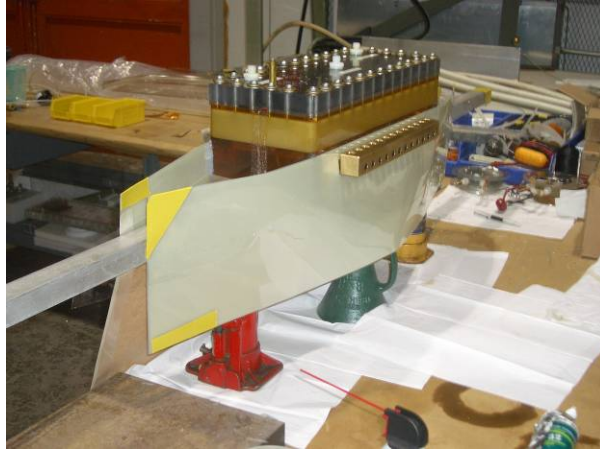


Figure 144. PI rail-gap switch after new Mylar packs were reattached and RTV applied

The next morning, the rail-gap switch was reattached to the bank- and load-side hot bus plates, and afterwards the trigger board was put back into place. Once all connections were made between the trigger board and the bank, the bank was ready again for tests. Figure 145 shows the PI bank after the repairs were completed.

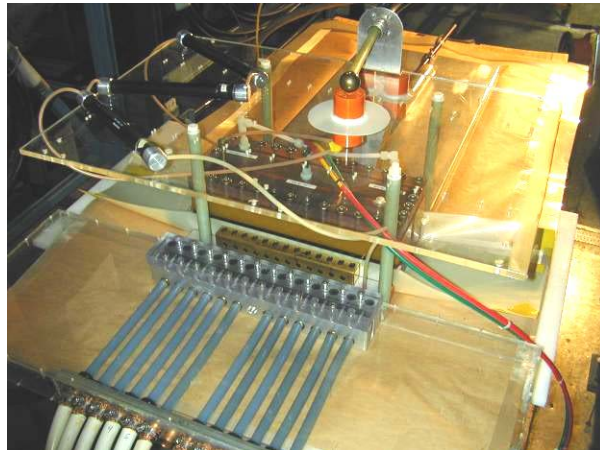


Figure 145. PI bank after repairs and reassembly was completed

Since completing the repairs, the PI bank has been successfully charged to and fired at voltages as high as ~60 kV with no further fault incidents.

### Main Bank

*Closing-Switch Trigger System.* As plasma tests were getting started there were a number of instances in which the Main bank was triggered early, at approximately the PI bank trigger time. Monitoring of the trigger pulse that was being sent to the Main bank's trigger system at both the



output of the DG-535 delay generator and at the Main bank trigger system revealed the delay generator and the trigger receiver were in fact sending and receiving the trigger at the correct time.

We looked at the Main bank's pre-fire detection system as a possible cause of the early triggering. Indeed, with the system disabled the Main bank was observed to trigger again at the correct time. This finding therefore showed that the Main bank's pre-fire detection sensor (located on the ground bus of the Main bank) was sensitive to the PI discharge. After more careful thought, it was not terribly surprising—the PI and Main banks are interconnected because they both drive the same theta coil load.

The signal from the pre-fire sensor on the Main bank was then monitored for several shots that did not include the operation of the Main bank. It was confirmed that the sensor response to the PI bank discharge was well above the voltage threshold required for the Main bank-trigger system to respond to it. By inserting a 5x attenuator in the pre-fire sensor's signal line, however, the sensor's response to the PI bank discharge was reduced to a level below that to which the trigger system would respond. Subsequent shots that included the Main bank then showed the Main bank triggering again at its appropriate time, and the pre-fire sensor response to the Main bank was still sufficiently large to ensure that the Main bank-trigger system would be triggered in the event of an actual Main bank pre-fire.

*Crowbar Switch Performance.* In Section 3.1.3.2.3 we described a number of modifications made to the Crowbar switch trigger-board circuit in an effort to improve the reliability of getting all four Crowbar rail-gap switches to conduct during each shot. We evaluated the effects of the final change this quarter as the FRC formation, translation, and capture tests were beginning. With some exceptions, the plasma shots tended to have all four Crowbar rail gaps conducting. However, vacuum shots, again with some exceptions, still tended to show three- and four-rail-gap current conduction in similar percentages as during previous tests.

As discussed in several earlier reports, such a variation in performance was somewhat problematic because of the need to have plasma- and vacuum-shot pairs to process the magnetic probe data and thereby calculate an excluded flux radius for the plasma. Rather than attempt to

make still further modifications to the Crowbar trigger-board circuit, it was decided this time to re-examine the time delay between the triggering of the Main bank and its Crowbar switch.

Five low-voltage tests with only the Main bank or with the Main bank with the PI and Bias banks were performed on 4 November. For these tests the Main bank-charge voltage was  $\pm 20$  kV, the PI bank-charge voltage was -33 kV, and the Bias bank-charge voltage was +2.8 kV. The Crowbar switch was not triggered in any these tests. Table 16 lists the approximate quarter-cycle time for the Main bank current as measured with either of the theta coil Rogowski current monitors or with the Main bank Rogowski coil.

Table 6. Main Bank Current Quarter-cycle Times vs. PI-to-Main Bank Trigger Delay and Load Conditions

Plasma or Vacuum	PI-to-Main Bank Delay ( $\mu$ s)	Current Maxima Measured With		
		Theta Coil Rogowski #2 ( $\mu$ s)	Theta Coil Rogowski #3 ( $\mu$ s)	Main Bank Rogowski ( $\mu$ s)
Vacuum	----	3.15	3.10	3.40
Vacuum	3.3	2.95	2.99	3.95
Plasma	3.3	2.96	3.09	3.82
Vacuum	4.4	3.39	3.26	3.48
Plasma	4.4	3.23	3.23	3.36

Table 16 also lists whether there was a plasma or vacuum load in the bore of the theta coil and what was the delay between the PI and Main bank-trigger times, if the PI bank was triggered.

Several interesting observations can be made. First, the two theta coil Rogowski coils show very similar quarter-cycle times, while the Main bank Rogowski coil, located at the cable header on the Main bank, shows a quarter-cycle time that is typically longer than the times measured with either of the theta coil Rogowski coils. Next, the quarter-cycle times change depending upon whether the PI bank is triggered or not and what the time delay is placed between the PI and Main bank triggers. However, little change is observed between plasma and vacuum-load shots.

When beginning the FRC formation, translation, and capture tests this quarter, the Main bank-to-Crowbar trigger delay being used was 3.06  $\mu$ s. This value had been established in June when the first tests were being performed with the Main bank in its new location and it was discovered that the bank quarter-cycle time had changed after moving it under the Shiva bank's B-arm. The

quarter-cycle times shown in the first row of Table 16 for the theta Rogowski coils continue to support this choice of Main bank-to-Crowbar switch trigger delay. However, the Main bank Rogowski measurement would suggest that the previous delay of 3.3  $\mu\text{s}$  should be used instead. When the PI bank is included in the tests—and the Main bank is triggered 4.4  $\mu\text{s}$  after the PI bank is triggered—the Main bank Rogowski data continues to suggest that a Main-to-Crowbar trigger delay of 3.3 ~ 3.4  $\mu\text{s}$  should be used. The theta Rogowski coil measurements indicate that a delay closer to 3.2  $\mu\text{s}$  should be used in this case.

After the data shown in Table 16 was compiled and examined, it was then decided to perform some additional tests and include the Crowbar switch again. Based upon the measurements obtained with the Main bank Rogowski coil (because this coil is measuring the current where the Crowbar switch is actually located) delays of 3.4  $\mu\text{s}$  and 3.3  $\mu\text{s}$  were used with vacuum and plasma tests, respectively. In both tests all four Crowbar rail gaps conducted. Tests then proceeded with bank voltages being raised and with the same Main-to-Crowbar trigger delay of 3.3  $\mu\text{s}$  being used for both plasma and vacuum tests. In all cases all four Crowbar rail gaps were now conducting. Two days later a delay of 3.2  $\mu\text{s}$  was used for the first plasma test (as might be suggested by the theta Rogowski coil measurements in the last two rows of Table 16). Only three out of the four Crowbar rail gaps conducted. Since then, the 3.3  $\mu\text{s}$  delay has been kept and in all tests all four of the Crowbar rail gaps have conducted reliably.

### 3.1.3.3 FRCHX-3

#### 3.1.3.3.1 *Operation of FRCHX Systems with Shiva Star Systems*

During the fall 2009 test series, in preparation for the fully integrated plasma compression shot, personnel began performing FRC formation, translation, and capture tests with the Shiva Star trigger system also being operated. Trigger delays were set such that the Shiva triggers occurred approximately 5.6  $\mu\text{s}$  and 10  $\mu\text{s}$  before the PI and Main bank triggers, respectively. A timing fiducial generated in the Shiva Star screen room was recorded along with the other FRCHX data channels to confirm this timing. The performance of these tests was useful in that they revealed immediately a pre-triggering problem in the PI bank-trigger system that was induced by the Shiva Star triggers.

A few weeks prior to performing these tests the configuration of the PI trigger system had been modified to match that of the Main bank and Crowbar trigger systems in anticipation of needing to make some modifications to shield the PI 40168 better from noise. Specifically, the high-voltage-output cable of the PI 40168 and the control and interlock cable between the 40168 and the MTG were each wrapped several times around a stack of ferrite cores (Figure 146).

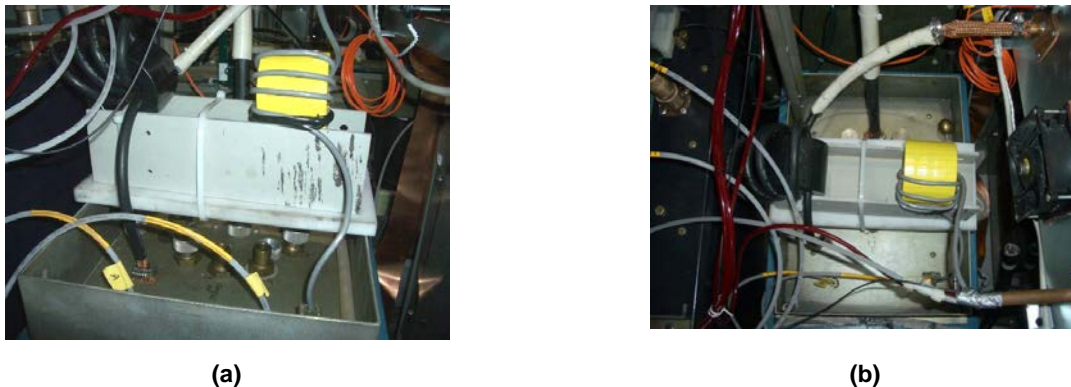
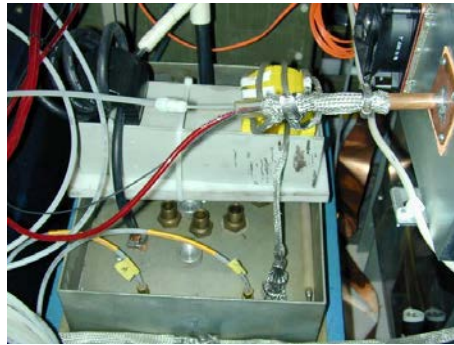


Figure 146. Cables between PI 40168 and MTG were wrapped around ferrite cores

Furthermore, all additional grounding connections beyond that provided by the 40168 high-voltage-output cable were removed, and the bundle of three ground cables tying the PI trigger system to the PI bank frame were connected to the MTG rather than to the 40168 Hoffman enclosure. Unfortunately, these changes proved to be insufficient for shielding the PI trigger system from noise induced by the Shiva Star triggers, so further changes were made.

First, the control and interlock cable between the 40168 and the MTG was run through a metallic ground braid to shield the wires better inside the cable bundle. In the process of carrying out this task, it was also discovered that the solder joint on the cutoff-waveguide feedthrough, by which this cable and several other lines exited the PI enclosure, was broken. The feedthrough was therefore removed from the enclosure, resoldered, and then mounted on the box again. A Variac being used to adjust the AC line voltage going into the 40168 Hoffman enclosure was moved inside the enclosure to shield it better and thereby reduce the likelihood of noise entering the enclosure through the AC lines. Figure 147 shows these changes.



(a)



(b)

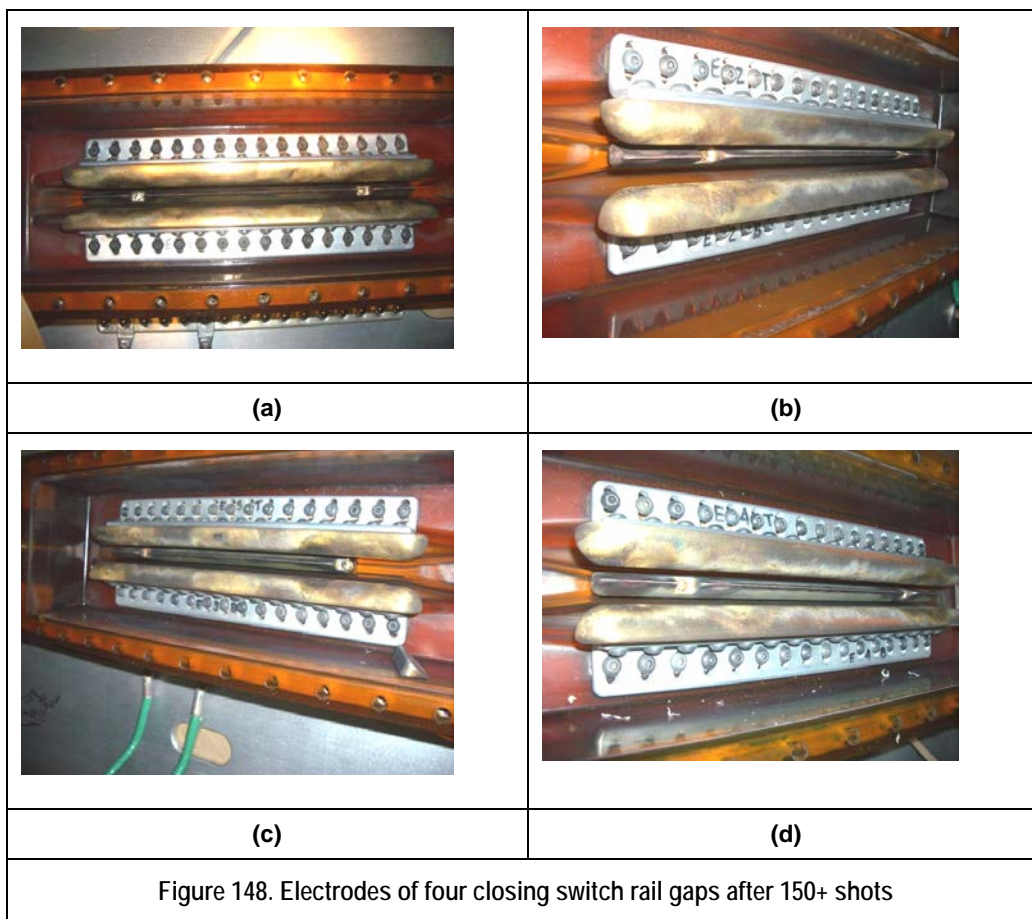
Figure 147. (a) Braid placed around 40168-MTG control cable; (b) Variac moved inside 40168 enclosure. Tests performed after these changes were implemented showed that the PI pre-triggering problem had been eliminated.

Additional plans called for conducting several charge-and-dump tests with the Shiva bank in tandem with FRCHX charge-and-dump tests, followed by a test in which all banks were fired together. The former tests would allow the appropriate time for starting the Shiva bank charge to be determined relative to starting the charging sequence for the FRCHX banks, as well as allow confirmation of the Shiva charge set-points calculated earlier. The purpose of the latter test, in which the Shiva bank would be fired into the resistive test load, would be to reveal any adverse effects that the Shiva bank discharge might have on the FRCHX pulsed power systems (particularly trigger systems) and diagnostics.

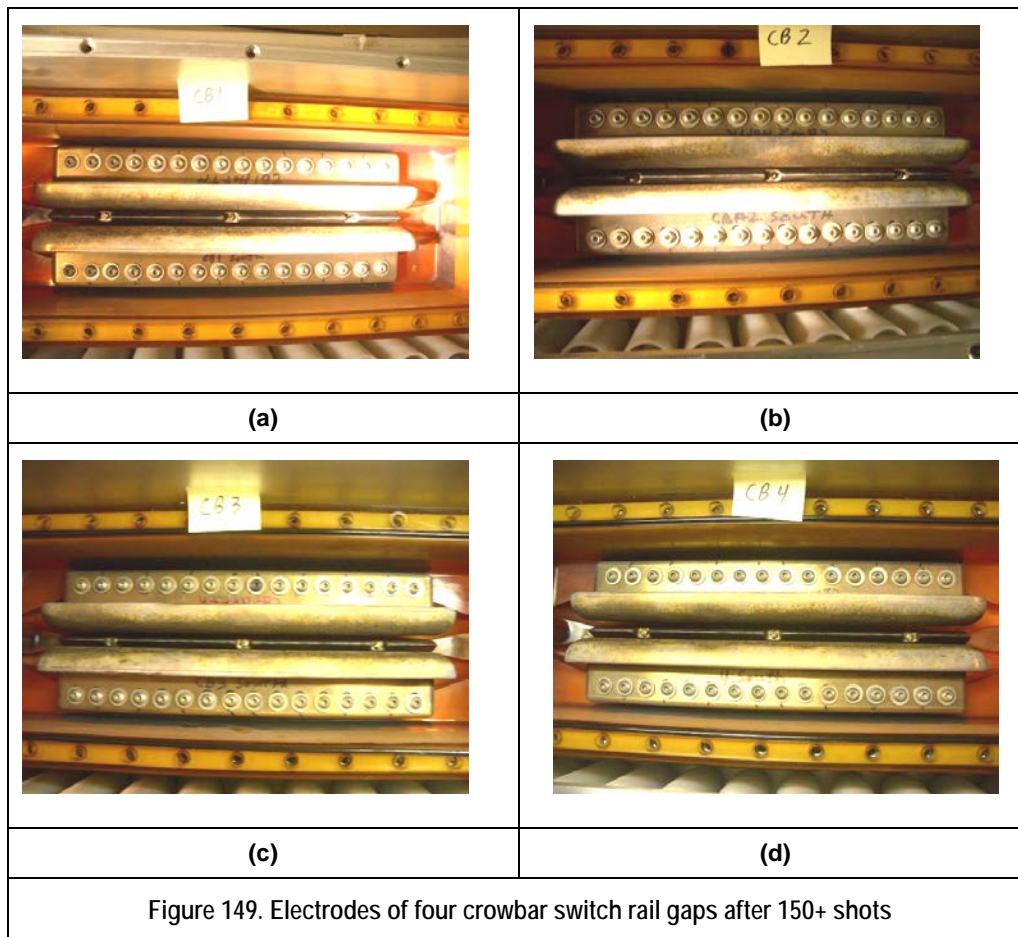
During final testing prior to the actual compression shot, the FRCHX pulsed power systems were found to operate quite reliably. As an example, the Bias bank, which had been the most problematic previously, only experienced one problem with its trigger isolation transformer at the beginning of the test campaign, which went from 13 January until 16 March 2010. After returning again to using the original transformer, which has fewer windings but more robust insulation on the windings, no further problems were encountered. There were no problems with the Lower Cusp bank, and as with the latter tests last fall, the Upper Cusp bank continued to be unused. Increased reliability with these banks' ignitrons can likely be attributed to a water chiller system brought on line at the beginning of the quarter to run chilled water through their outer

jackets. Separate chilling and circulating systems were borrowed from other projects on base, and these were set up near the Upper and Lower Cusp banks. Personnel then ran 0.375-in. polyethylene tubing between these units and the Bias, Guide/Mirror, and Upper and Lower Cusp bank ignitrons (connecting them all in series) to allow the chilled water to be circulated through the ignitrons.

There continued to be sporadic pre-fires of the Main bank throughout the period of testing. However, the bank was operated a record number of times—150+ shots without any cleaning being performed on either the closing or crowbar rail-gap switches. We show the rail-gap switch electrodes, with the covers were removed from the switches when they were finally being cleaned (Figure 148c, d; Figure 149). They showed no abnormal wear on any of their surfaces, though it was surprising to find that at some point during the test campaign the west end of the trigger electrode in rail-gap #3 of the closing switch had broken off (Figure 148c).





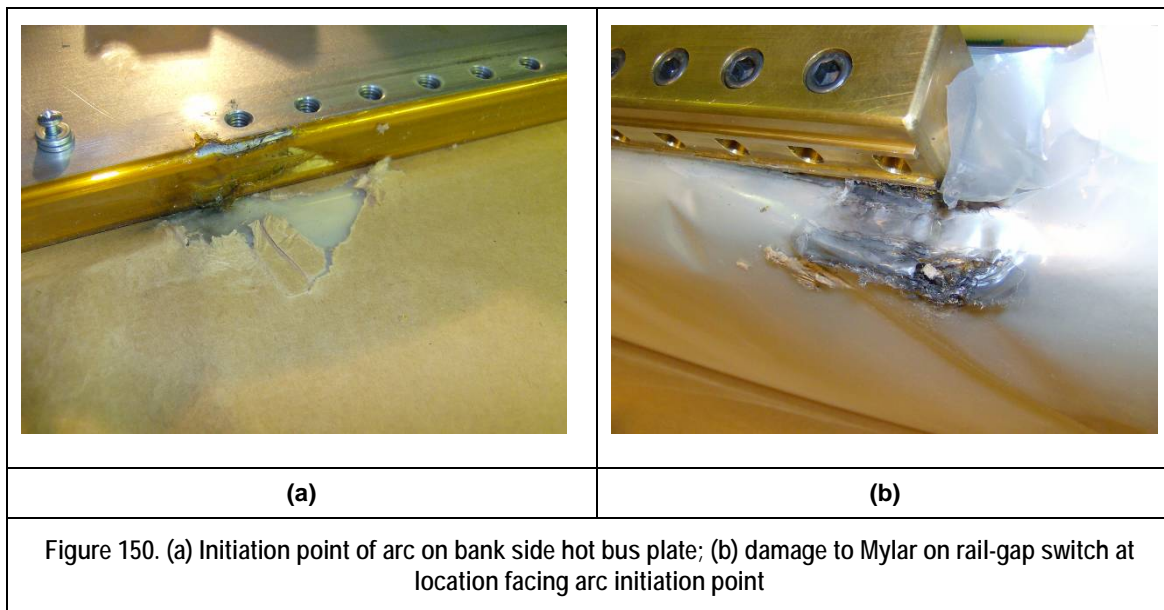


The point at where the break occurred was at the hole for the mounting screw, a weaker location structurally, and therefore the break may have been caused by age and/or over-tightening.

Only the PI bank and the Guide/Mirror bank and coils proved to be somewhat problematic. We detail the problems encountered with these systems and the various means employed to correct them in the rest of this section. For simplicity the problems are grouped according to the bank that they affected.

On 19 January 2010, an arc underneath the PI rail-gap switch, very much like the one that had halted tests the previous November, occurred during tests in which the PI bank voltage had been raised to 57 kV. Like that previous arc fault, the arc in this case originated from the hot bus plate, punching through the Kapton tape on the edge of this plate. It then burned through the layers of Mylar sheets attached to the bank side of the rail-gap switch, and propagated underneath the

switch over to the hot bus plate on the load side of the switch. Figure 150 shows the damage spot on the hot bus plate and the burned Mylar sheets on the rail-gap switch.



To reduce the likelihood of an arc occurring again in the future, a couple of changes were made as the bank was being put back together. First, the corners on the edge of the hot bus plate adjacent to the rail-gap switch were rounded further. Second, rather than using Kapton tape on that edge to attempt to suppress arc formation, which could trap pockets of air behind it and so still allow arcs to form, several coats of a high-voltage insulating paint were applied to that end of the plate (Figure 151).



Figure 151. Painted end of PI hot bus plate, where rail-gap switch is mounted



Lastly, to eliminate the air gap underneath the rail-gap switch in which an arc could propagate, SAIC's Jerry Parker suggested placing in this gap several lengths of Tygon<sup>®</sup> tubing that had a diameter slightly bigger than the height of the gap. When the switch is put into place, it then presses down on the Tygon tubing effectively turning the tubing into an arc barrier along the entire width of the switch. Figure 152 shows the placement of three such lengths of tubing. The red parachute cord was run through the tubes simply to straighten them out and to help them maintain their spacing with respect to each other.

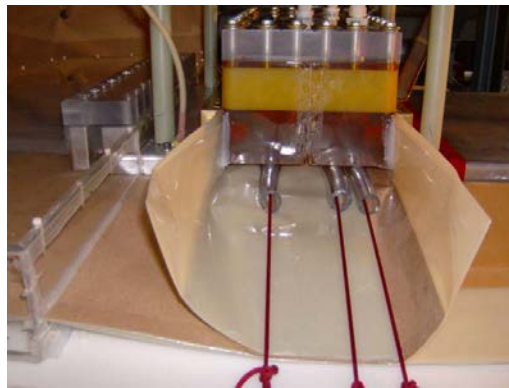
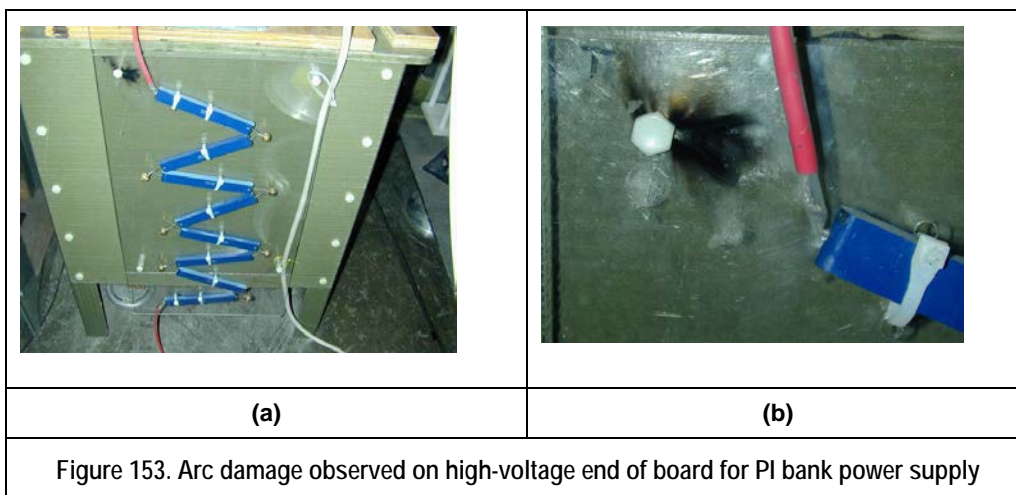


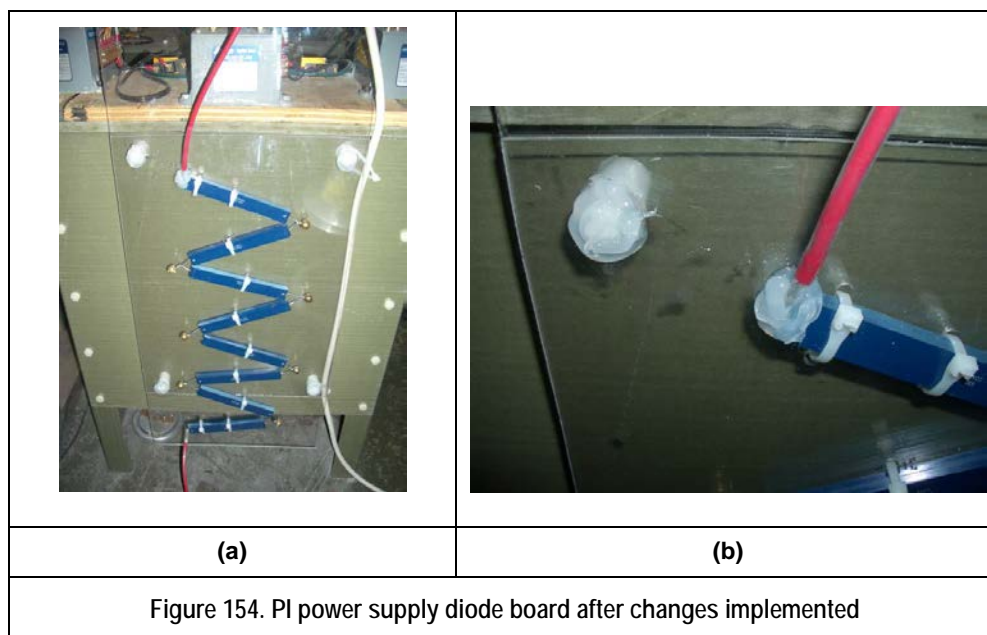
Figure 152. Tygon tubing placed underneath rail-gap switch to form arc barrier between bank and load sides of switch. Since the bank was rebuilt and these changes were implemented, the bank has been charged to as high as 70 kV and operated successfully without any further arcs underneath the rail-gap switch. At these higher voltages, however, there have now been some instances in which arcs have developed in the cable header.

When first raising the PI bank charge voltage to 70 kV, the bank began exhibiting signs of pre-firing after successfully charging to 68 kV. Increasing the switch pressure did not seem to help, and soon the bank would not charge to voltages that it had been able to charge to previously. Testing was halted, and it was then that arc damage was discovered on the power supply diode protection board (Figure 153).

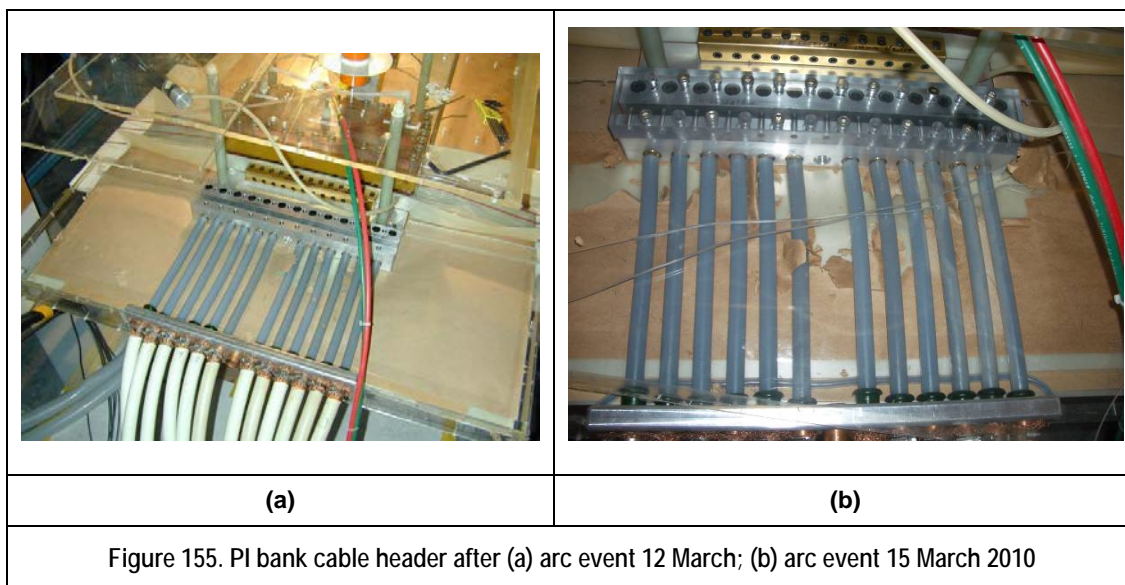


The apparent arc path was from the high-voltage end of the diode string to a bolt hole with an aluminum spacer on the back side of the Lexan mounting plate and from there to a bolt hole used to mount one of the Jennings switches.

To correct this problem, the Lexan mounting plate was cleaned, the aluminum spacer was replaced with a nylon spacer, nylon bolts were used to mount the closest side of the Jennings switch to the dump resistor stand, and RTV was placed around all the bolt holes and on the end of the last diode. Figure 154 shows the diode board after these changes were implemented; it was then possible to charge the bank to 70 kV.



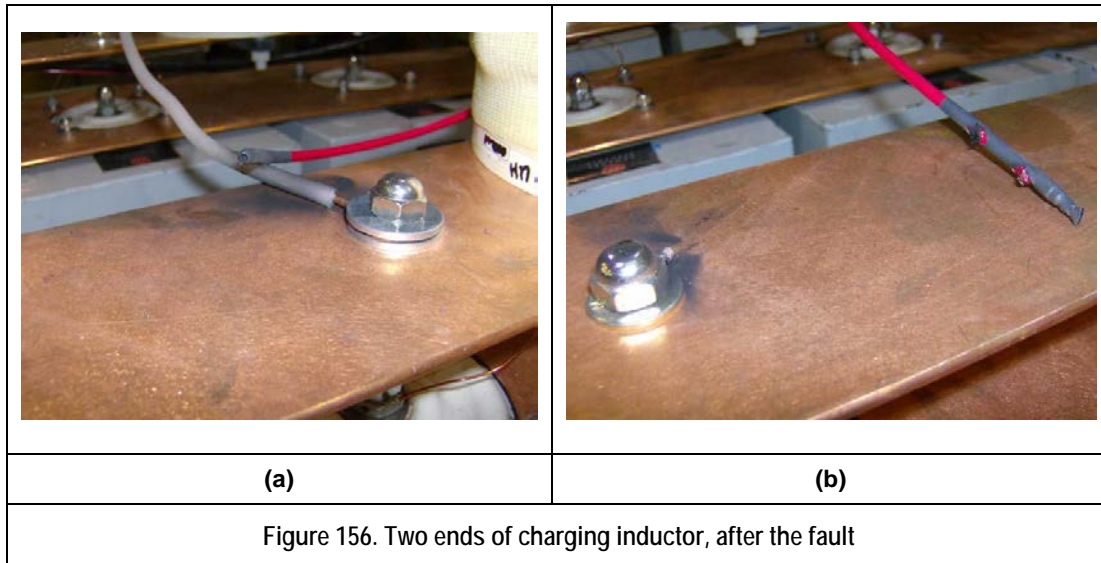
Once operation of the PI bank at 70 kV began, there soon began to be problems with arcing in the cable header (Figure 155).



After the first arc event on 12 March (Figure 155a), a clean 5-mil sheet of Mylar was placed under the cables; the torn paper on top of the Mylar in the header was replaced; the PI bank Rogowski coil, which had been removed for repairs, was replaced so it might also serve as a partial arc barrier; and procedures to begin flowing  $\text{SF}_6$  into the header during the time that the FRCHX banks were charging were implemented. Unfortunately, after all these changes were implemented, a second arc event occurred right away on 15 March (Figure 155b). This arc event also shattered the acrylic box that had been built up around the cable header to allow it to be backfilled with  $\text{SF}_6$ .

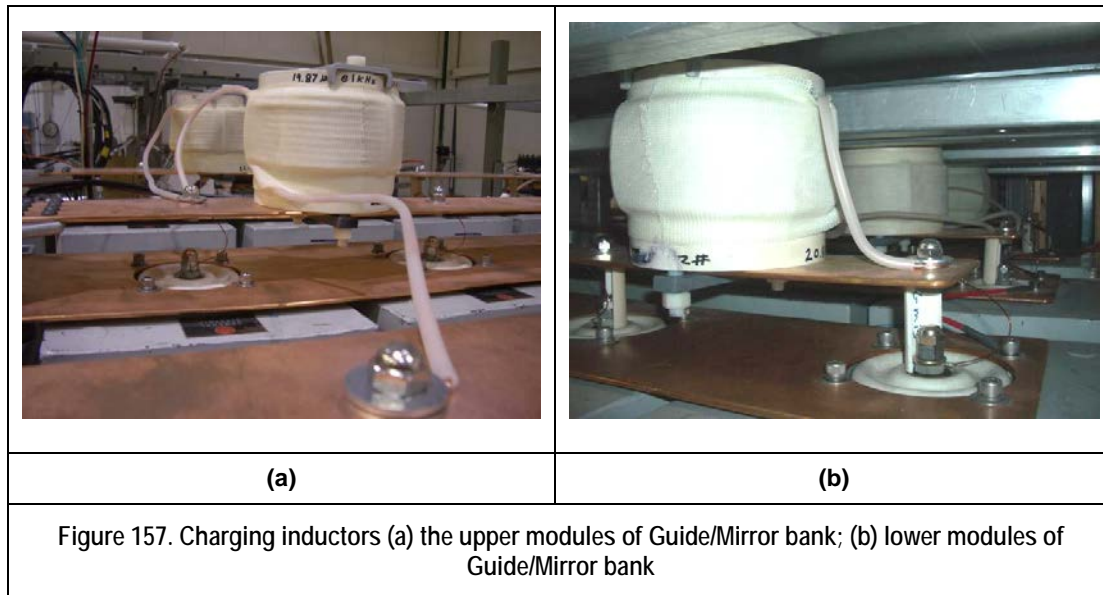
As an intermediate fix for the problem of the shattered Acrylic box, a plastic bag was taped over the header. The  $\text{SF}_6$  gas line instead of feeding gas at one end into the header volume was run underneath the cables in the header, capped off at the end, and punctured with the corner of a razor blade all along its length where it was underneath the cables. This arrangement allows the  $\text{SF}_6$  to be injected directly into the region where the arcs originate. PI bank voltages were also limited to 65 kV for near-term tests.

During the final test of the day on 22 January 2010, the charging inductor connecting Guide/Mirror bank modules 1 and 2 was damaged, apparently by excessive current flow (Figure 156).



Using a thicker gauge wire—0.125-in. diameter copper wire with a 0.375-in. diameter polyethylene dielectric around it—to wind the charging inductors was the most expedient solution to this problem, and appeared to work quite well. As a result, the module 1-2 charging inductor was rewound using the same wire used in the Oct-Dec quarter to fabricate the module 2-3, 5-6, and 3-6 charging inductors. It left only the inductor between modules 4 and 5 as the only surviving inductor that was wound with the original smaller-gauge wire. Though no obvious damage was found, it was decided to rewind this inductor to stave off any potential problems with it in the future. Figure 157 shows the two new charging inductors in place on the bank along with the others that had been rewound last quarter.





During the course of testing on 5 February 2010 the two leads of Guide coil #2 developed a short between them. This short was discovered as operators observed (on a video monitor) sparks being emitted from this location during the last test performed that day. Figure 158 shows the damage after testing was halted.

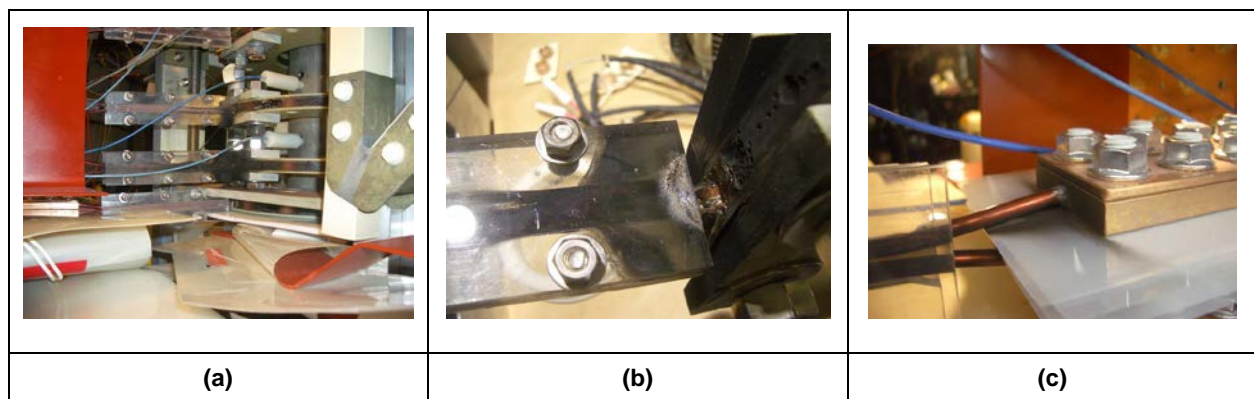


Figure 158. Arc damage produced when leads of Guide coil #2 developed a short

This event was the first failure of this type, and could have been precipitated by the flexing of the wires at this point each time the coils were pulsed. Fortunately, personnel were able to pull off the coils individually that were above Guide coil #2 from the Guide and Mirror coil assembly, without having to move the entire vacuum stand to an open area. (Moving the entire vacuum stand would have taken a considerable amount of time, because all the transmission-line cables, diagnostic cables, control lines, and gas lines would have needed to be disconnected and then

reconnected again afterward.) As it was, the task of replacing the damaged coil took approximately 4 days, although some of this time was spent fabricating the replacement. Likely because of their proximity to the arc spot on Guide coil #2, the Guide coil #3 current leads were blackened a little, as well, where they entered the potted windings of the coil. To make sure that it also had not been damaged, Guide coil #3 was also replaced at this time, as well.

To reduce the likelihood of a similar fault from occurring again, a layer of heat-shrink tubing will be placed around the copper wire leads of the coils when they are being fabricated. The shrink tubing extends several inches into the potted windings of the coils, and it should serve to provide some additional insulation between these two wires, which have across them the full voltage drop of the coil.

*Operation of the FRCHX Systems during the Shiva Star Dummy Load Test.* After several weeks of FRC formation, translation, and capture tests, plans were made to perform a small number of these tests while also operating the Shiva Star bank. The first such tests were to be charge-and-dump tests with the Shiva bank and all the FRCHX banks to practice charging all the banks simultaneously, followed by a test in which all the banks were fired together, the FRCHX banks forming and translating an FRC and the Shiva bank discharging into the Franklin resistor load (Figure 159).



Figure 159. Shiva Franklin resistor load, FRCHX vacuum stand in background

The former tests would allow the appropriate time for starting the Shiva Star bank charge to be determined relative to starting the charging sequence for the FRCHX banks, and the latter would uncover any adverse effects that the Shiva bank discharge might have on the FRCHX pulsed power systems (particularly trigger systems) and diagnostics.

Before performing either type of test, the Shiva Star triggers were incorporated first into the FRCHX tests. Though such tests were performed successfully earlier after making some changes to the PI bank 40168 enclosure, it was discovered that Shiva triggers were now causing the Main bank to trigger early. During the course of troubleshooting the problem, it was discovered that the Main bank pre-fire sensor cable was lying on part of the Shiva ground plane, and some of the Shiva trigger cables were coming into contact with some of the Shiva support structure, also in contact with the ground plane. After providing better isolation for both the pre-fire sensor cable and the trigger cables, the Main bank pre-fire problem went away.

Efforts then proceeded towards performing the charge-and-dump and charge-and-fire tests. Both were carried out on 2 March. For the charge-and-dump test the Shiva Star bank was charged to just under 85 kV, which is the target voltage for the compression-heating test, while the FRCHX systems were charged to the following voltages: Main bank—70 kV, PI bank—60 kV, Bias bank—5.2 kV, Lower Cusp bank—2.4 kV, and Guide/Mirror bank—4.6 kV. The Shiva charge was started 31 s into the FRCHX charge sequence to allow all banks to reach their target charge voltages at nearly the same time (at approximately 49 s into the FRCHX charge sequence).

For the charge-and-fire test, the Shiva Star target voltage was reduced to 60 kV, due to limitations imposed by the Franklin resistor load. The FRCHX charge voltages were kept the same. For all banks to reach their target charge voltage at nearly the same time again, the Shiva charge was started slightly later, at 36 s into the FRCHX charge sequence.

Both tests were successful in that personnel were able to bring the Shiva and FRCHX banks accurately to complete charge at approximately the same time, and during the charge-and-fire test the FRCHX systems operated reliably without any interference from Shiva triggers or the discharging of the bank. The Franklin resistor load also successfully received the Shiva discharge

energy and suffered no damage. It was, however, noticeably warm to the touch for many minutes after the test.

### 3.1.3.3.2 Overview of FRC Formation, Translation, and Capture Test Results

In this section, we review some of the data collected during the FRC formation, translation, and capture tests. The primary plasma diagnostics being employed during these tests included B-dot probes and flux loops, fiber-optic light probes, which monitor the visible light emission to give the axial location of the plasma, and laser interferometry, for a line-integrated measurement of the plasma density at the interferometer probe location.

A large portion of the winter 2010 diagnostic effort was directed toward implementing a second interferometer probe beam in the middle of the capture region both to verify capture and to obtain a measurement of the plasma density at this location. In addition, a new B-dot probe and flux loop pair were positioned near the peak of the upper mirror to enable determination of whether or not the magnetized plasma was escaping past the upper mirror. For the FRC formation, translation, and capture test setup, Table 17 shows a listing of all the diagnostics fielded around the FRCHX vacuum stand, along with their axial positions with respect to the top of the solid liner in the compression-heating experiment and their azimuthal positions with respect to the current feed for the theta coil.

Table 7. Positions of B-dot Probes, Flux Loops, Optical Fiber Probes, and Interferometer Probes

Location I.D.	B-dot Probes			Flux Loops	
	Distance from Top of Liner	Distance from Top of Liner	Azimuth	Distance from Top of Liner	Distance from Top of Liner
	(in.)	(cm)	(deg)	(in.)	(cm)
"T5"	1.37	3.49	180	0.97	2.45
"T4"	6.14	15.60	180	5.79	14.71
"T3"	9.43	23.95	180	9.09	23.09
"T2"	14.01	35.59	180	13.67	34.72
"T1"	17.88	45.42	180	17.66	44.86
"J"	26.17	66.47	90	25.87	65.71
"I"	27.70	70.36	90		



Location I.D.	B-dot Probes			Flux Loops	
	Distance from Top of Liner	Distance from Top of Liner	Azimuth	Distance from Top of Liner	Distance from Top of Liner
	(in.)	(cm)	(deg)	(in.)	(cm)
"H"	29.24	74.27	90		
"G"	30.77	78.16	90		
"F"	32.31	82.07	90		
"E"					
"D"	35.38	89.87	90		
"C"	36.91	93.75	90		

Location I.D.	Interferometer Probes			Optical Fiber Probes		
	Distance from Top of Liner	Distance from Top of Liner	Azimuth	Distance from Top of Liner	Distance from Top of Liner	Azimuth
	(in.)	(cm)	(deg)	(in.)	(cm)	(deg)
"T5"				0.27	0.68	180
"T4"	6.14	15.60	90-270	6.14	15.60	0
"T3"				9.43	23.95	0
"T2"				14.01	35.59	0
"T1"				17.88	45.42	0
"J"	26.93	68.40	90-270	26.17	66.47	45
"I"				27.70	70.36	45
"H"				29.24	74.27	45
"G"				30.77	78.16	45
"F"				32.31	82.07	45
"E"				33.84	85.95	45
"D"				35.38	89.87	45
"C"				36.91	93.75	45

Data collected during this test series from the original magnetic diagnostics continued to indicate that a magnetized plasma was in fact being translated from the formation region up and into the capture region. After the new upper B-dot probe (B-dot T5) was put into place, it was apparent

that the plasma was stretching past the upper mirror, but it was not completely moving past it. After a short excursion above the upper mirror, it was pulled back into the capture region. Furthermore, the probe's signal was observed to decrease as the Guide/Mirror bank charge voltage was slowly raised.

B-dots T3 and T4 in the capture region showed double-bumps, presumably due to the plasma bouncing between the mirrors on each end of the capture region, while only single bumps were seen on the lower B-dot probe signals at locations T1 and T2. Thus, the plasma did not appear to leave the capture region and return to the formation region. At a Guide/Mirror bank charge voltage of 4.7 kV, which was thought to correspond to a 2-T upper mirror field and that had previously been the target field for the upper mirror, the B-dot T-5 signal was observed to essentially go away completely, while only single bumps continued to be observed on the B-dot signals at T1 and T2 below the capture region. One might infer from these results that a "solid" capture was obtained with these parameters.

Getting the T4 interferometer probe beam on-line at that time to measure both the plasma density and lifetime in the capture region then became even more of a priority so that these results might be confirmed. The B-dot T4 signals from these tests were by themselves suggesting a lifetime of only approximately 5  $\mu$ s in the capture region; however, this lifetime was fairly consistent from shot to shot.

From this point forward the testing continued with the goal of varying the fields, bank timings, and pre-fill parameters in such a way as to raise the amplitude of the translation B-dot signals, which would imply an increase in the trapped flux in the FRC. The Bias field was slowly raised to provide more flux that could be trapped in the FRC. The PI field was raised, as well, to maintain the same percentage or greater of zero-crossing during its first half cycle, which appears to control the degree of the ionization of the pre-fill gas. Specifically, efforts were made to increase the PI zero-crossing from approximately 5–10% to 10–15% to see if more flux would then get trapped in the FRC. The time delay between the PI bank triggering and the Main bank triggering was also varied for this same purpose. PI-to-Main bank delays were varied

between tests from three-fourths of a PI period to two and three PI periods. The D<sub>2</sub> gas pre-fill pressure was also varied from 25 mTorr to 100 mTorr.

In summary, the shot parameters started out as follows in January 2010: Main  $V_{\text{charge}} - 70$  kV, PI  $V_{\text{charge}} - 57$  kV, PI-to-Main delay – one PI period (4.4  $\mu\text{s}$ ), Bias  $V_{\text{charge}} - 4.8$  kV, Lower Cusp  $V_{\text{charge}} - 2.0$  kV, Upper Cusp not energized, Guide/Mirror  $V_{\text{charge}} - 3.8$  kV, and D<sub>2</sub> pre-fill – 50 mTorr. As the parameter scans concluded in early March, the following parameters were deemed close to optimal: Main  $V_{\text{charge}} - 70$  kV, PI  $V_{\text{charge}} - 65$  kV, PI-to-Main delay – two PI periods (8.8  $\mu\text{s}$ ), Bias  $V_{\text{charge}} - 5.6$  kV, Lower Cusp  $V_{\text{charge}} - 2.4$  kV, Upper Cusp not energized, Guide/Mirror  $V_{\text{charge}} - 4.6$  kV, and D<sub>2</sub> pre-fill – 50 mTorr.

Figure 160 and Figure 161 show plots of the magnetic probe waveforms and the calculated excluded flux radii for two plasma and vacuum test pairs with the highest PI bank charge voltage, i.e., 70 kV, before problems began to occur in the PI bank cable header. Both plots are from 11 March 2010.

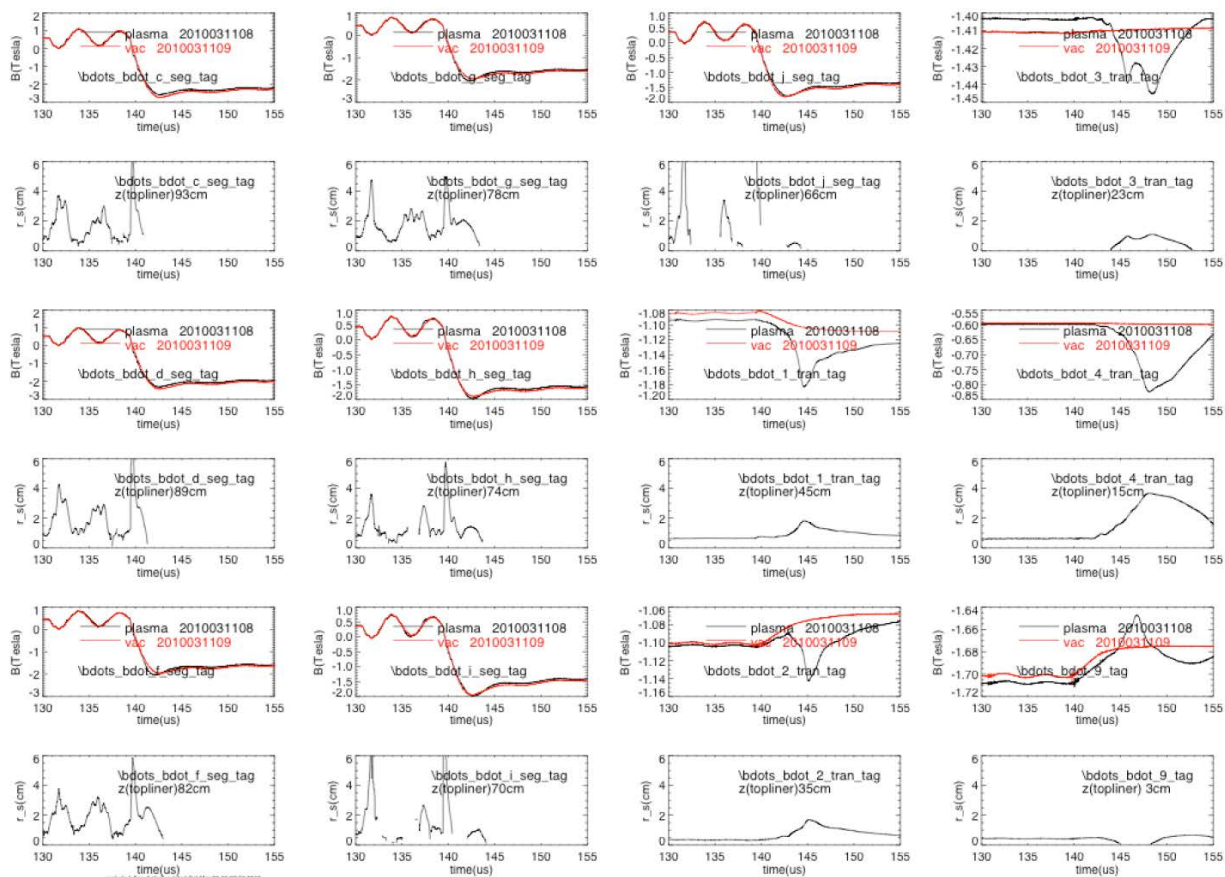


Figure 160. Magnetic diagnostic data and calculated excluded flux radii, Tests 8 and 9

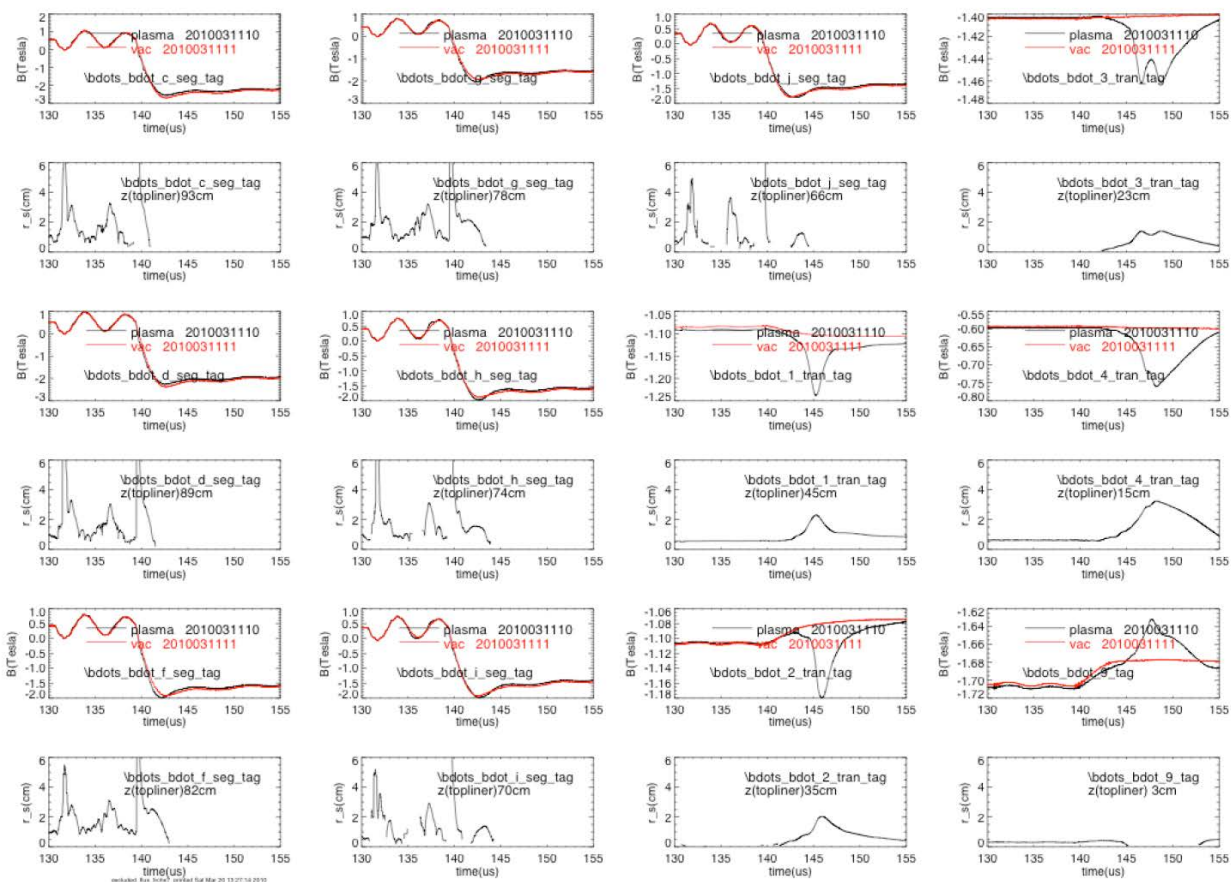
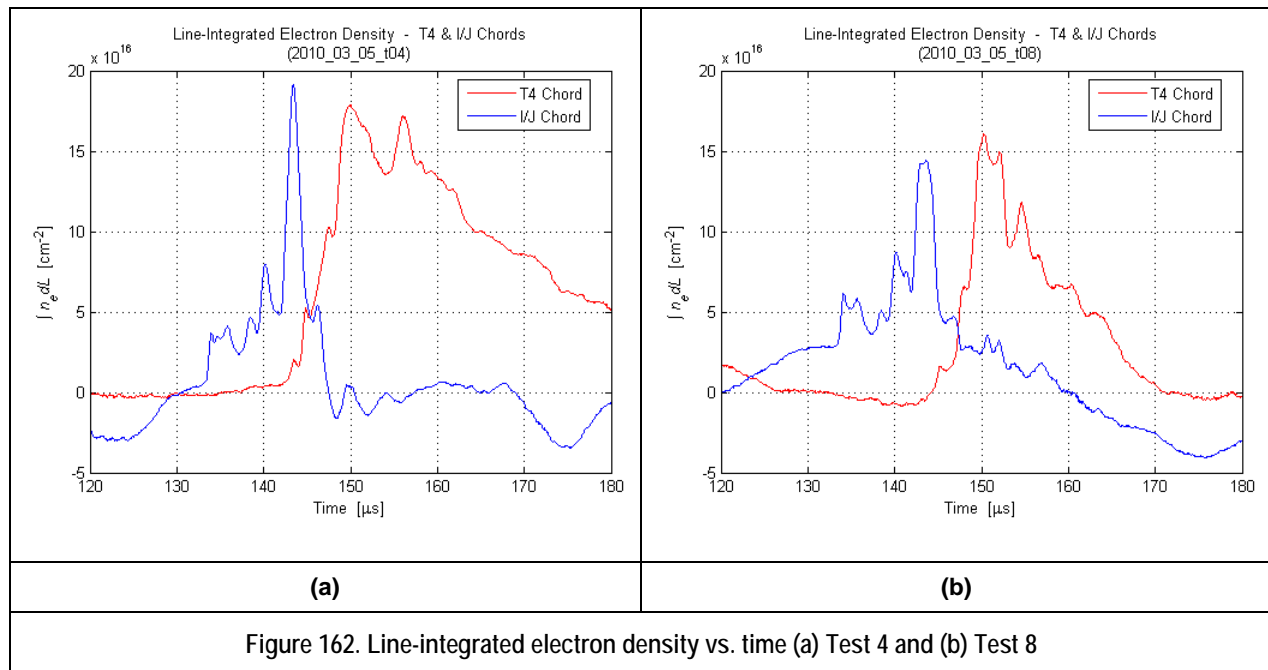


Figure 161. Magnetic diagnostic data and calculated excluded flux radii, Tests 10 and 11

The only difference between the two test pairs is the Bias bank charge voltage: 6.2 kV for Tests 8 and 9 and 6.0 kV for Tests 10 and 11. In some cases the excluded flux radii calculations are difficult to interpret; in others where the results are clearer, a radius of 1.5 to 3.5 cm seems to be the norm. These radii are, again, similar to those observed in the earlier tests with slightly lower PI and Bias voltages. The B-dot T4 signals also showed little change in width from earlier tests in the series, remaining at 5 to 10  $\mu$ s, depending upon where the measurement is made. However, amplitudes did not return to the levels observed during the earlier January tests, which were as high as 350 mT. As seen here, they are closer to 160 and 225 mT.

Figure 162 shows two plots of line integrated electron density measurements that were made during tests conducted earlier to those illustrated in Figure 160 and Figure 161 on 5 March.



As can be seen, plasma density lifetime in the capture region is observed to be significantly longer than the excluded flux lifetime, approximately 10-20  $\mu\text{s}$  FWHM. It would appear that a significant amount of non-FRC plasma travels up into the capture region, either in front of or behind the FRC that can account for the longer plasma lifetime.

The final tests for this experimental campaign were carried out on 15 and 16 March. The tests on these days were directed at finding the minimum Main bank voltage at which the plasma would enter the capture region. After finding this voltage, the Main bank and Guide/Mirror bank voltages were scaled upwards together in a series of tests. The baseline Guide/Mirror bank voltage was 4.6 kV, which was believed to correspond to a peak Lower Mirror field of approximately 1.56 T and a peak Upper Mirror field of approximately 1.96 T. The lowest Main bank voltage at which the plasma would enter the capture region with these fields appeared to be approximately 45 kV. During the compression heating test, the mirror fields were expected to be approximately 1.56 times higher, as the solid liner will have begun compressing the Mirror fields before the FRC arrives. Following through with such a scaling in these tests would have meant raising the Main bank voltage to 70.3 kV and the Guide/Mirror bank voltage to 7.2 kV. However, tests were halted at 53 kV and 5.4 kV because it was uncertain what the effect the increased field stresses would have upon the Guide and Mirror coils.

#### 3.1.3.3.3 *Shiva Star Plasma Compression Test Data*

The actual Shiva Star compression test took place on 16 April 2010. Some of the parameters, diagnostics, and data acquisition information for this shot include:

1. 85.0 kV / 84.9 kV target/actual capacitor bank charge voltage
2. 1.3 mF total bank capacitance
3. Two separate digitizing systems were in place for this experiment. One system, operated in the main Shiva Star screen room, controlled 11 Tektronix GPIB digitizing scopes. The other system contained 28 National Instruments PXI digitizing scopes. The PXI system was distributed among two RF-shielded enclosures in the Shiva high bay area and received its triggering from the main Shiva screen room. The GPIB system operated with 42 active data channels, and the PXI had 88 active data channels, for a total of 130 data channels.
4. Two radiography pulsers to take x-ray images of the liner. The imaging scheme employed had the heads at two different azimuthal locations. One head (RAD #1) was located at E arm, and the other (RAD #2) was located between C and D arms. Both heads imaged a field of view consisting of the liner region between Mirror Coils Nos. 1 and 2. The views were 90 degrees apart azimuthally.
5. Two PIN photodiodes to monitor the radiography imaging x-ray source production times.
6. Ten Rogowski coils to monitor discharge current (one per Shiva arm & four in the center section).
7. A single-turn Faraday fiber-optic probe to monitor the discharge current.
8. Three B-dot probes located near the load and 120 degrees apart at a radius of 9.36 cm.
9. Three voltage monitor probes to monitor the voltage on Shiva.
10. Four PMTs to monitor x-ray production from the imploding liner/FRC.

As is standard for Shiva Star capacitor bank shots, we had Rogowski coils at the end of each of the six transmission arms comprising the capacitor bank. After removing cable signal delays, the

average start time for these current signals is 1.231  $\mu\text{s}$ . This is the time that will be referenced when giving times with respect to the start of Shiva current. The individual arm Rogowski coil signals are shown in Figure 163, and their sum representative of the total current is shown in Figure 164.

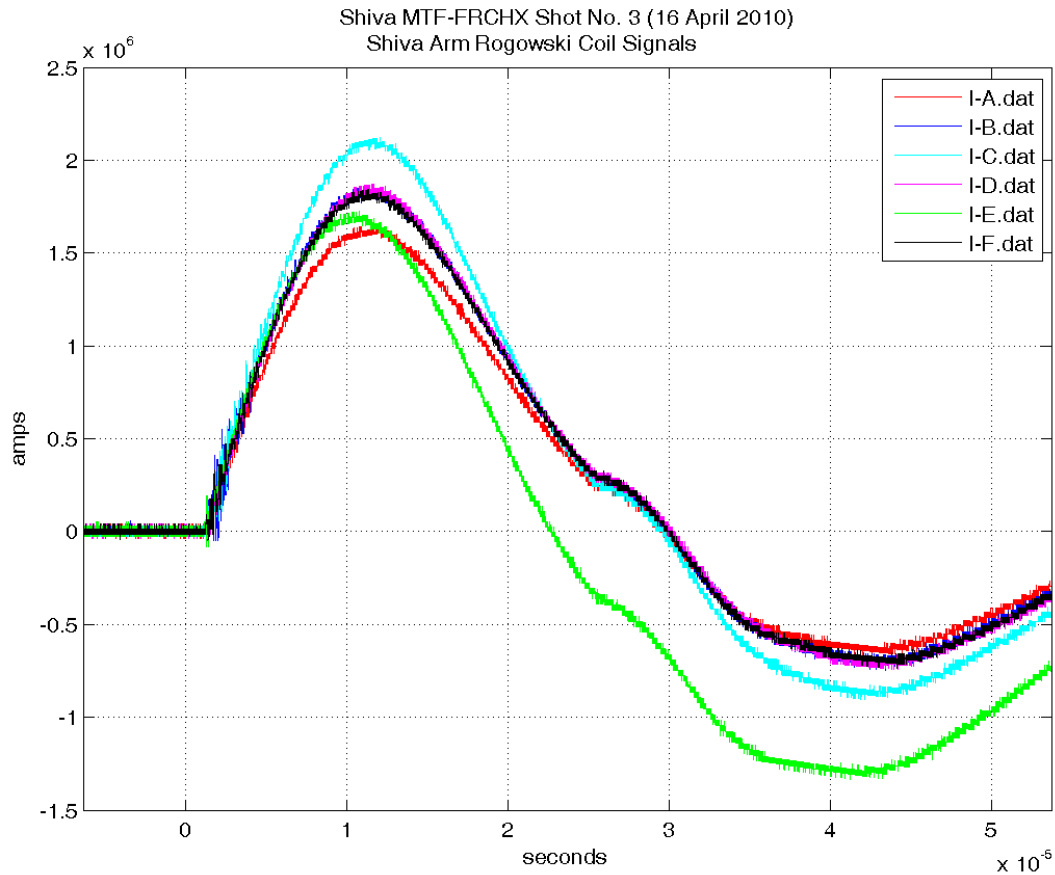


Figure 163. Shiva Star arm Rogowski coil signals for FRCHX-3



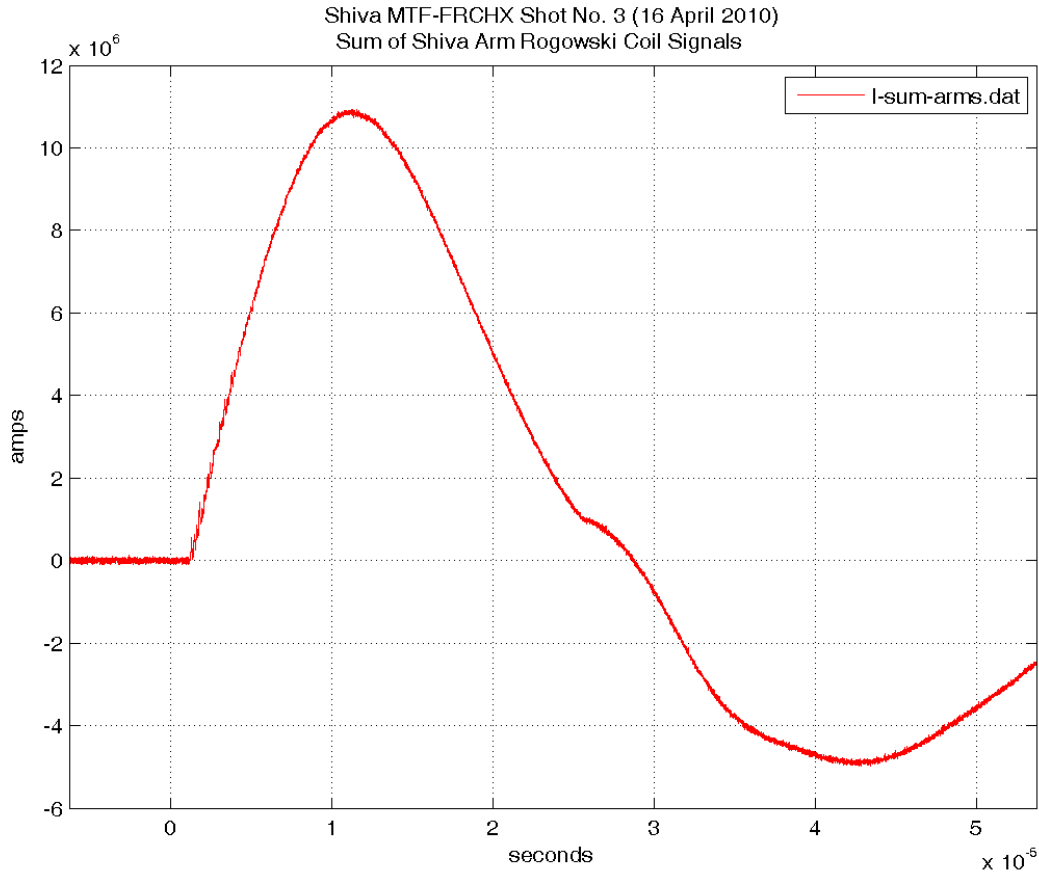


Figure 164. Shiva Star arm Rogowski coil signal sum for FRCHX-3

The peak value of the above signal is  $I_{\text{sum}} = 10.86 \text{ MA}$ , and it occurs at  $11.236 \mu\text{s}$  ( $10.005 \mu\text{s}$  after the start of Shiva current). The four (4) Rogowski coils located near the center section of the Shiva bank were divided into two groups with a pair of coils per group. Each pair of coils measures opposite halves of the discharge current, with each pair looped around the center in the same direction. Hence the prefix designation for the coil names is CW and CCW for clockwise and counter-clockwise, respectively. By summing the respective CW and CCW signals we get the total current delivered. By adding the summed CW and CCW signals together we should get zero current [i.e., the CW (CCW) signal is  $+ (-) \times \text{amps}$ ]. The value of current remaining after adding the summed CW and CCW data is the common-mode noise (CMN) current. This CMN current is divided in half and subtracted from the summed CW (CCW) data, and these results are referred to as the corrected CW (CCW) currents. The discharge current data are shown here in

Figure 165. The peak values of the above signals are  $I_{CW-1} = 5.46$  MA,  $I_{CW-2} = 5.46$  MA,  $|I_{CCW-3}| = 5.38$  MA,  $|I_{CCW-4}| = 5.50$  MA.

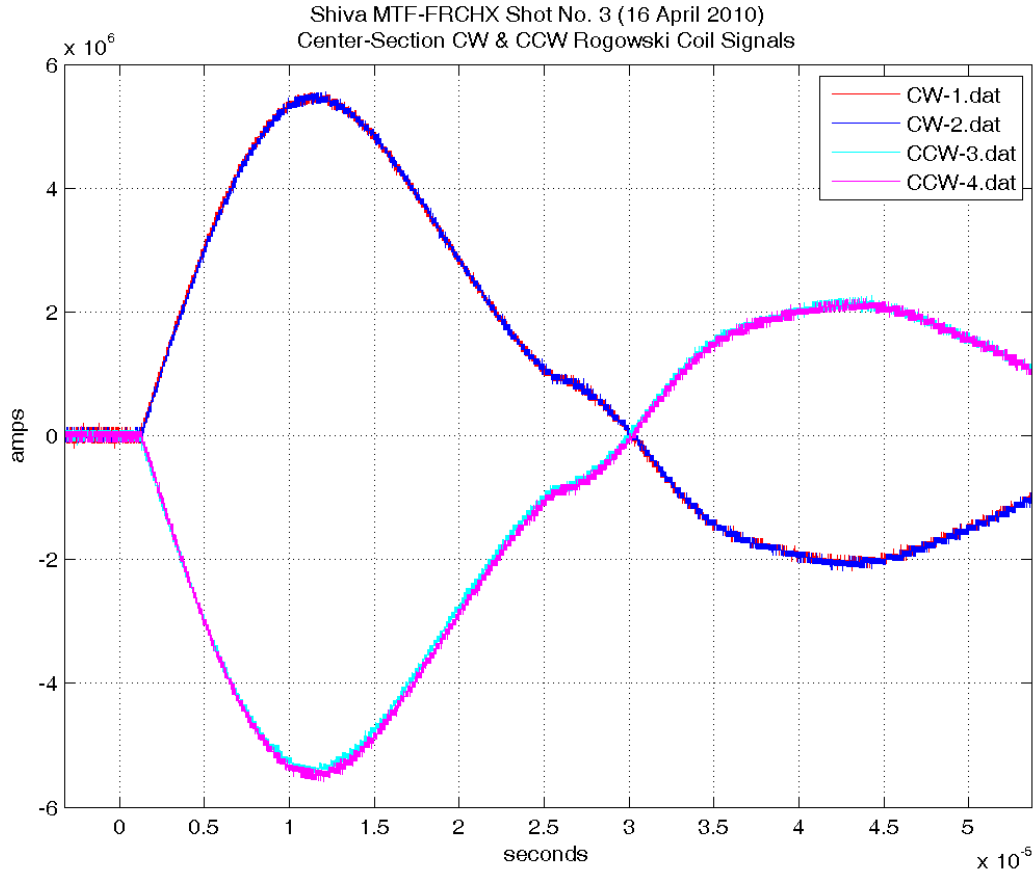


Figure 165. Shiva Star uncorrected center section Rogowski coil signals for FRCHX-3

Using the procedures outlined above, the common mode noise current and the two corrected CW/CCW discharge currents are calculated and shown below (Figure 166). The peak values of the above signals are  $I_{\text{corr-CW}} = -I_{\text{corr-CCW}} = 10.91$  MA and  $|I_{\text{CMN}}| < 50$  kA, with the peaks of the corrected CW/CCW Rogowski coil currents occurring at  $11.489 \mu\text{s}$  ( $10.258 \mu\text{s}$  after the start of Shiva current).

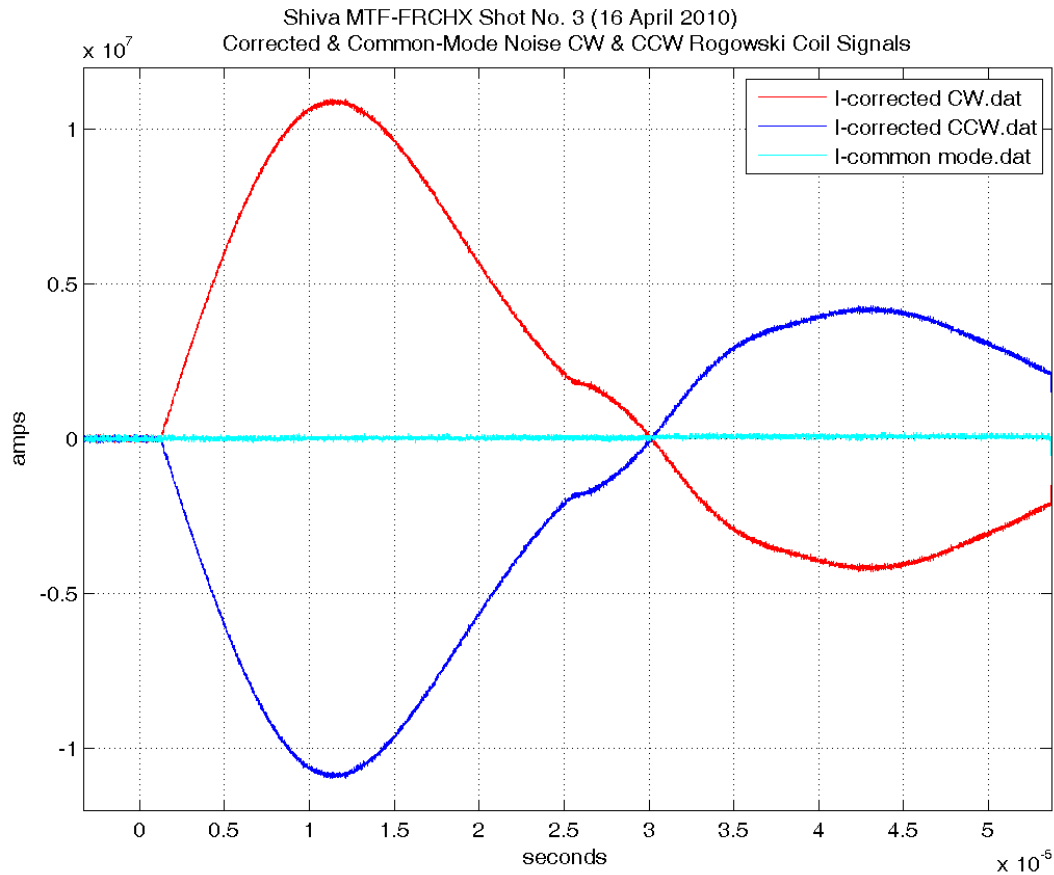


Figure 166. Shiva Star corrected center section Rogowski coil signals for FRCHX-3

There was a Faraday rotation fiber-optic probe installed for monitoring the Shiva discharge Current, as well as Rogowski coils. Physically, this probe was located very near the locations of the four CW/CCW Rogowski coils. The Faraday rotation probe is a single-turn design and has a sensitivity of 600 kA for a 90-degree phase change. The two Faraday rotation probe photodetector signals (designated 1A and 1B), which are a measure of the polarization angle of the laser light in the optical fiber used to sense the current, are plotted below (Figure 167), followed by a plot of the discharge current calculated from these two quantities (Figure 168). The peak current obtained with the Faraday rotation probe is 10.87 MA, and it occurs at 11.476  $\mu$ s (10.254  $\mu$ s after the start of Shiva current).

Shiva MTF-FRCHX Shot No. 3 (16 April 2010)  
Faraday Rotation Probe Signals

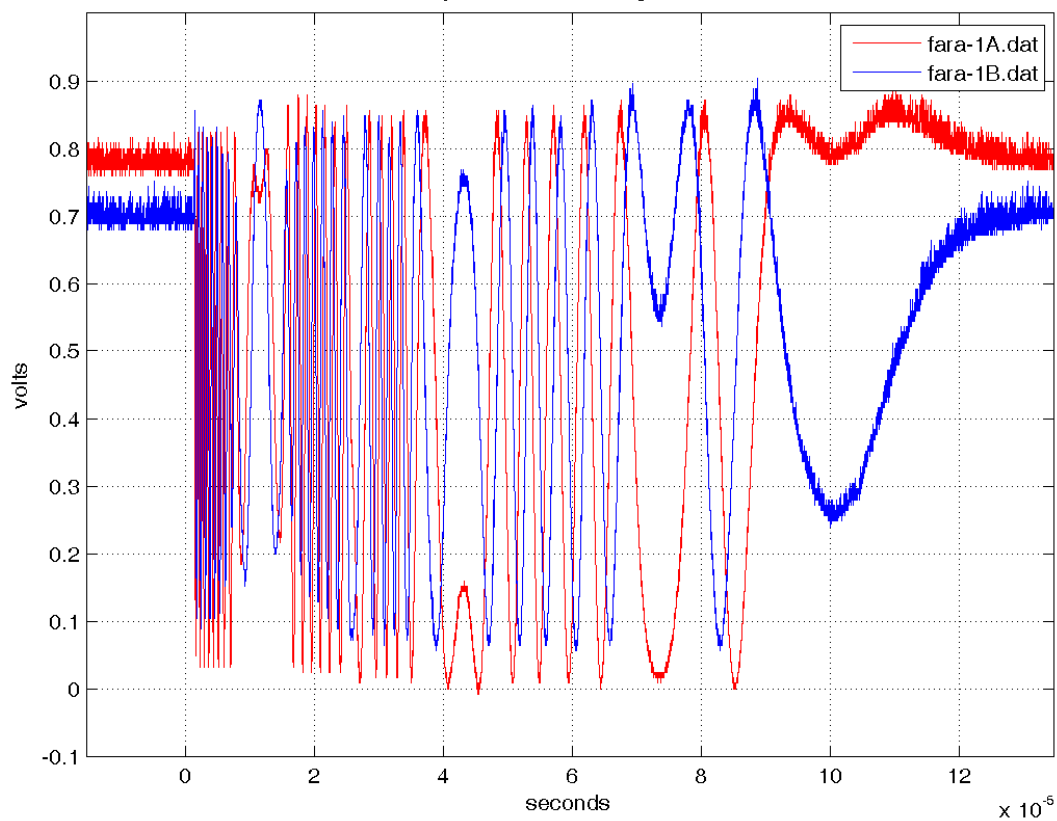


Figure 167. Raw Faraday rotation probe signals

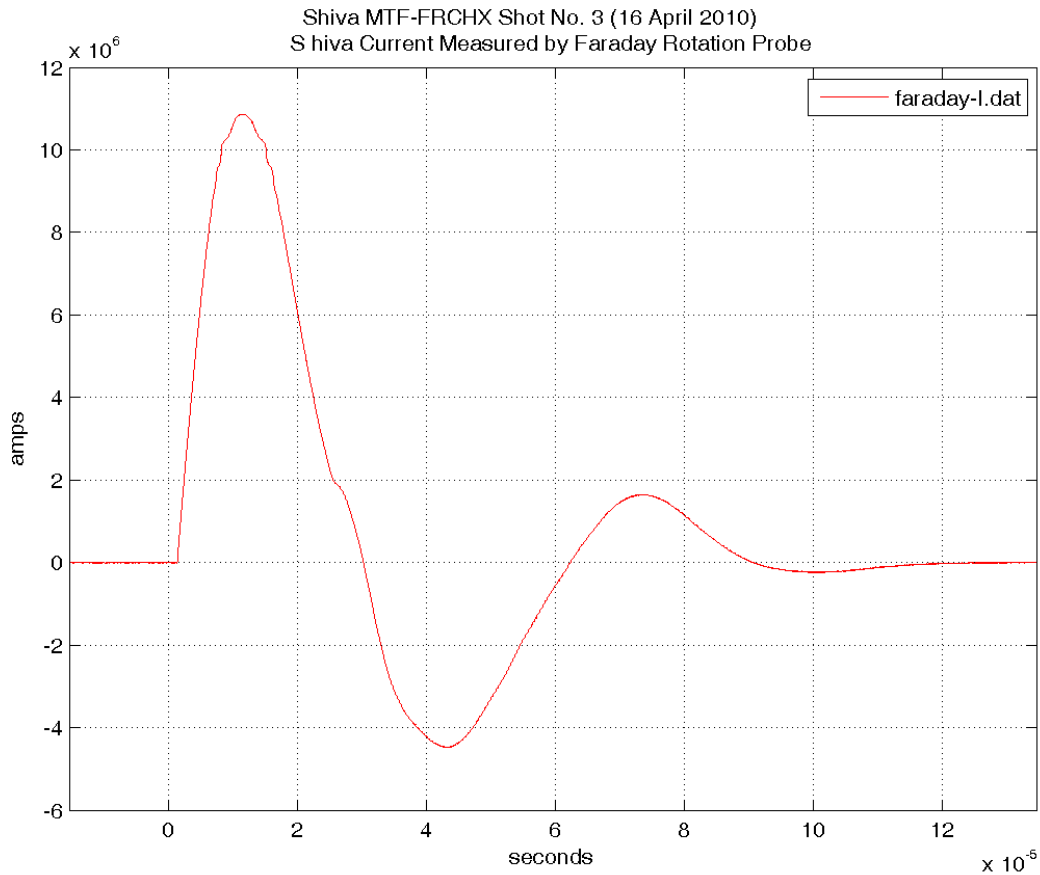


Figure 168. Interpreted current from the Faraday rotation signals

There were three B-dot probes in the vacuum region at a radius of 9.36 cm, placed 120 degrees apart, and located near the liner load in the lower center section. The three probes were azimuthally aligned such that first probe (B-dot no. 103) was centered along the middle of Shiva B arm, while B-dot probes nos. 104 and 106 were aligned with Shiva D and F arms, respectively. The discharge current as measured by these probes is shown below in Figure 169.

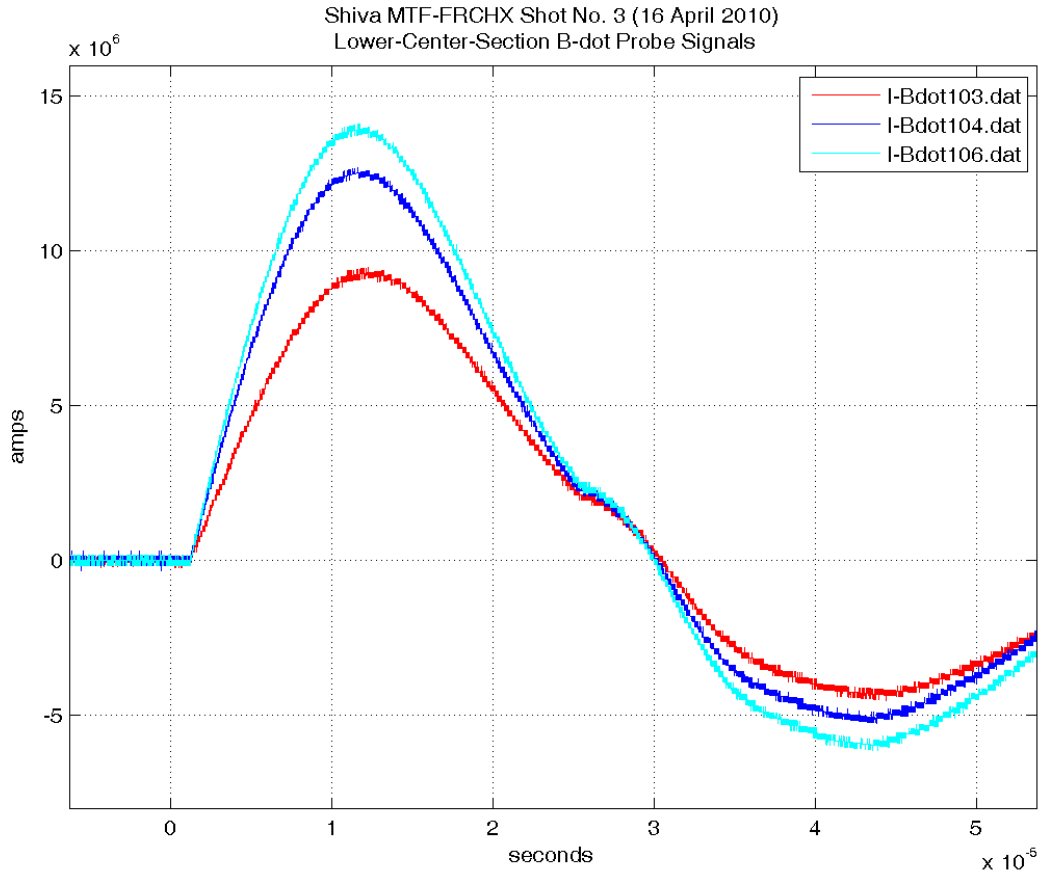


Figure 169. Current inferred from B-dot probes

Located on the lower portion of the Shiva transmission line hex plate are three (3) capacitive voltage probes. Physically, the probes are located at a radial position of 46 in and are labeled V1, V2, and V3. They are azimuthally positioned between Shiva arms A-B, C-D, and E-F, respectively. If zero degrees is defined to be along A arm, then V1, V2, and V3 are located at 30, 150, and 270 degrees, respectively. The overlay plot of the probe output signals is shown below in Figure 170.

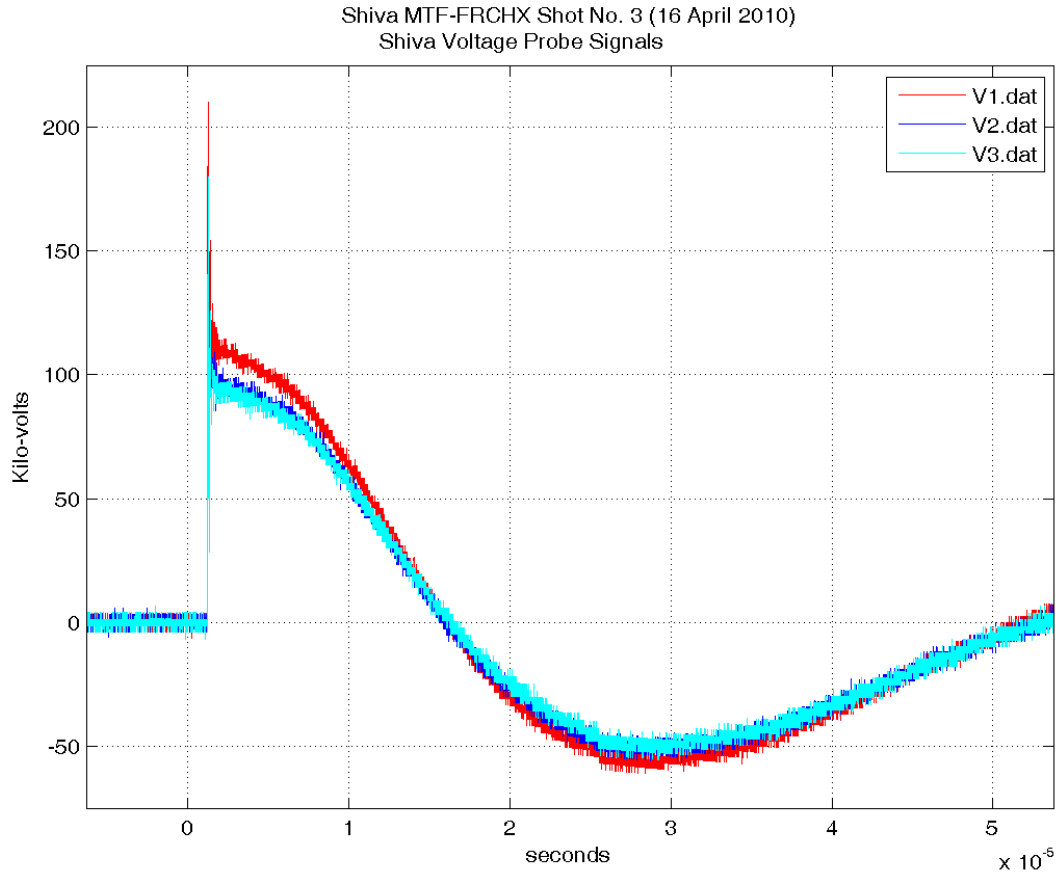


Figure 170. Shiva Star voltage probe signals

Two high-voltage anode-cathode heads were used to generate x-rays pulses designed to produce radiographic images of the imploding liner. Each Marx bank used to pulse the radiography heads was charged to 25 kV. The heads were at two different azimuthal locations. One head (RAD #1) was located along E arm, and the other (RAD #2) was located between C and D arms. Both heads imaged a field of view consisting of the liner region between Mirror Coils Nos. 1 and 2. The views were 90 degrees apart azimuthally.

Plots of the traces from the PIN photodiodes used to monitor x-ray production times are shown in the Figure 171. The desired times for the x-ray pulses were 21.8  $\mu\text{s}$  after the start of Shiva current for RAD #1 and 22.8  $\mu\text{s}$  after the start of Shiva current for RAD #2. Recalling that the start of Shiva Star current is at  $t = 1.231 \mu\text{s}$ , the times actually measured for signals shown were

21.711  $\mu\text{s}$  for RAD #1 ( $\Delta t = -89$  ns relative to desired time) and 22.985 for RAD #2 ( $\Delta t = +185$  ns relative to desired time).

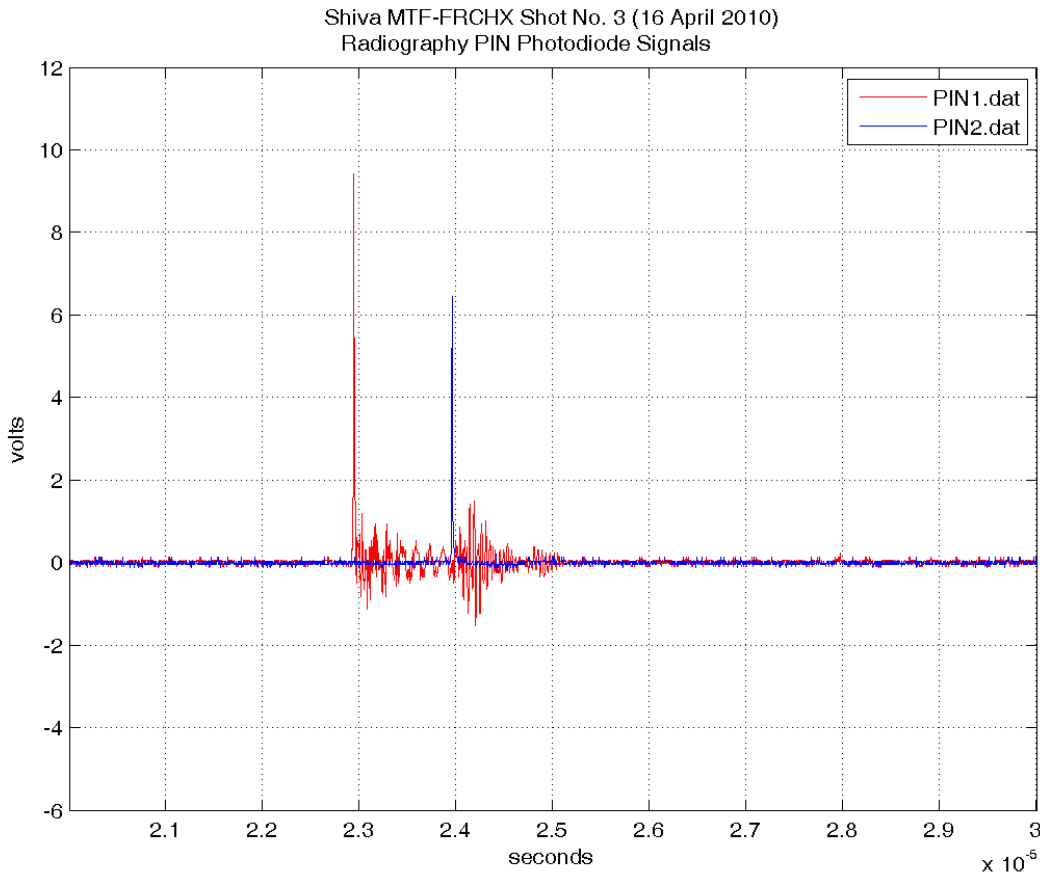


Figure 171. Radiography PIN Photodiode signals

For this experiment we used two 300 Kilovolt radiography (X-ray) imaging systems, operating at approximately 250 Kilovolts. To maximize imaging resolution we used our in-house-built x-ray tube heads with source spot sizes less than 1mm. Digital film was used for recording the all images. In each imaging film pack assembly we loaded two pieces of film with each film in its own separate “package”. The extra film was a “backup” in case of some unforeseen issue. Due to the guide mirror coils enclosing much of the liner, the only x-ray imaging region available was centered approximately 18.5 cm below the liner top plane. As such, both imaging systems were vertically position to view this region but were azimuthally separated to be perpendicular to each other. Also, because of guide mirror coil constraints, x-ray # 1 film pack needed to be mounted



between guide mirror coil electrode current feeds dictating a smaller film pack size for this imaging system. Both imaging systems needed to image thru approximately 6 cm of polyethylene (used for protection of the x-ray heads and film packs and to structurally support the guide mirror coils). Such a large amount of poly contributes to scatter and image quality is reduced.

The setup for the two 300-kV imaging systems is as follows:

1. X-ray system #1 was located at radius = 60 cm from centerline and its film pack was at a radius of 29 cm. This produces an image magnification = 1.51X.
2. The desired X-ray #1 system imaging time of 21.8  $\mu$ s actually came in at 21.711  $\mu$ s. This is 89 ns earlier.
3. X-ray #1 film pack suffered severe damage due to shot generated fragments and we were unable to retrieve the image from the damaged films.
4. X-ray system #2 was located at radius = 58 cm from centerline and its film pack was at a radius of 39 cm. This produces an image magnification = 1.68X.
5. The desired X-ray #2 system imaging time of 22.8  $\mu$ s actually came in at 22.985  $\mu$ s. This is 185 ns later.
6. X-ray #2 film pack also suffered significant damage due to shot generated fragments. However, we were able to extract the film and image data.
7. The static and shot images are a little bit difficult to read because we have a slotted outer conductor superimposed on the liner image. The outer conductor for this shot was divided into 16 equal segments. An interesting aside here is that these slotted segments became the deadly fragments that severely damaged the film cassettes. Next time we will use Kevlar for protection.

The radiographic images for the shot are shown in Section 4.1.2.

### ***3.2 Plasma System Development***

Based on the results of the plasma testing done prior to the FRCHX-3 Shiva Star compression shot, we knew that the plasma lifetime would be marginal, at best, for the compression experiment. Nevertheless, it was deemed important to demonstrate that the entire system, FRCHX plus Shiva-Star-driven liner, could be integrated.

Following FRCHX-3, we embarked on a prolonged campaign to attempt to increase the plasma lifetime by a variety of techniques. MHD simulation analysis by NumerEx showed that trapping sufficient poloidal magnetic flux in the FRC was a key, and previous research by several people argued that a rotational instability, the so-called  $n = 2$  instability could lead to enhanced flux loss and FRC plasma decay. To increase the flux trapping during formation, we developed two different systems to pre-preionize the gas using RF electric fields before PI discharge, and we performed calculations to help elucidate the problem of breaking down the gas via inductive electric fields (Theta discharge) when orthogonally oriented bias magnetic fields are present (the crossed-field ionization problem). We also developed the capability to use gas puff injection to limit the neutral background through which the FRC would have to travel to get to the trapping region from the formation region. It was postulated that the extra neutral gas with the static prefills could quench the plasma, thus lowering its temperature and conductivity, and thereby increasing the rate of flux loss by diffusion. To attempt to control the rotational instability, we developed and implemented a set of bias rings to create a radial electric field in the vicinity of the FRC that would counter the rotation via the resultant  $E \times B$  drift.

At the same time, we worked to continuously improve our ability to measure plasma characteristics, by developing new or improved diagnostic techniques. In particular, a crucial diagnostic for measuring plasma electron density with the possibility of resolving it in the radial dimension is laser interferometry, and we spent considerable effort improving our capability.

The diagnostic and data acquisition work is described in the next section, and details of the various techniques for increasing the plasma lifetime are described in the following section.

### **3.2.1 Diagnostic Development**

#### **3.2.1.1 Interferometer**

Early in the POP, the MTF four-chord HeNe laser-interferometer system was converted to a fiber-optic probe system. The purpose of this design change was to allow for the option of diverting any or all of the four probe beams into single-mode optical fibers whose collimated outputs could be used to probe different axial locations simultaneously [15]. This fiber-optic probe beam modification would enable us to place the interferometer system's optical table at a safe distance from the FRCHX experiment when destructive tests are performed involving plasma compression by a solid metal liner imploded by the Shiva Star capacitor bank. Single-mode optical fibers will transport the interferometer's probe beams to the FRCHX vacuum stand, where each beam will emerge from its fiber, be collimated, propagate through the plasma medium (thus experiencing a phase shift relative to its reference beam), and then be coupled to another single-mode optical fiber that will transport the phase-shifted beam back to the optical table to be recombined with its reference beam. While the ends of these fibers and the "launch" and "receive" fiber-optic probe assemblies and lenses will probably be destroyed during an imploding liner shot, all other interferometer optics and hardware will be located safely away from the Shiva Star center section.

In addition, fiber-optic probes would make it possible to obtain density measurements at various axial locations during FRC formation, translation, and capture tests that do not involve an imploding liner, thereby enabling us to track the behavior of the FRC at various points during its evolution in an effort to characterize its properties before an imploding liner-plasma-compression experiment is attempted.

As a first step toward developing fiber-optic probes for the interferometer system, a portion of the HeNe laser beam used for the probe leg of one of the four chords (chord no. 2) was injected into a single-mode optical fiber approximately 97 m in length after it emerges from the first beam expander. (A long run of fiber is used because the probe beams have to be transported over such distances when tests are performed under the center section of Shiva Star.) The fiber-coupler mount for the single-mode fiber is installed on an optical rail to have a variable path length of air between the beam expander and the input to the fiber. This adjustment is necessary

to obtain an optical path length that will yield an observable interference signal when the probe beam and its corresponding reference beam are recombined, as there are only certain fixed lengths of the fiber probe leg for which coherence between its signal and reference path signal is preserved. Figure 172 shows the fiber-probe test setup. The diagram overlaid on top of the photograph shows how two chords are being used to test the fiber-optic probe concept. One probe beam propagates through air, while the other is coupled to a long length of fiber to simulate the fiber probe beam path. In this configuration, both reference beams are propagating through air.

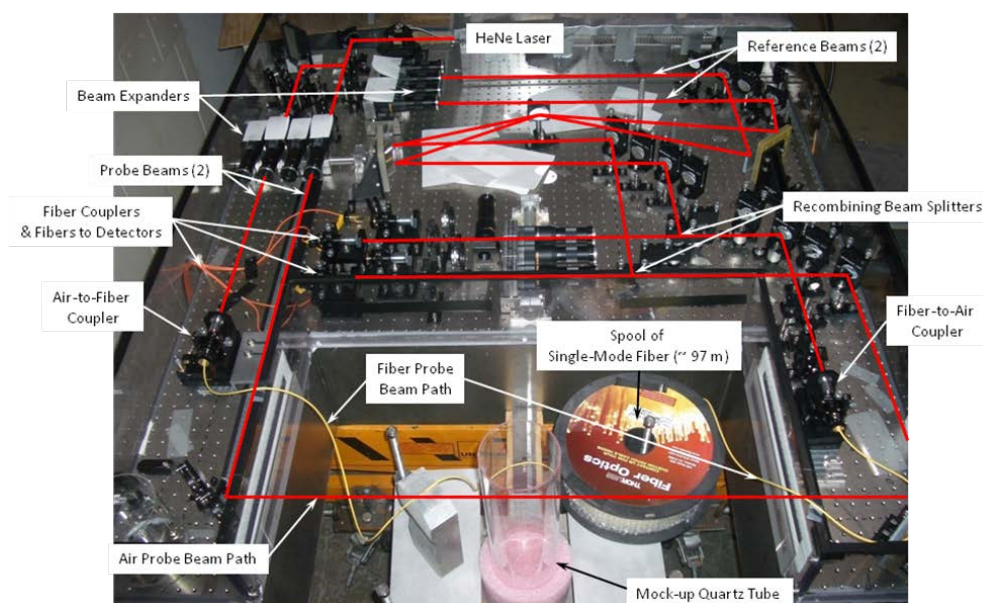


Figure 172. MTF four-chord interferometer system optical table

The probe beam emerging from the single-mode fiber is recombined with its corresponding reference beam, which still propagates through its original air path on the optical table, as has been done before to obtain an interference signal. After a fair amount of effort, an interference signal was obtained when recombining the beams from the fiber-probe leg and its air-path reference leg. Figure 173 shows representative oscilloscope traces of the 80-MHz sinusoidal interference signals obtained using both the fiber-probe beam and the air-probe beam from the central chord of the interferometer as it passes through a mock-up of the quartz tube in which the FRC is formed.

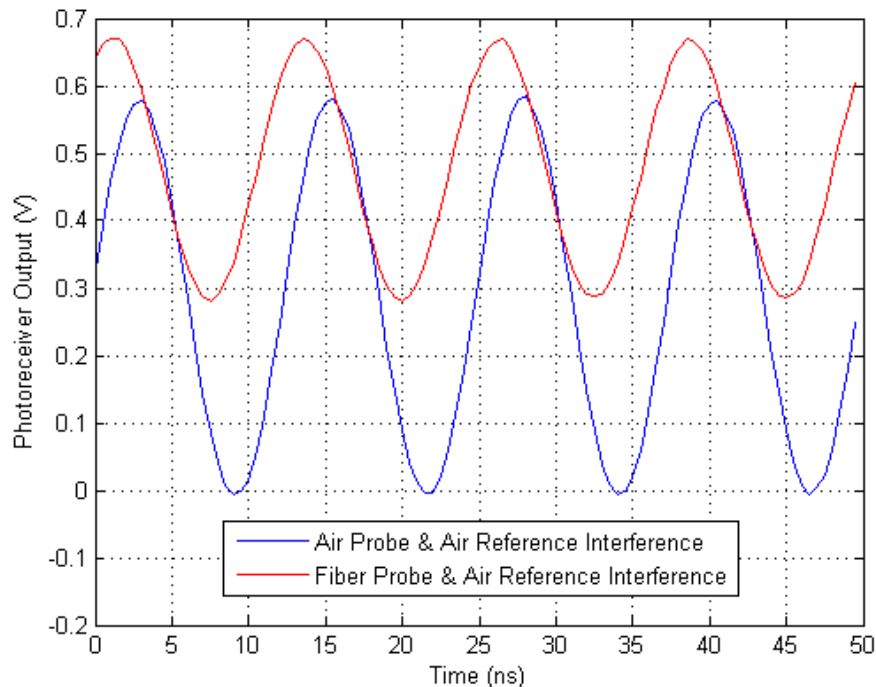


Figure 173. Interference signals at 80 MHz obtained from recombined probe and reference beams

The interference signal obtained from the recombined air probe and air-reference beams features a fringe contrast (or visibility) of 100%, indicating the best achievable interference signal. Fringe contrast is defined as  $(V_{\max} - V_{\min}) / (V_{\max} + V_{\min})$ . Loss mechanisms and other issues are encountered when propagating light through the single-mode fiber of the fiber-probe path; e.g., it is not possible to couple all of the incoming light from the probe beam into its optical fiber. Therefore, the best fringe contrast that can be obtained from that leg is less than optimal (in this case, about 40%), but still good enough to produce a discernible interference signal, indicating that at these levels it should be possible to make a measurement from which useful phase-shift data can be gathered when the probe beam actually passes through an FRC plasma.

However, during the course of observing these signals, it was found that the fiber probe and air reference interference signal is amplitude-modulated on a time scale that is much slower than the 80-MHz carrier wave. (The modulation appears to have a primary frequency component on the order of 40 kHz.) In contrast, the interference signal from air probe and air reference beam exhibits very little amplitude modulation on this time scale. An example of this effect is shown in Figure 174, with interference signals obtained from recombined probe and reference beams.

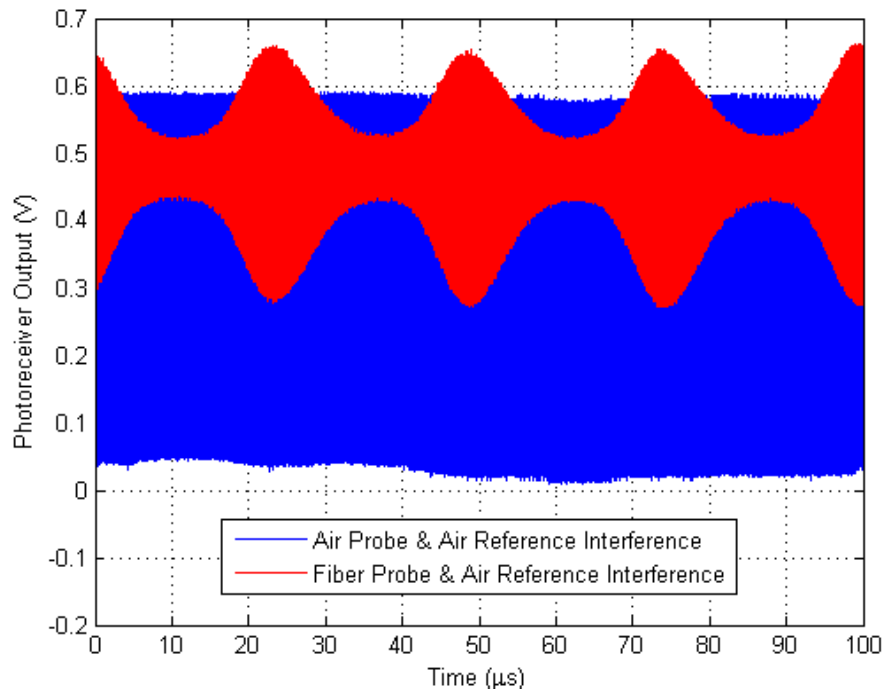


Figure 174. Interference signals showing amplitude modulated of fiber probe and air-reference-interference signal. The reasons for this amplitude modulation were not initially clear. A number of possible explanations, including the partial loss of coherence between the probe and reference beams due to thermal effects in the laser or propagation effects through the fiber, were considered. Because the modulation is taking place on a time scale that is not too different from that of measurements that will be made of the FRC plasma densities, it is important that this effect be mitigated as much as possible. One potential solution may involve sending the beam of the reference leg for this chord through a similar length of fiber instead of propagating it through air as is being done now. In this way, any effects arising from the introduction of a fiber path might be equalized between the two legs and thus cancel out. This hypothesis will be tested soon.

An important test of this diagnostic system is to see how sensitive its electronics and data acquisition system are to noise when the Shiva Star capacitor bank is fired for an imploding liner shot, either for magnetic-field compression alone or for an actual FRCHX shot with plasma. Such an imploding liner test was recently performed for magnetic-field compression. The interferometer optical table was situated at a safe distance away from Shiva Star with both the fiber probe and air-probe paths operating in the same configuration used for the signals appearing in Figure 171 and Figure 172. The “I” and “Q” outputs (in-phase and quadrature

components, respectively) of each of the four demodulator circuits were recorded as they would be during an actual FRC test with plasma. Therefore, each of the four channels has two signals (“A” and “B”) associated with it, corresponding to  $\cos\phi$  and  $\sin\phi$  for each of the four interferometer chords (where  $\phi$  is the phase shift). Because only two of the four channels were actually operational during this test—in this case, channels 1 and 3—the other two should display zero voltage output from their demodulator outputs. The results from this test are displayed in Figure 175–Figure 178.

Figure 175 shows the demodulator-output signals for Channel No. 1 measured during the Shiva Star imploding liner test. This channel corresponds to the air probe and air-reference-interference configuration and has the probe beam passing through a mock-up of the quartz tube that will be used during plasma formation, translation, and capture tests. Small Shiva trigger-noise spikes can be seen at around 150  $\mu\text{s}$ . As expected, both outputs are essentially constant because there is no plasma medium to introduce a phase shift. The slight amount of drift in the signals seen later in time is probably due to acoustic noise associated with the firing of Shiva Star.

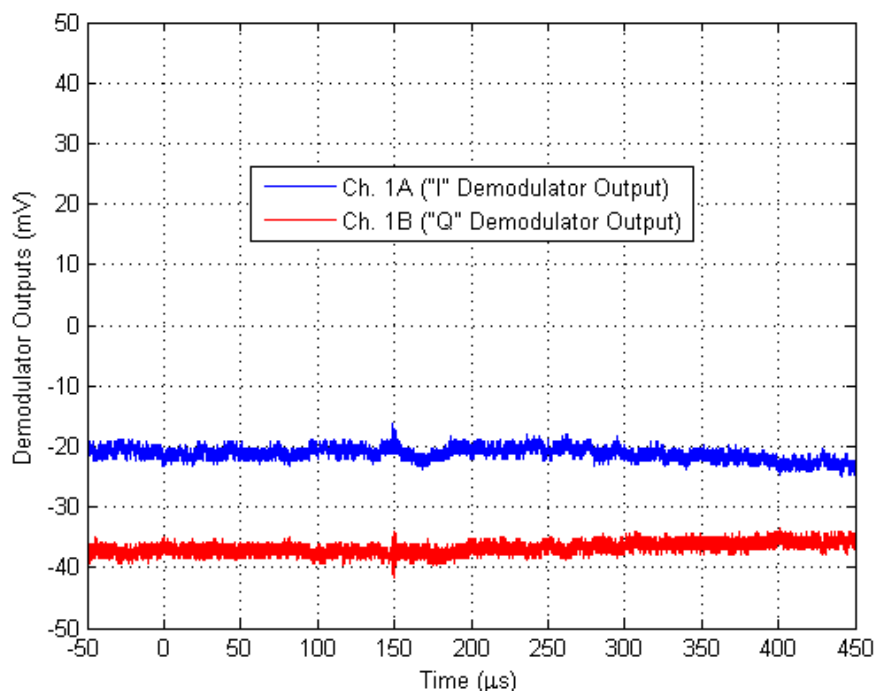


Figure 175. Demodulator-output signals for Channel No. 1, Shiva Star imploding liner test

Figure 176 shows the demodulator-output signals for Channel No. 2 measured during a Shiva Star imploding liner test. The corresponding probe-beam chord for this channel was not active for this particular experiment, so no interference signal is present. As expected, both signals are zero, with small Shiva trigger noise spikes occurring at around 150  $\mu\text{s}$ .

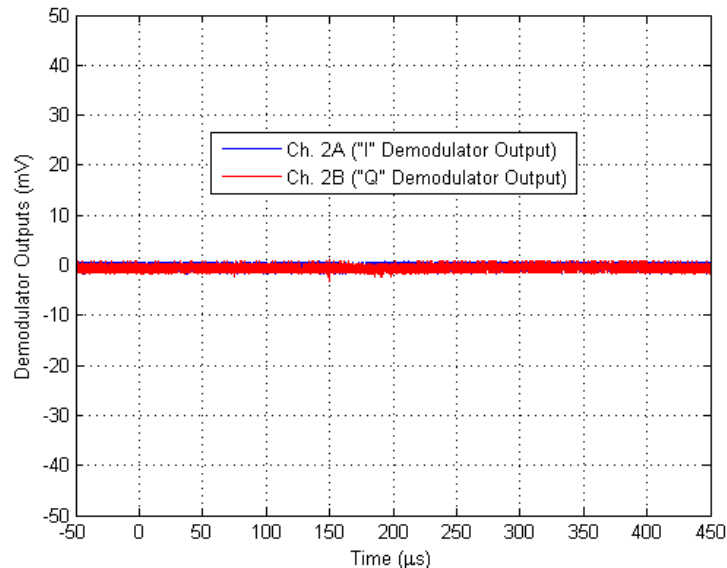


Figure 176. Demodulator-output signals measured for Channel No. 2, Shiva Star imploding liner test

Figure 177 shows the demodulator-output signals measured during a Shiva Star imploding liner test for Channel No. 3. Channel No. 3 corresponds to the fiber probe and air-reference-interference signal and has the probe beam propagating through a 97-m-long length of single-mode fiber. Because of the amplitude modulation that this interference signal has (Figure 174), both the I and Q components exhibit time-varying signals along with some DC offset. No Shiva trigger noise was observed. As with the data from Channel No. 1 shown in Figure 175, some drift is observed later in time, probably as a result of acoustic noise arising from the firing of Shiva Star.



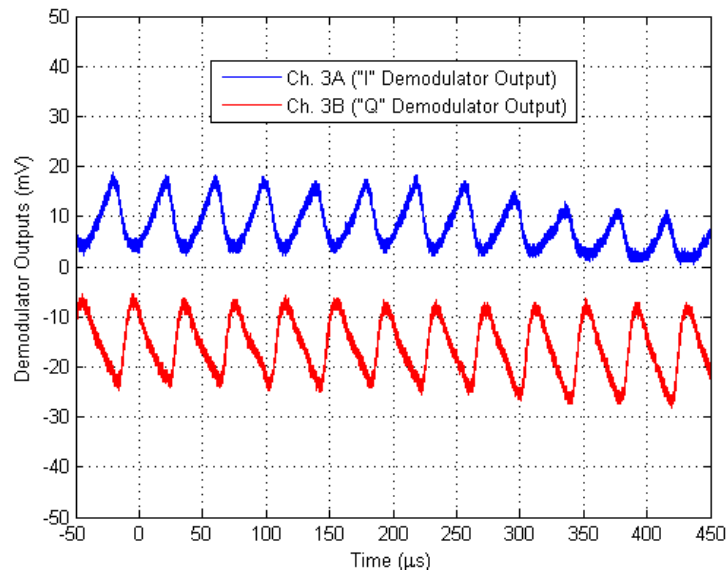


Figure 177. Demodulator-output signals measured for Channel No. 3, Shiva Star imploding liner test

Figure 178 shows the demodulator-output signals for Channel No. 4 measured during a Shiva Star imploding liner test. As with Channel No. 2, the corresponding probe-beam chord for this channel was not active for this particular experiment, and as expected, both signals are zero, with a small amount of Shiva trigger noise starting at around 150  $\mu\text{s}$ .

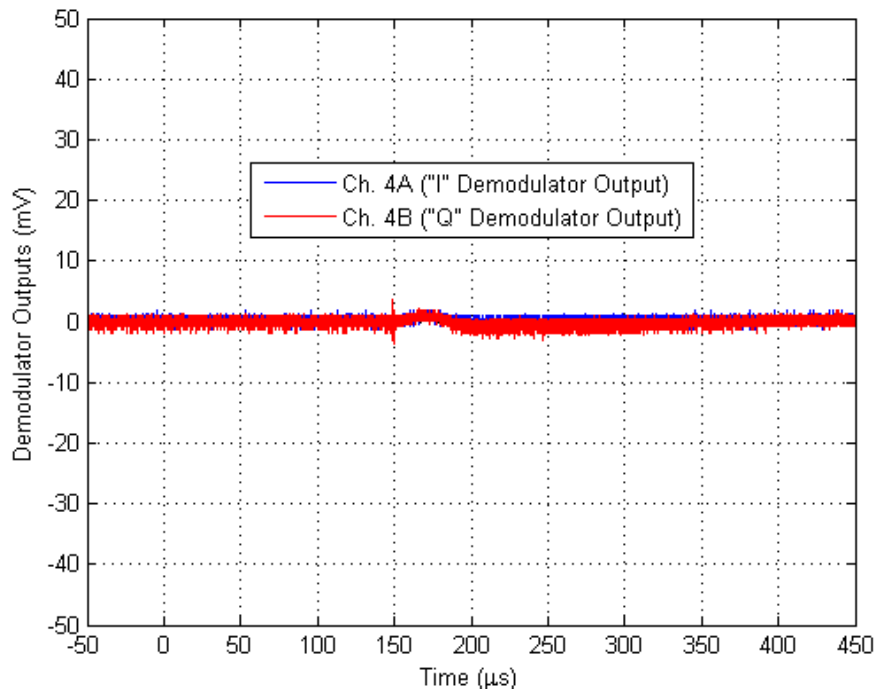


Figure 178. Demodulator-output signals for Channel No. 4, Shiva Star imploding liner test

All these signals appear as expected, with none of them featuring any significant amount of noise from the firing of Shiva Star. The shielding scheme for this system thus appears to be working well and should make it possible to obtain plasma-density measurements with good Shiva trigger-noise immunity during upcoming FRCHX plasma-compression tests.

As mentioned previously, a portion of the HeNe laser beam used for the probe leg of one of the four chords (chord no. 2) was injected into a single-mode optical fiber approximately 97 m in length for the purposes of initially testing the fiber-optic probe concept and establishing its viability. The probe beam emerging from the single-mode fiber was recombined with its corresponding reference beam, which propagates through its original 2.57-m-long air path on the optical table. An interference signal was obtained, but it was found that the fiber probe and air-reference-interference signal is amplitude-modulated on a time scale on the order of tens of kHz. In contrast, the interference signal from an air probe and an air-reference beam exhibits no amplitude modulation. Figure 179 shows an example of this effect on a time scale that clearly reveals the modulation obtained with fiber probe and air-reference path.

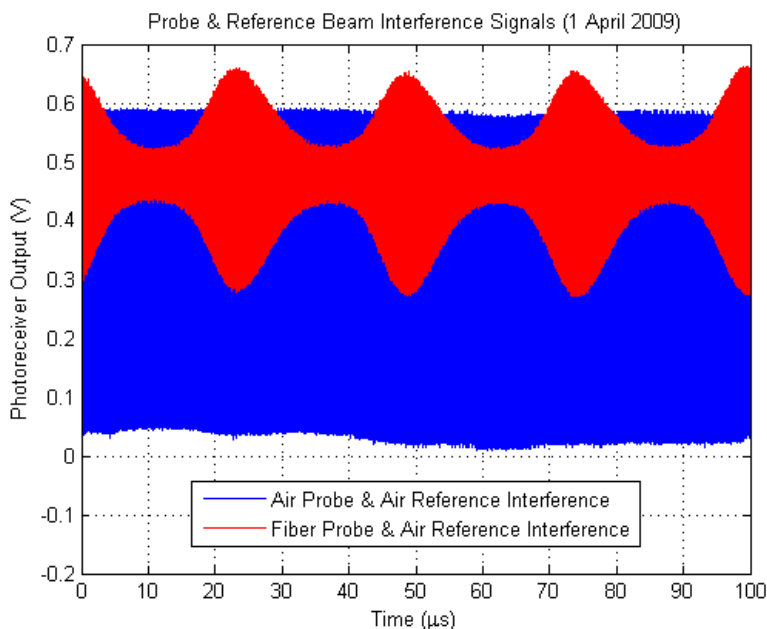


Figure 179. Interference signals from recombined probe and reference beams highlighting amplitude modulation. In addition, the type of modulation recorded here was also observed when the single length of 97-m-long fiber was cut into two segments, so that the probe beam also propagated through a

length of air path between its two fiber segments that simulated the portion of the probe beam that would actually pass through the quartz tube containing the FRC plasma. In this configuration, the total fiber length was about 91.4 m, and significant modulation of the interference signal still occurred.

After further experimentation and theoretical analysis, we concluded that the reason for the modulation has to do with the length of the single-mode fiber being used to transport the probe beam. It can be shown that there are only certain fixed lengths of the fiber-probe leg for which coherence between its beam and the reference path beam is preserved; it is the condition that must be met to obtain a good interference signal. When coherence between the probe beam and reference beam is preserved, the best interference signals that can be obtained are those for which  $V = 1$ , where  $V = (I_{\max} - I_{\min}) / (I_{\max} + I_{\min})$  is called the “visibility” of the interference signal and  $I_{\max}$  and  $I_{\min}$  are the maximum and minimum optical signals measured for the given signal. The requirement for maximizing the visibility translates into the condition that the difference between the optical path lengths of the probe beam and the reference beam must be  $2nL_{\text{cav}}$ , where  $n$  is an integer and  $L_{\text{cav}}$  is the length of the HeNe laser cavity.

If the line widths of the individual longitudinal modes of the multimode HeNe laser being used to generate our probe and reference beams are not taken into account, the condition for maximum interference-signal visibility imposes no constraints upon the ultimate fiber length that can be used to transport the probe beam from the interferometer optical table to the quartz tube containing the FRC plasma. As long as the length of the fiber is such that the aforementioned optical path length difference requirement of  $2nL_{\text{cav}}$  is met, the ultimate length of the fiber is limited only by what level of signal attenuation yields an acceptable signal-to-noise ratio.

In practice, however, the HeNe laser modes do have a finite spread in frequency, and further analysis shows that to maintain  $V \sim 1$  when this factor is taken into account, a maximum value of  $n$  is allowed. This value puts a limit on how long the fiber can be before it is impossible to maintain coherence between the probe and reference beam. For the case of our initial experimental parameters, we found that the maximum fiber length is on the order of 85 m (corresponding to  $n = 107$ ). Because our initial tests were conducted with a one-segment fiber

that was 97 m long and a two-segment fiber 91.4 m long, the fact that the interference signal exhibited substantial modulation is to be expected, even when the optical path length difference between the probe and reference beams was set to maximize the visibility. Once outside the “coherence zone” established by the maximum allowable value of  $n$ , the precise location of the longitudinal mode lines under the laser’s gain-curve effects can move due to variations in laser cavity length arising from acoustic modes of the laser tube. This “mode pulling,” which is a documented effect in lasers, is a likely cause of mode beating that manifests itself as an amplitude modulation of the interference signal.

Therefore, the solution to our modulation problem is simply to keep the length of fiber in our probe beam short enough. We tested our system with the probe beam going through two segments of fiber totaling 40 m in length, a distance that should amply satisfy the criterion discussed for the maximum fiber length that preserves the coherence between the probe and reference beams for our given experimental parameters. In addition, the portion of the probe-beam light propagating through the air gap between the “launch” and “receive” fibers was focused and collected with the use of microscope objectives in the fiber mounts in a manner similar to that which will be used when performing actual FRC electron-density measurements. This air path between the two segments of the fiber is approximately 2.1 m long. With the difference in optical path lengths between the probe and reference beams set to satisfy the requirement for maximum interference signal visibility, we obtained the data shown in Figure 180 for a probe beam propagating through two-segment fiber, 40 m long. There is no amplitude modulation of the signal on the time scale of interest.

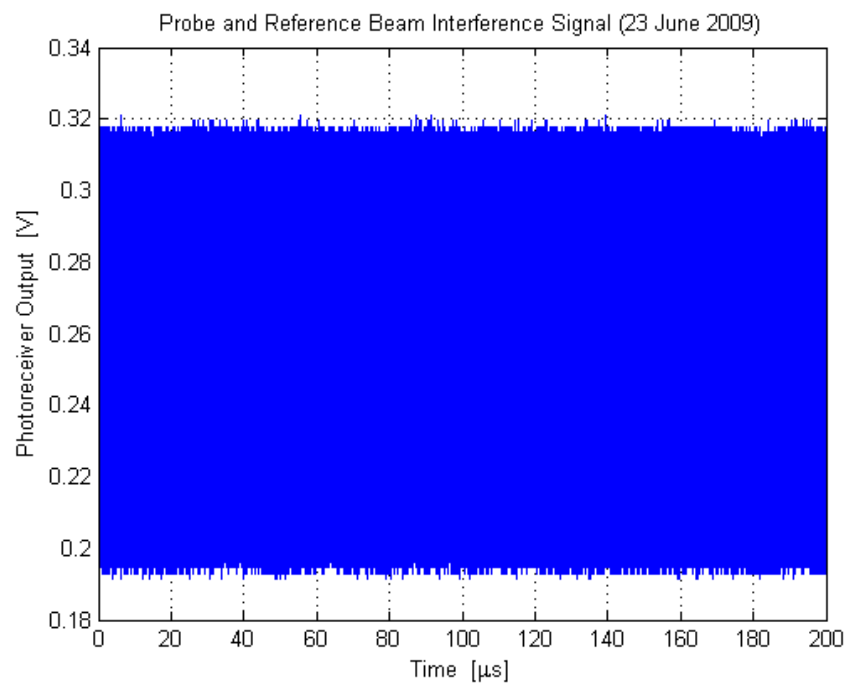


Figure 180. Interference signal obtained from recombined probe and reference beams

In Figure 181, an expanded view of the data clearly shows the 80-MHz sine wave of the interference signal.

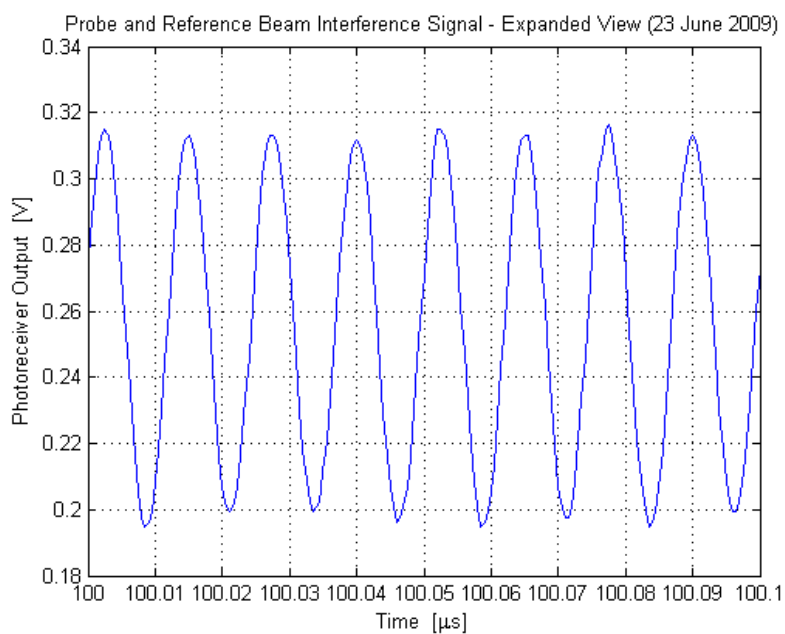


Figure 181. Expanded view of Figure 180 interference signal

The calculated visibility for the data shown is approximately  $V = 0.23$ . While this is considerably less than the maximum value of unity that should be observed under ideal conditions, the fiber-probe system is still capable of providing a useful interference signal even at these reduced levels of visibility. An interference signal with a peak-to-peak voltage level of about 120 mV, such as the one shown here, is still large enough to yield an acceptable signal-to-noise ratio, thus making it possible to perform a measurement from which useful phase-shift data can be gathered when the probe beam actually passes through an FRC plasma. The reasons for the reduced visibility has to do with effects such as fiber-coupling efficiencies at the points at which the probe beam transitions from air to the single-mode fiber and attenuation of the light as it propagates through a long length of fiber. These loss mechanisms lead to reduced signal levels in the probe beam relative to the reference beam.

With these measurements, we have shown that the interference-signal amplitude-modulation problem first observed when sending the probe beam through a long length of fiber can be eliminated by keeping the fiber length below a certain critical value. Thus, it should be possible to operate the four-chord interferometer successfully in a fiber-optic probe mode under conditions relevant to FRC formation, translation, and capture experiments. To this end, the interferometer optical table was recently repositioned so that it will closer to the FRCHX vacuum stand that is currently under the Shiva Star capacitor bank. In this way, the length of the fibers of each of the four probe beams that will eventually be fielded should be well below the limit required to avoid amplitude modulation of the interference signal. Figure 182 shows the optical table in its new location, between the “A” and “B” arms of Shiva Star. It should be noted that in its new location, the optical table will still be at a safe distance from the FRCHX experiment when destructive tests are performed involving plasma compression by a solid metal liner imploded by the Shiva Star capacitor bank.



Figure 182. Interferometer system optical table in new location between two arms of Shiva Star

Having shown that the fiber-optic probe-beam concept should be viable, we are now proceeding with converting the three remaining probe beams to fiber probes and installing the necessary hardware to field the full fiber-optic probe-interferometer system in time for a series of FRC formation, translation, and capture tests prior to the compression test with a solid imploding liner driven by Shiva Star. Our single-mode optical fibers will transport the interferometer's probe beams to the FRCHX vacuum stand, where each beam will emerge from its fiber, be collimated, propagate through the plasma medium (thus experiencing a phase shift relative to its reference beam), and then be coupled to another single-mode optical fiber that will transport the phase-shifted beam back to the optical table to be recombined with its reference beam.

The first chord served as a prototype for verifying that the fiber-probe approach can be fielded successfully on FRCHX before the remaining three chords are installed. In particular, the mechanical stability of the mounting scheme used for the fiber-probe optics (launch and receive fiber couplers plus two turning mirrors) had to be tested and, if necessary, improved upon, to ensure that forces arising from the pulsed magnetic fields and other sources of mechanical vibration (e.g., vacuum pumps) do not compromise the optical alignment of the system. After testing our optical configuration with one chord, the other three chords will be fielded to measure density at a total of four axial locations.

For the first chord, two fiberglass platforms were mounted on the sides of the FRCHX vacuum and field-coil stand to support the fiber couplers and turning mirrors required to send the probe beam through the FRC plasma that will be formed inside the quartz tube. Two single-mode optical fibers (the “launch” and “receive” fibers for the probe beam) were cut to the appropriate lengths, terminated, and installed. The fibers were run from the interferometer optical table located between the A and B arms of Shiva (Figure 183) to the Shiva center section (Figure 184) and then back to the optical table, where the probe and reference beams are recombined to form an interference signal.



Figure 183. Interferometer system optical table between A and B arms

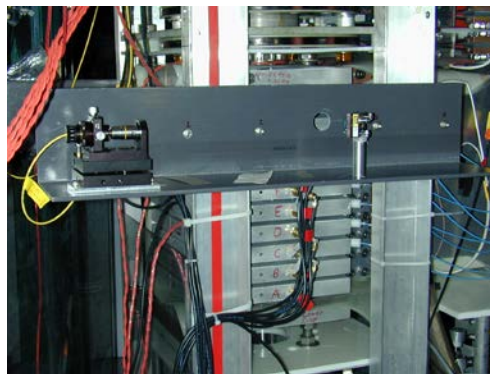


Figure 184. Fiberglass platform supporting the receive fiber coupler and its turning mirror

After aligning the optics to maximize the transmitted light through the single-mode fibers, the first probe beam was propagated through the quartz tube along a diameter situated in the gap between the “I” and “J” theta coil segments, and an interference signal of about 100 mV peak-to-



peak was observed. The signal featured very slight amplitude modulation, indicating that the fiber lengths are close to the lengths required to maintain coherence between the probe and reference beams. (As previously reported, the problem of amplitude modulation in the interference signal can be solved by choosing the length of the probe fiber such that it satisfies the criteria for preserving the coherence between the probe and reference beams for the given experimental parameters.) Minor adjustments to the length of the probe-beam air path on the optical table can be performed to eliminate the observed modulation altogether.

With the first fiber-probe beam chord installed and operating, the next step is to operate the interferometer during plasma formation and translation tests during which all the field coils are energized to determine the mechanical stability of the system and to measure the phase shift between the probe and reference beams so that line-averaged plasma-density measurements can be obtained. These tests should be underway shortly.

Having shown that the fiber-optic-probe beam concept should be viable, we proceeded with converting the three remaining probe beams to fiber probes. We installed the necessary hardware to field the full fiber-optic-probe interferometer system in time for a series of FRC formation, translation, and capture tests prior to the compression test with a solid imploding liner driven by Shiva Star. Our single-mode optical fibers will transport the interferometer's probe beams to the FRCHX vacuum stand, where each beam will emerge from its fiber, be focused as it propagates through the plasma medium (thus experiencing a phase shift relative to its reference beam), and then be coupled to another single-mode optical fiber that will transport the phase-shifted beam back to the optical table to be recombined with its reference beam.

The first chord of the MTF-FRCHX four-chord fiber-optic probe HeNe laser-interferometer system was operated during the fall of 2009. The primary concern during the initial phase of fiber-optic probe interferometry was the mechanical stability of the mounting scheme used for the fiber-probe optics—launch and receive fiber couplers plus two turning mirrors. Motion of the optical mounts arising from the forces due to the pulsed magnetic fields and other sources of mechanical vibration (e.g., vacuum pumps) must not compromise the optical alignment of the system, both during an actual shot (plasma or vacuum) and on a shot-to-shot basis. The goal is to

keep our probe beam alignment through the center of the quartz tube stable enough so that only occasional realignment of the optical system is required.

For the first chord, our initial mounting scheme consisted of two independent fiberglass platforms mounted on the aluminum beams of the FRCHX teststand. These platforms were positioned so that the probe beam propagated through the quartz tube along a diameter situated in the gap between the “I” and “J” theta coils. On one platform, the launch-fiber coupler and turning mirror were mounted; the receive-fiber coupler and turning mirror were mounted on the other platform located on the opposite side of the teststand. A good interference signal was obtained with this setup after initial probe-beam alignment through the center of the quartz tube prior to the start of plasma-formation tests.

Foam padding was placed between the platform and aluminum beams at their attachment points to provide some mechanical damping between the teststand and the optical platforms. However, after our first few plasma formation tests during which all the field coils were pulsed (Guide/Mirror, Bias, PI, and Main), it became apparent that this setup was not sufficiently stable. Optical alignment between the launch and receive fibers was lost on every shot of this type, requiring realignment prior to the next shot. This process can sometimes take longer than the time required to prepare for the next shot, so it was not a practical situation in terms of trying to maximize the number of shots taken on a given day.

After some additional thought and design work, a new optical platform was fabricated. It consists of a “U”-shaped G10 fiberglass platform that was mounted around the FRCHX teststand. Figure 185 shows the platform and probe beam optical components as fielded for plasma formation and translation tests.

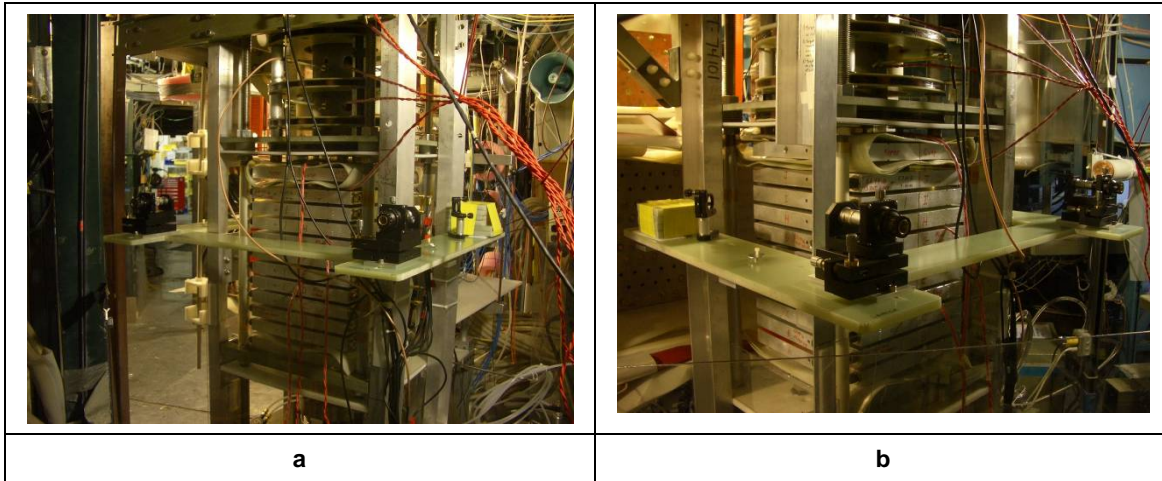


Figure 185. Single-chord fiber-probe interferometer G10 optical platform and associated components

To minimize the mechanical coupling between the aluminum frame of the FRCHX teststand and the optical platform, ultra-soft polyurethane pads (Sorbothane) were used to isolate the platform from the aluminum L-brackets upon which it rests. The L-brackets that support the platform are bolted to the aluminum beams of the FRCHX teststand.

With this configuration, the probe beam was again aligned through the center of the quartz tube in the gap between the I and J segments of the theta coil. We found that adequate optical alignment could be preserved for about two to three shots in which all the field coils were energized. After these shots, it was necessary to realign the probe beam, which is an improvement over the original setup. However, it is clear that further improvements need to be made to maintain alignment for a longer period of time.

To illustrate one of the best results obtained thus far, we present in Figure 186–Figure 189 interferometer data from a plasma-formation test, Test 13 from 12 November 2009.

Figure 186 shows the raw data from the I and Q demodulator circuit outputs, i.e., the “in-phase” and “quadrature” components of the interference signal, respectively, with respect to the 80-MHz carrier frequency of the heterodyned interferometer. An expanded view of these signals around the time of FRC formation is shown in Figure 187.

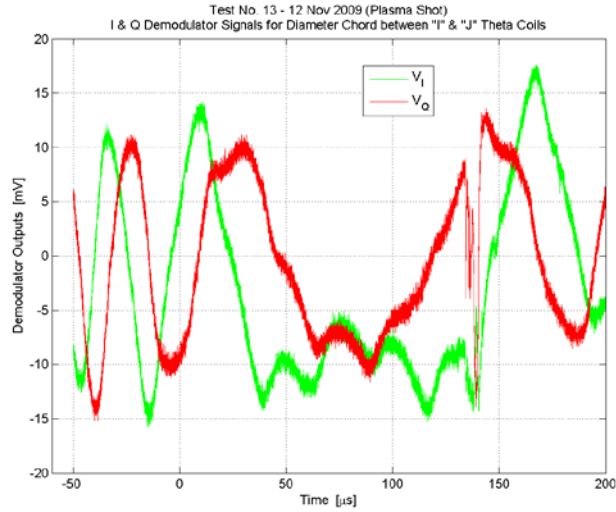


Figure 186. Plot of I and Q demodulator signals

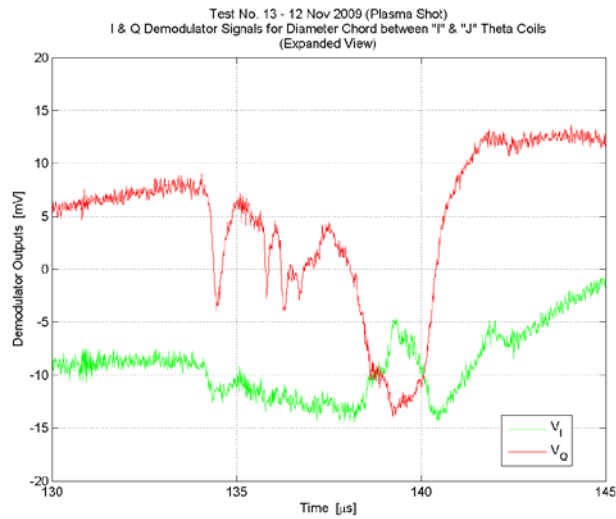


Figure 187. Expanded view of I and Q demodulator signals around the time of FRC formation

Figure 188 presents the result obtained when the demodulator signals are processed to obtain the electron density,  $n_e$ , assuming a 4-cm interaction-path length between the probe beam and plasma.

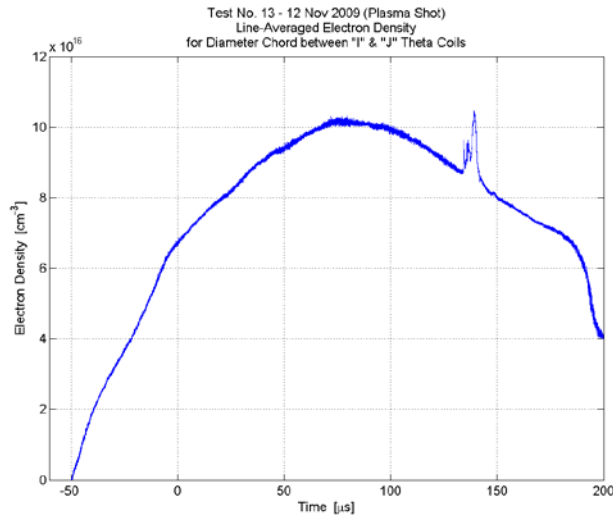


Figure 188. Plot of plasma-electron density

Figure 189 shows an expanded view of this result, also around the time of FRC formation.

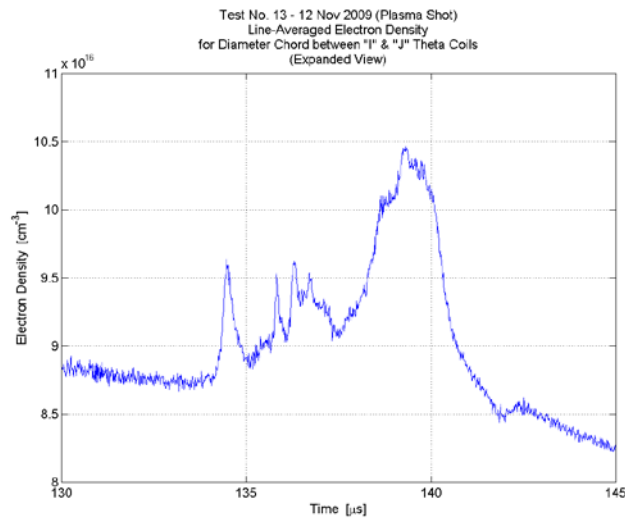


Figure 189. Expanded view of plasma-electron density around the time of FRC formation

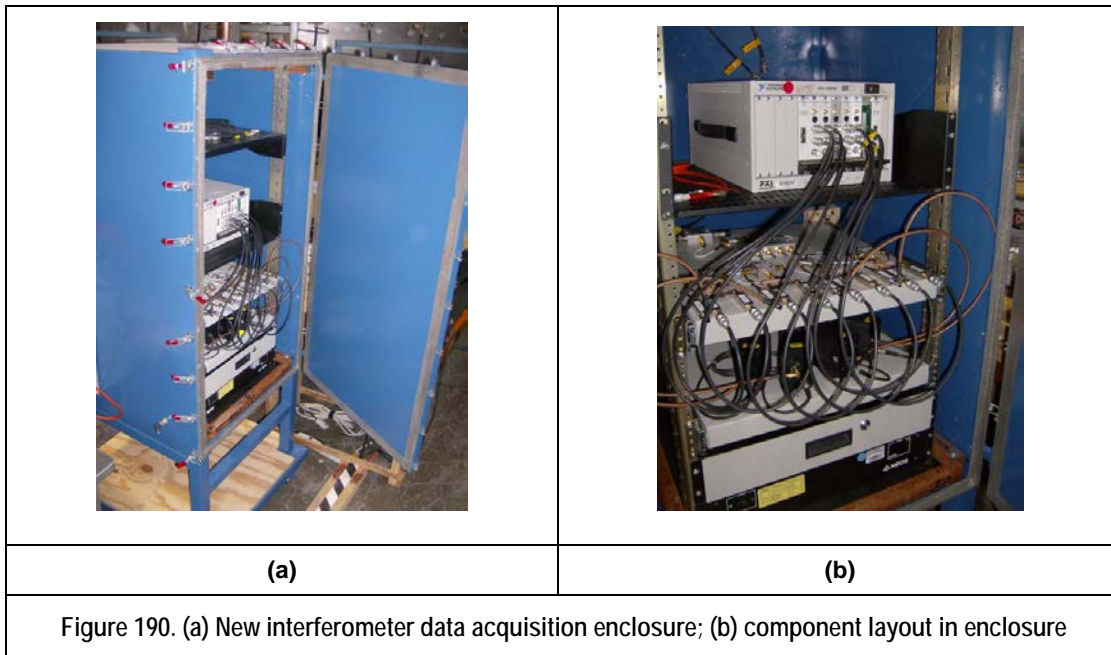
It should be noted that the results displayed for  $n_e$  in Figure 188 and Figure 189 have not been corrected for the mechanical motion of the FRCHX teststand and the optics on the G10 platform that occur due to the pulsed magnetic fields. Most of the contribution to this motion appears to come from the Guide/Mirror field. This motion changes the path length of the probe beam on the time scale of the shot, thereby introducing an additional component to the phase shift  $\phi$  that is used to compute the electron density. It should be possible to correct for this motion in future

shot series using data from a vacuum reference shot taken under the same conditions, provided this effect is not too large and that it is reproducible from shot to shot.

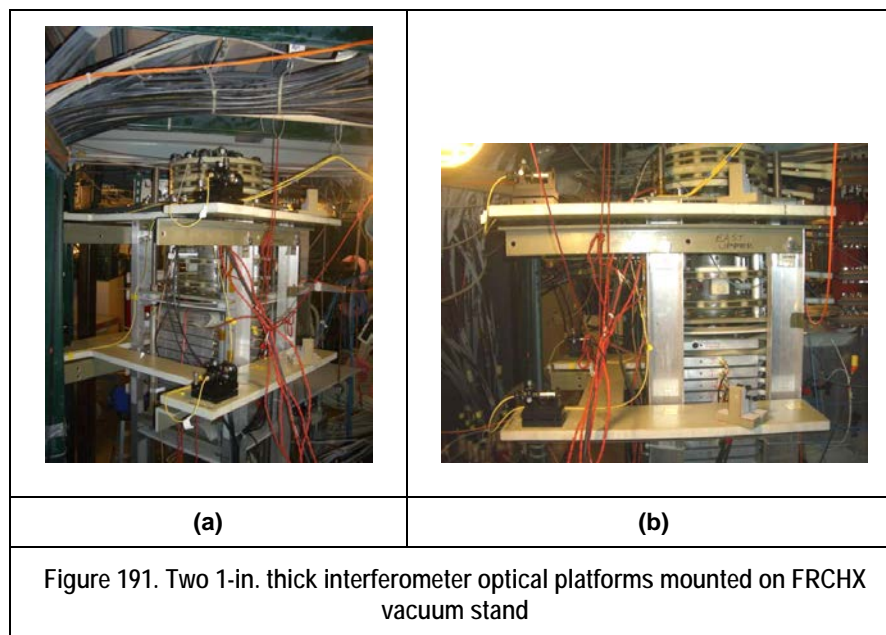
Not having done a vacuum correction for the effects of the pulsed magnetic field accounts for the fact that  $n_e$  is non-zero at  $t = 0$ , when there is no plasma present. As a result, the magnitude of the density shown in Figure 188 and Figure 189 is not accurate, but it serves to establish an order-of-magnitude estimate for the value of  $n_e$  and can also be used to estimate the change in electron density,  $\Delta n_e$ , that occurs around the time of FRC formation.

To mitigate against the problem of mechanical motion during a shot, a new design for the G10 optical platform has been developed in which the platform is 1-in. thick to provide greater stiffness. (The original one was 1/2-in. thick.) As in the original design of this type, Sorbothane pads will be used to isolate the platform as much as possible from the teststand and dampen any vibrations that are transmitted from the stand. In addition, the new design locates the fiber couplers and mirror mounts further away from the magnetic field coils. The interaction between the fringe fields emanating from the coils and the metallic components of our optical hardware also gives rise to forces that “bump” the optics and lead to misalignment. Positioning these components further away from the coils reduces the strength of this interaction. Finally, some of the hardware for our optical mounts is now made of G10 instead of aluminum, so that there is less metal that can couple to the magnetic field.

Because there was almost no space in the FRCHX data acquisition enclosure anymore, NumerEx and University of New Mexico (UNM) personnel began preparing a second shielded enclosure in January 2010 to house the interferometer’s electronics. The enclosure was set up with its own UPS to supply isolated battery power; its own PXI crate to record the data from each of the eight interferometer signal channels; and, similar to the FRCHX data acquisition enclosure, a set of three relays, which are energized with a pneumatic control, to allow the hot, neutral, and ground wires coming from the wall power to be disconnected. The cFP controller takes care of energizing the pneumatic control line to disconnect the wall power, at the same time that the original data acquisition enclosure is disconnected from wall power (right before each test). Figure 190 shows the new interferometer data acquisition enclosure as it was being set up.



Of somewhat greater importance were the tasks of bringing on line at least one more interferometer probe beam to measure the plasma density in the capture region, and of improving the stability of the optical platforms so that considerable realignment was not needed after every shot. Figure 191 shows two views of the improved “I-J” optical platform and the new “T4” optical platform above it, which was positioned for viewing in the center of the capture region.



Previously, 0.5-in. thick G-10 was used to fabricate the I-J probe's optical platform for tests; it was felt that further increasing the thickness of the platform to a 1-in. thickness would be a first step toward reducing vibrations. A second change to help reduce vibrations was to use one long (non-conducting) horizontal support for the optical platform, which was mounted to both vertical posts on each side of the FRCHX vacuum stand, rather than a pair of short supports mounted individually to the vertical posts. Such an arrangement, among other things, allowed support to be placed directly underneath the fiber couplers on each platform, which were approximately 12 in. out from the edge of the vacuum stand, thereby eliminating the need for additional G-10 blocks to be placed on the opposite end of the platform as counterweights. The ultra-soft sorbothane pads used previously to minimize the mechanical coupling between the vacuum stand frame and the optical platform were also used again with this new support scheme.

Another refinement to the platforms was to replace the small, metallic turning-mirror posts, which happened to be the components closest to the magnetic field coils, with stouter, non-metallic mirror mounts. The frame holding the mirror was also modified in that the steel ball bearing, on which the mirror pivoted, was replaced with a non-conducting plastic ball.

After having implemented all these changes, there was still considerable difficulty in maintaining the interferometer alignment between test shots. Despite these difficulties, however, NumerEx and UNM personnel were able to obtain credible density profiles, at both the I-J and T4 positions, during most plasma tests.

During the series of MTF experiments conducted in the fall of 2010, two chords of the MTF-FRCHX fiber-optic-probe HeNe laser interferometer system were successfully operated on a routine basis while conducting plasma formation, translation, and capture tests.

In anticipation of the next series of MTF experiments, the two chords previously used were readied once again for operation. The interferometer optical table, which is located between the A and B arms of Shiva, is shown in Figure 192.



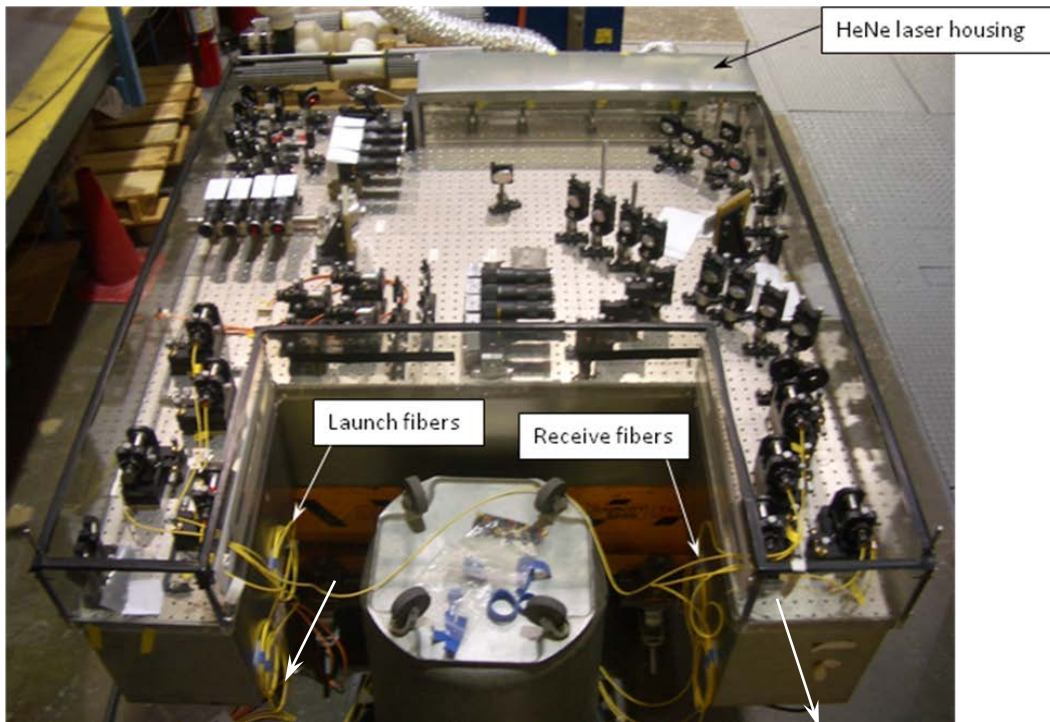


Figure 192. Optical table of the fiber-probe interferometer system

The probe beams are transported from the optical table to the MTF teststand and back to the table via single-mode optical fibers that are tens of meters long. Using an optical fiber setup enables us to conveniently probe the plasma at different axial locations without occupying space that would take away room needed for other diagnostics and hardware. In addition, when the experiment is located under Shiva for a liner implosion test, fiber probes make it possible to perform measurements during destructive tests without damaging a large amount of valuable optics. A photograph showing the launch and receive optical hardware for the two-chord system appears in Figure 193.

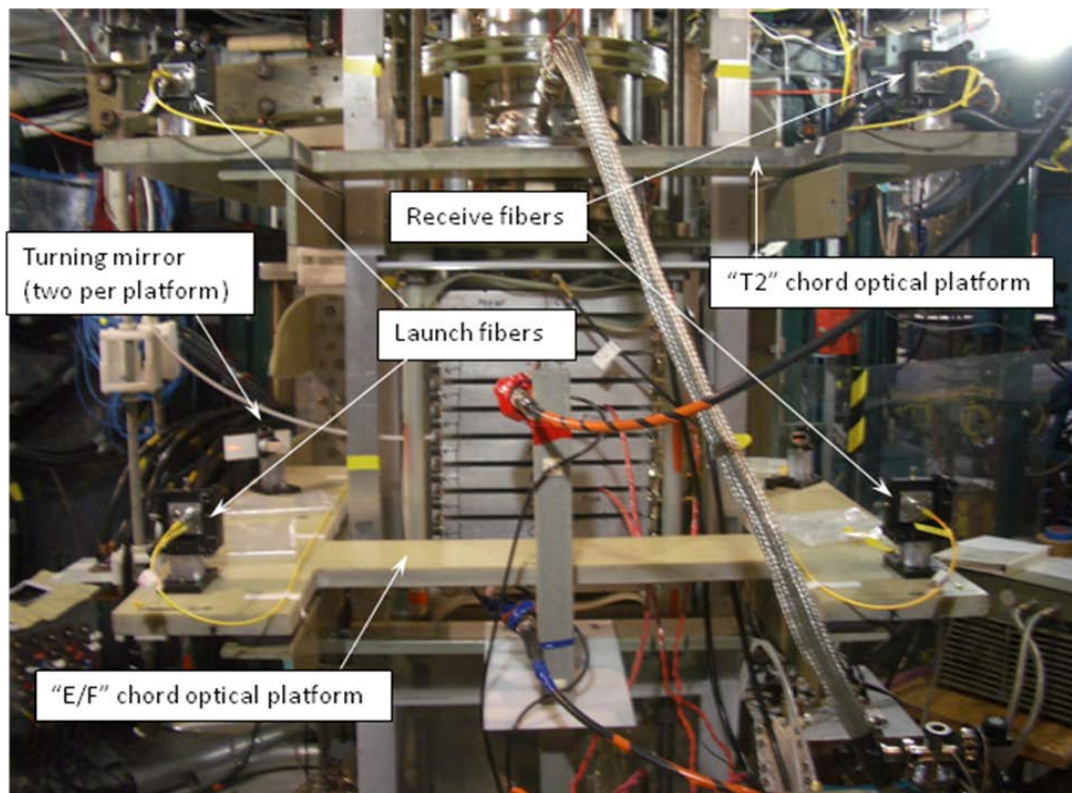


Figure 193. Launch and receive optics for "E/F" chord and "T2" chord at teststand

In addition to operating the two-chord system, work is underway to field a four-chord system in the near future that will utilize the full capability of our fiber-probe interferometer. A platform has been designed and fabricated on which the launch and receive optics will be mounted, as shown in Figure 194. The platform is made of G10 fiberglass to avoid interactions between the platform and the pulsed magnetic fields of the experiment that could affect optical alignment. Fiber couplers and turning mirrors used to launch the probe beams are on the right, and those for the receive optics are on the left in the figure.

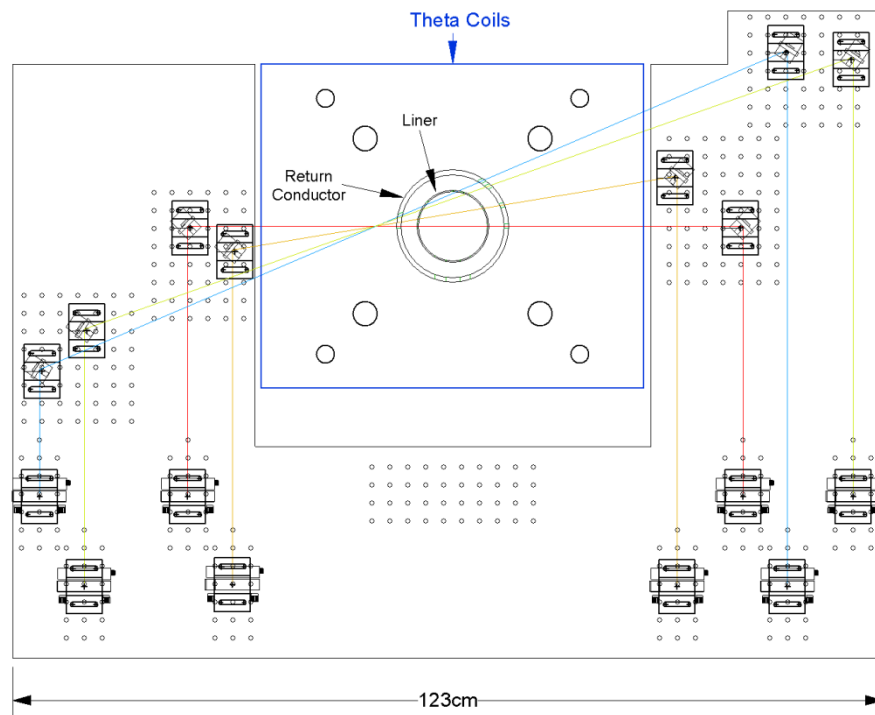


Figure 194. Diagram of optical platform to be used for four-chord fiber-probe interferometry system

Slots and holes were machined into a mock aluminum liner and return conductor identical to ones that would be used on a Shiva liner implosion test. Vacuum inside the liner will be maintained by curved quartz windows that will be secured to the slots on the liner using Torr Seal. These slots and holes will allow the probe beams to access the plasma at the axial location designated “T4” (15.6 cm below the top of the liner) once it has translated into the liner and been captured by mirror magnetic field created within it.

At this point, we had a fiber-probe interferometry system for MTF that works reliably and whose optics remain well aligned over the course of at least one full day of operation encompassing multiple plasma shots. The two-chord diagnostic has produced useful data and next would be expanded to operate with all four chords probing a single axial location within the mock liner at different impact parameters to obtain important density profile and symmetry information about the FRC plasma.

The interferometer optical table, which was located between the A and B arms of Shiva, is shown in Figure 195. Our system operates at the HeNe laser wavelength of 633 nm. The probe beams are transported from the optical table to the MTF teststand and back to the table via single-mode optical fibers whose total lengths are on the order of 40 meters for each chord. Using an optical fiber setup enables us to conveniently probe the plasma at different axial locations without occupying space that would take away room needed for other diagnostics and hardware. In addition, when the experiment is located under Shiva for a liner implosion test, fiber probes make it possible to perform measurements during destructive tests without damaging a large amount of valuable optics.

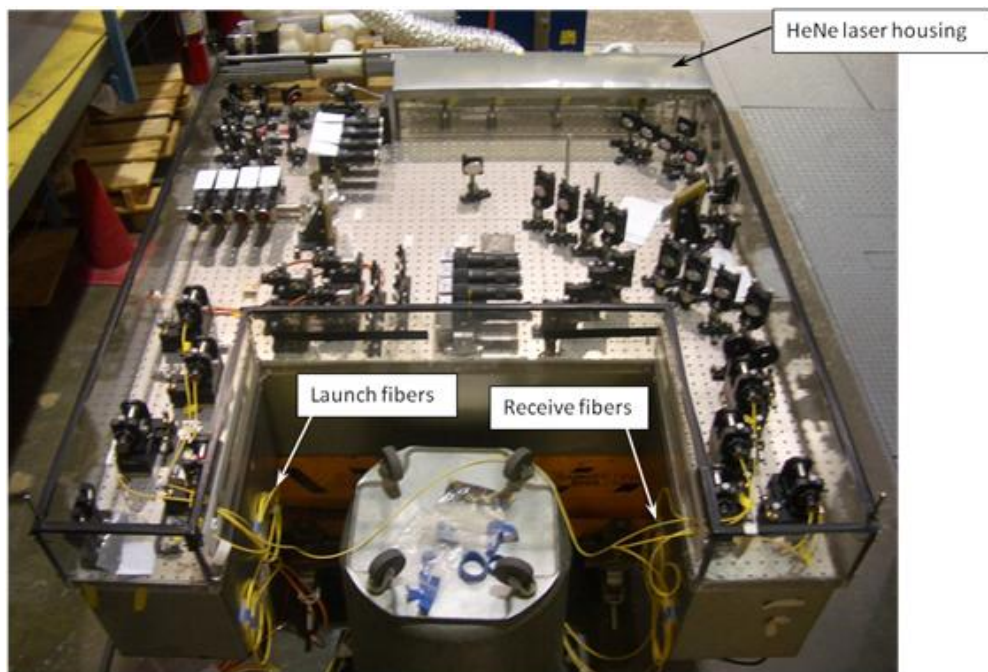


Figure 195. Optical table of the fiber-probe interferometer system

During the next series of MTF experiments, the FRC plasma was injected into a mock aluminum liner to simulate the conditions that would exist during an actual imploding liner test. It was important to characterize the plasma inside the liner as extensively as possible to learn how to extend the FRC's lifetime so that it lasts long enough for a successful implosion to take place. For the purpose of interferometry measurements, small slots and holes have been machined into the mock aluminum liner and return conductor assembly identical to ones that would be used on



a Shiva liner implosion test. These slots and holes will allow interferometer probe beams to access the plasma at the axial location designated “T4” ( $z = 15.6$  cm below the top of the liner) once the FRC has translated into the liner and been captured by the mirror magnetic field created within it.

To maintain the vacuum conditions required inside the liner while still allowing probe beam access to its interior, quartz windows whose radius of curvature closely matches that of the liner’s outer surface have been placed over the slots and holes and secured using Torr Seal. After the windows were bonded to the liner, the assembly was leak checked to confirm that the liner will hold a vacuum with the windows in place.

Optical assembly work on the G10 optical platform that will be used to field the four-chord system was also completed, and preliminary optical alignment was performed. A photograph of the optical mounts on the four-chord platform is shown in Figure 196.

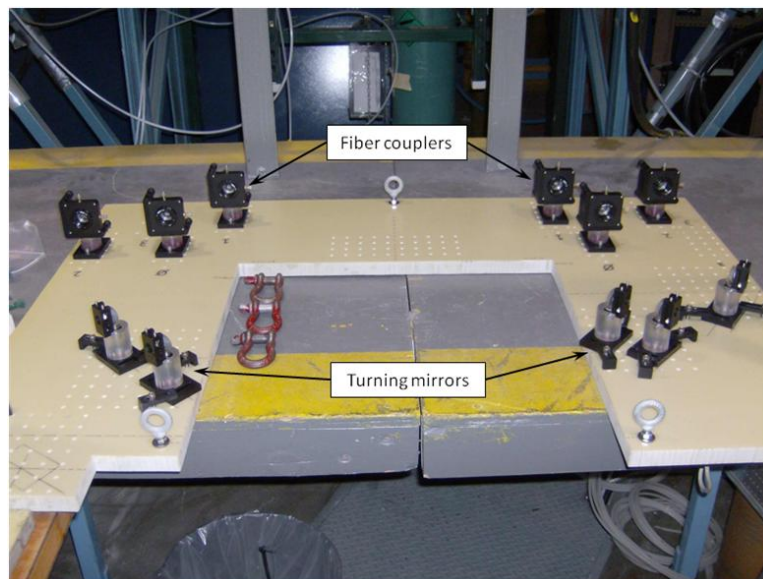


Figure 196. Optical platform for the four-chord interferometry system to be placed at T4 axial location  
The four-chord platform would be mounted on supports whose height along vertical aluminum beams of the teststand assembly can be adjusted to access different axial locations along the experiment. For now, the height will place the four beams at the T4 location where the diagnostic access holes in the liner and return conductor are located. A drawing illustrating the placement of the four-chord platform relative to the liner assembly and theta coils appears in Figure 197. The

coordinates of the turning mirrors and the angles of incidence for each mirror have been calculated to take into account probe beam deflections due to refraction at the quartz window interfaces, which can be fairly substantial for the two outermost chord beams given their angles of incidence at the windows. The mirrors have been oriented to give beam impact parameters of  $p = 0$  cm, 1.8 cm, 2.7 cm, and 3.9 cm inside the liner.

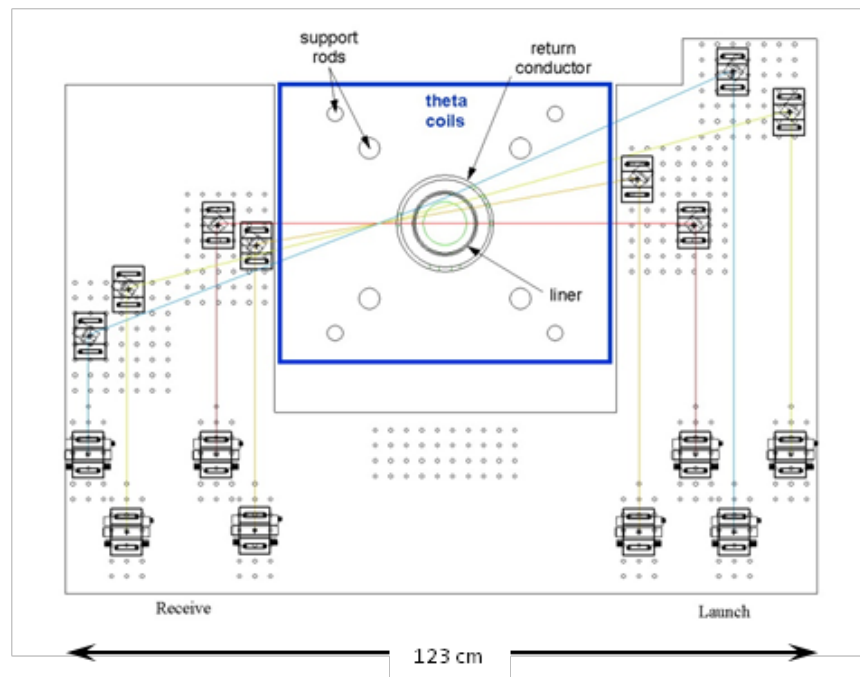


Figure 197. Diagram of the optical platform to be used for the four-chord fiber-probe interferometry system that will conduct density measurements of the plasma inside mock liner at different impact parameters

Figure 198 shows a photograph of the probe beam access holes on the return conductor on the side from which the beams are launched.

The platform is made of G10 fiberglass to avoid interactions between the platform and the pulsed magnetic fields of the experiment that could affect optical alignment.

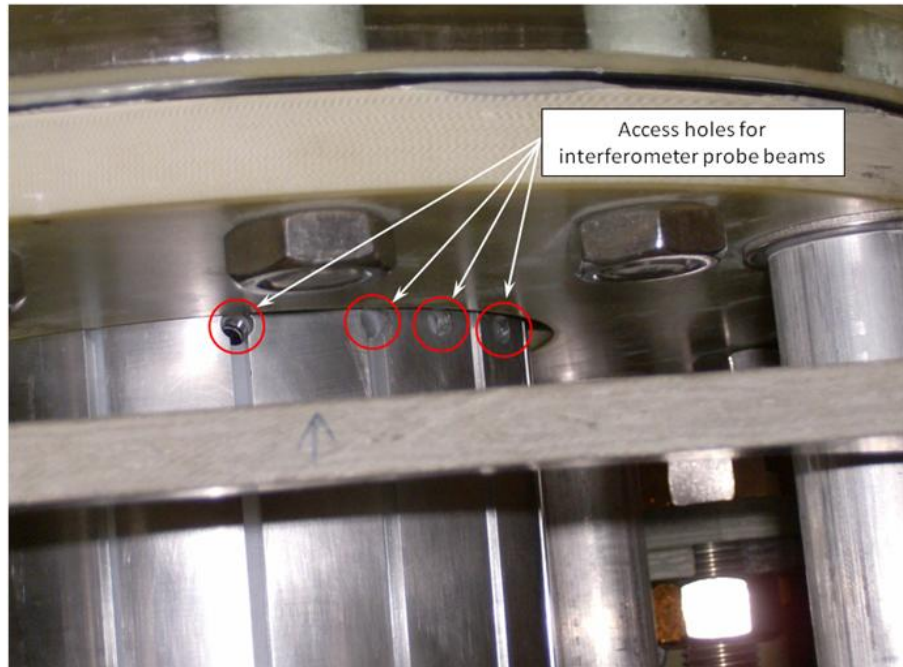


Figure 198. Access holes on slotted return conductor through which four interferometry beams can enter mock liner. Mock liner is situated inside return conductor with vacuum sealed quartz windows covering its access holes

After assembly of the vacuum system hardware, the four-chord platform was installed and its probe beams aligned through the liner.

In addition to the new four-chord platform system, we also retained the capability to field one of the two single-chord platforms that has been used on previous MTF experiments. This chord will probe the plasma along its diameter in the formation region between the E and F theta coil segments (corresponding to an axial location of  $z = 84$  cm below the top of the liner). The E/F chord platform has been mounted on the MTF teststand, its beam optics have been aligned through the quartz tube, and an interference signal for it has been obtained, so it is now operational for plasma tests. The E/F chord platform is shown in Figure 199.

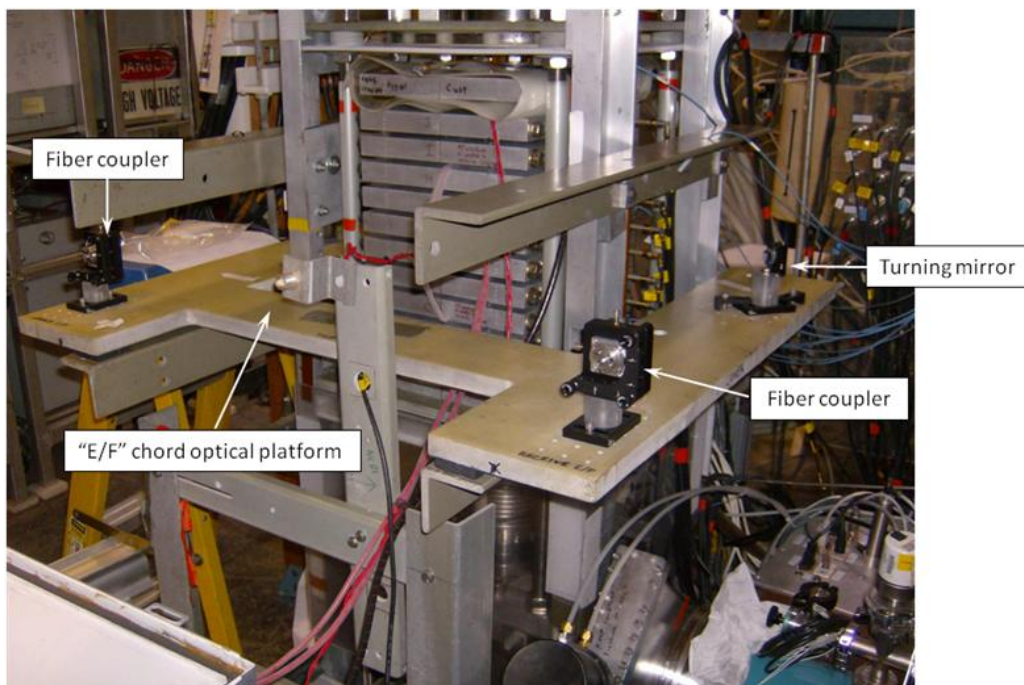


Figure 199. Optical platform for E/F diameter chord on MTF teststand—chord is now operational

Our plan at this time was to field three of the four chords at the T4 location (the ones with impact parameters of  $p = 0$  cm, 1.8 cm, 2.7 cm) and the single diameter chord ( $p = 0$  cm) at the E/F location for a total of four chords. This configuration would enable us to obtain density measurements in the formation region as well as in the liner on the same tests. When it is decided to field the fourth chord at the T4 location so that more complete density profile measurements can be obtained there, it is a simple matter to disconnect the fibers for the E/F chord and connect the fibers for the fourth T4 chord to bring the latter into the system. Probing the plasma at a single axial location inside the liner with four different beam impact parameters should enable us to obtain time-dependent density profile information via Abel and tomographic inversion techniques that have been previously used on other experiments with a similar interferometry apparatus.

In summary, we are now ready to field all four chords of the MTF fiber-probe interferometry system to utilize its full capabilities. In addition to probing a diameter chord through the formation region, as has been done before, we are now able to perform measurements with all four chords at a single axial location through the mock liner assembly. This feature will enable



us to obtain important information pertaining to plasma density profiles, FRC symmetry and rotation, and FRC lifetime data when the plasma is under conditions corresponding to a liner implosion experiment.

### 3.2.1.2 Data Acquisition and Other Diagnostics

#### 3.2.1.2.1 *Fiber Array Diagnostic*

For most of the duration of the plasma testing, we have fielded arrays of fiber optic probes with photodetectors at various axial positions within the experiment. These probes give information about passage of the plasma in translation and time of ionization in the formation region.

We have performed calibrations of a few photo detector systems to more fully determine light emission levels generated from FRCHX. For example, within the FRC formation region we have 10 similar optical fiber probes, each located within a theta coil segment and “aimed” radially inward towards the experimental centerline, utilizing in-house-built amplified photo detectors. Also within the formation region we implemented two other fiber-optic light collection assemblies utilizing narrow band wavelength filters and commercial Hamamatsu PMT detectors. The calculated photo detector sensitivities for these fiber-optic systems are presented in Table 18 and Table 19.

Table 8. Camac crate photo detector sensitivities

Detector #	Sensitivity (V/ W)	Sensitivity (W / V)
A1	NG	NG
A2	5.70E+004	1.75E-005
A3	6.50E+004	1.54E-005
A4	6.00E+004	1.67E-005
A5	6.30E+004	1.59E-005
A6	5.90E+004	1.69E-005
A7	5.50E+004	1.82E-005
A8	5.50E+004	1.82E-005
B1	6.40E+004	1.56E-005
B2	6.10E+004	1.64E-005
B3	5.70E+004	1.75E-005
B4	NG	NG
B5	5.90E+004	1.69E-005
B6	7.70E+004	1.30E-005
B7	7.70E+004	1.30E-005
B8	NG	NG

Table 9. Hamamatsu PMT 1 through PMT 5 sensitivities

PMT #	3 V bias	4 V bias	5 V bias	6 V bias	7 V bias	8 V bias	8.5 V bias	9 V bias
	K (W/V)	K (W/V)	K (W/V)	K (W/V)	K (W/V)	K (W/V)	K (W/V)	K (W/V)
1	6.0E-05	6.7E-06	1.3E-06	4.0E-07	1.6E-07	5.7E-08	3.7E-08	empty
2	1.9E-05	3.5E-06	7.3E-07	1.9E-04	7.1E-08	2.4E-08	empty	1.1E-08
3	2.9E-05	3.2E-06	7.1E-07	1.6E-07	5.0E-08	1.9E-08	1.2E-08	8.8E-09
4	1.6E-05	2.2E-06	4.0E-07	1.0E-07	3.3E-08	1.3E-08	empty	5.3E-09
5	1.7E-05	2.6E-06	5.3E-07	1.3E-07	4.5E-08	1.6E-08	empty	7.1E-09

We also determined the time response of the Hamamatsu PMT detectors. Using a TTL-type fiber optic transmitter with approximately 25 MHz response the detector output “1/e” time response and bandwidth were calculated to be 430 ns (814 KHz) and 230 ns (1.5 MHz) when driving 1-

M $\Omega$  and 5- $\Omega$  loads, respectively. A deconvolution algorithm was used to correct for the detectors' bandwidth response using the formula  $V = V_{\text{raw}} + \tau * V_{\text{raw}} / dt$ . Here,  $\tau$  is defined as the e-fold time for the output signal voltage level to change by a factor of 2.718. The plot overlay for  $V_{\text{raw}}$  and  $V$  is shown in Figure 200. It has been suggested this algorithm be incorporated into the LabVIEW auto post-processing routines.

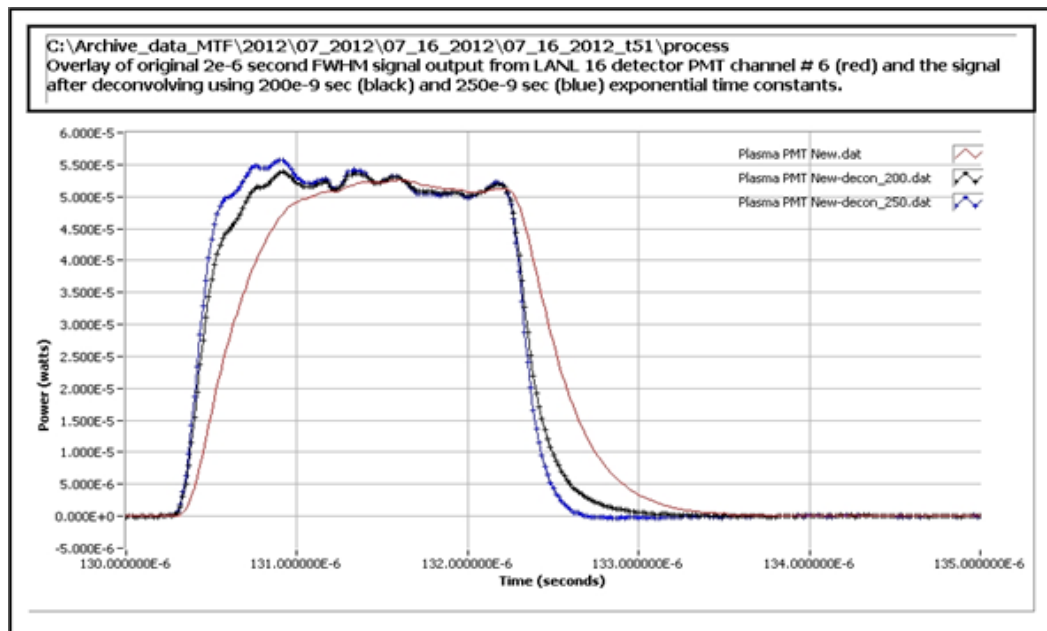


Figure 200. Plot overlay of the PMT signal before and after deconvolution

We implemented two more fiber optic light collection systems into the FRCHX experimental assembly. One such system uses two machined fiber holders, each containing two fibers. These fibers have 400- $\mu\text{m}$ -diameter core, radially positioned just outside the quartz tube for maximum light collection and orientated to view the experimental axial centerline. For most shots to date we have been fielding one pair of fibers with a Hydrogen/ Deuterium alpha ( $H_{\alpha}$ ) and beta ( $H_{\beta}$ ) filter (656 nm and 486 nm, respectively), while the other pair of fibers has only been filtered with a neutral density filter. A typical plot overlay of the emission light from the  $H_{\alpha}$  and  $H_{\beta}$  fibers is as shown in Figure 201. More work is needed to further post-process these signals to determine the FRC plasma temperature.

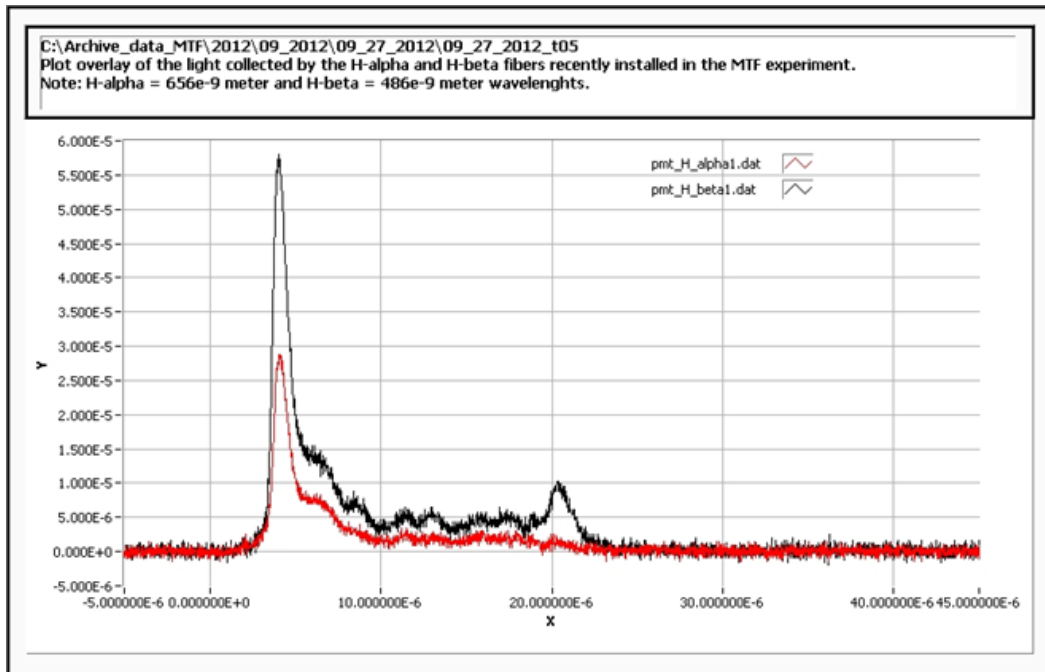


Figure 201. Plot overlay of the H $\alpha$  and H $\beta$  signals from FRCHX test

The other fiber optic light collection assembly involves eight fibers installed in a fixture such that each fiber is viewing a separate and distinct radial chord through the vacuum chamber. The collected light from each fiber is passed through a 546 nm narrow wavelength filter prior to collection by a Hamamatsu PMT-type detector. The purpose of this chord array is to process the eight channels of emission data using an Abel inversion algorithm so that the resultant emission is expressed as function of plasma radii. Figure 202 and Figure 203 are plot overlays of the emission light collected by each of the chord channels. For the test shown, the chord array was placed just above the J segment.

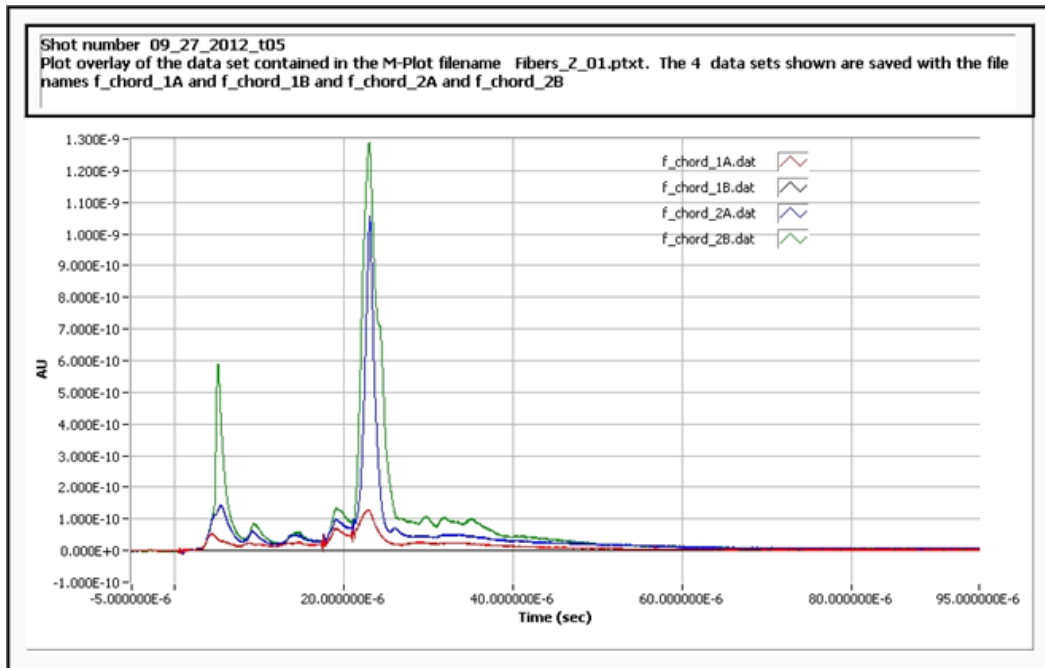


Figure 202. Plot overlay of the emission light collected by chords 1 through 4

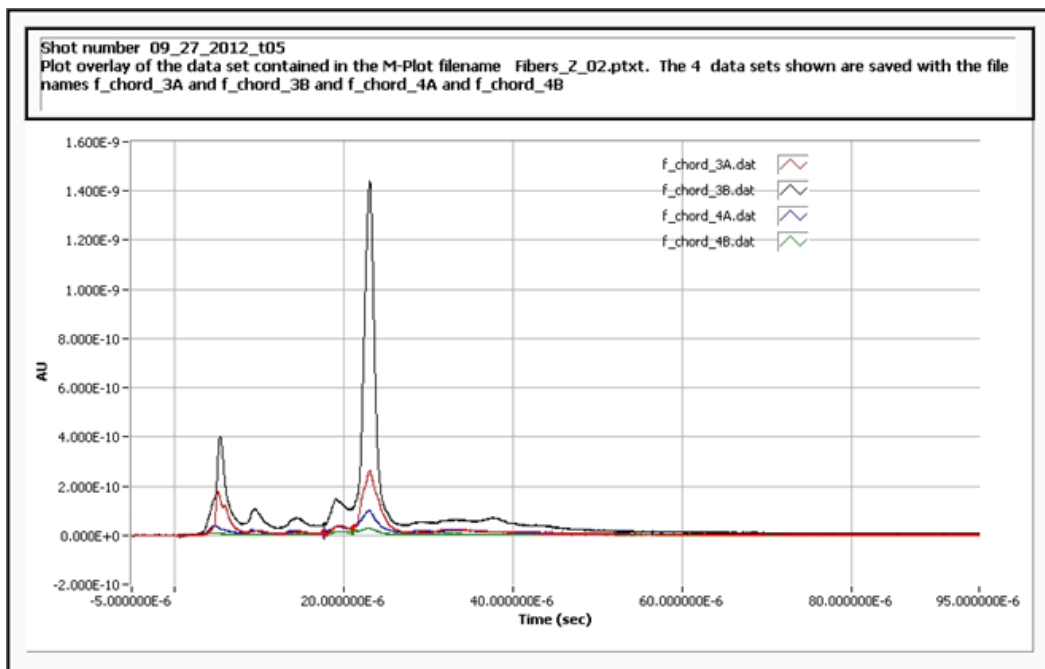


Figure 203. Plot overlay of the emission light collected by chords 5 through 8

Table 20 shows the Chord number, PMT number, and chordal length.

Table 10. Chordal length for each of the PMT data channels

Chord #	PMT #	chordal length (cm)
1A	9	7.5
1B	10	9.7
2A	11	10.8
2B	12	11.1
3A	13	10.9
3B	14	9.9
4A	15	8.1
4B	16	6.2

### 3.2.1.2.2 Flux Exclusion Radius Determination

The FRCHX experiment forms a plasma within a region of space filled initially with a nearly uniform magnetic field. The plasma conductivity acts to push out (exclude) magnetic flux injected in from the theta coils if its conductivity is high enough (or equivalently, its skin depth is small enough over the flux injection time). Typically, plasmas that are more conductive will have flux exclusion radii (FER) larger than plasmas with lower conductivity. One measure of the “robustness” of the plasmas generated during the FRCHX experimental effort is the FER for different shot conditions. Originally, the calculation of the FER was performed days after the shot events, it would be desirable to shorten this time period so that the calculated radius info is available within a few minutes after the shot. Such a calculation would be incorporated into the data acquisition program for near real-time processing and display after the FRCHX shot.

The flux exclusion radii formula can be derived if we first consider the total magnetic flux initially contained within the vacuum quartz tube given by:

$$\phi_{Tv} = \pi R_T^2 B_{Tv},$$

where  $R_T$  is the quartz tube inner radius and the vacuum field,  $B_{Tv}$ , is uniform and measured during vacuum discharge shots.

For a similar type shot but with a plasma (flux exclusion radius =  $R_X$ ), the total magnetic flux contained within the vacuum, outside the plasma, is given by

$$\phi_{TP} = \pi(R_T^2 - R_X^2)B_{TP},$$

where  $B_{TP}$  is the flux density in the vacuum outside the plasma as measured with a B-dot probe. The total flux is measured with a flux loop.

Taking the ratio of the total magnetic flux from the vacuum and plasma shots we obtain

$$\frac{\phi_{TP}}{\phi_{Tv}} = \left(1 - \frac{R_X^2}{R_T^2}\right) \frac{B_{TP}}{B_{Tv}}.$$

Rearranging and solving for  $R_X$  we obtain

$$R_X = R_T \sqrt{1 - \left(\frac{\phi_{TP}}{\phi_{Tv}}\right) \left(\frac{B_{Tv}}{B_{TP}}\right)}.$$

We implemented a computer program to calculate the flux exclusion radii that can also be executed by the main data acquisition program.

Active integrators, also became fully operational. They are now used with B-dot and flux-loop magnetic probes. They allow, for the first time, full recordings of magnetic field and flux for the entire time history of a shot (ms duration to allow the Guide/Mirror field to soak in). As a result, we have been able to automate the calculation of excluded-flux radius for the FRC. The current version of the integrators has fidelity over time scales up to 10 ms.

We also developed a new calibrator setup for the side-on fiber-optic probe array. Each fiber in the lower part of the array is threaded through a cavity drilled through each Theta-coil segment, and the ends are located approximately 3 in. from the quartz tube. The upper fibers are held in a fixture that ensures their ends are the same distance from the tube as the lower fibers. The acceptance angle of the fibers is approximately 3°. The fiber output is monitored by fast photodiodes, which are red sensitive. The signals are amplified by a factor of 10, and the amplifiers have a 14 MHz frequency response. There are currently 11 fibers in the array—8 in the theta-coil section (segments A, C, D, E, F, G, H, and J), one at the T0 location, one at T2, and one at the upper flange.

### 3.2.2 Gas Puff System

One of the potential issues with static gas prefill for FRC formation is that there is a significant mass of neutral gas surrounding the FRC plasma. Furthermore, the plasma must transport intact through the translation region and into the capture region within the liner. Since the extra gas (not used to form the plasma) is, in general, un-ionized, the closed magnetic field lines associated with the FRC pass readily through it, and the plasma undergoes plasma-neutral collisions that very likely cause loss of plasma internal energy. If the FRC could be created from a limited-extent gas, the neutral background would be reduced. That was the primary goal of the gas puff hardware implementation. Secondly, equipotential rings, which we envisioned implementing to help control the development of the  $n = 2$  rotational instability, would be problematic with a background gas. That is, the desired quasi-static potentials on the rings would almost certainly cause breakdown in the ambient neutral gas.

Therefore, we designed gas puff hardware that allows puffed gas injection into the formation region. The concept of operation is shown in Figure 204.

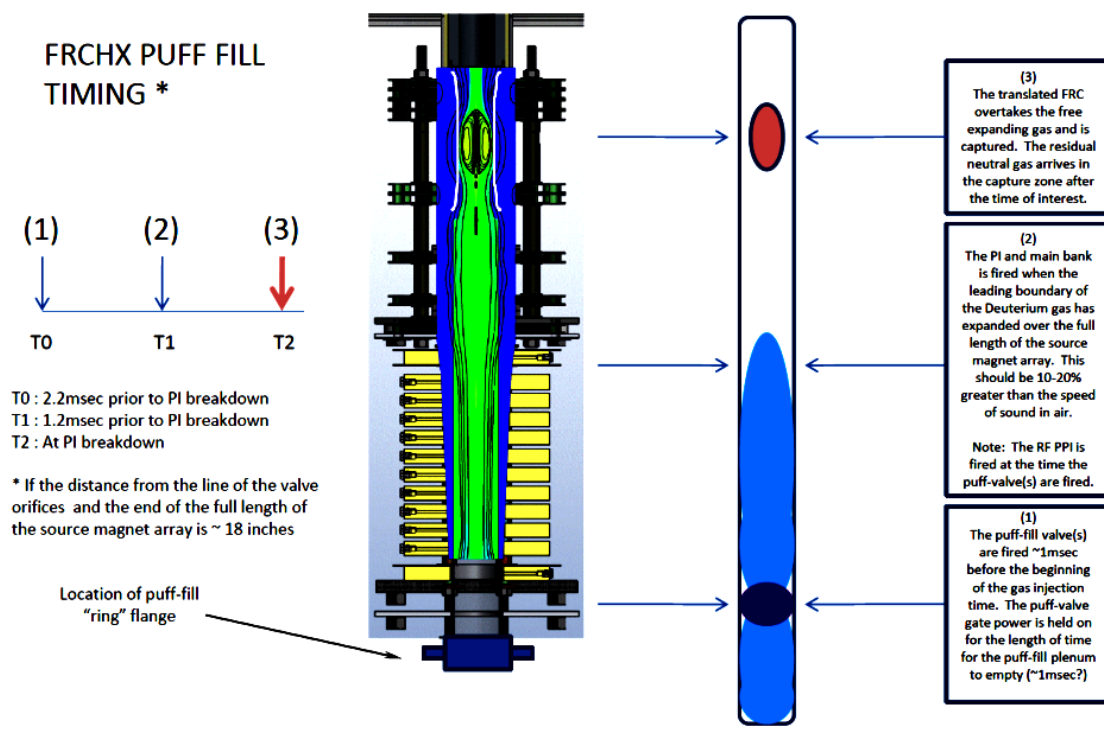


Figure 204. MTF FRCHX puff fill scheme



The puff-fill is based on an implementation of a similar system on the University of Washington (UW) TCS experiment that has generally improved lifetime performance. The FRCHX gas puff implementation uses two Parker Series 99 “extreme performance” valves. The Series 99 valves are made of 316L stainless steel with vespel and silver plated seals. A two-channel valve driver based on the UW TCS experiment design will be used to switch on the solenoid coils opening and closing the valves on a fiber optic command (see Figure 205). The general idea concerning the operation of the FRCHX puff-fill is to open the puff valves (located at the bottom of the vacuum stand just below the theta coils) with the correct timing so that the deuterium gas expands into the vacuum vessel; and, as the gas boundary expands across the theta coils the experiment fires and produces a translating FRC plasma that overtakes the expanding residual gas and translates into the capture region.

The Series 99 valves are operated at voltages much greater than their rated operating voltage but only for milliseconds, so up to a certain limit the valve solenoid coils will tolerate the higher applied voltages. There is protection circuitry built into the puff-fill driver circuit to prevent the greater voltages from damaging the puff-fill solenoid coils by overheating.

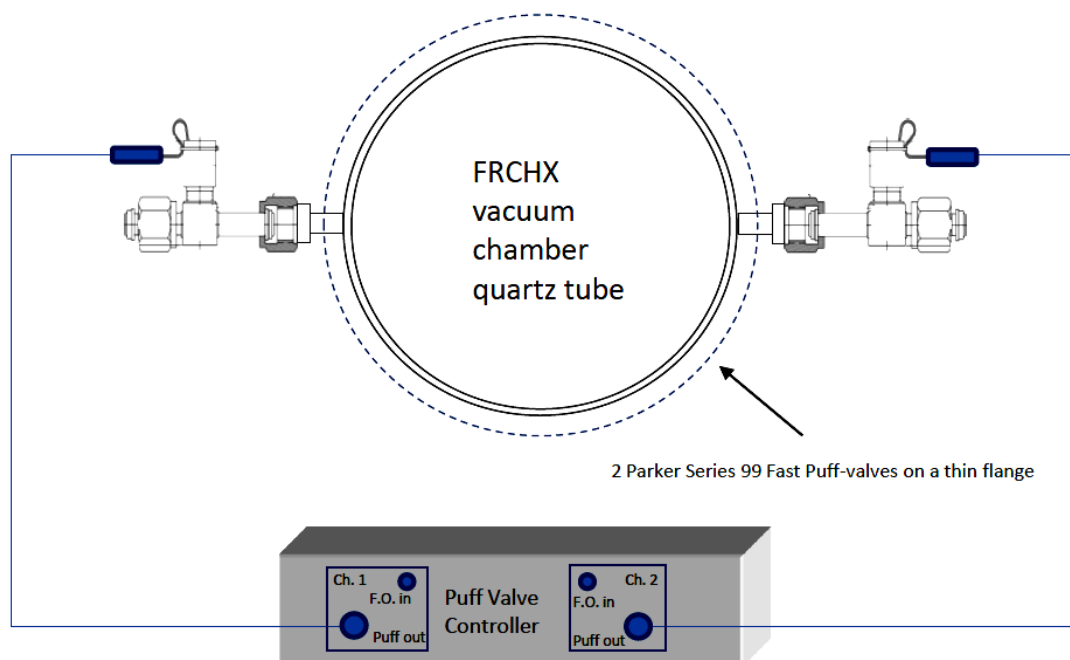


Figure 205. MTF puff-fill two-channel driver box

A teststand was designed and constructed to simulate the FRCHX vacuum chamber and to allow characterization of the puff-fill system separate from the FRCHX experiment. The design consists of a high-pressure gas plenum that is contained by a puff valve and a full-scale mock-up of FRCHX. After the puff valve opens, the gas enters the evacuated region where a gas front moves upward along the multi-sectioned representation of the actual experiment. A side-by-side comparison is shown in Figure 206. Timing between gas injection and subsequent liner implosion (with Shiva Star) is critical to ensuring that density and other properties of the plasma in the liner are optimum and that the gas has not spread throughout the vacuum volume to a level sufficient to cause flashover. This timing delay interval is extrapolated from a series of tests with the gas-puff hardware teststand.

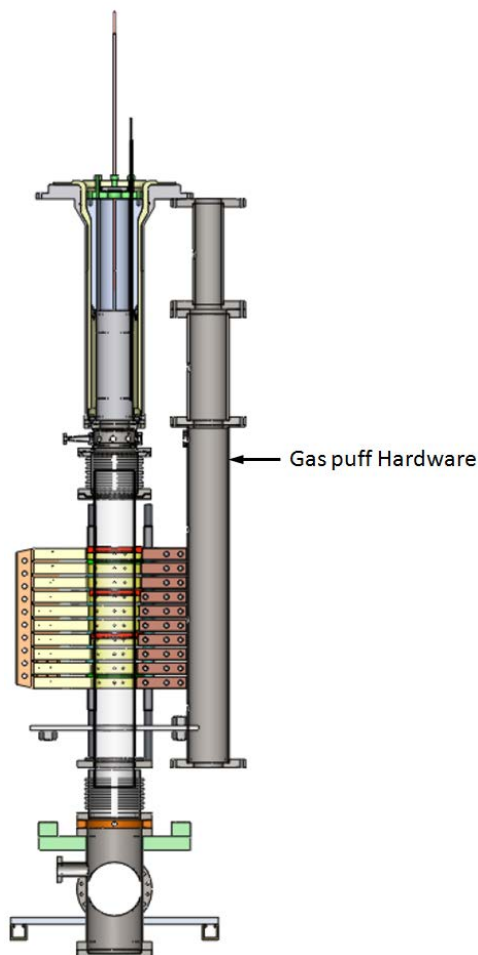


Figure 206. Comparison of gas puff hardware and actual experiment

Investigation of the gas front in the vacuum region is accomplished by monitoring the transient gas density simultaneously at six axial locations as shown in Figure 207.

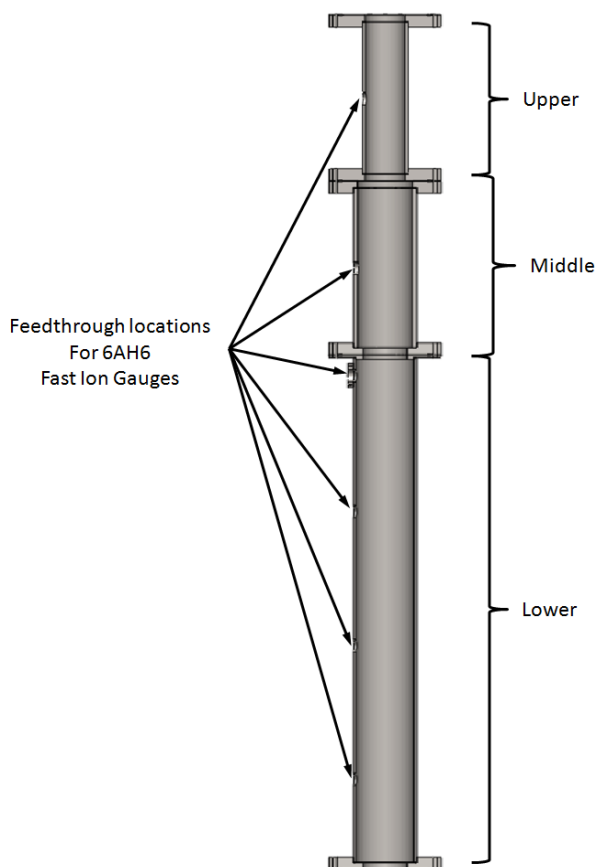


Figure 207. Locations of fast ion gauges for teststand mock-up

Each gauge in the lower section is used to provide data with regard to timing of the gas front with respect to the coils and subsequent discharge, while the gauges in the upper and middle sections measure the arrival of gas in the middle of each respective section. The gauges have vacuum-tight mounts and are oriented for optimum flowthrough. Pressures start in the high  $10^{-5}$  Torr range and end in the sub-Torr range after gas injection.

The gauges are modified 6AH6 pentode tubes. These particular pentodes were used successfully by AFRL on a previous experiment in which cylindrical gas shells were formed in electrode gaps. Past experience has showed that it is possible to obtain useful data with these pentodes. The interior of the pentode is open to the vacuum region between the inner and outer conductor and is used as a pressure gauge.

The pentode's glass tube is removed from the gauge while in an oxygen-free atmosphere. The glass is removed by scoring a circumferential line around the glass tube, approximately two-thirds down from the top, and then tapping the glass until it breaks. Approximately 100 6AH6 pentodes are on hand; only tubes that are to be used immediately have their glass tubes removed, and they are stored in either an inert gas atmosphere or vacuum until use.

A control circuit is used to monitor the 6AH6 gauges. The circuit shown in Figure 208 measures the ion and emitter current data.

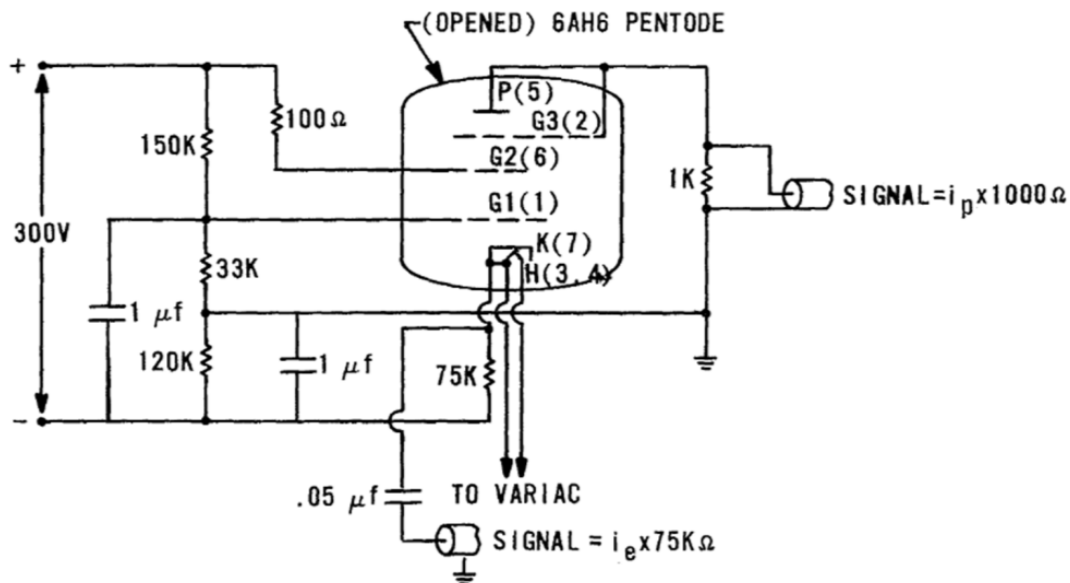


Figure 208. 6AH6 fast ion gauge control circuit

The numbers in parentheses after the tube emitter, collector, gate, and heater symbols represent the tube pin numbers;  $i_p$  is the collector ion current (proportionate to gas density);  $\Delta i_e$  is the change in the cathode emission current (monitored with a 50 ms time constant when connected to a 1 MΩ termination). Cathode emission current must be held constant for the pentodes to operate properly as ion gauges. However, the space-charge-limited cathode current increases as gas density increases.

Commercial, off-the-shelf (COTS) 8 in. MDC vacuum flanges, feedthrough ports, and tubing were machined in-house. The welding was done by a local vendor and the sections were cleaned and assembled in-house. The assembly consists of a high-pressure gas accumulator that is

contained by two gas puff valves and a full scale mock-up of the FRCHX represented by the three flanged sections. The mock-up contains the lower chamber (8 in Tee), bellows, mechanical gate valve, and plumbing hardware needed to pump down the assembly using a turbo pump. The setup was assembled and leak checked in a side lab. A side-by-side comparison of the designed setup and the actual setup is shown in Figure 209. Each position is referenced relative to the opening of the gas puff.

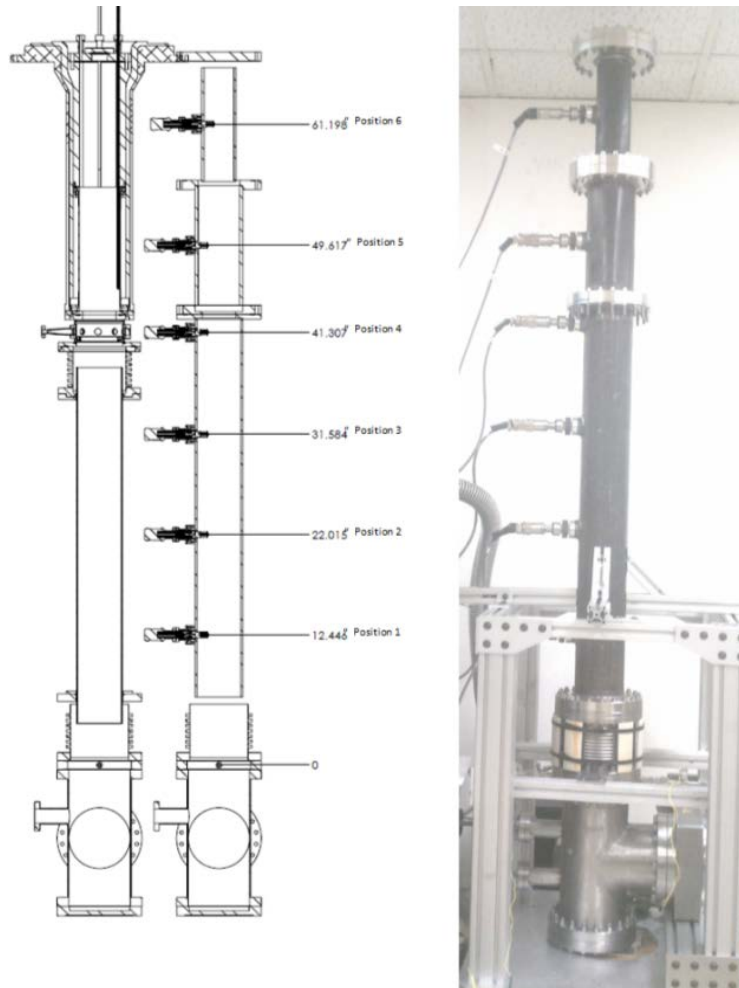


Figure 209. Comparison of the designed and actual gas puff hardware gas puff experiment

Initial timing tests varied the accumulator pressure and pulse width while maintaining consistent pulse amplitude of the gas puff valve. The initial puffs were set to 50 V driver voltage. Figure 210 shows the results of a 12.2 PSIA accumulator fill with a 5 millisecond pulse width. The main area of interest is the theta coil region of the experiment. This region is represented by positions

1, 2, and 3 on the teststand. When position 3 is in the 50 mTorr range the gas in position 6 needs to be near zero. The pressure at positions 1 and 2 should be approximately 100 mTorr. The red vertical line represents the time when Position 3 is at 50 mTorr. Positions 1 and 2 are fine with pressures of 75 mTorr and 55 mTorr, respectively; however, the pressure at Position 6 is too high at 15 mTorr.

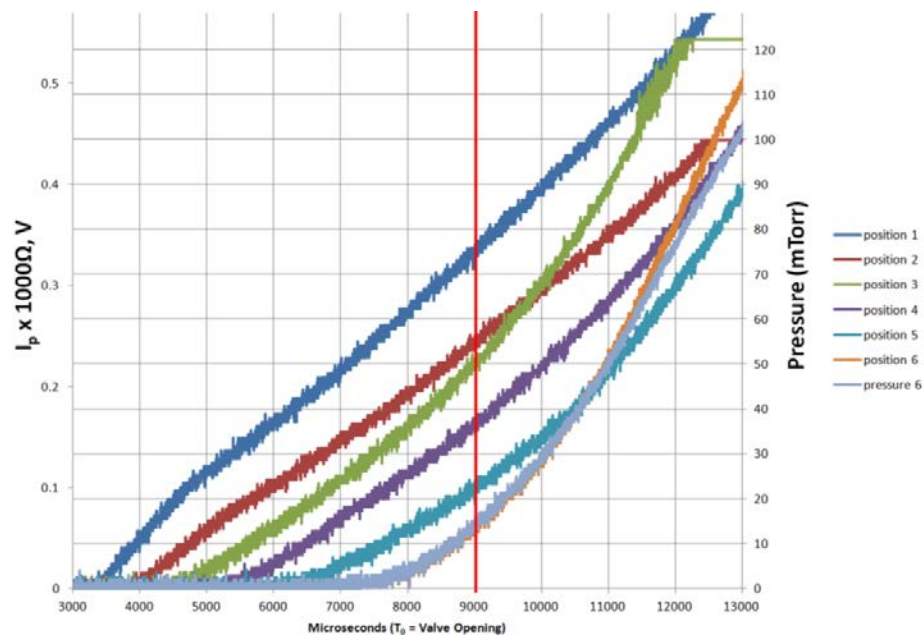


Figure 210. 12.2 PSIA, 5 ms gas puff pressure data

The thought was to try a lower pressure to see if the situation was exacerbated. Figure 211 shows the results of the lower accumulator gas fill pressure of 5 PSIA and a 5-ms pulse width. Once again, Positions 1 and 2 are fine with pressures of 65 mTorr and 50 mTorr, respectively; however, the pressure at Position 6 is too high at 30 mTorr.

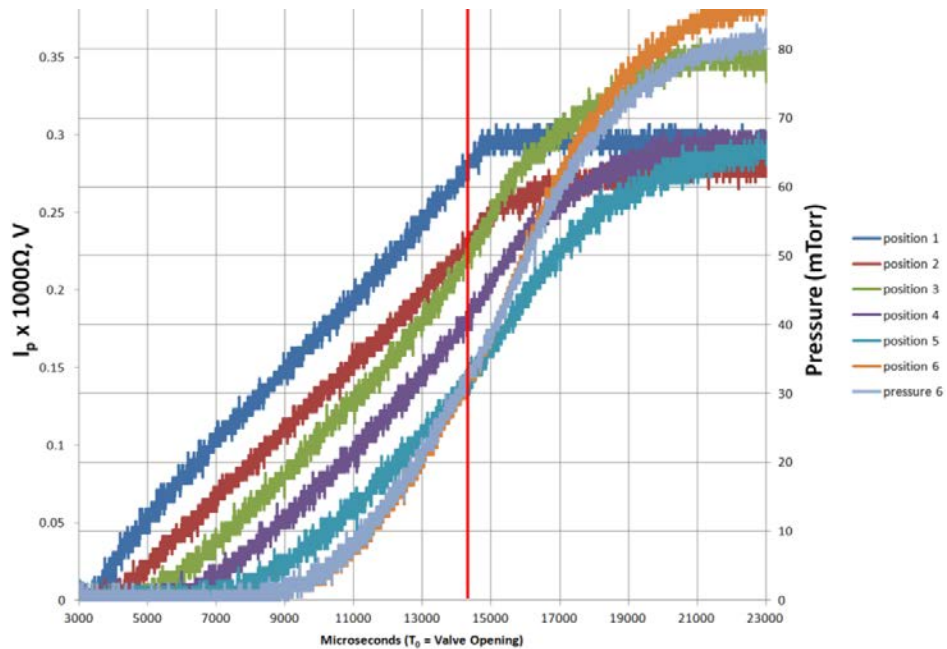


Figure 211. 5 PSIA, 5 ms gas puff pressure data

The next step was to try a higher pressure to see if the timing improved. Figure 212 shows the results of the higher accumulator gas fill pressure of 50 PSIA and a shorter 2.5 ms pulse width. Positions 1 and 2 are fine with pressures of 105 mTorr and 70 mTorr, respectively; the pressure at Position 6 is ideal with no gas response present until 250 microseconds later.

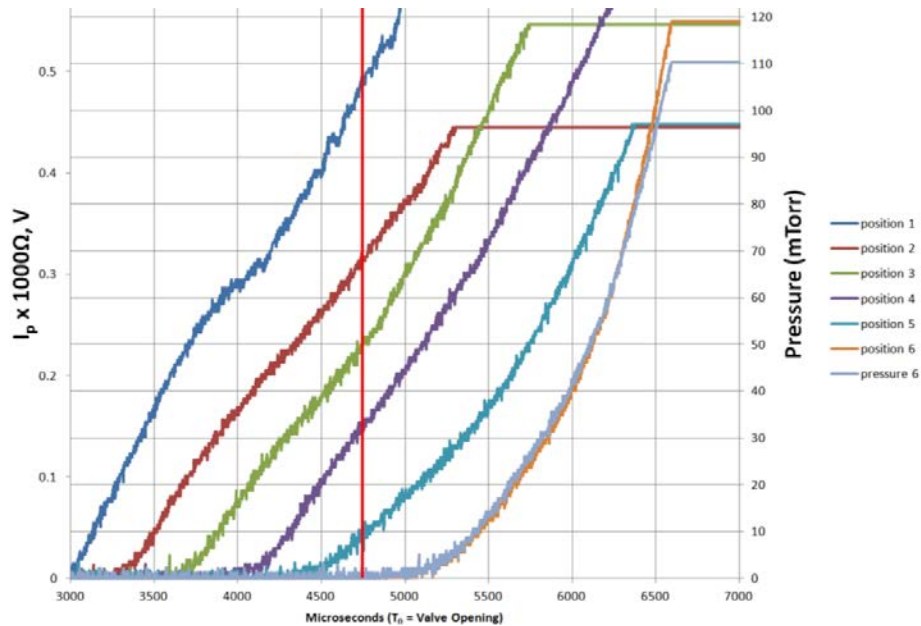


Figure 212. 50 PSIA 2.5 ms gas puff data

A test with two gas puff valves was also done, but the results were worse than with one and therefore abandoned. Two gas puff valves may be revisited at a later time if it is deemed possible to operate with a higher pulse amplitude and lower pulse width.

The next change was to raise the pulse amplitude and shorten the pulse width. Attempts to modify the circuit were attempted, but were unsuccessful. The ability to have an adjustable output voltage up to 100 V, while maintaining a regulated voltage of 5 V for the integrated circuits (ICs), turned out to be impractical. The only solution was to have independent power supplies. Three other power supplies were added. One was a 5 volt supply for the ICs and the other two were 24 volt supplies, in addition to the previous 48 volt supply, for a total pulsed output of 100 volts. When these modifications were complete, testing resumed to try to reduce the differential pressure between Positions 1 and 3, while maintaining no gas pressure in Position 6.

Repeatability tests with slightly less accumulator pressure and the lowest possible pulse width were done to see if the jitter was acceptable and to see if the differential pressure between Positions 1 through 3 could be lowered. Figure 213 shows the results of the lower accumulator gas fill pressure of 40 PSIA and a shorter 2.0 ms pulse width. This was shortest possible pulse width the gas puff valve was able to reliably operate at. Positions 1 and 2 are fine with pressures of 105 mTorr and 70 mTorr, respectively; the pressure at Position 6 is ideal with no gas response present until 100 microseconds later. This is a slightly tighter grouping of pressures relative to the 50 PSIA, 2.5 millisecond pulse widths done earlier. The jitter of the ion gauge responses seem to be negligible and the repeatability seems acceptable.



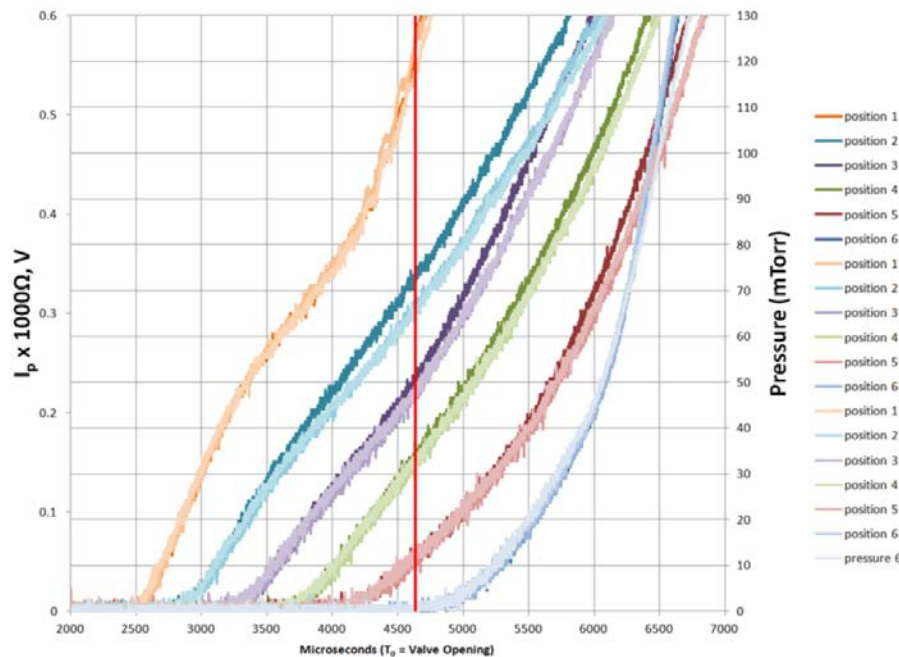


Figure 213. Three consecutive 40 PSIA, 2.0 ms gas puffs

In the figure, each color group represents a position, while each shade of the color group represents one of three experiments conducted. The red vertical line represents the time when Position 3 is at 50 mTorr. Positions 1 and 2 are fine with pressures of 105 mTorr and 70 mTorr, respectively; the pressure at Position 6 is ideal with no gas response present until 100  $\mu$ s later. This is a baseline for determining whether a shorter pulse width with a higher voltage would help the gas distribute more evenly and show better response times of the fast ion gauges. The following series of tests was done with a 100-V amplitude and shorter pulse width.

Figure 214 shows the results of a 40 PSIA accumulator fill with a 750- $\mu$ s pulse width at 100 V. Once again, this was the shortest possible pulse width the gas puff valve was able to reliably operate at. Position 1 is high with a pressure > 130 mTorr while position 2 is inadequate with a pressure of about 75 mTorr. The pressure at Position 6 is ideal with no gas response present until about 400  $\mu$ s later. The main concern, again, is the amount of jitter between experiments. We thought that the solenoid was not actuating fully and that the open time varied as a result. To have a fully activated solenoid, the pulse width was increased for the remaining gas puff tests.

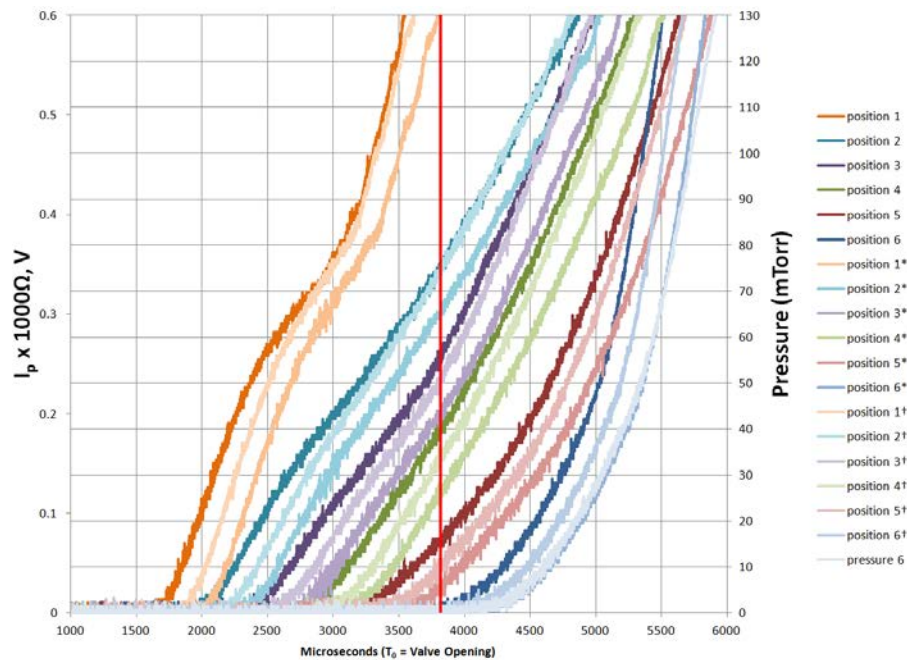


Figure 214. Three consecutive 45 PSIA, 750  $\mu$ s, 100 V gas puffs

The next thought was to try a slightly lower pressure and a slightly longer pulse width. Figure 215 shows the results of 40 PSIA, 1 ms pulse width at 100 V. Positions 1 and 2 are fine with pressures of 95 mTorr and 65 mTorr, respectively; the pressure at Position 6 is ideal with no gas response present until about 200  $\mu$ s later.

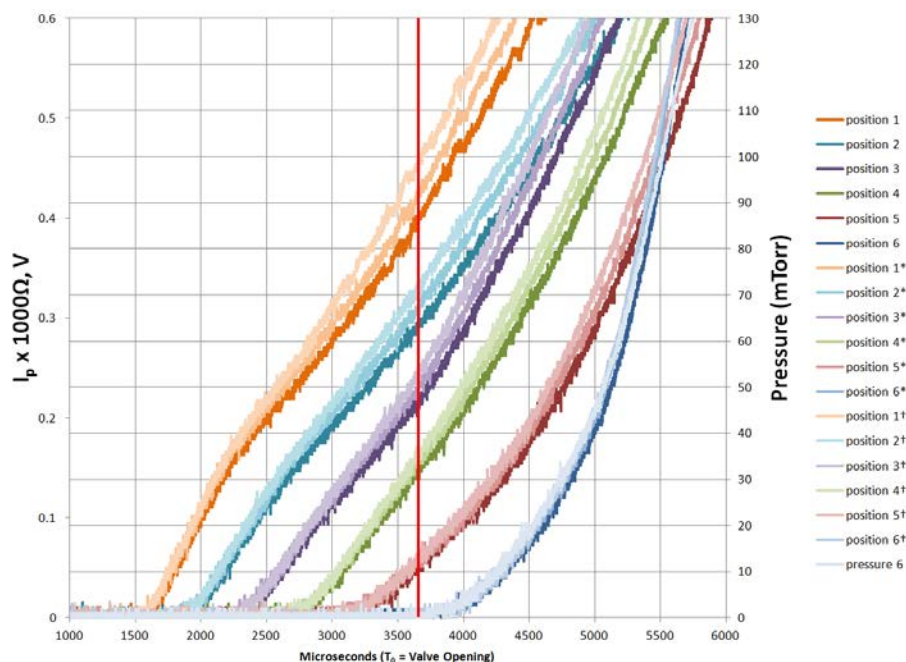


Figure 215. Three consecutive 40 PSIA, 1 ms, 100 V gas puffs

The next step was to try a lower accumulator pressure to see if the differential pressure improved. Figure 216 shows the results of the lower accumulator gas fill pressure of 35 PSIA, 1 ms pulse width at 100 V. Positions 1 and 2 are fine with pressures of 90 mTorr and 70 mTorr, respectively; the pressure at Position 6 is ideal with no gas response present until 250  $\mu$ s later.

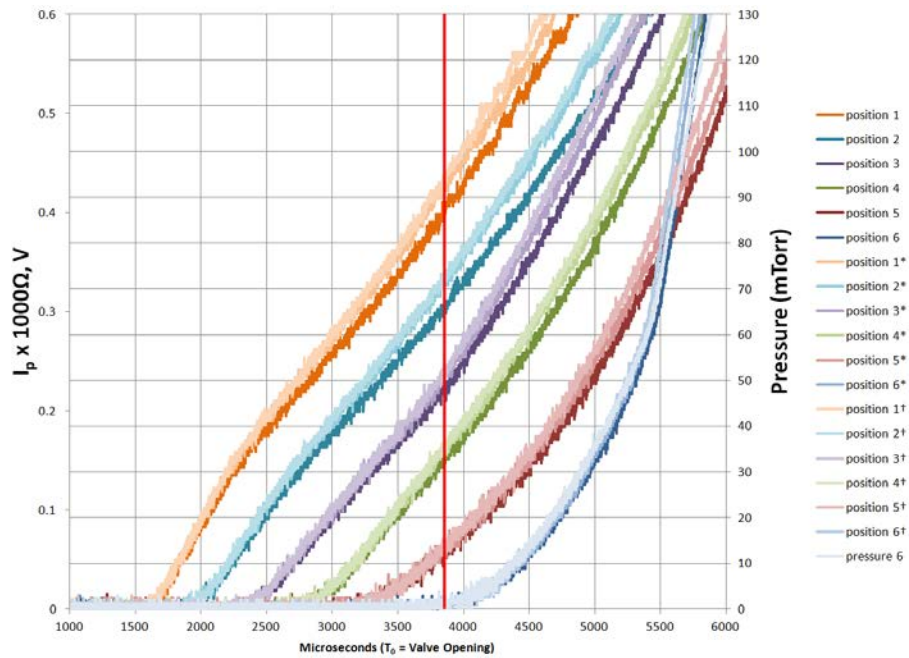


Figure 216. Three consecutive 35 PSIA, 1 ms, 100 V gas puffs

Again, a lower pressure was tried to see if the differential pressure improved. Figure 217 shows the results of the lower accumulator gas fill pressure of 30 PSIA, 1 ms pulse width at 100 V. Positions 1 and 2 are fine with pressures of 90 mTorr and 70 mTorr, respectively; however, the pressure at Position 6 is starting to rise at this point in time and is not acceptable.

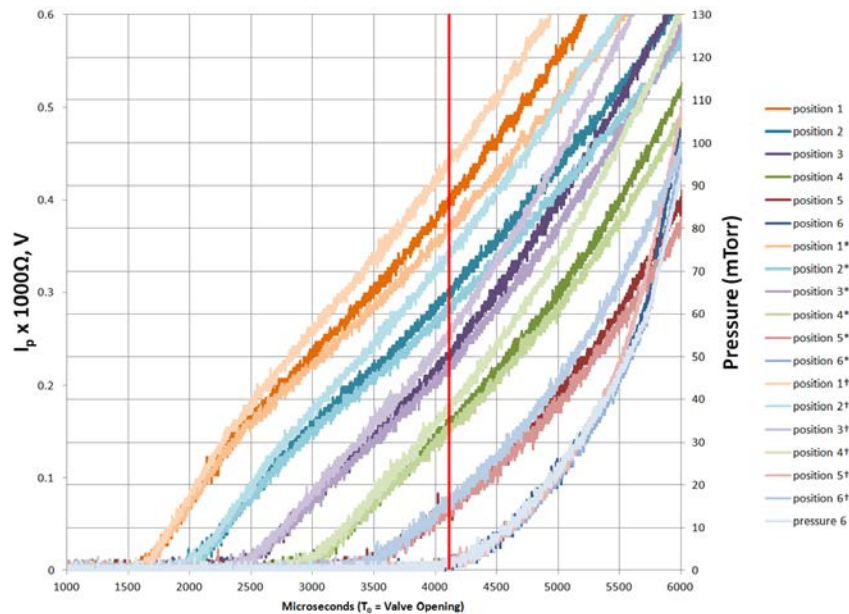


Figure 217. Three consecutive 30 PSIA, 1 ms, 100 V gas puffs

The gas-puff system that was tested on the teststand was moved into the high bay and installed on FRCHX. Appropriate plumbing and control systems were put in place to be fully compatible with existing plumbing and control. There were two main reasons for implementing gas puffing. First, there was concern about the effect of a large volume of neutral gas through which the FRC would have to pass en route from the formation region to the capture region. This gas could potentially quench the FRC plasma or collisionally slow it during passage – both causing enhanced flux decay prior to capture for compression. Second, we intended to implement equipotential rings DC biased to kV levels to attempt to control FRC rotation. Static gas fill at 50 mTorr would almost certainly break down in the field resulting from the biased rings. With the gas puffing properly tuned (i.e., proper delay, driver voltage, and plenum pressure), a dynamic fill of approximately 50 mTorr of deuterium could be delivered to the formation region with almost no neutral gas reaching the ring region. This strategy was tested off FRCHX, and it worked quite well. Photographs of the gas-puff driver electronics and their enclosure are shown in Figure 218 and Figure 2199, respectively.

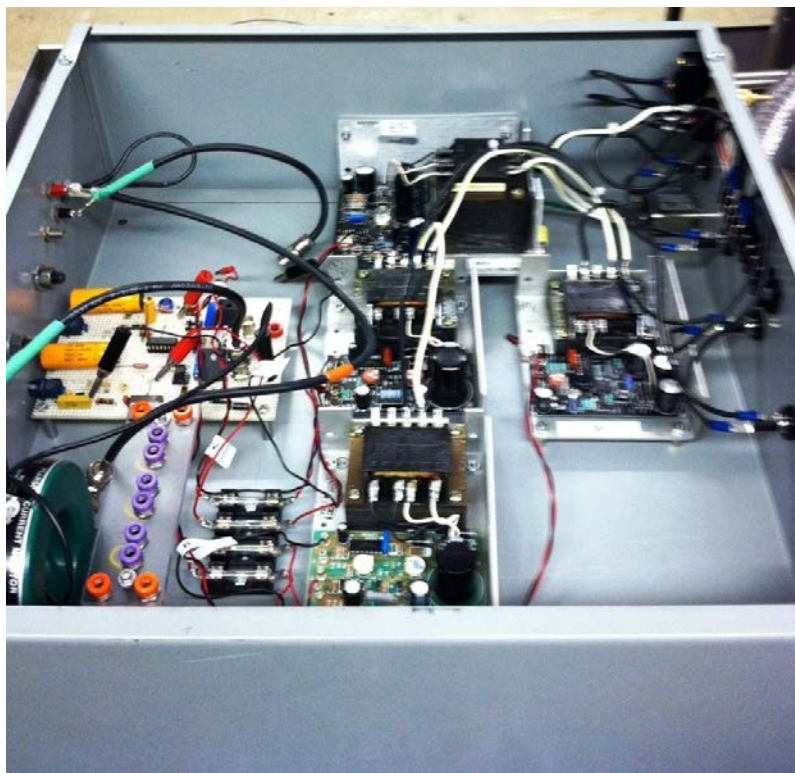


Figure 218. Gas-puff driver electronics





Figure 219. Gas-puff driver enclosure

Figure 220 shows the gas-puff valve assembly mounted on a ring prior to insertion into FRCHX; Figure 221 shows the valve on the experiment. Note that originally, we planned to drive two fast valves simultaneously, but as testing showed, one valve was adequate. One can see the blanked off port opposite the valve in the figures.



Figure 220. Puff-valve assembly



Figure 221. Puff-valve assembly mounted on the experiment

The gas puff valve driver was assembled in a noise resistant enclosure, as shown in Figure 222. The components consist of the gas puff valve driver circuit, a patch panel for selecting the output

voltage, a 5 V power supply for powering the driver circuit, and four 48 V power supplies for the output voltage.

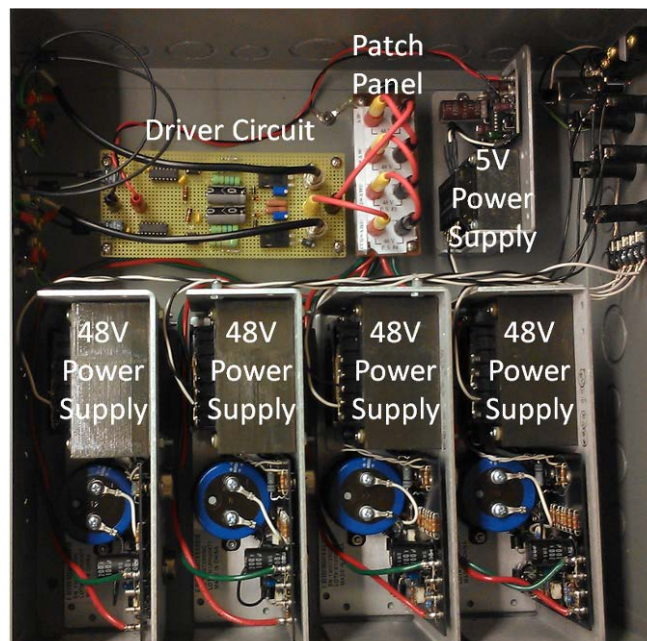


Figure 222. Gas puff valve driver enclosure

A schematic circuit of the driver is shown in Figure 223. The fiber optic input is first sent through an optical isolator to decouple the input and high voltage output. A 10-k $\Omega$  potentiometer is in series with a 2-k $\Omega$  resistor from the gate to the source of the 500-V MOSFET. The resistance discharges the 0.47  $\mu$ F coupling capacitor with a time constant ranging from 0.4 ms to 5.6 ms. The applied gate drive is approximately 8.3 V and the gate threshold is about 4 V. When the capacitor has discharged to about 4 V, the MOSFET turns off, independent of the optical input pulse length. Therefore, the length of the pulse to the valve is the lesser of the potentiometer setting or the optical input pulse.



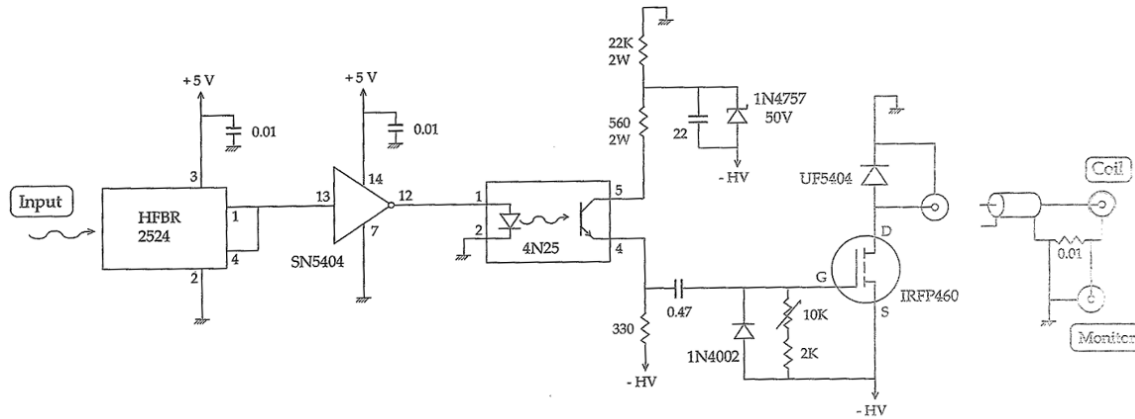


Figure 223. Gas puff valve driver circuit

The output voltage, -HV, can be selected as -48 V, -96 V, -144 V, or -192 V. A patch panel is used to jumper one, two, three, or all four of the 48-V power supplies in series. Each of the configurations is shown in Figure 224.

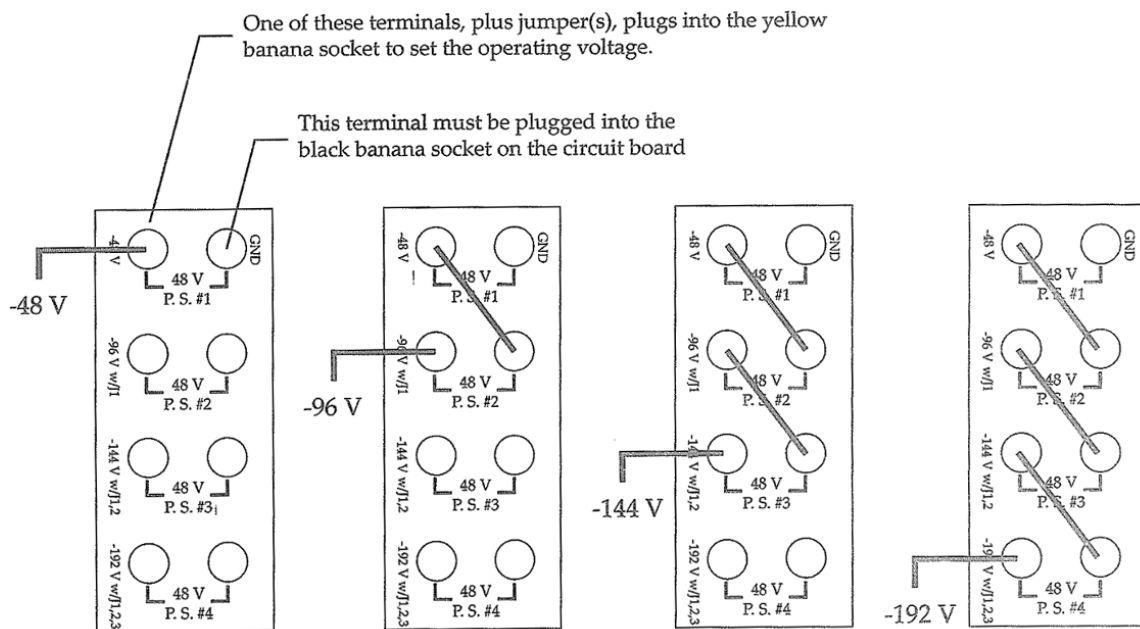


Figure 224. Power supply patch panel

Operation of the system was characterized with the test matrix shown in Table 11. The gas puff hardware operates reliably, is well-characterized, and is used routinely on FRCHX tests.

Table 11. Gas puff test matrix

Shot #	# of Solenoids	Pulse Width (ms)	Pressure (psig)	Voltage (V)
1	2	0.5	0.0	192
2	2	0.5	100.1	192
3	2	0.5	98.7	192
4	2	0.5	50.0	192
5	2	1.0	40.0	96
6	2	0.5	39.5	192
7	2	1.0	29.9	96
8	2	1.0	20.5	96
9	2	1.0	19.8	96
10	2	1.0	15.0	96
11	2	0.5	14.8	192
12	2	0.5	30.1	192
13	2	0.5	29.6	192
14	2	0.5	40.0	192
15	2	0.5	20.1	192
16	2	0.5	50.1	192
17	2	0.5	60.0	192
18	2	0.5	70.1	192
19	2	0.5	80.0	192
20	2	0.5	90.0	192
21	2	0.5	100.6	192
22	2	0.4	99.1	192
23	2	0.3	97.8	192
24	2	0.3	80.1	192
25	2	0.3	79.8	192
26	2	0.4	79.6	192
27	2	0.6	80.1	192
28	2	0.4	89.8	192
29	2	0.6	90.0	192
30	2	0.5	85.3	192
31	2	0.5	80.0	192
32	2	0.5	75.0	192
33	1	0.5	100.1	192
34	1	0.5	89.8	192
35	1	0.5	80.1	192
36	1	0.5	69.9	192
37	1	0.5	60.1	192
38	1	0.5	49.9	192
39	1	0.5	40.1	192
40	1	0.5	29.9	192
41	1	0.5	20.0	192

### 3.2.3 Preionization and Pre-Preionization

One of the issues with the present FRC formation is that the PI discharge, which produces an inductive azimuthal electric field, has difficulty ionizing the gas in the presence of the orthogonally directed (primarily in the axial direction) bias magnetic field that is needed to create the FRC poloidal flux. With the magnetic field, electrons that are born cannot travel unimpeded in the direction of the azimuthal electric field, because of the Lorentz force; they, instead, undergo quasi-circular orbits with a radius equal to the Larmor radius, until they suffer a

collision. That transverse magnetic fields inhibit electrical breakdown is well known, and in fact, it is used in magnetically insulated transmission lines.

In FRCHX, the polarity of the PI bank is such that its current creates a primarily axial magnetic field that opposes the existing bias magnetic field over its first half cycle. One would like for the gas to immediately ionize and become sufficiently conductive to impede diffusion of the entrained bias flux out of the plasma so that when reconnection occurs with the Main bank discharge the maximum amount of flux is trapped within the FRC, leading to relatively large excluded flux (or separatrix) radius and longer decay times. However, because of the bias field, gas breakdown is typically delayed until the PI magnetic field has effectively nulled out the bias field. Therefore, when ionization occurs, very little flux is available for trapping.

One thing that can be done – and has been done at other laboratories – to cause earlier breakdown during PI discharge, is to impose an RF electric field on the gas to enhance breakdown. Because of some success with this technique, we decided to implement it on FRCHX. Our first variant of an RF system was a long-pulse (1-ms to 10-ms) 1-kW system. It is described in Section 3.2.3.1.1. Later, it was suggested by Ed Ruden (AFRL) to try using a short, switched, charged cable transmission line to create a much higher-power transient RF pulse. We built and tested such a high-power RF (HPRF) system, and it is described in Section 3.2.3.1.2.

We also decided to examine the process of crossed-field gas breakdown using weakly-ionized plasma theory. The first attempt was dimensionless and done in an Excel spreadsheet. Based on the results, we developed a 2D cylindrically symmetric model for collisional ionization and diffusion model in FlexPDE<sup>®</sup>, a generalized partial differential equation solver. It used full tensor quantities for mobility and diffusion, and produced some interesting results. It is described in Section 3.2.3.2.

#### 3.2.3.1 Pre-Preionization Systems

Two varieties of RF electric-field pre-preionization have been developed and implemented. Chronologically, the first was a 1-kW long-pulse (1-10 ms) system patterned after a similar system developed previously. The second system was based on a high-power (> 1 MW) transient pulse formed by switching a charged cable transmission line. Each system is described below.

### 3.2.3.1.1 Long-Pulse RF

An RF pre-preionization system (applied prior to the main pre-ionization discharge) has been implemented for the FRCHX experiment. The present 46 MHz is based on a system used on previous experiments such as LSX and TRAP at the University of Washington, using a transmission-line-like capacitive coupling to the plasma that is terminated into a 50- $\Omega$  load resistor. The resistor is capable of the heat dissipation necessary for the duty cycle (2.5-kW operation at 10-ms pulse width). The system uses a large parallel plate capacitor configuration attached to the quartz vacuum chamber to apply a transverse (to the chamber axis) RF electric field. 46 MHz was identified as the optimal frequency for ionization. An important feature is a 50- $\Omega$  load during the deuterium gas breakdown. A schematic of the RF pre-preionization system is shown in Figure 225.

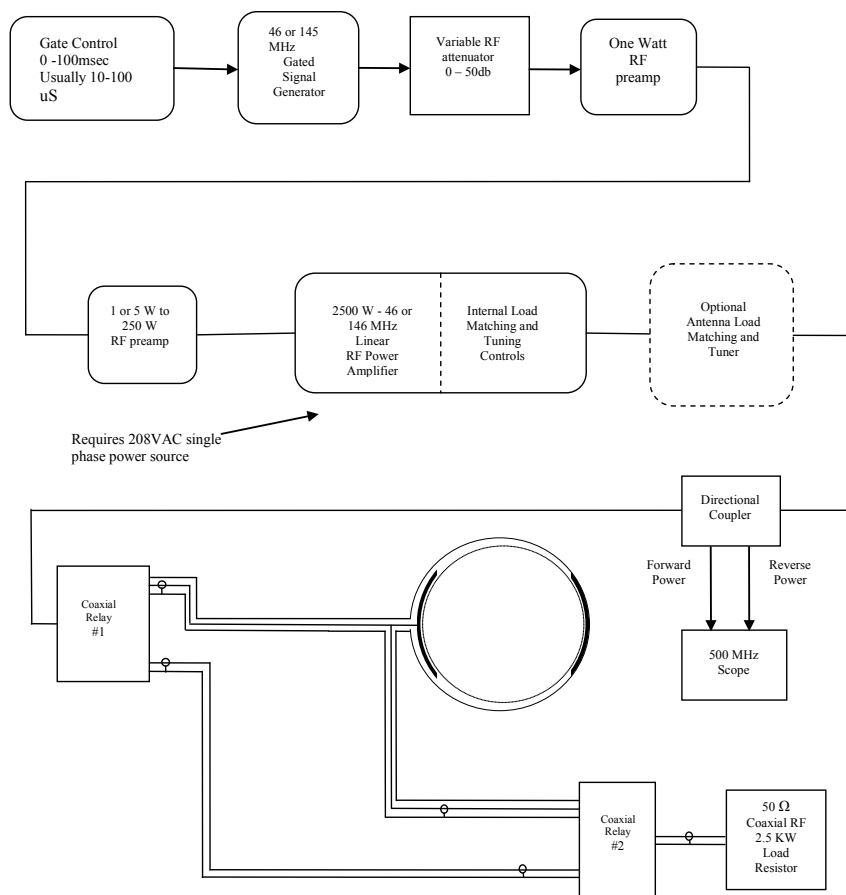


Figure 225. 46 MHz or 146 MHz LPRF pre-preionization system for MTF FRCHX

The RF system can be operated at a pulsed duration of up to 10 ms with a duty factor of 2% or less. When placed on the experiment the system must be load-tuned into an actual gas-plasma with the system being pulsed from 1 to 10 ms at a repetition rate of one pulse per second. If plasma formation does not occur, the tuning process is stopped after 3 minutes and not resumed for at least an hour. By default, the RF power amplifier is connected to a 50- $\Omega$ , 2500 W CW load resistor. The system once calibrated can be switched into the plasma chamber load just prior to each test shot and be switched back to the dummy load immediately after the test shot.

Several critical improvements were made to the long-pulse RF (LPRF) PPI system. In the first implementation, the quickest and easiest approach was taken to coupling the RF source into the deuterium gas. Electrodes were placed transverse to the vacuum quartz tube axis on opposite sides of the vacuum vessel quartz tube, which meant the RF electric field orientation was transverse to the direction of the magnetic field. This method of coupling was shown to work on previous experiments. However, the most appropriate direction for the RF E field is along the axis of the experiment, so that electrons are accelerated in parallel to the direction of the main B field, resulting in longer mean free paths and enhanced probability of collisionally ionizing the gas. Also with the RF coupling in the previous configuration, the means of matching the RF source to the experiment and plasma load was to treat the gas load as part of the transmission line; no provisions were made to match the transmission line to the experiment and gas-plasma load.

With the RF electric field applied along the axis, not only is it necessary to introduce a load-matching network on the experiment end due to the greater electrode gap distance that makes initial breakdown harder, but we can also now benefit from the much more efficient coupling of the transmission line and source, because they are well matched to the load. Figure 226 gives the overall plan of the modified configuration of the LPRF PPI system. The PIN Diode Fast Switch module can be bypassed to make the system operate in a 10-ms pulsed electron-seeding mode. In the fast switch trigger mode, the system is normally switched for a total time of up to 100  $\mu$ s with the RF diversion time as a variable internally set adjustment.

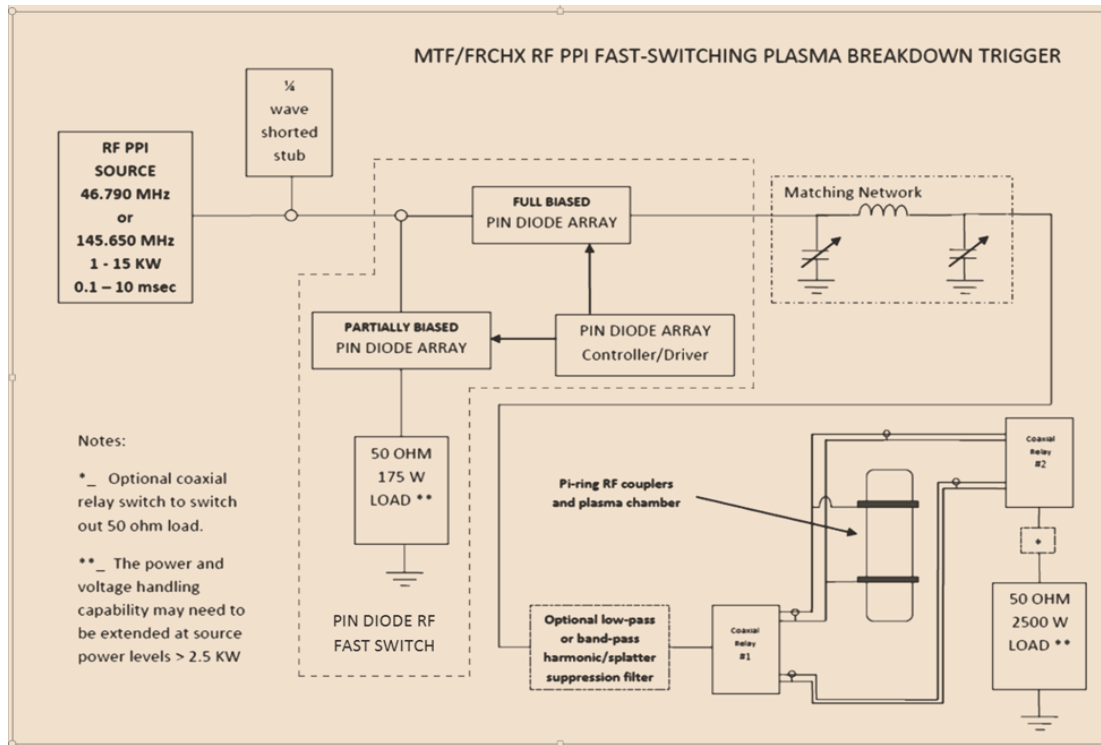


Figure 226. MTF FRCHX LPRF PPI modes of operation

The new configuration has been implemented and some early and successful tests have been accomplished on the system. The RF PPI source is the same setup as in our previous efforts shown in Figure 227. A new RF tube has been installed that has better emission characteristics, resulting in a 20% improvement of the source-power output from the earlier system.

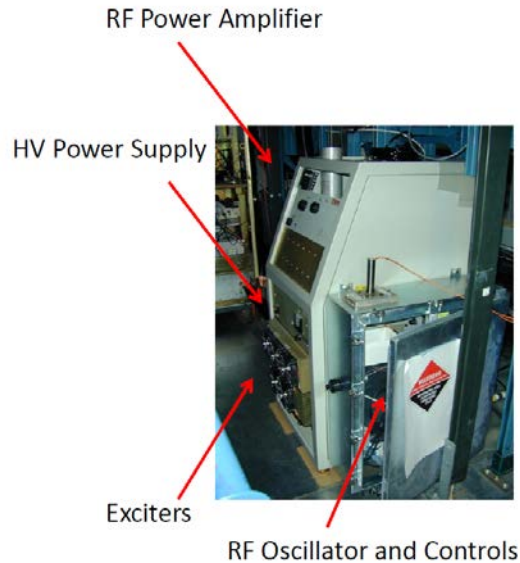


Figure 227. MTF FRCHX LPRF PPI 1 kW source

A new safety feature was been included in the new configuration, which is a quarter wave shorted stub. If a blocking capacitor in the RF source power amplifier plate circuit should fail and short the 2400-V power supply, voltage will get shorted out and trip the circuit breaker preventing the high voltage being exposed on the RF coupler surfaces and other parts of the distributed system. The RF power will not pass through the quarter wave stub so it will not be shorted out, only the DC component. The quarter wave stub has the additional advantage of improving suppression of harmonic components at the RF source output. Of course, quarter wave stubs need to be tuned to the frequency of operation, which in our present case is 46.79 MHz. A load-matching network has been recently installed that uses high Q high voltage vacuum dielectric tunable capacitors. They are used to very efficiently match the transmission line to the load. Some measurement of the coupling efficiency will be discussed.

Another addition to the previous system is a low-pass harmonic suppression filter. Many of the improvements to the LPRF PPI system have increased the power and voltage output of the system. Precautions are being taken to prevent radio frequency harmonic components that could leak out into the environment, should we go to higher-power operation (this, in addition to the advantage the in-line quarter wave stub gives us). A coaxial-switch system has been implemented to ensure that the default condition of the LPRF PPI system is to have the RF

output routed into the 50- $\Omega$ , 2500-W load only, as a good practice during operations. The new system is now more automatic and the gas-plasma load is switched in just prior to the experiment shot sequence; it is then returned to the default condition. In normal operation, the 50- $\Omega$ , 2500-W load is always connected in parallel with the experiment gas-plasma load, so the startup condition when the LPRF source is applied is a 50- $\Omega$  load. The system is carefully detuned as a compromise to a load impedance condition that is between the plasma load and the default load impedances. When the LPRF power is routed into the gas-plasma load, there is some RF leakage into the environment. During normal operation such leakage is acceptable for the very short RF “on” times that occur in our operations. With the compromise detuning, the voltage across the load when the RF is applied will be higher than for a nominally well matched system. The higher initial voltage offers the advantage of facilitating breakdown of the glow discharge; then, other physical processes will contribute to the sustained plasma glow.

The RF coupling rings at the experiment will be discussed later in detail. The complete system (excluding the PIN Diode RF Fast Switch, which is also discussed later) at the point of entry into the matching network has been tested with an HP 8510C network analyzer. When the system is tuned with the 50  $\Omega$  default load, the standing wave ratio (SWR) was measured at 1.07. When a simulated experiment load (12.5  $\Omega$ ) is switched in parallel to the default load the measured SWR is approximately 1.3. These conditions are certainly good workable power reflection values, especially compared to the previous estimated configuration, which had an SWR of more than 2.0. The RF source system was designed to survive such mismatched conditions for short periods of time. The present system is now coupled very efficiently so we can expect improved performance over the previous system.

Figure 228 shows the complete experiment side of the RF PPI system. The experiment structure is shown with two red rings representing the RF ring couplers mounted on each end of the theta coil assembly. The RF source is connected through the load-matching network to both ring coils, such that the RF E field is alternating between each ring; and as mentioned previously, the E field direction is now along the axis of the quartz tube and theta-coil magnet structure. The white box to the right of the experiment structure contains the matching network and harmonic



suppression filter, and the PIN Diode RF Fast Switch module that can be installed, removed, or bypassed depending on the LPRF PPI system configuration.

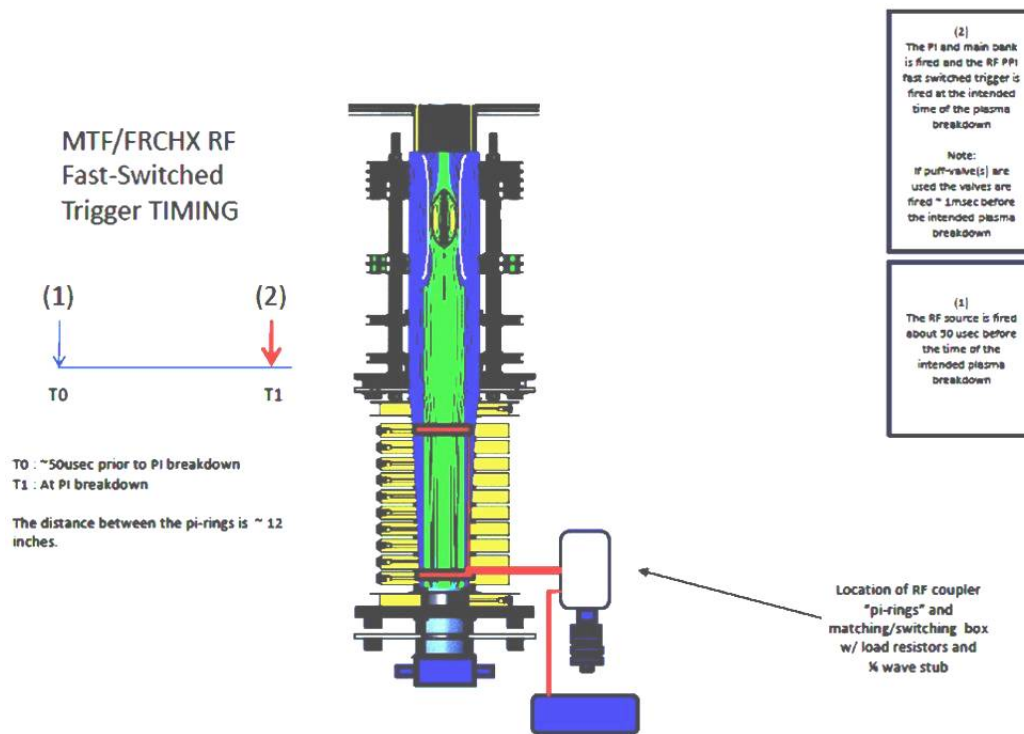


Figure 228. MTF FRCHX LPRF interfaced to the experiment

The first setup configuration is more like the original setup with the primary purpose of creating an RF-generated breakdown and glow discharge that provide a reasonably uniform field of free electrons. This setup configuration will be used in actual operation as a two-stage preionization system whose second stage is a high energy ringing pulsed power capacitor bank discharge through the magnet structure. Normally the RF source is gated on for about 10 ms before the PI high-energy pulsed-power bank system fires.

The non-triggered operation of the new system configuration was tested between FRCHX experimental campaigns. We show some open-shutter photos of gas ionization in the quartz tube in Figure 229. Using interim RF coupling rings and omitting the matching network box, we were not able to break down the deuterium gas over a distance greater than 9 in. With the matching network box, there was no difficulty in breaking down the gas and sustaining a glow discharge

over the full length of the theta coils, approximately 12 in. There is a reasonably uniform glow discharge over a wide range of fill pressures. The system was operating in the electron seeding configuration (i.e., without the PIN Diode Fast Switch) with the LPRF source gated on for 10 ms periods once every 2 s. Time exposure photographs were taken to show the glow discharge structure. During this test, one side of the theta coil assembly was removed so that side-on photographs could be taken. The RF coupling rings that we used had a foil width of  $\frac{1}{4}$  in and a  $\frac{1}{2}$ -in. azimuthal gap to prevent flux exclusion. The ring assembly used during the tests is apparent in the top left frame in Figure 229.

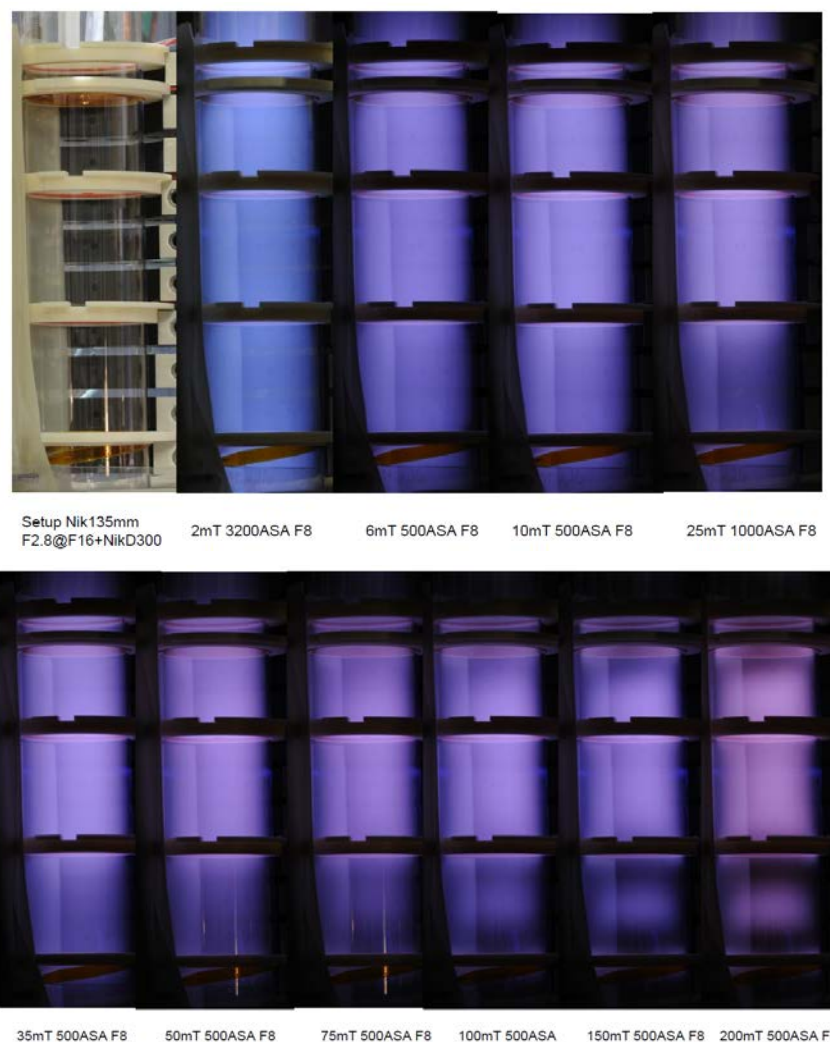


Figure 229. MTF FRCHX of RF glow gas breakdown over a range of fill pressures

During initial bank tests at high voltage, there was failure of the quartz tube caused by an arc to the theta coil assembly. This was due to a problem with the epoxy coating and not flux loop effects. The new RF ring assembly, shown in Figure 230, will be much better insulated and the foil width will be increased to  $\frac{3}{4}$  in. to increase the capacitive coupling to the gas-plasma load, and the gap in the ring will be increased to  $\frac{3}{4}$  in. as an added measure.

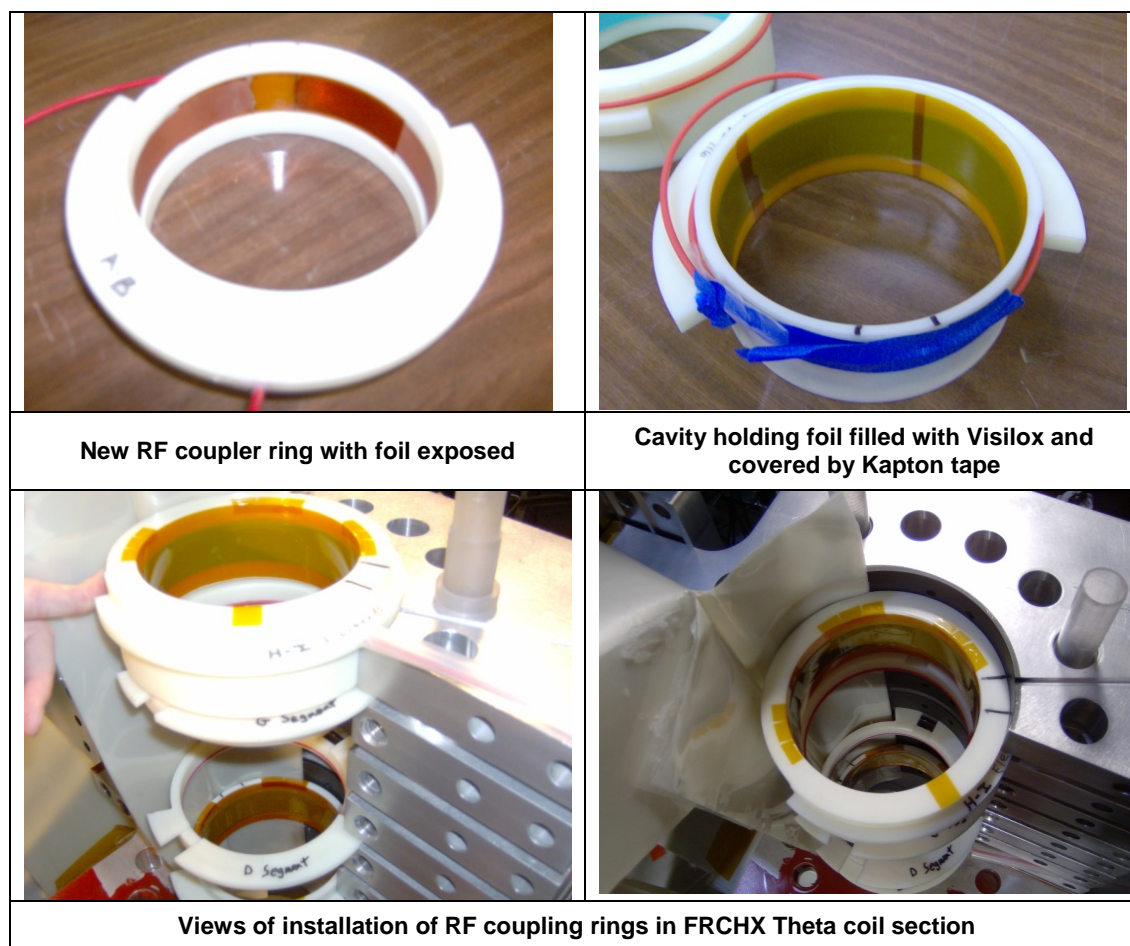


Figure 230. New RF ring assembly

As previously mentioned, the PIN Diode RF Fast Switch, shown in Figure 231 (a) and (b) is a module that is plugged into the RF PPI system inside the matching network box that also houses the harmonic suppression filter. Now that the PIN Diode RF Fast Switch module is being implemented, additional active control electronics are required to provide the level-shifted bias voltages to the RF PIN diodes along with internal logic, internal timers, dc-to-dc converters, voltage regulators, batteries, fiber optic signal interfaces, and air switching controls, shown in

Figure 231 (c). It is essential in this RF and capacitor bank pulsed power operating environment that the control electronics be completely isolated for both internal RF high power interference and the external pulse power switching noise. This means that the PIN Diode RF Fast Switch must be placed inside a matching network box. Then, the matching network box must be placed inside a larger box housing all of the control electronics and associated power supplies for isolation from the lab environment in proximity to the FRCHX experiment structure and capacitor banks.

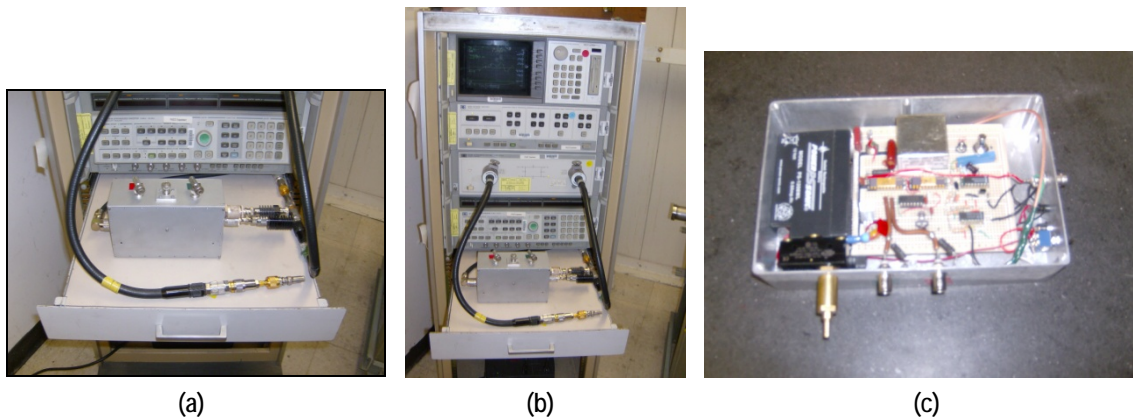


Figure 231. MTF RF PPI PIN diode fast trigger switch module and controller

The PIN Diode RF Fast Switch module houses two RF PIN switching diodes that either divert the RF power from the RF source into a diverter load or switches the RF power into the gas-plasma load that is also in parallel with a 50- $\Omega$ , 2500-W RF power resistor.

The RF PIN Diode Switch controller requires two 12 V batteries. One 12 V battery provides power to a +5 V regulator to supply logic, timing, and interface circuitry, and also to a 12V-to-300V, 1.5 W variable dc-to-dc converter, which, in turn, supplies the reverse bias voltage that is used to switch off the RF PIN diode. Since the PIN diode controller is designed to be versatile and operate with various RF PIN diodes with different switching parameters, the reverse bias voltage is variable from 0 V to 300 V. In this configuration the PIN diodes require a reverse voltage of 50 V or less. For performance reasons the PIN diode reverse voltage is set to approximately 35 VDC. To switch an RF PIN diode on, a current source is needed to supply up to 1A. Lower current levels will cause the PIN diode to act more as a variable attenuator. In the present configuration, due to the way the PIN diode control voltages are connected, a -3 V, 1 A

source is needed to switch on the PIN diodes. Another 12 V battery powering a -3 VDC regulator along with a load buffering capacitor is used for this purpose.

To control the operation of the PIN diodes that switch the RF power either into the diverter load or the gas-plasma load, an integrated circuit chip set was selected for use in the FRCHX RF trigger configuration. The integrated circuit chipset is advertised to be used for high power phased array radar control functions as well as other applications. The chipset facilitates the switching control levels that alternate between -2.5 VDC (-3 VDC under load) and in the present application +35 VDC for the reverse bias turn-off state. The present chipset can switch up to four PIN diodes between the on and off states with up to a 220 VDC reverse bias. The 300-VDC internal power supply is presently limited by a 200-V Zener diode to protect the chipset from overvoltage. The batteries supplying the power are turned on and with pneumatic air control switches by the FRCHX control system to conserve battery power during a day of operations, and the batteries recharge overnight. An additional 12 V battery is not related to the PIN diode controller, but is used to switch the coaxial RF relays that switch between 50- $\Omega$  load only and experiment load (as in Figure 226). It is also enabled by an air powered pneumatic control switch from the FRCHX control system. The PIN diode switching sequence is initiated by a fiber optic start trigger signal internally converted into a logic step voltage that causes an internal timer to initiate the RF power diverter sequence. Each time a state change is made to the PIN diode control chipset an "Output Enable Low" signal pulse is required, and that is the purpose of a dual timer chip.

Figure 232 gives some details of the various functions that have been described, and Figure 233 shows some actual waveforms of the operation of the PIN Diode RF Fast Switch. Before any control trigger is sent to the PIN diode controller, the RF PIN diode controller chipset is first in a high-impedance state and the PIN diodes have no controlling voltages.

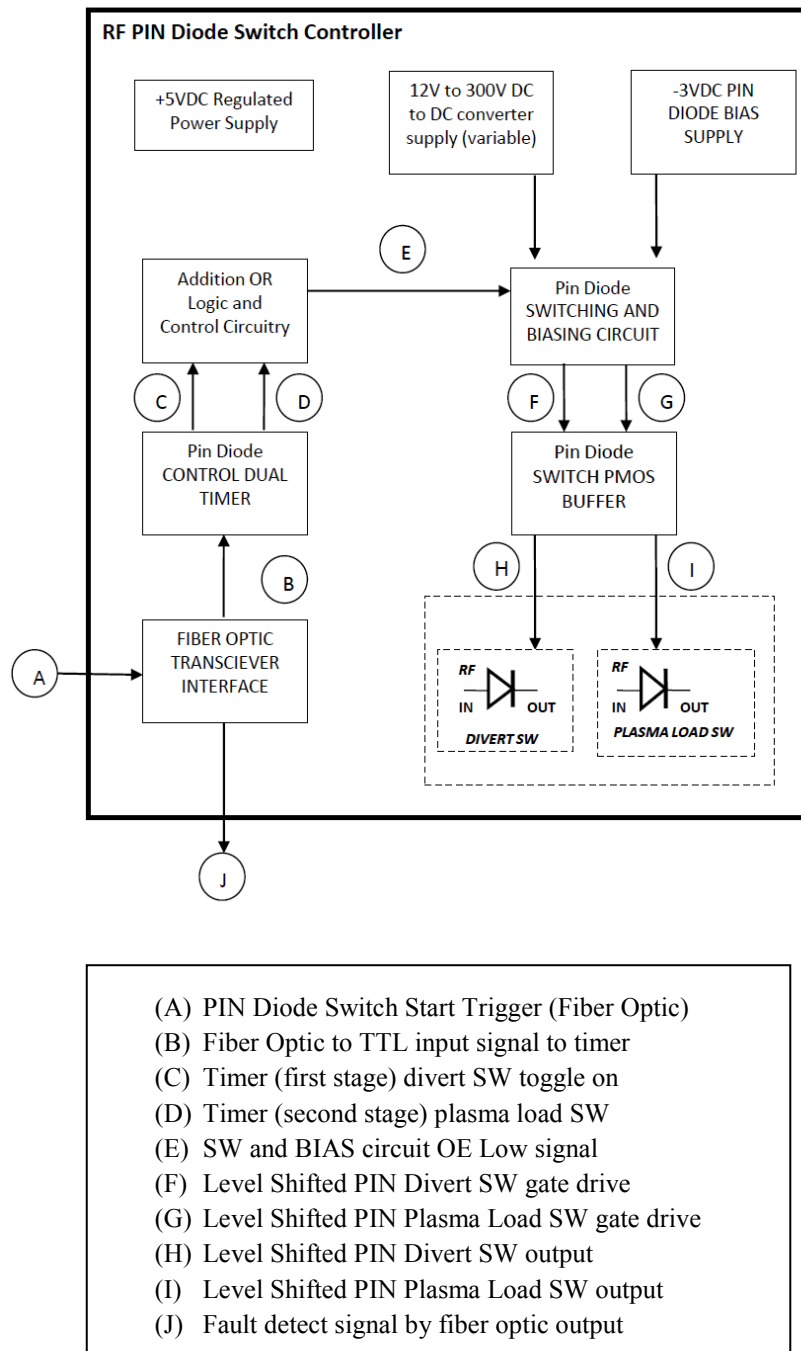


Figure 232. MTF FRCHX RF PPI Fast Switch plasma breakdown trigger controller



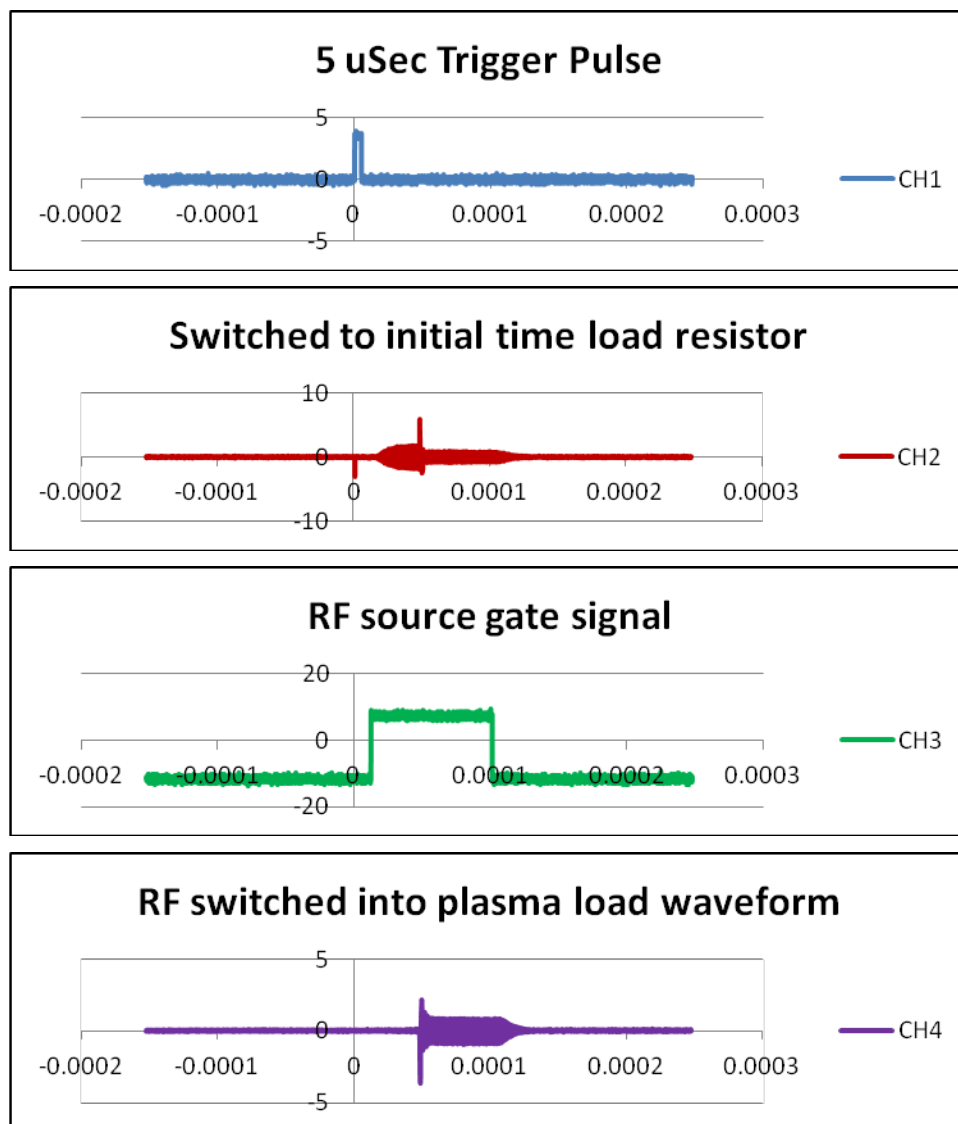


Figure 233. RF PPI PIN diode Fast Switch initial data showing switching parameters

SWR measurements have been made of the RF throughput. When the system is in the high-impedance state the reflected power SWR is approximately 1.2, and when the PIN diodes are switched on the SWR is approximately 1.08 at the RF operation frequency. There have been some difficulties with excessive switching transients that can cause component failures to happen. This situation was brought under control by making compromises in the switching time. Ultimately, we want to switch the RF trigger pulse on in much less than 1  $\mu$ s so work still needs to be done to resolve the problem. High-power RF will not be applied to the system until we are

confident that the switching transient problems are resolved and there is sufficient isolation between the RF power path and the PIN diode control level outputs.

To couple the RF energy into the neutral gas, electrodes were originally placed across a diameter near the center of the formation region on the outside of the quartz vacuum tube. During source operation, slightly enhanced breakdown was seen during the PPI discharge, but it was thought that the power level and coupling were insufficient to substantially ionize the gas. The problem was exacerbated because the direction of the RF electric fields was across the bias magnetic field lines, so that Larmor orbits would impede breakdown.

The higher power electronics just described allowed operation of the source in saturation mode, providing higher output power, and a harmonic suppression circuit was added. In addition, new electrodes were made from 7-mil thick,  $\frac{3}{4}$ -in. wide copper bands (Figure 234) around the tube above and below the formation region.



Figure 234. Copper strip electrode in holder

The electrodes had a  $\frac{3}{4}$ -in. circumferential gap to prevent flux exclusion (Figure 235), and they were insulated with Kapton tape. The completed electrode assembly, shown in Figure 236, surrounds the quartz tube. The two electrodes were separated by 30 cm.



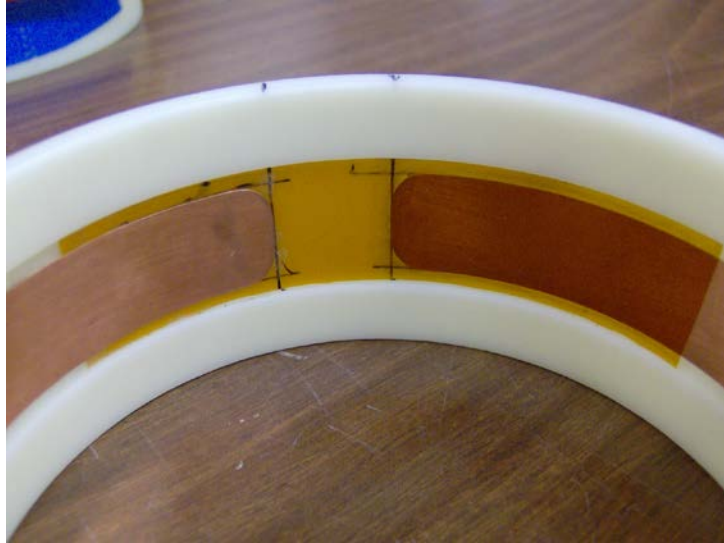


Figure 235. Circumferential gap in the electrodes to prevent flux exclusion



Figure 236. Electrode assembly surrounding quartz tube

With these electrodes, the orientation of the electric field is primarily axial, as calculated in Section 3.2.3.1.3, and almost in the same direction as the ambient magnetic field. This new electrode configuration was tested on FRCHX with a 50-mTorr deuterium static fill. Measurements of plasma light using optical fiber and a fast photomultiplier tube (PMT), and with a Hadland fast framing camera looking axially from below, were made with and without bias field and preionization field. A single interferometer beam probed electron density across a diameter of the tube in the middle of the formation region.

Initially, the RF source was operated in gated mode, but with filter circuits to suppress harmonics, the risetime into the quartz tube was approximately 500 ns. Different pulse lengths were tried, ranging from sub-microsecond to 10 ms. We saw that the delay to the beginning of plasma light varied considerably – often by several milliseconds – after RF pulse triggering, and more robust light signals were achieved only when the RF pulse was longer than 1 ms.

When the bias and preionization fields were applied, interferometer signals showed appreciable electron density, and fast photography showed radial compression of the plasma due to the PI bank discharge. Whereas earlier electron density did not rise until the PI magnetic field had essentially nulled out the bias field, with the new configuration breakdown occurred slightly before the field null. The conclusion we have drawn is that the new configuration and power levels have improved the ability to break down the neutral gas before the magnetic field and flux go to zero, and it should improve our ability to trap flux somewhat.

During the course of testing, it was discovered that one of the RF oscillator tubes had an inherent risetime at least as short as the switched-amplifier used with two other oscillators. After trying various switching schemes, it was decided to not use the high-power PIN diode switch, but rather just use the intrinsic risetime of the faster oscillator tube. This approach worked quite well.

#### *3.2.3.1.2 Transient RF*

A charged-cable high-power RF (HPRF) discharge device was built, and preliminary testing began on the teststand built for testing gas puff injection. The teststand has a quartz tube and RF electrodes, described in the previous section, identical to those on FRCHX. The transient HPRF source uses a triggered spark gap (Titan Pulsed Sciences model 40168) modified to accept a charged cable in place of its usual load capacitors. A schematic diagram of the cable-pulser setup is shown in Figure 237.

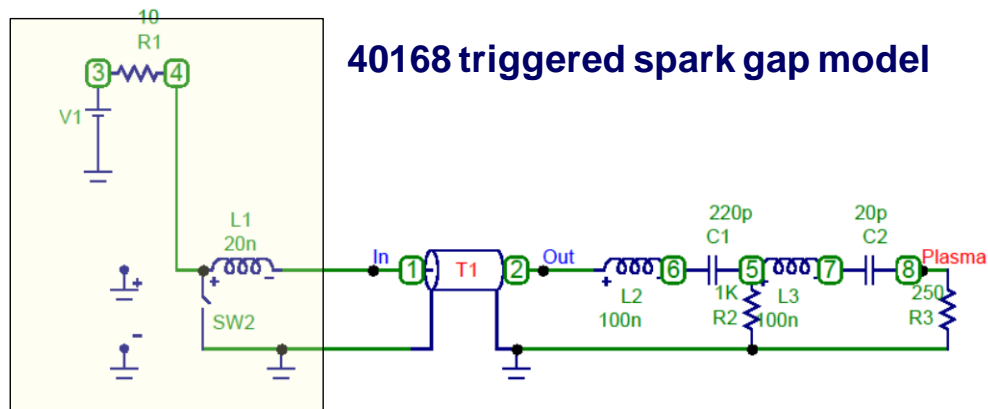


Figure 237. Micro-Cap model of cable discharge circuit

The initial device was constructed using a 15-ft-long pair of RG213 cables (24- $\Omega$  net impedance, 22.5-ns one-way transit time) charged to 10 kV. The upstream end of the cable was attached to the power supply and spark gap, and the downstream end attached to the quartz tube electrodes through 450-pF DC high-voltage blocking capacitors. A circuit diagram for the system is shown below in Figure 138. This circuit was used to calculate transient system response using Micro-Cap 10 (Spectrum Software).

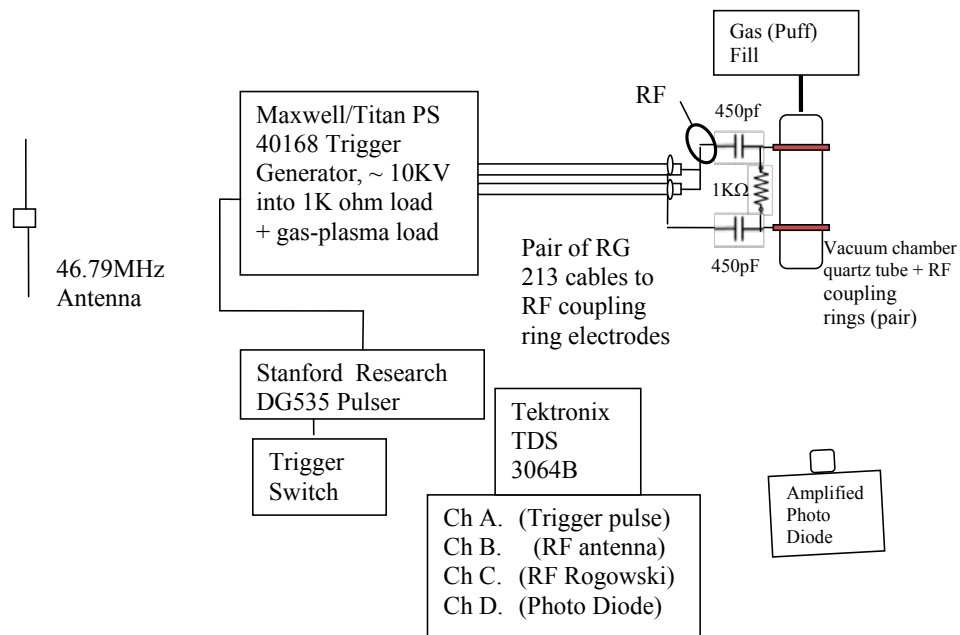


Figure 238. Cable pulser test setup

The spark gap's "no-break" and "self-break" voltages for ambient dry air pressure (approximately 12-13 psia) were determined to be 8 kV and 11 kV, respectively. The operating voltage for triggered spark gap operation was chosen to be 10 kV. With 50 mTorr – 100 mTorr deuterium in the tube, we found that breakdown was erratic, and it generally took a series of approximately 7.5 Hz conditioning pulses before breakdown occurred. A North Star PVM-5 high voltage probe was used to monitor voltage oscillations at the top of the spark gap, and a fast Fourier transform of the waveforms indicated a main frequency component of only about 8 MHz, in agreement with the Micro-Cap circuit simulation, so we expect the coupling through the quartz tube to be quite poor.

Figure 239 shows the test setup. The cable pulser is a Titan Pulse Sciences Model 40168 triggered spark gap that shorts the RG 213 charged cable that is terminated with a 440-pF blocking capacitor and parallel-load resistor. The resistor value was 1 M $\Omega$  for much of the testing, but was replaced with a 1 K $\Omega$  resistor after installation on FRCHX.

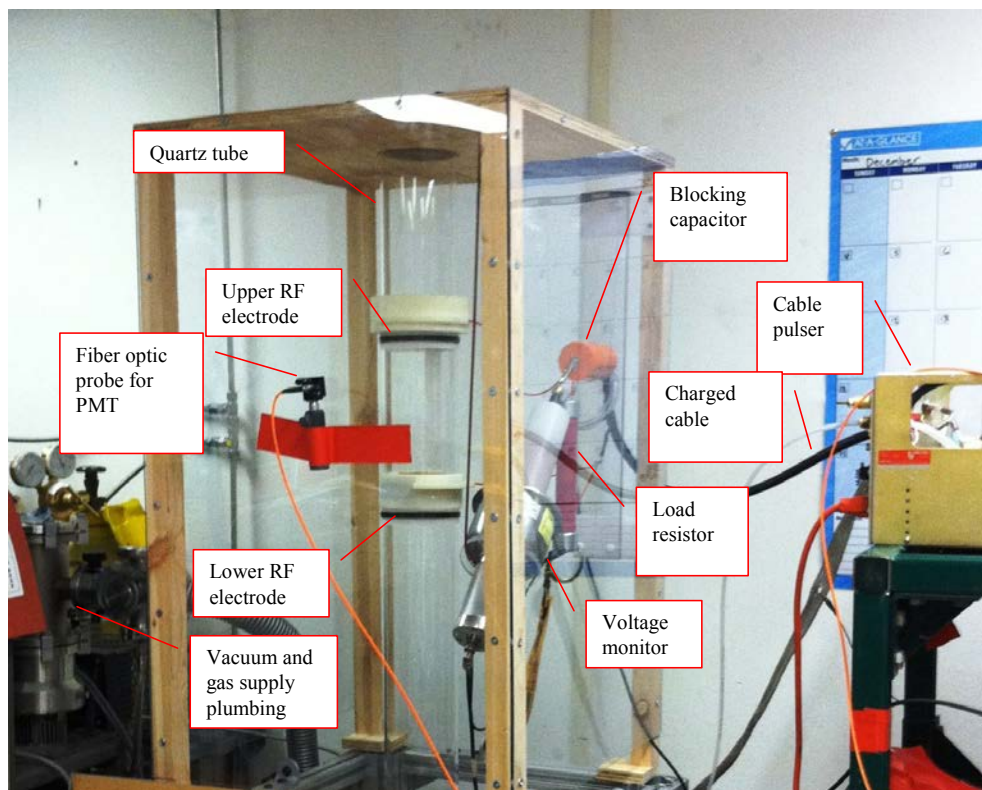


Figure 239. 40168 HPRF test setup

During early testing, the second charge cable was removed and the remaining cable shortened. The groundside blocking capacitor shown in the schematic was also removed. Although we started with a 10 kV voltage on the cable, we found we could operate with 20-kV charge voltage, and that value was used on the system installed on FRCHX. At that voltage, we were able to reliably breakdown the gas.

For installation of the system on FRCHX, the model 40168 had to be enclosed in an RF enclosure. This enclosure was built from a Hofman box, shown in Figure 240. One can see the AC-filter box, RF waveguide filters, and copper screen for the cooling fan. The 40168 was powered from a UPS.



Figure 240. RF enclosure for model 40168

#### 3.2.3.1.3 Implications for Plasma Conductivity and Flux Trapping

For good flux trapping during FRC formation, the plasma must be created rapidly and with high conductivity while the flux within the gas is high. Thus, there must be good ionization at the time of PI bank discharge. If the PI bank discharge is not strong enough to completely ionize the gas and heat it to a temperature corresponding to good conductivity, the flux will simply diffuse through the gas and not remain trapped.

The required conductivity can be estimated from simple diffusion theory. If we want the diffusion time to be at least 5  $\mu$ s over a plasma thickness of 1 cm, then the diffusivity,  $D$ , must be less than  $(1 \text{ cm}^2 / 5 \mu\text{s})$ , or about 20  $\text{m}^2/\text{s}$ , in mks units. Since the diffusivity is given by  $1/\mu_0\sigma$ ,

we see that the conductivity at the time the main formation discharge occurs should be at least  $4 \times 10^4$  siemens/m, in mks units.

We can also estimate what temperature the plasma must be to achieve that conductivity. The transverse conductivity is given by [16]

$$\sigma_{\perp} = \frac{ne^2\tau_e}{m_e}, \quad (1)$$

where  $n$  is the electron density,  $e = 1.6 \times 10^{-19}$  C is the electron charge,  $m_e = 9.1 \times 10^{-31}$  kg is the electron mass, and  $\tau_e$  is the electron collision frequency, given, in cgs units, by [17]

$$\tau_e = \frac{3\sqrt{m_e}(kT_e)^{3/2}}{4\sqrt{\pi}n\lambda e^4}. \quad (2)$$

Here,  $T_e$  is the electron temperature, in eV,  $k = 1.6 \times 10^{-12}$  erg/eV =  $1.38 \times 10^{-16}$  erg/K, and  $\lambda$  is the Coulomb logarithm. It is only weakly dependent on electron density and for fully ionized plasmas is in the range of 10 – 30. So, we see that the conductivity is nearly independent of electron density and roughly proportional to temperature to the 3/2 power.

We used Mathcad® (Parametric Technology Corporation) to solve the transcendental equations (1) and (2) for the electron temperature required for the conductivity estimated above. That value of electron temperature is 2 eV. Now, we must determine if the gas is fully ionized (implicit assumption in our conductivity estimate). The ionization of deuterium (or hydrogen) can be calculated from the Saha equation [18], written in terms of the fractional ionization ( $x = n_i/n$ , where  $n_i$  is the ionized hydrogen, or electron density, and  $n = n_i + n_0$  is the total ion/atom density) as

$$\frac{x^2}{1-x} = \frac{1}{n} \left( \frac{2\pi m_e kT}{h^2} \right)^{3/2} e^{-13.6 \text{ eV}/kT}. \quad (3)$$

Here,  $h = 6.6 \times 10^{-34}$  J·s is Planck's constant, and  $E = 13.6$  eV is the ionization potential for hydrogen. The fractional ionization, including dissociation from the analogous Saha equation,

and corresponding densities are plotted in Figure 241 and Figure 242, respectively, as a function of temperature for an assumed neutral molecular density of  $1.77 \times 10^{21} \text{ m}^{-3}$  corresponding to a pressure of 50 mTorr. As can be seen, hydrogen is completely ionized at 2 eV (23,200 K).

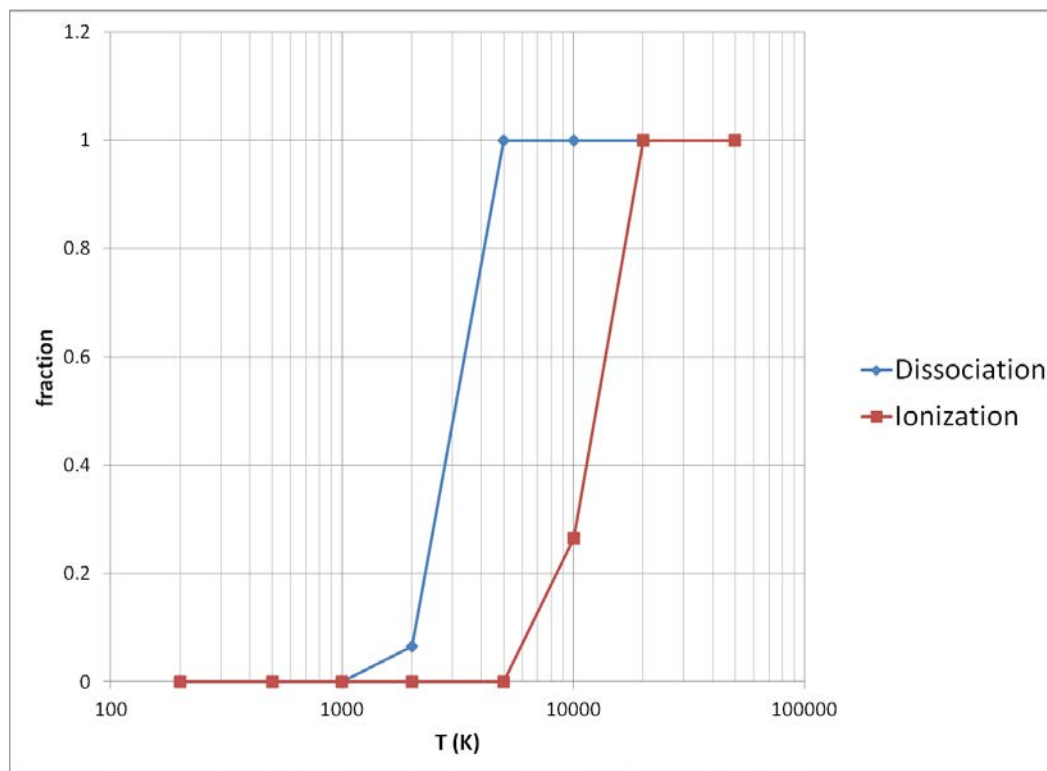


Figure 241. Hydrogen fractional dissociation and ionization from Saha equilibrium for a total number density of  $1.77 \times 10^{21} \text{ m}^{-3}$



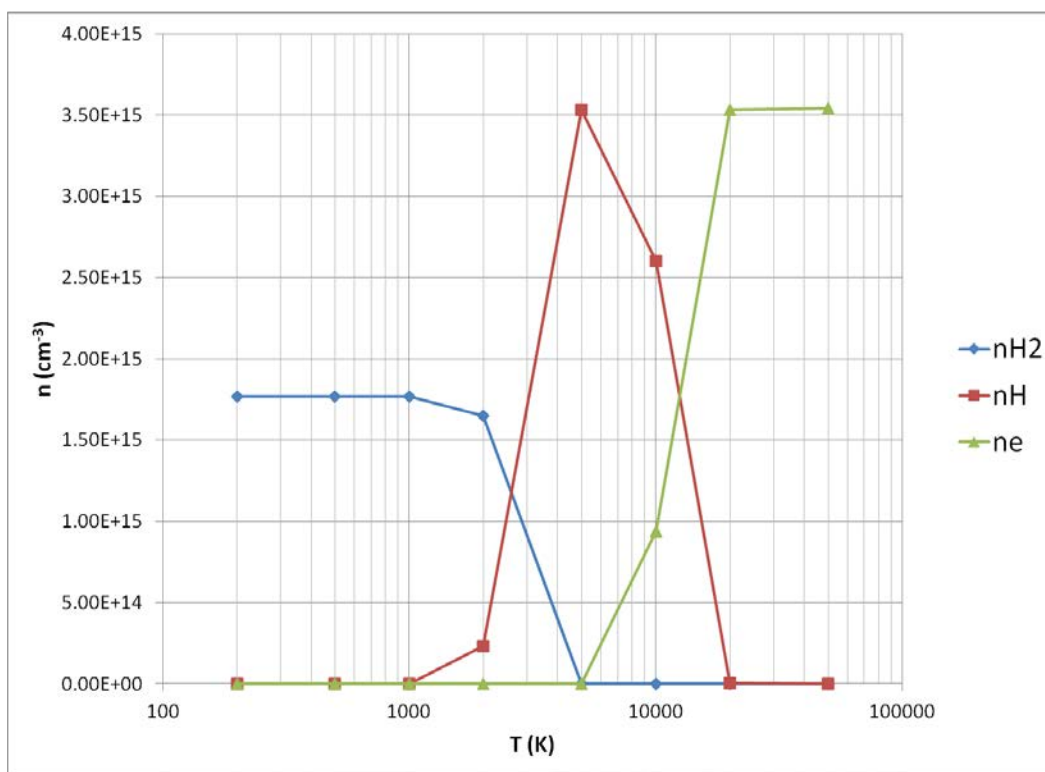


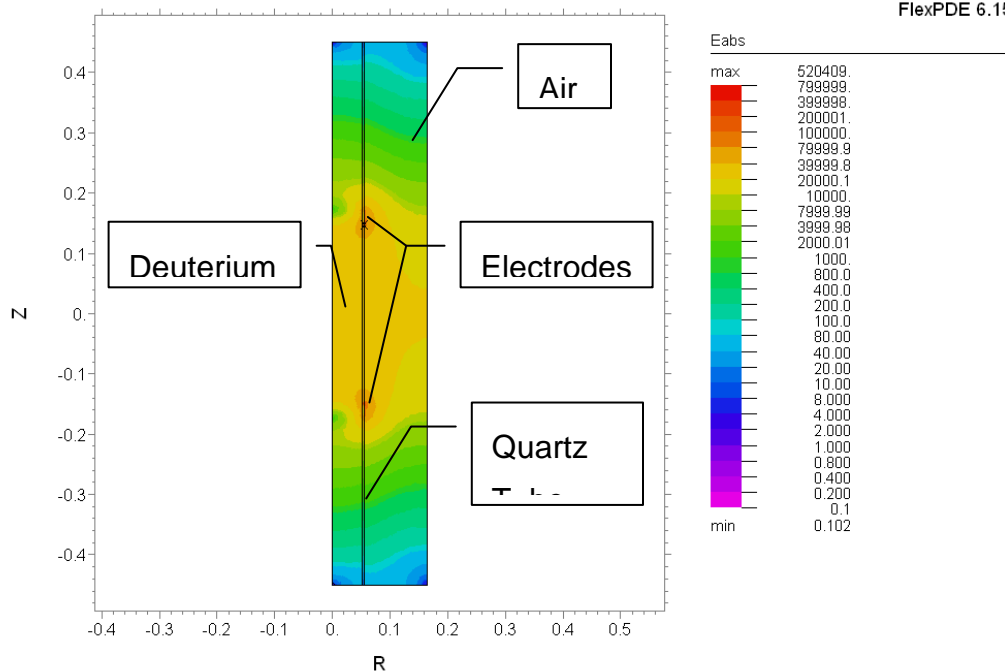
Figure 242. Densities of molecular, atomic, and ionized hydrogen as a function of temperature for a pressure of 50 mTorr from the Saha equation

We examined the electric potential and field distributions for the electrode system described above. We solved Poisson's equation for the potential in axisymmetric 2D using FlexPDE<sup>®</sup> (PDE Solutions, Inc.), both for the case before breakdown, then assuming the interior of the tube is conducting. From the latter, we were able to determine the effective capacitance of the electrode-quartz tube-plasma system. The relative dielectric constant for fused quartz is 3.75, and we ignored the effects of Kapton and dielectric epoxy used to seal the electrodes. The results for the potential and field strength are shown in Figure 243–Figure 250, for 10-kV applied voltage. For the pre-breakdown case, we find that the peak field at the inner surface of the tube is approximately 1.2 kV/cm. For the post-breakdown case, we calculate the capacitance between the electrode and plasma to be about 50 pF. From the electric field vector plots, one can see that the field is oriented primarily in the axial direction in the gas prior to breakdown, but almost purely in the radial direction across the quartz, post-breakdown.



RF Electrodes

15:02:45 1/17/12  
FlexPDE 6.15

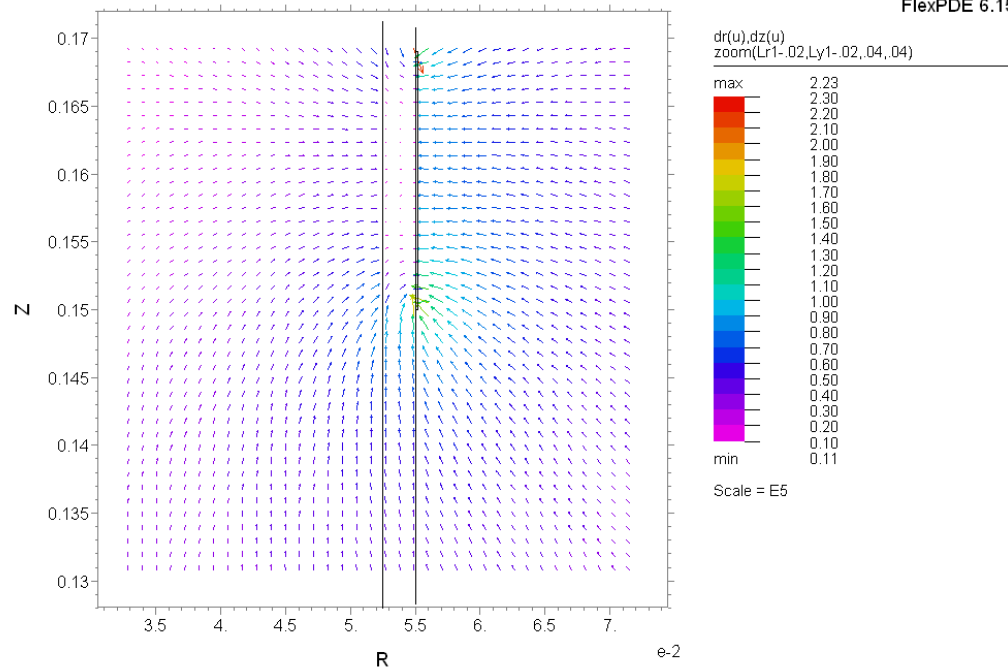


Efld02: Grid#1 P2 Nodes=8404 Cells=4123 RMS Err= 8.3e-5  
Vol\_Integral= 763.1973

Figure 243. Electric field strength in formation region—pre-breakdown, 10 kV applied

RF Electrodes

15:02:45 1/17/12  
FlexPDE 6.15



Efld02: Grid#1 P2 Nodes=8404 Cells=4123 RMS Err= 8.3e-5

Figure 244. Electric field vectors in vicinity of upper electrode—pre-breakdown case

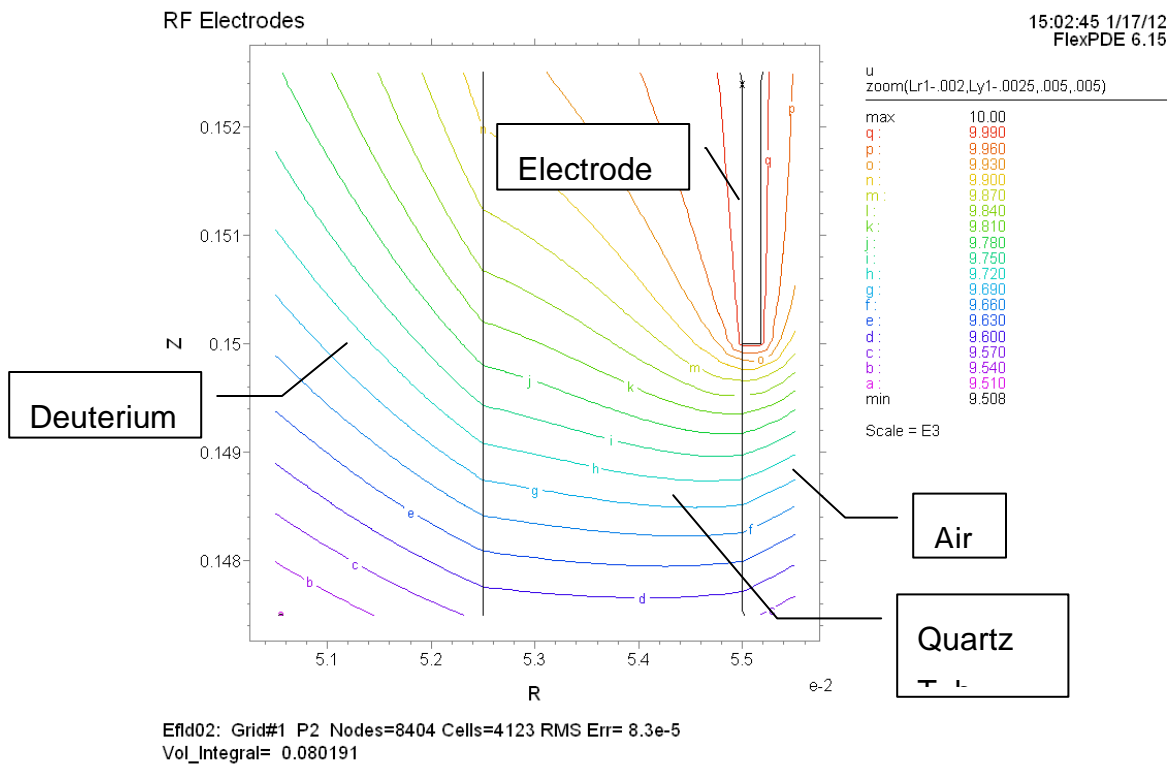
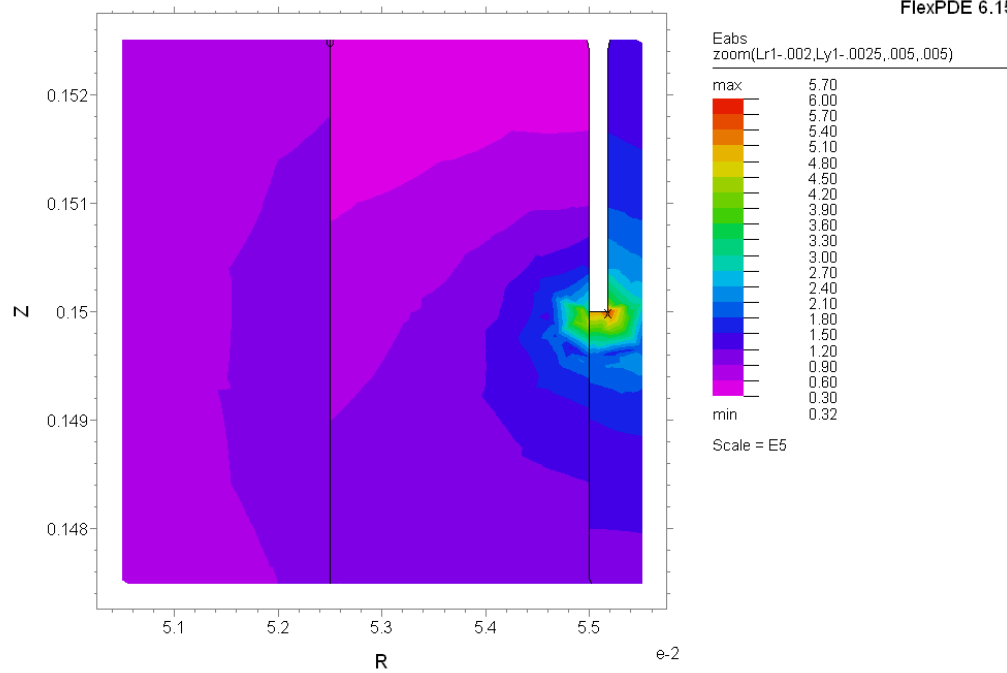


Figure 245. Equipotential contours near bottom of upper electrode—pre-breakdown

RF Electrodes

15:02:45 1/17/12  
FlexPDE 6.15

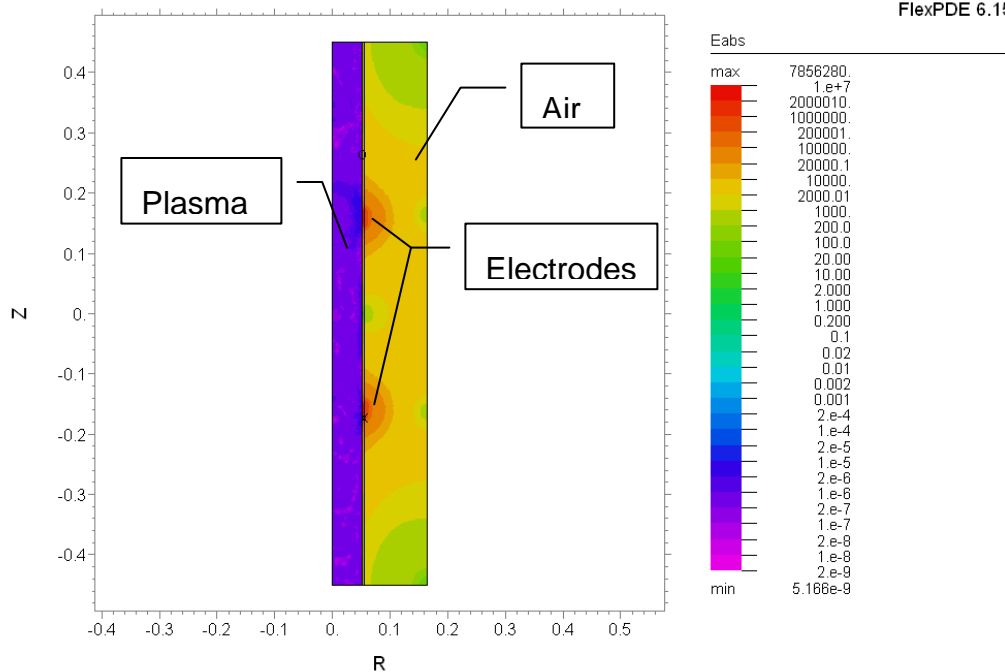


Efld02: Grid#1 P2 Nodes=8404 Cells=4123 RMS Err= 8.3e-5  
Q= -1.549042e-8 Vol\_Integral= 0.798631

Figure 246. Electric field contours near bottom of upper electrode—pre-breakdown

RF Electrodes

13:41:30 1/19/12  
FlexPDE 6.15

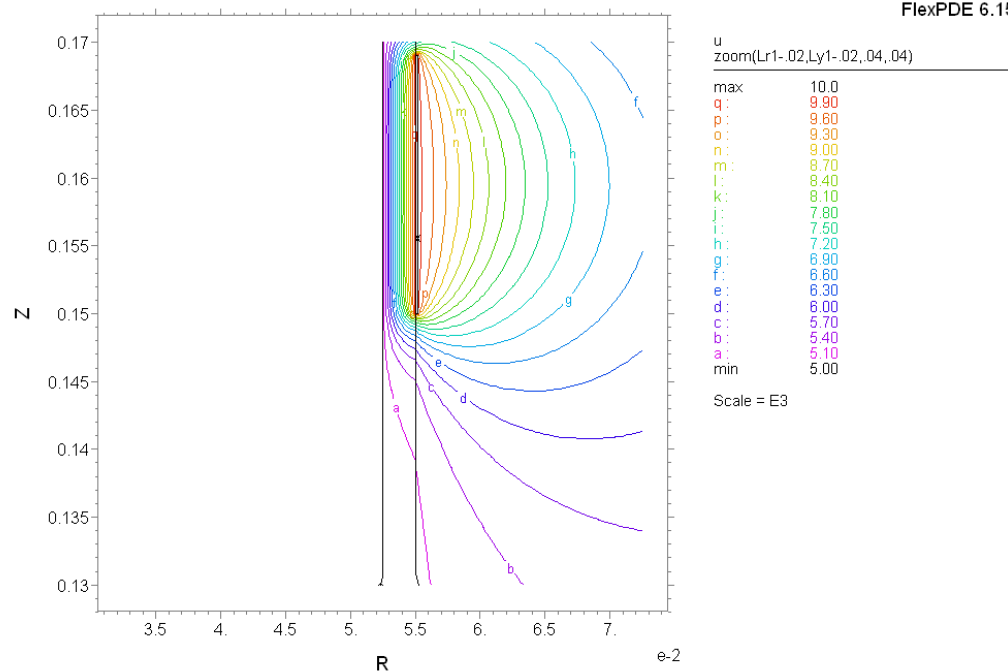


Efld03: Grid#1 P2 Nodes=8404 Cells=4123 RMS Err= 4.6e-4  
Vol\_Integral= 445.5818

Figure 247. Electric field amplitude in vicinity of electrodes—post-breakdown

RF Electrodes

13:41:30 1/19/12  
FlexPDE 6.15

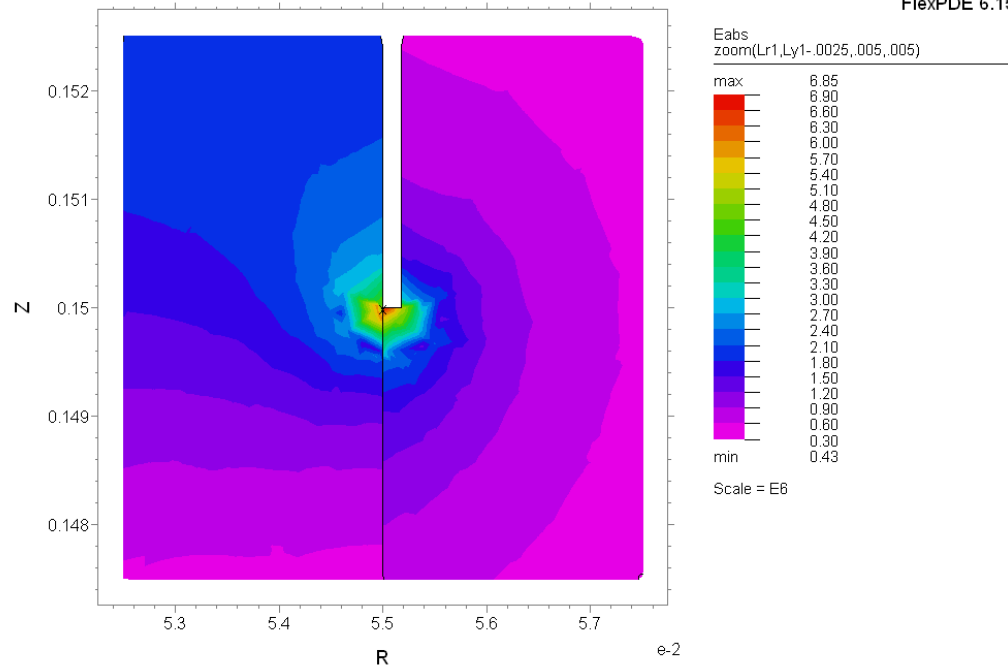


Efld03: Grid#1 P2 Nodes=8404 Cells=4123 RMS Err= 4.6e-4  
Vol\_Integral= 3.188741

Figure 248. Equipotential contours near upper electrode—post-breakdown

RF Electrodes

13:41:30 1/19/12  
FlexPDE 6.15



Efld03: Grid#1 P2 Nodes=8404 Cells=4123 RMS Err= 4.6e-4  
Q= -4.981211e-7 Vol\_Integral= 10.26233

Figure 249. Electric field strength near bottom of upper electrode—post-breakdown

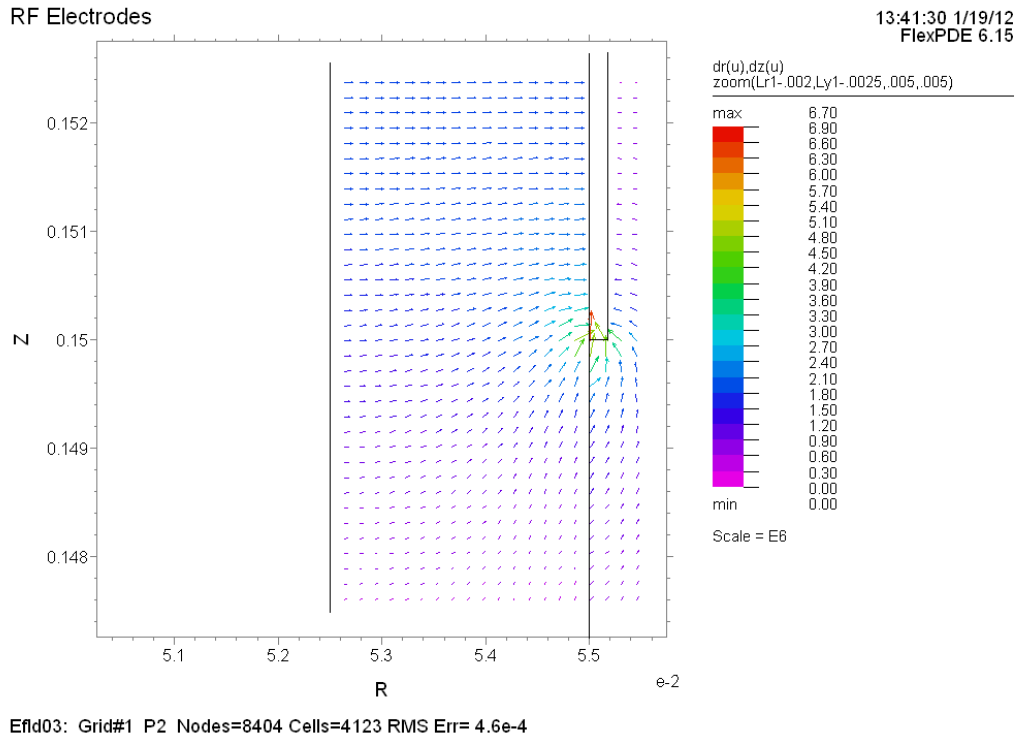


Figure 250. Electric field vectors near bottom of upper electrode—post-breakdown

### 3.2.3.2 Crossed-Field Ionization

In the FRCHX experiment, an FRC is produced for translation and subsequent compression. To preserve the plasma and field structure into compression, the FRC must have a lifetime of at least 20  $\mu\text{s}$ . In earlier experiments, the lifetimes achieved were typically no more than 10  $\mu\text{s}$ . Two keys were identified to substantially increase the lifetime: trap more initial flux in the FRC, and control development of the  $n=2$  rotational instability. Here, we present an analysis of controlled breakdown and ionization due to the preionization discharge we have been using to attempt to trap more initial flux.

The purpose of the PI discharge is to rapidly ionize and heat the plasma to sufficient temperature (approximately 2 eV) so that the electrical conductivity is high enough to prevent diffusion of flux out of the FRC.

The existing PI capacitor bank discharge is characterized by a frequency of approximately 230 kHz (1.1- $\mu\text{s}$  quarter cycle time), with a peak capacitor charge voltage of 60 kV. The



discharge current through the theta coils is an underdamped sine waveform produced from the series LRC circuit. The parasitic inductance associated with the bank itself, headers, and cable transmission to the theta coils dominates the total inductance of the circuit, so that the peak-inductive voltage at the inside wall of the quartz tube is only about 6 kV. This value was determined by estimating  $d\phi/dt$  assuming a uniform peak magnetic flux density inside the tube due to the discharge of 0.5 T. Therefore, peak inductive electric (E) field inside the 5.2 cm inner-radius tube is approximately 200 V/cm, and it decreases linearly with radius to zero on axis.

The ambient-magnetic field desired for initial trapping is approximately 0.5 T in the axial direction. With the E field oriented azimuthally, this is an electrodeless crossed-field breakdown configuration. In most parameter regimes for this configuration, electrical breakdown is inhibited compared to the case of no magnetic field. The main reason for this phenomenon is that the magnetic field impedes motion across the field due to cyclotron motion, although it affects both the ionization rate and radial diffusion loss rate.

In Section 3.2.3.2.1, we review the salient features of electron motion in crossed fields and present the basic theory of diffusion-controlled breakdown in Section 3.2.3.2.2. In Section 3.2.3.2.3, we present dimensionless, static calculations using parameters relevant to the FRCHX experiment, and in Section 3.2.3.2.4, we present a discussion of the calculations and implications for controlling crossed-field breakdown with inductive PI fields.

#### 3.2.3.2.1 Elementary Theory

The theory of single-charged particle motion in the presence of electric and magnetic fields is well known (see Chen [19], or Heylen [20]). The main feature in crossed electric and magnetic fields (strictly only for spatially uniform and constant fields) is cycloidal motion with the guiding center speed in the plane perpendicular to the magnetic field given by

$$\bar{v}_{E \times B} = \frac{\bar{\mathbf{E}} \times \bar{\mathbf{B}}}{B^2} = \frac{E_\phi}{B_z} \hat{r} \quad (4)$$

where we have assumed the geometry of FRCHX with azimuthal inductive electric field and axial magnetic field, so that  $\mathbf{E} \times \mathbf{B}$  is in the “perpendicular,” or radial direction for both ions and

electrons (the electric field direction is considered the “transverse” direction). If we assume a maximum inductive electric field of 200 V/cm and a magnetic flux density of 0.5 T, the  $E \times B$  electron drift speed is  $4 \times 10^4$  m/s, or 4 cm/ $\mu$ s, which is appreciable.

The motion about the moving guiding center is circular in the moving frame with speed  $v_{ExB}$ , so that the absolute maximum speed in the perpendicular direction is  $2v_{ExB}$ . In the transverse direction of the electric field the maximum speed is just  $v_{ExB}$ . Solving the equations of motion in the two orthogonal directions, one finds that

$$\begin{aligned}\bar{v}_\perp &= \frac{E_\phi}{B_z} (1 - \cos \omega_c t) \hat{r} \\ \bar{v}_T &= \frac{E_\phi}{B_z} \sin(\omega_c t) \hat{\phi}\end{aligned}, \quad (5)$$

where  $\omega_c$  is the cyclotron frequency, given by

$$\omega_c = \frac{qB}{m}. \quad (6)$$

Integrating eq. (5) over time yields the trajectories

$$\begin{aligned}r(t) &= \frac{E_\phi}{B_z} \left( t - \frac{\sin \omega_c t}{\omega_c} \right) \\ \phi(t) &= \frac{E_\phi}{\omega_c r B_z} (1 - \cos \omega_c t)\end{aligned}. \quad (7)$$

The radius of the orbits is the Larmor radius ( $r_L$ ), given by the ratio of speed to cyclotron frequency,

$$r_L = \frac{E_\phi}{\omega_c B_z}, \quad (8)$$

and it is inversely proportional to the square of the magnetic flux density. For the electrons,  $r_L$  is only  $4.55 \times 10^{-7}$  m at peak electric and magnetic field, while for protons (hydrogen nuclei), it is

$8.35 \times 10^{-4}$  m. Of course, the Larmor radius grows substantially as the net magnetic field approaches zero. We note that the direction of the electric field is given by Faraday's Law to be in the direction opposite to the direction associated with increasing magnetic field. Therefore, if the initial direction of the magnetic field from the PI discharge coil is opposite to the ambient magnetic field, the direction of the  $\mathbf{E} \times \mathbf{B}$  drift is radially outward over the first quarter cycle, then reverses direction (inward radially) over the next half cycle.

Although our inductive electric field varies roughly as a cosine function in time, the oscillation frequency is substantially below both electron-neutral collision and electron cyclotron frequencies ( $2.4 \times 10^8 \text{ s}^{-1}$  for 50 mTorr and  $8.8 \times 10^{10} \text{ rad/s}$  for 0.5 T, respectively). This means that the particle motion can be considered to be quasi-steady-state, using the instantaneous value of electric field.

The inductive electric field, however, is not uniform and varies linearly with radius. In this case, the field seen by an orbiting particle changes slightly over the orbit, and in general there is a finite Larmor radius correction to drift speed given by

$$\bar{v}'_{E \times B} = \left( 1 + \frac{r_L^2}{4} \nabla^2 \right) \frac{\bar{\mathbf{E}} \times \bar{\mathbf{B}}}{B^2}; \quad (9)$$

but, in the special case of  $E_\phi \sim r$ , the Laplacian is zero, and the  $\mathbf{E} \times \mathbf{B}$  drift speed is unaffected.

One can calculate, in detail, the single particle trajectories in the crossed fields, but the motion is dominated by the  $\mathbf{E} \times \mathbf{B}$  drift, except for the case of no magnetic field, where the electron acceleration, in the absence of collisions, is given by  $-eE/m_e$ .

To take electron-neutral collisions into account<sup>20</sup>, we note that the average time between collisions is  $\tau = 1/\nu_m$ , where  $\nu_m$  is the collision frequency, so that the average distance traveled in the transverse direction between collisions is

$$r\bar{\phi} = \frac{qE_\phi}{m\omega_c^2(1 + \nu_m^2/\omega_c^2)}. \quad (10)$$

Thus, the mean velocity in the transverse direction is

$$\bar{v}_T^B = \frac{qE_\phi}{m\nu_m} \frac{\nu_m^2/\omega_c^2}{(1 + \nu_m^2/\omega_c^2)}. \quad (11)$$

Similarly, the mean velocity in the perpendicular direction is found to be

$$\bar{v}_\perp^B = \frac{qE_\phi}{m\nu_m} \frac{\nu_m/\omega_c}{(1 + \nu_m^2/\omega_c^2)}. \quad (12)$$

Several things should be noted. First, there is no net drift in the azimuthal direction without neutral collisions. Second, the perpendicular velocity is just the **ExB** drift velocity, but reduced by the factor  $[1 + (\nu_m/\omega_c)^2]$ . Third, because for FRCHX  $\nu_m \ll \omega_c$ , except when the net magnetic field is zero, the perpendicular velocity is nearly the ExB drift velocity, but the transverse velocity is reduced by a factor of  $\nu_m/\omega_c$  with respect to the perpendicular velocity. One can define the angle between transverse and perpendicular velocities:

$$\tan \theta = \frac{\bar{v}_\perp^B}{\bar{v}_T^B} = \frac{\omega_c}{\nu_m} = \frac{qB}{m\nu_m}. \quad (13)$$

For FRCHX parameters,  $\tan \theta = 366$ , so the angle is very nearly 90 degrees and the electron trajectories are almost purely radial, as in the case of no collisions.

#### 3.2.3.2.2 Diffusion Theory

Elementary diffusion theory for weakly ionized plasmas is also covered in Chen [21], the variations on the basic theory in the presence of magnetic fields is covered by Brown [22], and the effects on electrical breakdown by Heylen [21], although the latter only for breakdown between electrodes. Here, we summarize the relevant theory.

The equation of continuity for electrons can be written as

$$\frac{\partial n_e}{\partial t} + \bar{\nabla} \cdot \bar{\Gamma}_e = s, \quad (14)$$

where  $s$  is the electron source rate and  $\bar{\Gamma}_e$  is the electron flux, given by

$$\bar{\Gamma}_e = n_e \mu_e \bar{E} - D_e \bar{\nabla} n_e. \quad (15)$$

Here,  $\mu_e$  is the electron mobility and  $D_e$  is the electron diffusion “constant,” or coefficient. The product of mobility and electric field gives the drift speed due to electric acceleration balanced by collisional slowing, as can be seen by setting the time derivative of the velocity to zero in the electron equation of motion and solving for the steady-state velocity. It is directly proportional to the electrical conductivity of a weakly ionized plasma.

The electron mobility, in the absence of magnetic fields, is given by

$$\mu_e = \frac{-e}{m_e \nu_m}, \quad (16)$$

where  $e$  is the electron charge,  $m_e$  is the electron mass, and  $\nu_m$  is the electron-neutral momentum transfer collision frequency. The collision frequency is linearly dependent on the neutral particle density above a few eV for hydrogen (similar to deuterium), and the accepted scaling is [21]

$$\nu_m [s^{-1}] = 4.8 \times 10^9 p [Torr] = 2.4 \times 10^8 s^{-1} \quad (17)$$

at 50 mTorr pressure.

Electron production is due to ionizing collisions between electrons and neutrals (deuterium molecules), and since the threshold ionization energy for deuterium in the ground state is 15.4 eV, one can see that only the higher energy electrons in the tail of the distribution function are responsible. Note that the only way that electrons can acquire sufficient energy to cause ionization, in the presence of crossed electric and magnetic fields, is to undergo multiple neutral collisions. The mean drift speed, for an electric field of 200 V/cm and a magnetic field of 0.5 T is  $4 \times 10^4$  m/s, or 4 cm/ $\mu$ s. This represents an energy of only  $4.55 \times 10^{-3}$  eV, far too low to cause ionization.

The electron source term,  $s$ , is the product of the electron number density ( $n_e$ ), ionization inverse mean free path ( $\alpha_l$ ), and electron velocity ( $v_e$ ), suitably averaged over distribution functions. The inverse mean free path is also known as the first Townsend coefficient, and it has been studied

since the early days of gaseous discharge investigations. The most common expression for  $\alpha_i$  is given by [23]

$$\alpha_i = C_1 p \exp \left[ -C_2 \left( \frac{p}{E} \right) \right]. \quad (18)$$

For hydrogen, the values of the coefficients are  $C_1 = 5$  ion pairs/cm-Torr and  $C_2 = 130$  V/cm-Torr, but the quoted range for validity in  $E/p$  is only 150-600 V/cm-Torr. Searches through the literature have been unsuccessful in finding other scaling for the much higher value of  $E/p = 4 \times 10^3$  V/cm-Torr, corresponding to the maximum preionization inductive electric field for FRCHX. However, data presented for  $\alpha/p$  plotted against  $p/E$  by Rose [24] for hydrogen and deuterium show both asymptoting to  $5 \text{ (cm-Torr)}^{-1}$  in the limit of  $p/E$  going to 0, which is consistent with eq. (18).

The diffusion coefficient in eq. (15) is more difficult to pin down. The formal definition of  $D$  is

$$D = \left\langle \frac{v^2}{3\nu_m} \right\rangle. \quad (19)$$

The problem here is the dependence on mean square velocity, and its dependence, in turn, on  $E/p$ . Reviews of the literature have turned up theoretical and experimental dependencies ranging from  $(E/p)^{0.71}$  to  $(E/p)^2$ . Crompton and Sutton [25] provided data up to  $E/p = 100$  V/cm-Torr, and the data appeared to asymptotically follow the power law

$$\bar{\varepsilon}[eV] = 0.357 \left( \frac{E}{p} \right)^{0.71}, \quad (20)$$

with  $(E/p)$  in V/cm-Torr, at the upper end of the  $E/p$  range.

If we assume only radial variations of quantities, we can ignore the mobility term in eq. (15). Further, if the diffusion coefficient is really constant and uniform, and we ignore sources for the time being, the continuity equation is

$$\frac{\partial n_e}{\partial t} = D_e \nabla^2 n_e, \quad (21)$$

which is the usual 1D radial diffusion equation. It can be solved analytically, and the solution is the sum of 0<sup>th</sup> order Bessel functions multiplied by decay constants. Higher order modes have faster decay rates, so that after some time, only the fundamental spatial mode persists. Forcing the density to go to zero at the radial boundary (wall of the tube for FRCHX) sets the radial variation as

$$n_e(r) = n_0 J_0 \left( \frac{\alpha_1 r}{R_w} \right). \quad (22)$$

Here,  $\alpha_1$  is the first zero of the Bessel function and equal approximately to 2.405. Now, the Laplacian of  $n_e$  can be replaced by

$$\nabla^2 n_e = -\frac{n_e}{\Lambda_r^2}, \quad (23)$$

where the fundamental diffusion scale length

$$\Lambda_r = \frac{R_w}{2.405}. \quad (24)$$

The threshold for electrical breakdown is when  $dn_e/dt = 0$ . Going back to the electron continuity equation, we see that the threshold occurs when collisional ionization is just balanced by diffusion loss:

$$\begin{aligned} \nu_i n_e &= D_e \nabla^2 n_e = -D_e \frac{n_e}{\Lambda_r^2}, \text{ or} \\ \nu_i &= \frac{D_e}{\Lambda_r^2}. \end{aligned} \quad (25)$$

When a magnetic field is present, that is orthogonal to the electric field, the effective ionization rate, mobility and diffusion coefficient change, as one might expect. The diffusion coefficient becomes a tensor,

$$D^B = \frac{\langle v^2 \rangle}{3\nu_m} \begin{bmatrix} D_T & D_\perp & 0 \\ D_\perp & D_T & 0 \\ 0 & 0 & D_\parallel \end{bmatrix}, \quad (26)$$

Here, the first row corresponds to the density gradient in the direction of the electric field ( $\phi$  direction for FRCHX), the second row corresponds to the perpendicular direction ( $r$  for FRCHX), and the third row corresponds to the direction of the magnetic field ( $z$  direction for FRCHX). The values of the three different multipliers in the matrix are

$$\begin{aligned} D_T &= \frac{(\nu_m^2 / \omega_c^2)}{(1 + \nu_m^2 / \omega_c^2)} \\ D_\perp &= \frac{(\nu_m / \omega_c)}{(1 + \nu_m^2 / \omega_c^2)}, \\ D_\parallel &= 1 \end{aligned} \quad (27)$$

and the diffusion coefficients in the transverse direction and perpendicular direction are reduced for high magnetic fields. Denoting  $D^0$  as the diffusion coefficient without magnetic field, eq. (21) becomes

$$\nu_i^B = D^0 \left( \frac{D_\perp}{\Lambda_r^2} + \frac{1}{\Lambda_z^2} \right). \quad (28)$$

Note that we have explicitly included diffusion in the axial direction, with

$$\Lambda_z = \frac{L}{\pi}, \quad (29)$$

and  $L$  is the axial distance from midplane to end wall. It becomes important when the axial diffusion length becomes comparable to the effective radial diffusion length



$$\Lambda_r^B = \frac{\Lambda_r}{\sqrt{D_{\perp}}} . \quad (30)$$

Equivalently, we can define a new diffusion coefficient,  $\Lambda_B$ , by

$$\frac{1}{\Lambda_B^2} = \frac{D_{\perp}}{\Lambda_r^2} + \frac{1}{\Lambda_z^2} . \quad (31)$$

The mobility is modified in the presence of a transverse magnetic field also and, when put into the formulae for electrical conductivity, results in Pedersen conductivity in the transverse direction and Hall conductivity in the perpendicular direction.

The modification of the first Townsend coefficient is [21]

$$\alpha_i^B = \frac{C_1 p}{\cos \theta} \exp\left(\frac{-C_2 p}{E \cos \theta}\right), \quad (32)$$

where  $\theta$  is the angle defined in eq. (13). Thus, one can see that at high magnetic fields, the exponential factor can become quite small, so that eventually, the reduction in ionization rate overcomes the reduction in diffusion loss rate.

### 3.2.3.2.3 Dimensionless Calculations for FRCHX Parameters

Based on the theory and empirical results presented above, we have evaluated various parameters for FRCHX. In all cases, we have assumed a neutral deuterium number density corresponding to a pressure of 50 mTorr, or  $1.77 \times 10^{15} \text{ cm}^{-3}$  molecular number density. This gives an electron-neutral collision frequency of  $2.4 \times 10^8 \text{ s}^{-1}$  and an electron mobility of  $7.33 \times 10^6 \text{ cm}^2/\text{V-s}$ . The magnetic flux density, when held constant, was 0.5 T, corresponding to an electron cyclotron frequency of  $8.79 \times 10^9 \text{ rad/s}$ . The electric field was varied from 0 V/cm to 2,000 V/cm (approximately one order of magnitude higher than obtained with the existing preionization capacitor bank). The quartz-tube radius is 5.2 cm, corresponding to a radial diffusion length of 2.16 cm. We have also assumed an axial diffusion length of  $100/\pi \text{ cm}$ , so that axial diffusion will be roughly comparable to radial diffusion at the tube wall for the full bias magnetic field value.

In Figure 251, we show a plot of the drift speeds calculated as a function of electric field for no magnetic field and full 0.5 T magnetic induction. One can see that the effect of the magnetic field is to decrease uniformly the drift speed by more than two orders of magnitude.

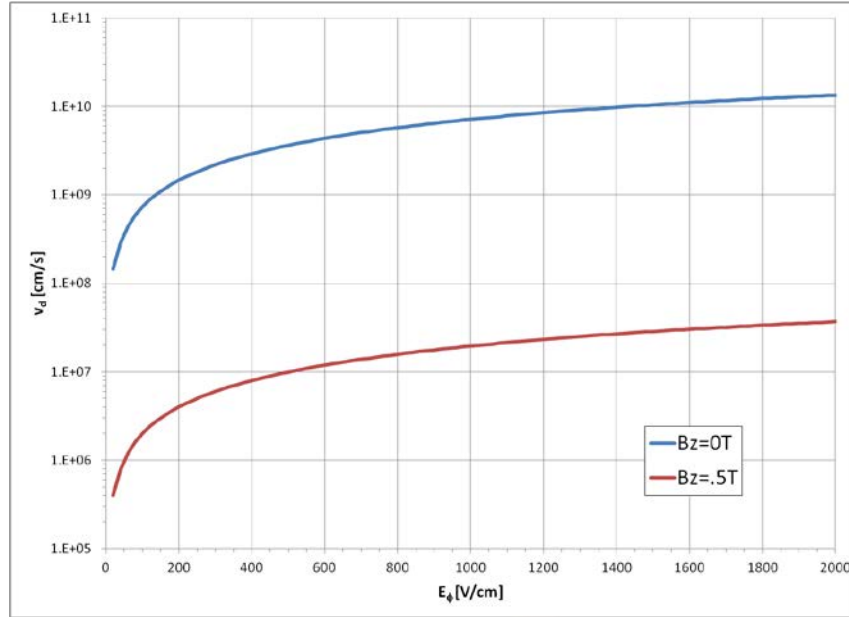


Figure 251. Drift velocities as a function of electric field with and without magnetic field

In Figure 252, we have plotted the first Townsend coefficient, the inverse mean free path for electron-neutral collisional ionization, as a function of electric field for the no-magnetic-field case and the full-magnetic-field case. The no-field case becomes constant above approximately 100 V/cm at 50 m Torr pressure because the exponential factor in eq. (15) approaches unity above this field value.

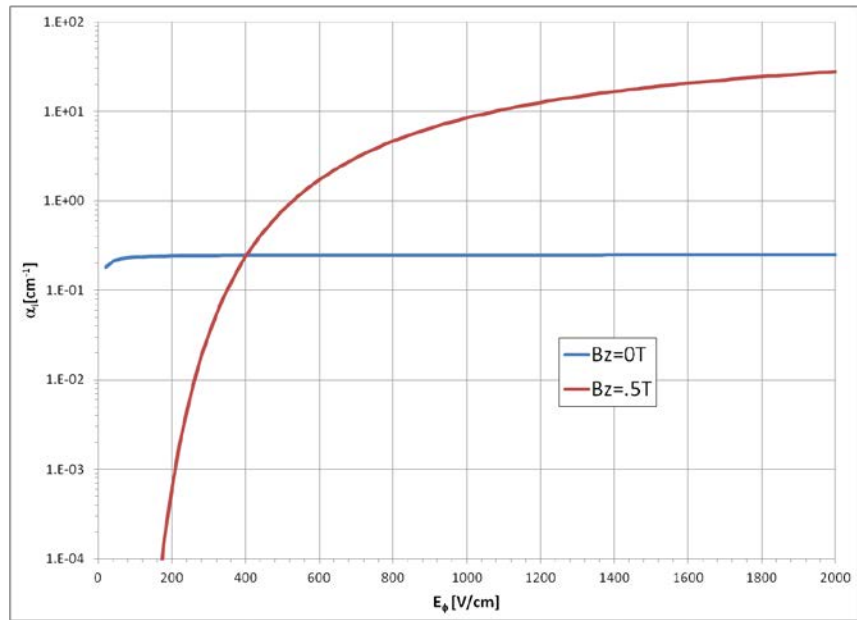


Figure 252. First Townsend coefficient (inverse ionization mean free path) as a function of electric field with and without magnetic field

In Figure 253 and Figure 254, we show the ionization rate and ionization exponentiation time, respectively, as functions of electric field for no magnetic field and full 0.5-T induction. The ionization time is important because it represents the shortest growth time for electron population, i.e., for no diffusion losses. One can see that the exponentiation time is already below 100 ns for electric-field values in excess of approximately 100 V/cm for the no-magnetic-field case, but that for 0.5-T induction, a 100 ns e-folding time is not achieved until the electric field exceeds 800 V/cm.

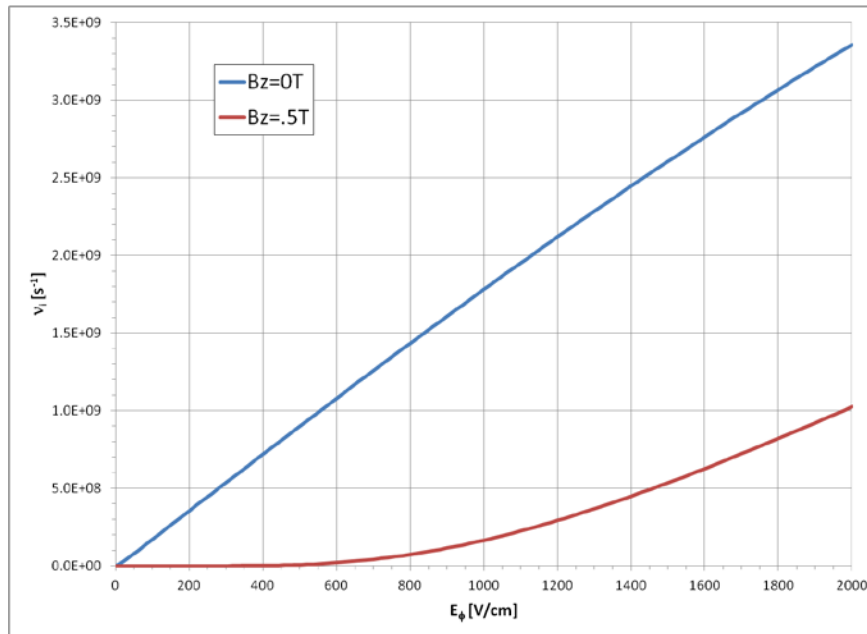


Figure 253. Ionization rate as a function of electric field with and without magnetic field

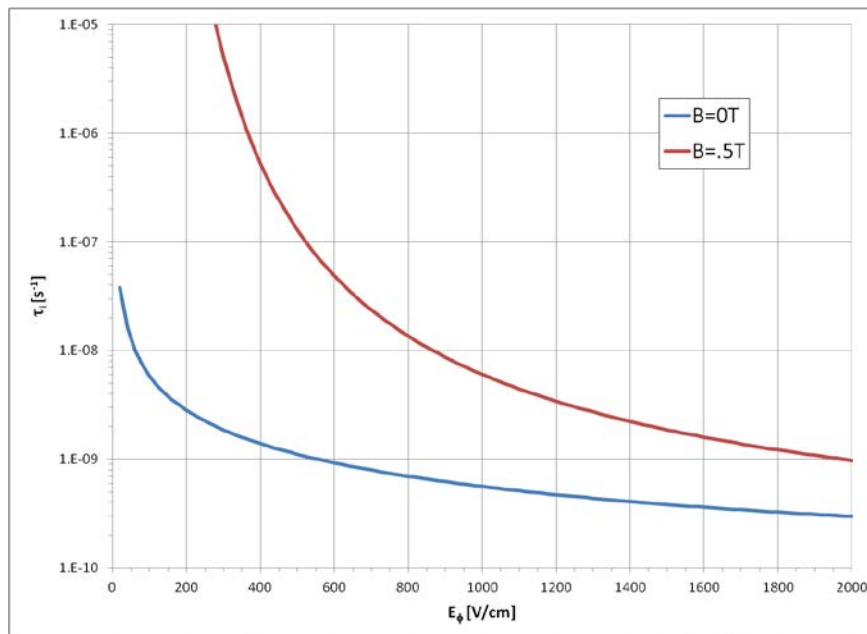


Figure 254. Ionization time as a function of electric field with and without magnetic field

Equation (20), the scaling of average electron energy as a function of  $(E/p)$ , is shown in Figure 255. We note again, some authors have deduced higher exponents for  $(E/p)$ , but usually at values well below 100 V/cm.

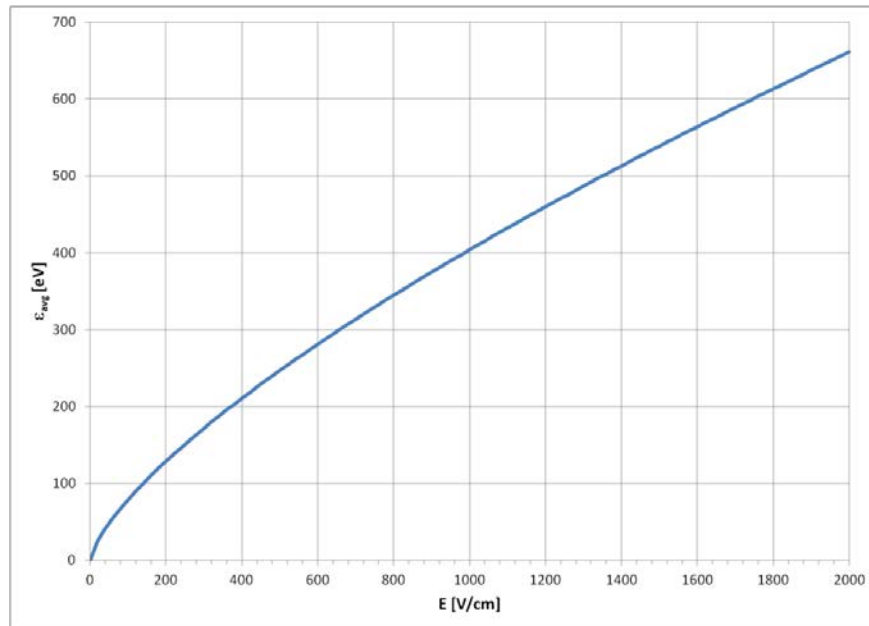


Figure 255. Average electron energy as a function of electric field

The diffusion coefficients for electrons, with and without magnetic field, are plotted in Figure 256 as a function of electric field. As is the case for the ionization rate coefficient, the diffusion coefficient is considerably reduced when the magnetic field is present.

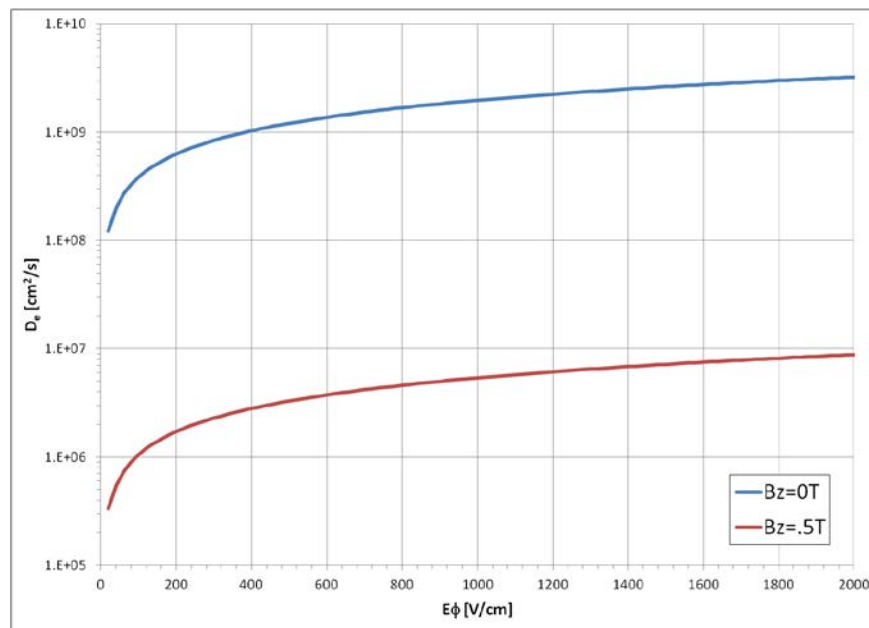


Figure 256. Electron diffusion coefficient as a function of electric field with and without magnetic field

In Figure 257, we show the ionization rates and diffusion loss rates as a function of electric field for both the no-magnetic-field and full-field cases.

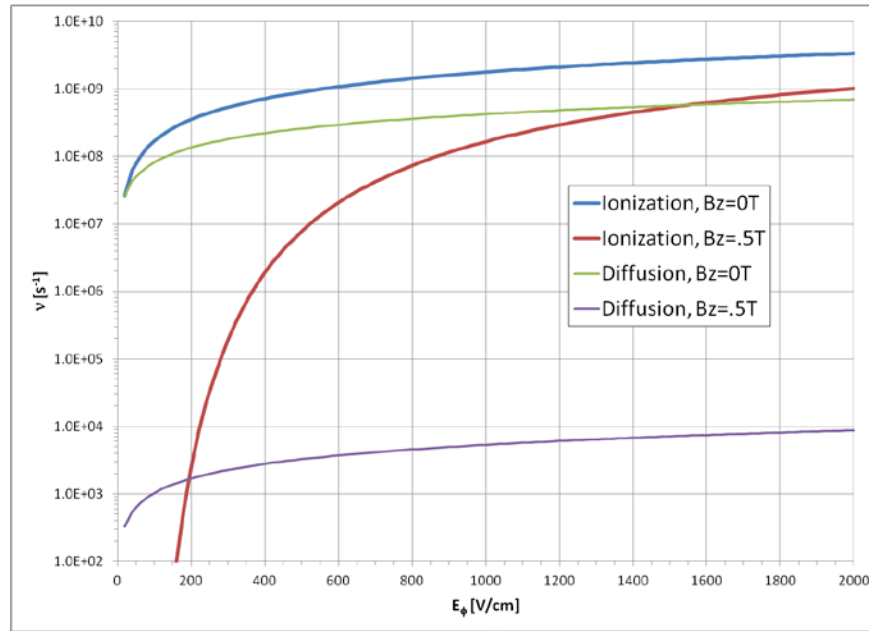


Figure 257. Ionization and diffusion loss rates as a function of electric field with and without magnetic field. For the no-field case, the ionization rate exceeds the diffusion loss rate for electric fields as low as 20 V/cm. However, for the full-field case, the ionization rate does not exceed the diffusion loss rate until the electric field exceeds approximately 190 V/cm, near the maximum inductive electric field produced by the FRCHX preionization discharge, and then only at the maximum radius corresponding to the inside radius of the quartz tube. This feature is shown more clearly in Figure 258, where we have plotted the effective, or net, electron growth rate (i.e., ionization rate minus diffusion loss rate). The zero crossing of the net rate represents the threshold for electrical breakdown.

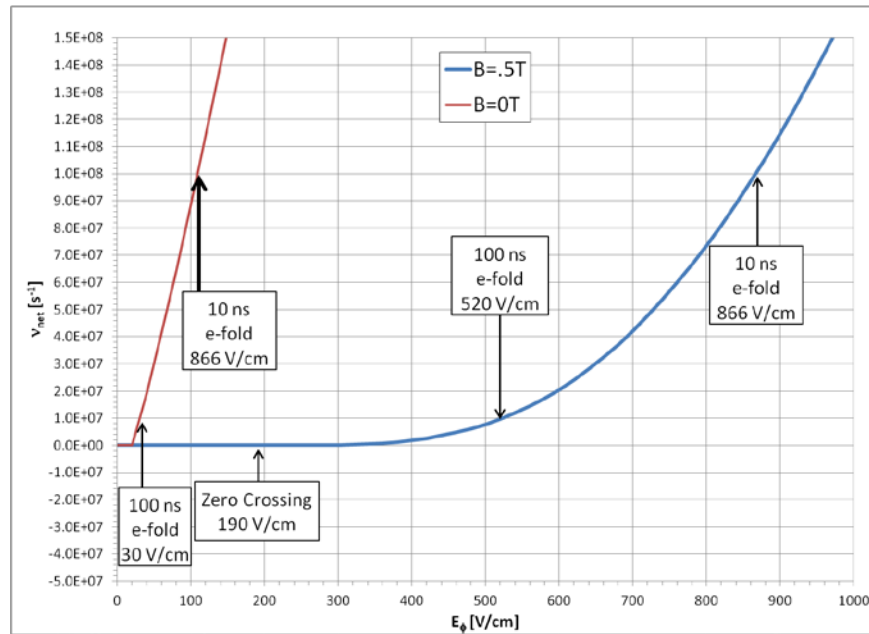


Figure 258. Net ionization-loss rates as a function of electric field with and without magnetic field

The inverse of the net rate is the exponentiation, or growth, time. One can see for the maximum field case, even though the threshold occurs at an electric field value of approximately 190 V/cm, the exponentiation time is long ( $> 1 \mu s$ ) for electric fields below approximately 400 V/cm, and that it only drops below 100 ns for electric fields above approximately 520 V/cm and below 10 ns for fields above 850 V/cm, considerably above the electric field achievable with our present preionization discharge circuit. One can also see why breakdown appears to start near the quarter-cycle time of the PI discharge, because at that time, the magnetic field approaches zero and the net ionization rates jump dramatically.

Whereas Figure 251–Figure 258 have shown parameter variations as a function of electric field for magnetic-flux densities of either 0 T or 0.5 T, Figure 259 and Figure 260 show how the net ionization/loss rate and exponentiation time vary with magnetic induction for electric-field parameters of 200, 400, 800, and 1,600 V/cm. If for example, one could achieve a peak-electric field of 400 V/cm, one can see from Figure 260 that a 100 ns exponentiation time is achieved only for magnetic flux densities below approximately 0.35 T, and for a 10 ns e-fold time approximately 0.15 T. For our present case of 200 V/cm maximum electric field, a 100 ns e-fold

time can only be achieved for magnetic-flux densities below approximately 0.15 T, and a 10 ns exponentiation time can only be achieved for magnetic-flux densities below only 0.05 T.

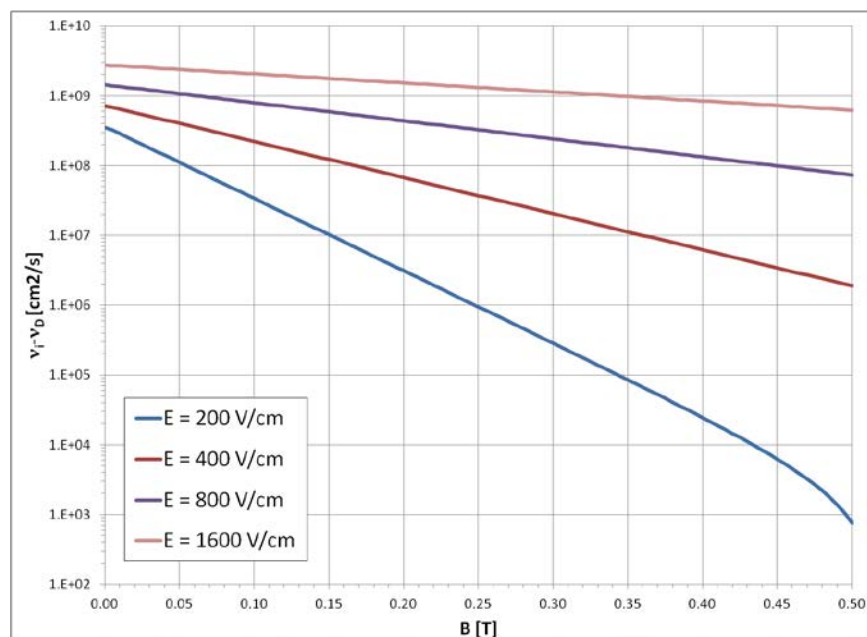


Figure 259. Net ionization rate as a function of magnetic flux density for various values of electric field

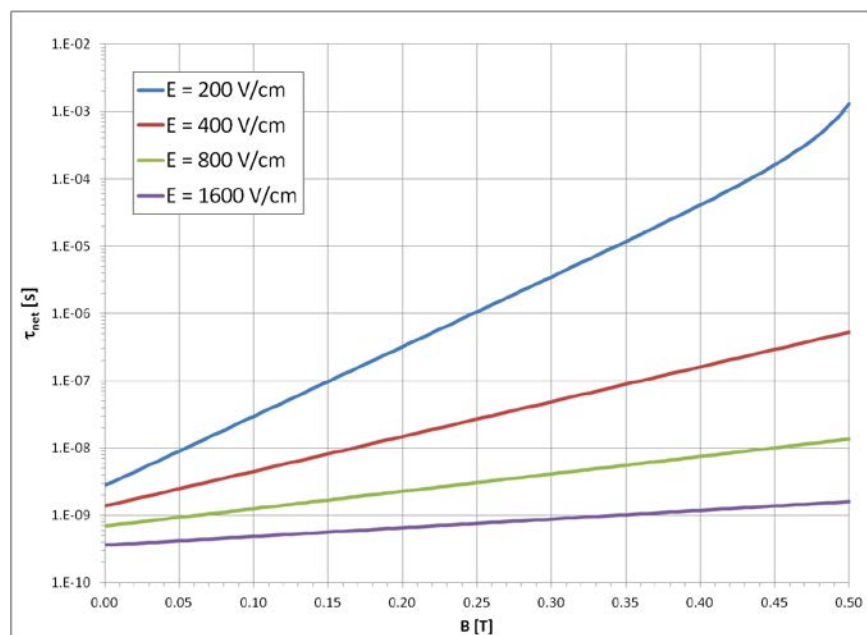


Figure 260. Net electron exponentiation time as a function of magnetic flux density for various values of electric field



Although the above analysis should only be considered as semi-quantitative, several conclusions can be drawn. Among them are:

- For a pressure of 50 mTorr, the presence of a transverse-magnetic field makes it harder to breakdown neutral hydrogen or deuterium.
- The magnetic-field inhibition of breakdown can be overcome by increasing the electric field.
- If the axial magnetic field lines terminate on the quartz-tube wall, then the diffusion-loss rates will increase and breakdown will require an even higher electric field.

There are other aspects that may further complicate the analysis. For example, we have assumed the electrons are free to migrate according to the equations presented. However, if the electron and ion fluxes due to diffusion differ significantly, charge imbalances can occur, leading to electrical polarization. The net effect of polarization is that the faster species will slow down and the slower species will speed up, so that the net diffusion coefficient will be between the two individual species' diffusion coefficients. This type of diffusion is called ambipolar diffusion, and it may be applicable to FRCHX preionization.

We have also ignored recombination in the electron continuity equation. That is generally a good approximation for weakly ionized plasmas, because the recombination rate is proportional to the square of the electron density. For gas breakdown, this approximation should be valid, but recombination will become increasingly important as the ionization increases.

We should also mention that several researchers have reported that they had to go to extreme lengths to keep the plasma from damaging their quartz containers and that for some breakdown studies involving RF discharges, they had to go to very short RF pulse lengths ( $< .5 \mu\text{s}$ ) to avoid introduction of silicon and oxygen into the plasma. Oxygen, especially, is problematic because it has an affinity for electrons; i.e., it has an appreciable attachment coefficient. The problem with release of wall material and tube damage may be exacerbated when the direction of  $\mathbf{ExB}$  is radially outward.

In previous experiments, such as FRX-A and FRX-B at Los Alamos [26], FRC formation was accomplished similarly to how it is done for FRCHX; i.e., there was a preionization discharge through theta coils prior to the main discharge. However, the peak PI voltages were higher than on FRCHX (80 kV and 75 kV, respectively, compared to 60 kV), the discharge frequency appeared to be higher (0.5  $\mu$ s and 0.6  $\mu$ s quarter cycle times, respectively, compared to 1.1  $\mu$ s). Furthermore, the theta coils in those experiments were larger diameter, and the non-coil series inductance was a lower percentage of the total inductance of the discharge circuits, so that the inductive electric fields in the gas were probably considerably higher than for FRCHX. The initial polarity of the discharges was the same as for FRCHX; i.e., so that the magnetic field from the first quarter cycle of the PI discharge opposed the bias field, but in FRX-A and FRX-B the PI discharge was allowed to resistively decay before the main discharge occurred. From the literature, it is not clear exactly when breakdown and rapid heating occurred with respect to the beginning of the PI discharge.

In his FRC review paper, Tuszewski [27] has said that “Despite extensive research and relatively good success at forming FRCs, the experimental approach remains largely an empirical process of trial and error.” Also, writing about various formation techniques, including high-frequency preionization theta discharges, he says “It is probably fair to say that, even though all of these PI techniques have proved workable, no one of them is clearly superior to the others... With proper choice of timing and amplitude (a very empirical process), most techniques have yielded FRCs with comparable parameters... However, it must be emphasized that, for a given PI scheme, slight departures from the ‘optimum’ conditions often lead to very poor FRC formation.”

As pointed out previously, the objective of preionization should be to rapidly ionize the gas and heat the resulting plasma to a temperature of approximately 2 eV, to successfully trap and hold the poloidal flux within the FRC. It seems that that process could occur given a strong enough electric field, so that the necessary heating would occur during the first quarter cycle of the PI discharge, with the polarity of the discharge such that the flux within the tube would increase during the first quarter cycle. Ideally, the main discharge would then trigger at the quarter cycle time of the PI discharge, so that minimal reversals in  $\mathbf{E}$  and  $\mathbf{E} \times \mathbf{B}$  would occur, and there would be no radial “breathing” of the plasma. An attempt could be made to rebuild the PI bank circuitry

to increase the charge voltage and frequency by configuring the bank capacitors in series (lowering the capacitance), and minimizing the inductance between the bank and the coil. Potentially, an order of magnitude increase in inductive electric field could be achieved.

If it turns out that those efforts are not sufficient to ionize the gas and heat the plasma adequately within the first quarter cycle, we recommend that the PI discharge be allowed to ring down (i.e., undergo enough oscillations that the amplitude damps to a small fraction of the initial amplitude) prior to discharging the main bank, similar to what was done on FRX-A and FRX-B. With this technique, even with limited power, the total energy available should be sufficient to heat the plasma to a high-conductivity state prior to main discharge. However, there is a caveat – if the gas does not break down until the magnetic field goes to zero, and then does so rapidly, the resultant plasma will exclude flux as the field rises again. This phenomenon may be the reason that historically, only approximately only 25% of the ambient flux has been trapped during formation.

#### *3.2.3.2.4 Two-Dimensional Dynamic Ionization Calculations*

In this section, we present results from 2D time-dependent ionization calculations performed with the generalized partial differential equation solving application FlexPDE<sup>®</sup>, based on the theory presented earlier. Limitations of the calculations are that they ignore the full electron and ion equations of motion (the electron equation of motion is assumed to be quasi-static due to the high electron-neutral collision frequencies), so that local charge neutrality is implicit. Still, they have all of the tensor mobility and diffusion coefficients. Another limitation is that the actual diffusion in the experiment is probably ambipolar, so that the ion diffusion must be accounted for. Since we do not have detailed information about ion diffusion, we have made, what we believe, are reasonable assumptions to account for it. We have estimated the effective diffusion rate by monitoring the decay of plasma light following ionization from the HPRF pre-ionization source. That effective diffusion time constant was measured to be approximately 1.9  $\mu\text{s}$ , resulting in an effective diffusion coefficient of approximately  $2.5 \times 10^6 \text{ cm}^2/\text{s}$ .

The calculations solve the electron continuity equation, eq. (14). They include collisional ionization, mobility, and diffusion. Some tests were conducted with recombination included, but

the effect was negligible for the parameters canvassed, so it was omitted from most calculations to reduce computation time. The calculations were run on an 8-core, 16-GB-RAM PC running a Windows 7 64-bit operating system. FlexPDE<sup>®</sup> was run multi-threaded, and considerable improvement in computation time was seen compared to lower capacity machines.

In Figure 261 we show results for the total electron population history for the case most closely resembling FRCHX in its present configuration, i.e., the initial Bias magnetic field is approximately 0.5 T in the axial direction, and the peak inductive electric field at the inside edge of the quartz tube is approximately 200 V/cm. One can see that for the first quarter cycle of the PI discharge (up to 1.1  $\mu$ s), the electron population is decreasing, and only reverses this trend once the second quarter cycle begins. The arrow on the figure points to the time at which the electron population is rapidly rising, which may be indicative of breakdown (1.3  $\mu$ s). At this time, the amplitude of the axial magnetic field is only 0.1 T, or 20% of the original value. If the plasma is formed at this time, only a small fraction of the initial bias flux would be trapped.

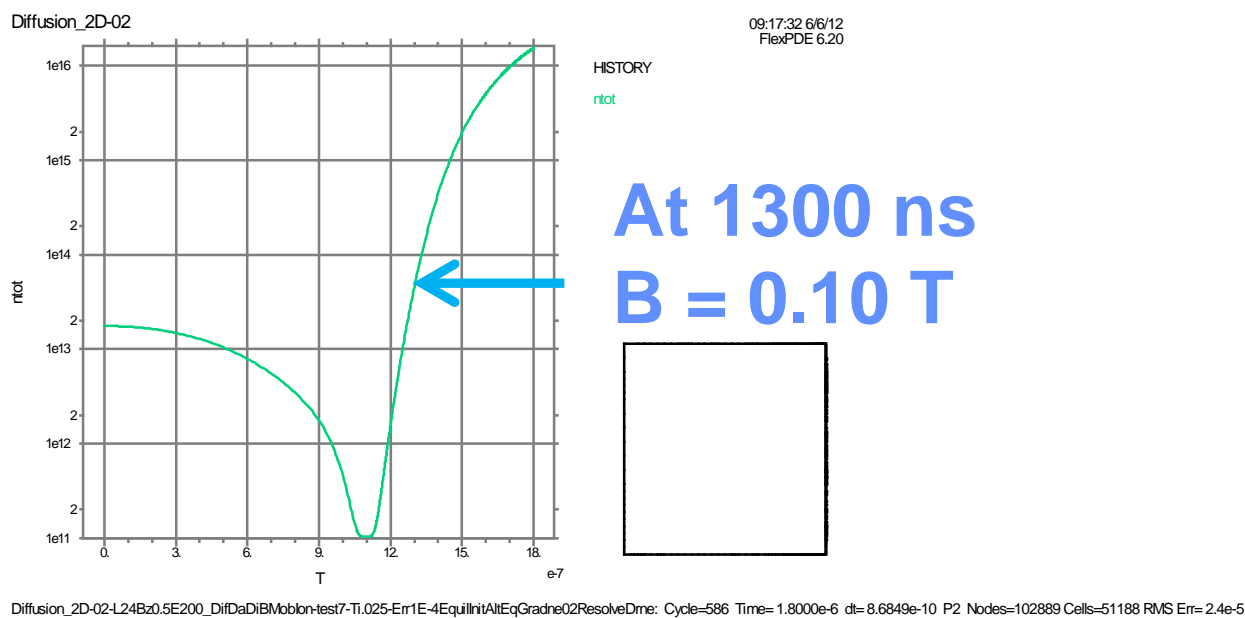


Figure 261. Electron population history for the case corresponding to the present FRCHX configuration

If we double the initial electric field at the chamber wall to 400 V/cm, while keeping the initial bias field at 0.5 T, we get the behavior shown in Figure 262. Now, appreciable electron population growth occurs in less than 1  $\mu$ s. We know that in general, for any given magnetic

field, there is some threshold value of transverse electric field for which breakdown occurs, and this simulation result seems to indicate that at 400 V/cm, we may have crossed that threshold.

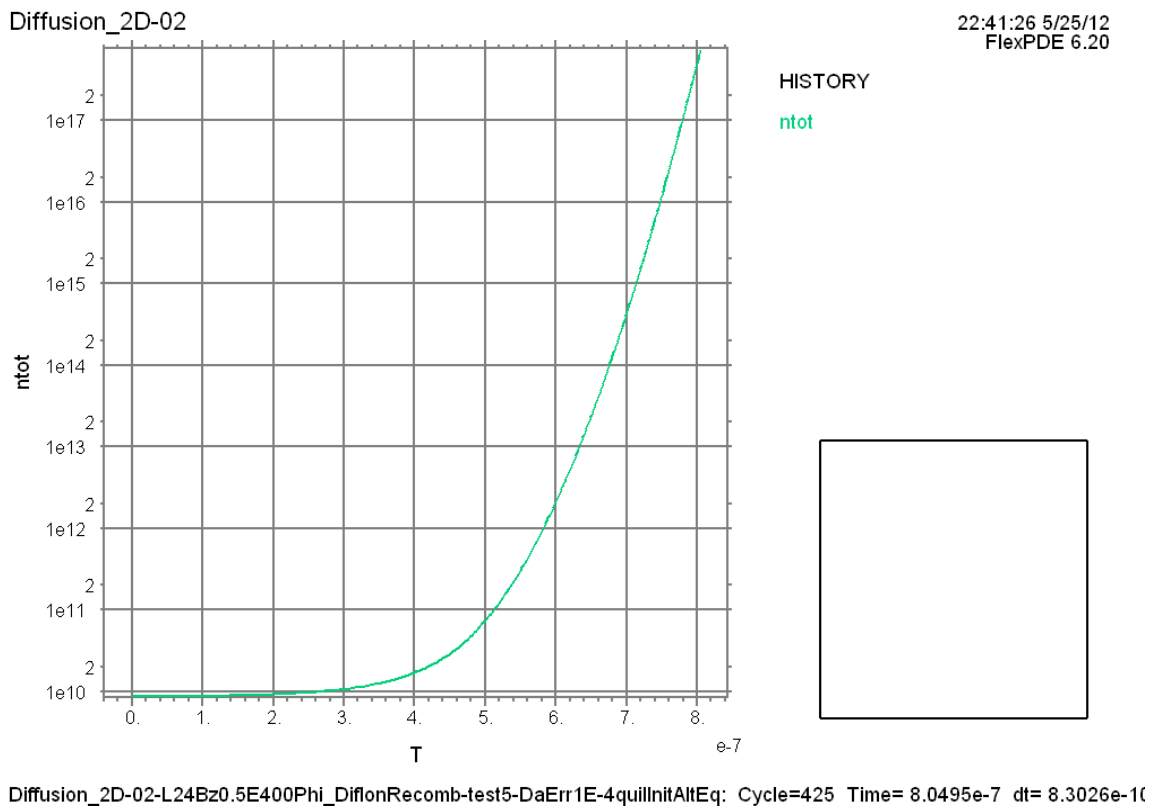


Figure 262. Electron population history for the case of 0.5 T bias field and 400 V/cm initial peak electric field

We have made some preliminary estimates to see what we could achieve if we tried to boost the initial peak inductive electric field from the PI bank. If we reconfigured the bank as a two-stage Marx, and we minimized series inductance between the bank and the Theta coils, we believe that we could apply an initial peak inductive electric field of approximately 665 V/cm. Figure 263 shows the electron population history for the case of 0.5-T Bias field and this value of inductive electric field. We see that the electron population has risen significantly by 180 ns, at which time the magnetic field inside the tube is 0.15 T.

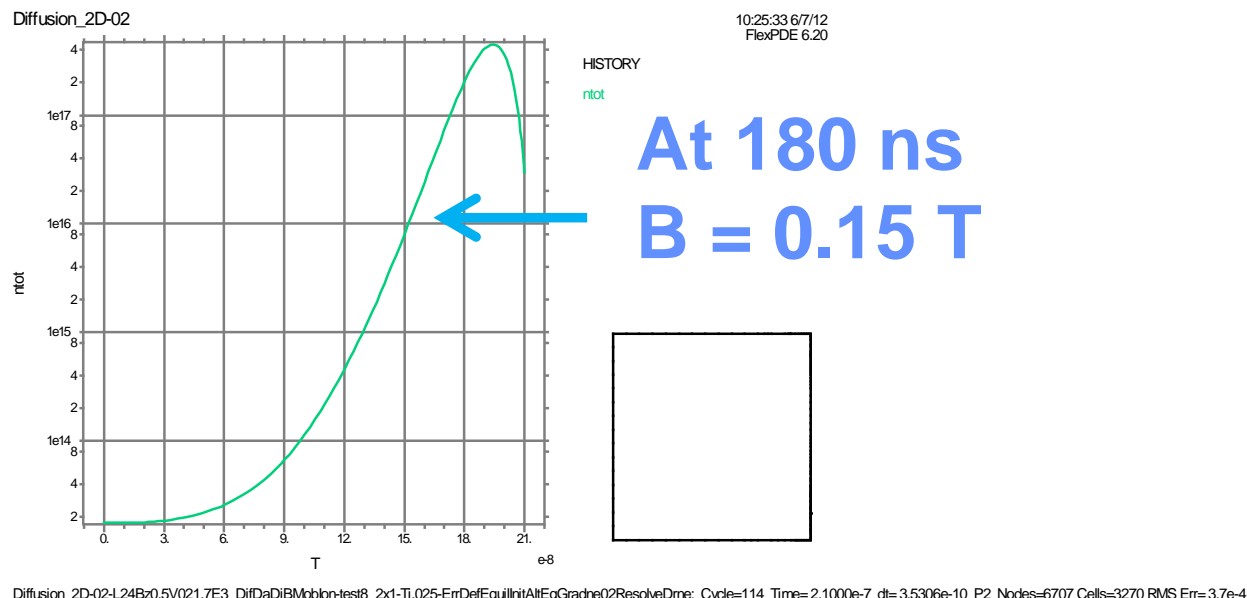


Figure 263. Electron population history for the case of 0.5 T Bias field and 665 V/cm peak initial electric field

The final example calculation we show, in Figure 264, is the case where we have reversed the polarity of the electric field with respect to the magnetic field (this could be achieved by reversing the polarity of the PI bank, for example). Again, we specified an initial Bias field of 0.5 T and used the previous electric field amplitude of 665 V/cm, but changed its sign. In this case, something dramatic has changed. Rapid ionization now occurs by about 90 ns after the beginning of the PI discharge, and at that time the magnetic field value has not changed appreciably from its initial 0.5-T value. If we could actually achieve plasma formation this early, the amount of flux trapped in the FRC would increase significantly compared to what we have been trapping.

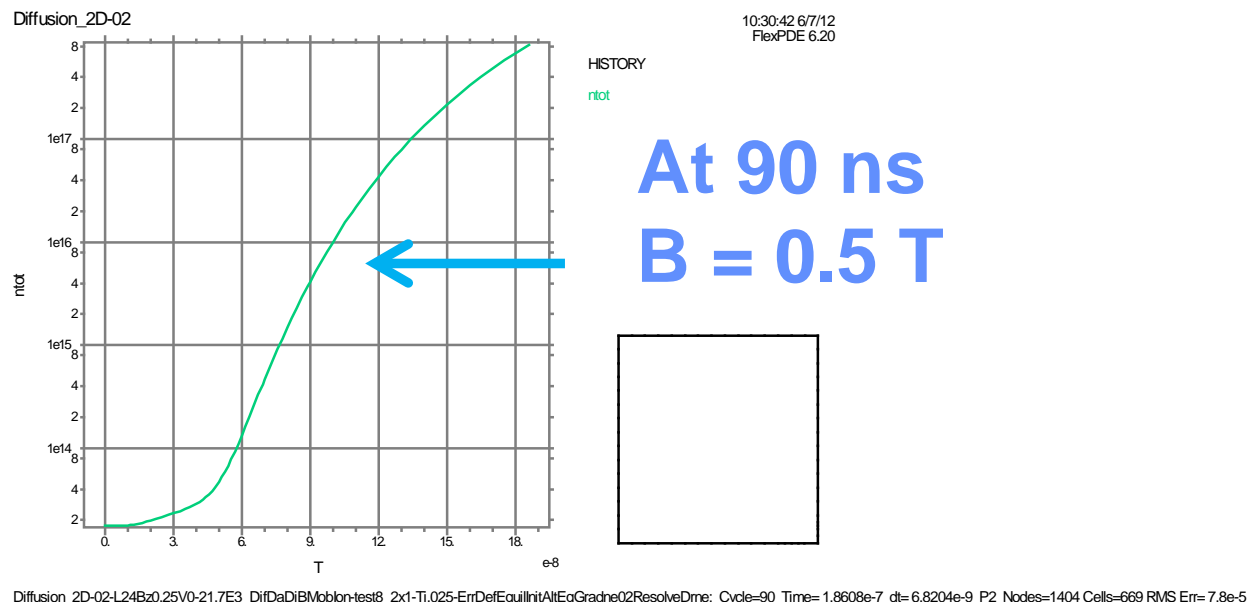


Figure 264. Electron population history for the case of 0.5 T Bias field and -665 V/cm electric field

### 3.2.4 Bias Ring System

Another issue for long plasma lifetime is stability. In particular, it is known that FRCs rotate and that the free energy associated with the rotation can drive an  $n = 2$  instability. This instability can cause disruption of the closed field structure of the plasma. We are developing an implementation of a technique to counter the tendency of the FRC to rotate. As shown by Steinhauer [28, 29], the rotation derives from electrical shorting of the electric field by a conducting wall where the FRC open-field lines exit from the formation region. In the equipotential ring approach, we decided to attempt to restore the electric field shorted out at the wall with a set of quasistatic potentials imposed on a set of annular rings in the region of the diverging magnetic field lines, as suggested by E. Ruden (AFRL) and shown schematically in Figure 265.

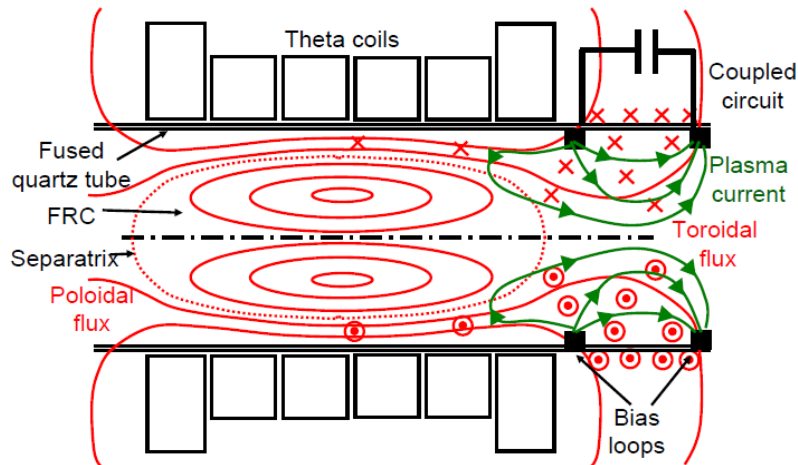


Figure 265. Magnetic field configuration with equipotential rings

In Figure 266, we show design drawings for the equipotential rings integrated into the FRC vacuum tube (a), the support and bias rod feedthrough flange (b), and the rings with their support and bias rods (c).

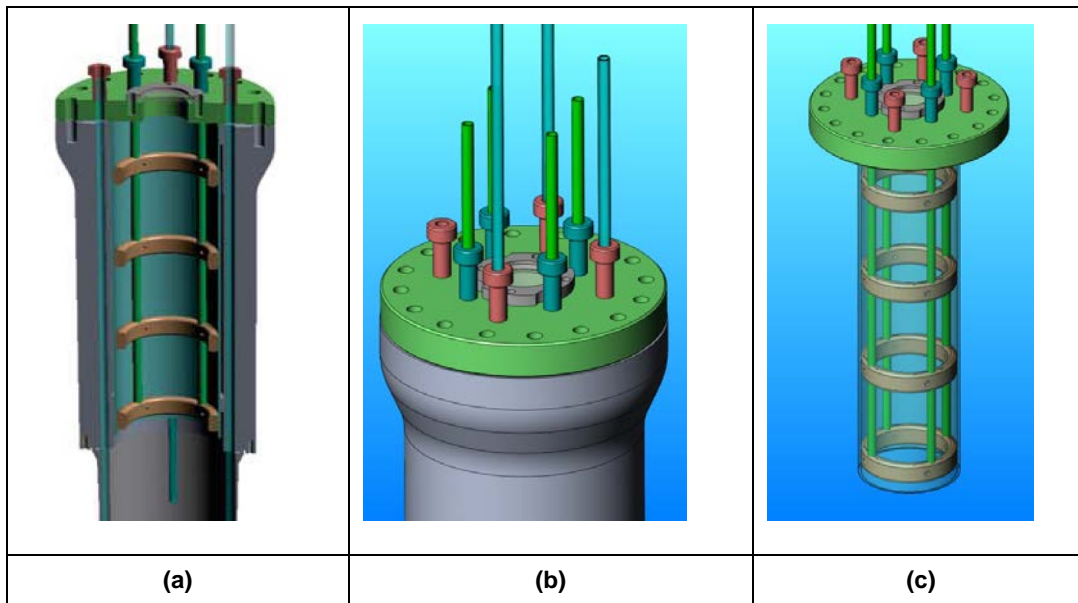


Figure 266. Design drawings for equipotential rings

Interior to the upper Shiva electrode bore, most of the open B field lines which envelop the FRC at the far end of the translation region exit the system through a layer of stainless steel and/or cold, dense, collisional, stagnant, weakly ionized gas/plasma obeying simple Ohm's Law. Over time, the resistive (simple Ohm's) boundary layer exposed to the plasma E field conducts current



until an equipotential boundary condition is established, leaving only diamagnetic flow near the wall. The boundary layer current introduces a toroidal component of the B field, sending a torsion wave down the open field lines, dragging the plasma along with it. The proposed solution is to insert conducting rings into boundary layer such that we can maintain the zero rotation  $\mathbf{E}$  field lines despite simple Ohmic losses. To avoid the need for switches and to minimize current load, gas puffing is needed.

Early in 2012, we completed fabrication of a set of the four equipotential rings, shown in Figure 266, for placement above the capture region in FRCHX. The rings are shown in Figure 267, and the placement of the assembly in the experiment is shown in Figure 268.

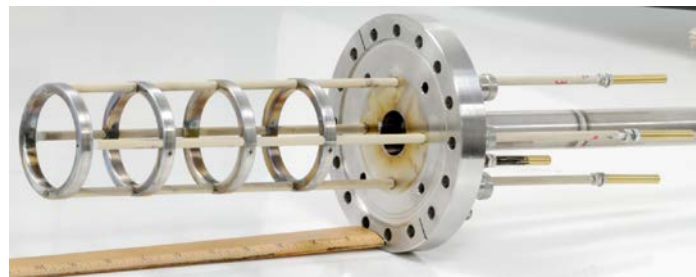


Figure 267. Equipotential ring assembly

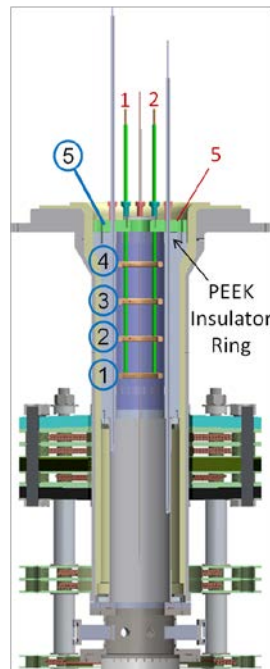


Figure 268. Location of EP rings in vacuum chamber

We also had the upper vacuum flange modified with a dielectric spacer so that the flange itself would be electrically floating. Originally, the rings were monitored passively for potential caused by plasma using a simple resistive divider. The vertical support rods allowed electrical connections to the voltage dividers. During shots with the monitors, potentials up to 1,000 V were recorded on ring 1 (closest to the liner mockup), with approximately linear reduction over rings 2-4 higher up. Based on these measurements, we designed a bias-capacitor bank to apply potentials roughly corresponding to the observed passive voltages measured. A schematic of the bias bank is shown in Figure 269 and the top of the 4 x 4 capacitor array that is mounted horizontally on a platform is shown in Figure 270. One can see the 4 x 4 array of capacitors, output wires to the ring connectors, bias resistor between ring 4 and flange (bank ground), and Pearson current monitors.

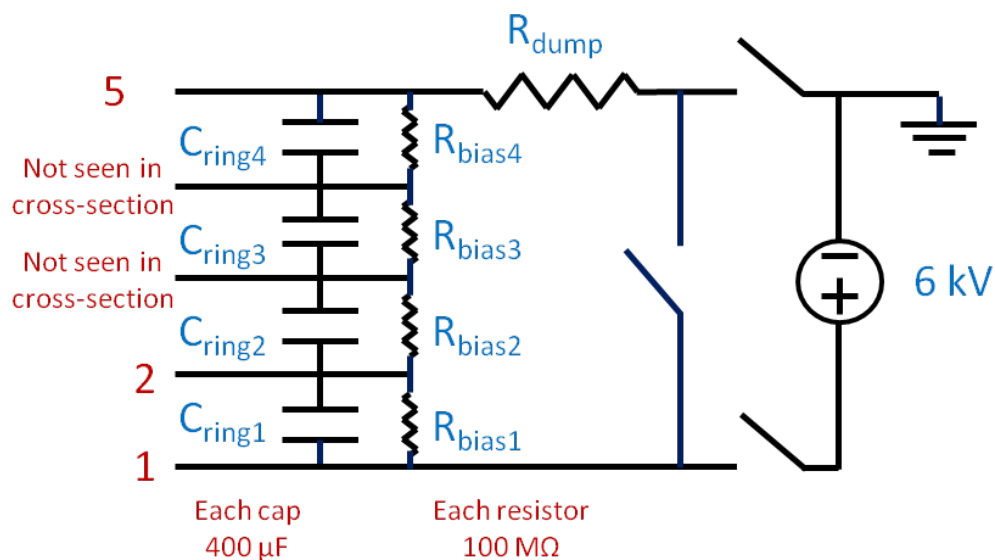


Figure 269. Bias circuit design for EP rings



Figure 270. Top of bias bank

The planned approach called for operating the rings, first, in passive mode and recording the potentials they floated to gauge how much active bias would be required. In Figure 271, we present data for equipotential rings in passive-monitor mode. The shot number was 03\_06\_2012\_t06. This was a gas-puff shot with cable discharge RF triggered  $87 \mu\text{s}$  before PI. Although the ring voltage signals are quite noisy, they show a peak voltage on ring 1 of approximately 800 V, and successively smaller voltages on the rings above ring 1. Also on the graph are B-dot signals at locations from T0 to T6 for timing comparisons, and timing marks to show the correlation between noise spikes and PI, main, and crowbar switches firing. Note that the T2 B-dot diagnostic had problems throughout this test sequence.

Based on this plasma potential data, we finalized the design of the active bias bank for the rings.

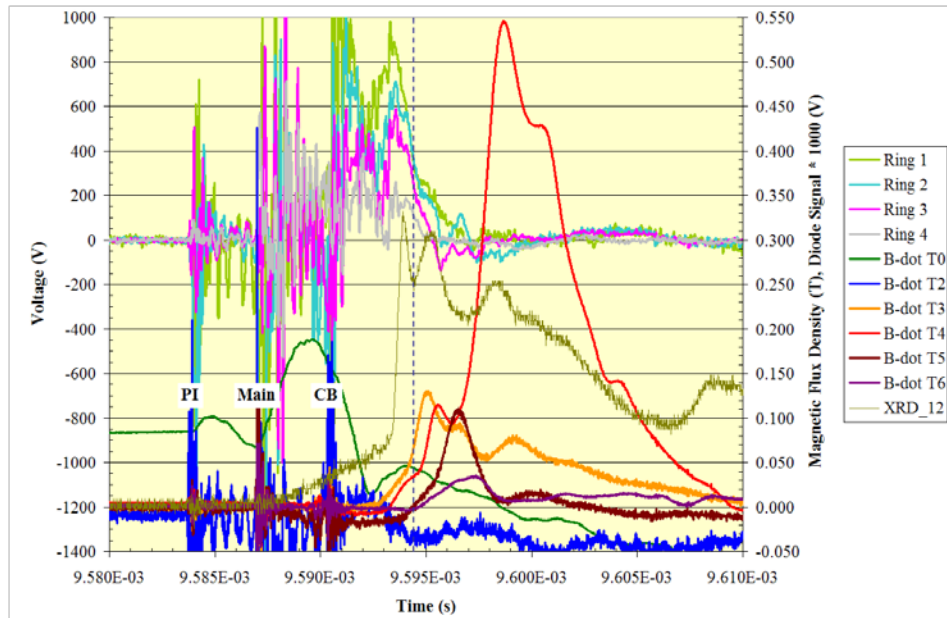


Figure 271. Equipotential ring voltage data

Figure 272 shows data from shot number 03\_14\_2012\_t07, which was a gas-puff shot with actively biased equipotential rings. Ring 1 had a voltage of 800 V applied. The four upper traces are current waveforms on the wires connecting the rings to the bias bank, taken with Pearson current transformers. One can clearly see that the current rate of rise is limited by the inductance of the circuit. Because of the inductive-voltage drop between the capacitors and the rings, the actual voltage on the rings is significantly lower than the original charge voltage on the capacitors, so that the effectiveness of the ring biasing is also limited. Based on this information, we decided to reconfigure the 4 x 4 ring bias bank to place all 16 capacitors in parallel and minimize the inductance of the circuit to try to maintain ring bias significantly longer.

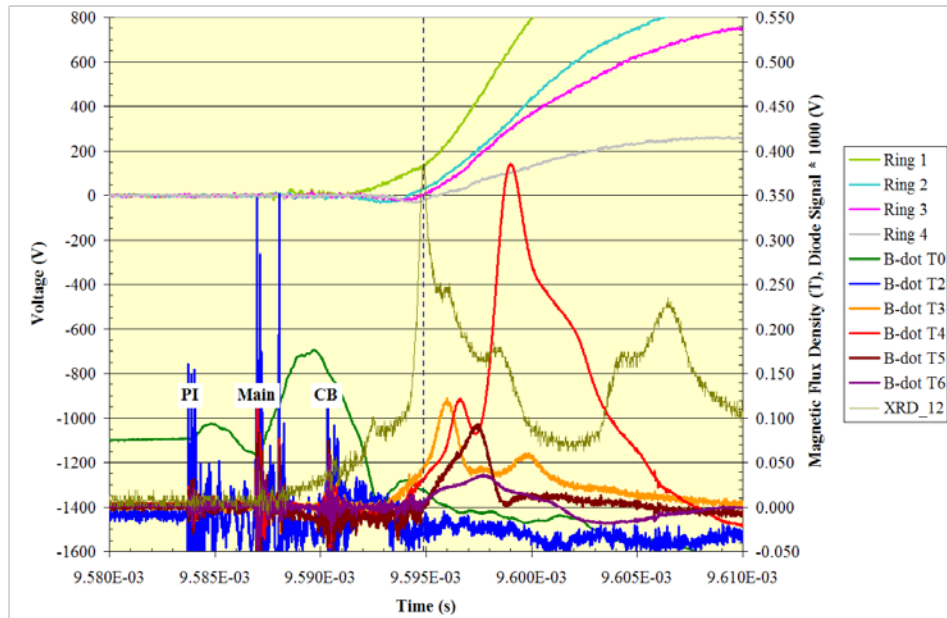


Figure 272. Actively biased ring current data

Even though the ring biasing was not optimal, we observed what appeared to be an effect (Figure 273). On all of these shots, we ran a 12-frame Hadland fast camera with axial view to observe visible light from the plasma. Without active ring biasing, we saw evidence of slow rotation of features in the images. With active biasing, the rate of rotation of these features appeared to slow, and even stop late in time. In Figure 273, we show a comparison of camera data for shot numbers 03\_14\_2012\_t07(with 800 V ring 1 bias) and 03\_14\_2012\_t08 (without ring bias). The parameters for the two shots were otherwise the same. Although difficult to see in the images, there appears to be a rotation of a feature in Test 8 by approximately  $45^\circ$  counterclockwise over the  $2 \mu\text{s}$  span of the images shown. In Test 7, there appears to be no rotation of features between the second and third images.

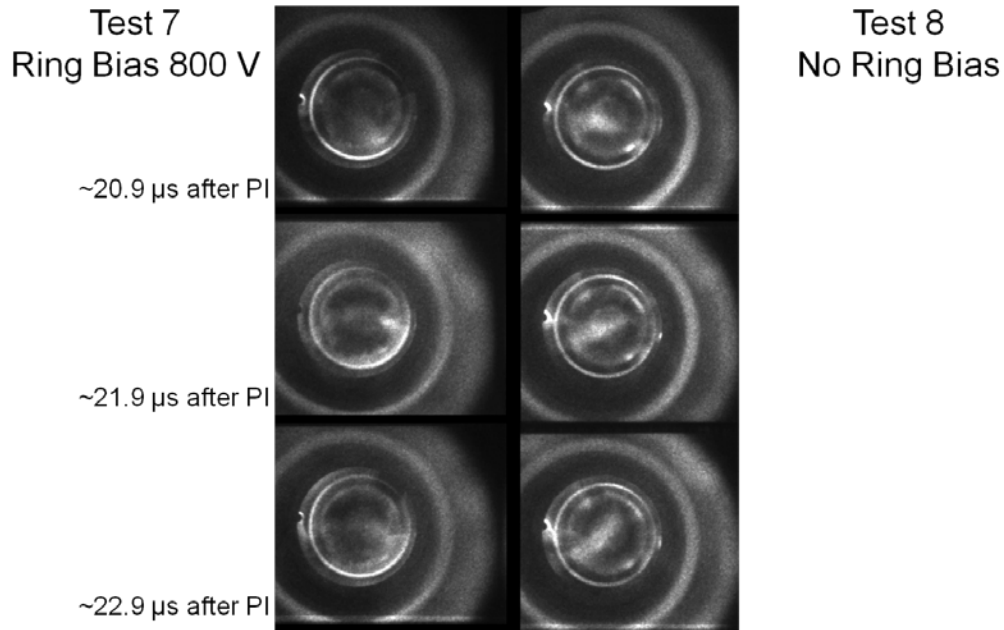


Figure 273. Comparison of fast camera images for shots with and without ring bias

The Ring bank consists of a 1.6-mf capacitor bank and a set of low inductance coaxial cables and SHV feedthroughs to lower the inductance of the previous bank system, as shown in Figure 274. The new ring assembly is shown in Figure 275. Note that based on results from the four-ring configuration that showed that the additional rings were not adding increased effectiveness, we decided to bias only one ring with respect to the upper flange (previously designated as ring 4). The additional ring shown in the figure is a trigger electrode that should enable initiating a ring bank discharge and producing conductive plasma to apply a radial electric field to the FRC in the formation region earlier in time.

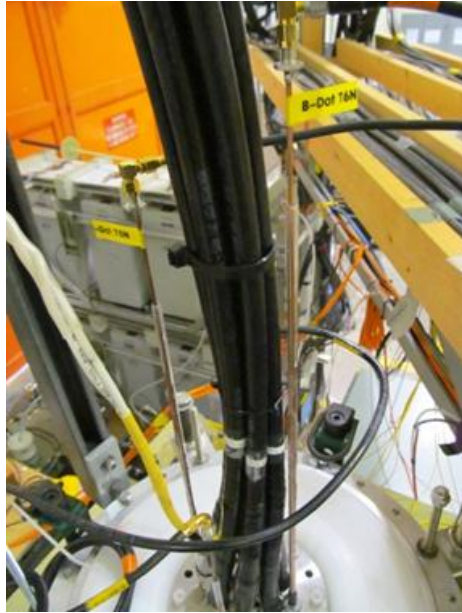


Figure 274. New cables installed to lower inductance of Ring bank system

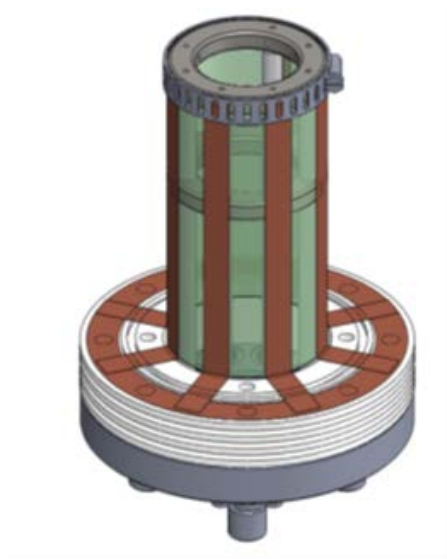


Figure 275. Copper strip shunts shown connected to ring assembly for resonance-inductance measurements

The new version of the Ring bank was installed on FRCHX and the EP ring assembly is presently in vacuum. A rough calculation of the bank inductance has been made based on the manufacturer's specifications of the bank components. A direct measurement of the bank inductance requires shunts (see Figure 275 and Figure 276) to be installed on the experiment side of the bank. Some bench prototyping of the tests has been accomplished.



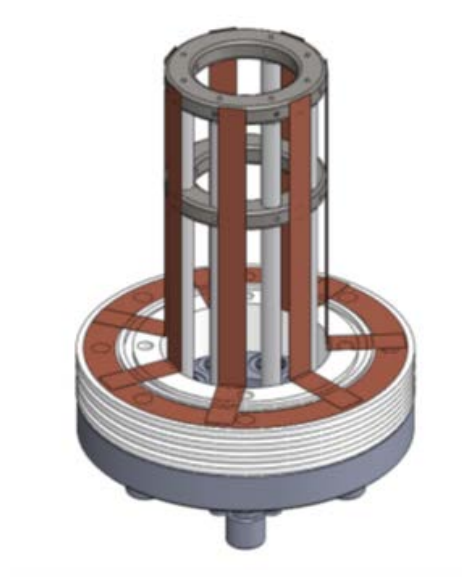


Figure 276. Another view of copper strip shunts

Figure 277 and Figure 278 are photographs of the bench test setup for the Ring bank characterization.



Figure 277. Bench mock simulation of Ring bank capacitance and inductance with 50-W amplifier





Figure 278. Close-up of mock-up bank to characterize resonance for deriving inductance

To lower the inductance of the present Ring Bank system, YK-198 coaxial cable was used. Manufacturer specifications indicate a cable impedance of  $13.6 \Omega$  and a rated inductance of 30.9 nH per foot. There are seven cables connecting to the Ring capacitor bank to the experiment end ring assembly. The average length of the seven cables is 149.5 in. The total inductance per cable is then 4.62 uH, so that the inductance of the set of seven cables in parallel is 660 nH. The Ring bank capacitance is 1.6 mf. The calculated resonant frequency of the bank capacitance with the inductance of the cables and the bank capacitance is  $f = 1/2\pi\sqrt{LC} = 4898 \text{ Hz}$ .

## 4.0 RESULTS AND DISCUSSION

### 4.1 Shiva Star Compression Tests

In this section, we show results of diagnostic measurements for the last two full-energy liner compression tests with the Shiva Star fast capacitor bank. The primary diagnostics that provided useful data were Shiva Star current monitors and x-ray radiography.

#### 4.1.1 FRCHX-2

An interesting plot overlay to see is that of the Shiva discharge currents, as measured by the sum of the arm Rogowski coils, the common-mode noise-corrected CW/CCW data, and the B-dot probes. Typically, the sum of the six arm Rogowski coil currents is about 7% less than the current measured by the Faraday rotation probe, which is usually taken as a more accurate diagnostic. Because no Faraday rotation current data is available for this shot, the sum of the arm currents was rescaled in amplitude by 1.07 and used as the benchmark to which the other current data is scaled. The corrected CW/CCW data set was therefore scaled by 0.94, and the data set from the three B-dot probes was rescaled in amplitude by 0.90, 0.90, and 0.85, respectively. Figure 279 shows how this procedure gives the plot overlay, all scaled to  $1.07 \times I_{\text{sum}}$ .

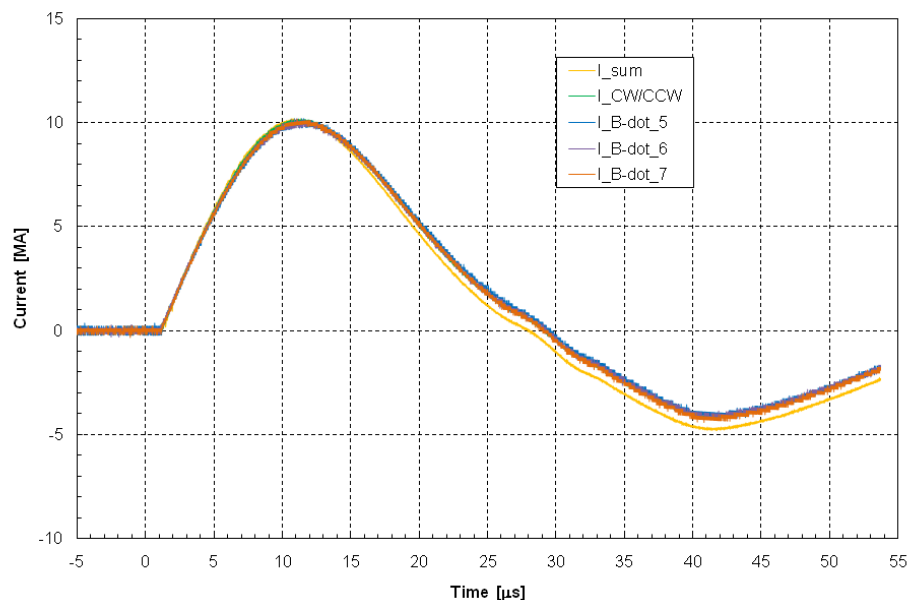
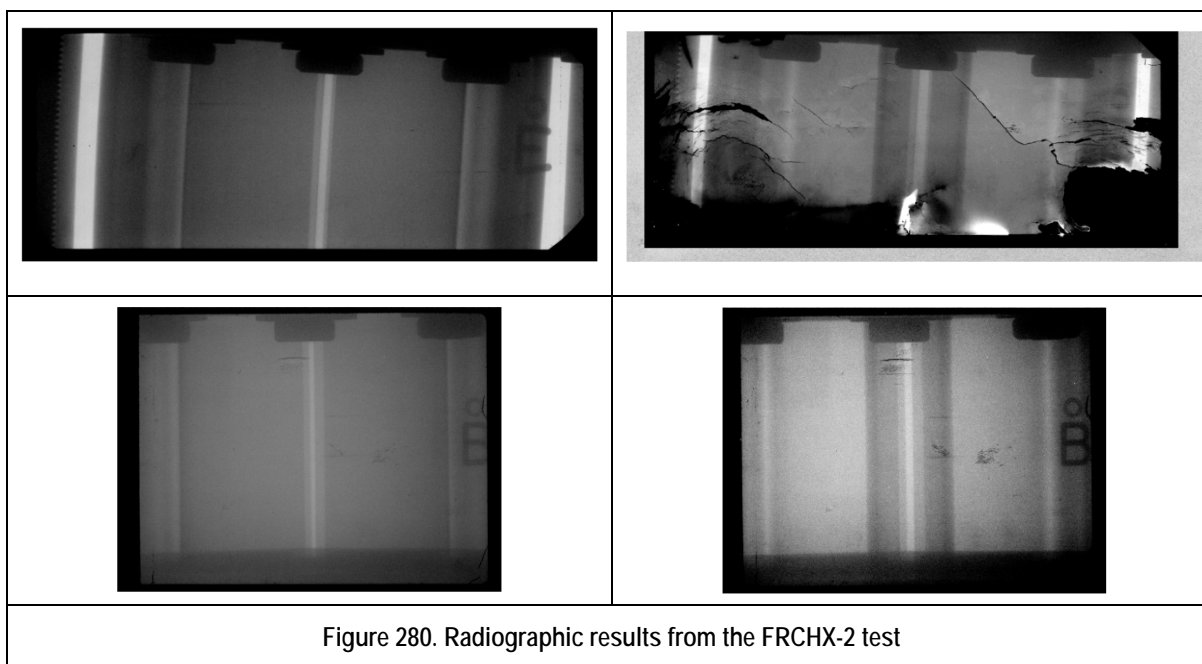


Figure 279. Overlay of arm Rogowski currents, load Rogowski currents, and upper return conductor B-dot probes signals

At approximately 10.640  $\mu\text{s}$  (the time of peak current as measured by the sum of the arm Rogowski coils) the currents are as follows:  $I_{\text{sum}}$  (1.00x scale) = 9.54 MA.  $I_{\text{sum}}$  (1.07x scale) = 10.21 MA,  $I_{\text{CW/CCW}}$  (0.94x scale) = 10.07 MA,  $I_{\text{B-dot5}}$  (0.90x scale) = 9.69 MA,  $I_{\text{B-dot6}}$  (0.90x scale) = 10.02 MA, and  $I_{\text{B-dot7}}$  (0.85x scale) = 9.89 MA.

In Figure 280, we show radiographic results for the FRCHX-2 liner shot. The top left image is the setup for the early dynamic radiograph. The top right image is the dynamic early radiograph at 21.813  $\mu\text{s}$  after the start of the liner implosion discharge. The bottom left image is the setup for the later dynamic radiograph. The bottom right image is the dynamic later radiograph, recorded at 22.797  $\mu\text{s}$  after start of liner implosion discharge. The liner outer diameter is 10 cm in the setup images. The liner outer diameters from the dynamic radiographs are 3.15 cm and 3.73 cm for the early and late radiographs, respectively.



We compare the liner OD dynamic data with an MHD simulation for the test in Figure 281. Also shown on the graph is the calculated magnetic field internal to the liner from the simulation. These simulations are highly accurate, as evidenced by the data points lying right on the radius curves. An overlay of the calculated Shiva Star current and the experimentally recorded current

is also in excellent agreement. From the calculation, the inferred peak magnetic field inside the liner at peak compression is in excess of 500 T.

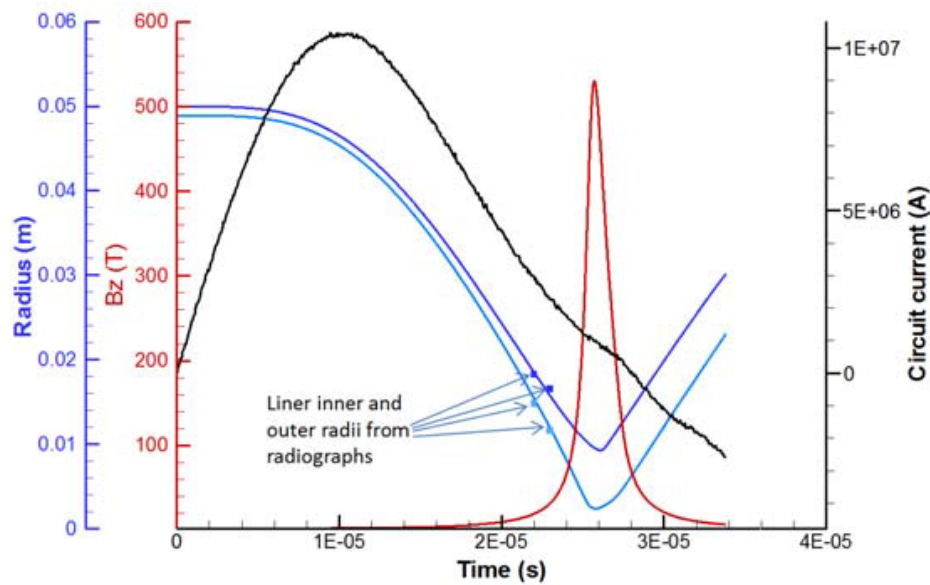


Figure 281. Results of a MACH2 MHD simulation for FRCHX-2, with radiographic data superimposed

#### 4.1.2 FRCHX-3

We show in Figure 282, an overlay of the various current diagnostic data from the FRCHX-3 fully integrated Shiva Star plasma compression experiment. The agreement is excellent, particularly over the first quarter cycle, and a peak current of nearly 11 MA was recorded.

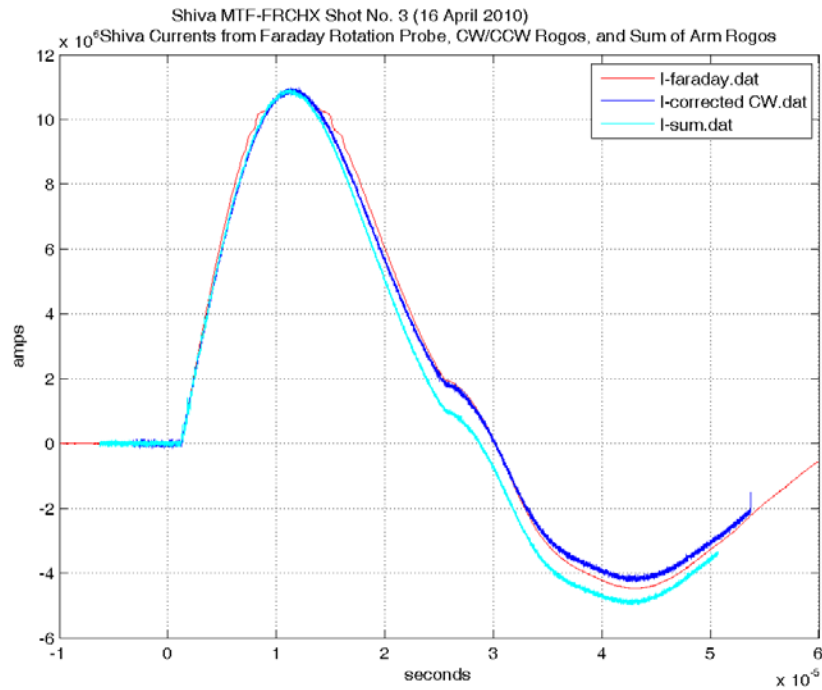


Figure 282. FRCHX-3 current diagnostics overlay

The static and dynamic images from the X-ray # 2 imaging system on FRCHX-3 are shown in Figure 283 and Figure 284, respectively. The shot imploding liner diameter measures 2.4 cm OD and 0.9 cm ID at an imaging time of 22.985  $\mu\text{s}$  with respect to the start of Shiva Star discharge current, indicating excellent liner compression.

Shiva MTF-FRCHX Shot No. 3 (16 April 2010)  
Radiography Imaging Unit No. 2  
Static Image

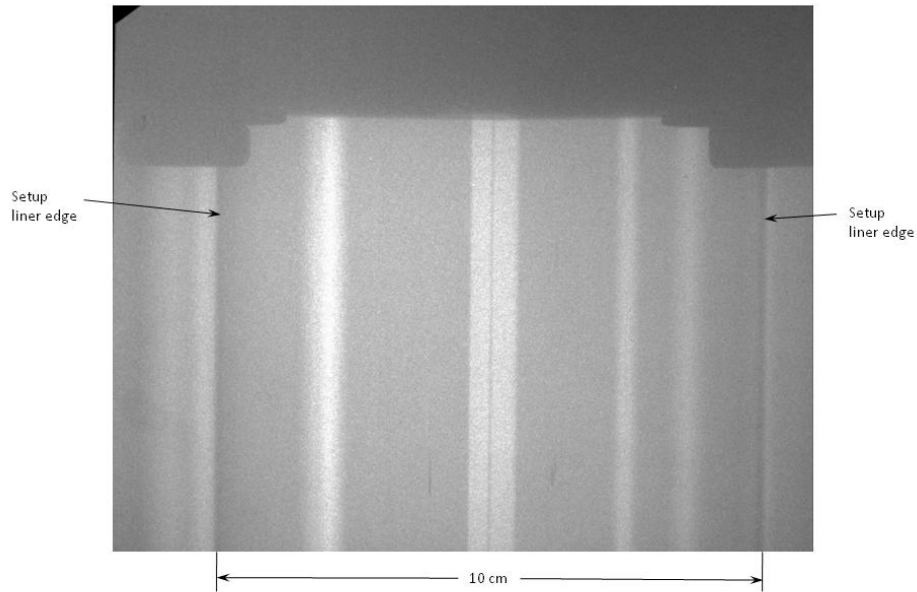


Figure 283. Radiography #2 static image

Shiva MTF-FRCHX Shot No. 3 (16 April 2010)  
Radiography Imaging Unit No. 2  
Shot image @  $t = 22.985 \mu\text{s}$  w.r.t. start of Shiva current

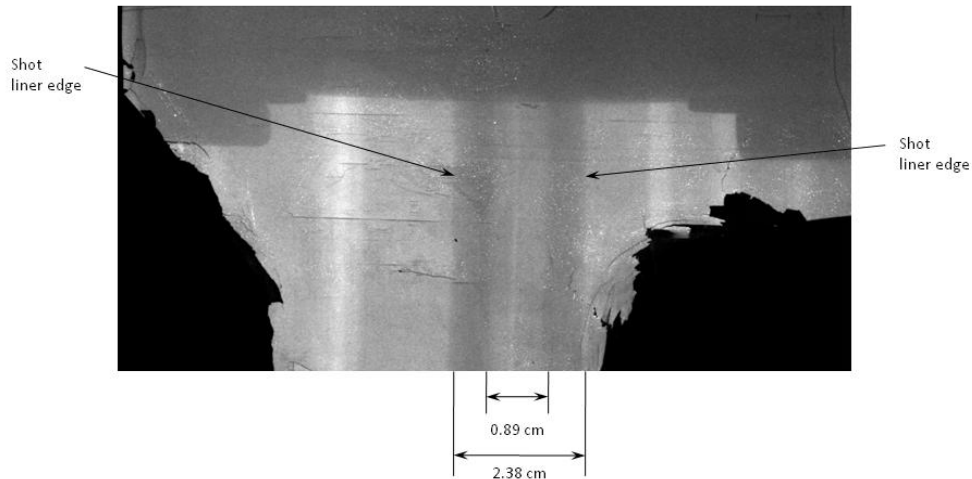


Figure 284. Radiography #2 dynamic image at  $22.985 \mu\text{s}$

## 4.2 Plasma System Development

In this Section, we show representative results from the plasma system development described in Section 3.2. Testing was nearly continuous over the contract, and the results were used to

maximize plasma lifetime, as well as characterize the plasma. It also provided an opportunity to study the effects of the various changes we made to the system. Figure 285 shows the result of one of the many field-mapping studies we did. In the figure, the “up” physical direction is to the left, as indicated by the layout drawing at the bottom of the figure. Note that the Mirror coils are located at the top and bottom of the liner. One can see a very distinct magnetic well formed by the coils, which were designed and placed based on transient diffusion calculations. The Guide coils are located between the liner/trapping region and the formation region, and they are powered in series with the Mirror coils. The Bias bank discharges into the segmented Theta coil in the formation region. The lower Cusp coil is located below segment A of the Theta coil, and it forces the reverse-direction Bias field lines to radially exit the system sharply. The fields were measured using large-area B-dot probes on axis; data set shown were taken at 6.1 ms after beginning the Guide/Mirror bank discharge, at a time when the fields were near maximum inside the liner. Such measurements tell us that we have a good axial field profile for FRC formation, translation, and trapping. They were used in MACH2 MHD simulations of the experiment.

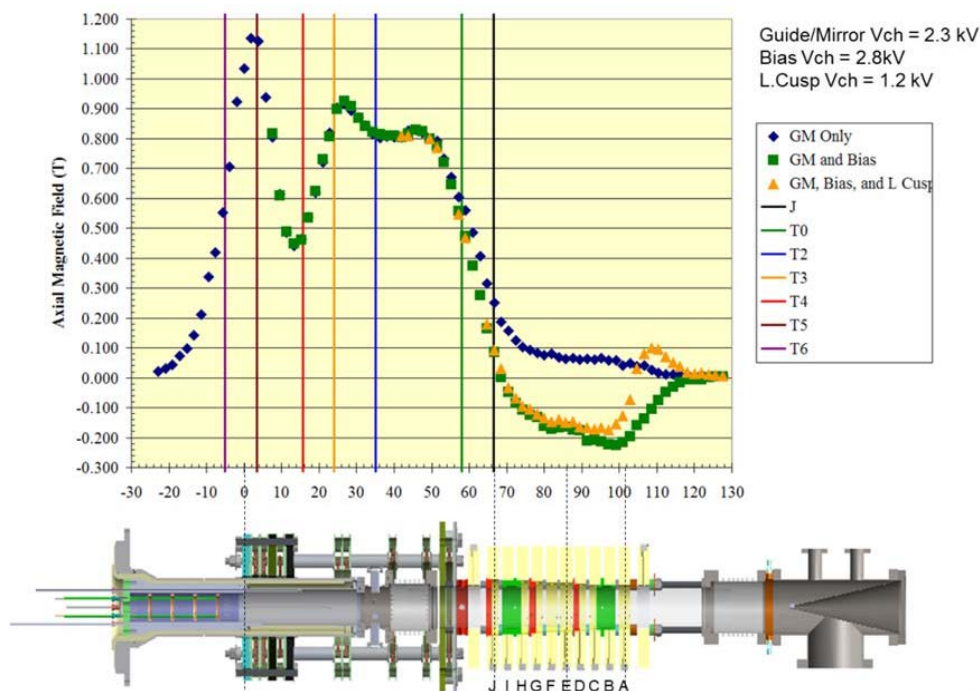


Figure 285. Field-mapping results for various combinations of coil bank discharges

Figure 286 shows the results, in terms of plasma electron density as measured by our multi-chord HeNe laser interferometer, of employing the LPRF pre-preionization system and the HPRF system in experiments conducted in February and March of 2012. One can see a fairly dramatic increase in density for the HPRF PPI source (shot 03\_06\_2012\_t04) in the trapping region at measurement location T4, compared to the two LPRF PPI shots on 02/14/2012 and the shot on 02/10/2012 without RF. Thus, we have shown that using at least our HPRF system can increase plasma density.

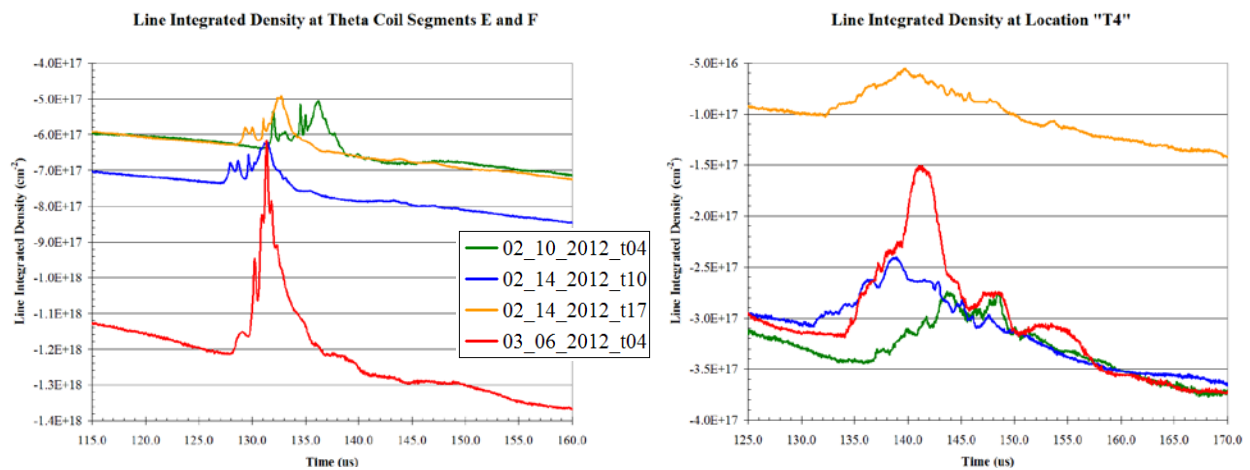


Figure 286. Electron density measurements with and without RF PPI

In Figure 287, we show the experiment configuration, with locations of magnetic coils, several diagnostics, and EP ring assembly, for reference. Note that the upper interferometer chordal probes are at the “T4” location, near the mid-plane of the liner. B-dot probes are also located here, as well as at several other locations from the formation region to above the liner.



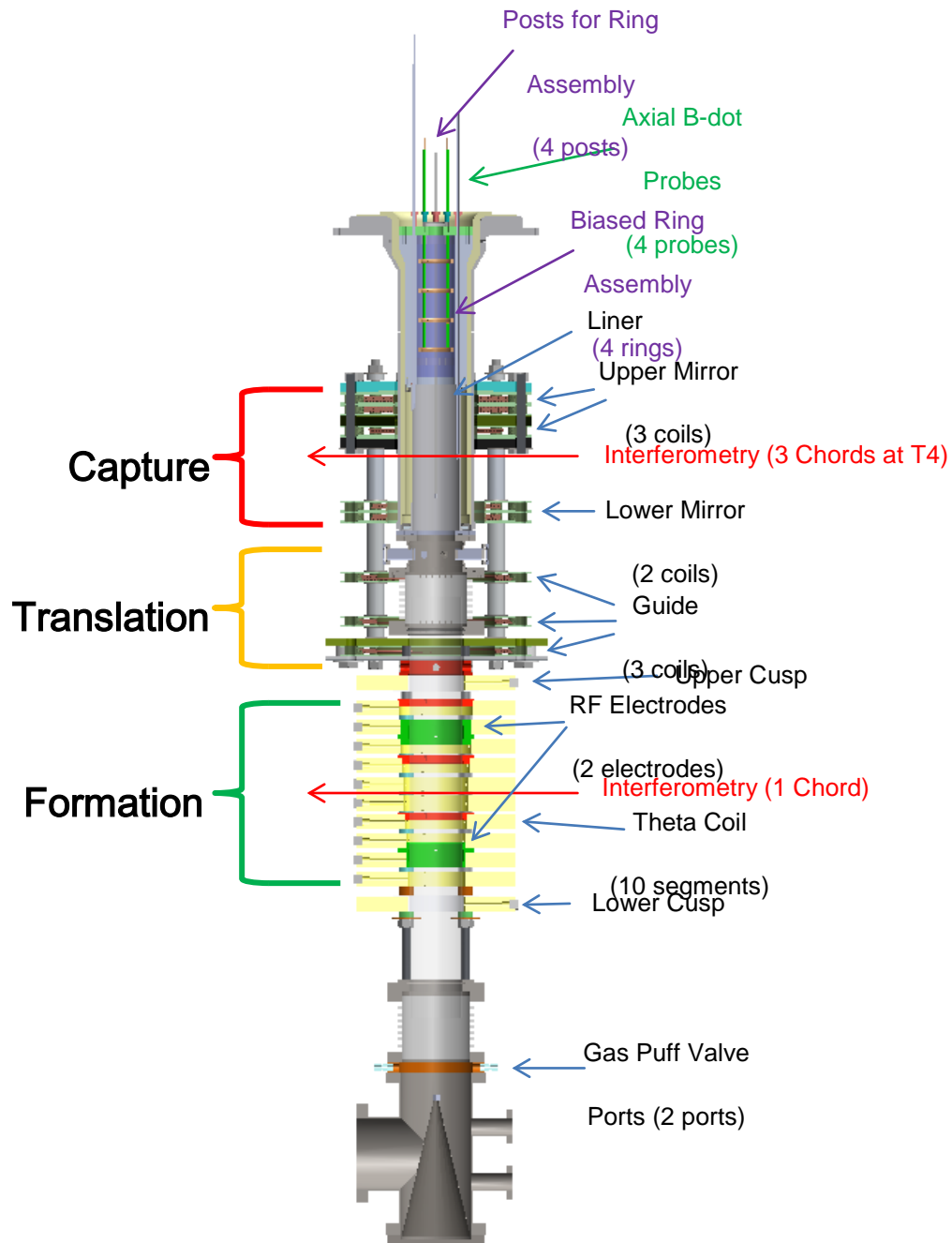


Figure 287. FRCHX configuration

In determining FRC plasma lifetime, we rely primarily on B-dot measurements and flux exclusion radius measurements at the T4 location (mid-plane of the liner). For example, we

show, in Figure 288, a comparison of T4 B-dot signals for a series of shots with lower voltage (60-KV main bank) discharges for various preionization (PI) to Main delays. Note that the nominal delay time of 3.3  $\mu$ s corresponds to  $\frac{3}{4}$  of one PI discharge cycle. For these shots the PI bank was charged to 49 KV, Bias bank was charged to 4.2 KV, Lower Cusp bank was charged to 1.8 KV, and Guide/Mirror bank was charged to 3.3 KV. The deuterium was puffed in from a 40-psi plenum, and there was no RF pre-preionization. A comparison of the two shots with either 3.3- $\mu$ s or 3.5- $\mu$ s delay shows relatively poor reproducibility, but we note that our time-gated spectrograph showed evidence of high oxygen impurity levels for all of the shots except the light blue (largest half-width) trace.

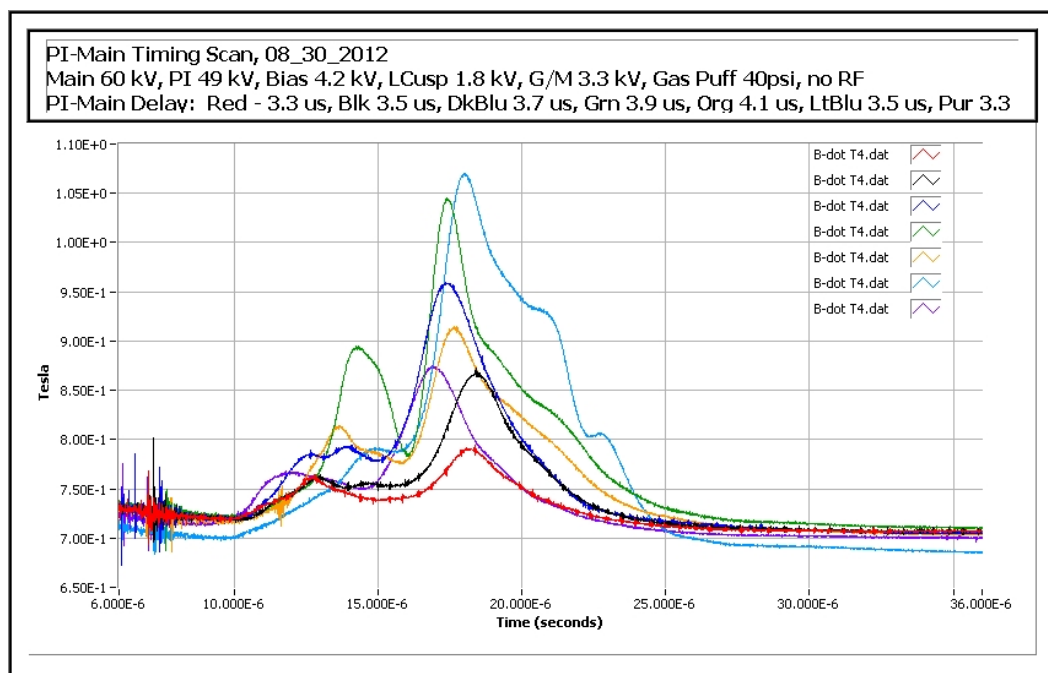


Figure 288. Comparison of T4 B-dot signals for various PI-Main delays for low-voltage operation

For a corresponding delay scan at full voltage (70 KV Main), there was more consistency, as shown in Figure 289. For these shots, the PI bank was charged to 57 KV, Bias bank to 4.9 KV, Lower Cusp bank to 2.1 KV, and Guide/Mirror bank to 3.8 KV. The gas puffing was done in the same manner as the low-voltage scan, and there was no RF PPI. For both scans there was no EP ring bias voltage. In the high-voltage scan, best T4 B-dot signal was observed for a 3.5- $\mu$ s delay, as for the low-voltage scan.

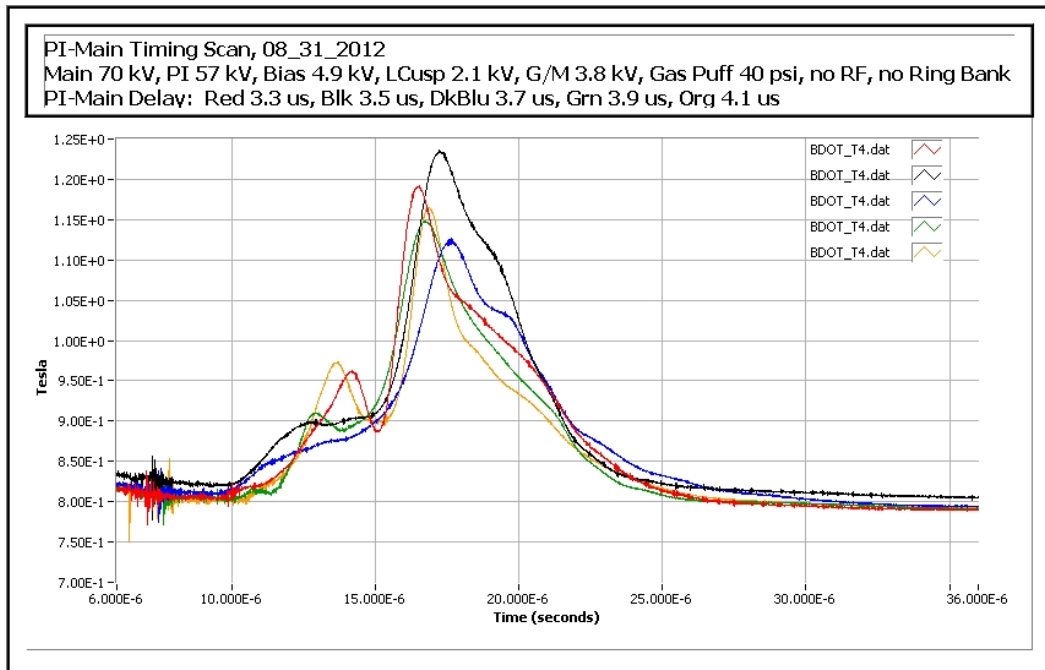


Figure 289. Comparison of T4 B-dot signals for various PI-Main delays for full-voltage operation

At the suggestion of G. Wurden (LANL), we tried longer PI-Main delays corresponding to later cycles of the PI discharge. Some of the data are shown in Figure 290. One can see that by delaying Main bank discharge until the second cycle of the PI bank discharge, we obtained a 1-3  $\mu$ s increase in T4 B-dot FWHM. Shot parameters were essentially the same as for Figure 288 and Figure 289.

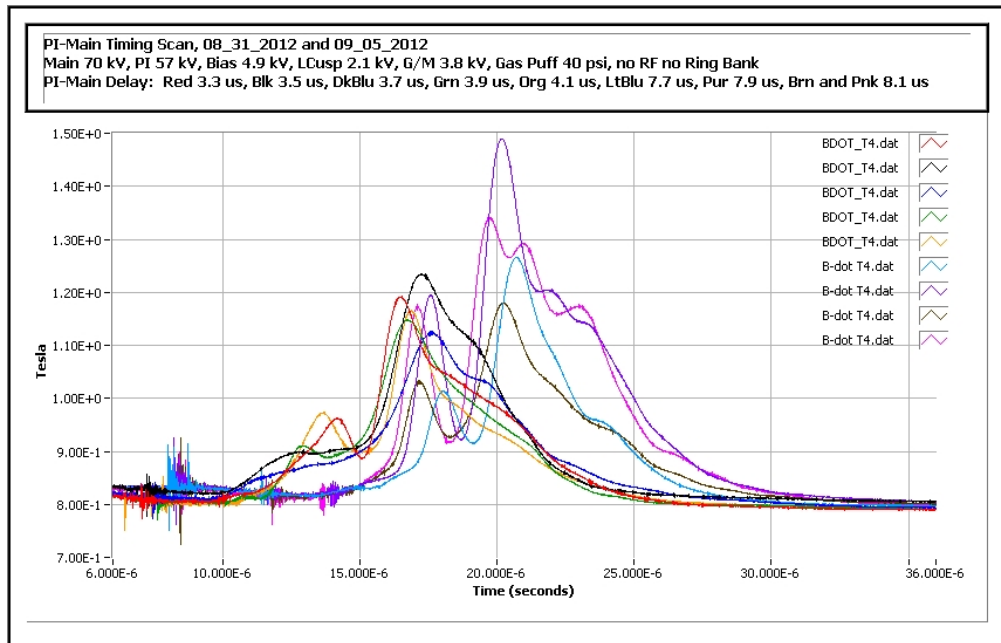


Figure 290. Comparison of first-cycle and second-cycle PI bank delays

In Figure 291, we show further data with Main bank triggered during the second PI cycle. Also shown in the figure is a shot with 50-mTorr static gas prefill. The fact that it had a greater FWHM than the gas puff shots suggested that our gas puff was not optimal.

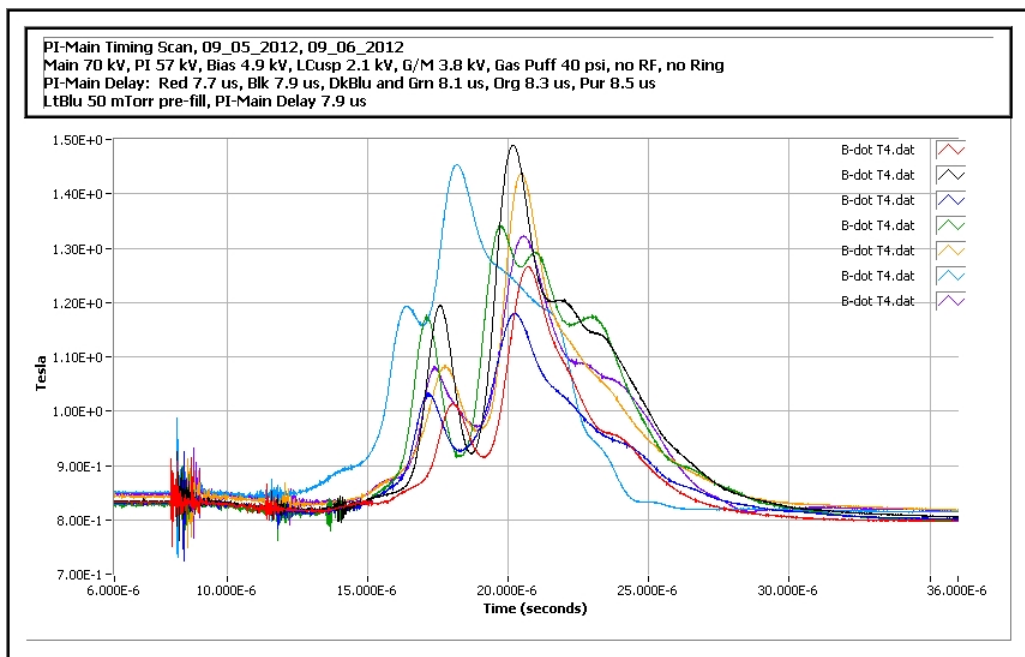


Figure 291. Comparison of second-cycle PI bank delays with gas puff and 50-mTorr static fill

When we compared data from shots with identical parameters from late August to early September, the later shots showed improvement, as shown in Figure 292. This caused us to speculate that the improvement could be due to vacuum vessel conditioning after being at atmosphere.

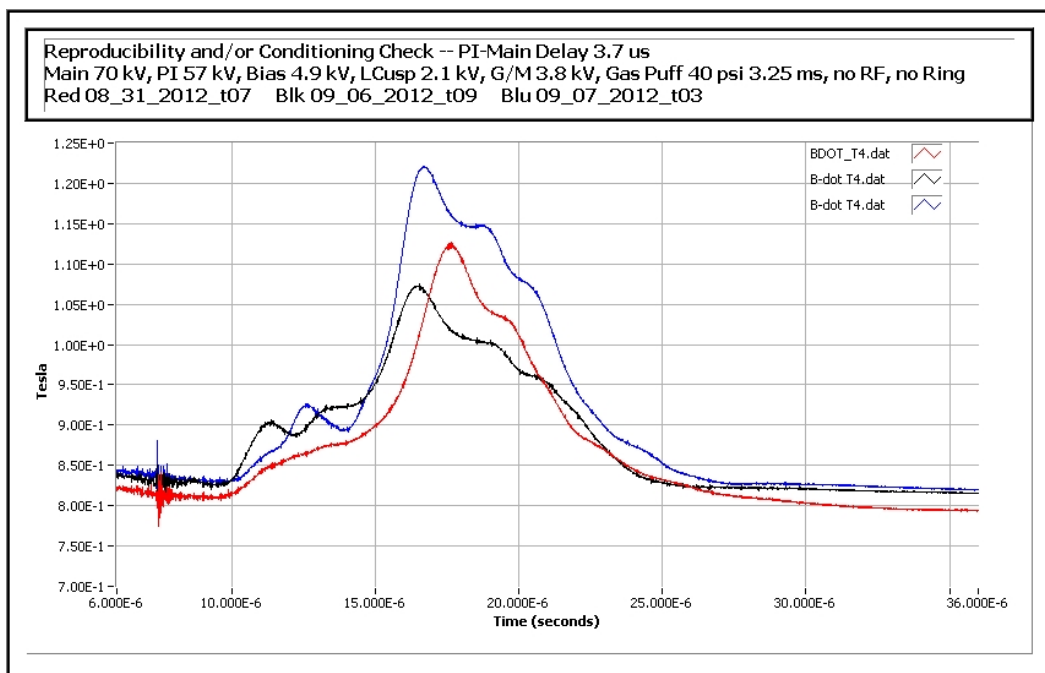


Figure 292. Comparison of data over conditioning of vacuum vessel

Because of the better performance of the static gas prefill of Figure 291, we performed a scan of gas puff delay to PI bank discharge time. These data are shown in Figure 293. For these shots, the PI-Main delay was kept constant at 3.7  $\mu$ s, and other shot parameters were the same as for previous shots. Largest FWHM of the T4 B-dot signals was seen for delays of 2.75 ms and 3.75 ms. We do not know why the intermediate delay of 3.50 ms was not as good.

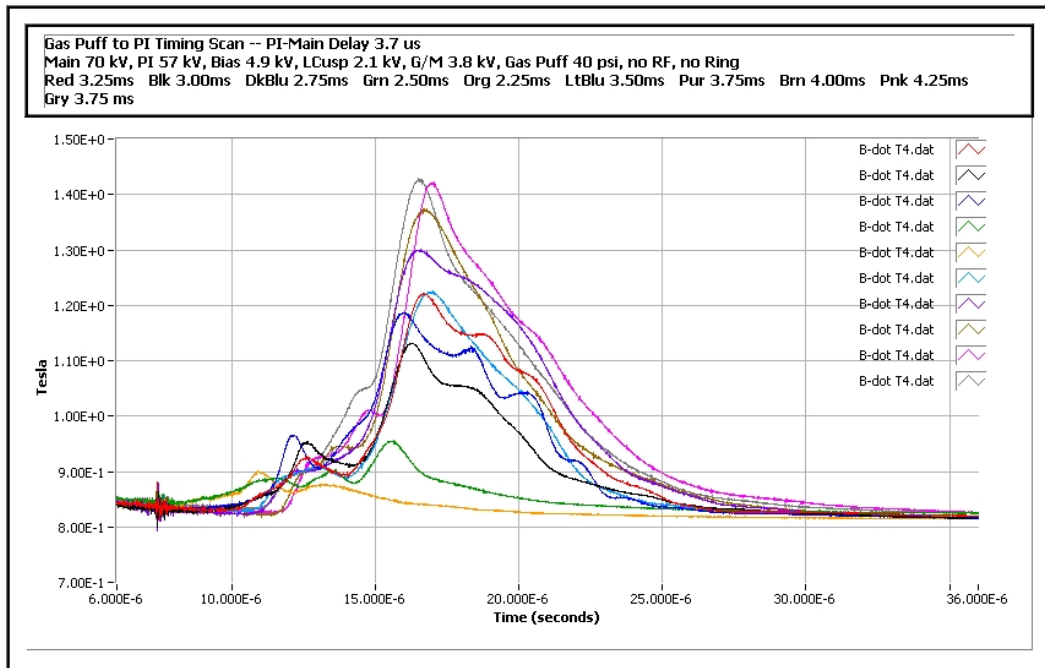


Figure 293. Comparison of different gas-puff-to-PI delays

We then repeated a partial scan of PI-Main delays with a puff-PI delay of 3.75 ms. These data are shown in Figure 294, and one can see general improvement in T4 B-dot FWHM.

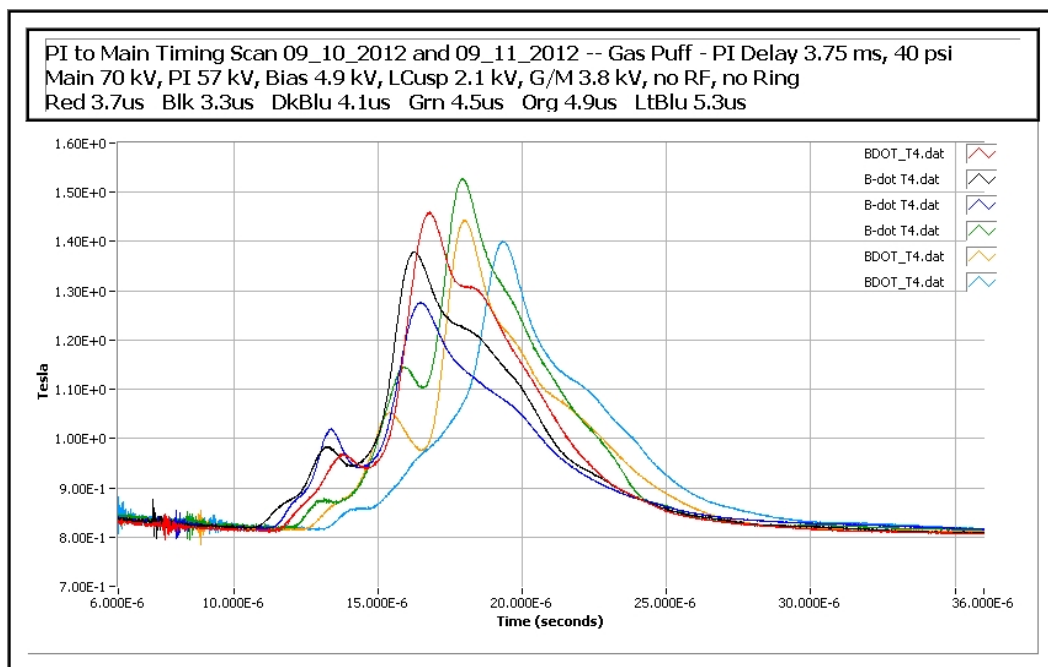


Figure 294. Comparison of PI-Main delays for 3.75-ms puff-PI delay

We also looked at the effect of delaying Main bank discharge, not only to the second cycle of the PI discharge, but to even later times corresponding to the third and fourth cycles. This data are shown in Figure 295 for B-dot signals at T4 and Figure 296 for corresponding flux exclusion radius measurements. The flux exclusion radius measurements were made from plasma-only data (i.e., no vacuum B-dot data). The FWHM of the flux exclusion radius measurements were typically 8-10  $\mu$ s.

Finally, we repeated the scans of PI-Main delays with puff-PI delay of 3.75 ms, but with low-power (1 KW) 10-ms-long RF pulse preceding PI discharge to approximately 20  $\mu$ s after PI discharge. A comparison to T4 B-dot data to the cases without low-power RF showed no discernible increase in plasma lifetime. We will perform analogous tests with high-power transient RF in the near future. When those tests are concluded, we will add the reconfigured EP ring rotation control. We do note that the results obtained above, without PPI and EP ring bias are comparable to results obtained earlier in the year with RF PPI and EP ring bias.

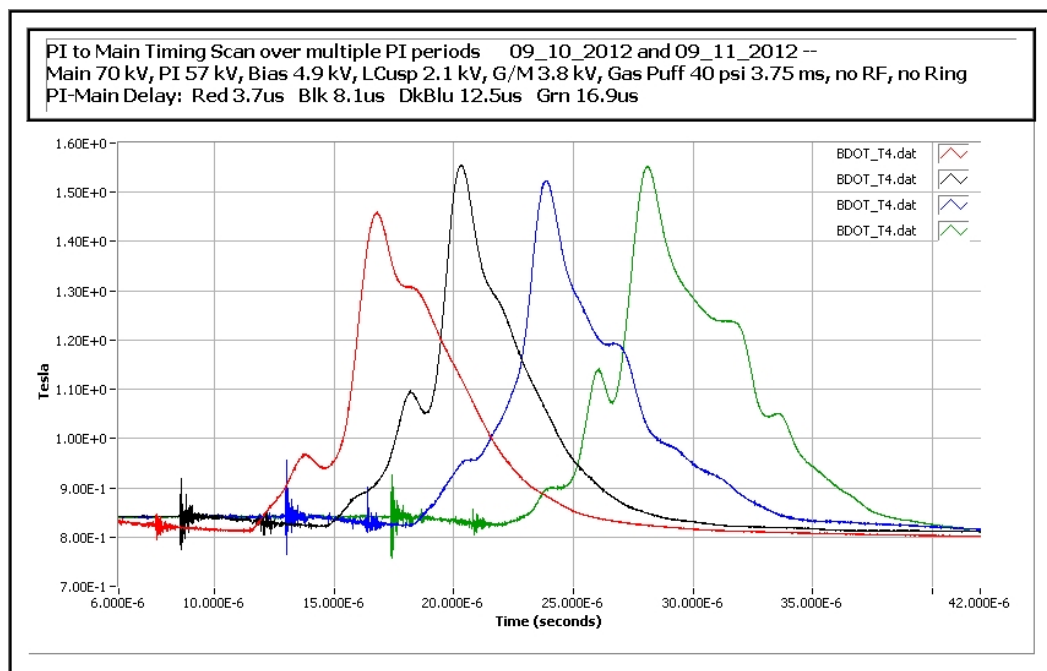


Figure 295. T4 B-dot data for multiple-cycle delays of PI to Main discharge

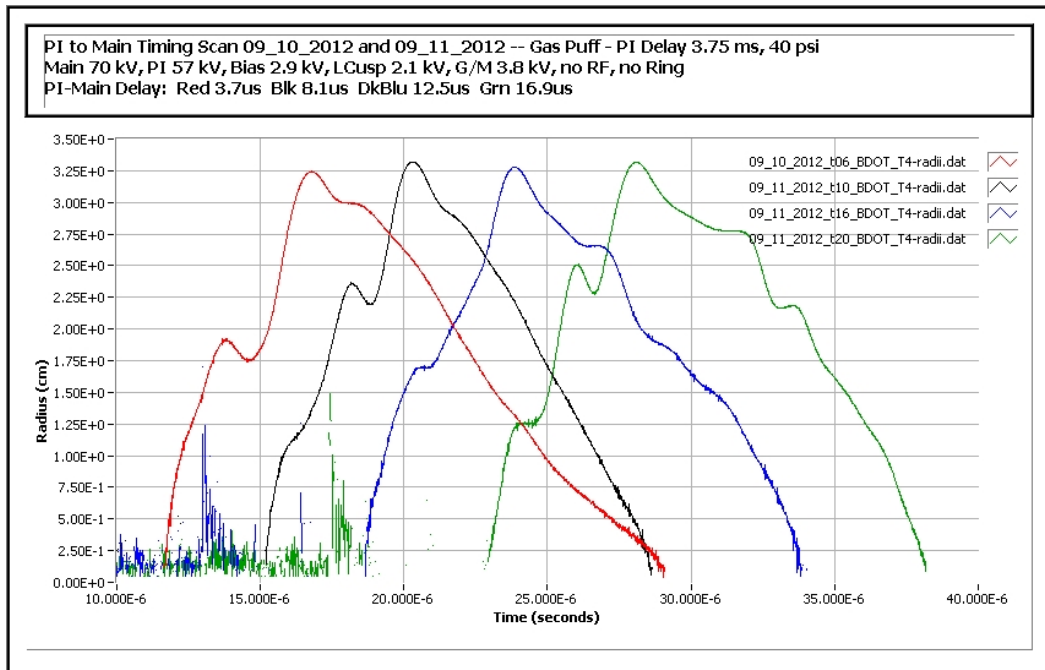


Figure 296. Excluded flux radius for the data of Figure 295

Experimentally, in the fall of 2012, as the use of the RF “pre-pre-ionization” systems, Biased Rings for FRC rotation control, and optimized gas-puff and bank timing parameters were explored in detail on FRCHX, FRC lifetimes (measured from approximately 2  $\mu$ s after Main theta discharge bank trigger when we estimate FRC formation to be essentially complete) were observed to be *typically between 14 and 17  $\mu$ s*, though in some cases *as much as 18 ~ 19  $\mu$ s* was measured. These values are *up by 21 ~ 36%* when compared with the lifetimes of *11 ~ 14  $\mu$ s* that were observed back in February 2012 and in earlier years. These lifetimes are still not quite long enough, however, to accommodate the 25- $\mu$ s time required for the solid liner implosion.



## 5.0 CONCLUSIONS

Based on the work described in Section 3 and the representative results shown in Section 4, we can conclude the following:

- We have been able to design, fabricate, and test successfully integrated and complex pulsed power systems for generating FRC plasmas.
- We have been able to integrate the plasma pulsed power systems with the Shiva Star pulsed power systems and operate them in an integrated fashion.
- We have been able to design a magnetic-flux compression experiment that produced a peak magnetic field in excess of 500 T.
- We have been able to perform dynamic diffusion calculations that allowed us to design and implement multiple sets of field coils to produce near-optimal magnetic field profiles for FRCHX.
- We have been able to reliably form, translate, and capture FRC plasmas.
- We have been able to create FRCs from dynamic (puffed) gas injection, as well as from static gas prefills.
- The puffed gas operation has allowed us to use electrically biased rings to affect the rotation of our FRCs, which is required to suppress growth of the  $n=2$  rotational instability.
- We have developed two types of RF electric field pre-ionization for FRCHX – a long-pulse (up to 10 ms), 1-kW system (LPRF), and a 20-MW transient (100 ns) high-power system (HPRF) – which operate at frequencies of 20–50 MHz.

The judicious use of the HPRF system has produced higher-density FRCs than what was produced without it.

We have performed a crossed-field ionization analysis that suggests means of improving the amount of poloidal magnetic flux entrained in FRCs produced by reversed-field theta discharges.

The FRC plasmas we have produced have pre-compression properties that are sufficient for compression to fusion conditions, with the exception of plasma lifetime (approximately 5  $\mu$ s too short for the 25-  $\mu$ s time required for Shiva-Star-driven liner implosions). However, the ability to trap more initial flux and control rotation should lead to longer-lived FRCs more suitable for liner compression.

## 6.0 RECOMMENDATIONS

Based on the work described in this report, we can make several recommendations for further work. Because the plasma lifetime that has been achieved (nearly 20  $\mu\text{s}$ ) is so close to what is required for liner compression by Shiva Star (25  $\mu\text{s}$ ), we recommend that work continue using the most promising techniques studied during this work. In particular, we believe that continued effort to enhance early-time ionization via high-power pre-ionization be continued.

In addition, the use of biased rings to control plasma rotation should be continued and further optimized. If the FRC trapped flux is great enough to extend the lifetime, as predicted by MACH2 MHD simulations, then it is quite possible that development of the  $n=2$  rotational instability will limit the plasma lifetime. Moreover, if the FRC is rotating when it is compressed, conservation of angular momentum dictates that the amount of compression for a given liner energy will be reduced compared to the case of no rotation.

There are two new approaches that we also advocate for potentially increasing the plasma lifetime. The first is the use of a coaxial plasma gun on axis to effectively bias the FRC and its surrounding space. Such a technique has been employed by Tri Alpha Energy Corporation, and, as a result, they have increased the lifetime of their FRC plasmas by a factor of three over what had been achieved before using the gun. Admittedly, their plasmas are larger and lower density than our FRCHX FRCs, and they are created, not by reversed field theta discharges, but rather by merging counter-streaming spheromaks. However, they were able to show, by the use of the plasma gun, that distortion and centering improved dramatically, and this stabilization is believed to be a major contributor to the increased plasma lifetime. The same should be true for our FRC plasmas.

Second, the crossed-field ionization analyses performed under this contract suggested that simply reversing the polarity of the preionization discharge may lead to significantly increased flux trapping in the FRC during formation due to the reversal of the  $\mathbf{E} \times \mathbf{B}$  drift from outward radially (i.e., into the chamber wall) to inward radially, allowing significant ionization during the first quarter cycle of the discharge. A further potential benefit would be the reduction of plasma

contaminants (in particular, oxygen, carbon, and silicon) due to plasma pile-up at the wall during the first quarter cycle of the discharge.

## 7.0 REFERENCES

1. Bondarenko B D "Role played by O. A. Lavrent'ev in the formulation of the problem and the initiation of research into controlled nuclear fusion in the USSR" *Phys. Usp.* 44, 844 (2001).
2. F. Winterberg, *Z. Naturforsch. A*, 19, 231 (1964).
3. See, for example, R. E. Siemon, I. R. Lindemuth, and K. F. Schoenberg, "Why MTF is a Low Cost Path to Fusion", *Comments Plasma Phys. Controlled Fusion* 18(6), 363 (1999).
4. R. Sherwood and F. L. Ribe, "Fast-Liner-Compression Fusion Systems," *Fusion* 1, Part B, 59-78 (1981).
5. R. Lindemuth, R. C. Kirkpatrick, "Parameter space for magnetized fuel targets in inertial confinement fusion," *Nuclear Fusion* 23(3), (1983).
6. V. N. Mokhov, V. K. Chernyshev, V. B. Yakubov, et al., "On feasibility of controlled thermonuclear fusion problem solution basing on magnetogasdynamical energy cumulation," *Dokl. AN SSSR* 247, 83-86 (1979).
7. J. H. Degnan, et al., "Compression of Plasma to Megabar Range using Imploding Liner," *Phys. Rev. Lett.* 82 (13) 2681-2684 (1999).
8. J. H. Degnan, et al., "Implosion of Solid Liner for Compression of Field Reversed Configuration," *IEEE Trans. Plasma Sci.*, 29 (1) 93-98 (2001).
9. See, for example, P. M. Bellan, *Spheromaks: A Practical Application of Magnetohydrodynamic Dynamos and Plasma Self-Organization*, Imperial College Press (2000).
10. L. C. Steinhauer, et al., "A white paper on FRC development," Redmond Plasma Physics Laboratory, unpublished (1998).
11. See, for example, M. Tuszewski, "Field Reversed Configurations", *Nuc. Fus.* 28(11), 2033-2092 (1988).
12. See, for example, J. H. Degnan et al. "Experimental and Computational Progress on Liner Implosions for Compression of FRCs," *IEEE Trans. Plasma Sci.*, 36(1), 80-91 (Feb 2008).
13. P. M. Barnes, et al., "The parallel operation of low-inductance high-current spark gaps without transit time isolation," *J. Sci. Instrum.* 44, pp 599-605 (1967).
14. E. Bishop, et al. "Low-inductance 100 kV switch (spark gap) for starting, diverting and clamping capacitor discharges," *Proc. Inst. Elec. Eng.* 113, pp 1549-56 (1966).
15. L. M. Smith et al., "A fiber-optic interferometer for in situ measurements of plasma number density in pulsed-power applications," *Rev. Sci. Instrum.* 74, 3324 (2003).

16. S. I. Braginskii, "Transport Processes in a Plasma," Rev. Plasma Phys., Vol. 1 ( Consultants Bureau, New York, 1965), p. 205.
17. J. D. Huba, NRL Plasma Formulary (Naval Research Laboratory, Washington DC, 2009), p. 37.
18. H. R. Griem, Plasma Spectroscopy (Academic Press, New York, 1966).
19. F. F. Chen, Introduction to Plasma Physics and Controlled Fusion (Plenum Press, New York, 1984), ch. 2.
20. E. D. Heylen, "Electrical ionization and breakdown of gases in a crossed magnetic field," IEE Proc., 127, Pt. A, 1980, pp. 221-244.
21. F. F. Chen, Introduction to Plasma Physics and Controlled Fusion (Plenum Press, New York, 1984), ch. 5.
22. S. C. Brown, Introduction to Electrical Breakdown in Gases (John Wiley & Sons, New York, 1966), ch. 2.
23. von Engel, Handbuch der Physik (Springer-Verlag, Berlin, 1956), Vol. 21, p. 504.
24. D. J. Rose, Phys. Rev. 104, 1956, p. 273.
25. R. W. Crompton and D. J. Sutton, Proc. Roy. Soc. A, 215, 1952, p. 467.
26. W. T. Armstrong et. Al., "Field-reversed experiments (FRX) on compact toroids," Phys. Fluids 24, 1981, pp. 2068-2089.
27. M. Tuszewski, "Field reversed configurations," Nucl. Fusion 28, 1988, pp. 2033-2092.
28. L. C. Steinhauer, "Plasma rotation in reversed-field theta pinches," Phys. Fluids 24, pp. 328-338, 1981.
29. L. Steinhauer, "Equilibrium rotation in field-reversed configurations," Phys. Plasmas 15, 012505,(2008).

## 8.0 ABBREVIATIONS

Term	Definition
1D	One-Dimensional
2D	Two-Dimensional
A	Amperes
AC	Alternating Current
AFB	Air Force Base
AFRL	Air Force Research Laboratory
AH	Ampere-Hours
Al	Aluminum
Ar	Argon
B	Magnetic Flux Density
BB	Blackbody
CB	Crowbar
CCD	Charge Coupled Device
CCW	Counter Clockwise
cFP	Compact Field Point
Cgs	Centimeter-Gram-Second
cm	Centimeters
CMN	Common-Mode Noise
COTS	Commercial Off The Shelf
CW	Clockwise
CW	Continuous Wave
D	Deuterium Atom or Ion
D <sub>2</sub>	Deuterium Molecule
dB	Decibel
DC	Direct Current
DE	Directed Energy
DEPS	Directed Energy Professional Society
DI	De-Ionized
DoD	Department of Defense

Term	Definition
D-T	Deuterium-Tritium Mixture
E	Electric Field
EMI	Electromagnetic Interference
EP	Equipotential
F	Farad
FCC	Federal Communications Commission
FER	Flux Exclusion Radius
FRC	Field Reversed Configuration
FRCHX	FRC Heating Experiment
FRX-L	Field Reversed Experiment - Liner
ft	Feet
eV	Electron Volts
H	Henries
HDPE	High-Density Polyethylene
HeNe	Helium-Neon
HERA	High Energy Research Applications
HERO	Hazards of Electromagnetic Radiation to Ordnance
HVPS	High Voltage Power Supply
IC	Integrated Circuit
ICF	Inertial Confinement Fusion
ID	Inside Diameter
in	Inches
J	Joules
K	Kelvin
kA	Kiloamperes
KAFB	Kirtland Air Force Base
keV	Kilo Electron Volt
kHz	Kilohertz
km	Kilometer
kN	Kilonewtons
kV	Kilovolt



Term	Definition
kW	Kilowatt
lb	Pounds
LED	Light Emitting Diode
m	Meters
M&S	Modeling and Simulation
MA	Megamperes
MAGO	<i>Magnitnoye Obzhatiye</i> , or Magnetic Compression
MCP	Microchannel Plate
mF	Millifarad
MHD	Magnetohydrodynamic
MHz	Megahertz
MIF	Magneto-Inertial Fusion
mH	Millihenries
mks	Meter-Kilogram-Second
mm	Millimeter
MOSFET	Metal-Oxide-Semiconductor Field-Effect Transistor
ms	Milliseconds
MTF	Magnetized Target Fusion
MTG	Master Trigger Generator
MW	Megawatt
MΩ	Megohms
mΩ	Milliohms
μF	Microfarads
μH	Microhenries
μs	Microseconds
μΩ	Microohms
N	Newtons
nF	Nanofarads
nH	Nanohenries
ND	Neutral Density

Term	Definition
NIR	Near Infrared
nm	Nanometers
ns	Nanoseconds
OD	Outside Diameter
Pa	Pascal
PDR	Preliminary Design Review
PEL	Permissible Exposure Limit
pF	Picofarads
PI	Preionization
PIN	Positive Intrinsic Negative (Detector)
PMT	Photomultiplier Tube
POC	Point of Contact
POP	Period of Performance
PPI	Pre-Preionization
PRS	Phillips Research Site
PS	Power Supply
psi	Pounds per Square Inch
psia	Pounds per Square Inch Absolute
PTA	Planar Trigger Amplifier
PXI	PCI Extension for Instruments
PVC	Polyvinyl Chloride
R&D	Research and Development
RF	Radio Frequency
RPM	Revolutions Per Minute
RTV	Room Temperature Vulcanizing
s	Seconds
scfm	Standard Cubic Feet Per Minute
SCG	Security Classification Guide
SIBR	Small Business Innovative Research
SF <sub>6</sub>	Sulfur Hexafluoride
SWR	Standing Wave Ratio

Term	Definition
T	Tesla (= Webers/m <sup>2</sup> )
TO	Task Order
V	Volts
Vp-p	Peak to Peak Voltage
W	Watts
Wb	Webers
Ω	Ohms

## DISTRIBUTION LIST

DTIC/OCF

8725 John J. Kingman Rd, Suite 0944

Ft. Belvoir, VA 22060-6218

1 cy

AFRL/RVIL

Kirtland AFB, NM 87117-5776

2 cy

Official Record Copy

AFRL/RDHP/James Degnan

1 cy